# II.C Next-Gen Lithium-Ion: Advanced Cathodes R&D

## II.C.1 Enabling High-Energy/Voltage Li-Ion Cells: Electrochemical Analysis and Evaluation (ANL, LBNL, NREL, ORNL)

**Daniel P. Abraham, Principal Investigator**
Argonne National Laboratory
9700 S. Cass Avenue
Lemont, IL 46039
Phone: 630-252-4332
E-mail: abraham@anl.gov

**Peter Faguy, Technology Manager**
U.S. Department of Energy
Phone: 202-586-1022
E-mail: Peter.Faguy@ee.doe.gov

Start Date: October 1, 2014 End Date: September 30, 2018
Total Project Cost: $4,000,000 DOE share: $4,000,000 Non-DOE share: $0

### Project Introduction

High energy density lithium-ion batteries are needed for transportation applications in order to increase the driving range of vehicles on a single charge. Towards this end, electrochemical cells containing near lithium-stoichiometric, manganese-bearing, nickel-rich layered oxides ($Li_{1+x}Ni_aMn_bCo_cO_2$, x typically <0.05) and graphite-bearing negative electrodes are being cycled to higher voltages (> 4.35 V) as part of the Applied Battery Research (ABR) for Transportation program. Cell lifetimes are, however, affected by these voltages with performance degradation being greater at the higher voltages. The cell electrolyte, typically containing carbonate-based solvents, is a major contributor to this performance loss as it tends to oxidize at the higher voltages leading to the generation of deleterious species that degrade the positive electrode. Hence, the development of electrolyte systems and stable interfaces that mitigate this performance degradation is a priority. This project is intended to "enable" high-energy/high-voltage (HE/HV) cells via new insights and/or understanding, not currently available, of why present materials/systems fail. This chapter deals with electrochemical investigations focused on gaining such insights and understanding; more specifically, studies relating to electrolyte and surface stability including solvents, additives, and surface coatings are presented.

### Objectives

The goals of this project are related to acquiring a deeper, fundamental understanding of the processes that influence the stability of NMC surfaces and the subsequent strategies, such as electrolyte formulations and surface coatings, which are aimed at stabilizing these surfaces under high-voltage operation, and are as follows:

- Identify additives, which when incorporated into the baseline electrolyte consisting of 1.2M LiPF6 in EC:EMC (3:7 w/w), denoted as Gen2, reduces cell degradation
- Provide an understanding of electrolyte-additive mechanisms through experimental and computational techniques
- Investigate fluorinated electrolyte systems with decreased activity at charged cathode surfaces
- Investigate the efficacy of coated surfaces, using various coating methods, under long-term electrochemical cycling

- Report and publish the knowledge gained so as to accelerate the development of high-energy/high-voltage cells that are suitable for vehicular applications

## Approach

The goals listed above will be pursued through the following experimental thrusts:

- Systematic study and evaluation of various ***additive systems*** to include:
  - Previously identified and new additive combinations
  - Electrochemical evaluation under standard project protocols
  - Development of Figure of merit (FOM) metrics for reliable evaluation of systems
  - Mechanistic determination of additive performance
- Investigation of ***fluorinated electrolytes*** and their electrochemical stability including:
  - Various electrolyte formulations
  - Measurements of oxidative stability
  - Characterization of cathode surface stability
- Electrochemical evaluation of ***coated cathode surfaces*** including:
  - NMC cathodes, modified with $Al_2O_3$-based coatings, using various wet-chemical processes
  - $Al_2O_3$-coated, NMC particles and electrodes using atomic layer deposition (ALD)

## Results

*Additive Systems*

In this work, all experiments were conducted using electrodes from ANL's cell fabrication facility (CAMP) with cell assembly and testing following the standard HE/HV protocols (Long et al., JES **163**, A2999, 2017) in a voltage window of 3.0-4.4 V vs. graphite. The additives in this study were chosen to mitigate the known effects of $Li^+$ trapping at graphite SEI layers or impedance growth arising at the cathode. Additives include 2,4,6-trivinylcyclotriboroxane (tVCBO), Prop-1-ene-1,3-sultone (PES), Phenyl boronic acid ethylene glycol ester (PBE), Li-bis(oxalato)borate (LiBOB),Vinylene carbonate (VC), Li-difluoro(oxalate)borate (LiDFOB), Tris(trimethylsilyl) phosphite (TMSPi) and Triethyl phosphite (TEPi). Additives are listed in Figure II-214b (right) according to their reported efficacy at either the anode or cathode.

To compare performance of the various additive compounds Figure of Merit (FOM) values were defined for cell Energy (relates to capacity) and Power (relates to impedance). These FOM values were based on cells containing the baseline (Gen2) electrolyte – for these cells the energy density decreases to 80% of its initial value (713 to 570 $Wh/kg_{oxide}$) after 170 cycles, and the power density decreases to 80% of its initial value (135 to 108 $mW/cm^2$) after 23 cycles. For the additive-bearing cells, the Energy FOM (FOME) is the extrapolated cycle number at which the energy density decreases to 570 $Wh/kg_{oxide}$ and the Power FOM (FOMP) is the extrapolated cycle number at which the power density decreases to 108 $mW/cm^2$; note that the FOM values do not depend on the initial energy and power density values of the additive-bearing cells.

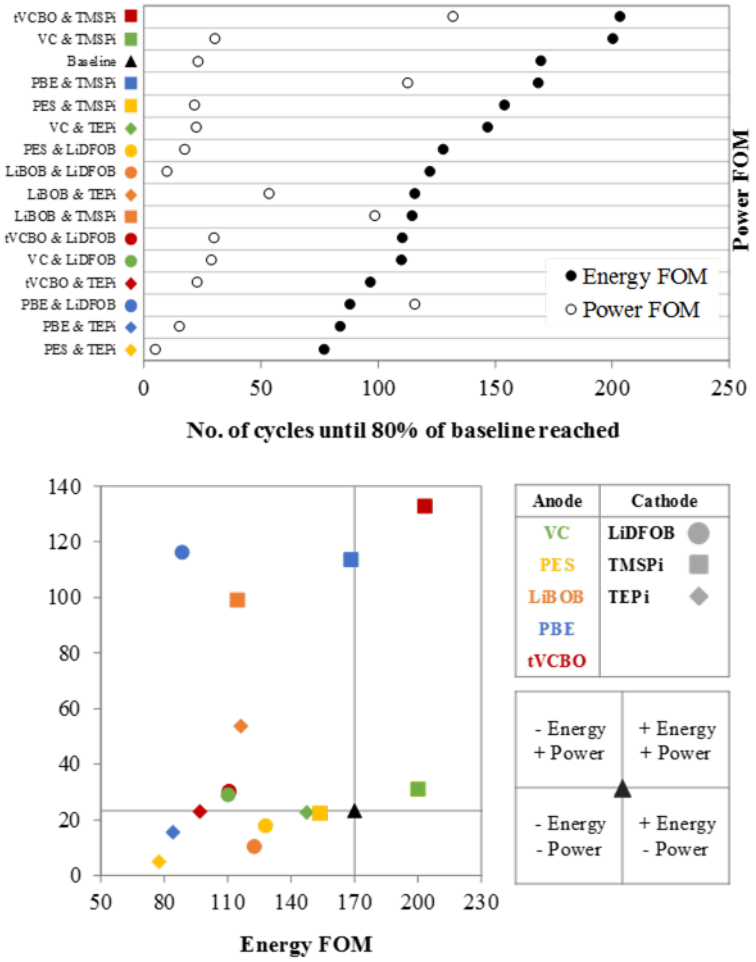


Figure II-214. (Top) FOME and corresponding FOMP values, in descending order, of tested additive combinations. (Bottom) Plot of FOMP vs. FOME for the additive systems tested.

Figure II-214 (left) shows the electrolytes in descending order of FOME and the corresponding FOMP. The plot indicates no obvious correlation and suggests that the mechanisms governing long-term energy performance are relatively independent from those that govern the long-term power performance of the cells.

Figure II-214 (right) shows a plot of FOMP vs. FOME. Here a direct comparison between the baseline system (located at the intersecting lines) and the additive systems can be made, where points in the top-right would indicate improved performance and point in the bottom-left degraded performance. An examination of the data shows that only cells with the 0.25% tVCBO + 1% TMSPi combination would have significantly better long-term energy *and* power retention than the baseline. The data in Figure II-214 represents a large amount of information and it is clear that the approach of combining standardized protocols and FOM values is a powerful approach. This methodology can be used to evaluate new electrolyte systems, optimize electrolyte formulations, and gain insights into the mechanisms of electrolyte behavior. Furthermore is has now been adopted to the study of cathode coatings.

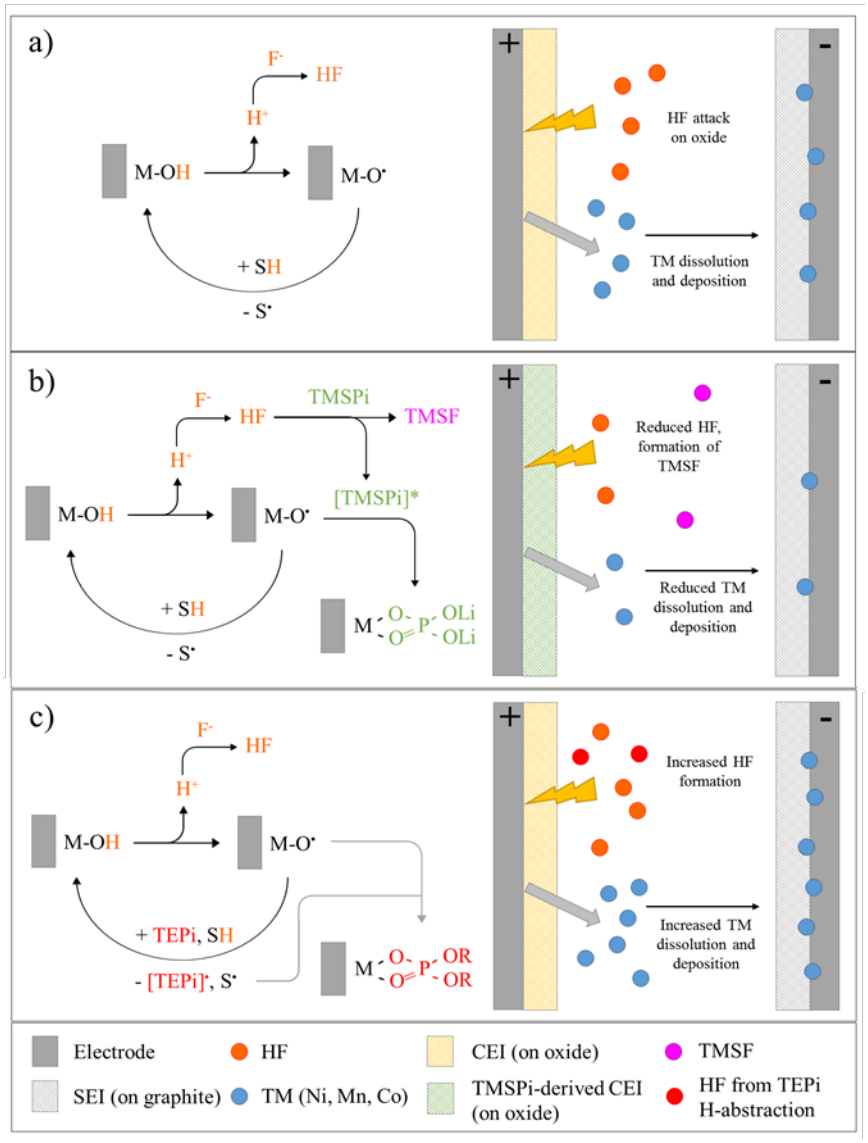


Figure II-215. Schematic depiction of the electrocatalytic cycle for the baseline electrolyte and the role of TMSPi and TEPi on the formation of oxide surface films and TM dissolution.

TMSPi has emerged as a useful electrolyte additive and the data in the FOM plots above indicate that this is an additive of interest. Therefore, TMSPi and the structurally analogous TEPi were further examined. Cycling data revealed lower capacity fade, lower impedance rise, and lower TM deposition on anodes for cells utilizing TMSPi compared to cells with TEPi. Furthermore, X-ray photoelectron spectroscopy (XPS) showed P- and O-rich surface films on the positive electrodes of TMSPi cells. These observations suggest that removal of TMS groups from the central P-O core of the TMSPi additive enables formation of a protective oxide surface film. In contrast, oxidation of the structurally analogous TEPi does not yield a protective positive electrode film, which results in inferior performance.

For baseline cells, the following degradation mechanism is proposed, shown in Figure II-215a. At higher voltages, reactive M-O• radicals abstract hydrogen atoms from solvent molecules generating solvent radicals and transient M-OH species. The abstracted hydrogen can react with fluorine species in the electrolyte to form corrosive acids (e.g., HF) that enhance TM dissolution from the oxide. These dissolved TMs can migrate and

deposit at the negative electrode and accelerate electrolyte reduction and $Li^+$ trapping in the SEI and, therefore, capacity fade.

For TMSPi, it is proposed that the reaction of the TMS groups with HF leads to the formation of trimethylsilyl fluoride (TMSF) and a phosphorus intermediate, [TMSPi*], Figure II-215b. In close proximity to the oxide surface the reactive M-O• species form bonds with the central P atoms of the [TMSPi*], leading to a P- and O-rich surface film, as detected by XPS. For these bonds to form, the scission of at least one TMS group must occur; however, the removal of two or all of the TMS groups from the central P-O moiety, prior to surface film formation, is possible. Quenching of reactive M-O• sites by the phosphorus-bearing film reduces hydrogen abstraction and in turn reduces formation of corrosive species. For TEPi, it is proposed that oxidation of TEPi occurs via hydrogen abstraction from the TEPi alkyl groups, initially generating more HF species compared to the baseline cell (Figure II-215c). Unlike TMSPi, TEPi does not initially form a surface film on the oxide electrode, allowing the M-O• catalytic centers to continue oxidizing solvent molecules and generating corrosive acids. Thus, increasing TM deposition at the negative electrode and accelerating capacity fade.

*Fluorinated Electrolytes*

The use of conventional organic carbonate electrolytes results in instabilities at the cathode/electrolyte interface that contribute to a loss of capacity and a rise in interfacial impedance. One strategy to address these instabilities is through new solvent designs that are more intrinsically stable at charged cathode surfaces. This project has developed a fluorinated, carbonate-based electrolyte and evaluated its electrochemical performance at high voltages in NMC-532//graphite cells (Gr). Preliminary results indicated potential benefits, especially at the cathode/electrolyte interface, relative to the baseline electrolyte (Gen2). However, details of the observed electrochemical properties are not well understood. This work aims to gain insights into the working mechanisms of fluorinated electrolytes when used in NMC//Gr systems cycled to high voltages (≥ 4.4 V).

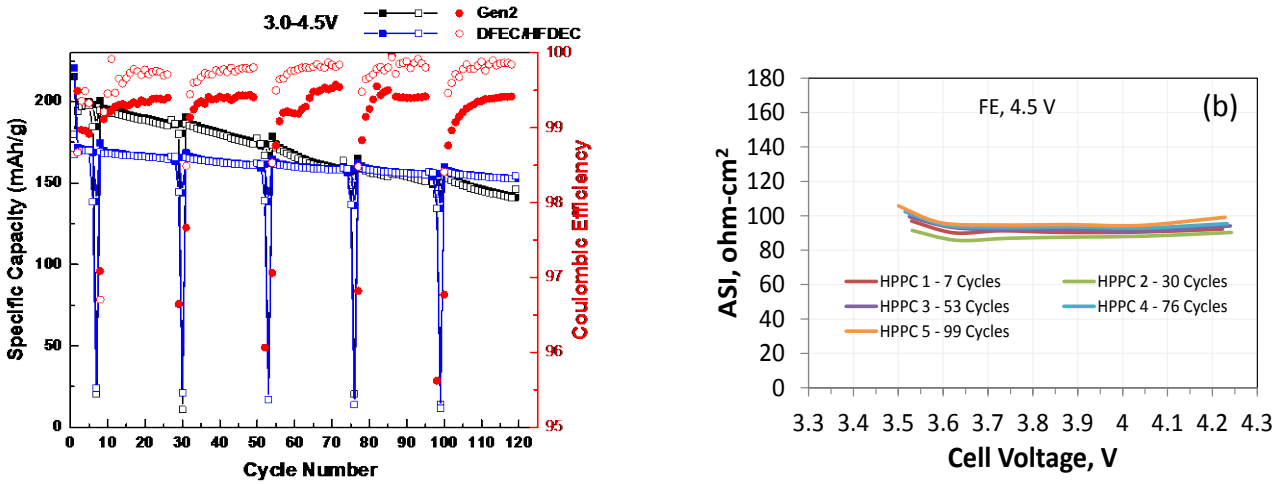


Figure II-216. a) Capacity and coulombic efficiency of NMC-532//Gr cells containing Gen2 and DFEC/HFDEC electrolytes cycled using a 4.5 V upper cutoff. b) ASI as a function of HPPC cycle for the DFEC/HFDEC cell shown in (a).

The fluorinated electrolyte developed in this project maintains the same 3:7 solvent ratio of cyclic carbonate to linear carbonate as the Gen2 formulation. However, EC is substituted with a difluoro cyclic carbonate, 4,5-difluoro ethylene carbonate (DFEC) and the EMC with a hexafluorinated diethyl carbonate, bis (2,2,2-trifluoroethyl) carbonate (HFDEC). The fluorinated formulation has a $LiPF_6$ concentration of 1.0 M and is abbreviated herein as DFEC/HFDEC. Figure II-216a shows capacity vs. cycle number and coulombic efficiency (right axis) for NMC-532//Gr cells containing the Gen2 electrolyte and DFEC/HFDEC electrolyte. The area specific impedance (ASI), as a function of hybrid pulse power characterization (HPPC) cycles, shown as low points in the cycling data of Figure II-216a, is presented in Figure II-216b.Three points of interest are observed. 1) DFEC/HFDEC results in the same first-cycle charge capacity as Gen2 but with lower first-cycle

efficiency, leading to lower initial cycling capacity; 2) the coulombic efficiency for the DFEC/HFDEC cell is significantly higher than the baseline Gen2 cell; 3) the ASI for the DFEC/HFDEC cell is initially higher than the Gen2 cell (~25 Ω•cm$^2$ for Gen2, not shown) but does not increase with cycling. Interestingly, Gen2 cells eventually (~75 cycles) show ASI values higher than those of the DFEC/HFDEC cell shown in Figure II-216b.

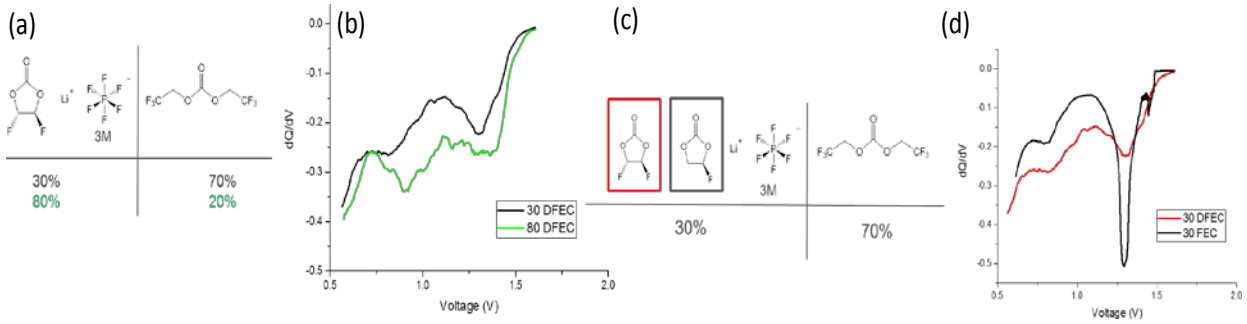


Figure II-217. a) and c) DFEC/HFDEC compositions (%). b) and d) corresponding dQ/dV profiles for each of the fluorinated compositions in Gr//Li cells on the first-cycle lithiation of graphite.

Figure II-217a and Figure II-217b show electrolyte compositions and dQ/dV profiles, respectively, for the first lithiation process of Gr//Li cells. Cells with 80% DFEC (20% HFDEC) showed significantly larger dQ/dV peaks at nearly all potentials relative to cells with 30% DFEC (70% HFDEC). These peaks are all at higher potentials than the dominant electrochemical activity of graphite, and thus are attributed to electrolyte reduction. Figure II-217c and Figure II-217d show that when 30% FEC is substituted for DFEC, there is substantially less reduction occurring below ~1.3 V. These data reveal that reduction of the DFEC component in the DFEC/HFDEC electrolyte is a major contributor the initial capacity loss and poor first-cycle efficiency observed in Figure II-216a. Several tests were also conducted to understand the origin of the high ASI values observed in Figure II-216b.

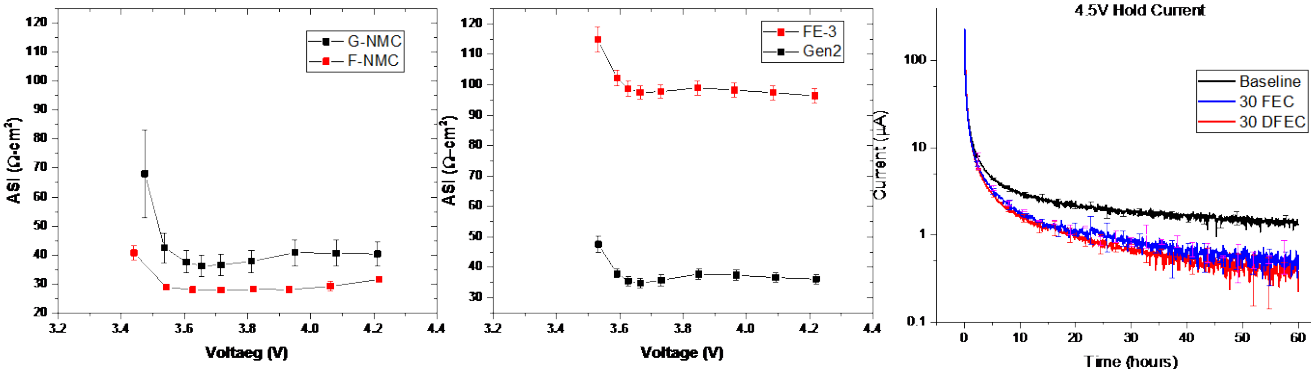


Figure II-218. a) and b) ASI values for various cell configurations as described in the text. c) Oxidation current vs. time at 4.5 V for NMC-532//Gr cells containing DFEC/HFDEC, FEC/HFDEC, and Gen2.

Figure II-218a shows ASI values for two cells containing Gen2 electrolyte as well as graphite anodes that had been previously formed using Gen2. However, the cathodes (NMC-532) of these cells were previously formed with either Gen2 (black curve) or DFEC/HFEC (red curve) electrolytes. The small impedance difference between these two conditions indicates that forming the cathode with the fluorinated electrolyte is not the source of the high impedance observed in Figure II-216b. Figure II-218b shows the ASI for two cells that both contain graphite anodes previously formed with DFEC/HFDEC electrolyte, and paired with pristine NMC-532 cathodes in cells containing either Gen2 (black curve) or DFEC/HFDEC (red curve) electrolytes. The large impedance change between these two cells, along with the data in 5a, shows that the formation environment of the graphite anode (or NMC cathode) is not the dominant contributor to high impedance. Clearly, the identity of the electrolyte itself is a major factor in determining the ASI observed in Figure II-216b. Finally,

Figure II-218c shows a plot of oxidation current vs. time (at 4.5 V) for NMC-532//Gr cells containing DFEC/HFDEC, FEC/HFDEC, and Gen2. Clearly, the fluorinated compositions lead to less oxidation current and thus greater stability at high voltages than the Gen2 baseline. These data taken together show that fluorinated electrolytes, and particularly the FEC/HFDEC composition, are of interest for high-voltage applications. Work is ongoing to better understand the nature of SEIs formed on graphite anodes using these, and other, fluorinated compositions.

*Coated NMC Cathodes*

Cathode coatings, particularly $Al_2O_3$, are often reported as beneficial to high-voltage operation. However, a wide variety of results can be obtained from the literature. This project is aimed at systematic studies of coatings in order to gauge their efficacy in enabling high-voltage performance. The systems tested included various NMCs coated by ALD (particles and electrodes) as well as wet-chemical methods (discussed elsewhere). Figure II-219 (top) and Figure II-219 (bottom) show summary data from a detailed study, conducted by Argonne's Cell Analysis, Modeling and Prototyping (CAMP) facility in collaboration with Forge Nano (Louisville, Co). Forge Nano delivered three coating levels of $Al_2O_3$ on NMC-532 powders to CAMP for electrode fabrication and testing. Sample A being the thinnest (2 ALD cycles) coating followed by samples B (4 cycles) and C (8 cycles). The table in Figure II-219 (top) shows cell formation and rate data of duplicate sets of full cell coin-cells.

| Sample | 1st Charge Capacity @ C/10 (mAh/g) | Irreversible Capacity Loss@ C/10 (mAh/g) | Avg. 1st Cycle Efficiency (%) | Reversible Discharge Capacity @ C/10 (mAh/g) | Reversible Discharge Capacity @ 1C (mAh/g) |
|---|---|---|---|---|---|
| Pristine | 215 | 31 | 84 | 180 | 169 |
| Sample A | 215 | 30 | 85 | 179 | 169 |
| Sample B | 220 | 34 | 84 | 179 | 168 |
| Sample C | 211 | 31 | 83 | 174 | 161 |
| Pristine | 221 | 35 | 85 | 178 | 168 |
| Sample A | 220 | 33 | 85 | 181 | 170 |
| Sample B | 219 | 33 | 85 | 179 | 167 |
| Sample C | 207 | 31 | 83 | 171 | 158 |

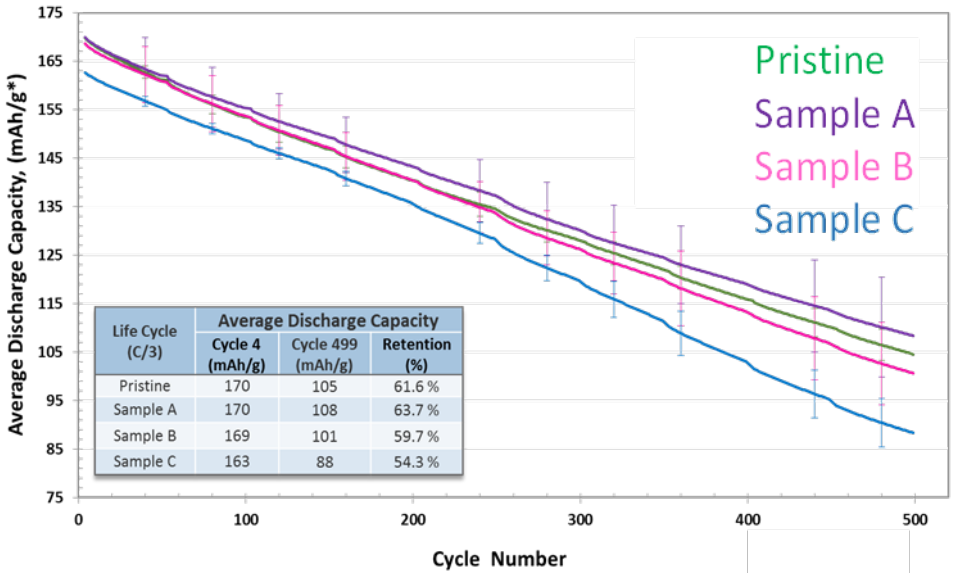


Figure II-219. (top) Cell formation and rate data for duplicate sets of coated NMC-532//Gr. (bottom) Cycle life plot of Set 1 data between 4.4-3.0 V, C/3 charge and discharge, 30°C.

Cells consisted of the coated cathodes, graphite anodes, and Gen2 electrolytes. All cells underwent formation, rate studies, HPPC, and cycle life testing. Figure II-219b shows cycle life testing of samples A, B, and C between 4.4-3.0 V at a C/3 charge and discharge rate. The main conclusions of this more detailed study can be arrived at from the data in Figure II-219. Specifically, ALD-$Al_2O_3$ coatings on NMC-532 did not significantly improve performance over the uncoated baseline under any of the conditions tested. A negative trend in performance was found with increasing ALD cycles (coating thickness). Preliminary data of ALD-$Al_2O_3$ coatings on electrode laminates, conducted at NREL, present similar conclusions with a possible NMC composition dependence for these coatings. For example, Figure II-220 shows NMC-532, 622, and 811 electrodes coated via ALD with $Al_2O_3$. No clear trend is observed for NMC-532 or 811, however, the NMC-622 data may indicate a net positive benefit. Future studies will focus on the effects of cathode composition on ALD coatings.

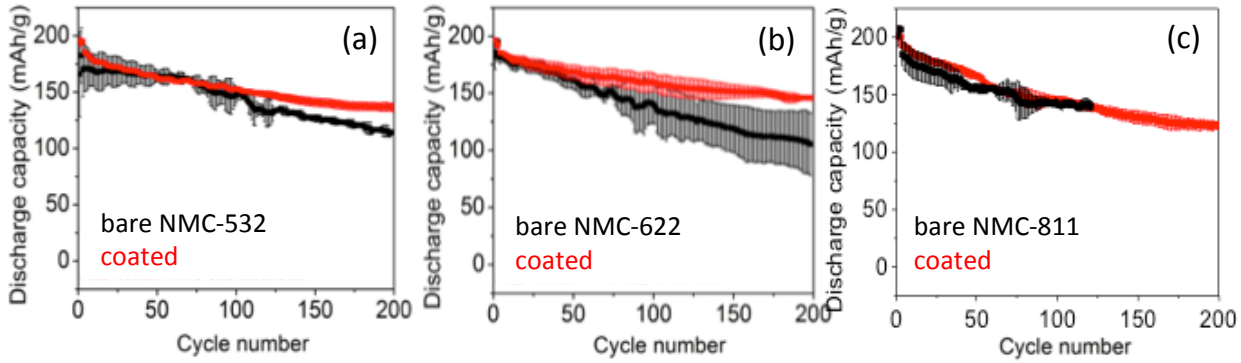


Figure II-220. $Al_2O_3$-coated NMC electrodes vs. graphite (a) NMC-532, (b) 622, and (c) 811. 3.0-4.5 V, 1C charge/discharge.

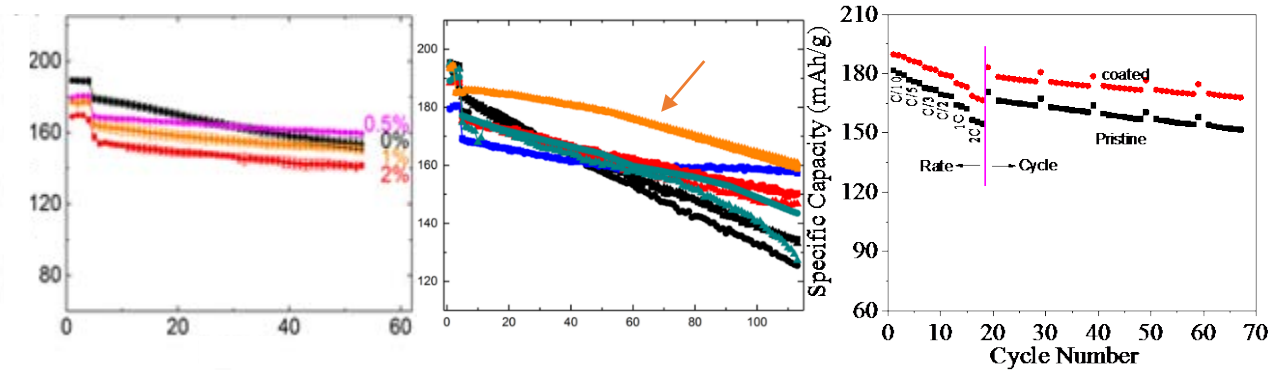


Figure II-221. NMC-532 powders wet-coated with $Al_2O_3$ by various wet-chemical methods as a function of (a) wt.% $Al_2O_3$, (b) Al salt/solvent system, and (b) 0.5 wt.% $Al_2O_3$ via a wet impregnation method.

Figure II-221a-c show wet-chemical coatings of $Al_2O_3$ on NMC-532 cathodes. In general, it can be observed that 1) thinner coatings lead to better performance; 2) the precursor/solvent system plays a role where Figure II-221b shows that 0.2 wt. % $Al_2O_3$, coated on NMC-532 by way of Al-isopropoxide in methanol, outperforms the uncoated material; 3) The wet impregnation method leads to greatly reduced initial impedance (not shown) and, subsequently, higher cycling capacities as a function of rate.

## Conclusions

- Protocols and Figure of merit values have been developed that allow for reliable comparisons of electrolyte formulations and insights into the mechanisms of their success or failure
- Fluorinated electrolytes have been developed that show increased stability at charged cathode surfaces and unique SEI films with enabling properties at graphite anodes
- $Al_2O_3$ coatings on NMC cathodes have been studied in great detail and, while findings thus far do not substantially support the idea that this particular material can enable long-term, high-voltage stability in NMC//Gr systems, certain synthesis conditions/methodologies show more promise than others
- Future studies will focus on select methodologies and their ability to promote stable surfaces in NMC//Gr systems at higher voltages.

**Chapter Acknowledgments** Daniel P. Abraham, John Zhang, Adam Tornheim, Meinan He, James A. Gilbert, Cameron Peebles, Ira Bloom, Ritu Sahore, Juan Garcia, Javier Bareño, Hakim Iddir, Chen Liao, Katherine Hurst, Robert Tenent, Chunmei Ban, Xuemin Li, Yongan Yang, Iyla A. Shkrob, Kaushik Kalaga, Stephen E. Trask, Bryant J. Polzin, Andrew N. Jansen, Alison Dunlop, Jack Vaughey, Binghong Han, Fulya Dogan, Wenquan Lu, Xin Su, Xiaoping Wang

## Key Publications

1. J.A. Gilbert, J. Bareño, T. Spila, S.E. Trask, D.J. Miller, B.J. Polzin, A.N. Jansen, D.P. Abraham, J. Electrochem. Soc. **164**, A6054 (2017).
2. A. Tornheim, C. Peebles, J.A. Gilbert, R. Sahore, J.C. Garcia, J. Bareño, H. Iddir, C. Liao, D.P. Abraham, Journal of Power Sources **365**, 201 (2017).
3. R. Sahore, C. Peebles, D.P. Abraham, J. Gilbert, I. Bloom, *Additive Effects in High-Voltage Layered-Oxide Cells: A Statistics of Mixtures Approach*, Journal of Power Sources, *accepted* (2017).
4. C. Peebles, R. Sahore, J.A. Gilbert, J.C. Garcia, A. Tornheim, J. Bareño, H. Iddir, C. Liao, D.P. Abraham, J. Electrochem. Soc. **164**, A1579 (2017).
5. I.A. Shkrob and D.P. Abraham, J. Phys. Chem. C **120**, 15119 (2016).
6. R. Sahore, A. Tornheim, C. Peebles, J. Garcia, F. Dogan, D. C. O'Hanlon, C. Liao, H. Iddir, Z. Zhang, J. Bareño, I. Bloom, *Methodology for understanding interactions between electrolyte additives and cathodes: a case of tris(2,2,2-trifluoroethyl) phosphite additive*, (*submitted*, J. Mat. Chem. A, 2017).

## II.C.2 Enabling High-Energy/Voltage Li-Ion Cells: Materials and Characterization (ANL, LBNL, NREL, ORNL)

**John Vaughey, Principal Investigator**
Argonne National Laboratory
9700 S. Cass Avenue
Lemont, IL 46039
Phone: 630-252-8885
E-mail: vaughey@anl.gov

**Guoying Chen, Principal Investigator**
Lawrence Berkeley National Laboratory
1 Cyclotron Road
Berkeley, CA 94720
Phone: 510-486-5843
E-mail: gchen@lbl.gov

**Peter Faguy, Technology Manager**
U.S. Department of Energy
Phone: 202-586-1022
E-mail: Peter.Faguy@ee.doe.gov

Start Date: October 1, 2014 End Date: September 30, 2018
Total Project Cost: $4,000,000 DOE share: $4,000,000 Non-DOE share: $0

### Project Introduction

The inability to charge commercially available $Li_{1+x}Ni_aMn_bCo_cO_2$ (NMC-abc, where x is typically <0.05), cathode materials beyond ~4.3 V (vs. graphite) without incurring excessive surface damage, electrolyte decomposition, structural instabilities, gassing, and loss of lithium inventory is a significant challenge in meeting next-generation energy storage targets. This project aims to understand the underlying failure mechanisms associated with these issues that prevent state-of-the-art Li-ion battery systems from achieving higher practical energy densities than are currently obtainable. To do so, several research thrusts have been established across the overall project including cathodes, electrolytes and additives, surfaces and interfaces, testing and analysis, modeling, and cell fabrication. In addition to these areas of focus, cross-cutting collaborations are targeted at obtaining information on the failure mechanisms of NMC//graphite (Gr) cells that affect systems-level performance when cycled at high voltages. This project is intended to "enable" high-energy cells via new insights and/or understanding, not currently available, of why present materials/systems fail. This chapter deals with the materials and characterization component of the project; more specifically, detailed studies of the structure and behavior of NMC surfaces, and their interactions with materials applied as surface stabilizers, as a function of synthesis are presented.

### Objectives

The goals of this project are related to acquiring a deeper, fundamental understanding of the processes that influence the stability of NMC surfaces and identify strategies, such as coatings, aimed at stabilizing these surfaces under high-voltage operation, and are as follows:

- Understand the complex relationships between NMC particle morphology and the associated, facet-dependent electrochemical properties

- Design, synthesis, and characterization of model systems that are directly compatible with experimental and theoretical approaches to allow for unique, atomic-scale insights into the reactivity of NMC surfaces
- Develop surface-sensitive, structural characterization tools that allow better correlations to be made between the morphology and composition of pristine and coated, Ni-rich cathodes, and their associated electrochemical properties
- Understand the effects of surface coatings on cathode interfaces and bulk structures as a function coating methodology (technique, annealing temperature, and coating content) and cathode composition
- Understand the effects of cathode composition on surface segregation, coating efficiency, and electrochemical performance of Ni-rich cathodes

## Approach

The goals listed above will be pursued through the following experimental thrusts:

- Synthesis of ***model systems*** that allow for detailed experimental and theoretical characterization of NMC surfaces including:
    - Single-crystal, NMC particles with well-defined compositions, sizes, and morphologies
    - Surface-modified particles
    - Thin-film, NMC cathodes
- Systematic studies of ***coated NMC particles*** using $Al_2O_3$ as a baseline, to include:
    - NMC composition (442, 532, 622, 811, NCA, and LCO)
    - Characterization and effect of initial surface-Li content and Li leaching
    - Aqueous vs. non-aqueous solvents coupled with various Al precursors with oxidizing and non-oxidizing associated anions
    - Post-synthesis annealing temperature and diffusion/solubility of Al, $LiAl_2O_3$, and $Al_2O_3$
    - Structure and morphology of coatings as a function of the above variables
    - Wet-chemical methods compared to atomic layer deposition (ALD)
    - Physical and electrochemical characterization

## Results

*Synthesis of Model Systems*

In this work, a modified molten-salt synthesis approach is used to fabricate layered, NMC single-crystal samples with well-defined particle morphologies, sizes, and compositions. In a typical synthesis procedure, stoichiometric amounts of transition-metal (TM) precursors, $Mn(NO_3)_2{\cdot}4H_2O$, $Co(NO_3)_2{\cdot}6H_2O$ and $Ni(NO_3)_2{\cdot}6H_2O$, are dissolved in a small amount of de-ionized water. A lithium source, $LiNO_3$, $Li_2CO_3$, or $LiOH{\bullet}H_2O$ is added to the solution followed by the addition of a flux, typically KCl (m.p. = 771°C) or CsCl (m.p. = 645°C). The mixture is then transferred into an alumina crucible, covered with a lid, and trace amount of residual water is removed by gentle heating at 200 C. The resulting dry powder is further heated at a controlled rate to an elevated temperature, typically 850°C or 900°C, and then soaked at the high temperature for 8-12 hours before cooling to room temperature. The final product is thoroughly washed with de-ionized water to remove the flux and dried in a vacuum oven overnight. Choice of precursors, flux, ratio between precursor and

flux, soaking time, and temperature can be adjusted to influence the uniformity and physical characteristics of the synthesized crystals.

Previously, crystal samples with varying TM ratios, including NMC-333, NMC-532, NMC-622, and NMC-811, were synthesized using the above procedures as shown in the SEM of Figure II-222. Importantly, these data were used to corroborate density functional theory (DFT) calculation carried out by Iddir et al., showing that, energetically, (012) surfaces dominate under highly oxidizing synthesis environments (see also II.A.3.iv). The (001) surface appears in all samples in a nearly constant fraction, while the coverage of (104) planes increases as the degree of crystal truncation increases, Figure II-222f. Furthermore, as shown in Figure II-223, these crystals can be fabricated into composite electrodes and cycled in electrochemical cells. These results support and verify the strategy of using "practical", model systems that can be directly understood by experiment, advanced characterization, and theory.

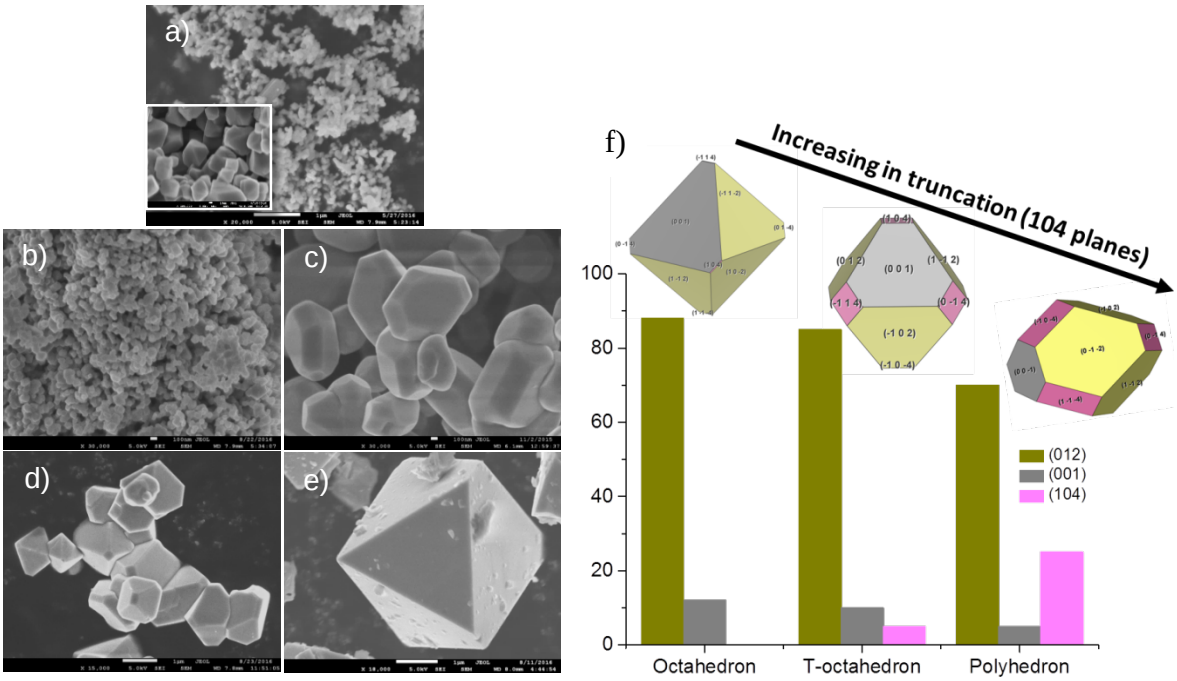


Figure II-222. NMC-532 crystal samples with varying particle sizes and morphologies: a) 50 nm, b) 100 nm, c) 1 µm, d) 1 µm, e) 10 µm and f) summary of surface facets and their fraction on NMC-532 crystals.

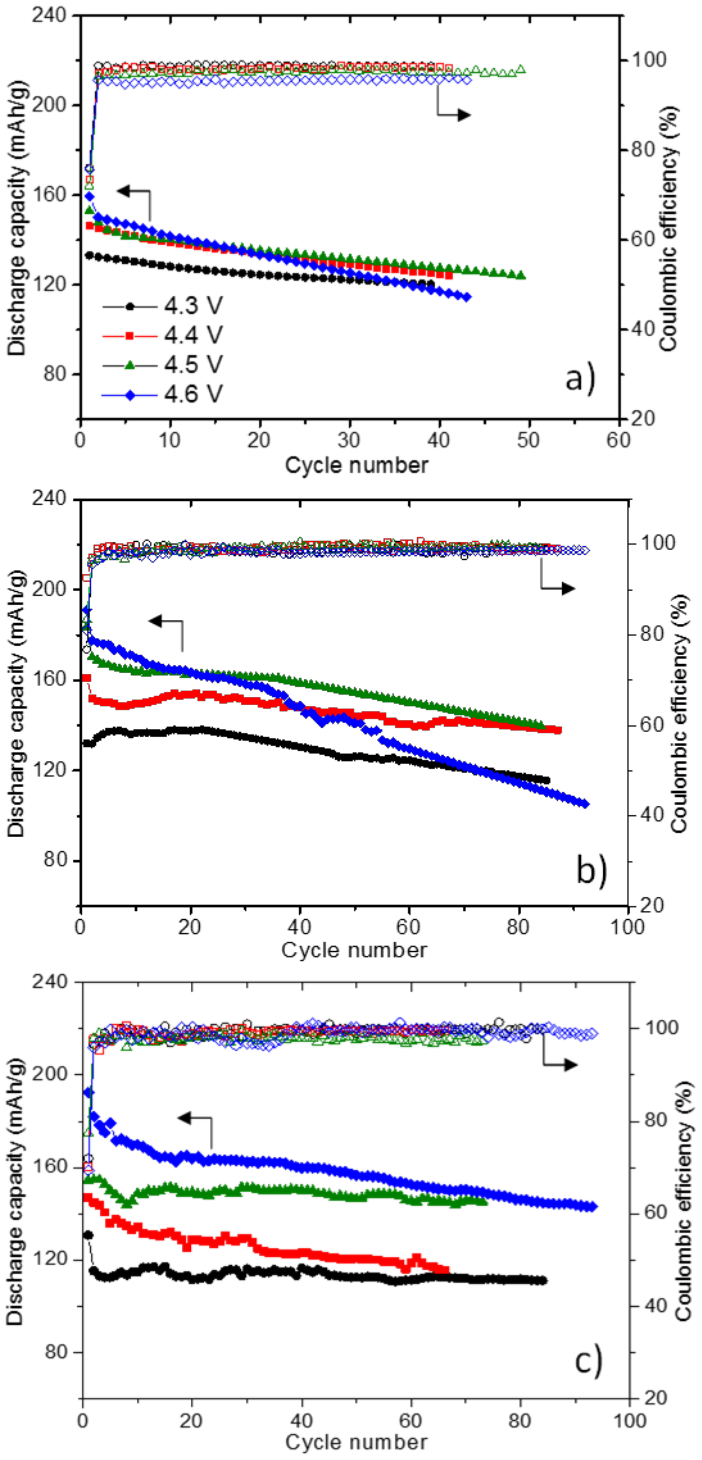


Figure II-223. Half-cell cycling stability comparison of NMC crystal cathodes: a) NMC-333 in 100 nm size, b) NMC-532 in 100 nm size and c) NMC-532 in 10 µm size.

Low-temperature (LT) synthesis routes (~500°C) were also explored, as part of a Go/No-Go milestone, in order to obtain other particle morphologies. Figure II-224a and Figure II-224b show SEM images of NMC-333 crystals synthesized through a LT route. Hexagonal nano-platelets, with an average particle size of 200-300 nm and a thickness of ~70-80 nm, were obtained and this particle morphology was found to be insensitive to NMC

composition. XRD data shows that the crystals adopted a phase-pure, layered structure. As such, a Go decision was made on pursuing these LT synthesis routes. High-resolution TEM (HRTEM) studies are underway to better understand the atomic-scale properties of these particles.

Spectroscopic characterization was performed on various NMC crystals to investigate the effect of Ni content on pristine surface properties. Figure II-224c and Figure II-224d show the soft X-ray absorption (XAS) data collected on NMC crystals with compositions of NMC-333, 532, 622, 811. All crystals had the same particle size of 1 µm and the same particle shape of truncated-octahedron (Figure II-222d), which is predominately enclosed by the (012) family of surface facets. The spectra were collected in either total electron yield (TEY) mode, which probes a depth of ~5 nm (e.g., surface), or fluorescent yield (FY) mode, which has a probing depth of ~50 nm (e.g., bulk). No obvious differences were observed in the oxidation states of Mn or Co (not shown), suggesting minimal impact of Ni concentration on similar surface planes. Ni oxidation state was found to increase along with the increase of Ni content, evidenced by the increasing intensity ratio of Ni *L*3 high/low peaks between 852-858eV (Figure II-224c). A comparison with the bulk Ni oxidation state, collected in FY mode (Figure II-224d), shows that surface Ni is more reduced than the bulk in all NMC crystal samples. The particles presented above, and variations thereof, will be used to investigate the atomic-scale, facet-dependent, electrochemical properties of NMC surfaces and inform further theoretical studies.

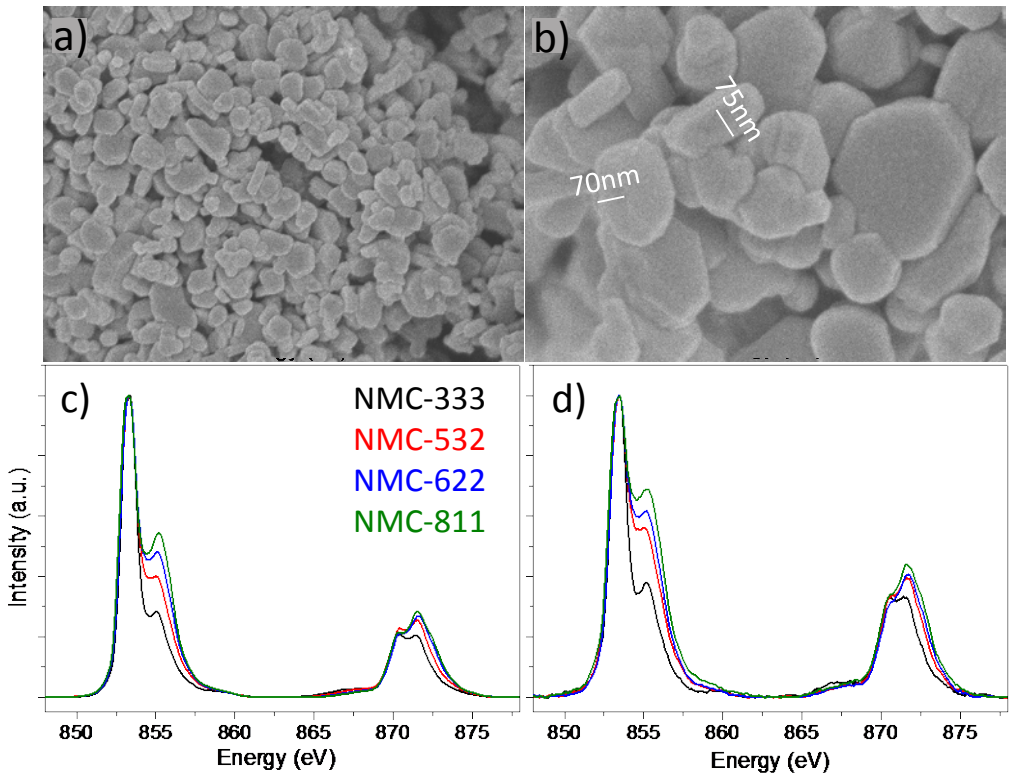


Figure II-224. a, b) SEM images of NMC-333 synthesized from a LT-synthesis route. c) TEY Ni *L*-edge and d) FY Ni *L*-edge XAS profiles.

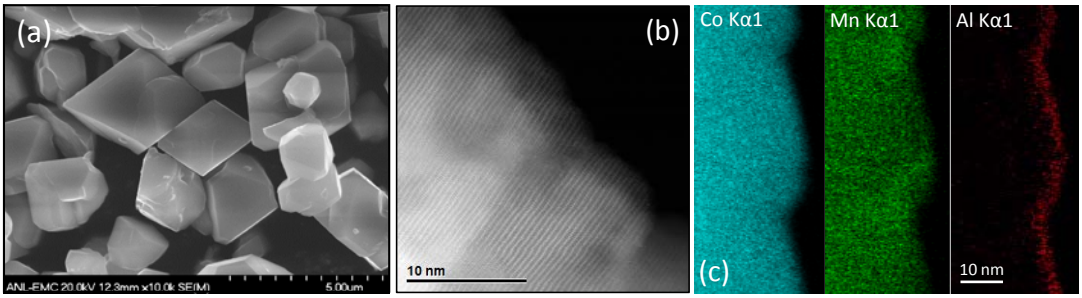


Figure II-225. a) SEM image of ~0.15$Li_2MnO_3$•0.85$LiCoO_2$ particles used for surface and bulk nickel doping. b) HRTEM image showing layered structure of the Ni-doped surface. c) EDS maps showing distribution of surface Al after ALD coating.

Figure II-225a shows single-crystal particles synthesized via a salt-flux method having a composition of ~0.15$Li_2MnO_3$•0.85$LiCoO_2$. The composite nature of the material gives $LiMn_6$-type ordering and Li sites within the TM layers. Treatment of these particles, in an acidic solution containing $Ni^{2+}$ cations, and subsequent annealing leads to the incorporation of $Ni^{2+}$ into the Li sites of the TM layers in an exchange process, thereby creating a Ni-doped, layered, R3-m-type of oxide. Depending on post annealing time/temperature, Ni can be doped primarily within the surface regions or distributed more deeply into the bulk. HRTEM data (b) and spectroscopy (not shown) reveals regions of Ni incorporated into a well-layered structure to a depth of ~20 nm for samples annealed at ~600°C. Preliminary XAS results show that the electrochemical behavior of Ni is different for samples annealed at 900°C (e.g., bulk incorporation of Ni) compared to 600°C (e.g., surface-doped Ni); even when protected by coatings such as $Al_2O_3$, Figure II-225c. Further analyses, as well as spectroscopic studies using various coatings and additives, are ongoing to better understand these systems and the role of surface vs. bulk nickel in nickel-rich cathodes.

Thin film cathodes have been produced by magnetron sputtering from NMC-442, 532, 622, 811, and NCA targets. XRD, ICP, and electrochemical profiles have been used to determine the sputtered phases and lithium contents of films produced under different processing conditions. Thin-film NMC-442, 532, and 622, heat-treated in air to 700°C, demonstrated proper phase content and voltage profiles but with low initial capacities for two, different film thicknesses (Figure II-226). NMC-811 and NCA sputtered films demonstrated voltage plateaus that did not agree with the established profiles for these materials, where ICP results indicated lithium-rich compositions for these films. Process optimization is ongoing.

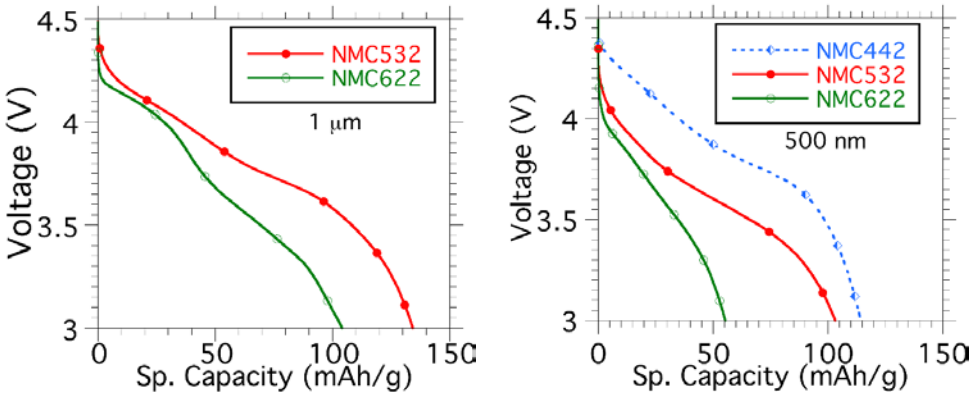


Figure II-226. Discharge profiles of NMC-442, 532, & 622 thin-film cathodes, 1 μm (left), and 500 nm (right).

*Coating Mechanisms and NMC Cathode Particles*

The effect of NMC metal ratios on surface and bulk composition, morphology, and electrochemical performance for $Al_2O_3$-coated samples was studied with NMC-532, 622, and 811 prepared with aqueous coatings, varying $Al_2O_3$ content, and annealing temperatures. Surface elemental distributions, local chemical

and atomic structures, surface species and bulk changes were examined by SEM, TEM, XRD, and solid-state nuclear magnetic resonance spectroscopy (NMR). Results show that with compositional change from 532 to 811, the $Al_2O_3$ coatings begin to diffuse into the bulk on high-temperature annealing due to Al compatibility with Ni-rich materials, Figure II-227a. Because diffusion of surface $Al_2O_3$ into the bulk of 811 is easier, and more evenly distributed when compared to 532 and 622, morphology differences can be observed, SEM Figure II-228a. $^{27}Al$ NMR data showed formation of a surface $LiAlO_2$ phase for all compositions when annealing temperatures increased to 800 °C. The diffusion of Al into the lattice was found to negatively affect electrochemical performance, indicating the importance of compatibility between surface coatings and bulk oxides.

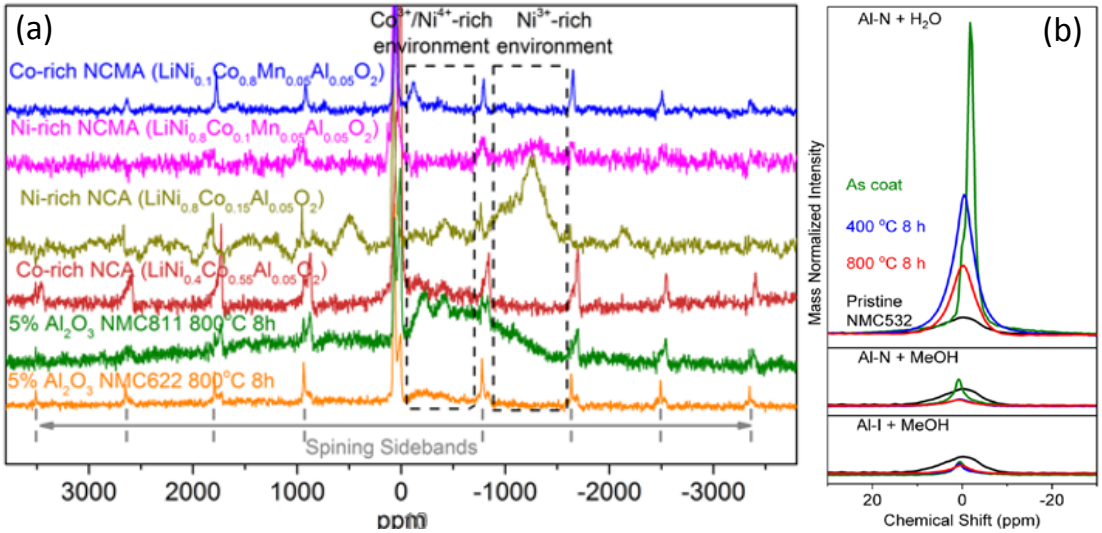


Figure II-227. a) $^{27}Al$ NMR spectra of 5 wt.% $Al_2O_3$-coated NMC-622 and 811 annealed at 800ºC for 8h, compared to Co-rich NCA, Ni-rich NCA and NCMA, and Co-rich NCMA. b) $^{7}Li$ NMR for $Al_2O_3$-coated NMC-532 with various salt/solvent systems.

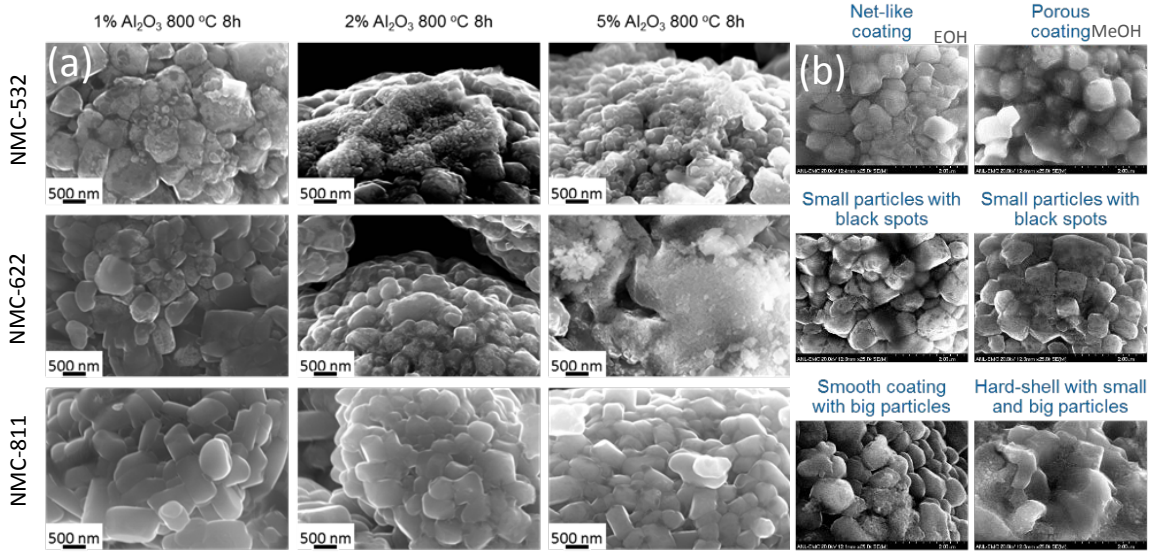


Figure II-228. a) SEM images of $Al_2O_3$-coated NMC-532, NMC-622, and NMC-811 with $Al_2O_3$ at 1, 2, and 5 wt.% annealed at 800ºC for 8 h. b) SEM images of $Al_2O_3$-coated NMC-532 with various aluminum sources, solvents, and annealing times.

NMR has also shown the presence of surface proton and lithium species, Figure II-227b. In addition, lower initial capacities in comparison to pristine samples were observed with aqueous solvents, suggesting possible

lithium loss or displacement from the bulk of cathode oxides during coating. In order to mitigate these challenges, alternative Al precursors and solvent systems were studied. Experiments were performed on NMC-532 with 2 wt.% Al-nitrate and isopropoxide as aluminum sources, and ethanol, methanol, and xylene as solvents. Coated samples were annealed at 400°C and 800°C to study the temperature effect on coating composition and electrochemical performance. Results show that surface-lithium contents after annealing are indeed influenced by choice of solvent (Figure II-227b), and particle morphologies are altered when changing both solvent and aluminum precursor, Figure II-228b. Furthermore, electrochemical performance was improved with the use of Al-isopropoxide/methanol in comparison to the Al-nitrate/water pair (II.C.1). Theoretical calculations have also been carried out on $Al_2O_3$-coated NMC surfaces and important insights gained on the interface structures of coated NMC materials (II.C.3).

## Conclusions

A major goal of the overall project is an atomic-scale understanding of the physiochemical properties of NMC surfaces and interfaces. In order to obtain unique insights into these materials, model systems were pursued that will allow for combined experimental and theoretical studies that can be correlated by practical experiments and tractable calculations. FY17 efforts have shown that well-defined, single-crystal particles can be synthesized and facet-dependent properties probed. In addition, model cathode particles and thin-film cathodes have been fabricated for combined spectroscopic and electrochemical characterization. Furthermore, a detailed study on the effects of NMC composition, precursors, solvents, and annealing conditions has been carried out to elucidate the mechanisms of protecting NMC surfaces by means of coating methods. It has been shown that all parameters act in concert to arrive at the final product and profoundly influence electrochemical performance. In particular, the propensity for lithium leaching in aqueous solvents, coating thicknesses, and the driving force for Al segregation and diffusion, both strong functions of TM content, play a particularly important role in realizing efficient particle coatings. The electrochemical properties of these and other coatings is presented in II.C.1.

**Chapter Acknowledgments** Guoying Chen, Jian Zhu, Jason R. Croy, Mahalingam Balasubramanian, Dan O'Hanlon, Hakim Iddir, Jack Vaughey, Binghong Han, Fulya Dogan, S. Sharifi-Asl, R. Shahbazian-Yassar, Gabriel M. Veith, Rose E. Ruther, Andrew Kercher, David Wood III, Lamuel David, Jagjit Nanda

## Key Publications

1. J. Garcia, J. Bareño, J. Yan, G. Chen, A. Hauser, J.R. Croy, and H. Iddir, Phys. Chem. C 121, 8290 (2017).
2. B. Han, T. Paulauskas, B. Key, C. Peebles, J.S. Park, R.F. Klie, J.T. Vaughey, and F. Dogan, ACS Appl. Mater. Interfaces **9**, 14769 (2016).
3. F. Dogan, J.T. Vaughey, H. Iddir, and B. Key, Appl. Mater. Interfaces **8**, 16708 (2016).
4. B. Han, C. Peebles, T. Paulauskas, J.T.Vaughey, F. Dogan, *Effects of Sintering Temperature and Cathode Composition on $Al_2O_3$ Coatings of Li-ion Cathodes*, 231st ECS Meeting, New Orleans, May 28th (2017).
5. B. Han, C. Peebles, T. Paulauskas, J.T.Vaughey, F. Dogan, *Characterization of $Al_2O_3$ Coatings on Li-ion Cathodes: Effects of Annealing Temperature and Composition*, 2017 MRS, Phoenix, April 17th (2017).
6. Binghong Han, Baris Key, Saul H. Lapidus, Juan C. Garcia, Hakim Iddir, John T. Vaughey, Fulya Dogan, ACS Appl. Mater. Interfaces, DOI: 10.1021/acsami.7b13597 (2017).

## II.C.3 Enabling High-Energy/Voltage Li-Ion Cells: Theory and Modeling (ANL, LBNL, NREL, ORNL)

**Hakim Iddir, Principal Investigator**
Argonne National Laboratory
9700 S. Cass Avenue
Lemont, IL 46039
Phone: 630-252-4505
E-mail: iddir@anl.gov

**Dennis Dees, Principal Investigator**
Organization: Argonne National Laboratory
Address: 9700 S. Cass Avenue
Lemont, IL 46039
Phone: 630-252-7349
E-mail: dees@anl.gov

**Peter Faguy, Technology Manager**
U.S. Department of Energy
Phone: 202-586-1022
E-mail: Peter.Faguy@ee.doe.gov

Start Date: October 1, 2014 End Date: September 30, 2018
Total Project Cost: $4,000,000 DOE share: $4,000,000 Non-DOE share: $0

### Project Introduction

The inability to charge commercially available $Li_{1+x}Ni_aMn_bCo_cO_2$ (NMC-abc, where x is typically <0.05), cathode materials beyond ~4.3 V (vs. graphite) without incurring excessive surface damage, electrolyte decomposition, structural instabilities, gassing, and loss of lithium inventory is a significant challenge in meeting next-generation energy storage targets. This project aims to understand the underlying failure mechanisms associated with these issues that prevent state-of-the-art Li-ion battery systems from achieving higher practical energy densities than are currently obtainable. To do so, a more complete description of the atomic-level structure and reactivity of NMC surfaces is needed. This chapter deals with atomistic and electrochemical modeling studies focused on understanding material surfaces and interfacial reactions as well as relating electrochemical performance measurements to diagnostic studies on lithium-ion cells.

### Objectives

The goals of this project are related to acquiring a deeper understanding of the atomic-scale processes that influence the structure and stability of NMC surfaces under various electrochemical environments by:

- Determination of surface structures and the driving forces for surface elemental segregation
- Theoretical predictions of electrolyte- and additive-NMC surface interactions
- Theoretical predictions of electrolyte decomposition and dissolution products and related effects
- Effect of NMC, transition metal (TM) composition on the synthesis of $Al_2O_3$-based NMC coatings
- Understanding the effects of side reactions and electrode crosstalk through electrochemical modeling

## Approach

The goals of the project will be accomplished through ***atomistic modeling*** using density functional theory (DFT) and ***electrochemical modeling*** using continuum-based transport equations combined with kinetic and thermodynamic expressions. All atomistic calculations were carried out by spin-polarized DFT as implemented in the Vienna Ab Initio Simulation Package (VASP). The exchange-correlation potentials are treated by the generalized gradient approximation (GGA) parametrized by Perdew, Burke, and Ernzerholf (PBE). The interaction between valence electrons and ion cores is described by the projected augmented wave (PAW) method. Furthermore, the GGA+U scheme is used for applying the on-site correlation effects among 3d electrons of the TMs, where the parameter of (U-J) is set to 5.96 eV, 5.00 eV, and 4.84 eV for Ni, Co, and Mn, respectively. The wave functions were expanded in the plane wave basis up to a kinetic energy of 500 eV. All surface calculations were performed using a periodically repeating slab separated by vacuum layers along the surface normal. A vacuum thickness of 10 Å was adopted to remove interactions between the slab layers. The lattice parameter of the supercell was fixed at its bulk value. All ions were allowed to relax until the total energy differences were no more than 0.003 eV. After geometry optimization within the DFT+U framework, electronic relaxation was performed using a single point calculation with the hybrid functional HSE06 to determine the surface energy at that level of theory.

NMC-111 is used as a model material because the TM-layer, ionic configuration is known. In order to establish the ion ordering in the TM layers, it is necessary to use a supercell that is at least three times bigger in the a and b directions than for a single-metal, layered material such as $LiCoO_2$. A k-point mesh of 3x3x3 was found sufficient to get accurate electronic energies for bulk calculations on this unit cell. Each ion has six neighbors consisting of groups of the other TMs arranged in a triangular shape. This ordering was found to be the most favorable using solid state NMR. This structure was also confirmed by DFT calculations of an initial set of 30 lowest-energy configurations determined based on electrostatic interactions only. The ordering can be explained based on the local charge balance. The sum of the electrovalencies of the nearest-neighbor cations should be equal to the charge of the anion in ordered rock-salt structures. Adsorption and reaction energies ($\Delta E$) were calculated using the following expression:

$$\Delta E = E_{surf+adsorbate} - E_{surf} - E_{adsorbate} \qquad (1)$$

Where $E_{adsorbate}$ is the energy of the isolated molecule in the vacuum, $E_{surf}$ is the energy of the bare slab, and $E_{surf+adsorbate}$ is the total energy of the molecule adsorbed on the slab. Bulk solvent effects were accounted for by using an implicit solvation model as implemented in the DFT code VASP. Additionally, calculations of reactions in solution were performed with the Gaussian 09 implementation of DFT at the B3LYP/6-31+G(d,p) level of theory. Frequency calculations were performed for all structures in order to determine the nature of the stationary points. The ultrafine integration grid was employed in all calculations.

## Results

*Atomistic Modeling*

**Oxidation mechanism of electrolyte molecules on pristine and delithiated NMC surfaces**

DFT calculations were used to estimate the interaction of electrolyte solvent molecules with the surfaces of NMC particles. Solvent molecules included ethyl methyl carbonate (EMC), ethylene carbonate (EC), hexafluorinated diethyl carbonate (HFDEC), and difluoro ethylene carbonate (DFEC), see II.A.3.iii. It was shown in an earlier report that the most reactive NMC facet is the (012) surface [1]. This facet was used as the prototype surface to determine cathode electrolyte interactions. Ab initio Molecular Dynamics (AIMD) was also used to explore the configuration space of the molecules over the surfaces. Several adsorption configurations were evaluated in order to find atomic positions that minimized the adsorption energy on the fully lithiated and delithiated NMC surfaces. The lowest energy configuration for EMC is shown in Figure II-229a. In this configuration the EMC molecule is chemically oxidized via hydrogen abstraction. The negative reaction energy denotes an exothermic reaction. The reaction produces a radical that is stable under the simulation conditions. However, this radical intermediate is highly reactive so its reactivity was tested by adding an alkene molecule to the simulation box. In the presence of an alkene the intermediate polymerizes

until a termination step is provided. Note that the hydrogen abstraction process transfers one electron to the lattice reducing a TM at the surface. EC interaction with the NMC (012) surface (Figure II-229b) takes place in an equivalent process. However, according to the calculated reaction energies, EC oxidation is more thermodynamically favorable than EMC oxidation. This indicates that EC would decompose preferentially in a Gen2 electrolyte. Contrary to EC and EMC, the fluorinated molecules HFDEC and DFEC do not react with the lithiated surface. The adsorption configurations of the fluorinated electrolyte molecules are shown in Figure II-229c and Figure II-229d. The interaction of HFEC and DFEC with the surface is weak, leading to an adsorption energy of -0.11 eV and -0.03eV respectively. There is no charge transfer during this interaction. Hence, no TM reduction is expected. The molecules interact in an analogous manner on the delithiated slab. On the other hand, the interaction of the additive Tris(2,2,2-trifluoroethyl) phosphite (TTFP) with the surface differs from the electrolyte molecules mentioned above. On the lithiated surfaces the interaction of TTFP is weak (ΔE=-0.04 eV). This matches the interaction of the fluorinated electrolytes molecules. In contrast, on the delithiated surface TTFP prefers to form a phosphorous-oxygen bond (Figure II-229e). The hydrogen abstraction is not favorable in this case, probably due to steric effects. Furthermore, the produced phosphate TTFPa molecule readily detaches from the surface without any energy barrier. Indeed, the reaction energy (ΔE=-3.1 eV) of taking an oxygen from the surface at this level of lithiation is very similar to the computed energy of oxidation of TTFP to TTFPa in solution (ΔE=-3.5 eV) [2, 3]. Oxidation of TTFP to TTFPa, creates an oxygen vacancy at the surface and leaves two electrons in the lattice that reduce the TMs. The reduction of the TMs and the creation of oxygen vacancies at the surface is likely the trigger of a surface phase change (e.g., layered to spinel).

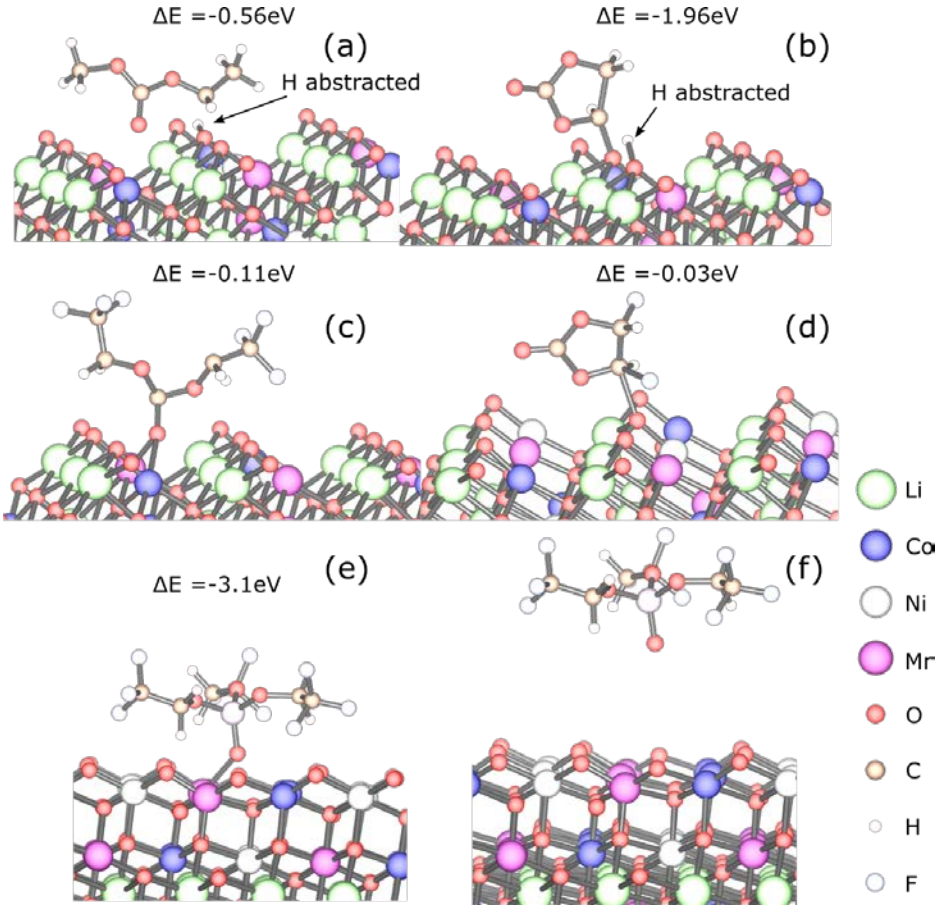


Figure II-229. Lowest energy configurations of electrolyte molecules on NMC (012) surface. (a) EMC, (b) EC, (c) HFDEC, (d) DFEC, (d) TTFP, (e) TTFP, (f) TTFPa

*Interaction of select additive decomposition products with NMC surfaces*

The interaction of the additive Tris(trimethylsilyl) phosphite (TMSPi) with the NMC (012) surface was also investigated. It was found that the decomposition products of TMSPi are stable on the surface in an oxidized state as phosphates. Figure II-230 shows the interaction of TMSPi with the delithiated (012) surface. The interaction of the additive is weak due to the steric effect of the bulky TMS groups. However, TMSPi can lose a TMS group (reaction with $PF_5$ and HF) and form a phosphate at the surface. The phosphate absorbs favorably at the surface. The absorbed species could produce a passivation effect at the cathode, in agreement with experimental findings that show a low impedance rise and much reduced TM dissolution (II.C.2). TMSPi was also compared with Triethyl phosphite (TEPi). Although the two additives are both phosphites, contrary to TMSPi, the TEPi leads to higher metal dissolution, higher impedance, and lower capacity retention [4, 5]. A more detailed mechanistic study is underway.

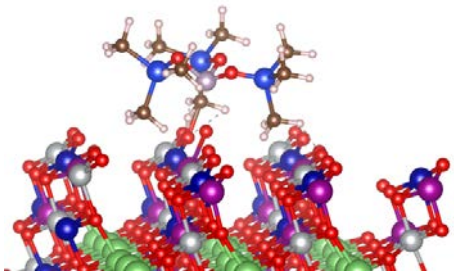

Figure II-230. TMSPi interaction with the delithiated NMC (012) surface.

*Transition metal segregation to specific NMC surfaces*

Calculations show that a thermodynamic driving force for Co segregation to the (104) facet of NMC surfaces exists [1]. However, no driving force was found for preferential segregation, via the TM layer, to the (012) surface. On the other hand, Ni segregation to (012) facets is related to surface-phase transformation. Previous work has found the (012) surface to be Ni rich. (See Figure II-231.) In order to gain some insights into these processes, a bulk Li/Ni anti-site defect formation energy of $E_f \approx 0.3\ eV$ was computed, which leads to an equilibrium concentration:

$$C = N_{conf} e^{\frac{-E_f}{RT}} \rightarrow 1.3\%$$

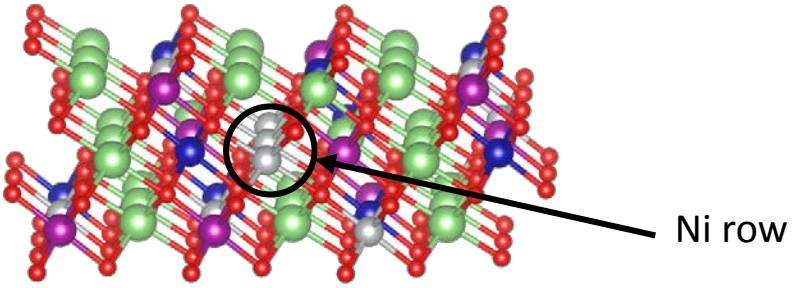


Figure II-231. Ni enriched NMC-111 (012) surface showing a stable arrangement of Ni in a row within the Li layer.

The energy of formation of a second anti-site defect in the same TM layer is ~1.8 eV. A third anti-site defect in the same TM layer produces a spinel-like region. The energy of formation of this defect is 0.4 eV. This indicates that the formation of rows of Ni in the Li layer near the surface is more favorable than randomly localized defects. This mechanism is likely at the origin of the observed formation of Ni-rich facets. However, in order to explore such surface-phase transformations (e.g., layered to spinel), thicker slab models need to be considered. Such systems are computationally expensive. Furthermore, to accurately describe key electronic structure features, hybrid functionals are required, adding to computational costs of DFT calculations. The convergence of the self-consistent loop is very hard to achieve at this level of theory and model sizes. However, good progress has been made and results are in preparation for publication.

*Theoretical Insights on how Transition Metal Composition Affects Alumina Coatings on Ni-Rich Cathodes*

A model slab for the (012) surface (Figure II-232) was used that was found to contribute the most to the overall surfaces of NMCs and was in agreement with the experimental results. Five layers of NMC-111 and two layers of α-$LiAlO_2$ on each side of the slab (symmetric configuration) were constructed. This configuration was chosen because α-$LiAlO_2$ is isomorphic with NMC. The matching unit cells produced a model with negligible strain. The likelihood of forming a different phase on top of the α-$LiAlO_2$ was investigated. In order to model this system, a disordered α-$LiAlO_2$ phase, which could be considered as a precursor to a phase transformation to γ-$LiAlO_2$, was constructed. The interface energy ($E_i$) between the $LiAlO_2$ layer and the NMC part of the material was computed as:

$$E_i = E_{LiAlO_2-surface} + E_{NMC-bulk} - E_{NMC-LiAlO_2}$$

Where $E_{LiAlO_2-surface}$ is the energy of a $LiAlO_2$ slab, $E_{NMC-bulk}$ is the energy of a bulk NMC-111 model with the same number of unit cells as the slab model, and $E_{NMC-LiAlO_2}$ is the energy of the NMC slab surface with a $LiAlO_2$ coating film. Figure II-233 shows the change in the interface energy with the thickness of the α-$LiAlO_2$ region. The energy decreases when the α-$LiAlO_2$ region increases. This result indicates that the α-$LiAlO_2$ phase could stabilize a different phase if the thickness of the film is larger than four atomic layers. Also, this is evidence of a possible presence of an interfacial α-$LiAlO_2$ between NMC and a different phase, such as γ-$LiAlO_2$.

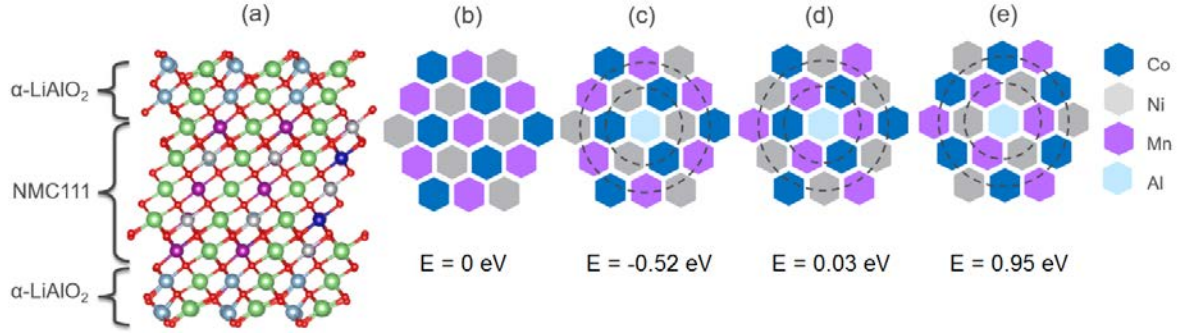


Figure II-232. (a) Model slab for the (012) NMC-111 surface coated with 2 layers of α-$LiAlO_2$. Light blue spheres represent Al, green spheres Li, purple for Mn, blue for Co, silver for Ni and the small red sphere represent O atoms. (b) Transition metal layer configuration for NMC-111, (c) Al swapped with Mn, (d) Al swapped with Ni, and (e) Al swapped with Co. The dashed circles represent the first and second nearest neighbors to Al atoms. The values of energy at the bottom of panels (c) to (e) represent the thermodynamic energy change after swapping Al from the surface layer with different transition metal centers in the bulk of NMC-111.

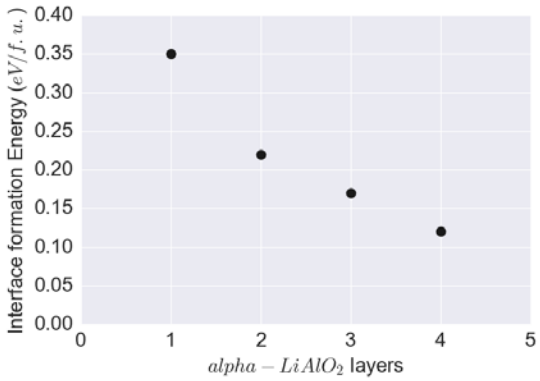


Figure II-233. Change in NMC/$LiAlO_2$ interface formation energy with thickness of α-$LiAlO_2$ and a disordered layer at the surface.

The ion ordering within the TM layer of NMC-111 is shown in Figure II-232b. This configuration allows the simulation of different environments for Al if different TM cations (from NMC) are swapped with Al from the surface $LiAlO_2$ layers. The only thermodynamically favorable configuration is the interchange of Al with Mn as shown in Figure II-232c. In this configuration the Al atom is exclusively surrounded by Ni and Co while the second nearest neighbors within the TM layer maintains the NMC-111 configuration. The negative number for the energy means that it is 0.52 eV more stable than the original configuration shown in Figure II-232b. All the configurations with Mn as a first neighbor (to Al) produce a positive change in energy with respect to the reference configuration (Figure II-232d and Figure II-232e). This result shows that Al prefers to be surrounded by Co and Ni cations (not Mn) in the TM layers of NMC. The existence of Mn in the TM layer can, therefore, greatly block the diffusion of Al from the surface to the bulk of the NMC particles. Previous work has also shown that there is a driving force for Co-Al clustering in Ni-rich environments.

**Electrochemical Modeling**

The focus of electrochemical modeling studies this year has been on side reactions and crosstalk in lithium-ion cells. An interesting study conducted within this program is utilized to establish and help calibrate a proposed model [6]. In that study, constant voltage relaxation currents for NMC//graphite (Gr), Li, or LTO, in standard and special coin and pouch cells, were measured over a wide range of voltages and conditions. Most noteworthy are the long relaxation time constant of 10s of hours and the final $\mu A/cm^2$ level currents observed. The study also proposes a series of side reactions on both electrodes (Figure II-234a).

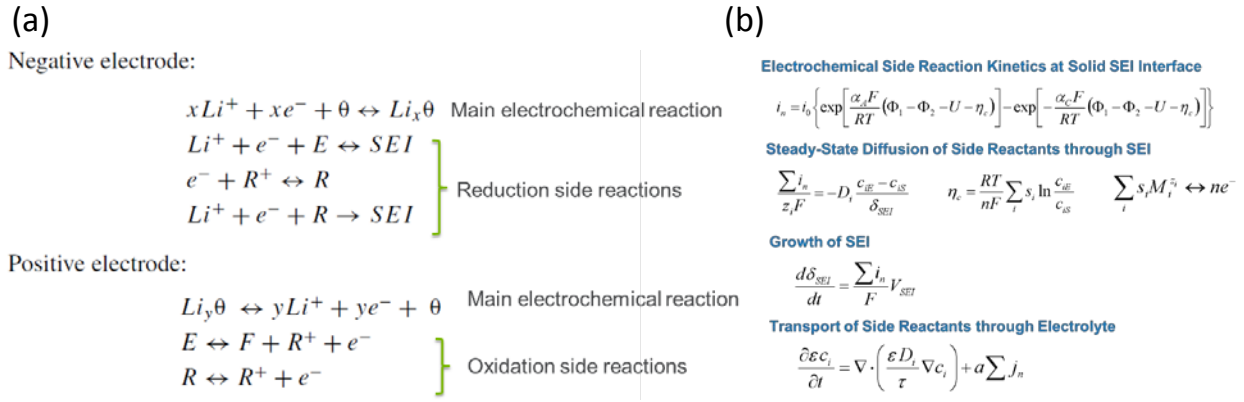


Figure II-234. (a) Proposed side reaction mechanism from ref. 11. (b) Electrochemical model for transport and reaction of side reaction components.

An earlier study on oversized negative electrodes indicated that long cell time constants can arise from edge effects [7]. Applying the electrochemical model to the present study, a long relaxation time constant was observed for the lithium concentration in the negative, however, the cell current relaxed relatively quickly. Ignoring the edge effects, the standard electrochemical model was modified to account for SEI growth, reactant species electrolyte transport, and side reaction kinetics and thermodynamics as given in Figure II-234b. Initial studies with the electrochemical model indicated that, when one electrode has a flat open circuit voltage (OCV) curve (e.g., graphite electrode) and one has a sloping OCV (e.g., NMC), the constant voltage relaxation current at long times is controlled by side reactions occurring at the electrode with the sloping OCV. A previous cell aging study was utilized in order to estimate the level of side reactions on the graphite negative [7]. As shown in Figure II-235, the slow relaxation can be modeled with a combination of SEI growth and reactant stabilization. This was accomplished with a relatively high initial side reactant concentration in the electrolyte and a slow SEI growth rate. While the current level and the long time constant can be matched, a close comparison of the relaxation indicates further improvement in the fitting is needed.

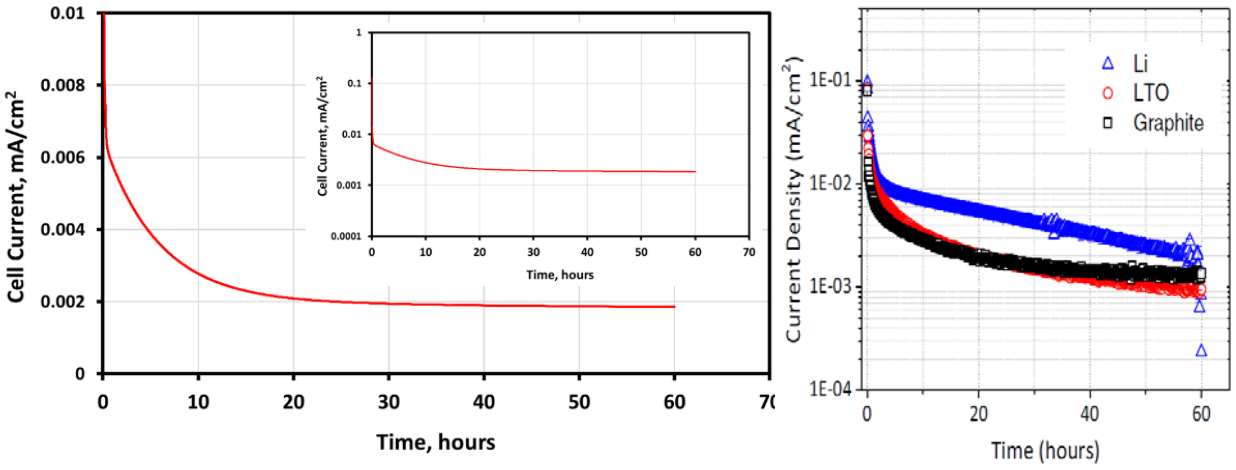


Figure II-235. (a) Full electrochemical model relaxation of an NMC//Gr cell. (b) Relaxation results with NMC cathode and indicated anode from ref. 11.

## Conclusions

DFT calculations have been used to understand the pristine structure of NMC cathode surfaces where the (012) facet of NMCs has been shown to be one of the most prevalent and reactive surfaces. The (012) structure was further utilized in calculations to understand the interaction of electrolyte solvent and additive molecules on pristine and charged cathodes. It was found that, in Gen2, EC preferentially oxidized relative to EMC via hydrogen abstraction and subsequent reduction of surface TMs. Conversely, select fluorinated solvents (HFDEC and DFEC) were found to interact only weakly with the cathode surface. Oxidation of the phosphite additive molecule, TTFP, was found as a possible trigger to surface oxygen loss and phase transformation, whereas the phospite additive molecule, TMSPi, was found to decompose on the (012) surface and create a passivating phosphate-based film. Interestingly, the use of a different phosphite molecule, TEPi, led to higher TM dissolution and impedance rise.

Studies on TM segregation have revealed a driving force for Co segregation to the (104) facet and the observed tendency for Ni segregation to the (012) facet of some NMCs was found to be related to the formation tendency of Li/Ni ant-site defects.

Detailed calculations of $Al_2O_3$-based coatings on NMCs suggest that an interfacial phase of α-$LiAlO_2$, between NMC surfaces and the bulk, coating phase, could stabilize surface structures such as γ-$LiAlO_2$. In addition, substitution of Al into the surfaces of NMCs favors Al surrounded by Co and Ni (e.g., Mn/Al exchange).

Initial electrochemical modeling results show that experimental data, related to side reactions and crosstalk in lithium-ion cells, can be understood in terms of a modified electrochemical model. Electrolyte transport of reactive species, SEI growth, and side reaction kinetics and thermodynamics were incorporated and qualitative agreement with experimental data was achieved. These results bode well for continuing studies aimed at understanding crosstalk in NMC//Gr systems.

**Chapter Acknowledgments** Hakim Iddir, Juan Garcia, Guoying Chen, Jian Zhu, Dennis Dees, Daniel P. Abraham, John Zhang, Adam Tornheim, Meinan He, James A. Gilbert, Cameron Peebles, Ritu Sahore, Juan Garcia, Javier Bareño, Chen Liao, Iyla A. Shkrob, Baris Key, Jack Vaughey, Binghong Han, Fulya Dogan

## Key Publications

1. Binghong Han, Baris Key, Saul H. Lapidus, Juan C. Garcia, Hakim Iddir, John T. Vaughey, Fulya Dogan, ACS Appl. Mater. Interfaces, DOI: 10.1021/acsami.7b13597 (2017).

2. Han, T. Paulauskas, B. Key, C. Peebles, J.S. Park, R.F. Klie, J.T. Vaughey, and F. Dogan, ACS Appl. Mater. Interfaces **9**, 14769 (2016).
3. F. Dogan, J.T. Vaughey, H. Iddir, and B. Key, Appl. Mater. Interfaces **8**, 16708 (2016).
4. B. Han, C. Peebles, T. Paulauskas, J.T.Vaughey, F. Dogan, *Effects of Sintering Temperature and Cathode Composition on $Al_2O_3$ Coatings of Li-ion Cathodes*, 231st ECS Meeting, New Orleans, May 28th (2017).
5. B. Han, C. Peebles, T. Paulauskas, J.T.Vaughey, F. Dogan, *Characterization of $Al_2O_3$ Coatings on Li-ion Cathodes: Effects of Annealing Temperature and Composition*, 2017 MRS, Phoenix, April 17th (2017).

## References


1. J. Garcia, J. Bareño, J. Yan, G. Chen, A. Hauser, J.R. Croy, and H. Iddir, Phys. Chem. C 121, 8290 (2017).
2. R. Sahore, A. Tornheim, C. Peebles, J. Garcia, F. Dogan, B. Key, D. O'Hanlon, C. Liao, H. Iddir, Z. Zhang, J. Bareño, I. Bloom, *Insights into the reactions of tris(2,2,2-trifluoroethyl) phosphite additive in high-voltage, lithium-ion cells* (*submitted*, J. Mat. Chem. A, 2017).
3. A. Tornheim, S. Sharifi-Asl, J. Garcia, H. Iddir, R. Shahbazian-Yassar, Z. Zhang. *Effect of electrolyte composition on rock-salt surface degradation in NMC cathodes during high voltage potentiostatic holds* (*in preparation*).
4. C. Peebles, R. Sahore, J.A. Gilbert, J.C. Garcia, A. Tornheim, J. Bareño, H. Iddir, C. Liao, and D.P. Abraham, D. P., J. Electrochem. Soc. **164**, A1579 (2017).
5. A. Tornheim, C. Peebles, J.A. Gilbert, R. Sahore, J.C. Garcia, J. Bareño, H. Iddir, C. Liao, and D.P. Abraham, D. P., Journal of Power Sources **365**, 201 (2017).
6. N. Vadivel, S. Ha, M. He, D. Dees, S. Trask, B. Polzin, and K. Gallagher, J. Electrochem. Soc. **164**, A508 (2017).
7. B. Long, S. Rinaldo, K. Gallagher, D. Dees, S. Trask, B. Polzin, A. Jansen, D. Abraham, I. Bloom, J. Bareno, and J. Croy, J. Electrochem. Soc. **163**, A2999 (2016).

## II.C.4 Studies on High Capacity Cathodes for Advanced Lithium-Ion (ORNL)

**Jagjit Nanda, Principal Investigator**
Oak Ridge National Laboratory
1 Bethel Valley Road
Oak Ridge, TN 37831-6124
Phone: 865-241-8361; Fax: 865-574-4357
E-mail: nandaj@ornl.gov

**Tien Duong, Technology Manager**
U.S. Department of Energy
Phone: 202-586-7836
E-mail: Tien.Duong@ee.doe.gov

Start Date: October 1, 2015 End Date: September 30, 2018
Total Project Cost: $400,000 DOE share: $400,000 Non-DOE share: $0

### Project Introduction

Development of high energy density, low-cost, and safe electrode materials is one of the key enablers for advanced batteries for transportation. Currently, one major technical barrier towards development of high energy density lithium-ion batteries is the lack of robust, high-capacity cathodes. Traditional layered $LiMO_2$ (M = Mn, Co, Ni, etc.) cathodes cannot reversibly cycle their entire Li supply (e.g., $x \leq 0.5$ in $Li_{1-x}CoO_2$). When charged beyond ~4.3 V vs. Li/Li+, many lithium-transition metal oxide cathodes undergo irreversible structural changes with concomitant oxygen gas evolution, resulting in irreversible capacity loss and voltage fade during cycling.[1-3] Understanding and addressing these structural instabilities is of vital importance to design next-generation cathode materials which can better utilize their Li supply without sacrificing cycle life.

In FY16, we developed $Li_2Cu_{0.5}Ni_{0.5}O_2$ cathodes which have a very high theoretical capacity of 250 mAh/g (assuming complete Li extraction).1 Nearly 400 mAh/g of capacity was obtained during the first charge, but only ~125 mAh/g was reversible. The large first-cycle irreversible loss is attributed to oxygen evolution and irreversible structural transformations. To address these issues, Q1 of FY17 focused on developing a new sol-gel synthesis route to produce carbon-coated Ni-rich $Li_2Cu_xNi_{1-x}O_2$ cathodes (x = 0.6).

We also developed $Li_2MoO_3$ cathodes which may be used as a structural stabilizing unit in layered-layered composite cathodes. [4, 5] $Li_2MoO_3$ has $R\bar{3}m$ symmetry and thus is expected to coherently blend with traditional layered $LiMO_2$ materials. Furthermore, Mo can access multiple oxidation states (e.g., Mo4+ - Mo6+), allowing for reversible Li storage in both the $Li_2MoO_3$ and $LiMO_2$ moieties. Finally, $Li_2MoO_3$ is expected to have improved oxidative stability compared to Li2MnO3 due to reversible anionic charge compensation.[4] To aid the development of composite x $Li_2MoO_3$ •(1-x)$LiMO_2$ cathodes, detailed structural analysis of the $Li_2MoO_3$ component was performed in FY17. The oxidative stability and structural evolution of these cathodes were evaluated using a suite of advanced characterization methods including in-situ mass spectrometry, Raman spectroscopy, synchrotron X-ray diffraction (XRD), and transmission electron microscopy (TEM). Combining the information gained from these experiments, new insights are made on the possible use of $Li_2MoO_3$ in layered-layered composite cathodes to be developed in FY18.

### Objectives

- Synthesize Ni-rich $Li_2Cu_xNi_{1-x}O_2$ cathodes with x = 0.2 and 0.3 and evaluate their high voltage capacity and oxidative stability [goal of > 225 mAh/g, 25 cycles].
- Complete *in-situ* and *ex-situ* x-ray, neutron, and spectroscopic studies of Ni-rich $Li_2Cu_xNi_{1-x}O_2$ and related high voltage cathode compositions.

- Synthesis of one particular class and composition of disordered cathodes-$Li_2MoO_3$ and/or Cr substituted $Li_2MoO_3$.
- Complete structural and electrochemical performance analysis of disordered cathodes-Li2MoO3 and/or Cr substituted $Li_2MoO_3$.

## Approach

We employ a number of synthesis routes including solid state, hydrothermal, solvothermal, and sol-gel reactions to produce cathode materials. The cathode compositions and phases are selected based on: (i) phase diagram analysis and modeling from work by Ceder and others, (ii) thermal safety, and (iii) materials availability and cost. When appropriate, we utilize ORNL's expertise to produce thin film electrodes with these new chemistries. Thin film electrodes do not require polymer binders or conductive carbon additives, and can therefore facilitate our understanding of the intrinsic properties of the cathode material. We also have an active interest in developing coatings that can improve cathode properties such as conductivity or interfacial stability. For optimizing our cathode synthesis process and improving cell level performance, we correlate electrochemical properties with information obtained from advanced characterization methods including micro-Raman spectroscopy, mass spectrometry, microscopy, and X-ray and neutron diffraction.

## Results

*Accomplishments*

- A sol-gel synthesis route was developed to produce carbon-coated Ni-rich $Li_2Cu_xNi_{1-x}O_2$ (x = 0.6). During the 1st charge cycle, the material undergoes an irreversible structural transition from orthorhombic to trigonal phase accompanied by oxygen loss.
- Synthesis conditions to produce phase-pure $Li_2MoO_3$ powders and sputtered thin films with the desired structure were identified.
- *In-situ* mass spectrometry studies demonstrate that $Li_2MoO_3$ cathodes have very stable lattice oxygen and do not evolve $O_2$ or $CO_2$ gases even when charged to very positive potentials (e.g., 4.8 V vs. $Li/Li^+$). This unique property makes $Li_2MoO_3$ a promising candidate for stabilizing the structure of layered-layered composite cathodes.
- Investigate solid-state and sol-gel synthesis routes to produce composite layered-layered cathodes with the general formula $xLi_2MoO_3•(1-x)LiMO_2$. Identify stable phases with the compositional space with x = 0.2 - 0.4 and M = Mn, Ni, and/or Co. The initial goal is to achieve capacities in the range of 225 mAh/g with low or minimal lattice oxygen evolution at potentials > 4.4 V vs. $Li/Li^+$.
- Explore fluorine substitution in Mo-based cathodes as a strategy to increase their operating potential and/or oxidative stability.
- Perform additional studies with the sputtered thin film $Li_2MoO_3$ cathodes. Unlike conventional slurry cast cathodes, the thin films have a dense structure which is absent of conductive carbon and polymer binder. These properties will facilitate interpretation of XPS and EIS experiments to better understand the fundamental characteristics (e.g., charge compensation mechanism, charge transfer kinetics, and Li transport rates) of $Li_2MoO_3$ cathodes.

*Redox Activity of Ni-Rich $Li_2Cu_xNi_{1-x}O_2$ Cathodes*

In FY16 we successfully synthesized $Li_2CuO_2$ and $Li_2Cu_{0.5}Ni_{0.5}O_2$ compositions and studied their capacity retention, oxidative stability, and structural transformation during cycling. Substituting 50% Ni at Cu sites improved the redox voltage and stability. In Q1 of FY17 we focused on stabilizing Ni-rich $Li_2Cu_xNi_{1-x}O_2$ with x = 0.60. This was necessary before trying to achieve a higher Ni-content of around 75%. Additionally, we aimed to improve the electrochemical kinetics by using adipic acid (AA) as a chelating agent which formed an amorphous carbon coating and reduced the primary particle size (determined from EDX and SEM, results

not shown). Figure II-236 shows cyclic voltammograms (CV) of $Li_2Cu_{0.4}Ni_{0.6}O_2$ synthesized with molar ratios of AA ranging from 0 to 0.75 relative to the overall metal-ion content. During the 1st charge cycle the material underwent an irreversible structural transition from orthorhombic to trigonal phase accompanied by oxygen loss as reported earlier. The 2nd cycle CV represents the signature of $Li_2Cu_xNi_{1-x}O_2$ redox activity with two broad oxidation peaks at 3.9 and 3 V. The corresponding reduction peaks were shifted by 300 mV towards lower voltage implying significant kinetic barrier. These electrochemical test data also show lower capacity compared to $Li_2Cu_{0.5}Ni_{0.5}O_2$, and as such, the focus during the remainder of FY17 was shifted to the development of disordered Mo-based cathodes.

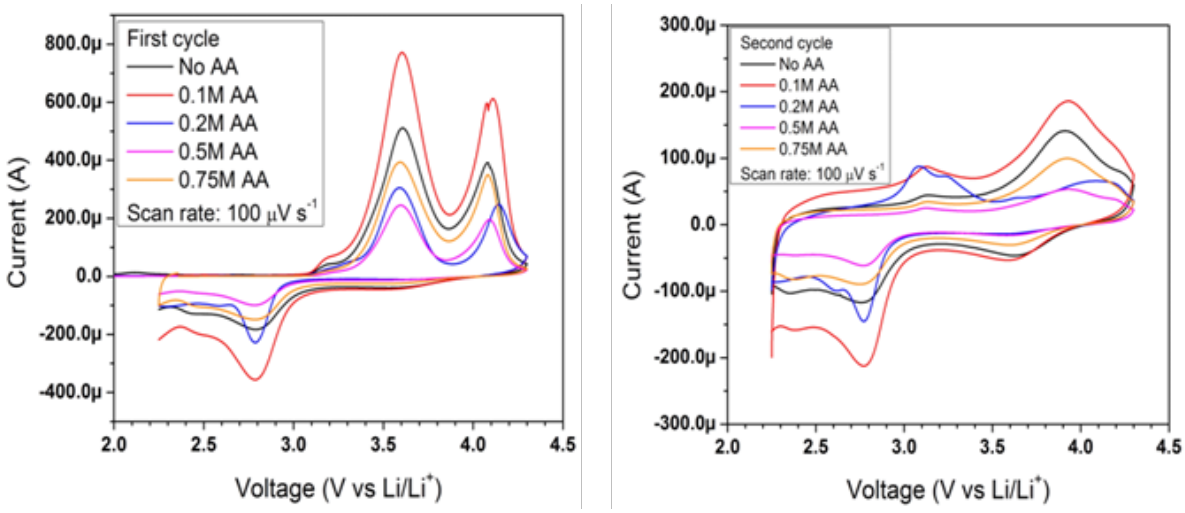


Figure II-236. CV during 1st and 2nd charge-discharge cycle for $Li_2Cu_{0.4}Ni_{0.6}O_2$ synthesized using sol-gel method using a chelating agent adipic acid (AA).

*Synthesis and Redox Properties of $Li_2MoO_3$ Cathodes*

We investigated the stability and oxygen activity of a new multi-lithium cathode composition, $Li_2MoO_3$. The goal of this study was not to use this material as a high voltage cathode candidate, but rather to consider this as one of the structural units for composite cathodes with the general formula $xLi_2MoO_3•(1-x)LiMO_2$. $Li_2MoO_3$ was synthesized through the reduction of $Li_2MoO_4$ powder at 675°C for 12 or 48 h under flowing $Ar/H_2$. As shown in Figure II-237a, the shorter reaction time resulted in mixed phases of $LiMoO_4$ and $Li_2MoO_3$, whereas the product obtained after 48 h contained phase-pure $Li_2MoO_3$ (used for all subsequent experiments) with $R\bar{3}m$ symmetry. The scanning electron microscopy (SEM) image in Figure II-237b shows the $Li_2MoO_3$ powder consisted of irregularly shaped particles which were on the order of 1 – 10 μm in size.

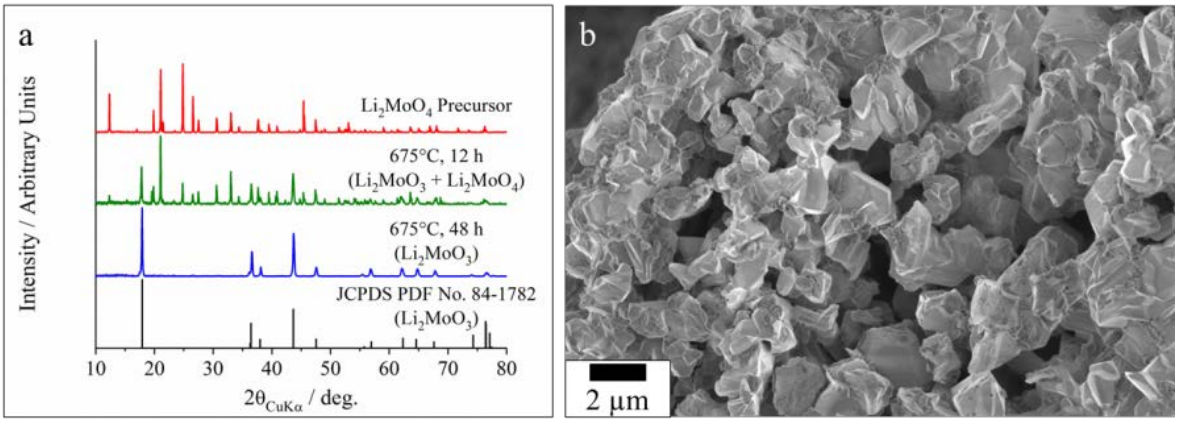


Figure II-237. (a) X-ray diffraction (XRD) patterns for as received $Li_2MoO_4$ precursor and the synthesized $Li_2MoO_3$. (b) Scanning electron microscopy (SEM) image of the synthesized $Li_2MoO_3$ particles.

The electrochemical properties of slurry cast $Li_2MoO_3$ cathodes were characterized through galvanostatic charge/discharge experiments in half cells. During the first charge cycle, a sloping potential profile over 3.6 – 4.8 V vs. $Li/Li^+$ was observed with a corresponding delithiation capacity of 223 $mAh/g_{Li2MoO3}$ (see Figure II-238a). The theoretical capacity of $Li_2MoO_3$ assuming complete Li extraction is 340 mAh/g, indicating 34% of the Li remained in the cathode structure after charging to 4.8 V. Upon the first lithiation cycle, a dramatically different profile was observed with a reversible capacity of 147 $mAh/g_{Li2MoO3}$ (corresponding to 0.86 Li cycled per Mo) and an average operating potential ~2.5 V vs. $Li/Li^+$. The large hysteresis between the charge and discharge steps suggests that an irreversible phase transformation occurred during the first cycle. During subsequent cycles, the cathode showed gradual changes to the voltage profile in which most of the redox activity occurred at potentials < 3.5 V vs. $Li/Li^+$ due to the oxidation/reduction of the Mo reaction center. The sloping nature of these profiles suggests that the lithiation/delithiation proceeded through a single, disordered phase rather than a two-phase intercalation reaction. After 50 cycles, the electrode exhibited moderate voltage fade with a reversible capacity of 119 mAh/g (see Figure II-238b). Note that the spurious data point at cycle 31 was due to a temporary power outage of the battery testing equipment.

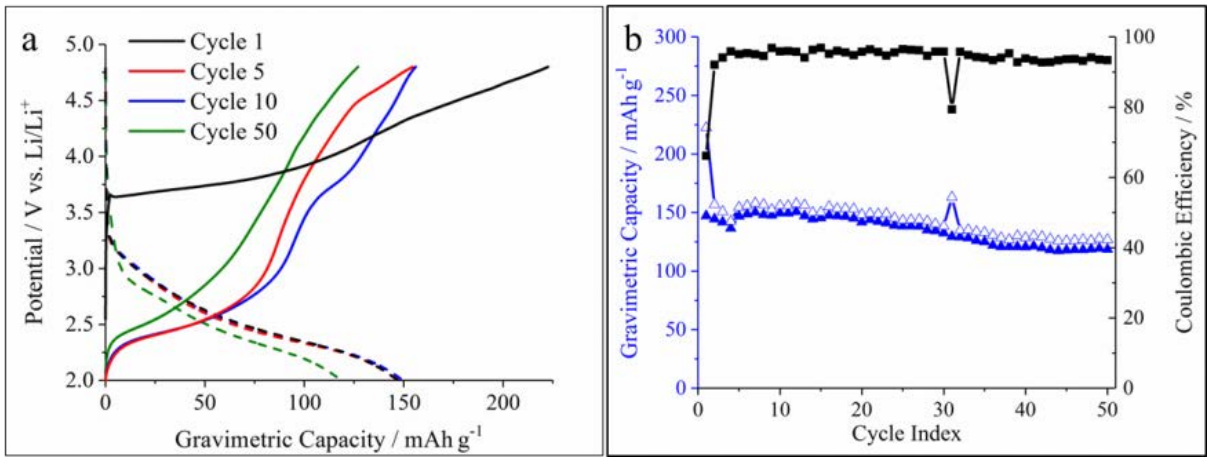


Figure II-238. (a) Charge/discharge curves and (b) cycling stability for a $Li_2MoO_3$ cathode cycled between 2.0-4.8 V vs. $Li/Li^+$ at 10 $mA/g_{Li2MoO3}$.

*Stability of Lattice Oxygen in $Li_2MoO_3$ Cathodes*

Under the aggressive cycling tests used in Figure II-238 (i.e., charging up to 4.8 V vs. $Li/Li^+$), the oxygen lattice in most conventional cathodes (e.g., $LiMO_2$) becomes unstable, resulting in evolution of $O_2$ or $CO_2$ gas and poor cycling stability caused by this irreversible structural change. To evaluate the oxidative stability of $Li_2MoO_3$, *in-situ* mass spectrometry was used to measure gas evolution which occurred during electrochemical delithiation/lithiation. The measured potential and gas profiles are shown in Figure II-239. After a 1 h rest at open-circuit, the background $O_2$ and $CO_2$ levels (due to evaporation of the electrolyte) were 0.23 and 0.16%, respectively. Upon galvanostatically charging/discharging the cell, the $O_2/CO_2$ gas levels remained at or below their baseline values, demonstrating that the lattice oxygen in $Li_2MoO_3$ is stable up to 4.8 V vs. $Li/Li^+$. Interestingly, the liquid carbonate-based electrolyte may be expected to decompose to $O_2/CO_2$ gases beyond its anodic stability limit (approximately 4.5 V vs. $Li/Li^+$), but this was not observed here. One possible explanation is that the electrolyte decomposed to form solid species which were not detectable with the mass spectrometry setup.

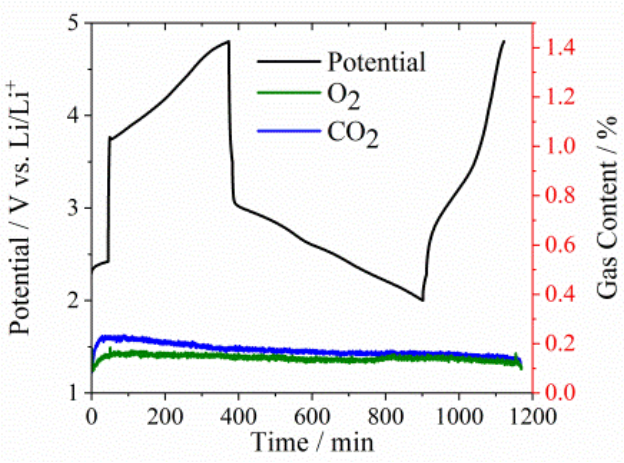


Figure II-239. *In-situ* mass spectrometry results showing the potential profile and measured $O_2$ and $CO_2$ levels evolved from the cell during charge and discharge.

*Structural Evolution of $Li_2MoO_3$ Cathodes*

A series of *ex-situ* X-ray diffraction (XRD) were performed to assess how the $Li_2MoO_3$ structure evolved during the first cycle. In these studies, the cathodes were cycled galvanostatically to predetermined voltage followed by a 5 h potential hold. The harvested cathodes were then thoroughly rinsed with dimethyl carbonate and dried prior to characterization. Figure II-240b shows synchrotron XRD patterns collected for the cathodes at various stages during initial lithiation/delithiation. For the pristine powder, the integrated intensity of the (003)/(104) diffraction peaks was 1.3, indicating the presence of a well-ordered R3m structure with little cation mixing (i.e., Mo was located primarily in the 3b sites).[6] The (003)/(104) ratio remained fairly constant (ranging from 1.3 to 1.5) during charging but decreased to 1.04 and 0.73 for electrodes discharged to 2.00 and 2.50 V vs. $Li/Li^+$, respectively. This result indicates that upon discharge, the $Li_2MoO_3$ became more disordered (i.e., some Mo migrated to the 3a sites) compared to the pristine sample.

In addition to changes in the (003)/(104) ratio, the $Li_2MoO_3$ diffraction peaks became broader with attenuated intensity during the first cycle, indicating a decrease in crystallinity. To qualitatively determine the extent of amorphization, the integrated intensity of the $Li_2MoO_3$ (003) diffraction peak was divided by that of the Al current collector's (111) peak. Since all samples had approximately the same loading ($2.77 \pm 0.80$ $mg_{Li2MoO3}/cm^2$), decreases in the $(003)_{Li2MoO3}/(111)_{Al}$ ratio correspond to lower crystallinity of the $Li_{2-x}MoO_3$ phase. The pristine electrode had a $(003)_{Li2MoO3}/(111)_{Al}$ ratio of 0.67 which rapidly decreased to 0.12 at the end of charge. Upon lithiation, this ratio remained relatively unchanged, indicating the $Li_2MoO_3$ irreversibly lost much of its crystallinity during the first charging cycle.

The irreversible structural transformation which occurred during the first cycle was also explored using *ex-situ* Raman spectroscopy. Figure II-240c shows Raman spectra for $Li_2MoO_3$ cathodes harvested at various stages during the first cycle. The pristine $Li_2MoO_3$ powder and slurry cast cathode exhibited several distinct Raman bands which agree well with previous reports.[5,7] The Raman signature was unchanged when charging to 3.75 V vs. $Li/Li^+$. However, when charging to 4.0 V (corresponding to a capacity of 113 mAh/g and a cathode stoichiometry of $Li_{1.33}MoO_3$), dramatically different spectra were recorded. Specifically, two broad bands appeared which were centered around 300 and 880 $cm^{-1}$ and contained multiple convoluted peaks. These features changed subtly throughout the lithiation/delithiation process, but the electrode clearly did not return to the original structure when re-lithiated to 2.0 V vs. $Li/Li^+$. These Raman results substantiate the conclusions drawn from the XRD analysis and indicate a disordered amorphous phase formed during the first cycle.

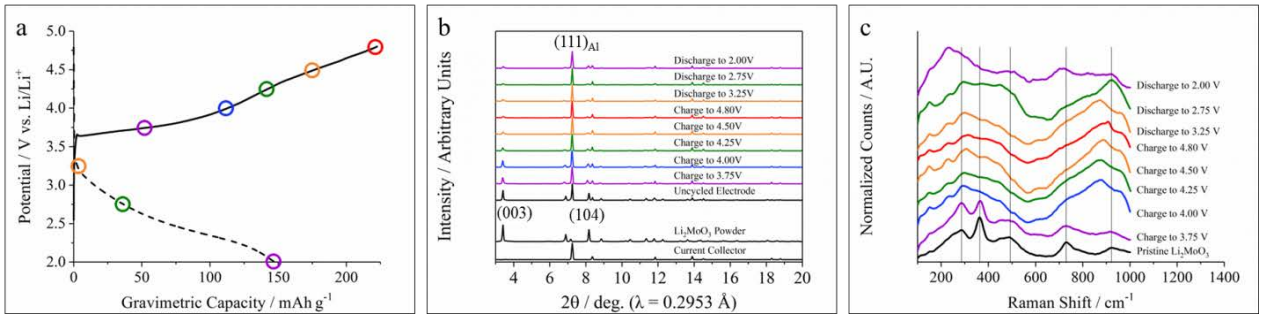


Figure II-240. (a) Charge/discharge curve during the first cycle of a $Li_2MoO_3$ cathode. (b) *Ex-situ* synchrotron XRD patterns collected at various stages during the first cycle. (c) *Ex-situ* Raman spectra collected at various stages during the first cycle.

To understand how the structure evolved beyond the first cycle, additional XRD data (using Cu Kα radiation, λ = 1.540562 Å) and Raman spectra were collected on cathodes in either the charged or discharged states after 10 cycles (results not shown here). The diffraction peaks of the electrodes after 10 cycles were extremely weak, and the Raman spectra contained broad bands similar to those observed during the first charge/discharge cycle (Figure II-240c). Overall, the results demonstrate the lithiation/delithiation of $Li_2MoO_3$ proceeded through an amorphous phase rather the crystalline solid solution mechanism proposed by Ma et al. [4]

The amorphous $Li_{2-x}MoO_3$ phase which formed during cycling was also characterized using *ex-situ* transmission electron microscopy (TEM). Figure II-241 shows the morphology (a-d) and selected area electron diffraction (SAED) patterns (e-h) for electrodes cycled 0, 1, 2, and 50 times. The pristine sample showed the presence of a highly crystalline $Li_2MoO_3$ phased as indicated by the periodic spacing of the diffraction spots (collected from the [100] zone axis). After 1 and 2 cycles, the SAED patterns contained a few, low intensity spots corresponding to a crystalline phase with $R\bar{3}m$ symmetry. However, these samples show predominantly diffuse patterns indicating the formation of amorphous phases nucleated randomly throughout the material. After 50 cycles (Figure II-241h), the SAED pattern was very diffuse, indicating the cathode became completely amorphous after extended cycling.

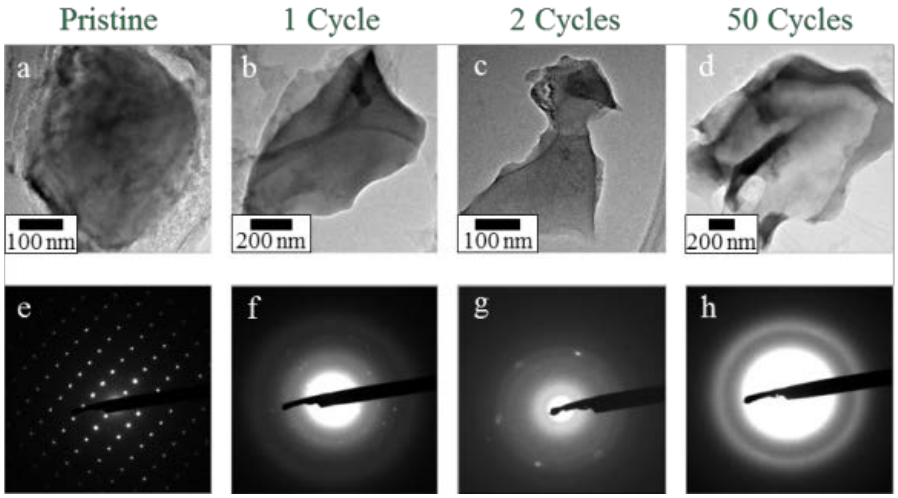


Figure II-241. (a-d) Transmission electron microscopy (TEM) images and (e-h) corresponding selected area electron diffraction (SAED) patterns for a $Li_2MoO_3$ cathode before cycling and after 1, 2, and 50 cycles.

*Investigation of Sputtered Thin Film $Li_2MoO_3$ Cathodes*

Interpreting *in-situ* and *ex-situ* data collected with traditional slurry cast electrodes is oftentimes complicated by the presence of conductive carbon and polymer binder which may produce signals that overlap with or dominate the desired signal from the active material. For example, the Raman scattering intensity from the conductive additive is generally much stronger than that of Li metal oxide cathode materials. Sputtered thin film cathodes composed entirely of active material can potentially resolve these issues, and thus experiments during Q4 focused on preparing and characterizing $Li_2MoO_3$ thin film cathodes for comparison with previous results obtained with traditional slurry cast electrodes.

$Li_2MoO_3$ films with thicknesses ranging from 1.0 – 1.2 µm were sputtered onto a Pt-coated $Al_2O_3$ substrate followed by heating at 675°C for 2 h under flowing $Ar/H_2$ (96/4). Figure II-242a shows a cross-sectional scanning electron microscopy (SEM) image of the resulting film which was uniform and dense in appearance. The X-ray diffraction (XRD) patterns in Figure II-242b demonstrate a phase-pure $Li_2MoO_3$ film with $R\bar{3}m$ symmetry was produced, and all diffraction peaks of this film could be assigned to either $Li_2MoO_3$ or the Pt-coated $Al_2O_3$ substrate.

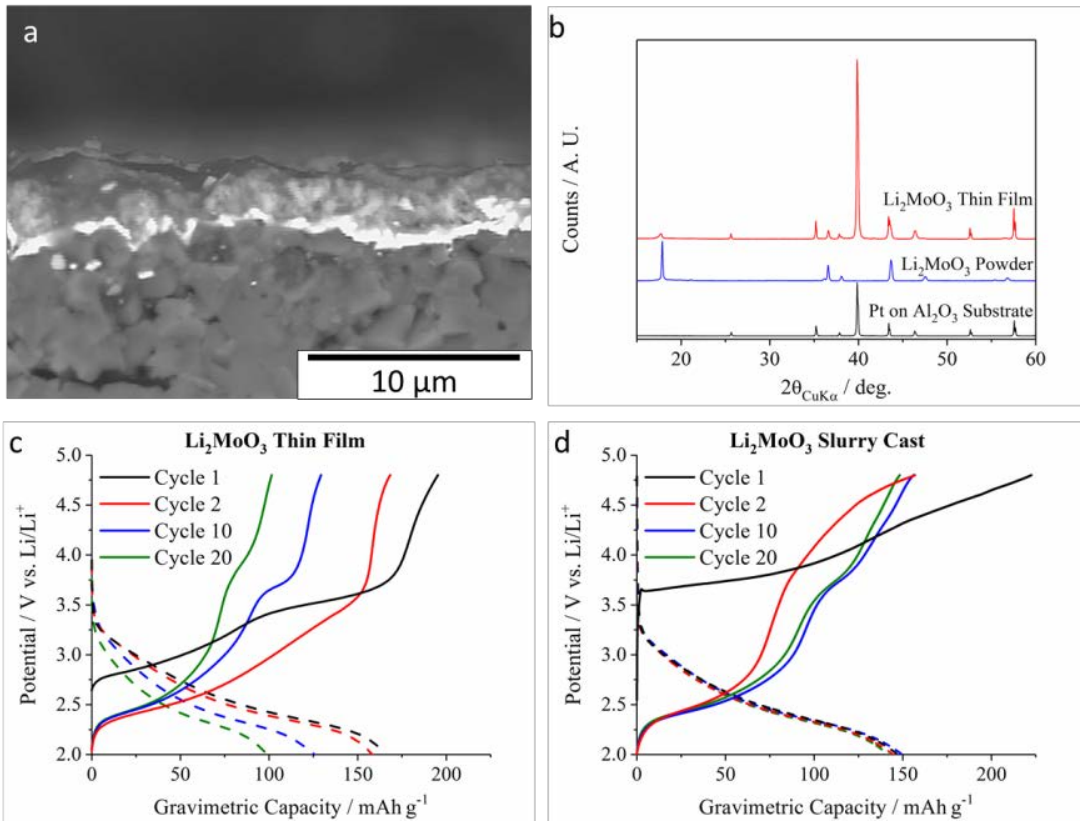


Figure II-242. (a) Cross-sectional SEM image of a sputtered thin film $Li_2MoO_3$ cathode. (b) XRD pattern of a sputtered $Li_2MoO_3$ thin film, $Li_2MoO_3$ powder, and the sputtering substrate (Pt on $Al_2O_3$). Galvanostatic charge/discharge curves for half-cells containing a (c) thin film $Li_2MoO_3$ cathode and (d) slurry cast $Li_2MoO_3$ cathode.

Galvanostatic charge/discharge experiments were conducted between 2.0 – 4.8 V for coin cells containing a $Li_2MoO_3$ thin film cathode and a Li metal anode. As shown in Figure II-242c, the cathodes exhibited an initial charge capacity of 190 mAh/g and reversible capacity of 166 mAh/g. The voltage profile and initial capacities of the thin films are in reasonable agreement with our previous studies on slurry cast $Li_2MoO_3$ cathodes (223 and 147 mAh/g, respectively, see Figure II-242d). However, while these slurry cast electrodes demonstrated excellent cycling stability, the thin film cathodes showed moderate capacity fade over 20 cycles. Future work

on the thin film $Li_2MoO_3$ cathodes will include additional synthesis and electrochemical characterization to understand the cause of this capacity fade. Despite this discrepancy, *ex-situ* Raman spectroscopy and XRD studies indicated that cycling the thin films induced a crystalline to amorphous transformation similar to that shown in Figure II-240 (results for thin films not shown). Unlike conventional slurry cast electrodes which contain complex pore structures, the planar structure of the sputtered thin films is ideal for studying the charge transfer kinetics and $Li^+$ transport rates in $Li_2MoO_3$ using electrochemical impedance spectroscopy (EIS). These experiments will be initiated in FY18 to provide complementary information to that obtained with conventional electrode architectures.

## Conclusions

A sol-gel synthesis route was developed to produce Ni-rich $Li_2Cu_{0.4}Ni_{0.6}O_2$ cathodes, but these materials exhibited lower capacity compared to $Li_2Cu_{0.5}Ni_{0.5}O_2$ developed in FY16. As such, the focus during the remainder of FY17 was shifted to the development of disordered Mo-based cathodes. For $Li_2MoO_3$ cathodes, an irreversible crystalline to amorphous transformation was initiated when charging to potentials $\geq$ 4.0 V vs. $Li/Li^+$. This amorphization reaction proceeded with further cycling, and there was no apparent crystallinity remaining in the cathode after 50 cycles. These conclusions are supported by complementary information obtained from X-ray diffraction (XRD), Raman spectroscopy, and transmission electron microscopy (TEM). Interestingly, the amorphization of $Li_2MoO_3$ did not prevent reversible Li storage from occurring. $Li_2MoO_3$ cathodes exhibited an initial reversible capacity of 147 $mAh/g_{Li2MoO3}$ with an average operating potential ~2.5 V vs. $Li/Li^+$. The cathodes retained 81% of their initial capacity after 50 cycles.

*In-situ* mass spectrometry studies demonstrated the amorphization of $Li_2MoO_3$ did not involve the release of lattice oxygen even when charged to very oxidative environments (i.e., 4.8 V vs. $Li/Li^+$). This observation makes $Li_2MoO_3$ quite unique compared to traditional $LiMO_2$ compounds which evolve significant amounts of $O_2$ and/or $CO_2$ at potentials > ~4.5 V vs. $Li/Li^+$. The excellent oxidative stability of $Li_2MoO_3$ may be a useful property to exploit in the preparation of layered-layered composites cathodes (i.e., $xLi_2MoO_3•(1-x)LiMO_2$). Various synthesis strategies will be explored in FY18 to produce such materials.

These studies broadly demonstrate the challenges associated with multi-lithium transition metal oxides, where there is close interplay between structure, transport, and oxygen loss that limits their use as high capacity cathodes for advanced lithium-ion systems.

## Key Publications


1. Probing Multiscale Transport and Inhomogeneity in a Lithium-ion Pouch Cell Using In-situ Neutron Methods, H. Zhou, K. Ann, S. Allu, S. Pannala, J. Li, H. Z. Bilheux, S. K. Martha, J. Nanda, *ACS Energy Letters* 1, 981-86 (2016)
2. High Capacity Cathodes for Advanced Lithium-ion: Challenges and Opportunities 11th Lithium Battery Power & Safety Conference, Nov 1st- 4th, 2016 Baltimore, MD [Invited]
3. Electrochemical Energy Storage Materials: From Transportation to Grid Storage, J. Nanda International Society on Advances in Electrochemical Science & Technology (ISAEST-11), Chennai, India December 7-9th (2016) [Invited]
4. Structural Transformations in High-Capacity $Li_2Cu_{0.5}Ni_{0.5}O_2$ Cathodes, R. E. Ruther, A. S. Pandian, P. Yan, J. N. Weker, C. Wang, J. Nanda, *Chem. Mater.* 29, 2997-3005 (2017)
5. Meso and micron scale chemical and morphological heterogeneities in high capacity battery materials, MRS Spring Meeting. April 17-21, 2017, Phoenix, Arizona [Invited]
6. Structural Transformations in High Capacity $Li_2Ni_{0.5}Cu_{0.5}O_2$ Cathodes, R. Ruther, J. Nanda et al., ECS Spring Meeting May 28th - June 1st 2017, New Orleans, USA

7. High Capacity Multi-lithium Cathodes for Advance Lithium-ion, J. Nanda and R. E. Ruther, *US Drive Highlights (Energy Storage), DOE* (2016)
8. High Capacity Multi-Lithium Oxide Cathodes and Oxygen Stability, R. E. Ruther, E. C. Self, and J. Nanda, *2017 AMR Meeting in Washington, DC* (2017)
9. Oxygen Stability of Disordered, Multi-Lithium Oxide Cathodes for Li-ion Batteries, E. C. Self, R. E. Ruther, G. M. Veith, and J. Nanda, *232nd Meeting of the Electrochemical Society in National Harbor, MD* (2017)

## References


1. R. E. Ruther, H. Zhou, C. Dhital, K. Saravanan, A. K. Kercher, G. Chen, A. Huq, F. M. Delnick, J. Nanda, Synthesis, Structure, and Electrochemical Performance of High Capacity $Li_2Cu_{0.5}Ni_{0.5}O_2$ Cathodes, *Chem. Mater.* **27**, 6746-6754 (2015).
2. M. Sathiya, G. Rousse, K. Ramesha, C. P. Laisa, H. Vezin, M. T. Sougrati, M. L. Doublet, D. Foix, D. Gonbeau, W. Walker, A. S. Prakash, M. Ben Hassine, L. Dupont, J. M. Tarascon, Reversible anionic redox chemistry in high-capacity layered-oxide electrodes, *Nat. Mater* **12**, 827-835 (2013).
3. R. E. Ruther, A. S. Pandian, P. Yan, J. N. Weker, C. Wang, J. Nanda, Structural Transformations in High-Capacity $Li_2Cu_{0.5}Ni_{0.5}O_2$ Cathodes, *Chem. Mater.* **29**, 2997-3005 (2017).
4. J. Ma, Y.-N. Zhou, Y. Gao, X. Yu, Q. Kong, L. Gu, Z. Wang, X.-Q. Yang, L. Chen, Feasibility of Using $Li_2MoO_3$ in Constructing Li-Rich High Energy Density Cathode Materials, *Chem. Mater.* **26**, 3256-3262 (2014).
5. J. Ma, Y. Gao, Z. Wang, L. Chen, Structural and electrochemical stability of Li-rich layer structured $Li_2MoO_3$ in air, *J. Power Sources* **258**, 314-320 (2014).
6. C. Julien, A. Mauger, K. Zaghib, H. Groult, Optimization of Layered Cathode Materials for Lithium-Ion Batteries, *Materials* **9**, 595 (2016).
7. D. Li, H. He, X. Wu, M. Li, Electrochemical behavior of submicron $Li_2MoO_3$ as anodes in lithium-ion batteries, *J. Alloys Compd.* **682**, 759-765 (2016).

## II.C.5 High Energy Density Lithium Battery (Binghamton University)

**M. Stanley Whittingham, Principal Investigator**
Binghamton University (SUNY)
85 Murray Hill Road
Vestal, NY, 13850
Phone: 607-777-4673
E-mail: Stanwhit@binghamton.edu

**Tien Duong, Technology Manager**
U.S. Department of Energy
Phone: 202-586-7836
E-mail: Tien.Duong@ee.doe.gov

Start Date: October 1, 2014 End Date: June 30, 2018
Total Project Cost: $1,265,773 DOE share: $1,265,773 Non-DOE share: $0

### Project Introduction

The project objectives are to develop the anode and cathode materials for high-energy density cells for use in plug-in hybrid electric vehicles (PHEVs) and in electric vehicles (EV) that offer substantially enhanced performance over current batteries used in PHEVs and with reduced cost. Specifically, the goal of this project is to enable cells with an energy density exceeding 1 kWh/liter. The carbon anode in today's Lithium-ion cells will be replaced with a tin-based anode with double the volumetric capacity of carbon. Similarly, the present intercalation cathodes will be replaced by materials, which are capable of reacting with up to two lithium ions per redox ion. Moreover, these cell reactions will occur within the stability limit of today's electrolytes, leading to longer-lived batteries.

### Objectives

We propose to develop the anode and cathode materials for high-energy density cells for use in plug-in hybrid electric vehicles (PHEVs) and in electric vehicles (EV) that offer substantially enhanced performance over current batteries used in PHEVs and with reduced cost. Specifically the primary objectvives are to:

- Increase the volumetric capacity of the anode by a factor of 1.5 over today's carbons by using a SnFeC composite conversion reaction anode
- Increase the capacity of the cathode by using a high capacity conversion reaction cathode, $CuF_2$, and/or using a high capacity 2 Li intercalation cathodes, $VOPO_4$.
- Enable cells with an energy density exceeding 1 kWh/liter.

### Approach

*Innovative Approach*

The approach of this "beyond Li-ion" battery concept is (a) to remove the volume intensive intercalation-based carbon anode in today's Li-Ion batteries, and replace it with a conversion reaction-based material, and (b) to replace the present cathodes that mostly react with less than one Li ion per transition metal ion with cathode materials that can react with more than one Li ion. This latter is similar to the concept of using the divalent magnesium with its two-electron transfer. However, we believe that moving two of the much more mobile singly charged lithium ions is more viable, and moreover today's electrolytes, SEI additives and cell technology can be used. Attainment of the goals proposed here will lead to a 50-100% increase in the volumetric and gravimetric energy storage capability of both the anode and the cathode, which will allow for the realistic attainment of the next generation batteries for PHEV vehicles. At the same time, the science

generated will be applicable to other energy storage systems, such as anodes for Li/S. The anode and cathode components in this approach are:

1. A SnFeC composite for the anode which reacts by a conversion mechanism giving $Li_xSn$ and Fe.
2. A $CuF_2$ containing material for the cathode which reacts with 2 Li ions by a conversion mechanism giving Cu and LiF.
3. A $VOPO_4$ containing cathode which reacts with up to 2 Li ions by an intercalation mechanism giving $Li_2VOPO_4$.

The optimized anode and cathode from the above will then be combined in a full cell.

## Results

We have achieved the following progress:

*The Fe/Sn/C anode*

Last year we reported the excellent cycling of the Fe/Sn/C composite anode formed by a mechanochemical process. This year we have developed an alternative approach, that is more scaleable, to produce a $Sn_2Fe/Sn_5Fe$ mixture. The first 550 cycles of this material are shown in Figure II-243 for two voltage regimes. Although charging to 1.5 volts leads to a larger capacity, much of the added capacity is at too large a potential to be useful in a full cell. The capacity can be increased slightly by replacing a part of the iron by copper as shown in Figure II-244. After 200 cycles the capacities were 465 mAh/g and 1.26 Ah/cc at the C/2, significantly higher than that of graphite.

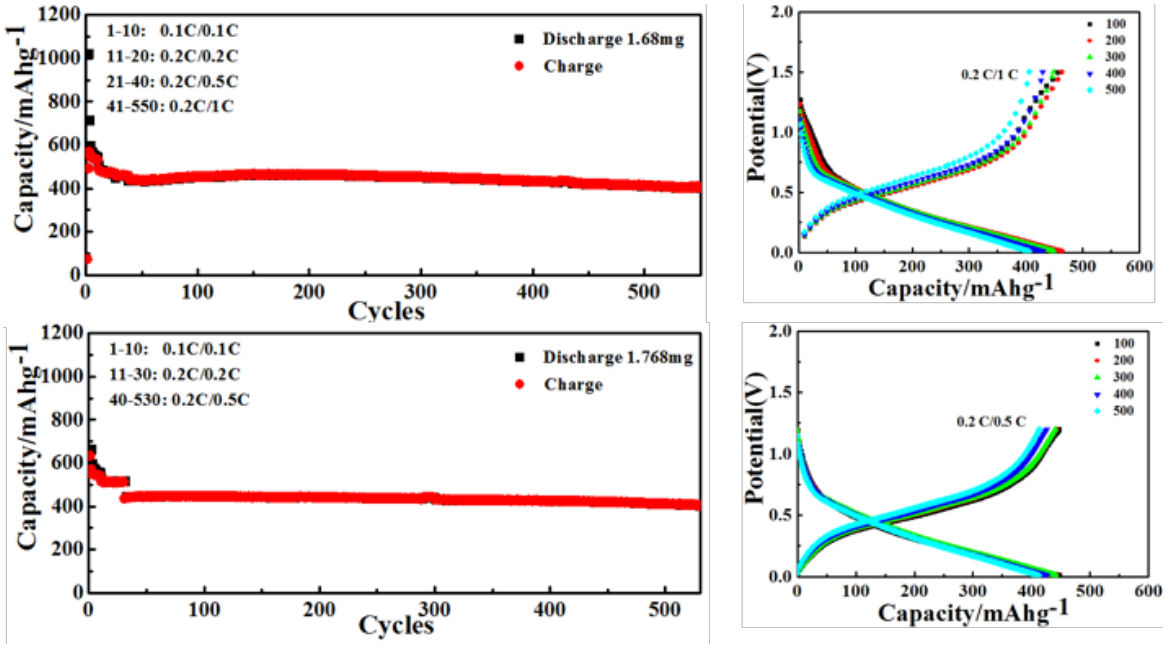


Figure II-243. Cycling capacity of the $Sn_yFe$ anode vs Li, in the voltage regimes (a) 0.01 – 1.5 volts and (b) 0.01 – 1.2 volts.

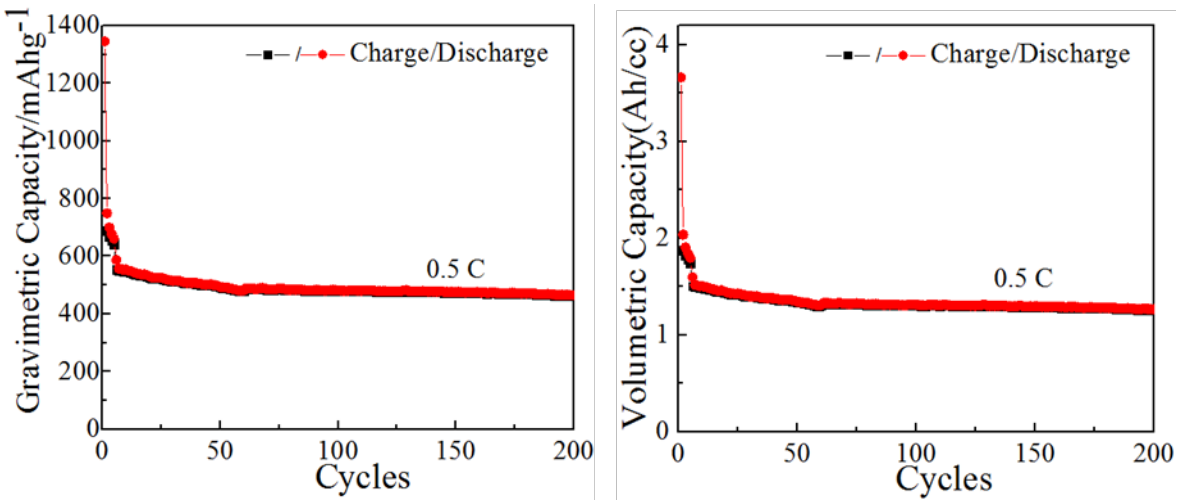


Figure II-244. Cycling capacity of the $Sn_yFeCu$ anode vs Li at a C/2 rate.

*The Cathode $CuF_2$*

We now better understand the challenges facing the $CuF_2$ cathode. It can be fully discharged to LiF and Cu metal achieving a capacity of over 500 mAh/g, but on recharge there is a competition between transport of $Li^+$ and $Cu^+$ ions to the anode in all the electrolytes we have studied including organic and ionic liquids, and organic and inorganic solid electrolytes. As a result, significant amounts of copper metal are plated out on the anode particularly at potentials above 3.5 volts, and the capacity rapidly decays on each cycle. The mixed $Cu_{0.5}Fe_{0.5}F_2$ cathode cycles much better, but a spectroscopic study indicates that this is a result of the Fe cycling from metallic iron to $FeF_3$.

*The Cathode $Li_xVOPO_4$*

The large particle size of $LiVOPO_4$ synthesized at elevated temperatures required that it be ball-milled to reduce the particle size to achieve high capacities. However, such ball-milling significantly degrades the crystallinity of the material. Ball-milling followed by a moderate temperature anneal, 450°C, was found to improve the crystallinity but not to that of the original crystalline $LiVOPO_4$. However, the smaller particle size is retained, and the electrochemical capacity is increased from 225 mAh/g to over 300 mAh/g as shown in Figure II-245(a). The rate capability is also increased achieving around 250 Ah/g at the C/2 rate. Increasing the annealing time to 20 hours reduces the capacity at all rates, as shown in Figure II-245(b).

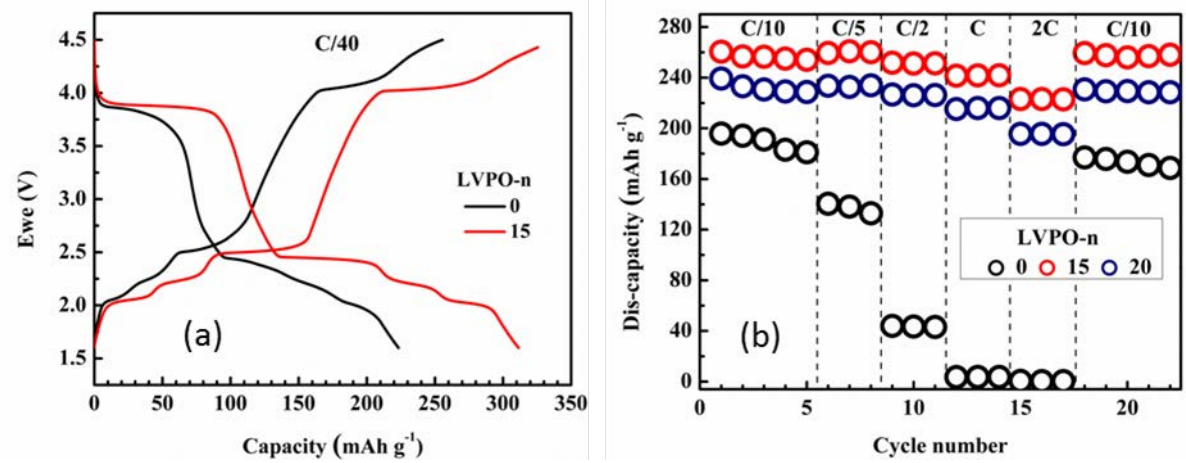


Figure II-245. (a) Cycling curve for $LiVOPO_4$ before annealing and after annealing for 15 hours, and (b) capacity retention and rate capability of $LiVOPO_4$ before annealing and after annealing for 15 and 20 hours.

Subsequent to the above finding, we developed a totally new synthesis approach that formed smaller particles in the initial step so that no ball-milling or annealing was required. The first five cycles vs a lithium anode of this material are shown in Figure II-246(a), and the excellent capacity retention is shown in Figure II-246(b). This material was used for the full cell tests described in the next section.

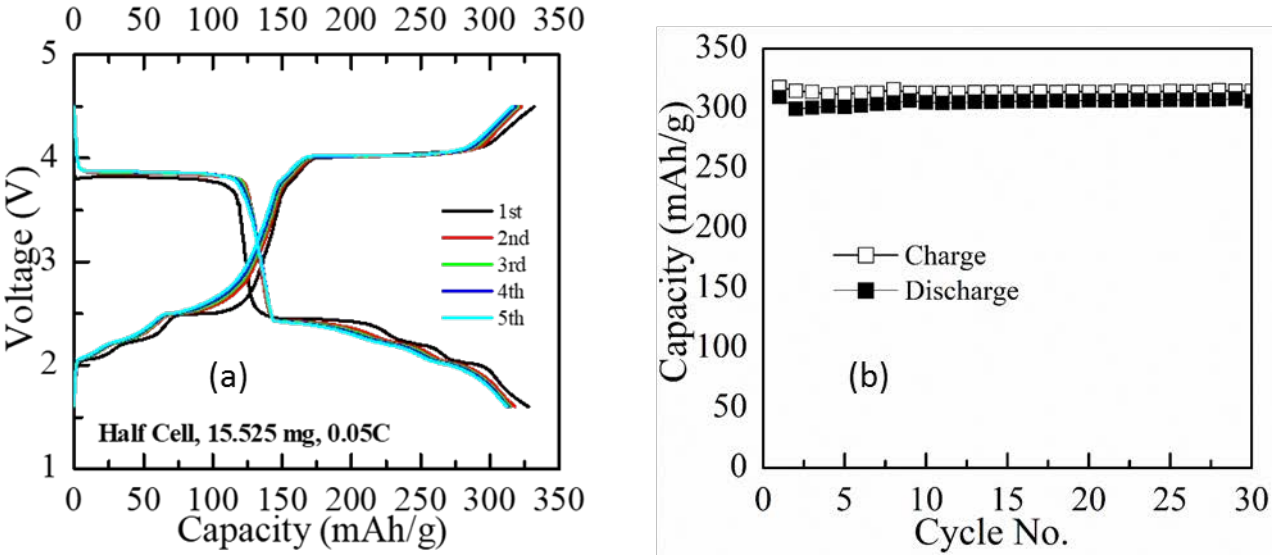


Figure II-246. (a) The first five cycles of $Li_xVOPO_4$ and (b) the capacity for the first 30 cycles vs a lithium anode.

*The Full Cell: Sn/Fe/C // $LiVOPO_4$*

The cell components were evaluated separately vs lithium metal to determine cell reproducibility. They were quite reproducible as shown in Figure II-247. A full cell was then constructed with a loading of the cathode exceeding 20 mg to ensure that a capacity exceeding the 4 mAh/g goal. This accomplishment is also shown in Figure II-247(c).

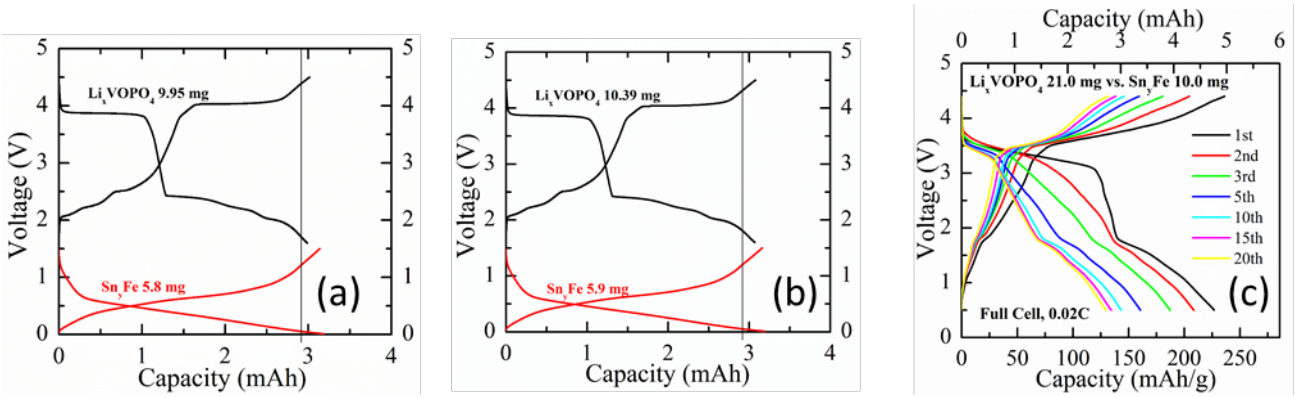


Figure II-247. (a) and (b) Two cells showing reproducibility of electrode components. (c) Cycling data for full cell showing achievement of 4 mAh goal.

To ameliorate the rapid capacity fading observed in Figure II-247, a study was made of the appropriate relative loadings of the two electrodes. The results are shown in Figure II-248. As can be observed an excess of the anode results in the highest capacity and capacity retention. Between 15 and 20 cycles were obtained in excess of the 4 mAh cell goal. However, there is still an unacceptably high capacity fade rate.

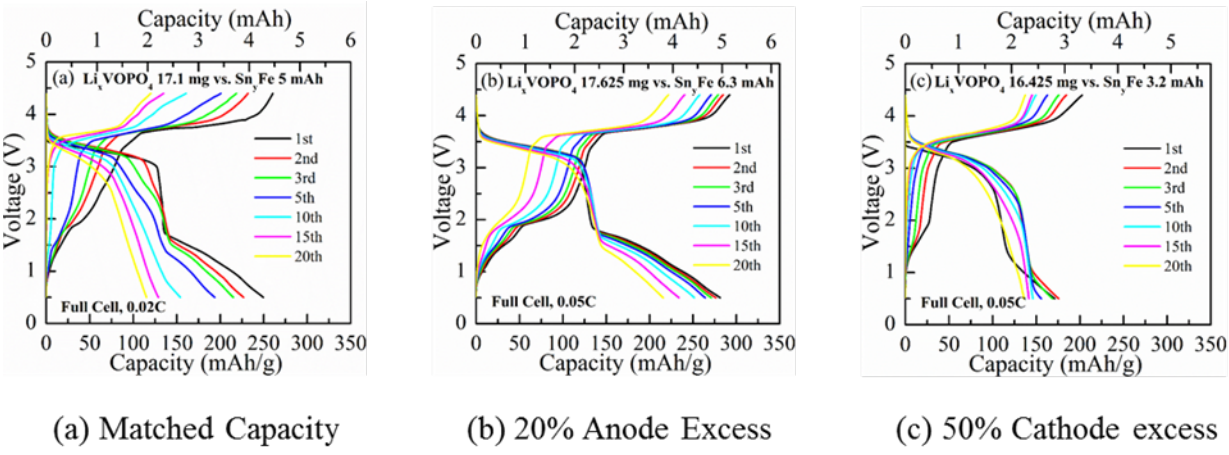


Figure II-248. Electrode Balancing. Cycling behavior of cells with (a) electrode capacity matched, (b) 20% excess anode, and (c) 50% excess cathode.

To ascertain the cause of this capacity fade, the impact of active material loading and of the anode material was determined. Figure II-249(a) and (b) show the impact of doubling the electrode loadings. Doubling the electrode loading has no negative impact, and in fact leads to better capacity retention. However, as shown in Figure II-249(c), the capacity fade is the same for the graphite anode as for the Sn/Fe anode suggesting the cause of the capacity fade is not related to the anode, but rather to the $Li_xVOPO_4$ cathode.

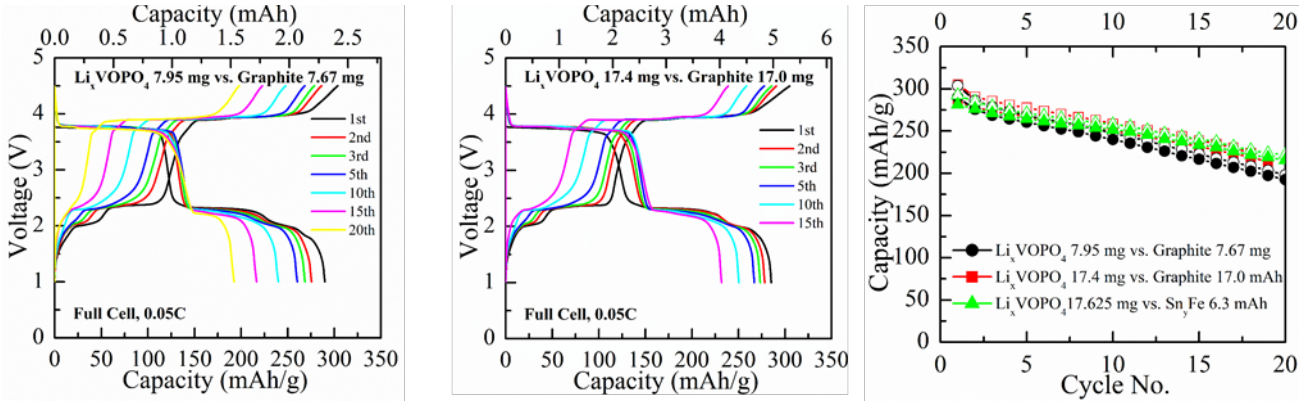


Figure II-249. Cycling of two $Li_xVOPO_4$ vs graphite cells with active materials loadings of 8 and 17 mg (left and center) indicating that loading is not a major factor in capacity fading. 17 mg loading allowed the achievement of the 4 mAh goal. (Right) Comparison of fade behavior of these two cells compared to one with a Sn/Fe anode suggesting that the fade is not due to the anode. a

The baseline couple for this study is the graphite//$LiFePO_4$ cell. A comparison with Sn/Fe//$Li_xVOPO_4$ shows that the latter has 70% more capacity when two lithium ions are intercalated than one lithium in $LiFePO_4$. Even when only one lithium ion is intercalated in $VOPO_4$ in the 4 volt plateau, the energy stored is comparable to that of LiFePO4 as shown in Figure II-250. The energy stored in this two electron lithium couple is much higher than that stored by the alternative, the two-electron one- magnesium ion intercalation couple.

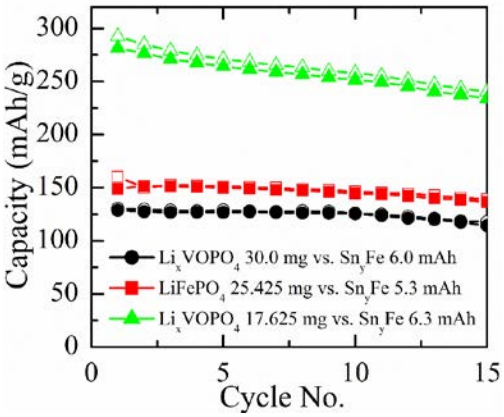


Figure II-250. Comparison of the cycling of $Li_xVOPO_4$ and $LiFePO_4$, showing that two Li cycling in $VOPO_4$ has a much higher capacity than that of $LiFePO_4$. One Li cycling in $VOPO_4$ has a comparable energy density to $LiFePO_4$.

## Conclusions

We have made significant progress in both the cathode and anode conversion materials. The $Sn_2Fe$/C composite has achieved well over 1.5 times the volumetric capacity of the graphitic anode based on the lithiated product. This has been achieved for over 500 full cycles and over a range of C rates. A second synthesis approach has been successfully developed, and copper

We have shown that copper fluoride electrodes have capacities around 500 Ah/kg on the first discharge at low rates, and that even at rates as high as C/5 the capacity remains above 400 Ah/kg. We have shown that on charging the Cu/LiF product of the discharge reaction, cuprous ions are transported through the electrolyte, whether liquid or solid, leading to plating of copper metal at the anode. In the mixed CuFe fluoride, the capacity after the first few cycles almost totally is due to the Fe redox.

We have shown that the two-electron redox cathode, lithium vanadyl phosphate, $LiVOPO_4$, can be readily cycled at rates up to 2C. It shows a substantially higher energy density than the alternative approach using magnesium.

Full cells comprising a SnFe anode and a $LiVOPO_4$ cathode have achieved over 4 mAh for 15 cycles, when there is a slight excess of the anode. The cycle life appears to be limited by the $LiVOPO_4$ cathode and not the anode. The capacity and energy density of this cell is much higher than the baseline cell, graphite//$LiFePO_4$.

## Key Publications

1. "ε- and β-LiVOPO4: Phase Transformation and Electrochemistry", ACS Appl. Mater. & Interfaces, 9, 28537–28541 (2017). Hui Zhou, Yong Shi, Fengxia Xin, Fredrick Omenya, and M. Stanley Whittingham. **DOI**: 10.1021/acsami.7b07895.

## II.C.6 Development of High-Energy Cathode Materials (PNNL)

**Ji-Guang Zhang, Principal Investigator**
Pacific Northwest National Laboratory
902 Battelle Boulevard
Richland, WA 99354
Phone: 509-372-6515
E-mail: Jiguang.Zhang@pnnl.gov

**Jianming Zheng, Co-Principal Investigator**
Pacific Northwest National Laboratory
902 Battelle Boulevard
Richland, WA 99354
Phone: 509-372-4762
E-mail: Jianming.Zheng@pnnl.gov

**Tien Duong, Technology Manager**
U.S. Department of Energy
Phone: 202-586-7836
E-mail: Tien.Duong@ee.doe.gov

Start Date: October 1, 2015 End Date: September 30, 2018
Total Project Cost: $1,200,000 DOE share: $1,200,000 Non-DOE share: $0

### Project Introduction

The lithium ion battery (LIB) is the most promising energy storage system for electric vehicles (EVs) and plug-in hybrid electric vehicles (PHEVs) that can help reduce environmental pollution and promote energy security in the United States. However, the large-scale market penetration of EVs has been hindered by several barriers, including limited energy density, high cost, and safety concern with cathodes in LIBs. Conventional layered oxide $LiCoO_2$ (LCO) has been widely used in LIBs developed for consumer electronics, but the high cost of cobalt and low lithium utilization (~0.5 Li) has limited its application for EVs. To enable the EVs to drive over 300 miles on a single charge and promote the market penetration of EVs, low-cost electrode materials with high tap density, high energy density, good rate capability, and long-term cycle life must be developed. Ternary layered oxides $LiNi_xMn_yCo_zO_2$ (NMCs) are promising cathode materials, because they combine the advantages of Ni, Co, and Mn in the structure. Replacement of Co with high Mn/Ni content also reduces production cost significantly. NMC cathode materials that have been successfully adopted in commercial LIBs, including $LiNi_{1/3}Mn_{1/3}Co_{1/3}O_2$ (NMC333) and $LiNi_{0.4}Mn_{0.4}Co_{0.2}O_2$ (NMC442), can deliver a reversible capacity of about 160 mAh $g^{-1}$ with very decent long-term cycling if they are charged to a voltage of 4.3 V vs. $Li^+/Li$. However, this capacity and energy density are still not sufficient to support high-energy Li-ion batteries for EVs.

We proposed to develop high-energy cathodes based on modified NMC, which can be charged to a high voltage with long-term stability. Extending the charge cutoff voltage is one simple method to increase the utilization of lithium ions in the NMC materials, but this is at the expense of shortened cycle life. Another efficient strategy to improve the energy density of NMC is to develop NMC materials with higher Ni content, which involves both the $Ni^{2+/3+}$ and $Ni^{3+/4+}$ couples and offers a high discharge capacity of more than 200 mAh $g^{-1}$. The energy density of Ni-rich NMC cathodes can reach ~800 Wh $kg^{-1}$ (calculated based on cathode only), which is 30% higher than that of conventional $LiCoO_2$ cathodes (570 Wh $kg^{-1}$). However, several technical challenges still exist with these Ni-rich NMCs due to their structural/interfacial instability and poor thermal stability. In FY17, we took several effective approaches, including grain boundary engineering, use of novel

electrolytes, and lattice doping, to enhance the structural/interfacial stability of Ni-rich NMC cathodes, which significantly improves their long-term cycle life.

## Objectives

- Develop high-energy cathode materials with improved safety for PHEV and EV applications
- Develop low-cost synthesis routes for environmentally benign cathode materials with long cycle life

## Approach

1. Engineer the grain boundary to enhance the structural integrity and interfacial stability of Ni-rich NMC materials.
2. Identify an optimized electrolyte that could efficiently stabilize the electrode/electrolyte interface of Ni-rich NMC cathodes.
3. Identify metal elements (Mg, Al, V, and Y) for lattice doping to enhance the cycling stability of Ni-rich NMC cathodes at high charge cutoff voltages. Electrochemical results demonstrated that Al doping helped improve the cycle life of Ni-rich NMCs.

## Results

*(1) Tailoring the grain boundary to improve the cycle life of Ni-rich NMC cathodes*

Lithium phosphate (LPO) solid electrolyte coating and thermal infusion technology was adopted to improve the structural integrity/stability of Ni-rich NMC cathodes, e.g., $LiNi_{0.76}Mn_{0.14}Co_{0.10}O_2$, and hence enhance their electrochemical performance.

The pristine Ni-rich $LiNi_{0.76}Mn_{0.14}Co_{0.10}O_2$ sample was composed of secondary particles of 10~15 μm that was constructed with primary particles of 100~300 nm (Figure II-251a). After atomic layer deposition (ALD), a thin layer of LPO was coated on the surface of secondary particles (Figure II-251b). Thermal treatment at 600°C infused the thin-film LPO into the interior grain boundaries of secondary particles (Figure II-251c), as confirmed by transmission electron microscope (TEM) energy dispersive spectroscopy (EDS) mapping (Figure II-251d). Electrochemical data (Figure II-251e, f) demonstrated that the as-coated cathode material delivered lower discharge capacity, because the coating layer blocked the fast lithium-ion diffusion pathways. With thermal treatment, the LPO-infused $LiNi_{0.76}Mn_{0.14}Co_{0.10}O_2$ secondary particles exhibited similar initial discharge capacity to that of the pristine material, but the long-term cycling stability of Ni-rich $LiNi_{0.76}Mn_{0.14}Co_{0.10}O_2$ was significantly improved. The LPO-infused material achieved 91.6% capacity retention after 200 cycles, which is much higher than the 79.0% retained by pristine material.

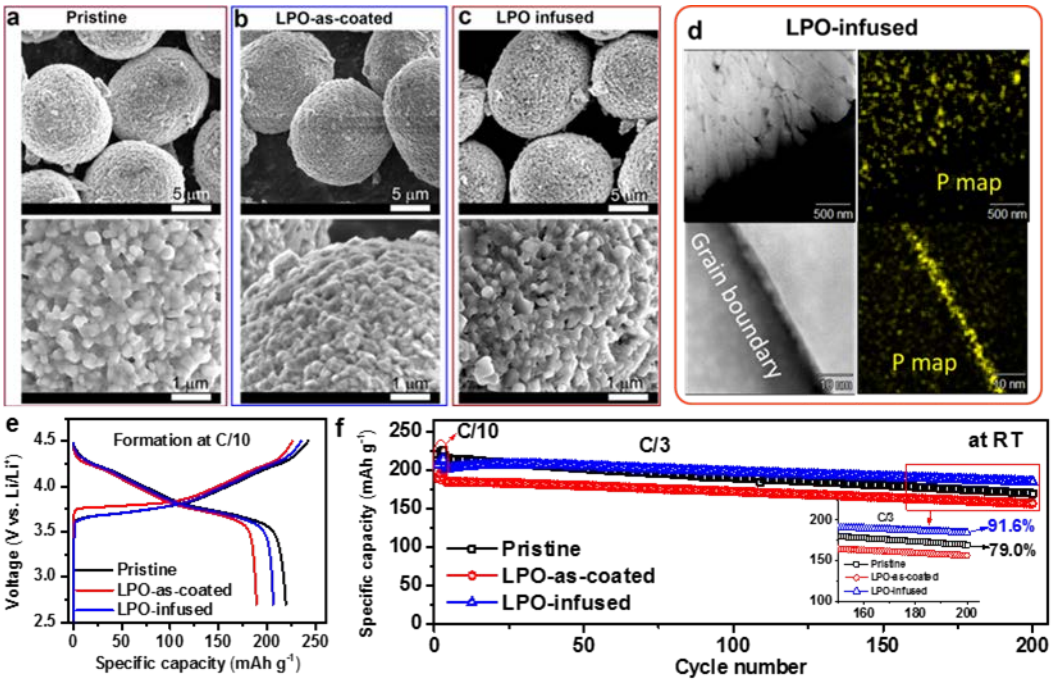


Figure II-251. (a-c) SEM images of (a) pristine, (b) LPO-as-coated, and (c) LPO-infused $LiNi_{0.76}Mn_{0.14}Co_{0.10}O_2$ cathode materials. (d) High-angle annular dark-field (HAADF) TEM images and EDS maps showing the presence of LPO at the grain boundary inside a secondary particle of $LiNi_{0.76}Mn_{0.14}Co_{0.10}O_2$. (e) Initial charge/discharge voltage profiles and (f) cycling performance of pristine and LPO-treated $LiNi_{0.76}Mn_{0.14}Co_{0.10}O_2$ cathode materials at C/3 between ~2.7 and ~4.5 V. Cathode electrode loading is ~4 mg $cm^{-2}$.

The functioning mechanism of LPO solid electrolyte coating was systematically investigated using focused ion beam (FIB) scanning electron microscopy (SEM), scanning TEM (STEM), and electrochemical impedance spectroscopy (EIS) analysis. The pristine material showed substantial crack formation after cycling (Figure II-252a), indicating a poor capability to accommodate the micro-strain generated during deep Li-ion extraction processes. Accompanying the crack formation, the electrolyte then penetrated into the interior of secondary particles along the crack network, leading to the formation of a resistive solid electrolyte interface (SEI) layer at the grain boundaries. This increased cell resistance, especially the charge transfer resistance. Therefore, the pristine material showed faster capacity fading. In contrast, the LPO-infused material exhibited greatly improved structural integrity upon cycling (Figure II-252c), with no obvious cracks being observed. This indicates that the LPO solid electrolyte network could effectively buffer the detrimental micro-strain generated during deep delithiation, contributing to superior long-term cycle life.

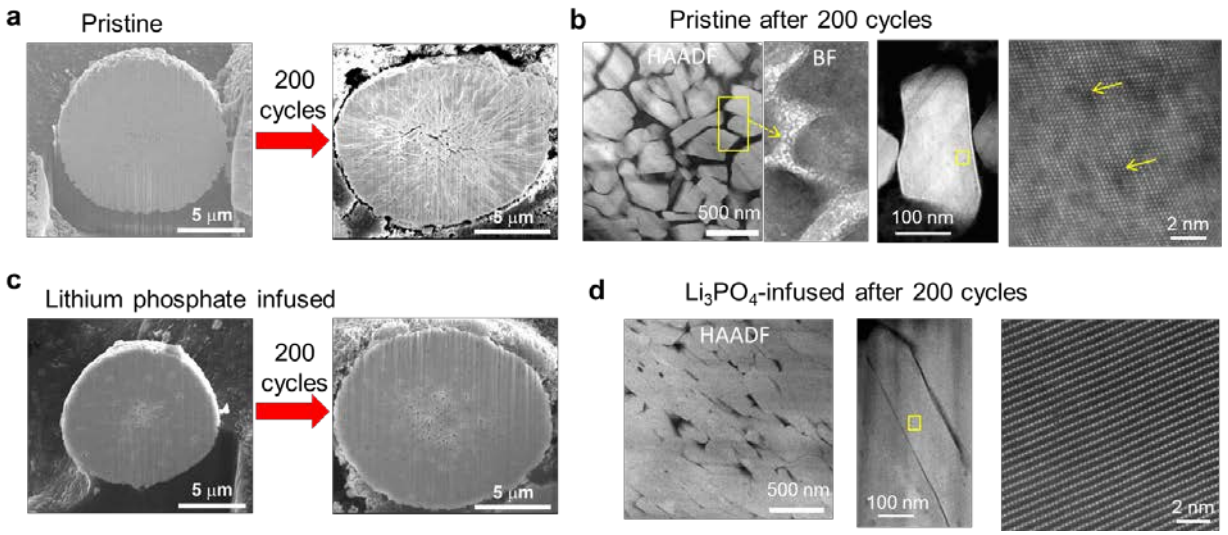


Figure II-252. Cross-sectional SEM images of (a) pristine and (c) LPO-infused $LiNi_{0.76}Mn_{0.14}Co_{0.10}O_2$ before and after 200 cycles at C/3 after 3 formation cycles at C/10 between ~2.7 and ~4.5 V. (b) HAADF/bright field (BF) and STEM images of pristine $LiNi_{0.76}Mn_{0.14}Co_{0.10}O_2$ material after 200 cycles. (d) HAADF and STEM images of LPO-infused $LiNi_{0.76}Mn_{0.14}Co_{0.10}O_2$ material after 200 cycles.

High resolution STEM was further employed to study the microstructural changes of pristine and LPO-infused $LiNi_{0.76}Mn_{0.14}Co_{0.10}O_2$ after electrochemical cycling. The pristine material before cycling showed a dense packing of the layered primary particles within the secondary particles. However, the unmodified material exhibited severe structural changes after 200 cycles at C/3 between ~2.7 and ~4.5 V (Figure II-252b). The grain boundaries between primary particles separated from each other and the gap between primary particles was filled with by-products of the parasitic side reactions between active material and the electrolyte. Also, the layered structure of Ni-rich NMC was transformed to disordered rock-salt structure. The degradation of the electrode crystal structure and the electrode/electrolyte interface was considered the main reason for the fast capacity decay of pristine Ni-rich $LiNi_{0.76}Mn_{0.14}Co_{0.10}O_2$. In contrast, the LPO-infused material showed well-maintained dense packing of the primary particles and well-preserved layered structure without serious phase transformation in the cycled particles (Figure II-252d). The enhanced structural and interfacial stability led to the greatly improved cycle life of Ni-rich $LiNi_{0.76}Mn_{0.14}Co_{0.10}O_2$. These fundamental findings validate the artificial solid electrolyte coating in conjunction with thermal infusion as a promising technology for developing stabilized Ni-rich cathode materials for high-energy-density Li-ion batteries.

*(2) Tailoring the electrode/electrolyte interface to improve the cycle life of Ni-rich NMC cathodes*

The electrode/electrolyte interfacial stability of the Ni-rich NMC cathode, i.e., $LiNi_{0.76}Mn_{0.14}Co_{0.10}O_2$ was enhanced by using an optimized electrolyte (E-optimized) composed of 0.6 M lithium bis(trifluoromethanesulfonyl)imide (LiTFSI), 0.4 M lithium bis(oxalate)borate (LiBOB), and 0.05 M $LiPF_6$ in ethylene carbonate (EC)-ethyl methyl carbonate (EMC) (4:6 by wt.), leading to significantly enhanced electrochemical performance.

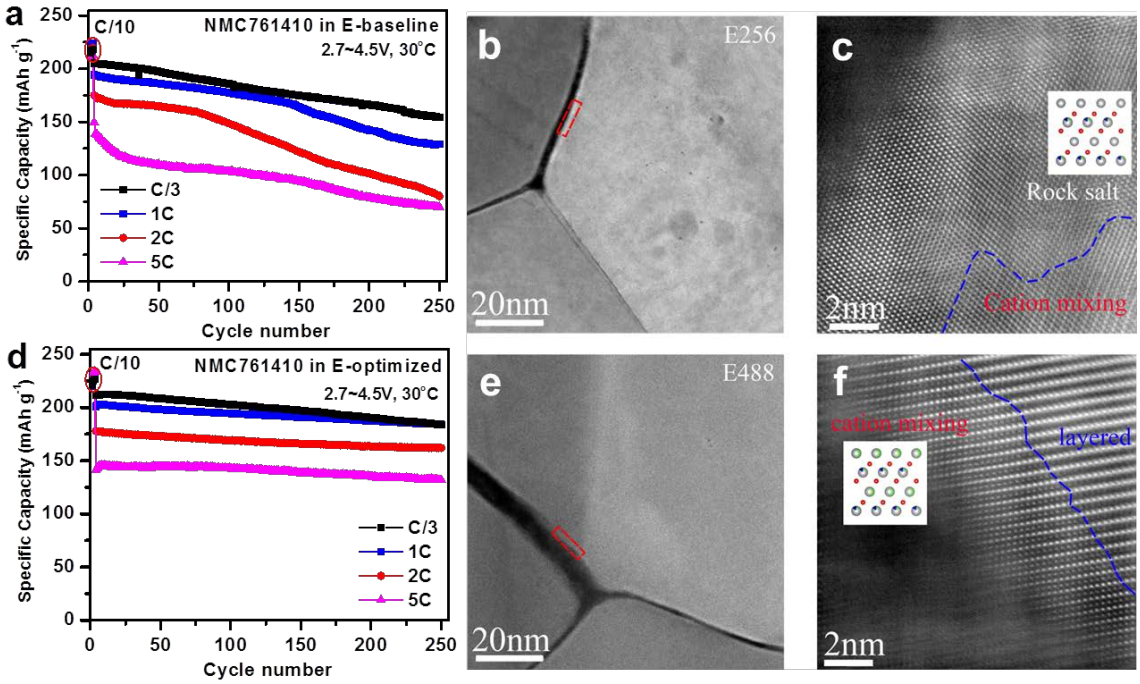


Figure II-253. (a, d) Cycling performance of Ni-rich $LiNi_{0.76}Mn_{0.14}Co_{0.10}O_2$ cathode in (a) E-baseline (1 M $LiPF_6$/EC-EMC) and (d) E-optimized (0.6 M LiTFSI, 0.4 M LiBOB, and 0.05 M $LiPF_6$ in EC-EMC) electrolytes during cycling at C/3, 1C, 2C, 5C rates (after 3 formation cycles at C/10) between ~2.7 and ~4.5 V. (b, c; e, f) HAADF-STEM images of Ni-rich $LiNi_{0.76}Mn_{0.14}Co_{0.10}O_2$ after 100 cycles at C/3 between ~2.7 and ~4.5 V in (b, c) E-baseline electrolyte and (e, f) E-optimized electrolyte.

The electrochemical performance data showed that, using optimized electrolyte, the Ni-rich $LiNi_{0.76}Mn_{0.14}Co_{0.10}O_2$ was able to deliver an initial discharge capacity of 220 mAh $g^{-1}$ and achieve 86.9% capacity retention after 250 cycles, far superior to those (215 mAh $g^{-1}$, 75.2% retention after 250 cycles) obtained in baseline electrolyte (1 M $LiPF_6$/EC-EMC) (Figure II-253a,d). Meanwhile, the advantage of using E-optimized for Ni-rich NMC is further evidenced by the much improved stability in long-term cycling at higher charge/discharge C rates of 1C, 2C, and 5C, as compared to those using E-baseline (Figure II-253a, d).

The mechanism of improved cyclability of the NMC cathode using E-optimized electrolyte was systematically investigated using SEM, TEM, x-ray photoelectron spectroscopy (XPS), and EIS. E-optimized has been previously proven to be much more stable with the Li metal anode, thereby suppressing the polarization increase occurring on the anode side. In addition, the E-optimized electrolyte greatly enhanced the surface structural stability of $LiNi_{0.76}Mn_{0.14}Co_{0.10}O_2$. Although similar particle cracking was observed in the two electrolytes, less corrosion and much less structural transformation (from R-3m layered to Fm-3m disordered rock salt) were detected at the particle surface of Ni-rich NMC cycled in E-optimized (Figure II-253e,f), as compared to those observed in E-baseline (Figure II-253b,c). This improvement can be ascribed to the absence of HF acidic species that could etch the cathode particle surface, resulting in the phase transformation from layered to disordered rock-salt phase. The enhanced surface structural/interfacial stability is regarded as the primary reason for the improved capacity retention and mitigated voltage decay of Ni-rich $LiNi_{0.76}Mn_{0.14}Co_{0.10}O_2$. The results highlight the importance of maintaining the particle surface structural/interfacial stability to enable the sustainable operation of Ni-rich cathode materials for high-energy-density Li-ion batteries.

*(3) Doping the lattice to enhance the cycling stability of Ni-rich NMCs*

Surface lattice doping has been adopted to enhance the cycling stability of Ni-rich NMC cathode materials at a high charge cutoff voltage of 4.5 V. Using the spherical $Ni_{0.68}Mn_{0.22}Co_{0.10}(OH)_2$ precursor, the effects of dopants on the electrochemical performance of $Li(Ni_{0.68}Mn_{0.22}Co_{0.10})_{0.99}M_{0.01}O_2$ (M = Mg, Al, V, or Y) were systematically investigated. The lattice-doped materials were prepared by mixing the $Ni_{0.68}Mn_{0.22}Co_{0.10}(OH)_2$ precursor (with a secondary particle size of ~10 μm) with the dopant precursors; the mixture was then blended with lithium hydroxides and annealed at the optimum calcination temperature of 775°C for 24 h. The cycling performance of the obtained 1%-metal-doped cathode materials was evaluated in lithium half-cells using baseline electrolyte (1 M $LiPF_6$/EC-EMC (4:6 by wt.)). Electrochemical performance results showed that the additional lattice doping slightly reduced the discharge capacity, due to electrochemical inactivity of the dopants (Figure II-254a). During long-term cycling, only the Al doping improved the capacity retention, while the other dopants (Mg, V, and Y) deteriorated the cyclability of the Ni-rich NMC cathodes (Figure II-254b, c).

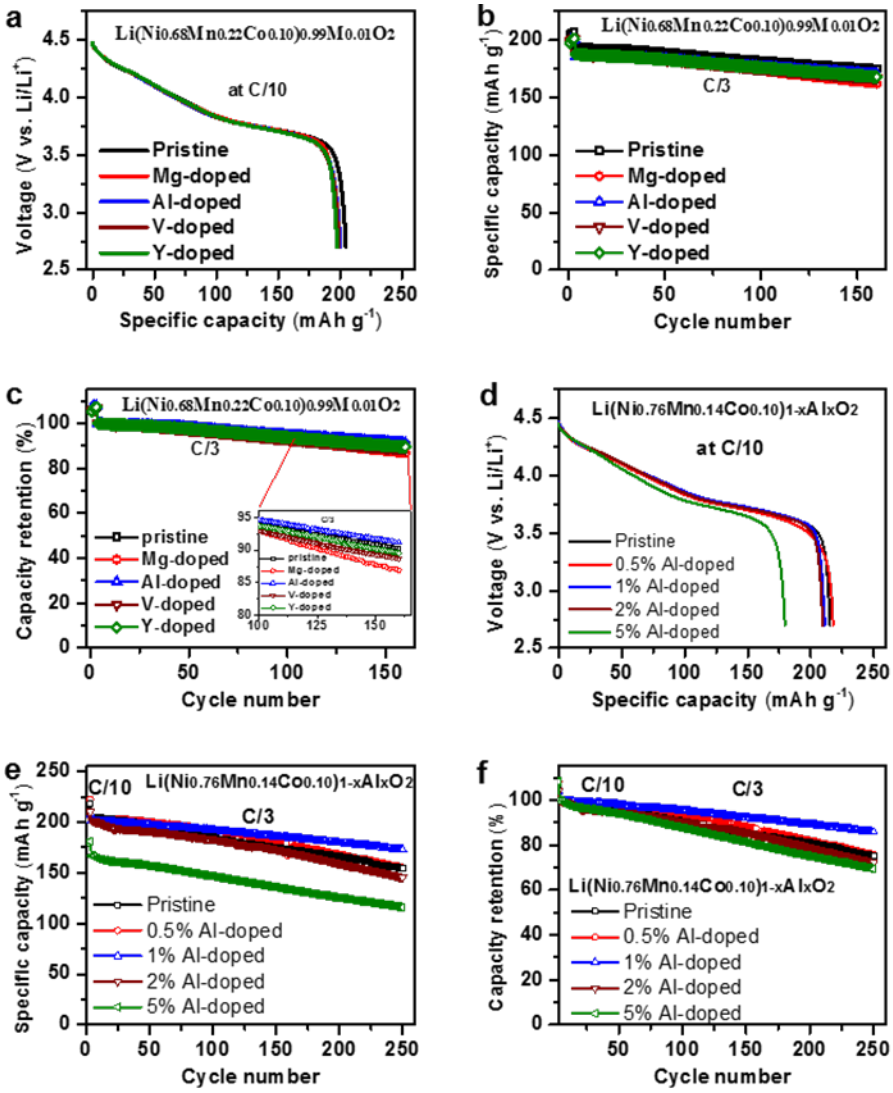


Figure II-254. (a) Initial discharge profiles at C/10, (b) cycling performance and (c) capacity retention of $Li(Ni_{0.68}Mn_{0.22}Co_{0.10})_{0.99}M_{0.01}O_2$ (M = Mg, Al, V, or Y) during cycling at C/3 after 3 formation cycles at C/10 (1C = 200 mA $g^{-1}$). (d) Initial discharge voltage profiles at C/10, (e) cycling performance and (f) capacity retention of $Li(Ni_{0.76}Mn_{0.14}Co_{0.10})_{1-x}Al_xO_2$ during cycling at C/3 after 3 formation cycles at C/10. Cathode electrode loading: ~4 mg $cm^{-2}$.

The effect of Al doping content on the electrochemical performance of another Ni-rich NMC $Li(Ni_{0.76}Mn_{0.14}Co_{0.10})_{1-x}Al_xO_2$ (synthesized at 750°C) was also investigated. The doping amount had significant effect on the long-term cycling performance of the Ni-rich NMC $Li(Ni_{0.76}Mn_{0.14}Co_{0.10})_{1-x}Al_xO_2$ (Figure II-254e, f). Increasing the doping amount to above 1% leads to decreased discharge capacity, owing to the electrochemical inactivity of Al (Figure II-254d). The pristine $LiNi_{0.76}Mn_{0.14}Co_{0.10}O_2$ showed relatively fast capacity fading during cycling, exhibiting a capacity retention of 75.2% after 250 cycles. With 0.5 mol% and 1 mol% Al doping, the capacity retention after 250 cycles was improved to 75.8% and 85.8%, respectively. Further increasing the Al doping amount to above 1 mol% led to fast capacity degradation. The materials with 2 mol% and 5 mol% Al doping showed inferior cycling stability, maintaining only 72.1% and 69.4% of their initial capacity, respectively, after 250 cycles. This could be because excess Al precursor could not be successfully doped into the layered structure lattice, but formed a thick coating on the surface, which dramatically increased the kinetic barrier for lithium ion transportation and the reversible lithium ion de/intercalation processes. The results suggest that both the doping elements and the doping amount must be carefully optimized in Ni-rich NMC cathodes to maximize their electrochemical performance.

## Conclusions

Three approaches were pursued to improve the structural and interfacial stability of high-energy-density Ni-rich NMC cathode materials for LIBs.

In the first approach, a thin $Li_3PO_4$ solid electrolyte layer was infused along the grain boundaries of Ni-rich $LiNi_{0.76}Mn_{0.14}Co_{0.10}O_2$ secondary particles via ALD coating and thermal infusion. The infused LPO solid electrolyte network could block the diffusion of electrolyte during cycling and act as an efficient buffer to minimize the detrimental influence of the micro-strain generated during deep delithiation. Therefore, the LPO-infused material showed well-maintained dense packing of the primary particles along with well-preserved layered structure without serious phase transformation even after long-term cycling. The homogeneous solid electrolyte coated material demonstrated significantly enhanced cycling stability, achieving the improved capacity retention of 91.6% after 200 cycles. These fundamental findings prove that artificial solid electrolyte infusion is a promising technology for prolonging the cycle life of high-energy-density Ni-rich cathode materials.

In the second approach, an optimized electrolyte (0.6 M LiTFSI, 0.4 M LiBOB, and 0.05 M $LiPF_6$ in EC-EMC) was shown to improve the electrode/electrolyte interface of Ni-rich $LiNi_{0.76}Mn_{0.14}Co_{0.10}O_2$. The optimized electrolyte significantly improved the long-term cycling stability of $LiNi_{0.76}Mn_{0.14}Co_{0.10}O_2$ at different C rates ranging from C/3 to 5C. In particular, when cycled at C/3, the capacity retention with E-optimized was increased to 86.9% after 250 cycles, far superior to the 75.2% retention obtained with E-baseline. In addition to improving the stability of the Li metal anode, another important reason for the improved cycling performance is formation of an enhanced CEI layer that can better protect the Ni-rich $LiNi_{0.76}Mn_{0.14}Co_{0.10}O_2$ cathode against electrolyte corrosion and suppress the structural transformation from layered to disordered NiO type rock-salt phase.

The third approach used in this work is lattice doping, which can effectively enhance the surface structural stability of Ni-rich NMCs. Several lattice dopants (Mg, Al, V, and Y) were investigated. Al dopant showed improved long-term cycling stability of Ni-rich materials including $LiNi_{0.68}Mn_{0.22}Co_{0.10}O_2$ and $LiNi_{0.76}Mn_{0.14}Co_{0.10}O_2$. With 1 mol% Al doping, the capacity retention after 250 cycles of a Ni-rich $LiNi_{0.76}Mn_{0.14}Co_{0.10}O_2$ cathode was improved to 85.8%, which is much better than that obtained for pristine material (75.2% after 250 cycles). Further increasing the Al doping amount above 1 mol% led to faster capacity degradation. This could be explained by an increased kinetic barrier for lithium ion transportation caused by excess Al precursor that could not be successfully doped into the material structure, but only existed as a thick coating layer. The results suggest that doping elements and doping amount should be carefully optimized to maximize the performance of Ni-rich NMC cathodes.

Based on the above achievements and fundamental understanding, future work will be focused on lattice modification, effective grain boundary engineering, and identification of effective electrolyte additives (or a combination of these) to maximize the long-term cycle life of Ni-rich NMC cathode materials. Any improvement identified in lithium half-cells will be further evaluated in full-cell configurations using graphite or a higher capacity Si/C composite as anode materials.

## Key Publications


1. The roles of oxygen non-stoichiometry on the electrochemical properties of oxide-based cathode materials, Jianming Zheng, Jie Xiao, and Ji-Guang Zhang, Nano Today, 11(5), 678-694 (2016).

2. Intragranular cracking as a critical barrier for high-voltage usage of layer-structured cathode for lithium-ion batteries, Pengfei Yan, Jianming Zheng, Meng Gu, Jie Xiao, Ji-Guang Zhang, Chongmin Wang, Nature Communications, 8, 14101 (2017).

3. Li- and Mn-Rich Cathode Materials: Challenges to Commercialization, Jianming Zheng, Seung Myeong, Woongrae Cho, Pengfei Yan, Jie Xiao, Chongmin Wang, Jaephil Cho, and Ji-Guang Zhang, Advanced Energy Materials, 7(6), 1601284 (2017).

4. Suppressed oxygen extraction and degradation of $LiNi_xMn_yCo_zO_2$ cathodes at high charge cut-off voltages, Jianming Zheng, Pengfei Yan, Jiandong Zhang, Mark Engelhard, Zihua Zhu, Bryant Polzin, Steve Trask, Jie Xiao, Chongmin Wang, Ji-Guang Zhang, Nano Research, https://doi.org/10.1007/s12274-017-1761-6.

5. High capacity and stable cathode materials, Jianming Zheng, Ji-Guang Zhang, Pengfei Yan, Chongmin Wang, Wengao Zhao, Shuru Chen, Wu Xu, U.S. Patent Application No. 15/597,025.

## II.C.7 *In situ* Solvothermal Synthesis of Novel High-Capacity Cathodes (BNL)

**Feng Wang, Principal Investigator**
Brookhaven National Laboratory
Sustainable Energy Technologies Department
Upton, NY 11973
Phone: 631-344-4388
E-mail: fwang@bnl.gov

**Jianming Bai, Co-Principal Investigator**
Brookhaven National Laboratory
National Synchrotron Light Source II
Upton, NY 11973
Phone: 631-344-2583
E-mail: jmbai@bnl.gov

**Tien Duong, Technology Manager**
U.S. Department of Energy
Phone: 202-586-7836
E-mail: Tien.Duong@ee.doe.gov

Start Date: October 1, 2015 End Date: September 30, 2018
Total Project Cost: $1,050,000 DOE share: $1,050,000 Non-DOE share: $0

### Project Introduction

Despite considerable interest in developing new battery electrodes, only a small number of known materials show real promise for achieving significant improvement in capacity and/or a reduction in cost. The preparation of new compounds or materials with unique properties often relies on trial and error as there are a variety of synthesis parameters (precursor concentration, temperature, pressure, p*H* value, cation type and reaction time, etc.) that can have a strong influence on the material properties (crystal structure, morphology, particle size) and electrochemical performance. Most synthesis reactions are carried out in a sealed autoclave and therefore the reactor is a black box – the inputs and outputs are known, but little is known about intermediate phases and overall reaction pathways. *In situ, real-time* probing of synthesis reactions can provide the details of reactions, elucidating intermediate phases and how temperature, pressure, time and the precursor concentrations affect the reaction pathways. The results of such studies enable strategies to optimize synthesis reactions, particularly the formation of materials of desired phases and properties. With a better understanding of the correlation between synthesis conditions, crystallization processes, and material properties, a rational design of advanced battery materials should emerge.

### Objectives

The goal is to develop novel high-capacity cathodes through synthetic control of the phase, stoichiometry and morphology.

### Approach

One unique approach taken in this project is to develop *in situ* techniques/capabilities for diagnostics and synthetic design of new battery materials using the world-best facilities at Brookhaven and other national laboratories. More specifically, synchrotron X-ray, neutron-based *in situ* techniques are developed and applied to studies of synthesis reactions during preparation of high-capacity cathode materials, allowing access to the structural chemistry involving intermediate and short-lived phases. Insights obtained from *in situ* studies will provide knowledge on how the synthesis conditions (temperature, pressure, p*H*, precursor concentration, etc.)

affect the kinetics and pathways of synthesis reactions. *Ex-situ* characterization conducted using synchrotron X-ray, neutron scattering, transmission electron microscopy (TEM), electron energy-loss spectroscopy (EELS) and various electrochemical techniques helps us to gain understanding of how structure, composition, and synthesis affect electrochemical performance. Together, *in situ* studies of synthesis process coupled with *ex situ* structural/electrochemical characterization of the synthesized materials provide a basis for synthetic design of phase-pure cathodes of desired stoichiometry and morphology.

## Results

### *In situ studies of synthesis reactions in preparing layered oxides*

In the last fiscal year, *in situ* studies were made on synthesis reactions in preparing $LiNiO_2$ and the Co-substituted variants ($LiNiCo_xO_2$), and with the insights gained from the studies, synthesis procedures were developed for making Ni-rich layered oxides with synthetic control of structural and electrochemical properties. The developed *in situ* approaches were further applied to studies of synthesis reactions in making $LiCoO_2$, $LiNiO_2$, and a series of solid solutions $LiNi_{1-x}(CoMn)_xO_2$ from hydroxide precursors. Synchrotron X-ray was employed for fast acquisition of high-resolution diffraction patterns with wide Q range, allowing access to intermediates and short-lived phases under real synthesis conditions.

Precursors were made from mixtures of Li source (LiOH) with transition metal hydroxides, $TM(OH)_2$ (TM = Ni, Co, Mn of varying molar ratios). Time-resolved synchrotron x-ray diffraction (XRD) patterns were recorded from the hydroxide mixtures upon heating from low to high temperatures. Figure II-255 shows representative contour plots of the XRD patterns recorded from intermediates at low temperatures (≤ 500°C) in preparing $LiNiO_2$ and $LiNi_{0.7}Co_{0.15}Mn_{0.15}O_2$ (NMC71515). The phase transformation process is overall similar in these two cases, both from initial hydroxides (space group: *p-3m1*) to the layered phase (*R-3m*). But more complex reaction occurred in the precursors containing 2 and 3 elements, along a much different pathway than that in those precursors containing only Ni or Co. For example, heat treatment led to decomposition of $Ni(OH)_2$ at ~230°C, giving rise to rock-salt (NiO), and no layered phase was observed at temperatures up to 500°C (Figure II-255a). In contrast, $Ni_{0.7}Co_{0.15}Mn_{0.15}(OH)_2$ transformed into structurally similar intermediates at temperatures between 218-313°C, and layered phase thereafter, through complex anionic exchange and cationic migration/re-ordering processes (Figure II-255b). Results from *ex situ* XRD measurements showed that, with elongated sintering time, the transformation from $Ni_{0.7}Co_{0.15}Mn_{0.15}(OH)_2$ to the intermediates occurred at a much lower temperature (~120 °C), and then to the layered at temperature as low as 200 °C. Quantitative structure analysis is now under way for better understanding of the synthesis process and dependence of kinetic pathway on transition element species in the precursors.

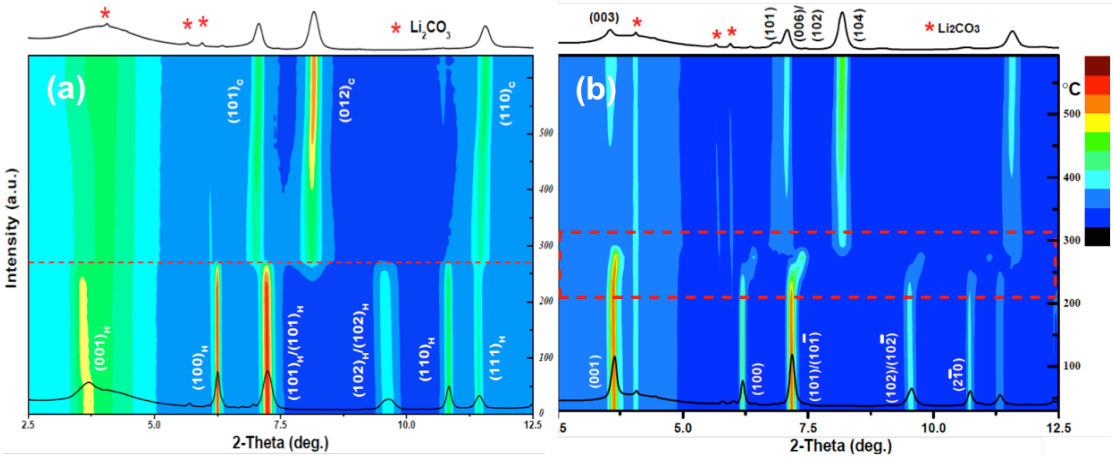


Figure II-255. *In situ* temperature-resolved synchrotron XRD for tracking structural evolution of intermediates in preparing (a) $LiNiO_2$, (b) NMC71515 from hydroxides (via solid-state reaction in $O_2$ flow with a heating rate of 5°C/min).

*Technique development for in situ probing cation ordering*

In addition to various *in situ* reactors built for X-ray experiments, a new design of *in situ* reactor, with configuration suited for neutron diffraction (ND) measurements was recently developed, with a gas-flow system integrated allowing for probing solid-state reaction under controlled atmosphere (Figure II-256a). The reactor has been used for *in situ* ND studies of synthesis reactions in preparing NMC71515. Figure II-256b shows one representative contour plot of temperature-resolved ND patterns from the measurements, revealing the entire reaction process, from the precursors (a mixture of Li/transition metal hydroxides) to intermediates, and then to the final layered NMC71515. The results are consistent with the *in situ* XRD observation (Figure II-255b), but more details were obtained from *in situ* ND measurements (particularly on cation ordering), owing to the unique capabilities of neutron scattering in detecting light elements (*e.g.*, Li) and differentiation of the involved transition metals (Ni, Mn, Co).

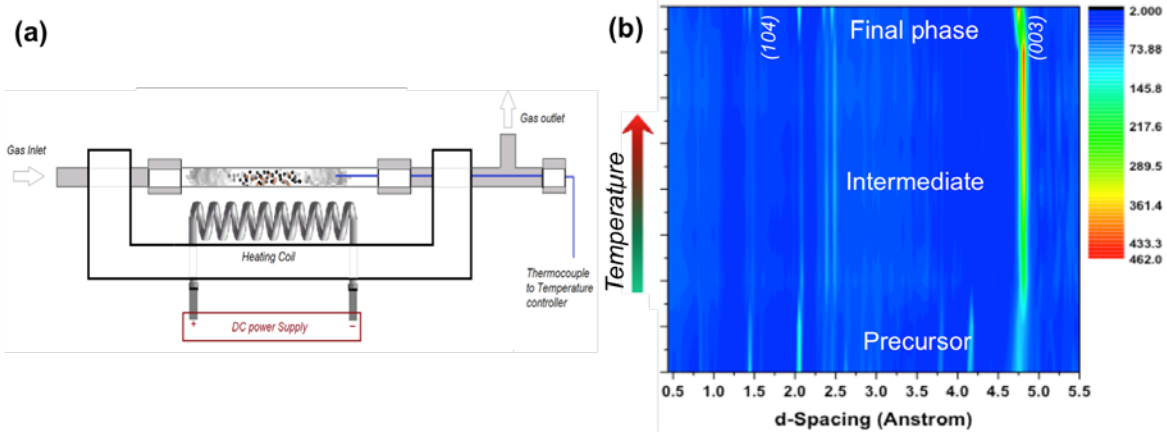


Figure II-256. (a) Setup for *in situ* neutron and synchrotron diffraction measurements. (b) Contour plot of temperature resolved *in situ* neutron diffraction patterns of intermediates during synthesis of NMC71515.

Details of the synthesis reactions can now be obtained through joint refinement of *in situ* XRD and ND data acquired from the same system (as demonstrated in Figure II-257), not only on the overall structural evolution, but potentially on the ordering of all the involved cations, thereby offering new insights into kinetic and thermodynamic parameters governing synthesis process in preparing Ni-rich layered oxides.

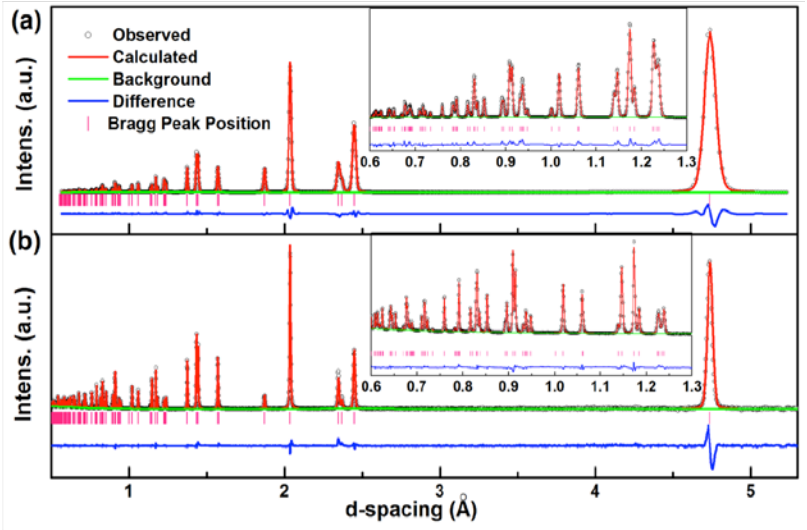


Figure II-257. (a) Synchrotron X-ray and (b) neutron diffraction patterns of the synthesized NMC71515, in comparison to that from structure refinement. The enlarged spectra in small d−spacing range are shown in the inset. In the plots, open circles are used for the observed data, red lines for the calculated data, pink bars for Bragg positions, blue lines for the difference between the observed and calculated data, and green lines for the refined background.

*Kinetic control of the cation ordering in NMC71515*

In addition to studies on the reaction pathway of the whole synthesis process (as given above), synchrotron and neutron-based *in situ* techniques were also applied to probing and synthetic control of the cation ordering in Ni-rich layered oxides subjected to heat treatment at high temperatures. Representative time-resolved synchrotron XRD patterns from NMC71515 are shown in Figure II-258a. The evolution of diffraction peaks, such as fast rise of (003) peak, indicates rapid improvement of cation ordering during the heat treatment and strong dependence on temperature (Figure II-258b-d).

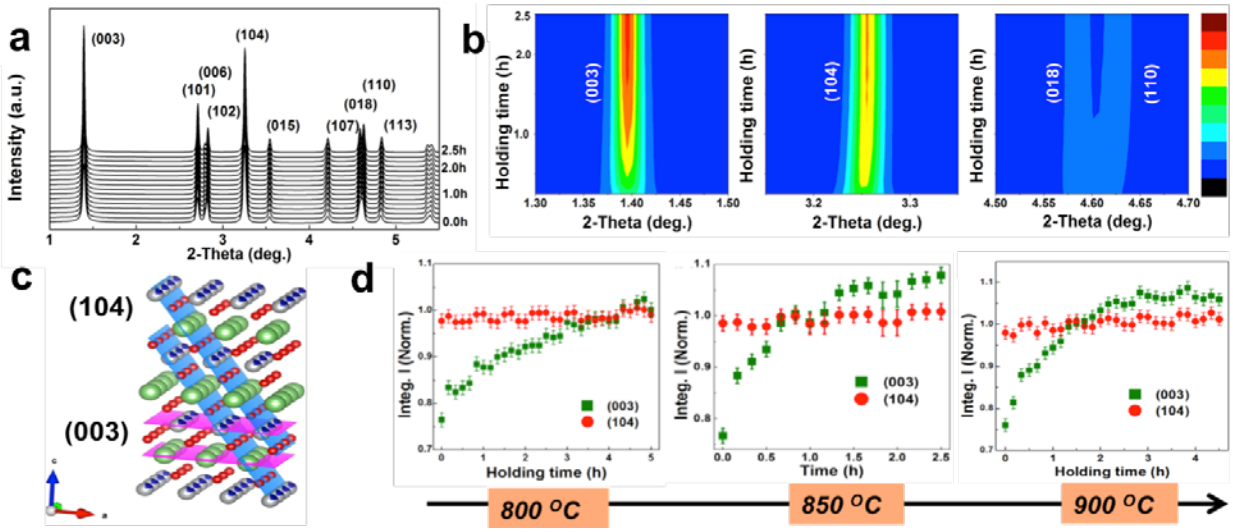


Figure II-258. (a) Representative time−resolved XRD patterns from NMC71515 during heat treatment (at 850°C). (b) Evolution of the reflections characteristic of layered structure. (c) Illustration of the atomic configuration and reflection planes of (104) and (003) in the layered structure. (d) Evolution of the integrated intensity of the (003) and (104) peaks.

Details on structural ordering processes, such as the evolution of Li-slab distance and Li/Ni disordering with holding time, were obtained through quantitative analysis of XRD data (Figure II-259a, b). The results from this study revealed a complex synthesis process, involving competition between cationic ordering and disordering processes (largely due to Li/O loss) that concomitantly occur during heat treatment. Treatment at elevated temperature would always facilitate the ordering process, but the ordering kinetics did not increase monotonically with temperature -- being compromised by the accelerated disordering with an increase of temperature. Kinetic control of the cationic ordering, *via* finely tuning heating temperature and time, was found to be crucial to optimizing structural ordering of the final products.

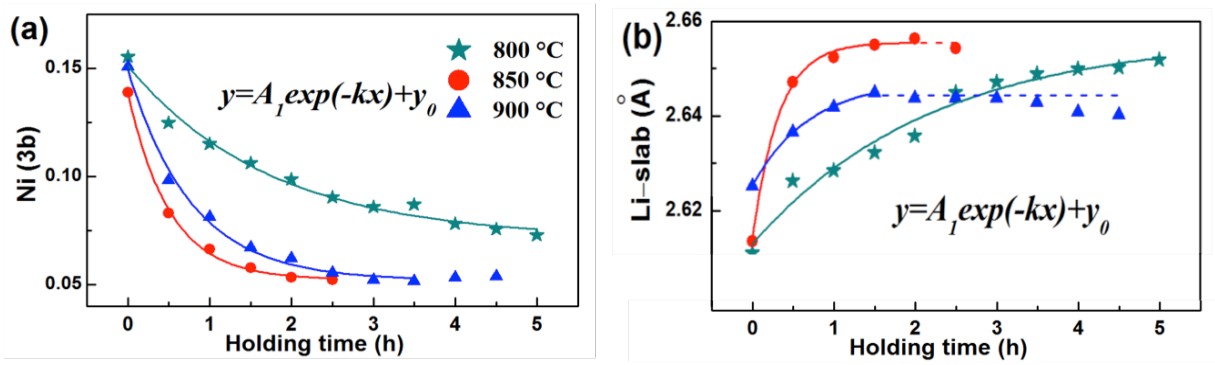


Figure II-259. (a) Evolution of cationic disordering (i.e., Ni ions at 3b sites and (b) Li–slab distance with holding. (Lines: fittings to y=A1exp(-kx)+y0.

The impact of synthesis conditions on the kinetic pathway and structural ordering of the final products was evaluated through *in situ* XRD, X-ray absorption spectroscopy (XAS), thermogravimetric analysis **(**TGA), and *ex situ* structural characterizations. The combined studies revealed a strong temperature dependence of the kinetics of cationic ordering in NMC71515 as a result of thermal-driven oxidation of transition metals and Li/O loss (Figure II-260a) that concomitantly occurred during heat treatment. In addition, particles grew quickly upon high-temperature treatment (Figure II-260b). Kinetic control of the cationic ordering and morphology, *via* finely tuning heating temperature and holding time, was found to be crucial to optimizing the electrochemical performance of the final products.

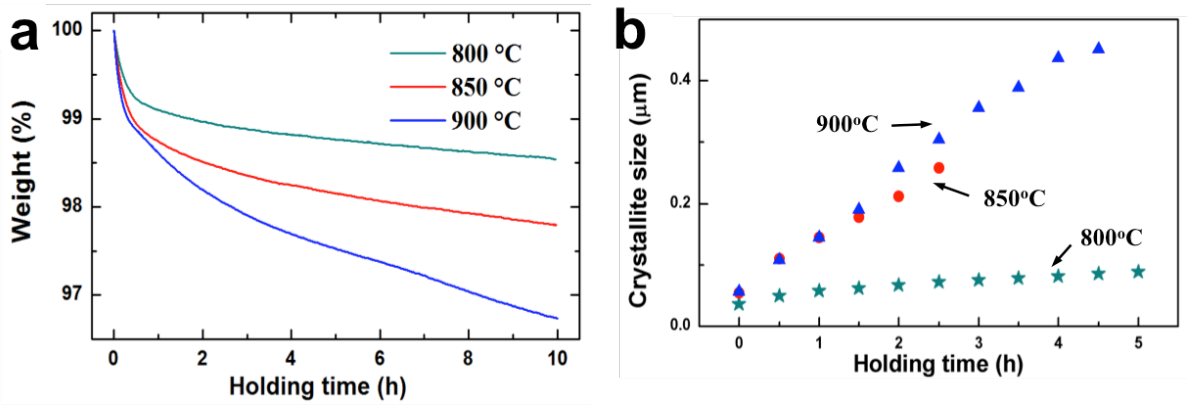


Figure II-260. (a) TGA curves of the precursors during holding at constant temperatures (800°C, 850°C, 900°C). (b) Evolution of crystallite size with holding time at the three temperatures (as labeled).

*Evaluation of synthesis conditions on the electrochemical performance of the final products*

The findings from this study enabled us to identify optimal conditions for synthesizing NMC71515 with low cationic disordering and high electrochemical activity. Figure II-261a displays the representative charge/discharge voltage profiles of synthesized materials, indicating much higher discharge capacity in the sample synthesized at 850° C, 197 mAh $g^{-1}$, compared to that obtained at 800 and 900°C, 162 and 174 $mAhg^{-1}$, respectively. In addition, a lower overpotential was obtained in the sample heated at 850°C. The measured electrochemical performance is in good agreement with structural analysis, that is, the sample heated at 850°C has low Li/Ni mixing at 3b sites, large Li slab, and moderate crystallite size. Excellent capacity retention was obtained in the three samples obtained at 800, 850, and 900°C, of 93.5%, 84.1%, and 84.5% after 50 cycles (Figure II-261b). The extension of electrochemical windows to 4.5, 4.7 V led to greatly increased capacity, but at the cost of capacity retention. The findings from this study provide new insights into synthetic design of high-Ni layered oxide cathodes.

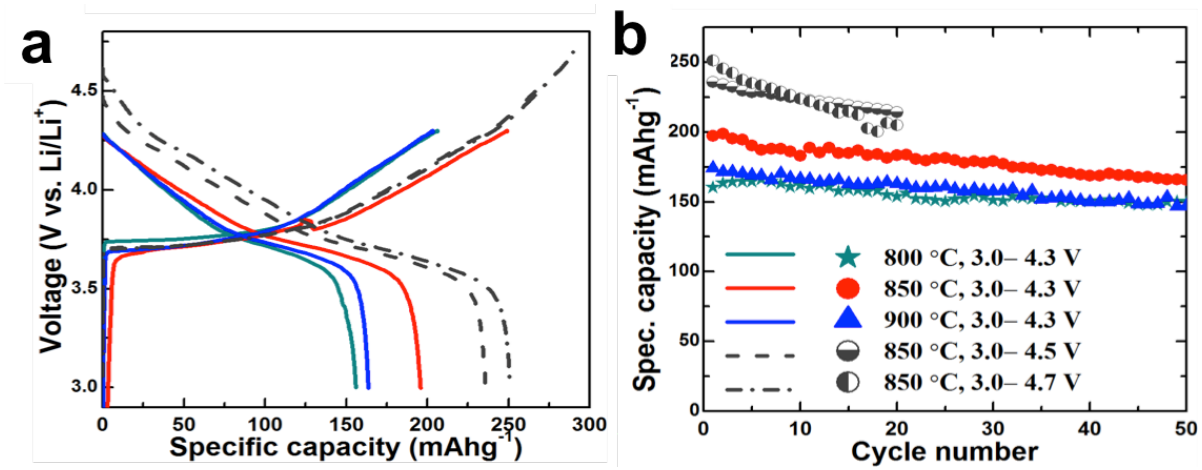


Figure II-261. Structural, chemical and morphological evolution in the intermediates of NMC71515 during heat treatment at 800°C, 850°C, 900°C. (a) Evolution of the cationic disordering (*i.e.,* occupancy of Ni ions at 3b sites). (b) TGA curves of the precursors during holding at constant temperatures. (c) Evolution of crystallite size with holding time.

## Conclusions

New capabilities were developed under this project, enabling *real time* probing of cation ordering in Ni-rich layered oxides during synthesis under controlled atmosphere. Details of the synthesis reactions can now be obtained through joint refinement of *in situ* XRD and ND data acquired from the same system, not only on the overall structural evolution, but the ordering of all the involved cations, thereby offering new insights into kinetic/thermodynamic parameters governing synthesis process in preparing Ni-rich layered oxides.

Following the previous studies on synthesis of $LiNiO_2$, $LiNi_{0.8}Co_{0.2}O_2$, *in situ* studies were further conducted on synthesis reactions in preparing high-Ni layered oxides, with focus on the specific composition of NMC71515, for getting deep insights into synthetic control of structural ordering in this type of materials. Time-resolved *in situ* HEXRD, XAS, ND were employed, coupled with quantitative data analysis, to track the kinetic reaction pathway and cationic ordering in the intermediates towards forming NMC71515 when subjected to high-temperatures heat treatment. The *real-time* observation revealed a dynamically competing cationic ordering/disordering process, arising from thermal-driven cationic oxidation and Li/O loss that concomitantly occurs during heat treatment. Through synthetic control of kinetic reaction pathway, the structural ordering of the final products was tuned for obtaining highly ordered NMC71515 with excellent electrochemical performance. The findings shed light on designing high-performance Ni-rich layered oxides through synthetic control of the kinetic reaction pathway and structural ordering in the materials.

In the future, *in situ* studies will be carried out for developing different types of cathodes, but with a focus on compositionally heterogeneous NMC layered oxides, wherein both high capacity and long cycling stability are expected to be achieved *via* synthetic control of local oxidation and ordering of cations in the materials.

## Key Publications


1. D. Wang, R. Kou, Y. Ren, C-J. Sun, H. Zhao, M-J. Zhang, Y. Li, A. Huq, J.Y.P. Ko, F. Pan, Y-K. Sun, Y. Yang, K. Amine, J. Bai, Z. Chen and F. Wang, "*Synthetic Control of Kinetic Reaction Pathway and Cationic Ordering in High-Nich Layered $LiNi_{0.7}Co_{0.15}Mn_{0.15}O_2$ Cathodes*", **Adv. Mater.** 29 (*2017*) 1606715.

2. Y-U. Park, J. Bai, L. Wang, G. Yoon, W. Zhang, H. Kim, S. Lee, S-W. Kim, J.P. Looney, K. Kang and F. Wang, "In situ Tracking Kinetic Pathways of $Li^+/Na^+$ Substitution during Ion-exchange Synthesis of $Li_xNa_{1.5-x}VOPO_4F_{0.5}$", **J. Am. Chem. Soc.** 139 (2017) 12504.

3. J. Zhao, W. Zhang, A. Huq, S.T. Misture, B. Zhang, S. Guo, L. Wu, Y. Zhu, Z. Chen, K. Amine, F. Pan, J. Bai, F. Wang, "*In-situ Probing and Synthetic Control of Cationic Ordering in Ni-rich Layered Oxide Cathodes"*, **Adv. Energy Mater.** 7 (2017) 1601266.

4. F. Wang, X. Wang, J. Graetz, P. Khalifah, "*Nanostructured Copper Vanadium Oxides as High-Capacity Cathodes for Lithium-ion Batteries"*, **US non-provisional patent** (*filed in Sept. 2017*).

5. ACS Spring Meeting, April 17-21, 2017, "*In-situ Structure-tracking Aided Design in Synthesis of Energy-Storage Materials*", F. Wang and J. Bai.

6. ACS Spring Meeting, April 17-21, 2017, "*Synthetic Control of Structural and Electrochemical Properties of High-Ni Layered Oxide Cathodes for Next-generation Li-ion Batteries*", D. Wang, M-J. Zhang, J. Bai and F. Wang.

7. MRS 2017 Spring Meeting, April. 17-21, 2017, "*In Situ* Tracking of the Structural Chemistry during Synthesis of Ni-Rich Layered Oxides as High-Energy Cathodes for Li-Ion Batteries", J. Bai, J. Zhao, D. Wang, J.Y. P. Ko, A. Huq and F. Wang.

8. Annual Merit Review, DOE, Washington, D.C. (June 5 – 9, 2017): "*In-situ Solvothermal Synthesis of Novel High- Capacity Cathodes*", F. Wang and J. Bai.

9. MRS 2016 Fall Meeting, *Developing High-Capacity Ni-rich Layered Oxide Cathodes for Li-ion Batteries via in-situ Synthetic Control of the Structure and Material Properties*, Nov. 27--Dec. 2, 2016, in Boston, Massachusetts, D. Wang, J. Bai, J. Zhao, W. Zhang, and F. Wang.

## II.C.8 Novel Cathode Materials and Processing Methods (ANL)

**Michael M. Thackeray, Principal Investigator**
Argonne National Laboratory
9700 South Cass Avenue
Lemont, IL 60439
Phone: 630-252-9184
E-mail: thackeray@anl.gov

**Jason R. Croy, Principal Investigator**
Argonne National Laboratory
9700 South Cass Avenue
Lemont, IL 60439
Phone: 630-252-9184
E-mail: croy@anl.gov

**Peter Faguy, Technology Manager**
U.S. Department of Energy
Phone: 202-586-1022
E-mail: Peter.Faguy@ee.doe.gov

Start Date: October 1, 2015 End Date: September 30, 2018
Total Project Cost: $500,000 DOE share: $500,000 Non-DOE share: $0

### Introduction

Research in lithium-ion batteries (LIB) is intensely focused on the development of next-generation systems capable of meeting ever-increasing demands placed on energy and power densities, while maintaining acceptable levels of cost and safety. Lithium- and manganese-rich, 'layered-layered' (LL), composite materials, $xLi_2MnO_3 \bullet (1-x)LiMO_2$ (M = Mn, Ni and Co; $0<x<0.5$), have received considerable attention owing to their high reversible capacities (~250 mAh/g) when compared to competing LIB cathodes that deliver capacities of <180 mAh/g (i.e., $LiCoO_2$, $LiMn_2O_4$, $Li_{1+x}Ni_{1a}Mn_bCo_cO_2$ (NMC) and $LiFePO_4$). In addition, Mn-rich materials are attractive due to their favorable cost and safety characteristics with respect to Co- and Ni-rich systems. However, key challenges to the wide scale adoption of LL composite cathodes remain. Notably, irreversible structural changes occur on the extraction of lithium from Li- and Mn-rich domains within the composite structure during first-cycle charge and "activation" above ~4.4 V (vs. $Li/Li^+$). These changes lead to subsequent voltage fade and hysteresis in the charge/discharge curves and slowly decrease the energy output of cells. Furthermore, the activation process leads to surface degradation that contributes to the material's poor rate performance, especially at low states of charge.

A promising approach to stabilizing LL structures has been to integrate a structurally compatible spinel component to form a complex, 'layered-layered-spinel' (LLS) composite. Previous work done under this project has shown that by controlling the amount of spinel integration, while limiting excess lithium contents, several metrics can be simultaneously improved. Specifically, voltage fade, rate capability, and first-cycle efficiencies are all enhanced for LLS cathodes with respect to their spinel-free, LL counterparts. In terms of surfaces, oxygen loss, surface reconstruction, and Mn dissolution are all surface issues that can contribute to poor cycle-life and rate performance of Li- and Mn-rich cathode materials and countless treatments/coatings have been tried in attempts to mitigate the adverse effects of unstable surfaces. Treatments have included carbons, phosphates, oxides, polymer coatings, and more. This chapter deals with efforts aimed at further stabilizing Mn-rich cathode materials. Specifically, a previously developed LLS composition is used to

systematically explore the effects of various surface chemistries and synthesis processes on rate and cycle-life of lithium-ion cells containing LLS cathodes.

## Objectives

- To develop low-cost, high-energy and high-power Mn-oxide-based cathodes for lithium-ion batteries that will meet the performance requirements of PHEV and EV vehicles
- Improve the design, composition and performance of advanced electrodes with stable architectures and surfaces, facilitated by an atomic-scale understanding of electrochemical degradation processes

## Approach

Exploit the concept and optimize the performance of structurally-integrated "composite" electrode structures with a prime focus on LLS materials. Alternative processing routes, in collaboration with Argonne's Materials Engineering Research Facility (MERF), will be investigated; Argonne National Laboratory's comprehensive synthesis and characterization facilities will be used to explore novel surface and bulk structures in the pursuit of advancing the properties of state-of-the-art cathode materials.

## Results

Several surface treatments and processing routes were investigated with respect to their efficacy in improving the cycle life and/or rate capability of a baseline LLS cathode. Preliminary studies aimed at optimizing the synthesis of a baseline LLS material were conducted using co-precipitation reactors at MERF, and within ANL's Chemical Sciences and Engineering (CSE) division. This effort resulted in high-quality LLS particles that were subsequently scaled to the ~1 kg level and used in surface-treatment studies.

The baseline LLS has a composition of ~$Li_{1.18}Mn_{0.54}Co_{0.18}Ni_{0.28}O_2$ with an integrated ~ 6% spinel component. Figure II-262a shows a scanning electron microscopy (SEM) image of the final, lithiated product. Particle analysis revealed a D50 (μm) = 20.7 and a reasonably high tap density of 2.0 g/cc. The material exhibited a reversible capacity of ~200 mAh/g when cycled between 4.45 – 2.5 V, after an initial activation cycle between 4.6 – 2.0 V, as shown in Figure II-262b. All electrochemical testing was carried out at 30°C using 15 mA/g charge and discharge currents in cells containing lithium-metal anodes.

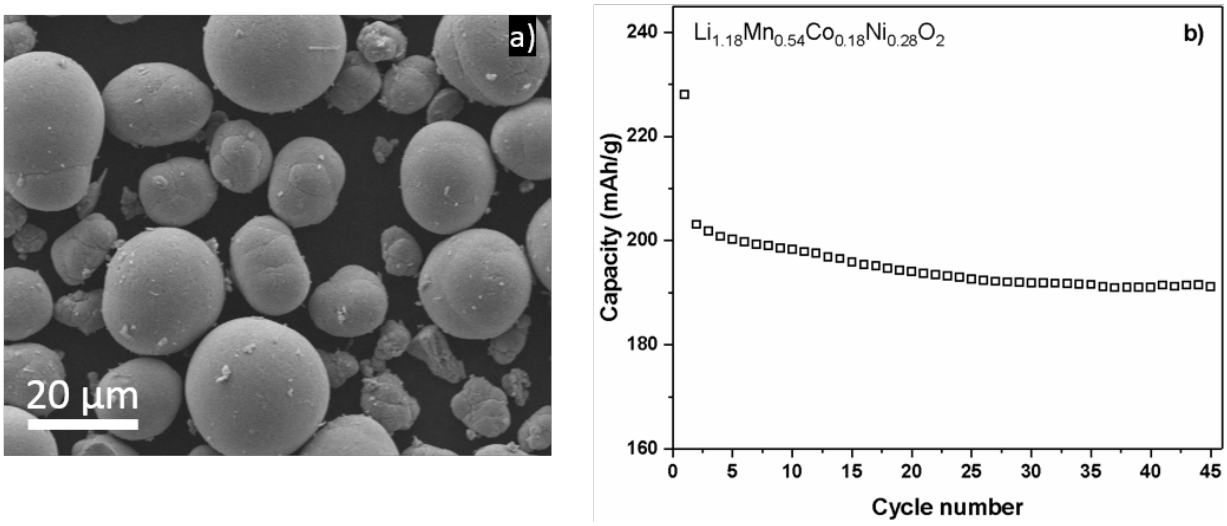


Figure II-262. a) SEM and b) cycle-life of the LLS baseline material used for all surface treatments. All electrochemical characterization was carried out at 30°C and 15 mA/g. Each material underwent an initial activation cycle between 4.6 – 2.0 V followed by extended cycling between 4.45 – 2.5 V vs. $Li/Li^+$.

The surface treatments consisted of three chemistries ($Li_2WO_4$, $Li_3PO_4$, and $Al_2O_3$) and their respective processing conditions. A summary of the processing conditions for each treatment is found in Table II-8. In short, each treatment was carried out via a wet-chemical method (aqueous) followed by several different post-synthesis annealing temperatures. The weight percent (wt.%) of each surface-treatment chemistry was previously optimized. In general, the capacity of the treated samples increased as the wt.% of the surface treatment decreased. The wt.% shown in Table II-8 for each surface-treatment chemistry exhibited improved cycle life while still maintaining an initial capacity similar to that of the baseline material (~ 200 mAh/g). SEM/energy dispersive spectroscopy (SEM/EDS) measurements on surface-treated samples suggest that homogenous coverage of the baseline material was achieved and that the morphology was unaffected during the surface treatments. Representative images are shown later in Figure II-265 (right).

**Table II-8: Surface treatments investigated on a LLS $Li_{1.18}Mn_{0.54}Co_{0.18}Ni_{0.28}O_2$ (~ 6% spinel)**

| Chemistry | Wt. % | Temp 1 | Temp 2 | Tem 3 | Temp 4 | Precursors |
|---|---|---|---|---|---|---|
| $Li_2WO_4$ | 2 | 500°C | 650°C | 850°C | -------- | $Li_2WO_4$ Sigma Aldrich |
| $Li_3PO_4$ | 1 | 100°C | 200°C | 550°C | 750°C | Lithium hydroxide and ammonium dihydrogen phosphate |
| $Al_2O_3$ | 0.5 | 100°C | 200°C | 400°C | 550°C | Aluminum nitrate nanohydrate |

The effect of post-treatment annealing temperature on the capacity retention for each of the surface-treatment chemistries is shown in Figure II-263(a-c). The untreated, baseline, LLS is shown as black squares in all figures. No clear trend was observed for samples treated with $Li_2WO_4$ with respect to the annealing temperature, Figure II-263a. However, a decrease in performance on going from 650°C to 850°C suggests that a volcano-type plot may result with more data points and that the optimum temperature is close to 650°C. Nonetheless, each of the samples treated with $Li_2WO_4$ exhibited superior cycle-life with respect to the baseline LLS. Surprisingly, the cycle-life improved as the annealing temperature was decreased for the samples treated with $Li_3PO_4$ (Figure II-263b) and $Al_2O_3$ (Figure II-263c). Interestingly, the samples treated at the lowest temperature of 100°C for both the $Li_3PO_4$ and $Al_2O_3$ (Figure II-263c) exhibited the best capacity retentions after 50 cycles. Overall, most of the surface-treated samples demonstrated improved capacity retention, irrespective of the chemistry. In fact, Figure II-263d reveals that the “best” sample for each of the surface chemistries produces similar capacity retention.

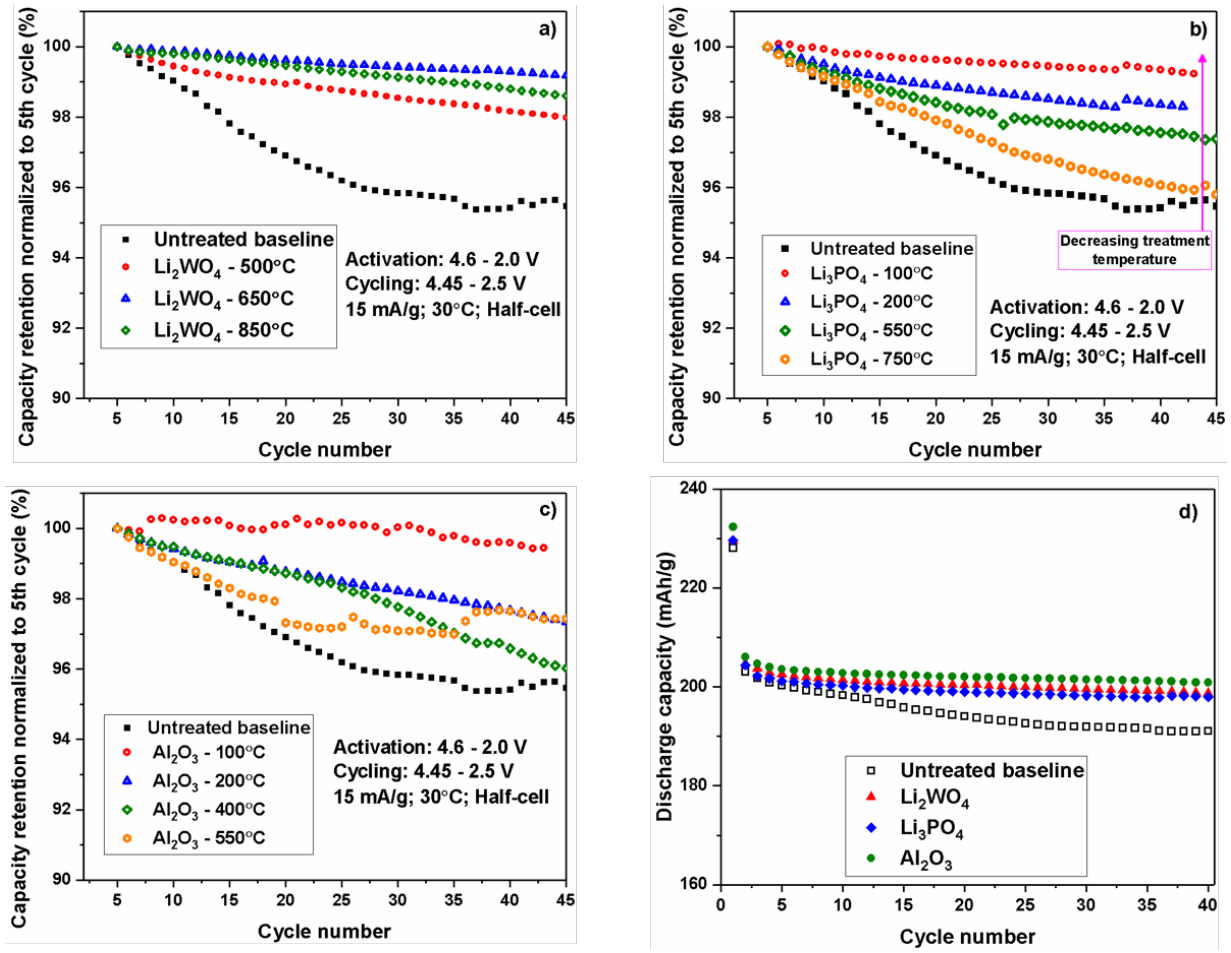


Figure II-263. Capacity retention vs. cycle number, as a function of post-treatment annealing temperature, for LLS samples that have undergone surface treatments with a) $Li_2WO_4$ b) $Li_3PO_4$ and c) $Al_2O_3$. The capacity retention was normalized to the discharge capacity delivered on the 5th cycle for each sample. d) A comparison of the cycle-life vs. cycle number of the baseline LLS with the best performing samples from each of the surface treatment chemistries presented in a)-c). All samples were cycled between 4.45 – 2.5 V (vs. $Li/Li^+$), at 15 mA/g, after an initial activation cycle between 4.6 – 2.0 V.

The rate performance of each of the samples was also tested at 30°C. An initial activation cycle was carried out between 4.6 – 2.0 V at 15 mA/g. All rate cycles were conducted between 4.45 – 2.5 V with a constant charge rate of 15 mA/g while the discharge rates were varied as shown in Figure II-264. As shown in Figure II-264(a-c), the post-treatment annealing temperatures did not affect the rate performances at low-to-intermediate currents (15 – 300 mA/g) for any of the surface chemistries investigated. However, at high currents (750 – 1500 mA/g) the rate performance of the surface treated samples revealed a direct correlation with the annealing temperature. The high rate performance of each surface chemistry improved as the annealing temperature decreased. In the case of the surface chemistries that contain lithium ($Li_2WO_4$ and $Li_3PO_4$, see Figure II-264(a-b), the sample treated with the highest annealing temperature performed similarly to the baseline LLS. While in the case of the surface chemistry that did not contain lithium ($Al_2O_3$, see Figure II-264c) the two samples treated at the highest annealing temperatures performed even worse than the baseline LLS. Similar to what was observed in the cycle life testing, a majority of the surface treatments improved the high rate performance of the underlying baseline material. The best performing samples for each of the chemistries are plotted against the baseline in Figure II-264d. The results suggest that similar improvements to the performance can be achieved with the appropriate annealing temperature after the surface treatment has been applied.

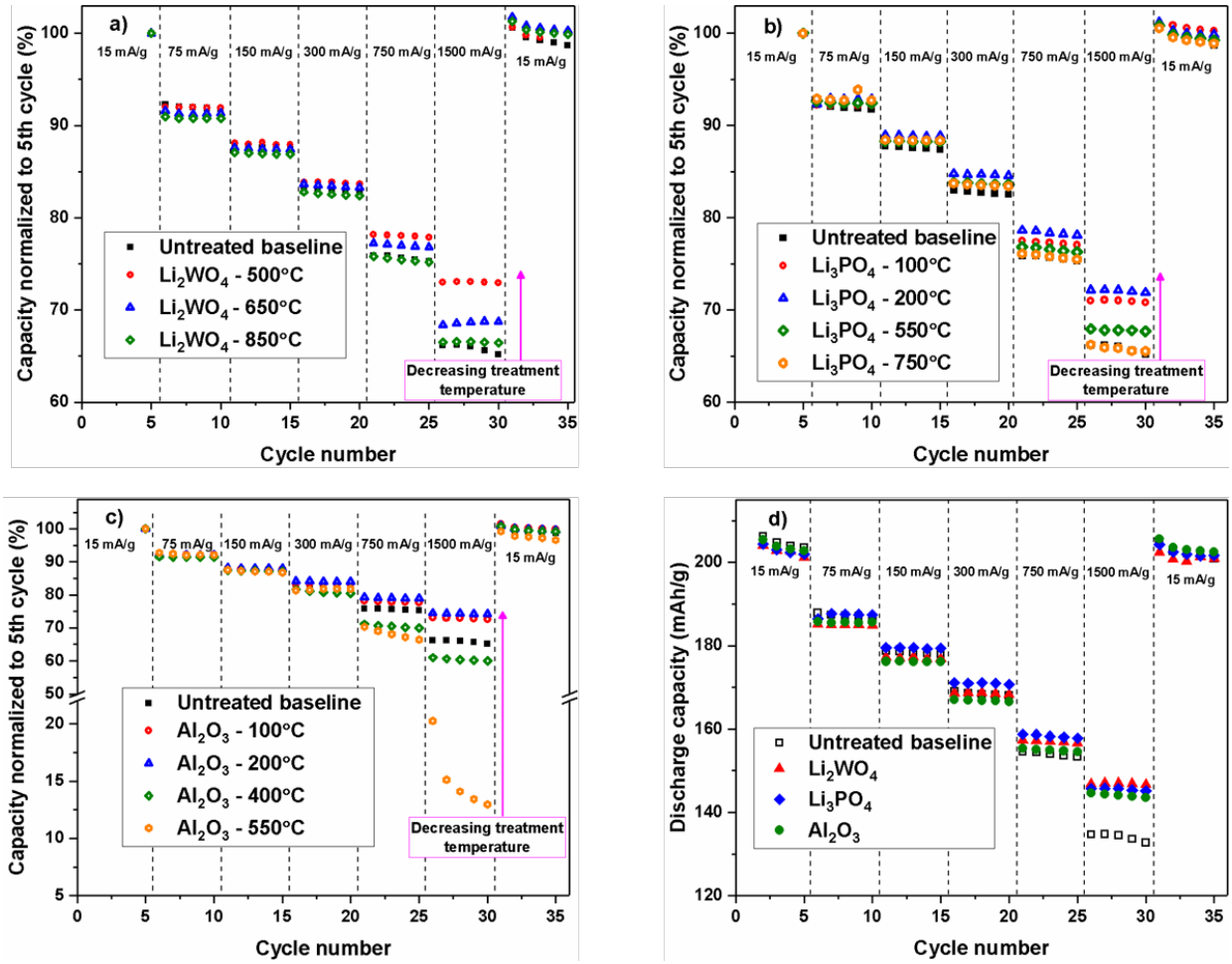


Figure II-264. Normalized capacity vs. cycle number, as a function of post-treatment annealing and discharge rate, for LLS samples that have undergone surface treatments with a) $Li_2WO_4$ b) $Li_3PO_4$ and c) $Al_2O_3$. The capacity of each cycle was normalized to the discharge capacity delivered on the 5$^{th}$ cycle for each sample. d) A comparison of the rate performance of the baseline LLS with the best performing samples from each of the surface treatment chemistries presented in a)-c). All samples were cycled between 4.45 – 2.5 V (vs. Li/Li$^+$) after an initial activation cycle (not shown in graph) between 4.6 – 2.0 V. Each charge cycle was carried out at 15 mA/g. The discharge currents were varied as labeled on each graph.

To gain a better understanding of the possible role lithium may be playing in the chemistry of the surface treatments, a series of samples was treated with 1 wt.% $Li_xCoPO_4$ with x = 0.25, 0.5, 0.75 and 1.0. The same LLS baseline material (~$Li_{1.18}Mn_{0.54}Co_{0.18}Ni_{0.28}O_2$ with ~ 6% spinel present) was used. In order to isolate the effect of the lithium content, the annealing temperature was kept constant (700°C). Each of the samples then underwent rate performance testing. The same protocol was used as before: initial activation cycle between 4.6 – 2.0 V followed by cycling between 4.45 – 2.5 V with a constant charge capacity of 15 mA/g. Each of the samples delivered a capacity of ~200 mAh/g when discharged at 15 mA/g, similar to the untreated baseline. The capacities delivered at subsequent discharge currents were normalized to respective, 5$^{th}$ cycle capacities. The results are shown in Figure II-265. Unlike the previous chemistries that were tested, samples treated with $LiCoPO_4$ all demonstrated superior rate performance, at all currents, when compared to the baseline LLS. Little to no difference was observed in samples with varied lithium contents in the surface treatments at discharge currents between 15 – 750 mA/g. Upon increasing the current to 1500 mA/g it was observed that, in general, the rate performance improved as the lithium content decreased in $Li_xCoPO_4$. Based on previous experiments with similar systems, it is hypothesized that phosphate-based (and other) treatments may leach lithium from cathode surfaces during processing. Subsequently, achieving optimized lithium contents and

structures, of both surface phases (e.g., $LiCoPO_4$) and the underlying cathode surfaces themselves, is not straightforward. The end product is dependent on processing parameters such as initial solution composition, pH, and post-annealing treatments. The strategy implied by the above results suggests an alternative route to incorporating integrated spinel phases at cathode particle surfaces via surface-treatment processing. Characterization efforts are ongoing to understand the phases present at the surfaces of these treated cathodes.

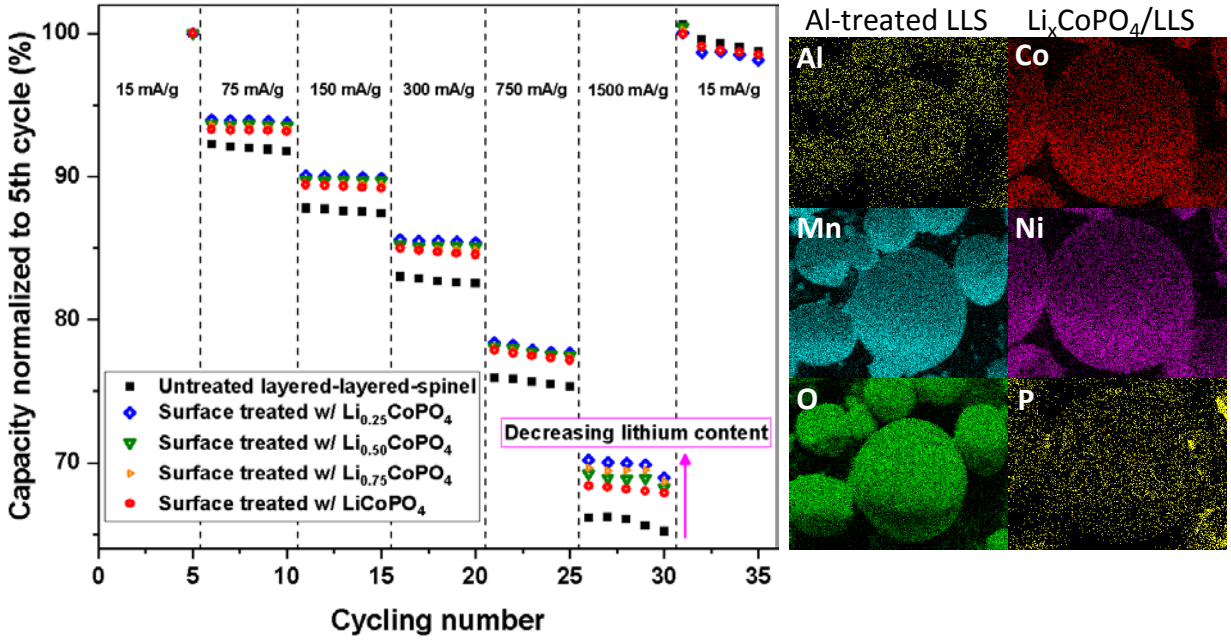


Figure II-265. (Left) Normalized capacity vs. cycle number, as a function of x in $Li_xCoPO_4$ surface treatments with x = 0.25, 0.5, 0.75 and 1.0. The capacity of each cycle was normalized to the discharge capacity delivered on the 5th cycle for each sample. All samples were cycled between 4.45 – 2.5 V (vs. $Li/Li^+$) after an initial activation cycle (not shown) between 4.6 – 2.0 V. Each charge cycle was carried out at 15 mA/g. The discharge currents were varied as labeled on the graph. (Right) EDS mapping of labeled elements for Al-treated LLS (left column) and $LiCoPO_4$ treated LLS (right column)

## Conclusions

The stabilization of Li- and Mn-rich, LLS, cathode particle surfaces was explored herein. From previous work done by this project, a baseline LLS composition of ~$Li_{1.18}Mn_{0.54}Co_{0.18}Ni_{0.28}O_2$, with ~ 6% integrated spinel, was scaled to the ~1 kg level and used for all surface treatments investigated. Among the parameters explored were surface-treatment chemistry and post-treatment annealing temperatures. Surface chemistries included both lithium- and non-lithium-containing oxides and phosphates. Interestingly, it was found that similar improvements to cycle-life and rate performance, with respect to the untreated baseline material, could be achieved by the appropriate choice of processing conditions for any of the given treatments, regardless of surface chemistry. In addition, lower-temperature, post-annealing conditions consistently led to better high-rate performance. Furthermore, the study revealed the complex interactions between particles surfaces and the solution chemistry. These interactions (e.g., Li leaching) were found to play an important role in determining the final electrochemical properties of surface-treated materials.

The results of this project show that surface treatments can indeed lead to improved performance of Mn-rich, LLS materials and that such treatments will be a critical and necessary aspect of future developments. However, due to the ambiguity of the observed improvements, where no surface chemistry resulted in a clear advantage over others, an important hypothesis might be formed to direct future research; as long as particle surface-treatments result in good uniformity of coverage with surface phases that do not obstruct Li-ion diffusion (e.g., thin or low-level treatments), enhancements over non-treated materials can be observed. It is

important to note that this hypothesis is not necessarily positive and may be particularly relevant to cells that do not utilize graphite anodes; where effects such as metal deposition at graphite surfaces leads to enhanced capacity fade. In this respect, ongoing experiments are looking at the efficiency of different treatments in mitigating metal dissolution from cathode surfaces. Finally, due to the unique surface properties and electrochemical mechanisms of Li- and Mn-rich materials, unique surface treatments and processing methods need to be developed in order to better address the novel challenges presented by these materials. Such materials and processes will be the focus of future work.

## Key Publications


1. Arturo Gutierrez, *The Next Generation of Li-ion Batteries for Transportation Applications: Perception, Promises and Problems*, University of Illinois Chicago, Chicago, IL, 08 November 2016. **Invited**

2. Jason R. Croy, Mahalingam Balasubramanian, Daniel C. O'Hanlon, Kevin G. Gallagher, Arturo Gutierrez, Eungje Lee, and Michael M. Thackeray, *The Pursuit of High-Capacity Cathodes for High-Energy Lithium-Ion Cells*, IBA 2017, Nara, Japan, 07 March 2017. **Invited**

3. A. Gutierrez, B. Yonemoto, M. He, E. Lee, R. Benedek, Y. Ren, H.M. Meyer II, J.R. Croy, and M.M. Thackeray, *Advancement of Li- and Mn-Rich High Energy Cathodes for Lithium-Ion Batteries*, Advanced Photon Source User Meeting (Lemont, IL), 9, May 2017.

4. M.M. Thackeray and J.R. Croy, *Tailoring Integrated Layered and Spinel Electrode Structures for High Capacity Lithium-Ion Cells*, ES049, DOE Vehicle Technologies Program Annual Merit Review (Arlington, VA), 5-9, June 2017.

5. J.R. Croy, *Development of Cathode Materials for Lithium-Ion Applications at Argonne National Laboratory*, ANL Battery Industry Day (Lemont, IL), 14, June 2017. **Invited**

6. Jason R. Croy, Michael M. Thackeray, Arturo Gutierrez, *Surface Treatment for Lithium Battery Electrode Materials*, U.S. Application filed 62/466,070.

## II.C.9 Design of High Performance, High Energy Cathode Materials (LBNL)

**Marca M. Doeff, Principal Investigator**
Lawrence Berkeley National Laboratory
1 Cyclotron Road, M/S 62R0100
Berkeley, CA 94720
Phone: 510-486-5821
E-mail: mmdoeff@lbl.gov

**Peter Faguy, Technology Manager**
U.S. Department of Energy
Phone: 202-586-1022
E-mail: Peter.Faguy@ee.doe.gov

Start Date: October 1, 2015 End Date: September 30, 2018
Total Project Cost: $1,800,000 DOE share: $1,800,000 Non-DOE share: $0

### Project Introduction

Ni-rich NMC ($LiNi_xMn_yCo_zO_2$; $x+y+z \approx 1$, $x \geq y+z$) cathodes have strong potential to increase energy density in lithium ion batteries in the near term, due to their high practical capacities (up to 200 mAh/g depending on Ni content and voltage limits used). As Ni content is increased, however, cycle life is diminished and safety is adversely impacted [1]. The aim of this project is to understand the surface, interfacial, and bulk properties of Ni-rich NMCs (in FY 2017, particular emphasis was placed on NMC-622), and how they affect the thermal and electrochemical properties.

Our previous work showed that NMC cathodes suffer from surface reconstruction to a rock salt-like phase under a variety of conditions including storage in electrolytic solution, normal cycling, and high voltage cycling [2]. The surface reconstruction is probably responsible for the first cycle coulombic inefficiencies that are commonly observed, even when using conservative voltage limits. In addition, high voltage cycling results in the formation of an unfavorable cathode/electrolyte interface (CEI) layer that increases cell impedance [3]. It is this rise in cell impedance, rather than deterioration of the bulk material, that results in capacity fading during cycling to high potentials. Driving forces in both of these phenomena are the high reactivity of surface Ni ions, and the strong tendency for Ni-containing oxides to lose surface oxygen, particularly at high states-of-charge. Soft X-ray absorption studies reveal that charge compensation occurs mainly on the transition metal ions in the bulk (primarily Ni in Ni-rich NMCs) but at the surface, oxygen has a greater tendency to undergo redox processes [4]. It is the high reactivity of surface oxygen that is responsible for surface reconstruction and formation of resistive reaction layers on particle surfaces via reactions with components in the electrolytic solution. One strategy to ameliorate these phenomena includes partial Ti substitution for Co. In NMC-442, the presence of Ti delays loss of oxygen to higher levels of delithiation [5]. Improved cycling behavior is observed for Ti-substituted NMC materials when delithiated to the same level as unsubstituted NMC during high voltage cycling [6]. Synthetic methods can also be used to make materials with reduced Ni contents on particle surfaces. NMC-442 made by a simple and scalable spray pyrolysis method, exhibited a graded composition such that the Ni content was naturally lower on both the primary and secondary particle surfaces than in the bulk [7]. Materials made by this method exhibited better cycling behavior to high potentials and decreased amounts of surface reconstruction. During FY17, we focused on NMC-622, with the goal of understanding the role of heterogeneity on the electrochemical properties by studying both chemically and electrochemically delithiated samples and comparing them. The results of this study showed that the electrolytic solution plays a critical role in the surface reconstruction and cathode/electrolyte interface formation. A number of experiments were also carried out to understand the thermal properties of NMC-622 by studying partially and fully delithiated materials by various synchrotron techniques to understand surface and bulk processes. Much of this work is still being analyzed and will be reported during the next fiscal year.

## Objectives

Our objectives are to understand what limits the cycling behavior of Ni-rich NMCs and to gain a deeper understanding of their thermal properties. Once this is done, methods to improve the robustness of the materials can be developed, ranging from partial substitution with Ti (for example), coatings, and synthetic strategies to reduce surface Ni content.

## Approach

We use a highly collaborative approach to understand electrochemical and thermal characteristics of Ni-rich NMC materials. In some cases, commercially provided materials are studied, but we also synthesize our own, either by classic co-precipitation methods or by spray pyrolysis. Chemically delithiated samples are compared to those prepared electrochemically. Electrochemical characterization is carried out in lithium half-cell configurations. A combination of synchrotron radiation and electron microscopy techniques (in collaboration with A. Mehta, D. Nordlund, T.-C. Weng, and Y. Liu at SSRL and H. L. Xin at BNL) are used to understand the surface and bulk characteristics of the NMCs (commercial materials, synthesized materials, chemically and electrochemically delithiated samples, etc). Several physical techniques (XRD, SEM, OES-ICP, etc.) are used to characterize materials before and after electrochemical cycling under a variety of conditions. Nanotomographic imaging (Transmission x-ray microscopy, TXM) at SSRL is used to determine chemical gradients in particles and correlate this with electrochemical behavior. Soft x-ray absorption spectroscopy (XAS) experiments carried out at SSRL are used to probe oxidation states of transition metals at particle surfaces and in the bulk as a function of their electrochemical history. These results are correlated with scanning transmission electron microscopy (STEM) and electron energy loss spectroscopy (EELS) experiments at Brookhaven National Laboratory to obtain a full understanding of what governs the behavior of NMCs as a function of composition, temperature and cycling history. For a full overview of the behavior of NMCs, the PI works closely with other PIs in the Advanced Battery Materials Research program, including R. Kostecki (interfacial characteristics using spectroscopy), W. Tong (novel materials), B. McCloskey (differential electrochemical mass spectroscopy to measure gas evolution), and C. Ban (NREL, atomic and molecular layer deposition for protective layers on cathode materials).

## Results

A comprehensive study to detail inhomogeneity in NMC-622 cathode materials was carried out in FY 2017. One goal of the study was to determine what differences there are between chemically and electrochemically delithiated samples. This is important because chemically delithiated samples are commonly use to model electrochemical processes in NMCs and other electrode materials. For this study, we subjected a commercial NMC-622 to partial chemical delithiation with either $NO_2BF_4$ or $Br_2$. $NO_2BF_4$ is a stronger oxidizing agent than $Br_2$; it is possible to completely delithiate NMCs with the former (although it is complicated by proton exchange), but not with the latter. We also partially charged a sample in an electrochemical cell and subjected another sample to full charge and then partial discharge. All samples were approximately in the halfway lithiated state, with some variation in the exact degree of delithiation.

Examination by scanning electron microscopy indicated that the chemically delithiated samples were damaged by the oxidation process, whereas the electrochemically prepared samples remained intact and particles resembled that of the pristine sample. Specifically, there was loss of contact between primary particles in the large secondary particles for the chemically delithiated samples. This is attributable to mechanical damage from stirring, and possibly to evolution of $NO_x$ gases from the sample treated with $NO_2BF_4$. Ni K-edge X-ray absorption spectroscopy was used to determine the oxidation state of Ni, which is closely related to the degree of lithiation (Co is also electroactive, but most charge compensation occurs at Ni). Shifts in the Ni K-edge were consistent with the coulometry in the case of the electrochemically prepared samples, or with the elemental analysis of the chemically delithiated material.

Representative multi-pixel averaged XANES spectra, histograms of the distribution of the Ni oxidation states (positions of the Ni K-edge) and 2 dimensional mapping of the Ni K-edge from the TXM experiments are shown in Figure II-266. These results reveal considerable heterogeneity in the Ni oxidation state in the pristine

commercial sample. Both chemically and electrochemically delithiated samples are more homogeneous, as the narrowing of the histogram peaks show. However, by carrying out the 2D mapping using a finer scale, heterogeneities in all of the partially delithiated samples can be observed (Figure II-267). In particular, Ni oxidation states are lower at the cracks in the chemically delithiated sample because these cracks, induced by mechanical damage, are exposed to the oxidant for a shorter period of time. Similar heterogeneities are seen in the samples treated with bromine (not shown). The source of the heterogeneity of the electrochemically oxidized samples are more likely due to disconnection of primary particles as they undergo redox-related volume changes.

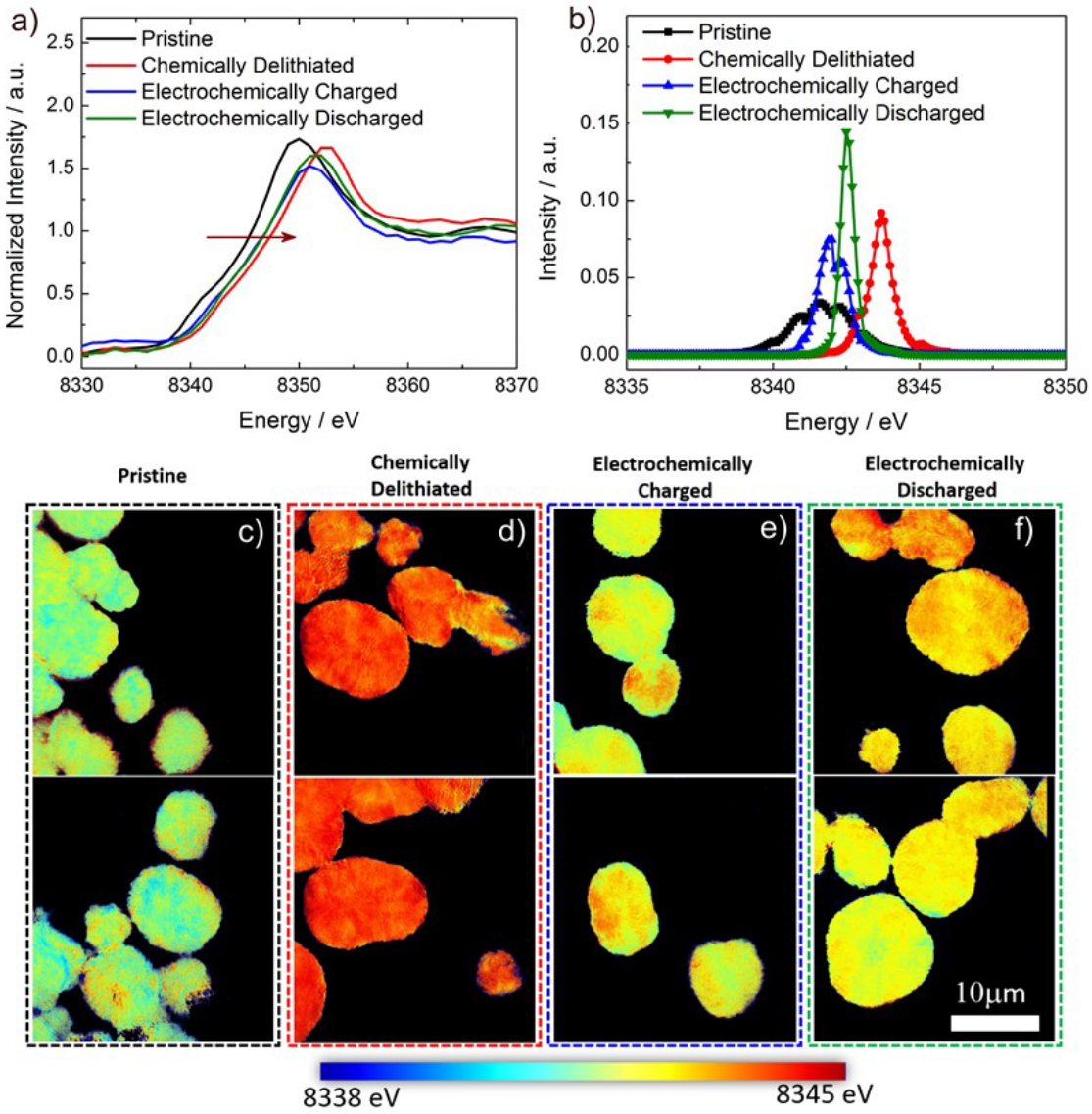


Figure II-266. (a) Representative multiple pixels averaged XANES spectra and (b) histogram of Ni K-edge shifts for pristine (black curve), chemically delithiated with $NO_2BF_4$ (red curve), electrochemically charged (blue curve) and electrochemically discharged (green) samples. 2D mapping of Ni K-edge in the samples (c) pristine NMC; (d) chemically delithiated NMC-622; (e) electrochemically charged NMC-622 electrode and (f) electrochemically discharged NMC-622.

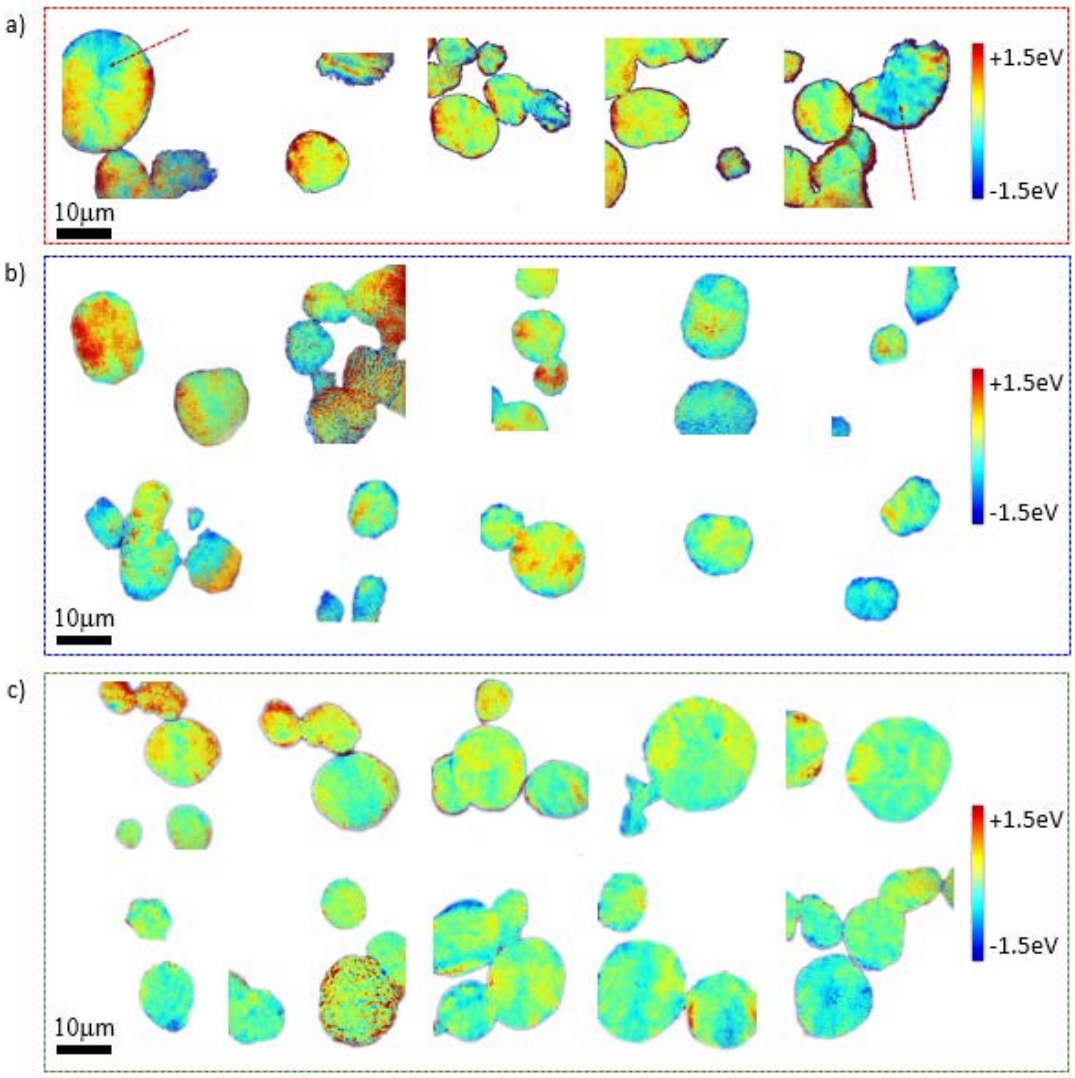


Figure II-267. Color mapping of (a) chemically delithiated NMC-622; (b) electrochemically charged NMC-622 electrode and (c) electrochemically discharged NMC-622 electrode. The color mapping was determined using the statistical peak energy as the center, and then -1.5eV (blue) and +1.5eV (red) as the two ends. Arrows point to regions of microcracks, which are less oxidized than surrounding areas.

Here dramatic differences can be observed among the different samples. In particular, the chemically delithiated sample shows almost no difference between the surface and the bulk. In contrast, a good deal of surface reconstruction is seen in the pristine sample already, and in the electrochemically delithiated sample. These differences can be quantified (Table II-9) and suggest strongly that exposure to the electrolytic solution drives the surface reconstruction. For the rock salt to form, metal ions must be reduced, but this requires something else to be oxidized. Components in the electrolytic solution serve this purpose during electrochemical oxidation, showing that surface reconstruction and CEI formation are intimately related. In the case of the chemical oxidation, there is no available material that can reduce the surface of the NMC particles and in turn be oxidized.

Table II-9: Relative L3 high to L3 low peak intensity ratio from nickel L-edge XAS spectra.

| $L_3$ high/$L_3$ low Intensity (γ) | Pristine | Electrochemically charged 50% | Electrochemically discharged 50% | Chemical delithiation 50% |
|---|---|---|---|---|
| $\gamma_{TEY}$ | 0.56 | 0.87 | 0.57 | 1.64 |
| $\gamma_{FY}$ | 0.83 | 1.28 | 1.04 | 1.78 |
| $\Delta = \gamma_{TEY} - \gamma_{FY}$ | 0.27 | 0.41 | 0.47 | 0.14 |

Figure II-268 shows Ni L-edge XAS results on the samples in two different modes. Total electron yield (TEY) probes about 5 nm into the particle surfaces, whereas fluorescence yield (FY) mode probes about 50 nm in, or into the bulk. Differences between the ratios of the two $L_3$ edges in the two different modes are diagnostic of surface reconstruction, as the rock salt surface layer contains metal ions in a reduced state compared to that in the bulk layered structure.

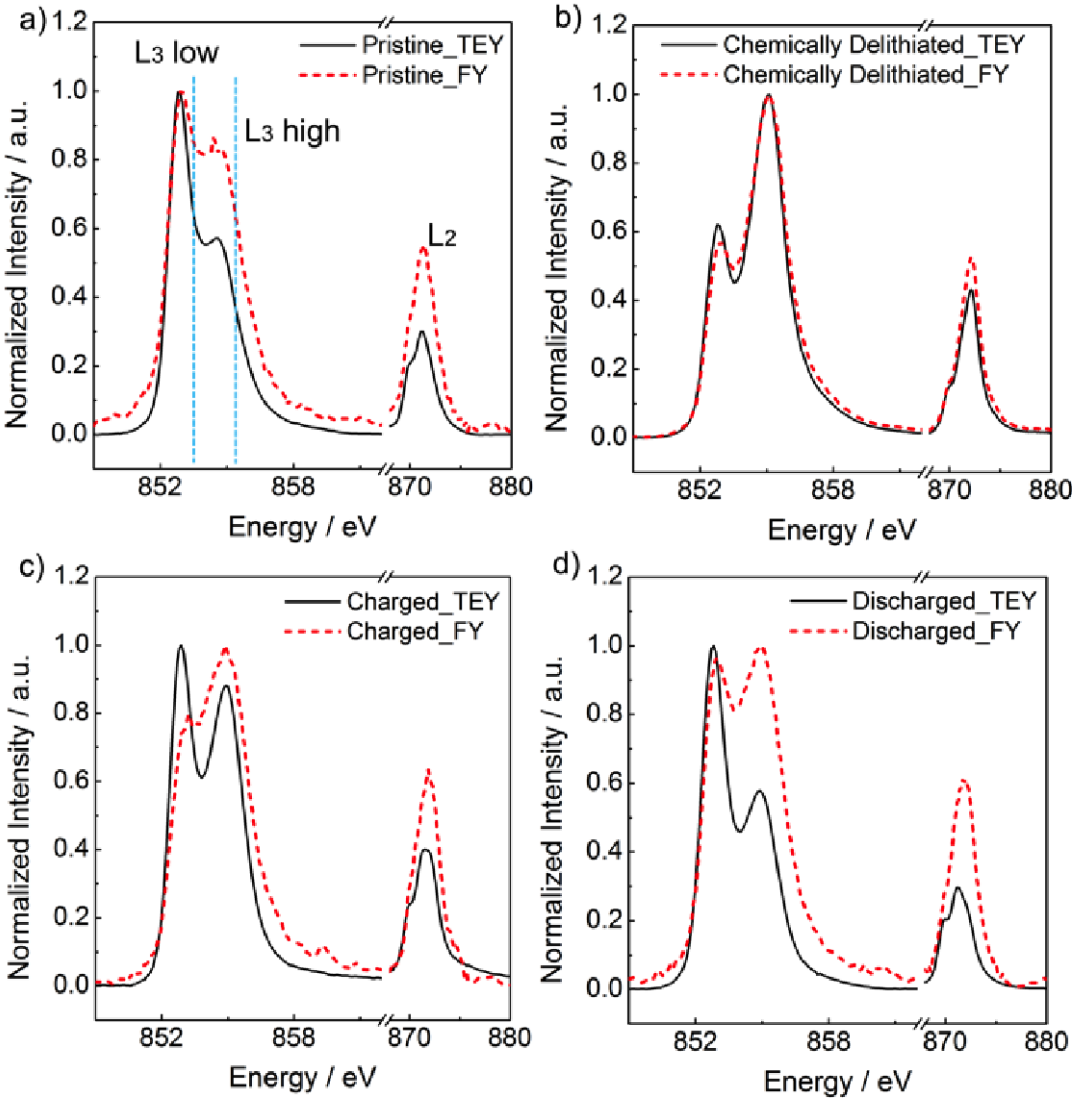


Figure II-268. Ni L-edge XAS spectra of (a) NMC-622 (b) chemically delithiated NMC-622; (c) electrochemically charged NMC622 electrode and (d) electrochemically discharged NMC-622 electrode collected using TEY (solid black curve) and FY (dashed red curve) modes.

## Conclusions

Commercial NMC-622 samples show considerable heterogeneity even in the pristine state. While chemical or electrochemical delithiation results in some homogenization, variations in oxidation states exist. These can be attributed to mechanical damage from the chemical oxidation process or disconnection of primary particles during electrochemical cycling. A significant finding is the fact that chemically delithiated samples show much less surface reconstruction than the electrochemically delithiated ones. This strongly suggests that contact with the electrolytic solution plays an important role in this phenomenon.

## References


1. H.-J. Noh, S. Youn, C.S. Yoon, and Y.-K. Sun, *J. Power Sources*, 233, 121 (2013).
2. Feng Lin, Isaac Markus, Dennis Nordlund, Tsu-Chien Weng, Mark Asta, Huolin L. Xin, and Marca M. Doeff, *Nature Commun***.** 5:3529, DOI: 10.1038/ncomms4529 (2014).
3. Feng Lin, Isaac M. Markus, Dennis Nordlund, Tsu-Chien Weng, Huolin L. Xin, and Marca M. Doeff, *Energy & Environ. Sci.* **7**, 3077 (2014).
4. C. Tian, D. Nordlund, H. Xin, Y. Xu, Y. Liu, D. Sokara, F. Lin, and M. Doeff, *J. Phys. Chem. A* submitted (2017).
5. Isaac Markus, Feng Lin, Kinson Kam, Mark Asta, and Marca Doeff, *J. Phys. Chem. Lett***.** 5, 3649 (2014).
6. S. Wolff-Goodrich, F. Lin, I. Markus, D. Nordlund, H. Xin, M. Asta, and M. M. Doeff, *Phys. Chem. Chem. Phys.* 17, 21778 (2015).
7. F. Lin, D. Nordlund, Y. Li, M. K. Quan, L. Cheng, T.-C. Weng, Y. Liu, H.L. Xin and M. M. Doeff, *Nature Energy* 1, 1 (2016).


## Key Publications


1. "Synchrotron X-ray Techniques for Studying Materials Electrochemistry in Rechargeable Batteries", Feng Lin, Yijin Liu, Xiqian Yu, Lei Cheng, Andrej Singer, Oleg G. Shpryko, Huolin Xin, Nobumichi Tamura, Chixia Tian, Tsu-Chien Weng, Xiao-Qing Yang, Ying Shirley Meng, Dennis Nordlund, Wanli Yang, and Marca Doeff, **Chem. Rev.** 10.1021/acs.chemrev.7b00007 (2017).
2. "Crystal Chemistry and Electrochemistry of $LiMn_{1.5}Ni_{0.5}O_4$ Solid Solution Cathode Materials", Wang Kan, Saravanan Kuppan, Lei Cheng, Marca Doeff, Jagjit Nanda, Ashfia Huq, and Guoying Chen **Chem. Mater.** DOI: 10.1021/acs.chemmater.7b01898 (2017).
3. "$Co_{11}Li[(OH)_5O][PO_3OH)(PO_4)_5]$, a Lithium-Stabilized, Mixed-Valent Cobalt (II, II) Hydroxide Phosphate Framework" J. Ludwig, S. Geprägs, D. Nordlund, M. Doeff, and T. Nilges, **Inorg. Chem.** DOI:10.1021/acs.inorgchem.7b01152 (2017).
4. "Direct Synthesis and Characterization of mixed-valent $Li_{0.5-\delta}CoPO_4$, a Li-deficient Derivative of the *Cmcm* Polymorph of $LiCoPO_4$", J. Ludwig, C. Alarcón-Suesca, S. Geprägs, D. Nordlund, M.M. Doeff, I. Puente Orench, and T. Nilges, **RSC Advances** 7, 28069 (2017).
5. "Enhanced Lithium Ion Transport in Garnet-type Solid State Electrolytes" Lei Cheng, Huaming Hou, Simon Lux, Robert Kostecki, Ryan Davis, Vassilia Zorba, Apurva Mehta, and Marca Doeff, **J. Electroceramics** DOI: 10.1007/s10832-017-0080-3 (2017).
6. "Synthesis and Characterization of Metastable, 20 nm-sized Pna21-$LiCoPO_4$ Nanospheres" Jennifer Ludwig, Dennis Nordlund, Marca M. Doeff and Thomas Nilges, **J. Solid State Chem.** 248, 9 (2017).

7. "Particle Size-controllable, Microwave-assisted Solvothermal Synthesis of the High-Voltage Cathode Material $LiCoPO_4$ using Water/Ethylene Glycol Solvent Blends" Jennifer Ludwig, Dominik Haering, Marca M. Doeff, and Tom Nilges, **Solid State Sciences,** 65, 100 (2017).

8. "Investigating the Intercalation Chemistry of Alkali Ions in Fluoride Perovksites", Tanghong Yi, Wei Chen, Lei Cheng, Ryan D. Bayliss, Feng Lin, Michael R. Plews, Dennis Nordlund, Marca M. Doeff, Kristin A. Persson, and Jordi Cabana, **Chem. Mater.**, 29, 1561 (2017).

9. "The Road to Solid State Batteries for Vehicle Applications" The 12th Pacific Rim Conference on Ceramic and Glass Technology, Waikoloa, HI, May 21-26, 2017. (invited)

10. "The Future of Energy Storage for Vehicle Applications" Marca M. Doeff, SVC TechCon 2017, 60th Annual Society of Vacuum Coaters Technical Conference, Providence RI, April 29-May 4, 2017. (invited)

11. "Studies on NMC and LLZO Materials for Lithium Batteries" Marca M. Doeff, Bosch Research and Technology Center, North America, Palo Alto CA, April 13, 2017. (invited)

12. "Materials for Next Generation Electric Vehicle Batteries" Materials Sciences and Engineering Colloquium, Fu Foundation School of Engineering and Applied Science, Columbia University, New York, NY March 24, 2017. (invited)

13. "Recent Progress on Battery Materials", Marca M. Doeff, The 2nd International Symposium on Renewable Energy Technologies", Sydney, Australia, Nov. 30-Dec. 4, 2016. (invited)

14. "Illuminating Performance Characteristics of Battery Materials Using Synchrotron Techniques: Advanced NMCs, Sodium-Ion Batteries, and Solid Garnet-Type Electrolytes" Marca M. Doeff, Energy Harvesting USA, Santa Clara CA, November 16-17, 2016. (invited)

15. "The Future of Solid State Batteries for Electric Vehicles" Marca M. Doeff, The Northern California Chapter of The American Vacuum Society, San Jose, CA November 16, 2016.

16. Design of High Performance, High Energy Cathode Materials" Marca M. Doeff 2017 DOE Annual Peer Review Meeting Presentation.

17. "Editorial for the JECR Special Issue on All Solid-State Batteries" J. L. M. Rupp, D. Rettenwander, J. Kilner, and Marca M. Doeff, **J. Electroceramics**, DOI 10.1007/s10832-017-0102-1 (2017).

18. "The Mechanism of Impedance Increase in Nickel-Rich NMC Cathodes" R.C. Lee, C. Tian, M. Doeff, and R. Kostecki, 232nd Meeting of the Electrochemical Society, National Harbor, MD, Oct. 1-6, 2017.

19. "Ionic Liquid Enabled High Energy-Density Lithium-Ion Batteries" T. Evans, D. Molina Piper, S.C. Kim, S. Han, M. Doeff, C. Ban, S.J. Cho, K.H. Oh, and S. Lee, 231st Meeting of the Electrochemical Society, New Orleans, LA, May 28-June 2, 2017.

20. "Controlling the Surface Chemistry of Cathode Materials for High Energy Rechargeable Batteries" F. Lin and M. M. Doeff, 231st Meeting of the Electrochemical Society, New Orleans, LA, May 28-June 2, 2017.

21. "Structural Stability of Nickel-Rich Layered Cathode Materials" Chixia Tian, Yahong Xu, Dennis Nordlund, Huolin Xin, Yijin Liu, and Marca Doeff. PRIME 2016, Honolulu, HI, October 2-7, 2016.

## II.C.10 Lithium Batteries with Higher Capacity and Voltage (UTA)

**John B. Goodenough, Principal Investigator**
The University of Texas at Austin
204 E. Dean Keeton St.
Austin, TX 78712
Phone: 512-471-1646
E-mail: jgoodenough@mail.utexas.edu

**Tien Duong, Technology Manager**
U.S. Department of Energy
Phone: 202-586-7836
E-mail: Tien.Duong@ee.doe.gov

Start Date: April 16, 2015 End Date: June 30, 2018
Total Project Cost: $398,000 DOE share: $398,000 Non-DOE share: $0

### Project Introduction

The dependence of modern society on the energy stored in a fossil fuel is not sustainable. A fossil fuel, once burned, is not recyclable; the gases from fossil-fuel combustion are already choking large population in major cities such as Beijing in China and Delhi in India. The introduction of an all-electric road vehicle powered by a rechargeable battery that is competitive in cost, safety, and convenience with today's road vehicles powered by the internal combustion engine would reduce, if not remove, the distributed air pollution generated on the highways of the world. Such a battery would also allow storage of electric power harvested from the sun's energy that arrives daily.

The flammable liquid electrolyte of the Li-ion battery of the wireless revolution has prevented the development with today's technology of a safe, cost-competitive battery that can compete with the internal combustion engine.

### Objectives

Replacement of the flammable liquid electrolyte with a solid electrolyte from which an alkali-metal anode can be plated/stripped reversibly and dendrite-free as the anode would provide a safe, rechargeable battery of higher volumetric energy density than the Li-ion battery, but the low cation conductivity of known solids and the problems of a solid/solid electrode/electrolyte interface with changing volumes of the electrodes have suppressed investigation of high-energy-density all-solid-state rechargeable batteries with a long charge/discharge cycle life. The objective of this project was to explore whether these problems can be overcome.

### Approach

Characterize several $Li^+$ solid electrolytes stable on contact with metallic lithium that provide dendrite free plating of a metallic-lithium anode. Investigate whether this solid electrolyte is stable with an aqueous and/or an organic liquid electrolyte. Develop a test cell with a lithium anode and a Cu cathode.

### Results

The project was conducted in collaboration with others in my group supported for parallel work. We have reported previously only results obtained with regard to milestones specified by this project. Here, our previously supported results are placed in the broader context of our collaboration effort.

We began with the choice of a ceramic solid $Li^+$ electrolyte that would not be reduced on contact with metallic lithium The $Li_7La_3Zr_2O_{12}$ (LLZO) with the garnet structure had been reported to have a room temperature $Li^+$

conductivity $\sigma_{Li} \approx 10^{-4}$ S cm$^{-1}$, and we had improved the bulk conductivity to $\sigma_{Li} \approx 10^{-3}$ S cm$^{-1}$ by substituting Ta for Zr in $Li_{6.5}La_3Zr_{1.5}Ta_{0.5}O_{12}$ (LLZT), but we found the materials to be highly hygroscopic; $Li_2CO_3$ and LiOH formed at the surface of the grains reduce performance. Both LiOH and $Li_2CO_3$ are Li-ion insulators, which leads to a large grain-boundary resistance of the garnet electrolyte and the lithium/garnet interface also has a large plating/stripping impedance. We used LiF to increase the stability of the garnet electrolyte LLZT against moisture and carbon dioxide in air; the grain-boundary and interfacial resistances were reduced significantly, which makes LLZT a possible solid electrolyte in Li–S batteries.

To demonstrate the advantages of the LiF modification that decreases the interfacial resistance, Li-S cells with a LLZT and a LLZT-2LiF solid electrolyte were assembled. The solid electrolyte can efficiently block the polysulfide shuttle, which is a severe problem in Li-S batteries. The total resistance of the cells with LLZT and LLZT-2LiF in Figure II-269(a) were 1000 and 2620 Ω cm$^{-2}$, respectively. The cells with LLZT and LLZT-LiF display well-defined discharge/charge plateaus and low overpotentials. The cell with LLZT-2LiF exhibited a much lower gap (0.34 V) between charge and discharge voltages than that with LLZT (0.59 V) at the current density of 200 μA cm$^{-2}$. The much reduced interfacial resistance allows the cells to be cycled at high current densities. As shown in Figure II-269(c), discharge capacities of 1137, 1074, and 1042 mAh g$^{-1}$ can be obtained at the rates of 100, 200 and 300 μA cm$^{-2}$, respectively. Notably, since the polysulfide shuttle can be completely blocked by the solid electrolyte, the hybrid cells assembled also exhibit a stable cyclability at 200 μA cm$^{-2}$. The reversible capacity stabilized at 988 mAh g$^{-1}$ after 100 cycles with the retention of 93% of the stabilized capacity in the second cycle (Figure II-269(d)). Furthermore, the Coulombic efficiency maintains almost 100% over the subsequent 100 cycles, which is much higher than the Li–S cell without garnet in Figure II-270, indicating that the solid electrolyte can successfully block the polysulfide shuttle during the whole cycling processes.

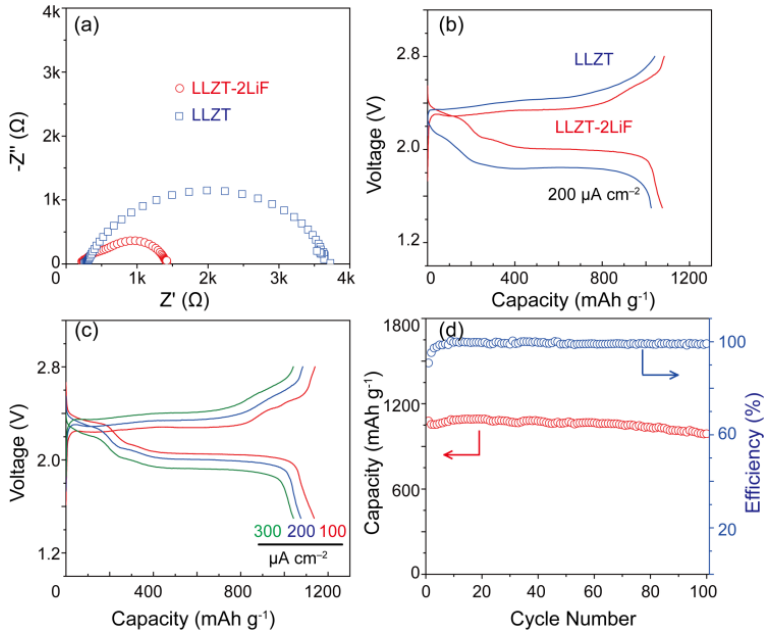


Figure II-269. (a) The impedance plots of a Li–S battery, (b) charge and discharge voltage profiles of a Li–S battery (b) with LLZT and LLZT–2LiF as a separator, (c) charge and discharge voltage profiles of a Li–S battery with LLZT–2LiF at different current densities, (d) capacity retention and cycling efficiency of the Li–S battery.

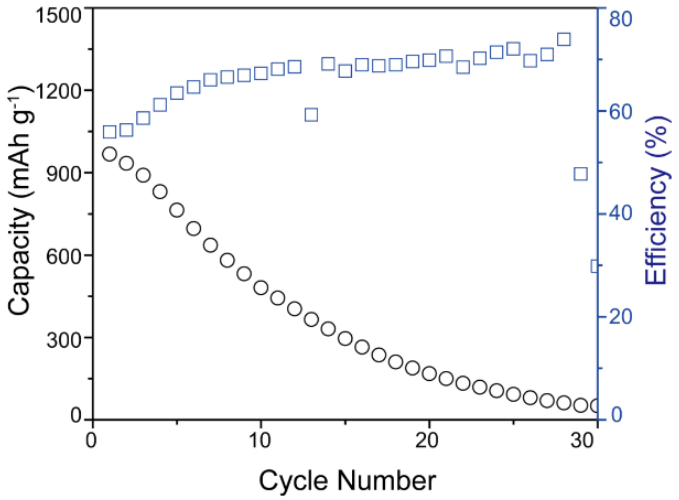


Figure II-270. Cycling stability and Coulombic efficiency of the Li-S cell without solid electrolyte nor $LiNO_3$ additive.

Although we were able to reduce the $Li_2CO_3$ contamination by introducing LiF at the grain surfaces, removal of $Li_2CO_3$ was not complete, so we turned to investigate a ceramic with the perovskite structure. (In subsequent work, we have developed a preparative procedure that removes all the $Li_2CO_3$ and shown that the garnet is then wet by a Li-metal anode to give dendrite-free plating/stripping of a lithium anode with little interface impedance; the cells operate well at 60°C.)

In the second quarter, we investigated a perovskite $Li^+$ solid electrolyte, $Li_{1/8}Sr_{7/16}Hf_{1/9}Ta_{1/4}O_{32}$ (LSHT) that we could make 99.9% dense by spark plasma sintering. LSHT has a room-temperature Li–ion conductivity $\sigma = 4.4 \times 10^{-4}$ S $cm^{-1}$ and a small activation energy of 0.33 eV from 298 to 420 K (Figure II-271). Another advantage of LSHT is its good stability in air; unlike the garnet electrolyte which reacts with moist air to form $Li_2CO_3$, there is no $Li_2CO_3$ detectable with a Raman shift at 1080 $cm^{-1}$on the surface of a perovskite LSHT pellet after exposure to air for 3 months.

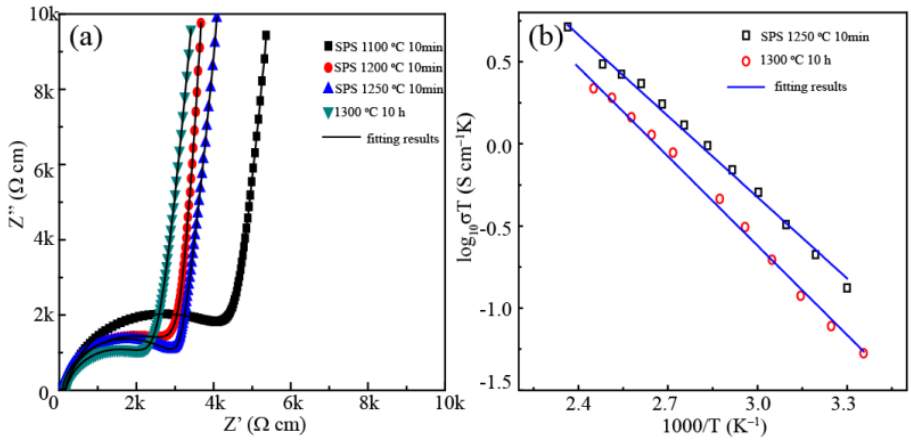


Figure II-271. (a) Impedance spectra and (b) Arrhenius plot of LSTH pellet fired by spark plasma sintering.

Because of its stability, LSHT shows a small interfacial resistance with a solid polymer electrolyte and commercial organic electrolyte; moreover, it is chemically and electrochemically stable with a polysulfide catholyte. An all-solid-state Li/$LiFePO_4$ battery with LSHT as electrolyte had a small resistance, high coulombic efficiency of 99.5~100 %, and long cycling life (Figure II-272). A Li-S battery with dense LSHT as

a separator that blocks the polysulfide transport towards the Li–metal delivered an initial discharge capacity of 1100 mAh $g^{-1}$, had a high coulombic efficiency of 99.5 %, and kept 93 % capacity after 400 cycles.

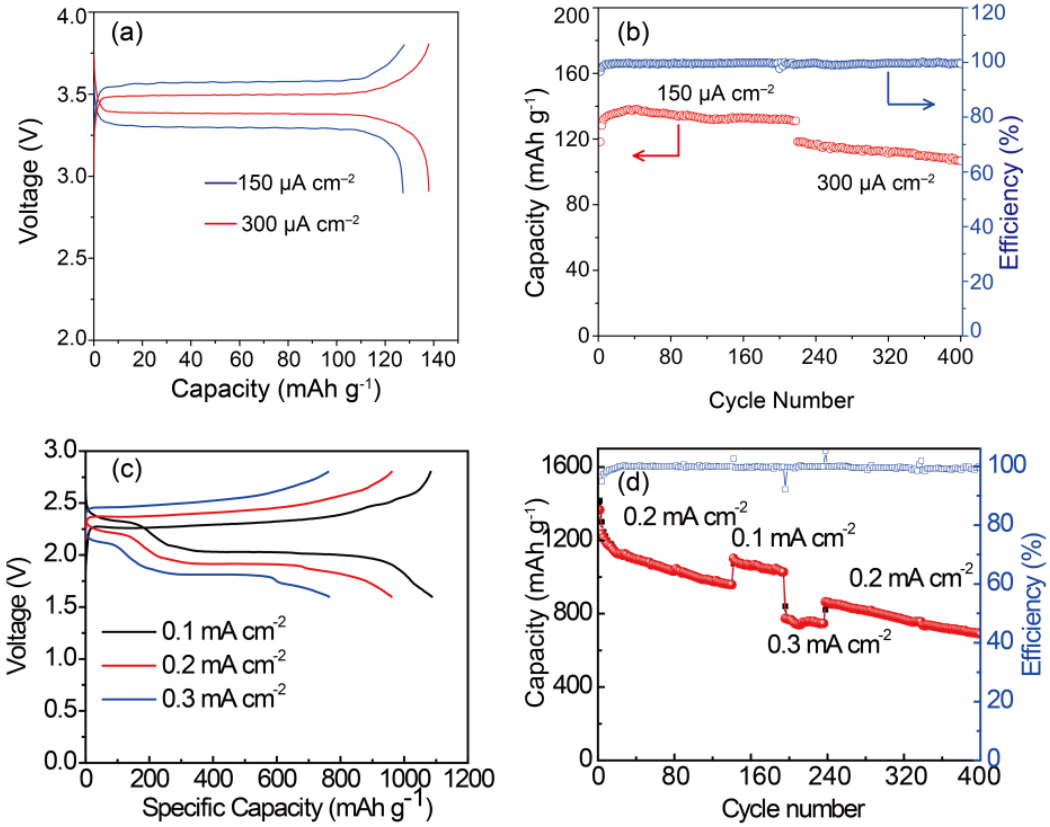


Figure II-272. (a) Charge and discharge voltage profiles of Li/LSHT/$LiFePO_4$ at 150 and 300 μA $cm^{-2}$. (b) Capacity retention and cycling efficiency of the $LiFePO_4$/Li cells. (c) Charge and discharge voltage profiles of a Li–S battery with LSHT at different current densities. (d) Capacity retention and cycling efficiency of the Li–S battery.

In the third quarter, we studied a new battery concept with the $Cu^+/Cu^0$ redox couple in the cathode of an all-solid-state lithium battery. In this concept, the $Cu^+/Cu^0$ redox couple determines the cell voltage and a solid $Li^+$ electrolyte provides $Li^+$ ions. We have used a cross-linked poly(ethylene glycol) methyl ether acrylate (CPMEA; Figure II-273) membrane with LiTFSI salt as the solid electrolyte. The membrane was shown to be electrochemically stable up to 4.8 V vs. Li at 65°C. A battery-grade Cu foil was used as a cathode current collector and a $Cu^+/Cu^0$ redox source. The Cu foil was directly placed on one-side of the CPMEA membrane, and a lithium metal foil was placed on the other side.

Figure II-274 shows an initial charge/discharge voltage curve of the solid-state Li cell at 70°C. During charging, a constant voltage plateau at ~ 3.5 V vs. Li was observed, which corresponds to the electrochemical Cu dissolution via the $Cu^+/Cu^0$ redox reaction. Li plating occurs at the anode while the dissolved $Cu^+$ ions keep the charge neutrality of the polymer electrolyte. During the following discharge, two voltage regions were noticed, one at ~3.3 V and the other at ~2.1 V. The upper voltage region should be responsible for the $Cu^+/Cu^0$ redox couple. However, the corresponding capacity is only about a half of the charging capacity. It is partly because the initially dissolved $Cu^+$ ions diffuse away from the Cu foil owing to the concentration gradient, and therefore, the diffusional overpotential increases as the electrochemical $Cu^+$ reduction proceeds at the Cu surface during discharge. The results suggest that higher $Li^+$ and $Cu^+$ concentrations are necessary to increase cell capacity and reaction kinetics. For the lower voltage reaction at ~ 2.1 V, the discharge mechanism is not understood yet, and further study is needed.

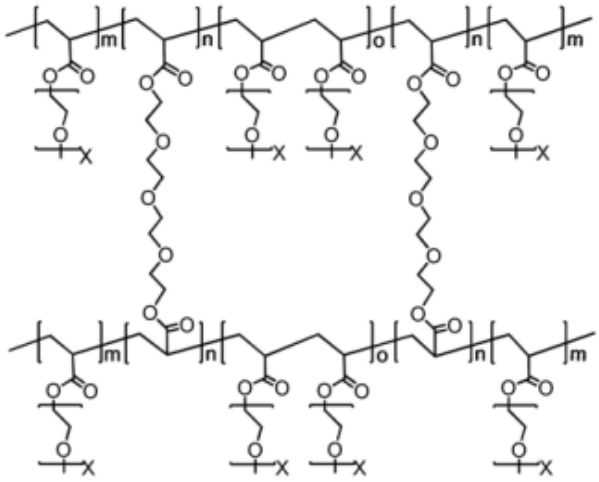

Figure II-273. Structure of CPMEA.

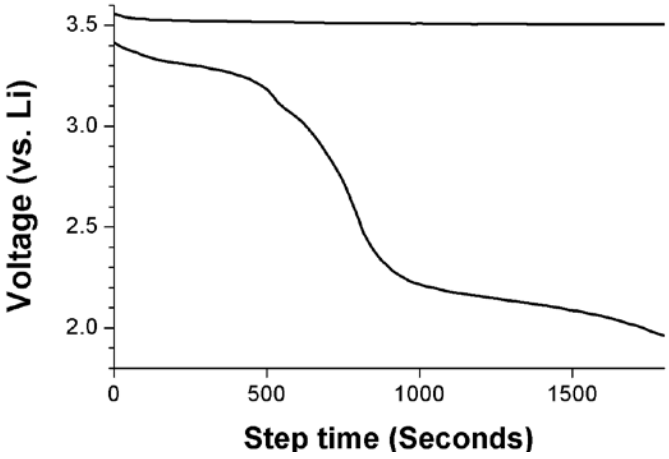


Figure II-274. Charge/discharge voltage curves of all-solid-state Li/CPMEA-LiTFSI/Cu cell at 70°C.

In the fourth quarter, the $Cu^{+}/Cu^{0}$ redox couple in the cathode was tested in a quasi-solid-state lithium battery cell. To collect more reproducible cell data, we have fabricated a gel polymer electrolyte membrane based on PVDF-HFP instead of the crosslinked polymer membrane, CPMEA. LiTFSI and poly(ethylene glycol) methyl ether acrylate were added to the PVDF-HFP solution in acetone; the clear solution was then cast on a Teflon dish. After vacuum drying at 50°C overnight, the membrane was used as a separator in a quasi-solid-state cell. We investigated several experimental parameters that affect the electrochemical performance of the $Cu^{+}/Cu^{0}$ redox couple.

*Electrochemical feed of $Cu^{+}$ ions into the separator membrane and its effect on the discharge capacity*

First, we have made coin half-cells with Cu foil as the cathode and Li metal as the anode. During the first charge, Cu dissolves into the polymer membrane and exhibits a voltage plateau at around 3.4 V. The electrochemical oxidation time was changed (10, 20, and 40h at 20 μA and 60°C) to control the $Cu^{+}$ concentration in the membrane and to check its effect on the discharge capacity (Figure II-275). The results suggest that (i) a higher $Cu^{+}$ concentration in the membrane is needed to promote $Cu^{+}$ conduction and deliver a higher reversible capacity, (ii) $Cu^{+}$ diffusion away from the cathode interface must be solved to enhance the Coulombic efficiencies, and (iii) Cu plating at the Li surface should be prohibited.

*Chemical feed of $Cu^{2+}$ ions into the separator membrane and its effect on the discharge capacity*

Second, to enhance electrochemical performance, vacuum-dried $Cu^{2+}$ perchlorate was chemically incorporated into the polymer composite during the membrane fabrication. $Cu^{2+}$ concentration was set to be 1:1 ratio to the $Li^{+}$ concentration. The Cu-incorporated membrane couldn't be solely used as a separator owing to the spontaneous $Cu^{2+}$ reduction reaction at the Li surface: a bare gel polymer membrane was introduced between the Li anode and the Cu-incorporated membrane. Figure II-276 shows the charge/discharge voltage curves of the coin cell with Cu foil as the cathode. The cell was charged first and then discharged at 20 μA and 60°C. Compared to Figure II-275, the discharge capacity was greatly improved. It is clear that having sufficient Cu ion concentration in the membrane is critical to deliver a higher cell capacity and a higher Coulombic efficiency.

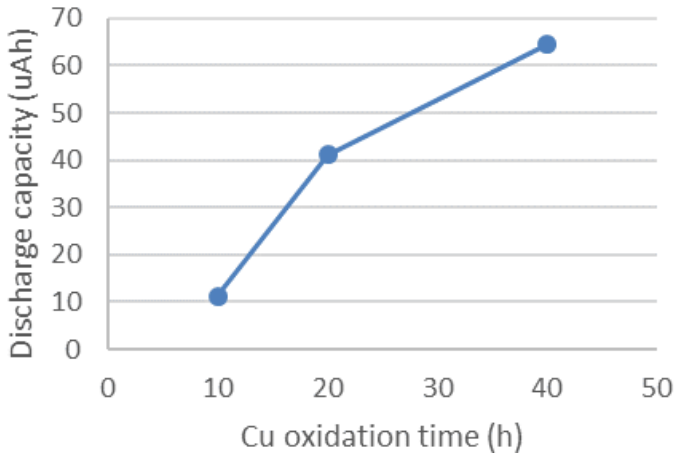


Figure II-275. Cu oxidation time and the corresponding discharge capacity.

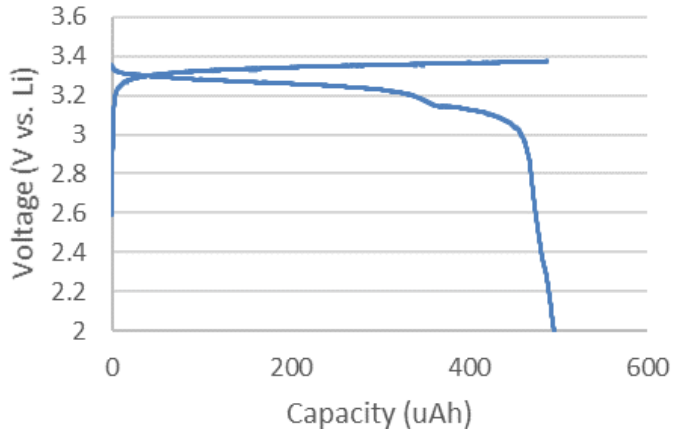


Figure II-276. Charge/discharge voltage curves of the Cu cathode.

## Conclusions

The data have shown that dendrite-free alkali-metal anodes can be plated reversibly with low plating/stripping impedance if the alkali-metal wets the solid electrolyte, i.e., if the anode-electrolyte bonding is stronger than bonding of the alkali metal with itself, and if the solid electrolyte is not reduced on contact with metallic lithium. Moreover, the solid electrolyte can block soluble species from the cathode as in a Li-S cell. Investigation of a new concept was initiated in the last half of the years; it consists of plating/stripping of metallic lithium on the anode and of metallic copper on a copper cathode with a dual-electrolyte system, the ceramic solid electrolyte contacting the anode.

## Key Publications

1. K. Park, J. B. Goodenough, “Dendrite-suppressed lithium plating from a liquid electrolyte via wetting of $Li_3N$”, Adv. Energy Mater. DOI: 10.1002/aenm.201700732.

## II.C.11 Exploiting Co & Ni Spinels in Structurally-Integrated Composite Electrode (ANL)

**Michael M. Thackeray, Principal Investigator**
Argonne National Laboratory
9700 S. Cass Aveue
Lemont, IL 60439
Phone: 630-252-9184
E-mail: thackeray@anl.gov

**Jason R. Croy, Principal Investigator**
Argonne National Laboratory
9700 S. Cass Aveue
Lemont, IL 60439
Phone: 630-252-9184
E-mail: croy@anl.gov

**Peter Faguy, Technology Manager**
U.S. Department of Energy
Phone: 202-586-1022
E-mail: Peter.Faguy@ee.doe.gov

Start Date: October 1, 2015 End Date: September 30, 2018
Total Project Cost: $500,000 DOE share: $500,000 Non-DOE share: $0

### Project Introduction

The structural instability of lithium- and manganese-rich, $xLi_2MnO_3 \cdot (1-x)LiMO_2$ (M=Mn,Ni,Co), 'layered-layered' (LL) materials, at high states of charge, is a critical barrier to their implementation in commercial battery systems [1]. One promising strategy to enhance structural stability has been to incorporate a spinel component to form complex, structurally-integrated, 'layered-layered-spinel' (LLS) electrodes [2-5]. LLS spinel, and even layered-spinel (LS), composites have been explored with positive results utilizing the incorporation of stoichiometric, manganese-based spinels such as $Li_{1+y}Mn_{2-y}O_4$ or $LiNi_{0.5}Mn_{1.5}O_4$. However, several interesting options for integrated spinel components have yet to be studied. For example, lithiated cobalt-rich spinels, $LiCo_{1-x}M_xO_2$ (M=metal cations), may be attractive as alternative spinel components for several reasons: (1) $LiCo_{1-x}M_xO_2$ (alternatively, $Li_2[Co_{2-2y}M_{2y}]O_4$) spinels have close-packed structures with a rock-salt stoichiometry, making them compositionally and structurally compatible with layered structures such as $LiMO_2$ and $Li_2MnO_3$; (2) Relative to that of manganese and nickel, cobalt has a lower propensity to migrate during electrochemical redox reactions ($Co^{3+/4+}$) at high potentials [6], thereby, possibly helping to mitigate voltage fade with cycling; and (3) Lithium extraction from a lithiated cobalt-rich spinel component, $Li_{2-x}Co_{2-2y}M_{2y}O_4$ ($0 \leq x \leq 1$), occurs at a potential (~3.6 V) [7, 8] significantly higher than that of its lithiated manganese-oxide spinel analogue, $Li_2Mn_2O_4$ (~2.9 V) [9, 10]. This chapter deals with efforts within this project to develop stable, Co-based spinels as possible end-member compounds for integration into more complex LLS systems in order to realize stable, high-energy, Mn-rich cathode materials capable of meeting the cost and safety requirements of EV and PHEV vehicle applications.

### Objectives

The objective of this project is to stabilize high-capacity, structurally-integrated (LL), Mn-rich cathodes by introducing a stabilizing spinel component into the parent electrode with a particular emphasis on lithium-cobalt-oxide and lithium-nickel-oxide spinel components that accommodate lithium at ~3.5 V vs. metallic lithium.

## Approach

The approach is to design, synthesize and characterize new spinel-related materials, compositions and structures that operate between 3 to 4 V and to determine their structural/electrochemical property relationships. This information will be used to identify the most promising spinel components that can be used, in low concentration, to stabilize high capacity $xLi_2MnO_3 \bullet (1-x)LiMO_2$ (M=Ni, Mn, Co) electrode structures.

## Results

*Synthesis of Co-based, lithiated-spinel materials with cation substitutions*

### Impurities

$LiCo_{1-x}M_xO_2$ (M = Ni and Mn) materials, synthesized at low temperature (LT), have lithiated spinel structures that could be used as stabilizing components in high capacity, lithium- and manganese-rich composite cathodes. After exploring a large portion of the LT-$Li(Co_{1-x-y}Ni_xMn_y)O_2$ compositional phase space, it was found that Ni and Mn substitution improves the phase purity and electrochemistry of lihtiated-spinel cathodes. However, impurity phases are easily formed during LT synthesis, and thus the range of Ni and Mn substitution has to be limited to a small degree in order to obtain monophasic materials. The formation of impurity phases is related to the relative stability of possible oxide phases in a given overall composition. For example, in lithiated-spinel $Li(Co_{1-x}Mn_x)O_2$ compounds, the transition metal (TM) cations should maintain an overall oxidation state of +3 to satisfy the charge neutrality condition. However, Mn cations having a preference for the +4 oxidaton state will drive the stabilization of a Li-Mn(IV)-O impurity phase, as shown in previously reported examples of LT-$Li(Co_{1-x-y}Ni_xMn_y)O_2$ materials with high Mn contents.

Different from the stoichiometric LT-$LiCo_{1-x}M_xO_2$ compounds, that have a Li:TM ratio of 1, the LT-$Li_{1-x}(Co_{0.9-x-y}Ni_yMn_x)O_2$ composition is designed to maintain the Mn(IV) oxidation state by decreasing Li content with Mn substitution. In Figure II-277a, LT-$Li_{1-x}(Co_{0.9-x-y}Ni_yMn_x)O_2$, with x = 0.1 and 0.2, do not show an impurity phase related to Mn(IV) cations, however, the peaks for $Co_3O_4$ are clearly detected; the decreased Li content in $Li_{0.9}(Co_{0.8}Ni_{0.1}Mn_{0.1})O_2$ and $Li_{0.8}(Co_{0.7}Ni_{0.1}Mn_{0.2})O_2$, devised to maintian the Mn(IV) oxidation state, actually induces the formatin of a $Co_3O_4$ impurity phase. For the x = 0.4 sample, a third phase, denoted as LT-LMO, is observed in addition to the LT-spinel and $Co_3O_4$ phases. From the analysis of the LT-$LiMnO_2$, the LT-LMO phase is identified as a $Li_2MnO_3 \bullet Li_4Mn_5O_{12}$ composite phase. The high-resolution x-ray diffraction (XRD) pattern of LT-$LiMnO_2$ (Figure II-277b) shows the presence of a spinel structure while the additional peak marked with an asterisk suggests superstructure ordering of Li/Mn as in $Li_2MnO_3$. The electrochemical behavior of LT-$LiMnO_2$ further confirms the composite structure by clearly exhibiting characteristics of both $Li_2MnO_3$ and $Li_4Mn_5O_{12}$ in the voltage curves of Figure II-277c. These results, combined with previous data, point to $Co_3O_4$ spinel, $Li_xNi_{1-x}O$ rocksalt, and a $Li_2MnO_3 \bullet Li_4Mn_5O_{12}$ composite as the main impurity phases during the low-temperature synthesis of 'NMC spinel' materials. Therefore, alternative synthesis routes that can deter the formation of those stable impurity phases, such as soft chemistry methods, need to be explored.

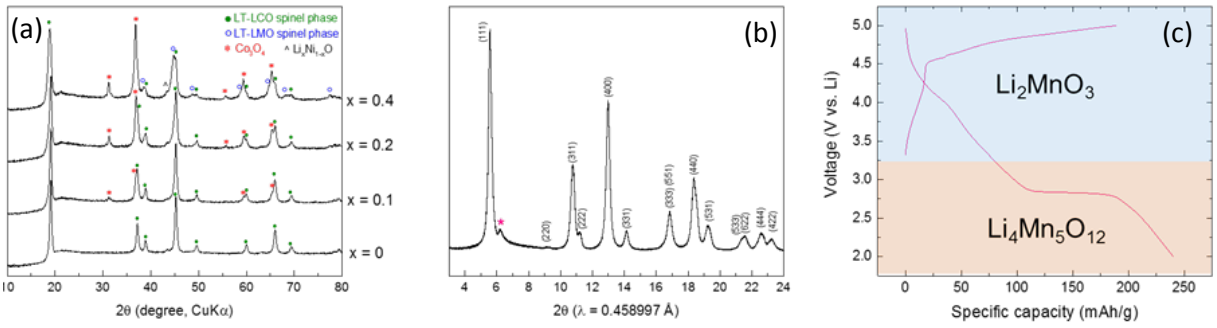


Figure II-277. (a) XRD patterns of LT-$Li_{1-x}(Co_{0.9-x}Ni_{0.1}Mn_x)O_2$, (b) high-resolution XRD and (c) electrochemistry of the low-temperature product with the $LiMnO_2$ composition (LT-LMO phase).

**Al-substitution**

The effect of Al substitution on the structure and electrochemical properties of LT-LCO was also explored. This approach was adopted because of the important role that Al substitution plays in fortifying the structures of several well-known, lithium-TM-oxides, such as layered $LiNi_{0.8}Co_{0.15}Al_{0.05}O_2$ (NCA) and lithium-manganese-oxide spinel materials. A series of Al-substituted $LiCo_{1-x}Al_xO_2$ (LCO-Al) samples was synthesized by sol-gel reactions of metal acetates and glycolic acid; the resulting sol-gel precursors were subsequently fired in air at 400ºC (LT) or at an intermediate temperature of 600ºC (IT).

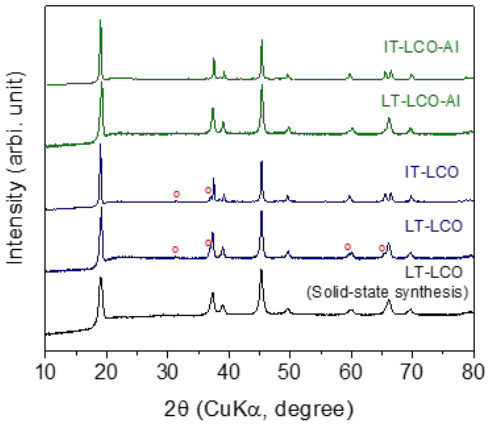


Figure II-278. XRD patterns of sol-gel $LiCoO_2$ (LCO) and $LiCo_{0.85}Al_{0.15}O_2$ (LCO-Al) samples fired at 400ºC (LT) or 600ºC (IT). XRD pattern of LCO, synthesized by solid-state reaction, is shown for comparison. Red circles indicate the peaks for $Co_3O_4$.

In Figure II-278, the LT-LCO sample is indexed to a cubic spinel structure, consistent with products made by solid-state synthesis at 400ºC. LT-LCO particles prepared by the sol-gel method were observed to have a larger crystalline size (smaller FWHM) relative to solid-state LT-LCO, and to contain a $Co_3O_4$ impurity phase that was also apparent in IT-LCO samples, but in lower concentration (reduced peak intensities). The IT-LCO product prepared at 600ºC had a well-defined layered structure, indicated by the split of the (018) and (110) peaks at ~66º 2θ, unlike the materials prepared by solid state reaction that required a higher synthesis temperature (≥700ºC) to produce well-ordered layered structures.[1] LCO-Al samples had a similar structure to their LCO analogues but did not contain a $Co_3O_4$ impurity phase. The lower firing temperature required to order the lithium and TM ions and the growth of larger crystallites in the final products suggest that, relative to solid state reactions, the sol-gel method lowers the kinetic barriers to the formation of well-defined LCO structures. Voltage profiles of lithium cells with LT-LCO and LT-LCO-Al cathodes showed two voltage plateaus corresponding to layered (3.9 V) and spinel (3.6 V) components, whereas cells with IT-LCO and IT-LCO-Al electrodes exhibited only the 3.9 V plateau, corroborating the XRD data (Figure II-279a and Figure II-279b). Al-substitution improves the cycling stability of both LT and IT electrodes (Figure II-279c).

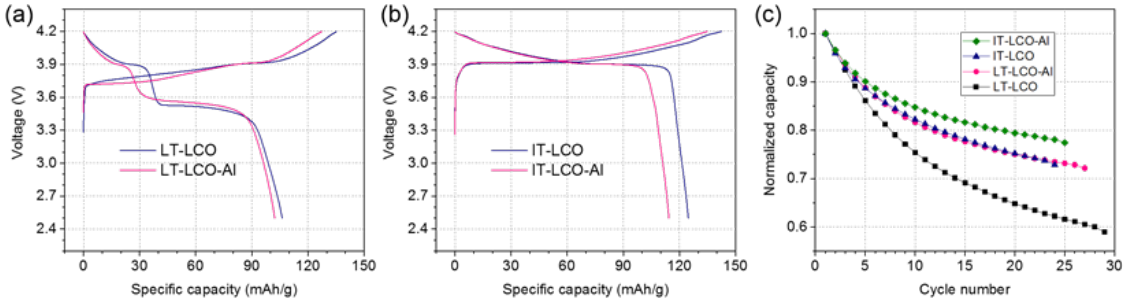


Figure II-279. (a, b) Initial voltage profiles and (c) normalized capacities of the sol-gel prepared samples.

*Modified sol-gel synthesis method for layered-spinel composite cathodes*

Encouraged by the improved performance of the Al-substituted, Li-Co-O spinel materials, prepared by the sol-gel route, synthesis efforts were expanded to prepared LS composite materials via a modified sol-gel method. Previous reports have discussed the structure and electrochemistry of LS $Li_2MnO_3$•$LiMn_2O_4$ cathodes. For these lithium-manganese-oxide materials, with relatively simple elemental components, the formation of structurally-integrated, layered and spinel domains is readily achieved by high-temperature firing of homogeneously-mixed precursors. However, such simple synthesis routes rely on thermodynamic phase segregation into composite structures and, therefore, have limitations in preparing multi-element samples. As such, alternative synthesis routes that enable more precise control over compositional and structural arrangements at the nano-scale are desired and hence a modified sol-gel process was explored to synthesize a LS $Li_2MnO_3$•$LiNi_{0.5}Mn_{1.5}O_4$ composite structure in which a heterogeneous distribution of Ni and Mn in the component phases is required.

Single-phase powder samples of layered $Li_2MnO_3$ and spinel $LiNi_{0.5}Mn_{1.5}O_4$ were prepared by a sol-gel method. An aqueous solution of metal acetates (Mn or Mn/Ni) was added to a glycolic acid or citric acid solution at 70ºC and ammonium hydroxide was used to adjust the pH values to between 7-9. The final solutions were dried under stirring until a gel was formed. The gel products were fired at 400ºC to remove the

polymer precursors and subsequently heat-treated at 800ºC, for 12 hours, to produce well-crystallized powder samples of $Li_2MnO_3$ and $LiNi_{0.5}Mn_{1.5}O_4$. To produce a LS $Li_2MnO_3$•$LiNi_{0.5}Mn_{1.5}O_4$ composite structure, the $Li_2MnO_3$ and $LiNi_{0.5}Mn_{1.5}O_4$ sols were mixed together prior to gel formation. With continued stirring and heating, the mixed sol quickly formed a gel. The gel product was then decomposed at 400ºC and heat-treated under the same conditions as those used for the single-phase powder samples (800ºC, 12 hours).

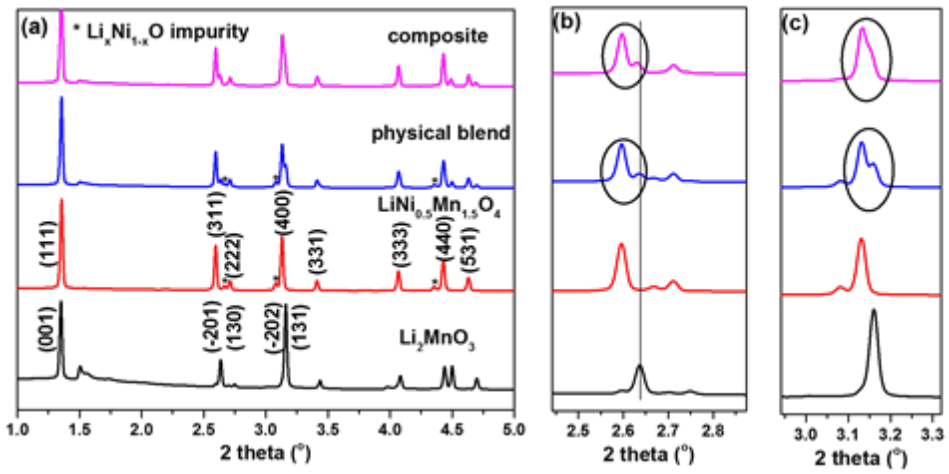


Figure II-280. (a) Synchrotron XRD of $Li_2MnO_3$, $LiNi_{0.5}Mn_{1.5}O_4$, a 1:1 physical blend of the two, and a $Li_2MnO_3$•$LiNi_{0.5}Mn_{1.5}O_4$ composite. (b, c) Enlarged regions ranging from 2.5° to 2.8° 2θ and from 3° to 3.3° 2θ, respectively.

For comparison, a physical blend of the $Li_2MnO_3$ and $LiNi_{0.5}Mn_{1.5}O_4$ powders, in a 1:1 molar ratio, was also prepared. The synchrotron XRD patterns for the composite material in Figure II-280(a-c) show a merging of the peaks for each single-phase component together with some peak broadening. This merging effect is noticeably different in the corresponding XRD patterns of the physical blend, indicating a more complex structure than the simple mixture. In Figure II-281(c), the electrochemical profiles for the composite material display the characteristics of both $Li_2MnO_3$ (Figure II-281b) and $LiNi_{0.5}Mn_{1.5}O_4$ (Figure II-281a), but with much improved electrochemical performance relative to the physical blend of the individual components (Figure II-281d). These X-ray and electrochemical data indicate that the modified sol-gel method provides an effective route to produce structurally-integrated electrode materials.

*Lithium intercalation mechanism of lithiated spinel $LiCoO_2$*

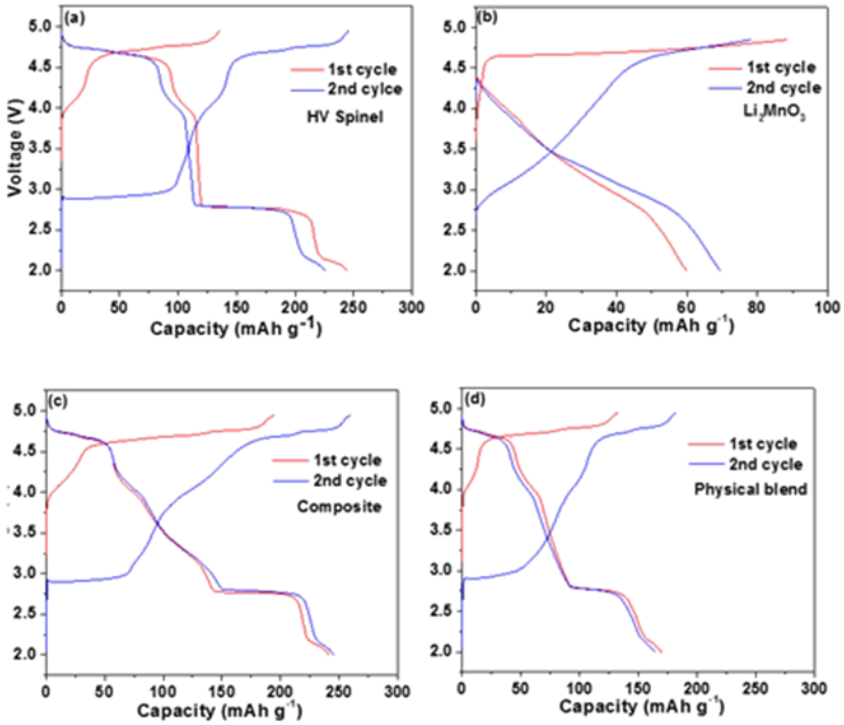


Figure II-281. (a) Initial voltage profiles of spinel $LiNi_{0.5}Mn_{1.5}O_4$, (b) layered $Li_2MnO_3$, (c) a $Li_2MnO_3 \bullet LiNi_{0.5}Mn_{1.5}O_4$ composite, and (d) a 1:1 physical blend of the two components. (4.8 – 2.0 V at ~C/15 against Li metal).

An interesting electrochemical behavior observed in the lithiated spinel $LiCo_{1-x}M_xO_2$ materials is a unique voltage hysteresis between the charge (~3.7 V) and discharge (~3.5 V) processes, which is more prominent than that in layered $LiCoO_2$ or spinel $LiMn_2O_4$. In order to understand the lithium deinterlacation mechanism that is responsible for such a prominent voltage hysteresis, ex-situ XRD analyses and DFT calculations were conducted. Figure II-282a shows the initial voltage curve of a Li/LT-$LiCo_{0.9}Ni_{0.1}O_2$ cell. The points where the cycled electrodes were exracted for ex-situ XRD measurement are marked on the curve. In Figure II-282b, the corresponding ex-situ XRD data indicates no significant structural changes. Detailed examination of the (311) and (400) peaks, however, reveals a reversible change in their relative intensities ($I_{(311)}/I_{(411)}$) during the charge-discharge cycle: $I_{(311)}/I_{(411)}$ increases during charging and decreases during discharging (Figure II-282c; $I_{(311)}/I_{(411)}$ = 0.44, 0.64, and 0.45 for the patterns (1), (4), and (6), respectively). The $I_{(311)}/I_{(400)}$ value is dependent on the relative $Li^+$ occupancies of tetrahedral ($T_d$) *vs*. octahedral ($O_h$) sites in the spinel structure. For example, $I_{(311)}/I_{(400)}$ is greater for the $\{Li\}_{[tet]}Co_2O_4$ spinel structure than for the $\{Li_2\}_{[oct]}Co_2O_4$ lithiated spinel structure as compared in the simulated XRD patterns in Figure II-282d. Therefore, the ex-situ XRD result suggests $Li^+$ migration from $O_h$ to $T_d$ sites during charging and from $T_d$ to $O_h$ sites during discharging.

Kinetic mechanisms for the Li (de)intercalation process(s) from the $LiCoO_2$, lithiated-spinel structure were investigated by DFT simulations wherein the energetically most favorable lithium vacancies were created in every lowest-energy, model structure of $Li_{16-x}Co_{16}O_{32}$. The DFT calculations found that (1) $Li^+$ migration from $O_h$ to $T_d$ sites is favorable during charging; (2) meta-stable structures such as $\{Li\}_{[tet]}\{Li_{10}\}_{[oct]}Co_{16}O_{32}$ form during charging until the $\{Li_{0.5}\}_{[tet]}CoO_2$ structure is stabilized at the end of charge; (3) the discharge process follows the equilibrium reaction pathway between the $\{Li_{0.5}\}_{[tet]}CoO_2$ and $\{Li\}_{[oct]}CoO_2$ structures; (4) the voltage for the meta-stable path is ~0.2 V higher than that for the equilibrium path. These experimental and thoeretical data corroborate each other and provide a deeper understanding of the electrochemcial and structural behavior of cobalt-based, lithiated-spinel cathodes.

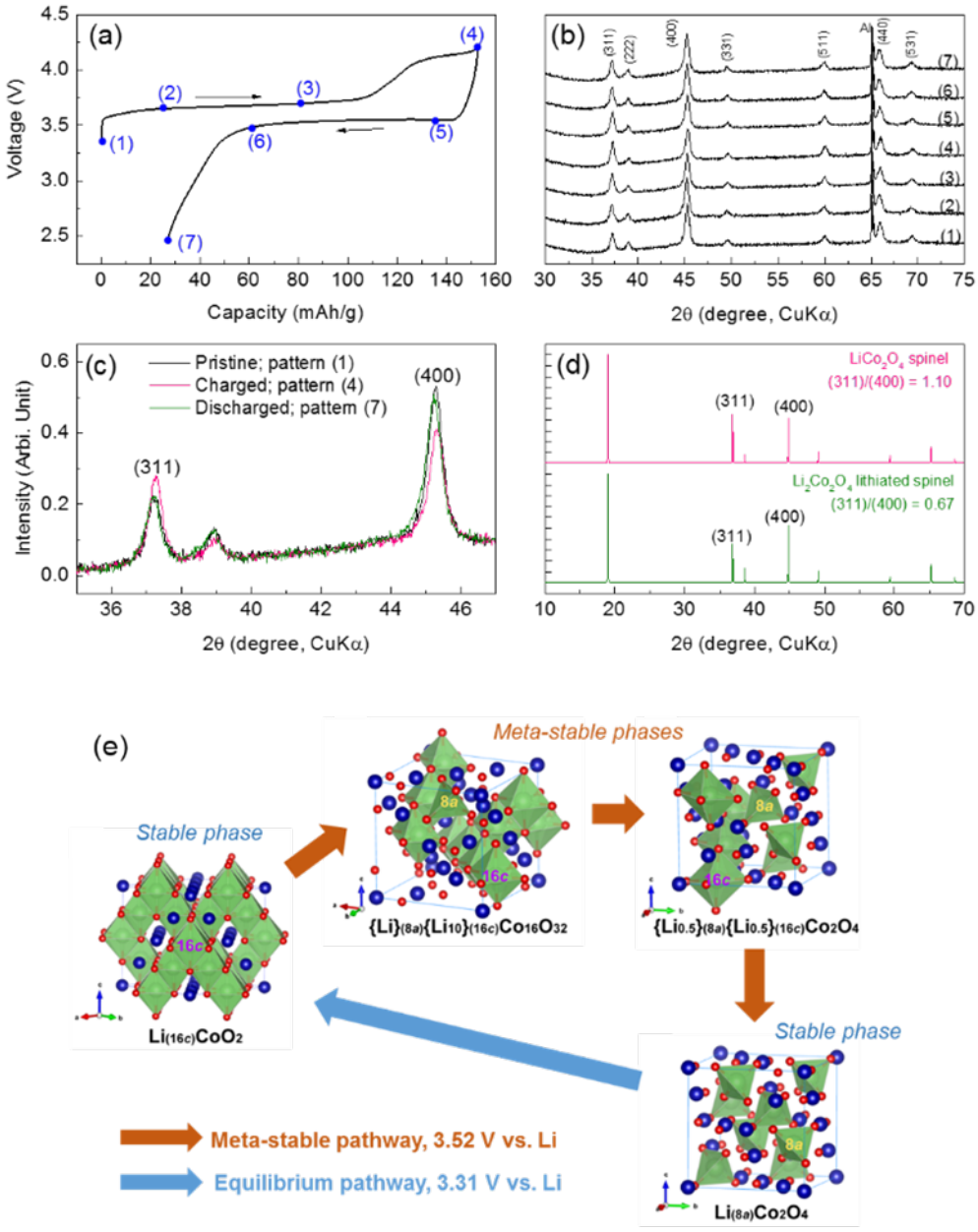


Figure II-282. (a) Voltage profiles of a Li/LT-$LiCo_{0.9}Ni_{0.1}O_2$ cell showing the points where ex-situ XRD data were collected, (b) corresponding ex-situ XRD patterns, (c) magnified view of the (311) and (400) peaks, (d) simulated XRD patterns of $\{Li\}_{[tet]}Co_2O_4$ spinel and $\{Li2\}_{[oct]}Co_2O_4$ lithiated spinel, and (e) Li (de)intercalation mechanism(s) suggested by DFT calculation.

## Conclusions

- A better understanding of the complex relationships that exist between synthesis, composition, structure, and electrochemical performance of lithiated-spinel, Li-Co-Ni-Mn-O materials has been acquired via systematic synthesis, characterization, and computational efforts
- Layered $Li_2MnO_3$, spinel $Li_4Mn_5O_{12}$, spinel $Co_3O_4$, and rock salt $Li_xNi_{1-x}O$ are identified as common impurity phases that could be generated depending on compositions and synthesis conditions

- Inactive Al substitution is proven to be a promising strategy to stabilize Co-based, lithiated-spinel structures and improve cycling performance
- The synergistic advantage of atomic incorporation between layered and spinel structures has been confirmed in $Li_2MnO_3$•$LiNi_{0.5}Mn_{1.5}O_4$ composite materials prepared by a modified sol-gel synthesis route
- DFT calculations and ex situ XRD data suggest that lithiated-spinel, $LiCoO_2$ follows asymmetric reaction pathways during charge (meta-stable pathway) and discharge (equilibrium pathway) processes, that are responsible for its large, voltage hysteresis.

## Key Publications

1. M.M. Thackeray and J.R. Croy, *Tailoring Integrated Layered and Spinel Electrode Structures for High Capacity Lithium-Ion Cells*, ES049, DOE Vehicle Technologies Program Annual Merit Review (Arlington, VA), 5-9, June 2017.
2. E. Lee, J. S. Park, H. Kim, Q. Li, F. C. Castro, J. Wu, V. P. Dravid, S. Kim, C. Wolverton, P. Yan, C. Wang, R. Benedek, J. R. Croy, and M. M. Thackeray, *Coherently Integrated Layered-Spinel Cathodes for Lithium-Ion Batteries*, 68th Annual Meeting of the International Society of Electrochemistry (Providence, RI), August 27 - September 1, 2017.

## References

1. J. R. Croy, M. Balasubramanian, K. G. Gallagher, A. K. Burrell, Acc. Chem. Res. 48, 2813 (2015).
2. S.–H. Park, S.–H. Kang, C. S. Johnson, K. Amine and M. M. Thackeray, Electrochem. Comm. **9**, 262 (2007).
3. D. Kim, G. Sandi, J. R. Croy, K. G. Gallagher, S.-H. Kang, E. Lee, M. D. Slater, C. S. Johnson and M. Thackeray, J. Electrochem. Soc. **160**, A31-A38 (2013).
4. B. R. Long, J. R. Croy, J. S. Park, J. Wen, D. J. Miller, and M. M. Thackeray, J. Electrochem. Soc., **161** (14) A2160-A2167 (2014).
5. E. Lee, J. Blauwkamp, F. C. Castro, J. Wu, V. P. Dravid, P. Yan, C. Wang, S. Kim, C. Wolverton, R. Benedek, F. Dogan, J. S. Park, J. R. Croy, and M. M. Thackeray, ACS Appl. Mater. & Interfaces, **8**, 27720 (2016).
6. J. Reed and G. Ceder, Chem. Rev. **104**, 4513 (2004).
7. R. J. Gummow, M. M. Thackeray, W. I. F. David and S. Hull, Mater. Res. Bull. **27**, 327 (1992).
8. R. J. Gummow and M. M. Thackeray, J. Electrochem. Soc. **140**, 3365 (1993).
9. M. M. Thackeray, W. I. F. David, P. G. Bruce and J. B. Goodenough, Mater. Res. Bull. **18**, 461 (1983).
10. J. M. Tarascon and D. Guyomard, J. Electrochem. Soc. **138**, 2864 (1991).

## II.C.12 Discovery of High-Energy Li-Ion Battery Materials (LBNL)

**Wei Tong, Principal Investigator**
Lawrence Berkeley National Laboratory
1 Cyclotron Road, MS62R0203
Berkeley, CA 94720
Phone: 510-486-7084
E-mail: weitong@lbl.gov

**Peter Faguy, Technology Manager**
U.S. Department of Energy
Phone: 202-586-1022
E-mail: Peter.Faguy@ee.doe.gov

Start Date: October 1, 2015 End Date: September 30, 2018
Total Project Cost: $450,000 DOE share: $450,000 Non-DOE share: $0

### Project Introduction

Currently, the commercial Li-ion batteries adopt a wide use of intercalation cathodes such as layered lithium metal oxide, spinel-type lithium manganese oxide, and olivine-type lithium iron phosphate. However, these cathodes can only deliver a reversible capacity of 140 - 170 mAh/g based on the cationic redox. Attempt to charge layered oxides to higher potentials (> 4.7 V) results in a higher initial capacity (> 200 mAh/g), but leads to an irreversible phase transformation and ultimately a capacity decay. Recently, Li-, Mn-rich layered oxides have demonstrated a high reversible capacity of > 250 mAh/g, which outperforms most of the commercially available Li-ion cathodes. However, this family of compounds experience a series of structural rearrangement and gas evolution, demonstrating continuous voltage/energy decay over the extended cycles. In this project, we propose to develop new Li-rich metal oxides that utilize Ni2+/Ni4+ redox, meanwhile, incorporate a second transition metal (TM) that is located on the first and second row in the periodic table, which is designed to stabilize the crystal structure and/or contribute electrochemical redox. The presence of Li excess in the structure is expected to increase the number of Li diffusion paths, therefore, enable more accessible Li.

### Objectives

- Develop a cathode that can cycle > 200 mAh/g while exhibiting minimal capacity and voltage fade
  - Target at Li-rich compositions in Li-Ni-O chemical space that utilizes Ni2+/Ni4+ redox to potentially overcome capacity limitation per TM
  - Integrate a second TM on the first and second row to improve structural stability and/or contribute electrochemical redox
- Gain in-depth understanding on the correlation between composition and electrochemistry in Li-rich metal oxides
  - Understand the participation/contribution of cationic and anionic redox in electrochemistry
  - Investigate the potential impact of TMs on oxygen reactivity

### Approach

This project integrates material design, synthesis, physical and electrochemical evaluation to search for new high capacity cathodes within Li-Ni-O chemical space. We initiated our material synthesis efforts with Li, Mn-rich layered oxide to identify the optimal synthetic condition via a facile solid-state reaction that is ultimately employed for the synthesis of Li-rich Ni-based metal oxides. Integration of a second TM is expected to

stabilize structure and/or contribute electrochemical redox. The materials are subjected to a variety of synchrotron-based radiation and spectroscopy techniques to characterize the crystal structure and electronic structure of both TMs and oxygen.

## Results

We first studied the correlation between the synthesis and electrochemical performance to identify the key variables that govern the electrochemical properties. $Li_{1.2}Mn_{0.6}Ni_{0.2}O_2$ (LNMO) samples were synthesized *via* solid-state method using $Li_2CO_3$, $Ni(OH)_2$, and $MnCO_3$ precursors. Raw materials were mixed by either High Energy (HE) or medium Energy (ME) mechanical milling process, and then annealed at 950ºC. The effect of the synthetic condition, include milling energy, milling time, and annealing time on the electrochemical performance was studied. Figure II-283a and Figure II-283b shows the XRD patterns and the first cycle voltage profiles of four LNMO samples synthesized with various conditions. Overall, all the samples demonstrated similar XRD patterns that are consistent with those reported in the literature, and no significant effect of the synthetic condition on the crystal structure of LNMO was detected by XRD. In contrast, we clearly observed the effect of synthetic conditions on the electrochemical performance. Despite of the similar voltage profiles, consisting of an electrochemical activation plateau around 4.5 V as well as a sloping voltage profile during the discharge, it can be clearly seen that LNMO sample prepared at a high energy for 3 h and annealing for 15 h delivered the highest discharge capacity (259 mAh/g), corresponding to 0.82 Li per formula. In comparison, the discharge capacity of the sample prepared at a medium energy was only 215 mAh/g. This capacity was about 17% lower compared to the best sample (HE3h_15h), although the XRD patterns of these two samples were similar. This clearly translates into the difference in LNMO active materials rather than process variables (*i.e.*, slurry formulation, electrode fabrication, and cell assembly). Simply comparing these two samples led to a combined effect of milling method and annealing time. The optimal synthetic condition for LNMO will be used to prepare other Li-rich metal oxide cathodes.

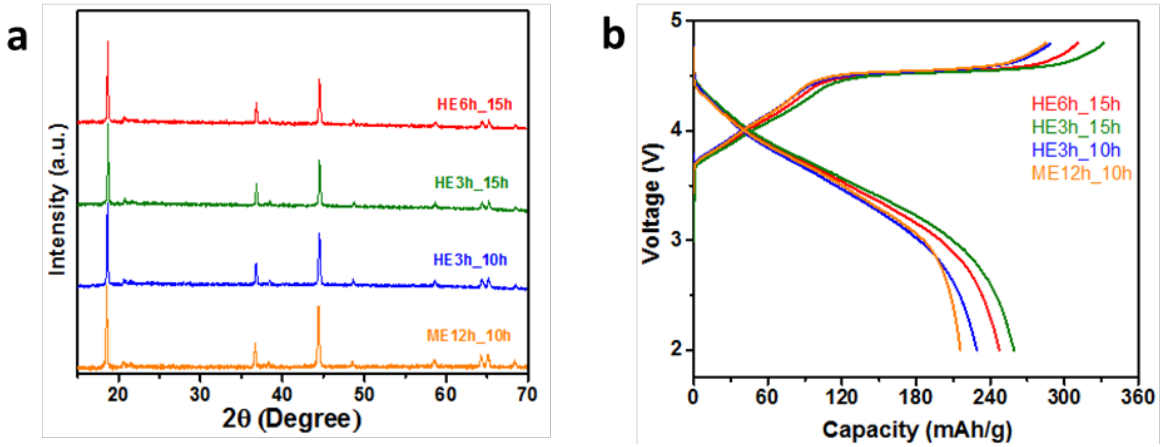


Figure II-283. (a) X-ray diffraction patterns of of $Li_{1.2}Mn_{0.6}Ni_{0.2}O_2$ samples prepared by a solid-state method. Samples are denoted by milling energy followed by milling time_annealing time. (b) The first cycle voltage profiles of $Li_{1.2}Mn_{0.6}Ni_{0.2}O_2$ samples prepared by a solid-state method. Cells were cycled between 4.8 and 2 V at a current of 25 mA/g.

In the second quarter, different transition metals (TM = Mn, Ru, Sn, Mo, Nb, Ti, V) with a general formula of $Li_{2-x-y}Ni_xTM_yO_2$ ($0 < x, y < 1$) were synthesized *via* a solid-state reaction using the optimal synthetic condition identified above for LNMO. Selection of the second TM was mainly based on the theoretical capacity. The XRD patterns of the as-produced samples are presented in Figure II-284. Samples that incorporate Ru, and Sn showed very similar XRD patterns to that of LNMO. A shift in XRD peaks was observed due to the difference in ionic radius of these three TM cations. For TM = Mo, more X-ray diffraction peaks were observed, however, it can be seen that the major characteristic peaks of LNMO were reserved along with more diffraction peaks in the two-theta region of 20 - $35^0$. The crystal structure seemed consistent with those of the samples

with TM = Mn, Ru, Sn. Careful search and match of TM = Mo pattern in the ICDD database showed a consistency with $Li_4MgWO_6$, which belongs to the monoclinic crystal system. For the other TMs we tested, the crystal structure of the final products was very different, as shown in Figure II-284b. For both Ti and Nb, the XRD patterns can be easily assigned to the disordered rock salt phase. Although NiO possesses a rock salt structure, the complete absence of any XRD peak that is related to lithium and another TM precursors or byproducts suggests incorporating Ti and Nb very likely led to the formation of a disordered rock salt phase in the final products. As for TM = V, $Li_3VO_4$ was a thermodynamically favorable phase in our synthesis and observed as the major phase along with NiO. The electrochemical properties of the as-produced samples were tested, the Ru compound, which showed good electrochemical performance, was used for detailed characterization.

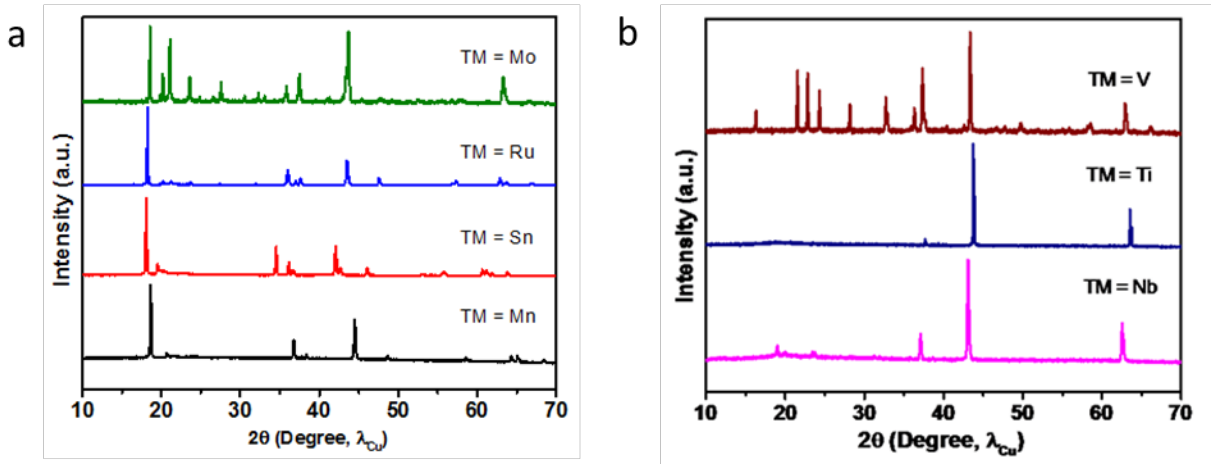


Figure II-284. (a) XRD patterns of $Li_{2-x-y}Ni_xTM_yO_2$ (TM = Mn, Sn, Ru, Mo), exhibiting layered structure. (b) XRD patterns of $Li_{2-x-y}Ni_xTM_yO_2$ (TM = Nb, Ti, V), exhibiting non-layered structure.

The first cycle voltage profiles and differential capacity (dQ/dV) plots of $Li_{1.2}Ni_{0.2}Ru_{0.6}O_2$ and $Li_{1.2}Ni_{0.2}Mn_{0.6}O_2$, denoted as LNRO and LNMO, are shown in Figure II-285. The LNRO sample demonstrated a charge capacity of 239 mAh/g and a discharge capacity of 213 mAh/g, leading to a coulombic efficiency of 88.9%. In comparison, LNMO sample exhibited a coulombic efficiency of 75.0%. Both samples revealed a common feature of about 1 $Li^+$ removal during the charge process, but noticeably different charge profiles. Instead of exhibiting a long plateau at 4.55 V in LNMO, a sloping curve with most of the capacity extracted below 4.5 V was observed for LNRO. This difference was also pronounced in the dQ/dV curves (Figure II-285 c, d). The charge profile of LNMO was characterized by a strong anodic peak at 4.55 V, corresponding to the extended voltage plateau, as well as two weak anodic peaks around 3.8 and 4.1 V associated with $Ni^{2+}/Ni^{4+}$ oxidation. This strong anodic peak in the high voltage region was absent during the charge of LNRO, instead, a relatively strong peak at 3.65 V was observed to superimpose with some minor peaks at 3.75 and 4.1 V. The corresponding cathodic peaks, which were clearly visible in the LNRO, unlike the LNMO, were located around 3.7 and 3.4 V.

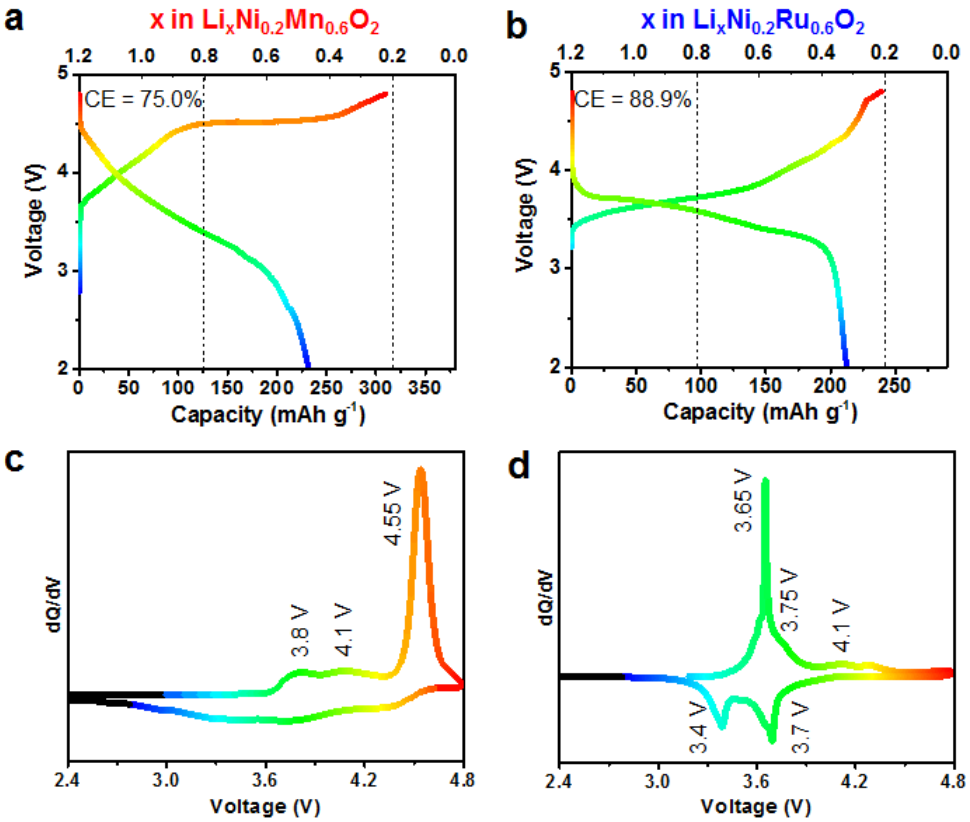


Figure II-285. The first cycle voltage profile of (a) LNMO and (b) LNRO; Differential capacity (dQ/dV) plot of (c) LNMO and (d) LNRO. Cells were cycled between 4.8 and 2.0 V at a current density of 5 mA/g at room temperature.

LNMO and LNRO showed a similar crystal structure, which was confirmed by Rietveld refinement and HRTEM analysis (Figure II-286). Both LNMO and LNRO samples fit the structural model of monoclinic solid solution, and electron diffraction (ED) patterns and fast Fourier transformation (FFT) results along the [001] and $[30\bar{1}]$ zone axis of *C*2/*m* and *C*2/*c* from LNMO and LNRO particle showed high structural consistency.

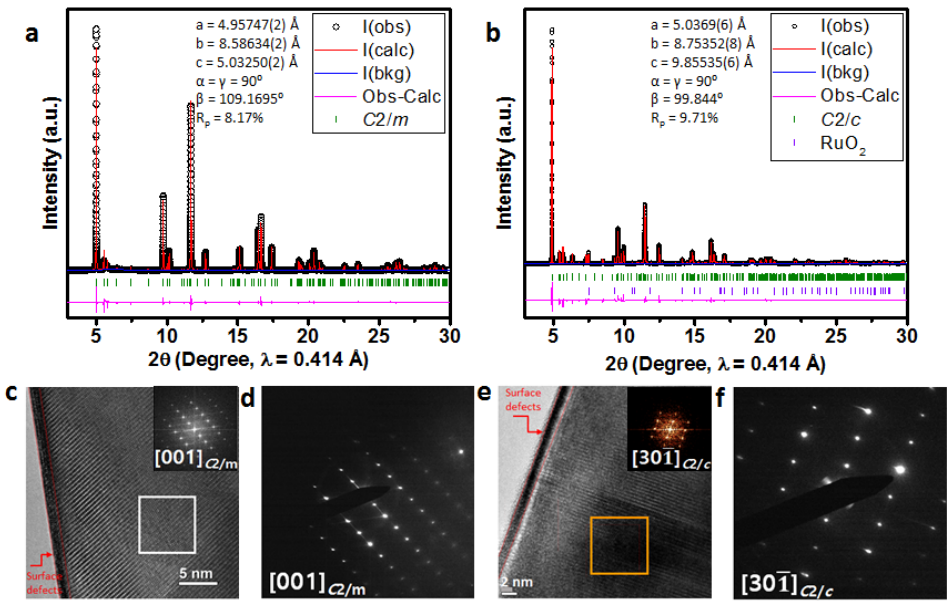


Figure II-286. XRD Rietveld refinement of (a) LNMO, monoclinic *C*2/*m*, and (b) LNRO, monoclinic *C*2/*c*; HRTEM image of (c) LNMO, (e) LNRO with FTT of the selected area; ED pattern of (d) LNMO, (f) LNRO.

To understand the different electrochemical behaviors in LMNO and LNRO of similar structure, the cationic redox of Ni and Ru were examined by X-ray absorption spectroscopy (XAS). The Soft XAS Ni Li-edge spectra of LNRO and LNMO is shown in Figure II-287. Ni L3-edge exhibits splitting features at high and low energy, the ratio between which is in accordance with Ni valence state. In comparison with reference compounds, Ni was determined to be 2+ in both pristine LNMO and LNRO. Upon charging, an increase in Ni L3-edge peak at the high energy suggests the oxidation of Ni. Further increasing charge voltage to 4.8 V did not lead to an obvious change in Ni oxidation state, suggesting the completion of Ni redox by 4.5 V and 4.3 V for LNMO and LNRO, respectively. The Ni valence state reverts back to its divalent state after the first discharge, as the discharged material spectra are similar to those of the pristine material. Comparison between FY and TEY mode for both compounds revealed a slight Ni reduction at the surface of the charged electrodes, as evidenced by a slight decrease in the relative intensity of the TEY Ni L3-edge feature compared to the analogous FY spectra at high energy. Meanwhile, the Ni oxidation state during charging process was lower in LNRO compared to that in LNMO.

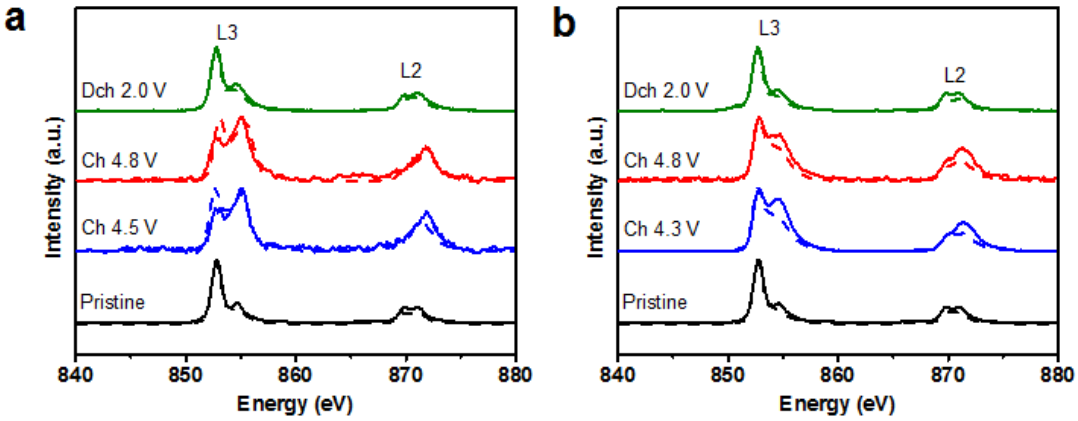


Figure II-287. sXAS Ni L-edge spectra of (a) LNMO, (b) LNRO electrodes at different states of charge. Solid and dash line indicate FY (~ 50 nm depth) and TEY (2 - 5 nm depth) mode, respectively.

We further investigated the anionic oxygen redox in both compounds by resonant inelastic X-ray scattering (RIXS). In O K-edge RIXS maps (Figure II-288), the RIXS intensity was plotted against the excitation energy (y axis) and emission energy (x axis). For LNMO electrodes (Figure II-288a), one relatively large fluorescence feature was observed at an excitation of ~ 529.2 eV ($t_{2g}$ orbitals) along with a relatively small feature at ~ 531.5 eV ($e_g$ orbitals) in the pristine state. Upon charging, the 529.2 eV feature tended to grow due to its more covalent nature (corresponding to Ni oxidation). The most striking phenomenon was the appearance of an additional feature (marked by arrow) at an excitation energy, 530.9 eV, between the pre-edge peaks, but at a slightly lower emission energy (~ 1 eV) in LNMO at 4.8 V charge. More importantly, this additional feature disappeared and the other two pre-edge features reverted to their original states at 2 V discharge. In contrast, the main features of the LNRO spectra (Figure II-288b) were similar to those of LNMO, except at slightly different excitation energies, 528.5 and 531.1 eV. However, at 4.8 V charge, the new feature at 530.9 eV excitation observed in LNMO was absent in LNRO. We hypothesize this additional feature that appears at 530.9 eV excitation and 523.2 eV emission energy is a direct evidence of the participation of electrons from anionic oxygen in the electrochemistry of LNMO. Therefore, we infer minimal electrons from anionic oxygen participate in the electrochemistry of LNRO, instead, Ni and Ru are electrochemically active.

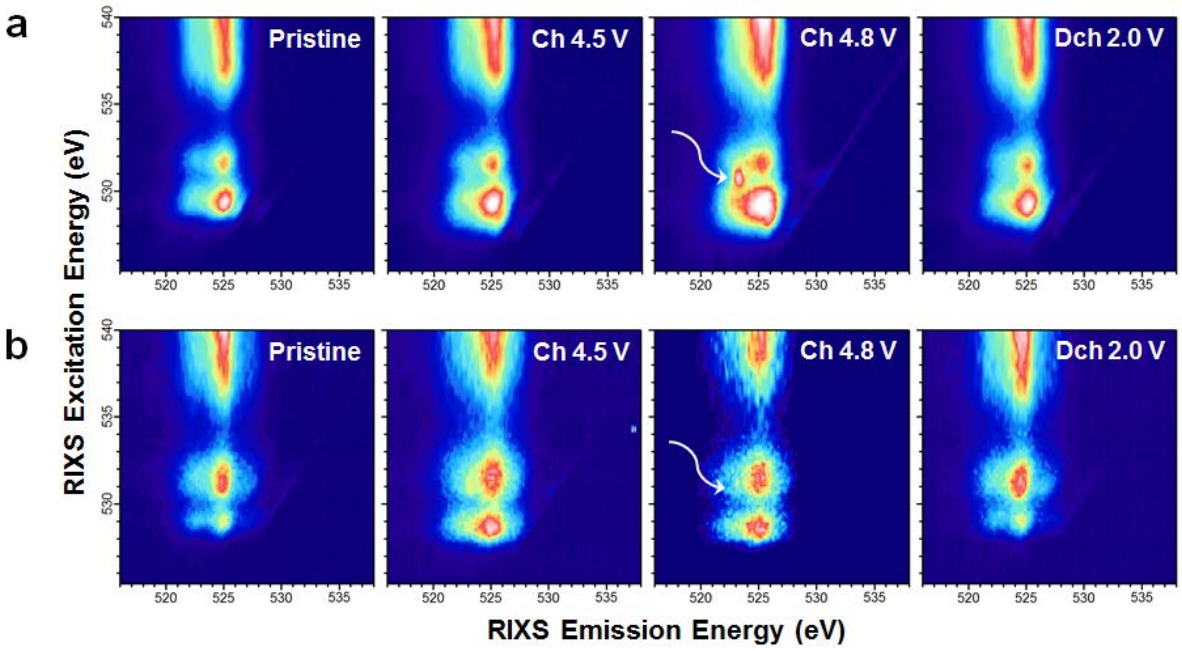


Figure II-288. O K-edge RIXS maps of (a) LNMO and (b) LNRO electrodes at various states of charge. The while arrow indicates the specific oxygen redox state that is absent in LNRO.

As discussed above, Ni is electrochemically active in both LNMO and LNRO, the additional capacity was contributed by the participation of electrons from O in LNMO. For LNRO, the reversible Ru redox is anticipated because the RIXS maps of O K-edge imply that lattice oxygen is not contributing to charge compensation. To verify our hypothesis, in-situ hard XAS (Figure II-289) were collected on Ru K-edge during the first cycle of LNRO. Compared to the X-ray absorption near edge spectra (XANES) of the reference compounds the oxidation state of Ru was determined to be 4+ in pristine LNRO (Figure II-289a). Upon charging, the Ru edge gradually shifted from its pristine state to higher energies, indicating Ru was oxidized. Meanwhile, the Ru edge moved back to the lower energy and almost to its original valence state upon discharge. On the other hand, extended X-ray absorption fine structure (EXAFS) shown in Figure II-289b exhibits two distinct shells around 1.4 and 2.3 Å, corresponding to Ru-O and Ru-TM interactions, respectively. The two shells shifted slightly to smaller distances as a result of Ru oxidation during the charge process, then reverted back to their pristine distances after discharge, indicating the reversible nature of the Ru redox process

during LNRO cycling. In further support of the Ru redox reversibility, no obvious change in amplitude of the Ru-O and Ru-TM shells was observed, revealing no change in Ru coordination during the electrochemical process. In-situ XAS results clearly demonstrated the electrochemical activity of Ru and its good reversibility during electrochemical cycling, lending support to our earlier hypothesis that lattice oxygen redox did not participate in charge compensation during Li insertion/extraction.

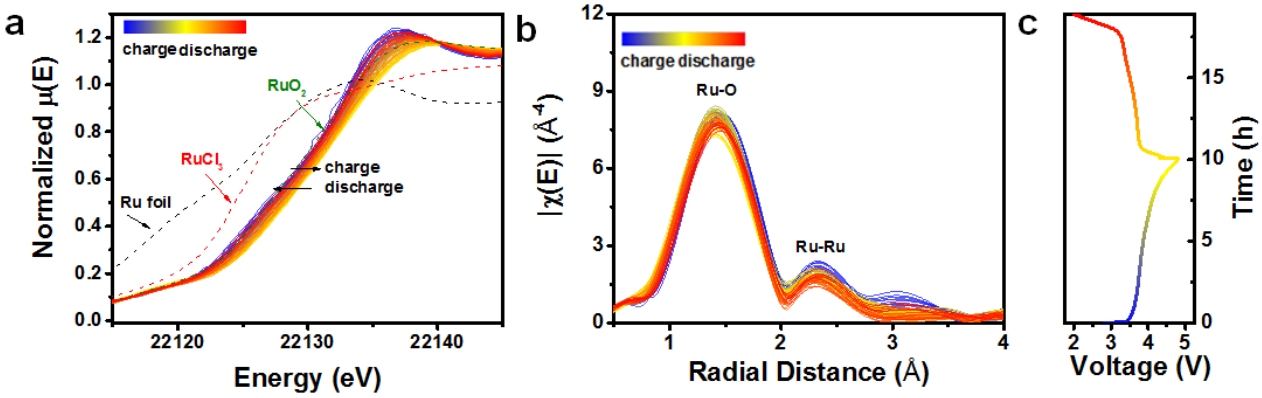


Figure II-289. In-situ (a) XANES and (b) EXAFS of Ru L-edge; (c) in-situ voltage profiles of LNRO during the first cycle. The in-situ cell was charged at C/10 and discharged at C/7.

## Conclusions

In conclusion, optimal solid-state synthesis of Li-, Mn-rich layered oxides was identified and employed to synthesize a series of Li-rich metal oxides through the combination of Ni and a second TM beyond Mn (*i.e.*, Ru, Sn, Mo, Nb, Ti, V). The initial synthetic efforts led to the formation of two types of phases, layered oxides and disordered rock salts. In FY17, we focused on $Li_{1.2}Ni_{0.2}TM_{0.6}O_2$ (TM = Mn, Ru) and performed detailed characterization on crystal structure and charge compensation mechanism in both compounds. We observed three interesting phenomena from these two compounds: (1) they exhibited a similar crystal structure, (2) they enabled a similar amount of $Li^+/e^-$ (de)insertion during the charge-discharge process, but (3) they demonstrated distinctly different charge voltage profiles, as evidenced by 4.55 V plateau in LNMO *vs.* none in LNRO. Using combined X-ray spectroscopy techniques, we illustrated the charge compensation mechanism and verified the electrochemical activity of Ni and O in LNMO and Ni and Ru in LNRO. In particular, a signature of anionic oxygen redox was directly observed using RIXS to map the O K-edge in cycled LNMO, whereas the absence of this signature in charged LNRO indicated no such oxygen redox in LNRO. The sharp contrast between LNMO and LNRO clearly demonstrates the critical role that TM plays in the anionic oxygen activity in Li-rich metal oxides. Moreover, these two compounds of similar crystal structure, but distinct contrast in oxygen activity, offer us a platform to elucidate the correlations between structural evolution and oxygen redox. We will study the structural evolution of these two compounds upon cycling to understand its impacts on subsequent electrochemical behaviors for Li-rich metal oxides. Meanwhile, the structural and electrochemical properties of the as-produced Li-rich metals oxides by incorporating other TMs will be evaluated as well.

## Key Publications

1. J. Xu, S. Renfrew, M. A. Marcus, M. Sun, B. D. McCloskey, W. Tong*, "Investigating $Li_2NiO_2$-$Li_2CuO_2$ Solid Solutions as High-Capacity Cathode Materials for Li-Ion Batteries," Journal of Physical Chemistry C, 121, 11100-11107 (2017).

2. J. Xu, F. Lin, M. M. Doeff, and W. Tong*, "A Review of Ni-based Layered Oxides for Rechargeable Li-Ion Batteries," Journal of Materials Chemistry A, 5, 874-901 (2017).

3. J. Xu, E.-Y. Hu, D. Nordlund, A. Mehta, S. N. Ehrlich, X.-Q. Yang, and W. Tong*, "Understanding the Degradation Mechanism of Lithium Nickel Oxide Cathode for Li-ion Batteries," ACS Applied Materials & Interfaces, 8, 31677-31683 (2016).

4. C. Ma, J. Alvarado, J. Xu; R. Clément, M. Kodur, W. Tong, C. Grey, Y. S. Meng, "Exploring Oxygen Activity in the High Energy P2-Type Na0.78Ni0.23Mn0.69O2 Cathode Material for Na-ion Batteries," Journal of the American Chemical Society, 139, 4835-4845 (2017).

5. W. Tong*, G. G. Amatucci, "Silver Copper Fluoride: a Novel Perovskite Cathode for Lithium Batteries," Journal of Power Sources, 362, 86-91 (2017).

6. Z. Xing, Y. Qi, Z. Tian, J. Xu, Y. Yuan, C. Bommier, J. Lu, W. Tong*, D. Jiang, and X. Ji, "Identify the Removable Substructure in Carbon Activation," Chemistry of Materials, 29, 7288-7295 (2017).

## II.C.13 Model-System Diagnostics for High-Energy Cathode Development (LBNL)

**Guoying Chen, Principal Investigator**
Lawrence Berkeley National Laboratory
1 Cyclotron Road
Berkeley, CA 94720
Phone: 510-486-5843
E-mail: GChen@lbl.gov

**Peter Faguy, Technology Manager**
U.S. Department of Energy
Phone: 202-586-1022
E-mail: Peter.Faguy@ee.doe.gov

Start Date: October 1, 2016 End Date: September 30, 2019
Total Project Cost: $550,000 DOE share: $550,000 Non-DOE share: $0

### Project Introduction

To meet DOE targets for Li-ion batteries intended for vehicular applications, electrode materials with high-energy density and high stability are needed. Critical performance issues associated with electrode structural and morphological instabilities, side reactions with the electrolyte, and transport limitations are sensitive to material's properties such as chemical compositions, crystal structures, surface facets, and particle sizes. Advances in materials development, therefore, require a better understanding of these relationships between properties and functions, yet this has been difficult to achieve on conventional aggregated secondary particles. This project addresses these challenges in a systematic way, by synthesizing single-crystal version of the commercially promising yet complex electrode materials, obtaining new insights into the materials utilizing state-of-the-art analytical techniques that are mostly inapplicable or ineffective on conventional secondary particles, and subsequently establishing the relationships between structure and function. The goal is to use these findings to rationally design and synthesize advanced electrode materials with improved performance.

### Objectives

This project will use a rational, non-empirical approach to design and synthesize next-generation high-energy, high-voltage cathode materials. Combining a suite of advanced diagnostic techniques with model cathode materials and model electrode/electrolyte interfaces, the project will perform systematic studies to achieve the following goals: 1) obtain new insights into solid-state chemistry, particularly cationic and/or anionic redox activities during charge and discharge of lithium transition-metal oxides, 2) gain fundamental understanding on cathode/electrolyte interfacial chemistry and charge transfer process as well as the impact of operating voltage window, 3) reveal performance- and stability-limiting properties and processes in high-energy, high-voltage cathodes, and 4) develop strategies to mitigate the structural and interfacial instabilities.

### Approach

Prepare single crystals of Li-rich transition-metal oxides with well-defined physical attributes. Perform advanced diagnostic and mechanistic studies at both bulk and single-crystal levels. Global properties and performance of the samples will be established from the bulk analyses, while the single-crystal-based studies will utilize time- and spatial-resolved analytical techniques to probe material's redox transformation and failure mechanisms.

### Results

Recently, it has been shown that some Li-excess transition-metal (TM) oxides are capable of delivering very large capacities by utilizing both TM and oxygen redox centers. One such example is $Li_{1.3}Nb_{0.3}Mn_{0.4}O_2$ ($Li_{1.3}$NMO) reported by Yabuuchi et al., which can deliver a specific energy up to 950 Wh/kg at 60 °C. As Mn is

the only redox active TM that capable of producing ~120 mAh/g with the $Mn^{3+}/Mn^{4+}$ reaction, the mechanism for the extra capacity, the possible involvement of bulk oxygen redox and its reversibility in long-term cycling, are not understood. To this end, a series of uniform micron-sized crystals of Li-rich niobium/tantalum manganese oxides with a formula of $Li_{1.4-x}Nb_{0.4-x}Mn_{0.2+2x}O_2$ ($x$ = 0, 0.1, 0.2, M = Nb, $Nb_{0.5}Ta_{0.5}$ and Ta) were synthesized by a molten salt method. In a typical synthesis procedure, stoichiometric amounts of $Li_2CO_3$, $Nb_2O_5/Ta_2O_5$ and $Mn_2O_3$ were used as precursors. To compensate the loss of lithium at elevated temperature, 10% excess of $Li_2CO_3$ was used. The precursors were mixed in a small amount of ethanol/acetone and ball-milled in a zirconia jar for 12 h. The resulting powder was then mixed with the KCl flux (m.p. = 771°C) in an R value of 2.5 or 5 (R is defined as the molar ratio between the flux and the total transition metals) and further grinded for 15 mins. The mixture was transferred into an alumina crucible covered with a lid, heated in a tube furnace at 950°C under Argon atmosphere for 12 h, and then cooled to the room temperature.

Figure II-290 shows the morphology of the synthesized $Li_{1.3}$NMO sample as well as the structural refinement results. The particles are uniform large spheres with an average size of 5 µm (Figure II-290a). Joint synchrotron X-ray and neutron Rietveld refinements (Figure II-290b and Figure II-290c) confirmed the cation-disordered rock-salt structure with a space group of $Fm\bar{3}m$ and a lattice parameter of 4.1954(1) Å. No oxygen vacancy was found in the pristine sample.

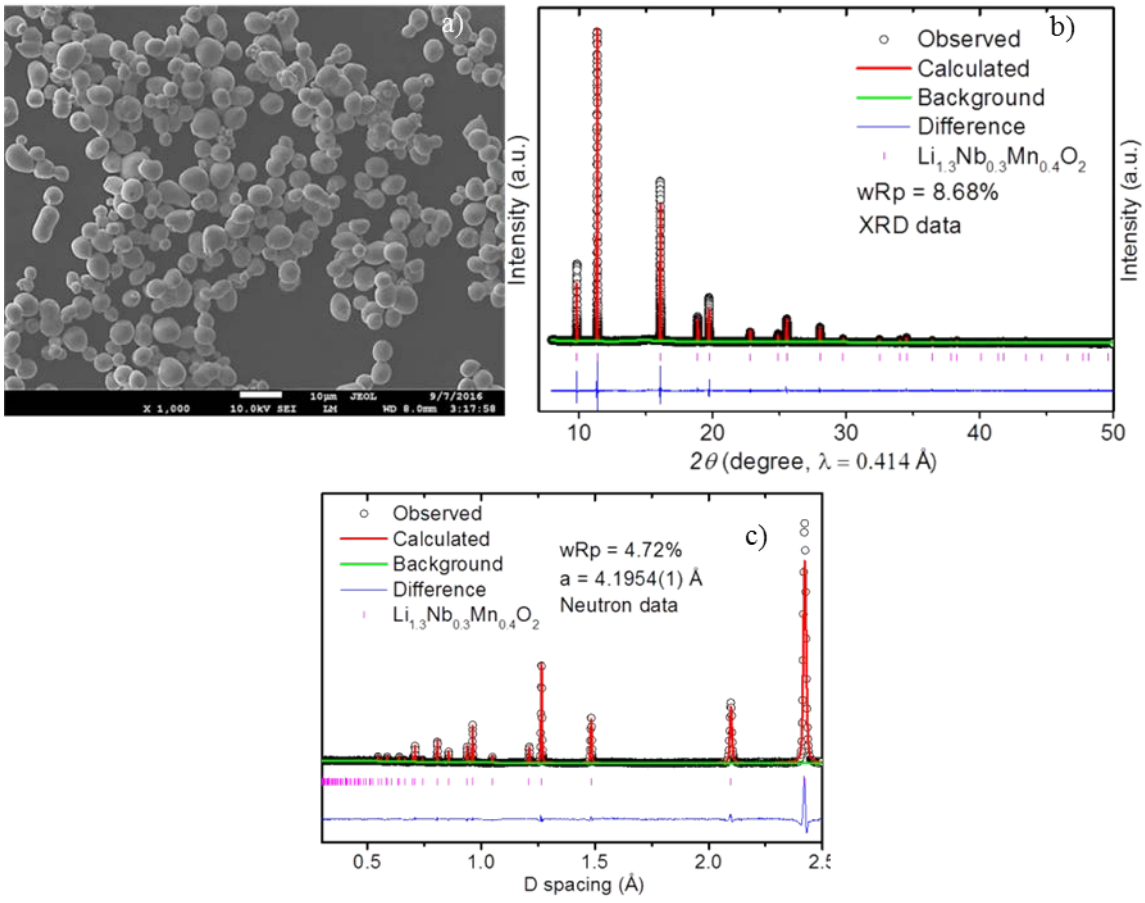


Figure II-290. a) SEM image, b) and c) Rietveld refinements of synchrotron XRD and neutron patterns of $Li_{1.3}$NMO sample.

The electrochemical performance of $Li_{1.3}$NMO crystals was evaluated at room temperature in a half-cell configuration. Due to high resistance and poor utilization of large particles, only limited capacities were obtained on composite electrodes made with the as-synthesized micron-sized crystals. In a modified procedure, the crystal size was reduced and electronic conductivity improved by ball-milling the oxide crystals together

with a carbon black additive in a $Li_{1.3}NMO$: carbon weight ratio of 80:20. The mixture was then added into the standard carbon and polyvinylidene fluoride (PVdF) slurry in an N-methyl-2-pyrrolidone (NMP) solvent and cast onto the Al current collector. The final weight ratio of active material: carbon additive: PVdF binder in thus prepared electrodes was 56:34:10. The electrodes were assembled into half-cell coin cells with a 1M $LiPF_6$ in 1:1 (v/v) ethylene carbonate (EC): diethylene carbonate (DEC) electrolyte and cycled at room temperature at a constant current of 10 mA/g between 1.5 and 4.8 V. Figure II-291a shows the voltage profiles of the first 4 cycles. In the sloping region, the voltage increased steadily from the open circuit voltage (OCV) of 3.0 V to 4.3 V which delivered a specific capacity of ~115 mAh/g. Whereas in the plateau region, the voltage only increased slightly from 4.3 V to 4.5 V before it rapidly increased to the cut off voltage of 4.8 V. A specific capacity of ~215 mAh/g was obtained above 4.3 V on the first cycle, leading to a total charge capacity of 330 mAh/g. An overall sloping discharge profile was observed which delivered a total discharge capacity of ~290 mAh/g at the cutoff voltage of 1.5 V. Two guidelines, one showing the theoretical capacity originated from the $Mn^{3+}/Mn^{4+}$ redox couple (118 mAh/g) and the other showing the theoretical capacity based on Li content (383 mAh/g), are also shown in Figure II-291a. It is clear that both charge and discharge capacities are significantly larger than the theoretical capacity of the $Mn^{3+}/Mn^{4+}$ redox. The charge capacity obtained in the sloping region is consistent with the capacity from the $Mn^{3+}/Mn^{4+}$ redox couple, suggesting that $Mn^{3+}/Mn^{4+}$ may be the sole redox process occurring in this region below 4.3 V. In the 2nd cycle, there is an overall decrease in the charging voltage of the sloping region which led to an increased capacity of ~180 mAh/g upon reaching 4.3 V. This signals a reduction in polarization in the electrode. The plateau region became somewhat sloping but voltage increase remained slow. With cycling, the degree of sloping gradually increased and the capacity obtained from this "plateau region" continued to decrease. The same trend was also observed on the discharge capacity. These results obtained from room-temperature cycling are comparable to what was obtained at 60ºC by Yabuuchi et al., suggesting that the crystal samples may have a kinetic advantage compared to the polycrystalline samples synthesized using the solid-state method.

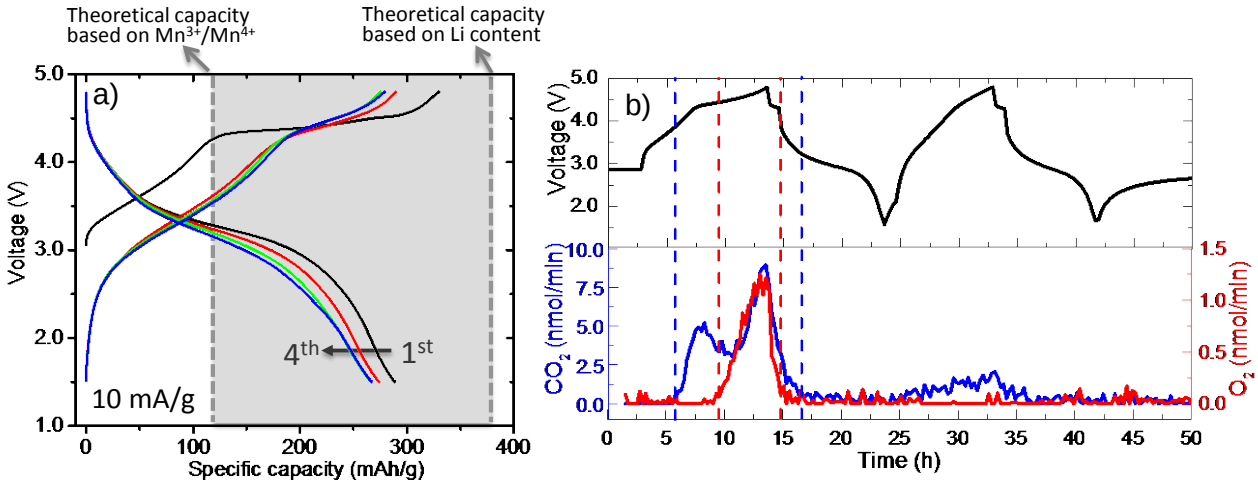


Figure II-291. a) Voltage profiles of $Li_{1.3}NMO$ half-cell cycling and b) DEMS measurement: (top) Voltage profile and (bottom) $O_2$ and $CO_2$ gas evolution.

*Operando* differential electrochemical mass spectroscopy (DEMS) was used to further examine the oxidation process of oxygen anions. Figure II-291b shows the results obtained during the first two cycles at a constant current density of 25 mA/g. During the 1st cycle, both $CO_2$ and $O_2$ evolution were detected. $CO_2$ evolution began around 3.8 V during the charge (the 1st blue guideline in the figure) and completed around the mid-discharge cycle (the 2nd blue guideline). There was an increase in intensity around the mid-plateau after the onset of $O_2$ evolution and the peak $CO_2$ evolution was reached at the end of charge at 4.8 V. Oxygen gas was not detected until the mid-plateau region at about 4.5 V (the 1st red guideline), which also peaked at the upper cut-off voltage of 4.8 V. Oxygen evolution completes at the beginning of 1st discharge after the resting step (the 2nd red guideline). The cumulative $CO_2$ and $O_2$ evolved from the first cycle were 1.53 µmol and 0.11

µmol, respectively, from a cathode that contained 2.66 mg of active materials. In the 2nd cycle, the amount of $CO_2$ was reduced from 1.53 µmol to 0.46 µmol while negligible $O_2$ evolution was detected. Combined with the cyclic voltammetry (CV) studies, the results reveal that capacity contribution from O extraction from the oxide lattice occurs above ~4.5 V. While both $O_2$ gas evolution and lattice oxygen oxidation occur in the first charge, the following cycles only involves the redox of $O^{2-}$ to $O^{n-}$ ($0 < n < 2$) species, signaled by the single oxidation peak at 4.5 V on the CV. The continuous decrease in peak intensity along with scanning indicates that the lattice anion redox process is highly irreversible.

In order to gain further insights on structural and chemical changes during the first charge, chemical oxidation was used to extract various amounts of Li from $Li_{1.3}NMO$ crystals. Delithiated $Li_xNb_{0.3}Mn_{0.4}O_2$ ($Li_xNMO$) samples were prepared by chemical reaction in a $NO_2BF_4$ solution in acetonitrile, with the lithium content ($x$) controlled by the mole ratio between the oxide and the oxidizing agent. Figure II-292 shows the synchrotron XRD and neutron patterns of the series with various lithium content of $0 \leq x \leq 1.3$, collected at 11-BM at the Advanced Photon Source (APS) and BT1 at National Institute of Standards and Technology (NIST), respectively. With decreasing $x$, the cell dimension reduces while the rock-salt crystal structure maintains. Two separate regions, a single phase region with $0.9 < x \leq 1.3$ and a two phase region with $0 < x < 0.9$, were found, suggesting the involvement of distinctively different redox activities.

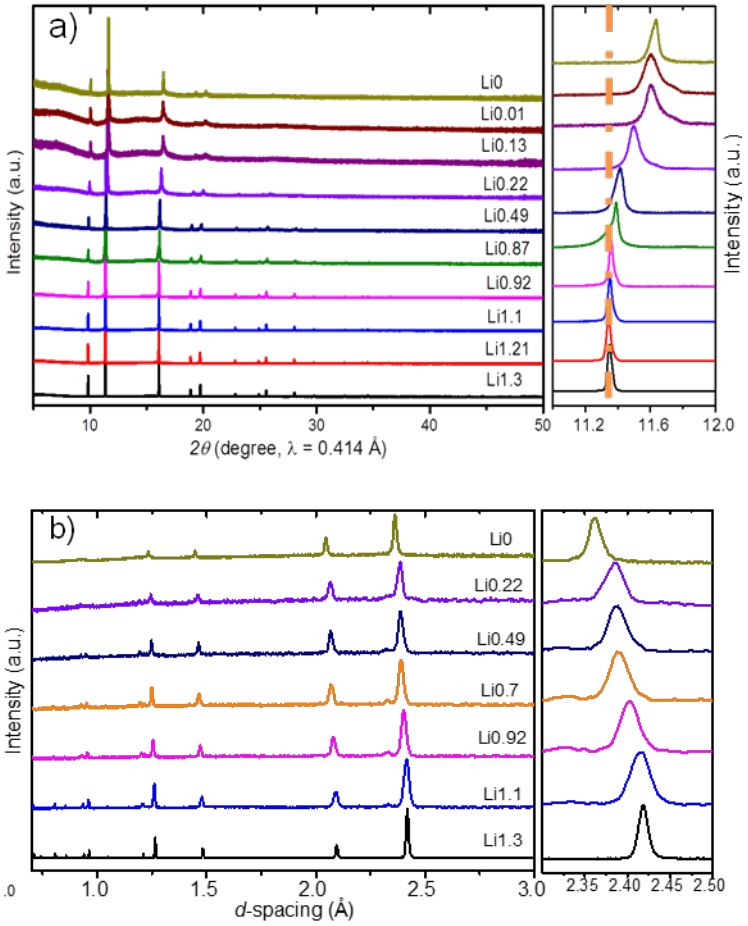


Figure II-292. a) Synchrotron XRD and b) neutron patterns of chemically delithiated $Li_xNb_{0.3}Mn_{0.4}O_2$ ($0 \leq x \leq 1.3$) crystal samples.

The unit cell volume and phase fraction as a function of Li content were constructed from the refinement and shown in Figure II-293a and Figure II-293b, respectively. The Vegard's law is only followed in region I where the total volume change is *ca.* 0.2%. This is consistent with the participation of simple cation redox from $Mn^{3+}$ to $Mn^{4+}$ along with the extraction of 0.4 $Li^+$ from $Li_{1.3}NMO$. Complex mixed oxygen activities are likely involved in region II, where Phase 2 and Phase 3 with the same rock-salt crystal structure but different lattice dimension evolves along with the extraction of Li. Smaller sized Phase 3 reaches the maximum fraction when *x* is ~0.5 whereas Phase 2 becomes the main phase with further Li removal. Combining with the results from the electrochemical studies, we propose that lattice $O^{2-}$ oxidation to $O^{n-}$ ($0 < n < 2$) mainly occurs in Phase 3 whereas loss of O from the lattice mainly occurs in Phase 2. This was further supported by results from the joint X-ray and neutron refinements which revealed that ~2 mol.% and 7.8 mol.% of oxygen ion vacancies exist in the delithiated $Li_xNb_{0.3}Mn_{0.4}O_{2-\delta}$ with $x$=0.2 and 0, respectively. The kinetic properties of delithiation is evaluated by the relationship between the molar ratio of oxidant/oxide used and the residual Li content in the sample (Figure II-293c), as determined by ICP. While a linear relationship is apparent in region I, significant deviation is seen in region II, further confirming the complex nature of mixed anion activities at lower Li contents.

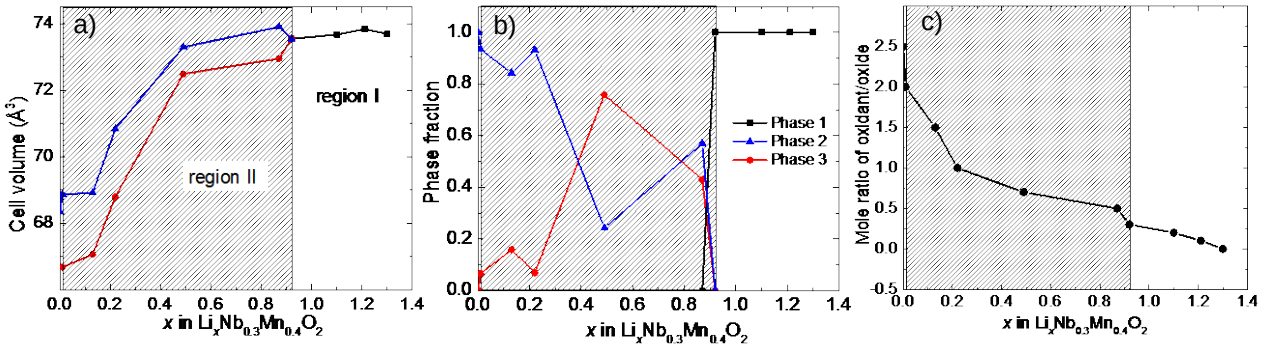


Figure II-293. a) and b) Cell volume and phase fraction as a function of x in delithiated $Li_xNMO$ samples, and c) The relationship between the molar ratio of oxidant/oxide and residue Li content in chemically delithiated $Li_xNMO$ samples.

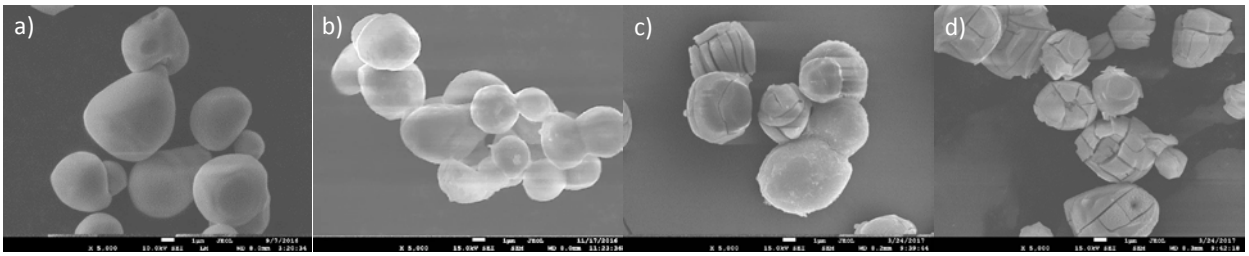


Figure II-294. SEM images of chemically delithiated $Li_xNMO$ crystal samples: a) x=1.3, b) x=1.1, c) x=0.76, and d) x=0.13.

Figure II-294 shows the changes in particle morphology along with the decrease of x in LixNMO crystals. The particles with a lithium content above 0.9 remain intact but significant cracking was observed when the lithium content is less than 0.9, likely a combined effect of cell volume change (7.3% total) and oxygen evolution during the process.

Figure II-295a-Figure II-295c show the Mn *K*-edge hard X-ray absorption spectra (hXAS) collected on pristine and chemically delithiated $Li_xNMO$ crystal samples. In the Mn pre-edge region (Figure II-295b), there is a clear division in peak intensity below and above Li0.9, suggesting a change in Mn local environment. Figure II-295c shows the expanded view of the X-ray absorption near-edge structure (XANES) region. Above Li0.9, Mn *K*-edge energy continuously shifts to a higher value in a near linear fashion which then becomes constant below 0.9. This trend is further revealed in Figure II-295d where the relationship between Li content and Mn XANES edge position, defined by the interception of the spectrum at 1/2 of the normalized intensity,

is shown. Combined hXAS, XRD and neutron results confirm that cation redox involving $Mn^{3+}/Mn^{4+}$ only occurs in the single phase region above Li0.9. Below Li0.9, Li extraction occurs with the complex oxygen redox activities that involve two rock-salt phases.

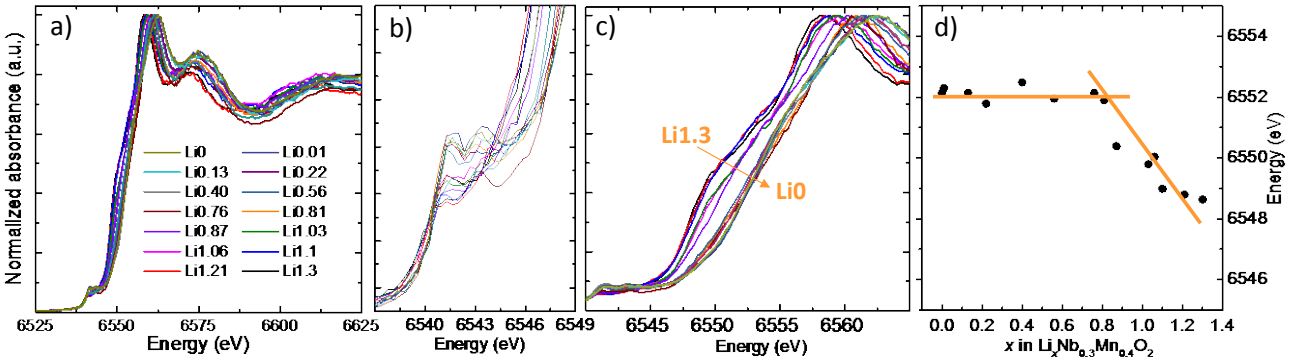


Figure II-295. Mn K-edge hard XAS measurements of $Li_xNMO$ crystals: a) hard XAS spectra, b) expanded view of the pre-edge region, c) expanded view of the XANES region and d) relationship between Mn edge position and Li content in the samples.

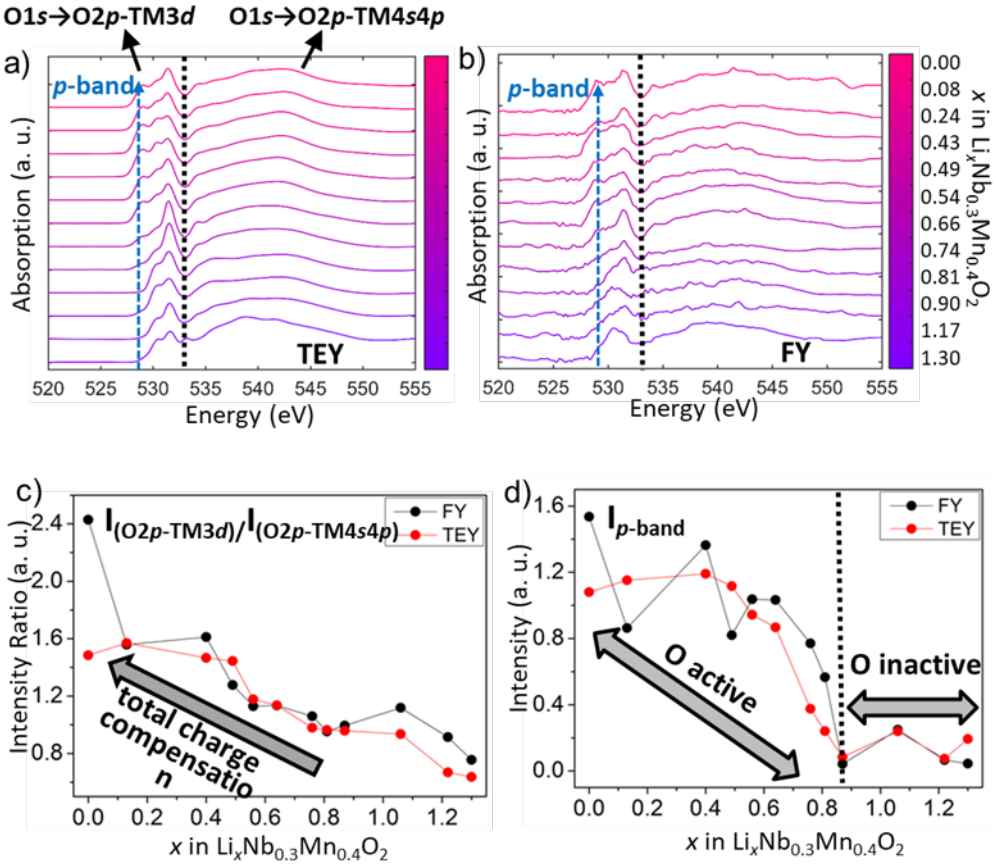


Figure II-296. a) and b) O K-edge soft XAS spectra obtained in TEY and FY modes, c) and d) Intensity ratio between the pre-edge and post-edge absorption peaks and Intensity of the p-band as a function of Li content. In a) and b), black dashed line divides the pre- and post-edge regions and the blue dashed arrow follows the evolution of the p-band intensity.

Evaluation on oxygen activities during 1st delithiation was then carried out by soft XAS measurements at the Stanford Synchrotron Radiation Lightsource (SSRL). Depth profiling from surface to bulk was achieved by using two different detectors in total electron yield (TEY) and fluorescence yield (FY) modes that have a typical probing depth of 5 and 50 nm, respectively. Figure II-296a and Figure II-296b show the evolution of TEY and FY O *K*-edge XAS spectra as a function of Li content in $Li_xNMO$. In both cases, the spectra can be separated into the pre-edge region and post-edge region at the black dashed line (533 eV). Features in the post-edge region are often attributed to O1*s* → O2*p*-TM4*s*4*p* hybridization while those in the pre-edge region are attributed to O1*s* → O2*p*-TM3*d* hybridization. The pre-edge region is therefore of most interest and may be used as a qualitative measure for holes generated from electron extraction either from oxygen or TM at the O2*p*-TM3*d* energy level. As expected, both TEY and FY spectra exhibit significant increase in the pre-edge peak intensity with Li extraction from $Li_{1.3}NMO$ which is demonstrated by the continuous increase in the ratio between the pre-edge peaks and post-edge absorption peaks (Figure II-296c). A new low-energy shoulder peak at 529 eV also appeared and gradually grew along with delithiation, suggesting the involvement of additional O-TM hybridization (referred to as *p*-band) during the process. Due to the similarity between the *p* band and the pre-edge absorption peak observed in peroxide and super-peroxide species, we speculate this new hybridization arises from the interaction between oxygen anions as a result of oxygen redox activities. Further quantification shows that the initial *p*-band intensity in the pristine $Li_{1.3}NMO$ is extremely low which remains nearly constant below Li content of ~0.9 (Figure II-296d), suggesting negligible interactions between oxygen anions or oxygen redox activities. As *x* decreases to below 0.9, there is a rapid increase in the *p*-band intensity and it continues to rise until full delithiation ($x = 0$). The results indicate an increase in oxygen valence states in this region and the participation of oxygen redox for charge compensation. Note that the *p*-band intensity in the $x < 0.9$ region is generally higher in the FY mode than that in the TEY, consistent with a difference in oxygen activities mostly involving $O^{2-}$ anion oxidation to $O^{n-}$ ($0 < n < 2$) species in the bulk and lattice O loss on the surface.

## Conclusions

In conclusion, we demonstrated the effective use of model-system-based diagnostic studies by synthesizing one of the high-capacity Li-rich oxide cathode materials, $Li_{1.3}Nb_{0.3}Mn_{0.4}O_2$, in micron-sized single crystals and using it as a platform to understand the charge compensation mechanism during Li extraction and insertion. We explicitly demonstrate that the oxidation of $O^{2-}$ to $O^{n-}$ ($0 < n < 2$) and $O_2$ loss from the lattice dominates at 4.5 and 4.7 V, respectively. While both processes occur in the first cycle, only the redox of $O^{2-}/O^{n-}$ participates in the following cycles. The lattice anion redox process triggers irreversible changes in Mn redox, which likely causes the voltage and capacity fade observed on this oxide. While a single-phase behavior involving only $Mn^{3+/4+}$ redox was observed in $0.9 < x < 1.3$, a two-phase behavior involving $O^{2-}/O^{n-}$ ($0 \leq n < 2$) reactions was seen in $0 < x < 0.9$. Approximately 7.8 mol.% of oxide-ion vacancies were found in the fully delithiated $Li_0Nb_{0.3}Mn_{0.4}O_{2-\delta}$. Morphological damage with particle cracking and fracturing was broadly observed when O redox is active, revealing additional challenges in utilizing O redox for the development of high-energy cathodes. Efforts on material modification to influence the extent of oxidation of $O^{2-}$ to $O^{n-}$ ($0 < n < 2$) and $O_2$ loss from the lattice as well as strategies to improve oxide performance are underway.

## Key Publications


1. S. Kuppan, Y. Xu, Y. Liu and G. Chen, "Phase Transformation Mechanism in $LiMn_{1.5}Ni_{0.5}O_4$ Cathode Particles Revealed by Single-crystal Hard X-ray Microscopy," *Nature Communications*, **8**, 14309 (2017). DOI: 10.1038/ncomms14309.

2. S. Kuppan, A.K. Shukla, D.Membreno, D. Nordlund and and G. Chen, "Revealing Anisotropic Spinel Formation on Pristine Li- and Mn-Rich Layered Oxide Surface and Its Impact on Cathode Performance," *Advanced Energy Materials*, **7**, 1602010 (2017), DOI: 10.1002/aenm.201602010.

3. Y. Ma, Y. Zhou, C. Du, P. Zuo, X. Cheng, L. Han, D. Nordlund, Y. Gao, G. Yin, H. L. Xin, M. M. Doeff, F. Lin, and G. Chen, "A New Anion Receptor for Improved Interface between the Lithium- and

Manganese-rich Layered Oxide Cathode and the Electrolyte," *Chemistry of Materials*, **29** (5), 2141 (2017). DOI: 10.1021/acs.chemmater.6b04784.

4. W. H. Kan, S. Kuppan, L. Cheng, M. Doeff, J. Nanda, A. Huq and G. Chen, "Crystal Chemistry and Electrochemistry of $Li_xMn_{1.5}Ni_{0.5}O_4$ Solid Solution Cathode Materials," *Chemistry of Materials*, **29** (16), 6818 (2017). DOI: 10.1021/acs.chemmater.7b01898.

5. S. Kuppan, A.K. Shukla and G. Chen, "Single-crystal Based Diagnostics for Li-ion Battery Cathode Development," PRiME 2016, Honolulu, HI, October 2016.

6. Y. Ma, Y. Zhou, G. Yin, F. Lin and G. Chen, "A New Anion Receptor for Improved Interface Between the Lithium- and Manganese-Rich Layered Oxide Cathode and the Electrolyte," PRiME 2016, Honolulu, HI, October 2016.

7. W.-H. Kan, S. Kuppan and G. Chen, "Advanced High-energy Cathode Materials for Lithium-ion Batteries," 2016 Bay Area Battery Summit, Menlo Park, CA, November 2016.

8. J. Kan, T. Yan and G. Chen, "Rational Design and Development of Advanced Lithium Battery Materials" Energy Technology Area Lab Director's Review, Berkeley, CA, January 2017 (invited).

9. J. Kan and G. Chen, "Rational Design and Development of Advanced Lithium Battery Materials" Energy Technology Area Lab Town Hall Meeting, Berkeley, CA, March 2017 (invited).

10. G. Chen, "Design and Synthesis of Advanced High-Energy Cathode Materials," DOE Hydrogen Program and Vehicle Technologies Program Annual Merit Review and Peer Evaluation Meeting, Washington, DC, June 2017.

# II.D Next-Gen Lithium-Ion: Diagnostics

## II.D.1 Interfacial Processes (LBNL)

**Robert Kostecki, Principal Investigator**
Lawrence Berkeley National Laboratory
1 Cyclotron Road
Berkeley, CA 94720
Phone: 510-486-6002
E-mail: r_kostecki@lbl.gov

**Tien Duong, Technology Manager**
U.S. Department of Energy
Phone: 202-586-7836
E-mail: Tien.Duong@ee.doe.gov

Start Date: October 1, 2016 End Date: September 30, 2017
Total Project Cost: $440,000 DOE share: $440,000 Non-DOE share: $0

### Project Introduction

Li-ion batteries are inherently complex and dynamic systems. Although often viewed as simple devices, their successful operation relies heavily on a series of complex mechanisms, involving thermodynamic instability in many parts of the charge/discharge cycle and the formation of metastable phases. This paradigm of Li-ion system operation usually drives the battery toward irreversible physical and chemical conditions that lead to battery degradation and failure.

The requirements for long term stability of Li-ion batteries are extremely stringent and necessitate control of the chemistry at a wide variety of temporal and structural length scales. Progress towards identifying the most efficient mechanisms for electrical energy storage and the ideal material depends on a fundamental understanding of how battery materials function and what structural/electronic properties limit their performance. This in turn necessitates the development and use of new characterization tools to monitor these processes.

The design of the next generation of Li-ion batteries requires a fundamental understanding of the physical and chemical processes that govern these complex systems. Although some significant advances have been made to prepare and utilize new materials efforts towards the understanding of their operation mechanisms and degradation modes have been insufficient and/or unsuccessful.

This project provides better understanding of the underlying principles that govern the function and operation of battery materials, interfaces and interphases, which is inextricably linked with successful implementation of high energy density materials such as $Li[Ni_xMn_yCo_z]O_2$ compounds (NMCs) in Li-ion cells for PHEVs and EVs. A systematic evaluation of the NMC material composition, and cell history on the surface reconstruction, transition metal dissolution, oxygen loss phenomenon is proposed for this work, using *in situ* surface-sensitive optical spectroscopy and microscopy. These results will supplement other characterization efforts within this Task and ultimately will be used to design and synthesize robust NMC materials that can cycle stably to high potentials and deliver >200 mAh/g at coulombic efficiency close to 100%. A better understanding of the underlying principles that govern these phenomena is inextricably linked with successful implementation of high energy density materials such as Si and high voltage cathodes in Li-ion cells for PHEVs and EVs.

## Objectives

This collaborative project involves the development and application of advanced experimental methodologies to study and understand the mechanism of operation and degradation of high capacity NMC materials for Li-ion cells for PHEV and EV applications. The main objectives of this task are:

- Provide critical understanding of basic principles that govern the function and operation of active materials, composite electrodes and Li-ion battery cells that is necessary for successful implementation of high energy density materials in Li-ion cells for PHEVs and EVs.
    - Establish direct correlations between electrochemical performance, interfacial phenomena, surface chemistry, morphology, topology and degradation mechanisms of ABMR baseline materials, electrodes and cells.
- Propose and evaluate remedies to interfacial and materials instability e.g., artificial surface coatings (e.g., ALD) and/or structures, novel electrode architectures, electrolyte additives etc.
- Develop, adapt and employ new advanced experimental techniques and methodologies to guide development of novel EES materials, electrodes and battery systems.
    - Obtain detailed insight into the dynamic behavior of molecules, atoms, and electrons at electrode/electrolyte interfaces at resolution that is adequate to the size and function of basic chemical or structural building blocks

## Approach

Apply *in situ* and *ex situ* far- and near-field optical multifunctional probes to obtain detailed insight into the active material structure and the pysico-chemical phenomena at electrode/electrolyte interfaces of stoichiometric NMCs with high Ni contents such as 622 and 523 compositions materials at a spatial resolution that corresponds to the size of basic chemical or structural building blocks. The primary goal of these studies is to unveil the structure and reactivity at hidden or buried interfaces and interphases that determine material, composite electrode and full cell electrochemical performance and failure modes. The proposed work constitutes an integral part of the concerted effort within the BMR Program and it supports development of new cathode materials for high-energy Li-ion cells. The specific research tasks include:

1. Study interfacial reactions between organic electrolytes and Ni-rich NMC.
2. Investigate the impact of surface reconstruction layer(s) on the electrochemical behavior of the NMC cathode.
3. Obtain detailed insights into the mechanism and interdependence of interfacial phenomena at Ni-rich NMC cathodes.

This project focuses on high Ni content NMC compositions such as 523 and 622, which are expected to achieve high discharge capacities even within conservative electrode potential limits. The *in situ/ex situ* investigations of the surface reconstruction into rock salt on NMC samples of different morphology and composition were carried out in sync with with similar studies by X-ray techniques (M. Doeff, LBNL) and directly linked with investigations interfacial reactivity toward organic electrolytes.

In close collaboration with the BMR Cathode Group, NSOM, FTIR-ATR and environmental XPS were used to monitor surface reactions and identify their intermediates and end-products on binder and carbon-free model NMC samples to investigate the spatial-chemical composition of surface layers. This is a collaborative effort with the LBNL ALS IR beam line 5.4.1 scientists to adopt and employ a synchrotron-based tunable IR source to overcome spectral range limitation of the tunable lasers and/or inadequate intensity of the glow bar IR source. This new and unique experimental setup constitutes a major breakthrough in the diagnostics of electrochemical interfaces, and Li-ion systems in particular.

## Results

We analyzed the relationship between the reconstruction layer on the surface of nickel-rich NMC (Ni:Mn:Co=5:3:2) particles and its electrochemical properties. For this purpose, an artificial reconstructed surface layer was produced by storing the NMC powder for 10 days in 1M $LiPF_6$ in EC/DEC 1:2 electrolyte at 60 $^oC$. The NMC powder was then washed and sonicated in DEC, and dried in vacuum. The resultant surface rock-salt layer is expected to have a similar thickness as the one that evolves from electrochemical charging and discharging as reported in the literature. The pristine (NMC) powder and the powder with a surface reconstruction layer (NMC/R) were then used to prepare composite electrodes for electrochemical tests in a standard coin cell configuration.

After 200 charge-discharge cycles at 0.5 C between 2.0-4.7 V, both the NMC and NMC/R cells show similar capacity retention ca. 61% of the original discharge capacity (Figure II-297a). Interestingly, NMC/R electrode showed consistently lower polarization than pristine NMC Figure II-297(b)-(d)). The polarization difference between NMC and NMC/R is about 0.2 V for discharging and 0.1 V for charging at 50 % state of charge for 200$^{th}$ cycle. This demonstrates that in fact, the existence of the reconstruction layer improves the cell performance by inhibiting the impedance growth during cycling.

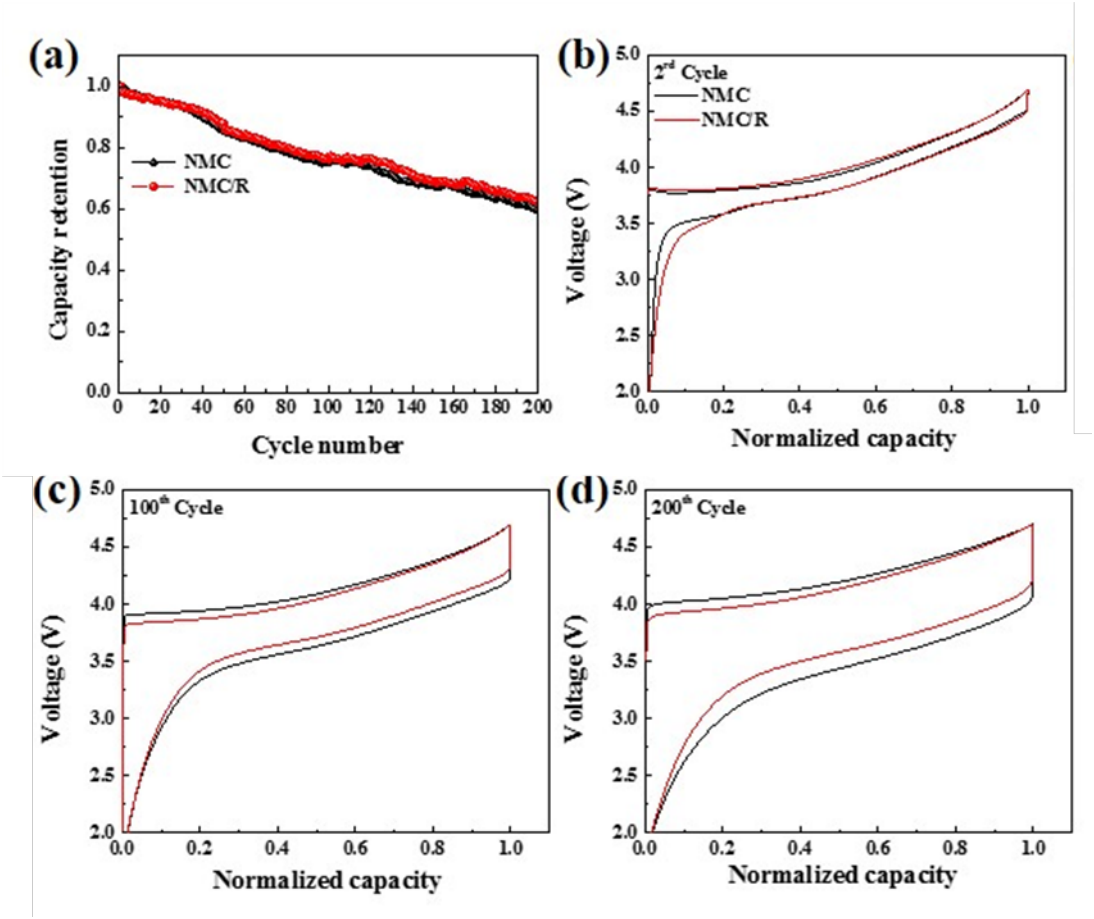


Figure II-297: (a) NMC and NMC/R electrodes capacity retention, and (b-d) charge discharge voltage profiles.

To clearly identify possible origins of the impedance growth, the electrochemical impedance spectroscopy was employed at selected cycles (Figure II-298 a,b). The high frequency semi-circle can be assigned to the contact resistance ($R_s$) i.e., electronic resistance between the current collector, conductive additive and the active material. $R_s$ is highly related to the electron percolation in the composite electrode. The mid-frequency semi-circle can be assigned to the charge transfer resistance ($R_{ct}$) at the interface between the active material and the electrolyte. Those resistances can be obtained by fitting the spectra using an adequate equivalent circuit model (Figure II-298 c,d). Both electrode materials show similar trends with $R_{ct}$ variations that continuously increases over 90 cycles. However, $R_s$ for the pristine NMC electrode is not only higher but it grows substantially during cycling whereas $R_s$ for the NMC/R electrode is relatively low and it remains constant during cycling.

Lin et al. [1] demonstrated that reconstruction layer at NMC surface has lower valence state of the transition metal than in the bulk. Our earlier work [2] inferred the electrolyte decomposition mechanism that relates to the catalysis effect at high-charge-state transition metal surface. Thus, lower interfacial activity toward the electrolyte of MeO-rich surfaces may inhibit electrolyte decomposition and slow down accumulation of the reaction products, which are mainly responsible for creating ionic and electronic barriers in the composite electrode.

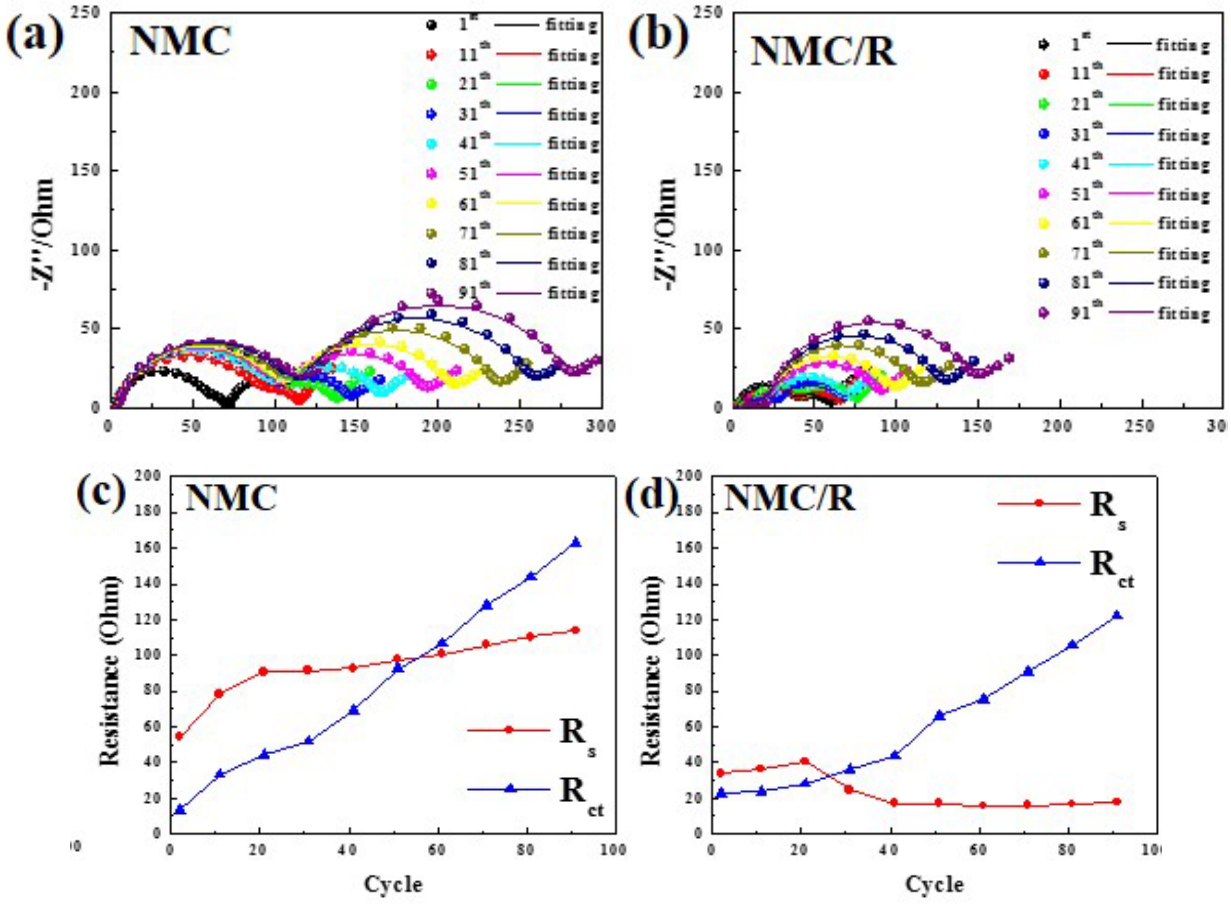


Figure II-298: Nyquist plots of coin cells with NMC (a) and NMC/R (b) cathodes. $R_s$ and $R_{ct}$ extracted from the impedance data for NMC (c) and NMC/R (d) electrodes.

Then we evaluated the effect of an artificial surface reconstruction layer on the electrochemical performance of the nickel-rich NMC (Ni:Mn:Co=5:3:2) cathode and its effect on the degradation mechnism of the NMC electrode. We used X-ray absorption spectroscopy in total electron yield mode (XAS-TEY) to probe the valence state of transition metal ions in NMC at shallow depths (2-5 nm) from the particle surface. Figure II-299 shows XAS-TEY spectra of the pristine nickel-rich NMC powder and NMC/R powder samples after surface modification process at Ni, Co and Mn L-edge. The absorption peaks at 852.5 eV and 854 eV correspond to $Ni^{2+}$ and $Ni^{3+}$, respectively. NMC/R exhibits lower $Ni^{3+}/Ni^{2+}$ peak ratio than pristine NMC, which indicates that NMC/R material has higher concentration of $Ni^{2+}$ at the surface. Co and Mn L-edge spectra display $Co^{2+}$ and $Mn^{2+}$ shoulders at 778 eV and 639 eV next to the main $Co^{3+}$ and $Mn^{4+}$ peaks at 780.5 eV and 642.5 eV, respectively. Higher intensities of $Co^{2+}$ and $Mn^{2+}$ peaks in NMC/R spectra also points toward surface enrichment with $Co^{2+}$ and $Mn^{2+}$. In other words, XAS-TEY spectra provide a direct evidence of a surface reconstruction layer, which was artificialy created in NMC/R particles upon a long-term exposure to the electrolyte at elevated temperatures. The (II) valance state of Ni, Co and Mn at the surface is consistent with the presence of a rock salt structure thin-film, which has been reported elsewhere by different groups.

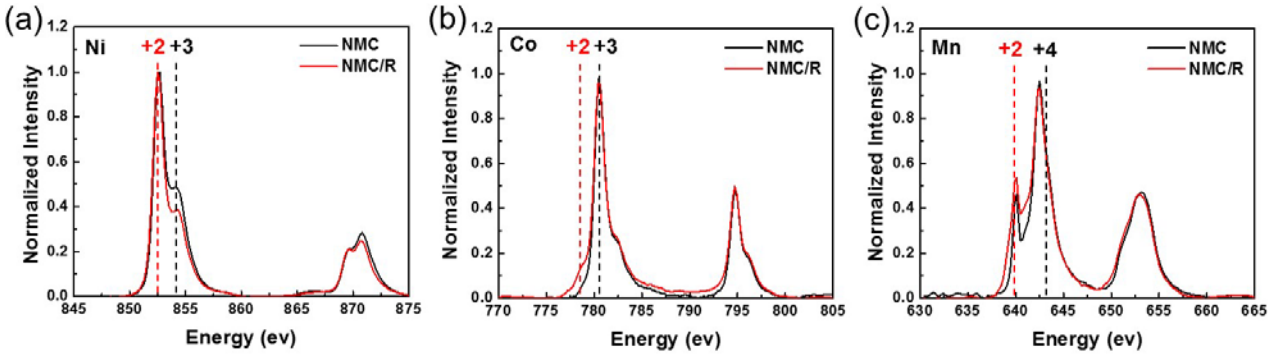


Figure II-299: XAS-TEY of NMC and NMC/R powders on the range L-edge of (a) Ni, (b) Co and (c) Mn.

Composite cathodes were fabricated with pristine NMC and NMC/R powders and then cycled at 0.5 C between 2-4.7 V in coin cells equiped with Li anode and 1M $LiPF_6$ EC/DEC (1:2 wt%) electrolyte. The cycled cathodes were washed in DEC and dried in vacuum. Figure II-300 shows XAS spectra of the cycled electrodes at Ni, Co and Mn L-edge. The Ni L-edge spectrum of the NMC electrode shows a notable decrease of the $Ni^{3+}$ peak at 854 eV after cycling whereas the cycled NMC/R electrode shows no such a change. Interestingly, the surface composition of the NMC and NMC/R electrodes after cycling becomes almost the same. Co and Mn L-edge spectra show increased peak intensities at 778 eV, 639 eV and 641eV, which is associated with higher surface concentrations of $Co^{2+}$, $Mn^{2+}$ and $Mn^{3+}$, respectively. However, the extent of surface reduction in NMC/R is much smaller than in NMC after cycling. It appears that the rate of formation of the reconstruction layer and associted proceses (e.g., Me dissolution, surface film formation) during cycling is strongly dependent on the initial state of the surface.

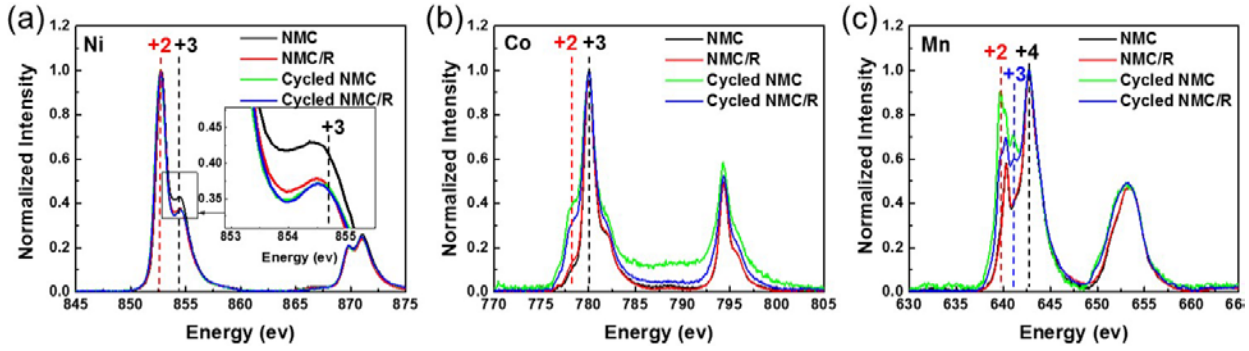


Figure II-300: (a) XAS-TEY of cycled NMC and NMC/R electrodes on the range L-edge of (a) Ni, (b) Co and (c) Mn.

W also studied changes in the surface morphology of model NMC cathodes during operation at potentials above 4 V in 1M $LiPF_6$ in EC/DEC (1:2 vol.). To enable a high-resolution surface analysis by *in situ* AFM, a nominally flat, binder-free and conductive-additive-free NMC thin-film electrode was produced by pulsed laser deposition (PLD) directly on an aluminum substrate, using NMC (Ni:Co:Mn = 5:3:2) target. A Raman spectrum (Figure II-301a) of the model NMC/Al electrode shows vibrational modes typicall for layered hexagonal structure ($R\bar{3}m$) [3] which are consistent with the spectrum of standard NMC 532 powder. The electrochemical performance of the thin-film NMC/Al electrode was evaluated in a coin cell against with Li-foil counter electrode in 1M $LiPF_6$ in EC/DEC (1:2 vol.). The cyclic voltammetry curve (Figure II-301b) of the model electrode displays similar redox features as a typical NMC composite electrode. The *in situ* three-electrode AFM cell with the NMC/Al working, Li-foil counter and reference electrodes is shown in Figure II-297c. The cell was operated in He-filled environmental chamber under saturated DEC partial vapor pressure to prevent drying of the electrolyte during the experiment. NMC electrode was charged at constant potential steps from OCV (~3.4 V) to 4.7 V (Figure II-301c) for 30 min at each step before AFM imaging.

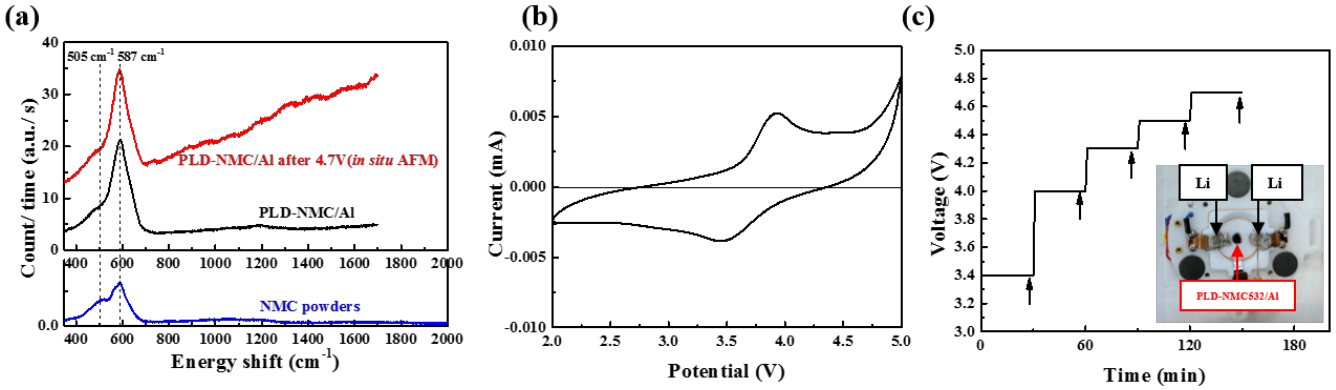


Figure II-301: (a) Raman spectra of NMC powder (blue), PLD-NMC/Al electrode (black) and PLD-NMC/Al electrode after 4.7 V charged (red). (b) Cyclic voltammogram of PLD-NMC/Al electrode at the 3rd cycle. (c) The voltage-time profile of electrode during in situ AFM experiment. The arrows point at the time when AFM images were acquired. (Insert: *in situ* AFM cell.)

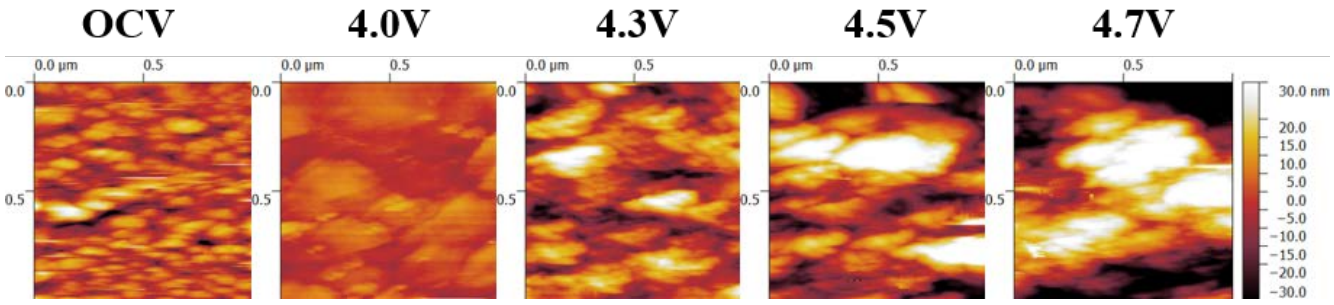


Figure II-302: 1 x 1 µm AFM images of PLD-NMC/Al electrode after 30 min. polarization at each potential

The AFM images of the NMC surface at OCV (~3.4 V), 4.0, 4.3, 4.5, 4.7 V are shown in Figure II-302. The pristine electrode is composed of tightly packed 100-150 nm NMC grains. After charging to 4.0 and 4.3 V the NMC particles tend to agglomerate and form ~300 nm clusters, and larger 500 nm aggregates at 4.5 V and 4.7 V. At potentials <4.3 V, the cluster surface morphology still shows individual 100 nm grains of NMC. However, at higher potentials (>4.5 V), the observed changes in surface morphology can be also assigned to a surface film formation. The NMC/Al electrode was removed from the AFM cell after polarization at 4.7 V, washed in DEC and probed by *ex situ* Raman spectroscopy (Figure II-301a). The spectrum shows a strong fluorescence background and weak features in 800-1600 $cm^{-1}$ range, which indicate possible formation of β-ketone coordination complexes similarly to LMNO [2]. These results provide a direct insight into the surface

film formation process, which otherwise is difficult to observe by other diagnostic methods especially in NMC composite cathodes. At the end of anodic polarization the film is ca. 10 nm thick and it may give rise to formation of electronic and ionic barriers, which can contribute to the commonly observed degradation modes of NMC cathodes in Li-ion batteries.

## Conclusions

- Surface reconstruction layer is NOT the root cause of impedance rise and capacity fade fading of the Ni-rich NMC electrode.
    - "Pristine" NMC material and NMC with the artificially induced surface reconstruction layer exhibit similar initial electrochemical behavior.
- NMC material with the artificially induced surface reconstrType equation here.uction layer shows better long-term cycle performance than "pristine" NMC".
    - Surface reconstruction layer on NMC surface suppresses oxidation of EC/DEC, inhibits electrolyte oxidation, surface film formation and Me dissolution during cycling
- Artificially induced surface structure reconstruction can be an effective strategy of reducing NMC surface reactivity

This study not only determines the mechanism of surface reduced layer formation but also offers unique insight into its direct and indirect impact on the electrochemical performance and interrelated mechanism of interfacial phenomena at high-voltage cathodes.

## Key Publications


1. Lei Cheng, Huaming Hou, Simon Lux, Robert Kostecki, Ryan Davis, Vassilia Zorba, Apurva Mehta, and Marca Doeff, "Enhanced Lithium Ion Transport in Garnet-type Solid State Electrolytes", Journal of Electroceramics, accepted
2. Robert Kostecki, Angelique Jarry, Maurice Ayache, Hans A. Bechtel, Michael C. Martin, 253rd ACS National Meeting & Exposition: Advanced Materials, Technologies, Systems and Processes, April 2-6, 2017, San Francisco, USA (invited lecture)
3. Robert Kostecki, Maurice Ayache, Hans A. Bechtel, Angelique Jarry, Michael C. Martin, "IR spectroscopy and Imaging Interfaces in Silicon Anode", 20th Topical Meeting of the International Society of Electrochemistry, 19-22 March 2017, Buenos Aires, Argentina
4. Robert Kostecki, "Probing charge and mass transport phenomena across interfaces and interphases in Li-ion batteries", Nanomaterials for Applications in Energy Technology Gordon Research Conference February 26-March 3, 2017, Ventura, CA, USA (invited lecture)
5. Robert Kostecki, "The Mechanism of NMC Cathodes Dissolution in Organic Carbonate Electrolytes", 57th Battery Symposium, November 29, 2016, Chiba-City, Japan (invited lecture)
6. Robert Kostecki, Maurice Ayache, Simon Lux, "Near-Field IR Imaging and Spectroscopy of Interfaces and Interphases in Li-ion Electrodes", 230th Meeting of The Electrochemical Society, Honolulu, Hawaii, USA, October 2-7, 2016
7. Robert Kostecki, "Probing charge and mass transport phenomena across interfaces and interphases in Li-ion batteries" Telluride Science Research Center Workshop: Interfacial Chemistry and Charge Transfer for Energy Conversion and Storage, July 25-29, 2016, Telluride, CO (invited lecture)

8. Angelique Jarry, Paul Pearce, Bryan Eichhorn, and Robert Kostecki, “Role of the transition metal dissolution species formed at Li-ion positive electrode materials on the battery performance and failure modes”, 18th International Meeting on Lithium Batteries, June 19-24, 2016, Chicago, Illinois, USA

9. Robert Kostecki “Understanding Charge and Mass Transport Across Interfaces and Interphases in Batteries” SIRBATT Workshop “*Controlling Lithium Battery Interfaces”*, Orlando, USA Friday 27th May 2016. (keynote lecture)

## References

1. Lin F, et al., *Nat. Commun.* 5, (2014).

2. Jarry, A. et al., *J. Am. Chem. Soc.*, 137, 3533-3539 (2015).

3. R. E. 4, A. F. Callender, H. Zhou, S. K. Martha and J. Nanda, *J Electrochem Soc*, **162**, A98 (2015).

## II.D.2 Advanced *in situ* Diagnostic Techniques for Battery Materials (BNL)

**Xiao-Qing Yang, Principal Investigator**
Chemistry Division
Brookhaven National Laboratory
Bldg. 555, Brookhaven National Lab.
Upton, NY 11973
Phone: 631-344-3663
E-mail: xyang@bnl.gov

**Seongmin Bak, Co-Principal Investigator**
Chemistry Division
Brookhaven National Laboratory
Bldg. 555, Brookhaven National Lab.
Upton, NY 11973
Phone: 631-344-4142
E-mail: xyang@bnl.gov

**Tien Duong, Technology Manager**
U.S. Department of Energy
Phone: 202-586-7836
E-mail: Tien.Duong@ee.doe.gov

Start Date: October 1, 2016 End Date: September 30, 2017
Total Project Cost: $600,000 DOE share: $600,000 Non-DOE share: $0

### Project Introduction

This proposed project was focused on developing advanced diagnostic characterization techniques to investigate these issues, obtaining in-depth fundamental understanding of the mechanisms governing the relationship between the structure and the performance, and providing guidance and approaches to solve these problems. The unique approach of this proposed project is the development and application of combined synchrotron-based in situ X-ray techniques such as x-ray diffraction (SXRD), pair distribution function (PDF), hard and soft x-ray absorption (XAS and SXAS), together with other imaging and spectroscopic tools such as high resolution transmission electron microscopy (HRTEM), scanning transmission electron microscopy (STEM), mass spectroscopy (MS), X-Ray fluorescence microscopy (XRF) and transmission x-ray microscopy (TXM). For advanced Li-ion battery technologies, the revolutionary approaches using new generation of materials for cathode, anode, electrolyte, and separator are in the horizon. The new generation of cathode materials such as high voltage spinels ($LiMn_{2-x}Ni_xO_4$) and/or Li-rich high energy density $Li_{1+x}(NiMnCo)O_2$ composite materials together with high energy density Si-based anode materials will significantly increase the energy density of the LIB cells. However, many technical barriers must be overcome before the large scale commercialization of these new materials can be realized. This proposed project will use the time-resolved x-ray diffraction TR-XRD and absorption (TR-XAS) developed at BNL to study the kinetic properties of these materials with structural sensitivity (TR-XRD) and elemental selectivity (TR-XAS). This project will develop and apply the HRTEM, TXM and PDF techniques to study the mechanism of capacity and performance fading of cathode and anode materials. Another important issue is the thermal stability of new cathode materials which is closely related to the safety of the batteries. This problem will be studied using the combined TR-XRD, TR-XAS with mass spectroscopy (MS). This project also proposes to develop a novel in situ X-ray fluorescence (XRF) microscopy combined with X-ray absorption spectroscopy (XAS) technique, which will enable us to track the morphology and chemical state changes of the electrode materials during cycling. We will further develop this novel technique utilizing the new unique capability of TES beamline at NSLS II, with

better signal/noise ratio and spatial resolution to do diagnostic studies of the cathode and anode materials of advanced Li-ion batteries. In summary, this proposed project supports the goals of VTO, the Battery and Electric Drive Technologies, and BMR program by developing new diagnostic technologies and applying them to the advanced Li-ion battery systems to provide guidance for new material development.

## Objectives

The primary objective of this project is to develop new advanced in situ material characterization techniques and to apply these techniques to support the development of new cathode and anode materials with high energy and power density, low cost, good abuse tolerance, and long calendar and cycle life for the next generation of lithium-ion batteries (LIBs) to power plug-in hybrid electric vehicles (PHEV). The diagnostic studies will be focused on issues relating to capacity retention, thermal stability; cycle life and rate capability of advanced Li-ion batteries.

## Approach

- Using nano-probe beamline at NSLSII to study the elemental distribution of new solid electrolyte materials for Li-ion and Na-ion batteries
- Using pair distribution function (PDF) techniques to study the effects of multiple cycling for $Li_2Ru_{0.5}Mn_{0.5}O_3$ cathode material with and without pre-lithiation (Micro structural defects were intentionally generated) to improve the performance of high energy density materials.
- Using high resolution transmission electron microscopy (TEM) to obtain multiple dimensional (3D + elemental, valence state, and time) mapping of new cathode materials for advanced Li-ion batteries.
- Using transmission x-ray microscopy (TXM) to do multi-dimensional mapping of cathode materials
- Using A combination of time resolved X-ray diffraction (TR-XRD) and mass spectroscopy (MS), together with *in situ* soft and hard X-ray absorption (XAS) during heating to study the thermal stability of the electrode materials
- Using *in situ* XRD and XAS, to study the new concentration gradient cathode materials to improve the cycle life of Li-ion batteries
- Using quick x-ray absorption spectroscopy and time resolved x-ray diffraction techniques to study the kinetic properties and the structural changes of $Li_{1-x}Ni_{1/3}Co_{1/3}Mn_{1/3}O_2$ cathode material during high rate charge process to improve high rate capability of Li-ion batteries.

## Results

*1. Using pair distribution function (PDF) to correlate the voltage and capacity fading with micro-structural defects of $Li_2Ru_{0.5}Mn_{0.5}O_3$ as a model compound for (LMR) high energy density cathode materials.*

In FY 2017, this project carried out the studies on the structure of $Li_2Ru_{0.5}Mn_{0.5}O_3$, as a model compound for Li and Mn rich (LMR) high energy density cathode materials using pair distribution function (PDF) to correlate the voltage and capacity fading with micro-structural defects. Figure II-303a shows that PDF peaks correspond to characteristic bond distances while the amplitude of the peak is relating to the coordination number. Take $LiNiO_2$ as an example, the first peak (in red) is mainly from transition metal—oxygen bond and the peak position correspond to the transition metal—oxygen bond length. The second peak (in blue) is mainly from transition metal—transition metal bond. The PDF data for pristine state and "OCV-1V-3V" state are shown in Figure II-303b, providing structural information in the scale of around 50 Å. It can be seen that in the short-range region (Figure II-303c) which covers from 1.6 Å to around 20 Å, the two data sets are almost identical. This indicates that at the scale of a unit cell dimension, the pristine state and "OCV-1V-3V" state have very similar atomic arrangements, suggesting their crystal structure are basically the same. However, when it comes to long range data sets as shown in Figure II-303d, there is obvious difference between these two states. For the pristine state, there are still well-defined structural features at R value as high as 50 Å.

However, for “OCV-1V-3V” state, these structural features are gradually lost when R is greater than 35 Å, indicating that the coherently scattering domain is on the scale of several nanometers

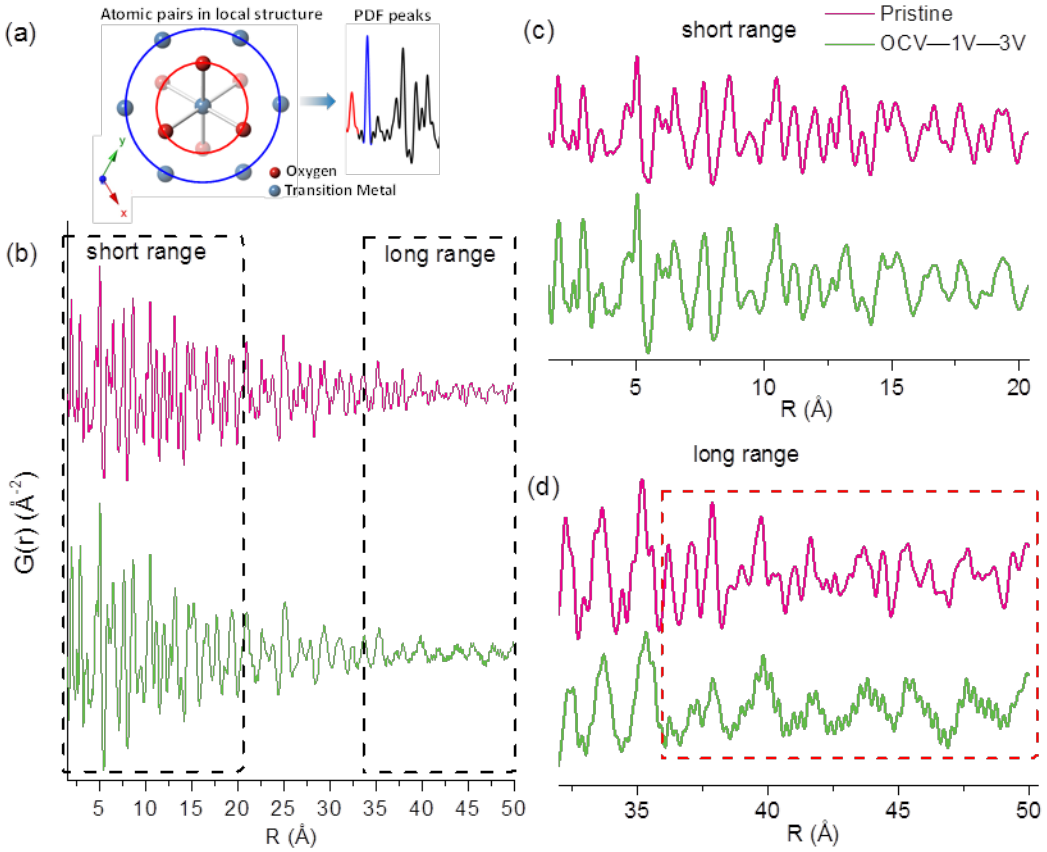


Figure II-303. (a) Illustration of PDF showing that peaks correspond to characteristic bond lengths. (b) Ex situ PDF data of pristine sample and “OCV—1V—3V” sample (c) zoomed in data on the short range region of ex situ PDF data and (d) zoomed in data on the long range region of ex situ PDF data.

*2. Using scanning transmission electron microscopic (STEM) to correlate the voltage and capacity fading with micro-structural defects of $Li_2Ru_{0.5}Mn_{0.5}O_3$*

In FY 2017 this project also carried out the structure studies of $Li_2Ru_{0.5}Mn_{0.5}O_3$, as a model compound for Li and Mn rich (LMR) high energy density cathode materials using scanning transmission electron microscopic (STEM) to correlate the voltage and capacity fading with micro-structural defects in this type of materials. Microstructure changes and nano-sized microstructural defects created by prelithiation process can be directly observed by comparing the Z-contrast annular dark-field scanning transmission electron microscopic (ADF-STEM) images taken on pristine and prelithiated samples. Figure II-304a (left panel) shows the atomic-resolution ADF-STEM image of the pristine material, indicating good crystallinity with typical features of the layered structure. After prelithiation, the material (right panel, Figure II-304a) shows great loss of the crystallinity, forming domains that orient differently from each other with large amount of additional grain boundaries created. It can be seen that these domains are at the scale of several nanometers, confirming previous analysis of XRD and PDF results. The process is illustrated in Figure II-304b.

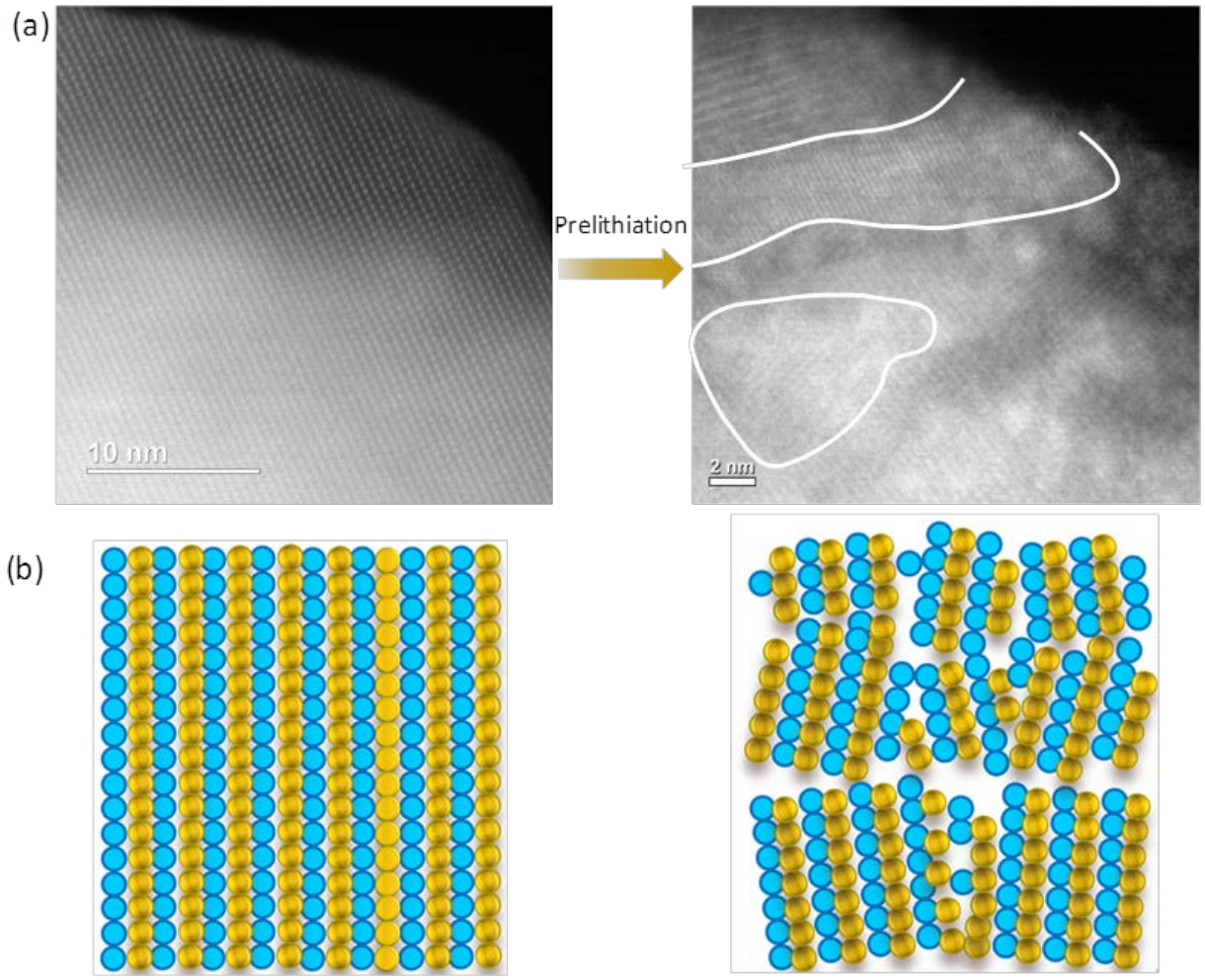


Figure II-304. (a) Illustration of PDF showing that peaks correspond to characteristic bond lengths. (b) Ex situ PDF data of pristine sample and "OCV—1V—3V" sample (c) zoomed in data on the short range region of ex situ PDF data and (d) zoomed in data on the long range region of ex situ PDF data

*3. Using synchrotron-based x-ray diffraction (XRD) and absorption (XAS) to correlate the voltage and capacity fading with micro-structural defects of $Li_2Ru_{0.5}Mn_{0.5}O_3$*

In FY 2017, this project also completed the structure studies of Li2Ru0.5Mn0.5O3, as a model compound for Li and Mn rich (LMR) high energy density cathode materials using synchrotron-based x-ray diffraction (XRD) and absorption (XAS) to correlate the voltage and capacity fading with micro-structural defects in this type of materials. The prelithiated sample experiences more reduction. As shown in Figure II-305a. Figure II-305a indicates that transition metal cations in both "OCV-1V-(4.6V-2V)20Cy" sample and "OCV-(4.6V-2V)20Cy" sample experience reduction during cycling. This is true both for Mn and Ru as seen from the edges shifting to the lower energy in both Mn K-edge and Ru K-edge spectra. Oxygen release is not only exacerbated by the micro structural defects, but also promotes the formation of defects. Evidence comes from ex situ XRD studies shown in Figure II-305b. The figure is separated by a dash line in the middle. The upper part corresponds to the prelithiated case and the lower one to the normally cycled case. Compared with the normally cycled case, samples in the prelithiated case show much greater peak broadening and this broadening effect increases as the cycle number increases. Oxygen release and microstructural defects also accelerates spinel formation. This can be seen from Figure II-305c which gives the evolution of lattice parameter c to lattice parameter a ratio during cycling.

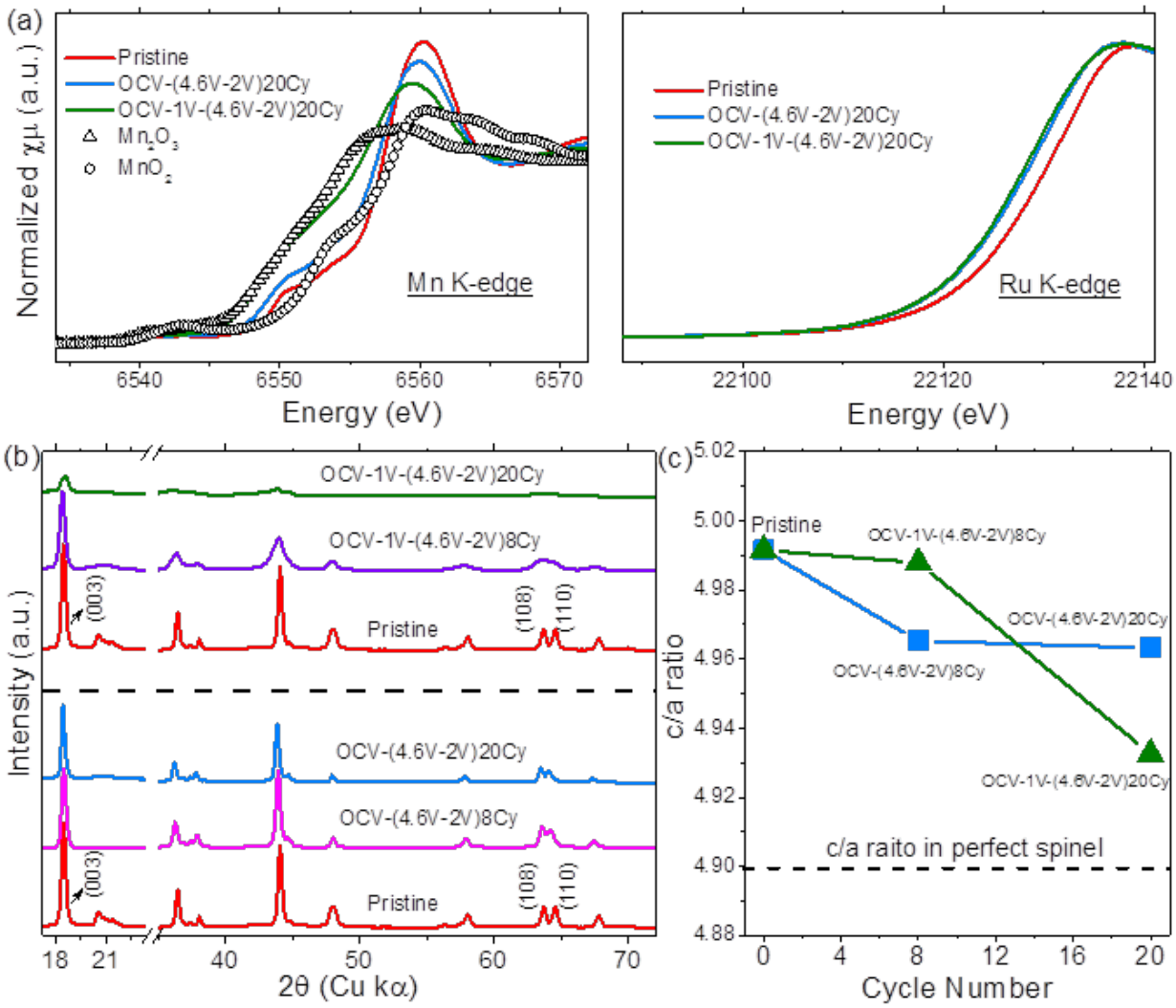


Figure II-305. (a) ex situ Mn K-edge and Ru K-edge XAS data of pristine $Li_2Ru_{0.5}Mn_{0.5}O_3$ sample, sample normally cycled 20 times and sample cycled 20 times but first prelithiated, with references of $Mn_2O_3$ and $MnO_2$ shown. (b) Ex situ XRD patterns of two cases (with (003), (108) and (110) peaks indexed according to the space group $R\bar{3}m$): pristine sample, cycled 8 times and cycled 20 times for the normally cycled case (the part below the dash line); pristine sample, cycled 8 times and cycled 20 times for the prelithiated case (the part above the dash line). (c) The ratio between lattice parameter c and lattice parameter a as a function of cycle numbers. The dash line shows the c/a ratio in perfect spinel.

*4. Using scanning transmission electron microscopic (STEM) to correlate the voltage and capacity fading with micro-structural defects of $Li_{1.2}Ni_{0.15}Co_{0.1}Mn_{0.55}O_2$*

In FY 2017, this project focused on the structure studies of $Li_{1.2}Ni_{0.15}Co_{0.1}Mn_{0.55}O_2$ for Li and Mn rich (LMR) high energy density cathode materials using scanning transmission electron microscopic (STEM) to correlate the voltage and capacity fading with micro-structural defects in this type of materials. To pinpoint the structure nucleation and evolution, we performed atomic-resolution annular dark-field scanning transmission electron microscopic (ADF-STEM) imaging, spatially resolved electron energy loss spectroscopy (EELS), and ADF-STEM tomography. Using ADF-STEM tomography, the 3D internal structures of the cathode material before and after 15 charge-discharge cycles were reconstructed. The 3D rendered reconstructions in Figure II-306 qualitatively shows that a new population of large pores had formed in the interior of the cycled particle after 15 cycles. By analyzing the pore size distributions (Figure II-306c and Figure II-306d), it can be quantitatively concluded that the large pores observed in Figure II-306b belongs to a new modal that did not appear in the

pristine samples. The volume weighted distribution shows that the large-pore modal contributes to the majority of porosity in the material. As the formation of the large pores are correlated with charge cycles, they are very likely formed by nucleating vacancies that had been left behind by oxygen loss, agreeing well with the "lattice densification" model.

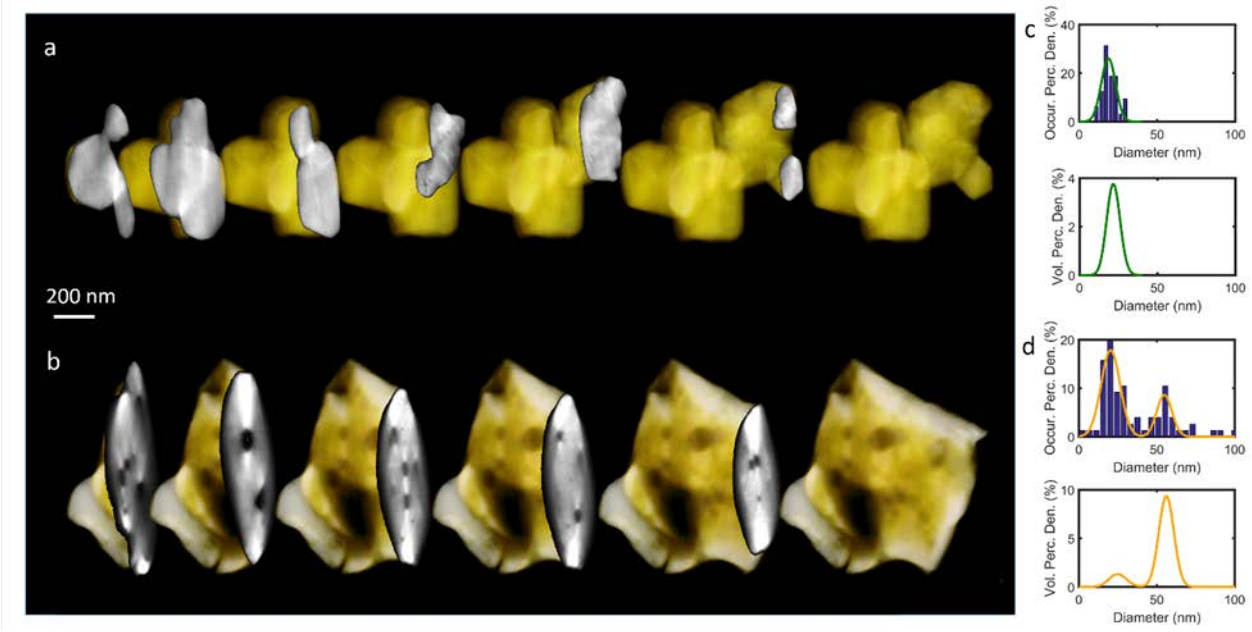


Figure II-306. Three-dimensional electron tomography reconstructions of (a) pristine, (b) after 15 charge-discharge cycles of $Li_{1.2}Ni_{0.15}Co_{0.1}Mn_{0.55}O_2$ material. The internal pore size distribution weighted by occurrence (upper) and by volume (lower) of (c) the pristine materials and (d) the sample after 15 cycles.

## Conclusions

The effects of micro structural defects on the voltage fade studied in this project can provide valuable guidance in finding the paths to suppress voltage fade in LMR materials. For some Li-ion battery cathode materials, small particle size is favored because the reduced lithium ion transport length can enhance the electrochemical reaction and high rate capability. A classic example is $LiFePO_4$, which has dramatic improvement in electrochemical performance when the crystallite size is small enough. Recent studies on $Li(Ni_{0.5}Mn_{0.3}Co_{0.2})O_2$ indicate that small particle size may also be beneficial for conventional layered materials. However, for LMR materials with the problem of oxygen loss at high voltage, the situation is quite different. In this project, using XRD, PDF, and TEM, the effects of accelerating oxygen loss by micro structural defects including grain boundaries are clearly demonstrated. Such effects are very likely to be caused by the increased surface area of materials with smaller particle size as well. Therefore, in order to suppress the voltage fade in LMR materials, it is necessary to (1) minimize the level of microstructural defects; (2) modify the surface of LMR materials with protection layer. There are recent examples of improving electrochemical performance, especially suppressing voltage fade, by applying surface modification using $Al_2O_3$, $AlF_3$ and even lithium-conducting materials like LiPON and $LiFePO_4$. The results of structural studies reported in this project provide important scientific base for using surface protection approaches such as coating to suppress the voltage fade in LMR materials.

## Key Publications


1. Yahong Xu, Enyuan Hu, Feifei Yang, Jeff Corbett, Zhihong Sun, Yingchun Lyue, Xiqian Yu, Yijin Liu, Xiao-Qing Yang, Hong Li, "Structural integrity—Searching the key factor to suppress the voltage fade of Li-rich layered cathode materials through 3D X-ray imaging and spectroscopy techniques", Nano Energy, Volume 28, October 2016, Pages 164–171, DOI: 10.1016/j.nanoen.2016.08.039

2. Jing Xu, Enyuan Hu, Dennis Nordlund, Apurva Mehta, Steven N. Ehrlich, Xiao-Qing Yang, Wei Tong*, "Understanding the Degradation Mechanism of Lithium Nickel Oxide Cathode for Li-ion Batteries", ACS Appl. Mater. And Interfaces, 2016, 8 (46), pp 31677–31683, Publication Date (Web): November 1, 2016. DOI: 10.1021/acsami.6b11111

3. Ji-Young Kim, Sang Hoon Kim, Dong Hyun Kim, Dieky Susanto, Se Young Kim, Won-Young Chang, Byung Won Cho, Won-Sub Yoon, Seong Min Bak, Xiao Qing Yang, Kyung Wan Nam*, Kyung Yoon Chung*, "Electronic structural studies on the improved thermal stability of $Li(Ni_{0.8}Co_{0.15}Al_{0.05})O_2$ by $ZrO_2$ coating for lithium ion batteries", Appl Electrochem (2017), First Online: 21 March 2017, DOI:10.1007/s10800-017-1062-5

4. Jue Liu, Pamela S Whitfield, Michael R Saccomanno, Shou-Hang Bo, Enyuan Hu, Xiqian Yu, Jianming Bai, Clare P Grey, Xiao-Qing Yang, Peter G Khalifah, "In situ Neutron Diffraction Studies of Ion Exchange Synthesis Mechanism of Li2Mg2P3O9N: Evidence for Hidden Phase Transition", J. Am. Chem. Soc., 2017, Publication date: 2017/7/6, DOI: 10.1021/jacs.7b02323

5. Feng Lin, Yijin Liu, Xiqian Yu, Lei Cheng, Andrej Singer, Oleg G Shpyrko, Huolin L Xin, Nobumichi Tamura, Chixia Tian, Tsu-Chien Weng, Xiao-Qing Yang, Ying Shirley Meng, Dennis Nordlund, Wanli Yang, and Marca M Doeff, "Synchrotron X-ray Analytical Techniques for Studying Materials Electrochemistry in Rechargeable Batteries", Chemical Review, Publication date (web): 2017/9/29, DOI: 10.1021/acs.chemrev.7b00007.

6. Feng Lin, Yijin Liu, Xiqian Yu, Lei Cheng, Andrej Singer, Oleg G Shpyrko, Huolin L Xin, Nobumichi Tamura, Chixia Tian, Tsu-Chien Weng, Xiao-Qing Yang, Ying Shirley Meng, Dennis Nordlund, Wanli Yang, and Marca M Doeff, "Synchrotron X-ray Analytical Techniques for Studying Materials Electrochemistry in Rechargeable Batteries", Chemical Review, Publication date (web): 2017/9/29, DOI: 10.1021/acs.chemrev.7b00007.

## II.D.3 NMR and Pulse Field Gradient Studies of SEI and Electrode Structure (University of Cambridge)

**Clare Grey, Principal Investigator**
Department of Chemistry
Lensfield Road
Cambridge, CB2 1EW
United Kingdom
Phone: +44(1223)336509
E-mail: cpg27@cam.ac.uk

**Tien Duong, Technology Manager**
U.S. Department of Energy
Phone: 202-586-7836
E-mail: Tien.Duong@ee.doe.gov

Start Date: October 1, 2016 End Date: September 30, 2017
Total Project Cost: $275,000 DOE share: $275,000 Non-DOE share: $0

### Project Introduction

The ability to cycle a battery for the multiple cycles requires that a stable solid electrolyte interphase (SEI) is formed on the electrodes of a Li-ion battery. Without such a stable SEI, breakdown of the electrolyte continues unhindered because a battery operates outside the stability of the electrolyte (below approx. 1.3 - 0.8 V vs. Li), leading to loss of electrolyte (and Li) from the cell, and thus, an increase in resistance of the cell. Although electrolytes have been optimized to form a stable SEI on graphite, the commercial anode material, the push to utilize very high energy density anodes such as Si, Sn and Li metal presents new challenges. For example, lithiation of Sn and Si involves significant volume expansion (e.g., 300% for Si), due to the large volume occupied by the lithium in the $Li_xSi$ and $Li_xSn$ alloys. During prolonged cycling, cracks develop, exposing fresh surface for continuous SEI growth. Practically, this means that the composite phase that makes up the SEI must be flexible and able to accommodate these expansions and contractions. Risk reduction strategies exploited to develop commercial Si/Sn-based anodes generally involve mixing graphitic carbon with Si/Sn, to make use of reversible capacity from both graphite and Si/Sn. In practice, this actually accentuates the SEI problem because the electrode must be cycled to low potentials so as to access the full graphite capacity. This results in even more severe SEI formation, either due to the formation of more heavily reduced $Li_xM$ species (e.g., $Li_{15+x}Si_4$) or due to more severe volume expansion, which may result in the exposure of fresh surface. Strategies for SEI stabilization have been proposed but without a detailed understanding of SEI structure and composition a rational path forward is not obvious.

In principle, Li metal is a promising anode material due to its exceptionally high energy density, with a specific capacity > 3800 mAh $g^{-1}$. Much effort has been made to use metallic Li anodes in rechargeable Li-ion batteries and its use is fundamental to the high energy densities quoted for Li-air and Li-sulfur battery technologies. However, the practical application of Li metal to rechargeable batteries has been prevented due to serious drawbacks associated with morphological changes of the Li metal following continuous stripping and plating. In particular, dendrite growth causes severe safety concerns and eventual cell failure. Continual SEI formation on the Li microstructures consumes $Li^+$. Furthermore, the nature and thickness of the SEI appears to affect the mechanism of microstructure formation on the Li metal anode. Thus, it is important to understand the nature of the SEI that forms on Li and to determine how this affects dendrite formation.

In addition, Na-ion batteries are an attractive option for low-cost and environmentally benign energy-storage technologies. While a number of Na cathode materials have now been identified [1-2], hard carbons represent the best materials identified to date as anode materials [3-4] since graphite shows almost no ability to store Na

electrochemically. Extremely high capacity is also observed for Sn-based materials, but they suffer from capacity fade, in part due to uncontrolled SEI formation. Furthermore, the composition of the SEI that forms on these anodes is poorly understood. Na-ion batteries are a more sustainable alternative to the existing Li-ion technology and could alleviate some of the stress on the global Li market as a result of the growing electric car and portable electronics industries. Overall, fundamental research focused on understanding the structural and electronic processes occurring on electrochemical cycling is key to devising rechargeable batteries with improved performance. The major technique used in this work is NMR and our surface (SEI) studies are complemented by studies that focus on elucidating the short range structural changes that occur within the electrodes themselves.

## Objectives

Here, we will use spectroscopic tools, such as multinuclear nuclear magnetic resonance (NMR) to provide molecular-level insight into the SEI that forms on Si, where thick SEIs typically grow and where SEI stability is one key aspect hindering the commercialization of this technology. The focus during this grant period will be to determine how additives (e.g., fluoroethylene carbonate (FEC)) and charging parameters (e.g., voltage) influence the composition and stability of the SEI. Fundamental studies of SEI structure *in operando* will be complemented by a synthetic program aimed at preparing new Si coatings based on phosphazene (P-N) elastomeric polymers to increase Coulombic efficiency. Further, the nature of the SEI is one factor that appears to control the type of Li/Na microstructures that form on the metal electrodes during cycling. To test this hypothesis, we will use magnetic resonance imaging (MRI) to investigate Li dendrite vs. moss formation in different electrolytes as a function of salt concentration and with different additives. Finally, we will compare Li and Na metal anode chemistries to determine the composition, morphology, and stability of local structures that form on sodiating anodes such as Sn and hard carbons.

## Approach

Perform multinuclear NMR, IR and X-ray photoelectron spectroscopy (XPS) of SEI composition. NMR and MRI studies of dendrite formation. $^{23}$Na *in-* and *ex-situ* NMR studies of Na battery materials.

## Results

### *Substitution in layered Na cathode materials*

We have investigated a series of different layered Na cathode materials to understand how cation substitution of nominally inert ions such as Mg and Li affect the structural transformations that occur at high voltages (when most Na ions are removed), and how Na mobility is altered in these phases. An in-depth investigation of the effect of Mg doping on the electrochemical performance and structural stability of $Na_{2/3}MnO_2$ with a P2 layer stacking was performed by comparing three compositions: $Na_{2/3}Mn_{1-y}Mg_yO_2$ where y = 0.0, 0.05, 0.1. Mg substitution leads to smoother electrochemistry, with fewer distinct electrochemical processes, improved rate performance and better capacity retention (Figure II-307). The improved electrochemistry upon Mg substitution was attributed to more gradual structural changes upon charge and discharge, as observed with synchrotron, powder X-ray, and neutron diffraction. Mg doping reduces the number of $Mn^{3+}$ Jahn-Teller centers and delays the high voltage phase transition that occurs in P2-$Na_{2/3}MnO_2$. The $^{23}$Na ssNMR data provides direct evidence for fewer oxygen layer shearing events, leading to a stabilized P2 phase, and an enhanced $Na^+$ ion mobility up to 3.8 V vs. $Na^+$/Na upon Mg doping. By comparing the $^{23}$Na NMR spectra of the x = 0, 0.05 and 0.1 phases (Figure II-308), less spectral complexity was noted, with fewer resonances observed on Mg substitution. For example, the y = 0.10 sample, contains only a single $^{23}$Na resonance for Na contents of between 0.67 and 0.4, consistent with rapid $Na^+$ mobility in between the layers. A weak signal centered at around 1100 ppm forms due to the OP4 phase, which contains alternating octahedral and prismatic environments for Na in the Na metal layers. The relative concentration of this phase (which is formed by layer shearing) decreases with increasing Mg content. The y = 0.05 Mg-doped phase exhibits one of the best rate performances reported to date for Na-ion cathodes with a P2 structure, with a reversible capacity of 106 mAh $g^{-1}$ at the very high discharge rate of 5000 mA $g^{-1}$. In addition, its structure is highly reversible and stable

cycling is obtained between 1.5 and 4.0 V vs. $Na^+/Na$, with a capacity of approximately 140 mAh $g^{-1}$ retained after 50 cycles at a rate of 1000 mA $g^{-1}$.

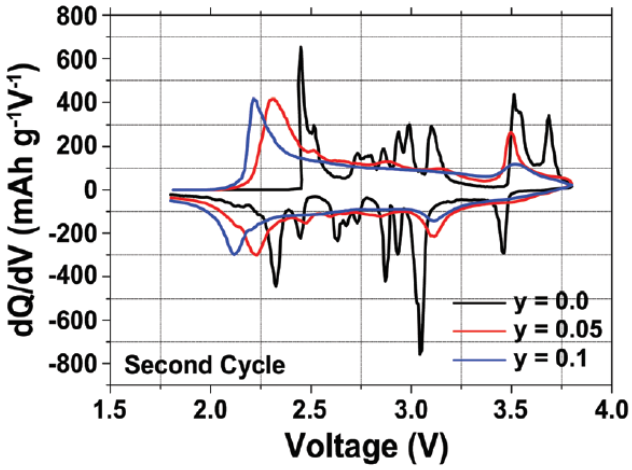


Figure II-307. Differential capacity vs. voltage plots of the $Na_{2/3}Mn_{1-y}Mg_yO_2$ (y = 0.0, 0.05, 0.1) compositions.

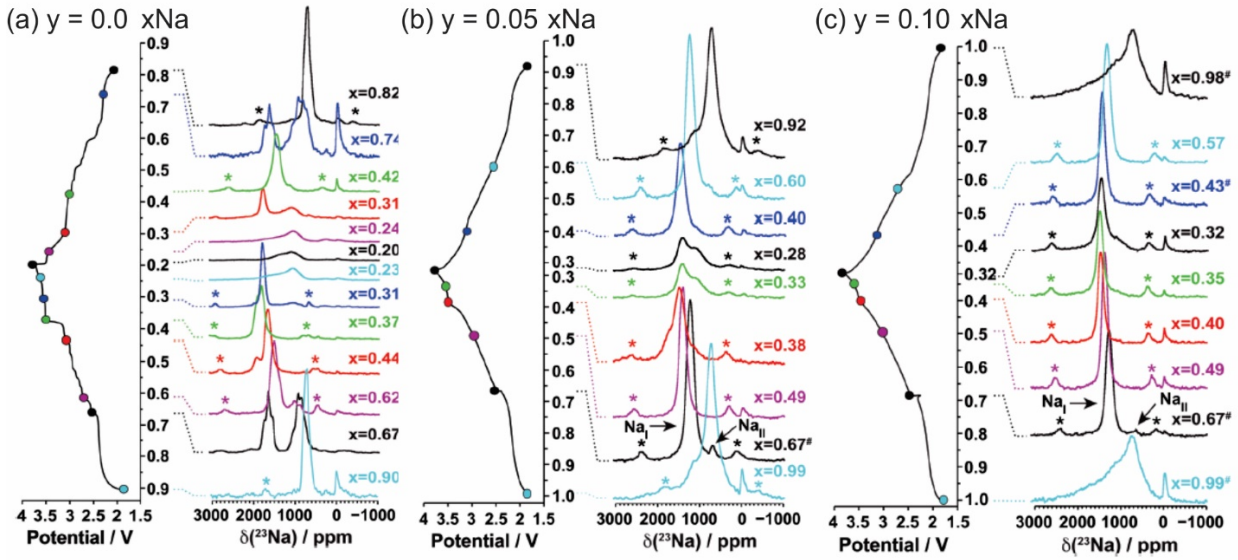


Figure II-308. Ex-situ $^{23}Na$ MAS ssNMR spectra collected on cells stopped at different points along the first electrochemical charge/discharge cycle of $Na_{2/3}Mn_{1-y}Mg_yO_2$, where y = 0.0, 0.05, 0.1 for (a), (b), and (c), respectively. Spectra are scaled according to the number of scans collected during the experiment, the amount of sample in the rotor, and the NMR signal decay obtained from $T_2$ relaxation time measurements. Hashes indicate samples for which a lack of experimental data prevent proper scaling of the spectrum. Asterisks indicate spinning sidebands.

This study has been complemented by $^{23}Na$ NMR investigations of local structure and electrochemistry of P2-$Na_x[Li_yNi_zMn_{1-y-z}]O_2$ (x,y,z ≤ 1); direct evidence for rapid $Na^+$ mobility in these phases was obtained.

*Na dendrite growth*

*In situ* $^{23}Na$ NMR studies have been performed on the Na dendrites that form on Na metal anodes to complement previous work on Li microstructural growth in the group [5-7]. Quantification of the $^{23}Na$ NMR signal during electrochemical cycling indicates that Na metal deposits with a morphology associated with an

extremely high surface area (Figure II-309a), and that the deposits continuously accumulate, even in the case of galvanostatic cycling at low currents (e.g., 0.5 mA $cm^{-2}$, Figure II-309c orange).

Two distinct regimes for the electrochemical cycling of Na metal are observed that have implications for the application of Na anodes. At low currents (0.5 mA $cm^{-2}$), the Na deposits are partially removed upon reversing the current (Figure II-309b, c, orange), while at higher currents (1 and 2 mA $cm^{-2}$) there is essentially no removal of the deposits in the initial stages (Figure II-309b, c, blue and black, respectively). At longer times, high currents show a significantly greater accumulation of deposits during cycling, again indicating a much lower efficiency of removal of these structures when the current is reversed. Analysis of the current–time transients performed in a separate experiment were interpreted in terms of a change in the mechanism of nucleation from a progressive (time dependent) nucleation mechanism at the overpotentials observed for the lower current density of 0.5 mA $cm^{-2}$ to instantaneous at higher currents. For instance, the fraction of high surface area Na metal deposits measured with NMR compared to the accumulated mass calculated from Faraday's law revealed that at low currents, smooth deposition and stripping occurs, while at high currents, rough deposition and less efficient removal is present (Figure II-309d). We proposed that the different and fewer microstructures that are formed at lower currents are more readily removed on cycling.

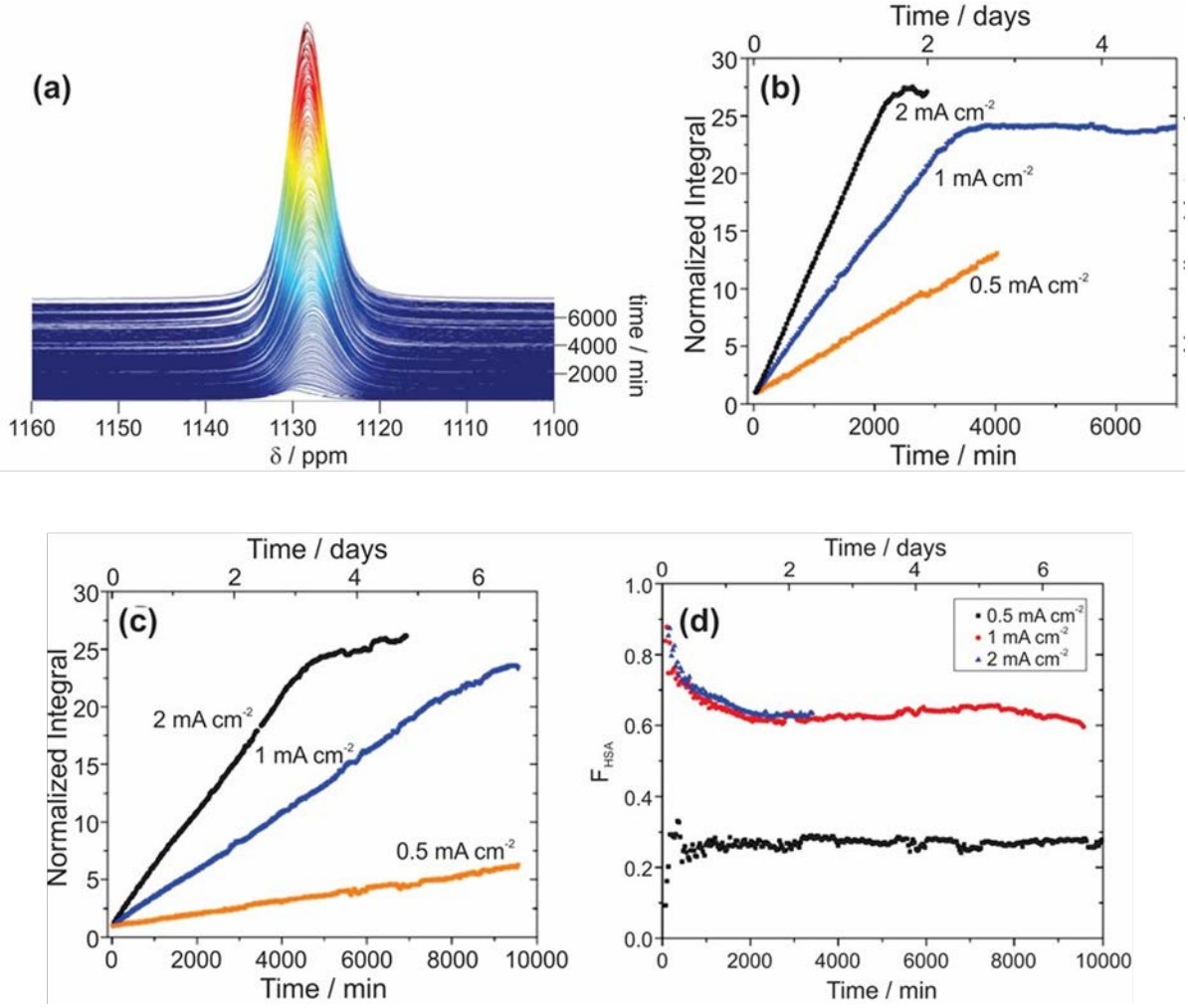


Figure II-309. (a) $^{23}Na$ NMR spectra as a function of time during galvanostatic cycling at 2 mA $cm^{-2}$, showing high surface area Na metal deposits growing in. (b,c) Integral of the normalized $^{23}Na$ metal resonance for (b) continuous galvantostatic deposition and (c) galvanostatic cycling at three different current densitites. (d) Fraction of high surface area ($F_{HSA}$) Na during galvanostatic cycling at various current densities. A ratio of 1 indicates completely rough deposition and 0 indicates smooth deposition.

Unfortunately, despite differences in the nucleation and growth processes, both mechanisms yield microstructures that continue to grow as cycling progresses. Overall, dendrite formation appears to be more severe for Na metal anodes in comparison to Li metal anodes, with significant dendrite/microstructure formation occurring at low current densities, as probed by *in situ* $^{23}$Na NMR experiments. However, the microstructures that form at low currents can be partially removed on reversing the current, which is not the case for the dendrites formed at higher currents. Differences in the mechanisms of nucleation of dendrites may account for some of these differences. Further investigation into the role of SEI in both Na and Li dendrite formation will be key to elucidating the physical origin underpinning the differences observed between these two systems.

### Sn anodes for Na-ion batteries

The goal of this study was to understand the phases formed during Na insertion in high capacity Sn anodes for Na-ion batteries. *Ab initio* random structure searching (AIRSS) and high-throughput screening using a species-swap method allowed us to explore the phase chemistry of the Na-Sn system and predict new structures. These structures were linked to experiments using *operando* pair distribution function (PDF) analysis, X-ray diffraction (XRD), $^{23}$Na solid-state nuclear magnetic resonance (ssNMR), and *ex situ* $^{119}$Sn ssNMR. Here, we identified: (i) the number and nature of the crystalline phase(s) formed during the first electrochemical process; (ii) the structural features of the amorphous phase formed during the second electrochemical process; and (iii) the phase formed during the third process.

Figure II-310a shows electrochemical data for a Na-Sn cell compared to theoretical predictions. From *operando* PDF and ssNMR (Figure II-310b-d), XRD measurements and theoretical calculations, we proposed the following discharge mechanism for the Na-Sn system:

- Process 1: Sn → $NaSn_3$
- Process 1′: Sn, $NaSn_3$ → $NaSn_2$
- Process 2: $NaSn_2$ → *a*-$Na_{1.2}Sn$
- Process 2′: *a*-$Na_{1.2}Sn$ + $NaSn_2$ → *a*-$Na_{1.2}Sn$ + expanded $Na_{1+x}Sn_2$ (solid solution)
- Process 3: *a*-$Na_{1.2}Sn$ + expanded $Na_{1+x}Sn_2$ → $Na_{4.4}Sn_2$
- Process 3′: $Na_{4.4}Sn_2$ → $Na_{4.75}Sn_2$ (solid solution)
- Process 4: $Na_{4.75}Sn_2$ → $Na_{15}Sn_4$
- Process 4′: $Na_{15}Sn_4$ → $Na_{15+x}Sn_4$

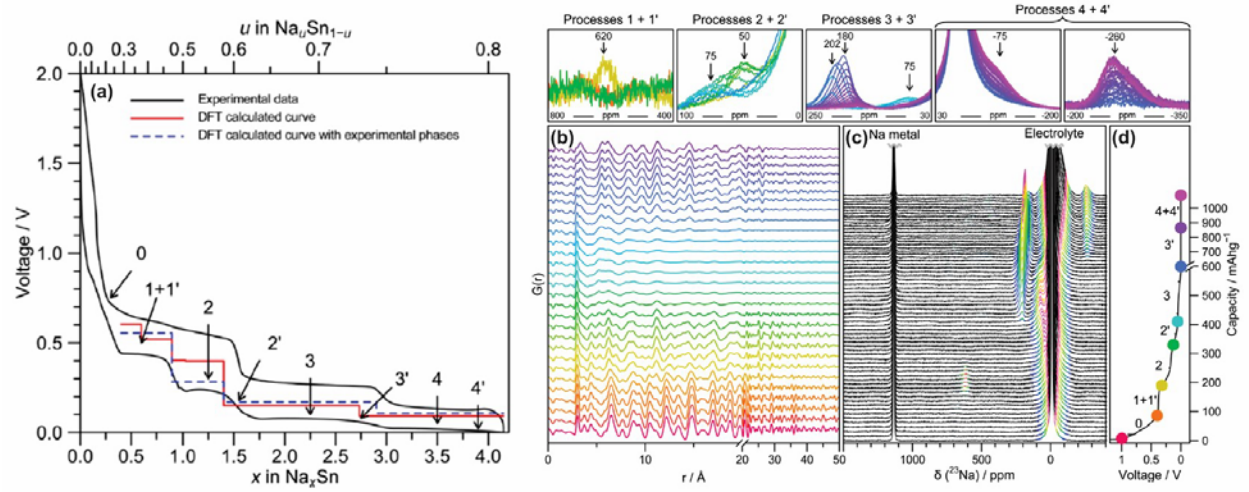


Figure II-310. (a) Experimental (black) electrochemistry of a Na-Sn cell cycled at C/20 between 2 and 0.001 V compared to theoretical (red/blue) predictions. (b) Operando PDFs and (c) $^{23}$Na NMR spectra for Na-Sn cells aligned with the corresponding electrochemistry (d).

The first electrochemical process of Na insertion into Sn results in the conversion of crystalline Sn into a layered structure consisting of mixed Na/Sn occupancy sites intercalated between planar hexagonal layers of Sn atoms ($NaSn_3$, Figure II-311, left panel). Following this, $NaSn_2$, which is predicted to be thermodynamically stable, forms. $NaSn_2$ contains hexagonal layers closely related to $NaSn_3$, but has no Sn atoms between the layers. In Process 2, $NaSn_2$ is broken down into an amorphous phase of approximate composition $Na_{1.2}Sn$, which is predicted to exhibit Sn chains. *Operando* ssNMR and PDF refinements show evidence that further reaction with Na results in the formation of structures containing Sn-Sn dumbbells, which interconvert through a solid-solution mechanism in Process 3'. These structures are based upon $Na_{5-x}Sn_2$, with increasing occupancy of one of its Na sites commensurate with the amount of Na added Figure II-311b, right panel). Finally, ssNMR results indicate that the final product, $Na_{15}Sn_4$, can store additional Na atoms as an off-stoichiometry compound, $Na_{15+x}Sn_4$, analogous to previous observations in the Li-Si system. Taken together, this work provides the first evidence for significant solid solution behavior and resulting metastability in the Na-Sn system. These findings have further implications beyond the Na-Sn system, highlighting the fact that even a system under apparent thermodynamic control, the nature of electrochemical alloying means that kinetic considerations remain of primary importance.

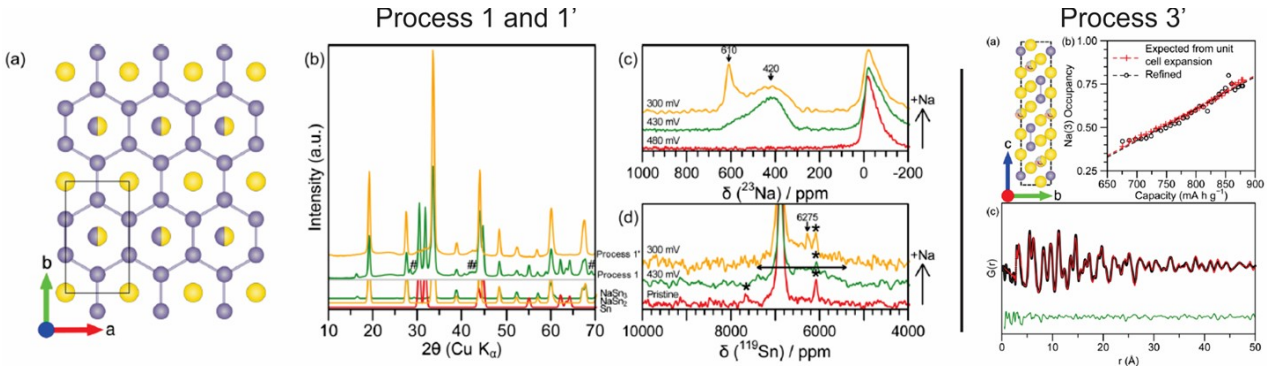


Figure II-311. Left panel: (a) Structure of $NaSn_3$-Pmmm with Na in yellow and Sn in purple (b) operando XRD patterns (c) ex situ $^{23}Na$ and (d) $^{119}Sn$ 60 kHz MAS NMR at the end of process 1 and 1'. Right panel: (a) Structure of $Na_{5-x}Sn_2$ (b) occupancy vs Na site 3 vs time spent on process 3' (c) fit of the PDF corresponding to the first frame in process 3'.

### *SEI on Si anodes for Li-ion batteries*

The primary aim of this study was to understand how the electrolyte additive fluoroethylene carbonate (FEC) enhances the stability of the SEI formed on Si anodes. The organic species formed on Si nanowires (SiNWs) in both the standard carbonate-only electrolyte (LP30) as well as LP30 with 10% FEC were characterized with solution and solid-state NMR techniques, including dynamic nuclear polarization (DNP). SiNWs were used here as model systems, since they can be prepared as binder-free anodes that cycle for multiple cycles without losing electrical contact.

After long-term cycling, $^{1}H$ solution NMR shows that LP30 decomposes and forms a variety of soluble oligomers in addition to the transient formation of lithium ethylene decarbonate (LEDC, yellow shading, Figure II-312a). Addition of 10 vol% FEC into the electrolyte suppresses the decomposition of EC/DMC (Figure II-312b,c), that is correlated with an increased Coulombic efficiency in the electrochemical cycling data after the first few cycles. To facilitate a more in-depth characterization of the electrolyte products in the presence of FEC via 1D and 2D NMR (e.g., $^{13}C$-$^{13}C$ COSY, $^{1}H$-$^{13}C$ HMBC, $^{1}H$-$^{13}C$ HSQC to assign red shaded peaks x, y, and z), $^{13}C$-enriched FEC was synthesized, which ultimately allowed a detailed structural assignment of the organic SEI. The $^{1}H$ and $^{13}C$ NMR spectra provide compelling evidence for the defluorination of FEC to form soluble vinoxyl species ($HCOCH_2OR$) and VC. The formation of VC, rather than LVDC, was unambiguously determined, the assignment being based on the *J*-coupling pattern that arises from the uniform $^{13}C$ labelling of FEC and the subsequent breakdown products (Figure II-313).

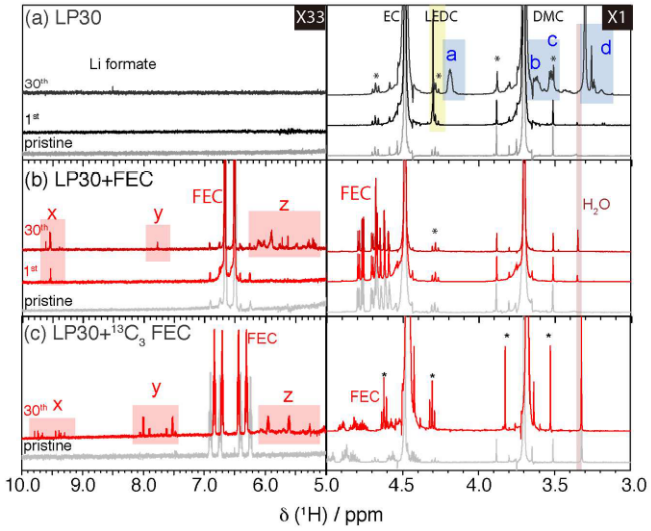


Figure II-312. $^{1}H$ solution NMR of (a) LP30, (b) LP30 + FEC, and (c) LP30 + 10 vol% $^{13}C_3$-FEC before cycling (pristine), and after the 1st and 30th cycles. $^{13}C$ satellites are marked with an asterisk.

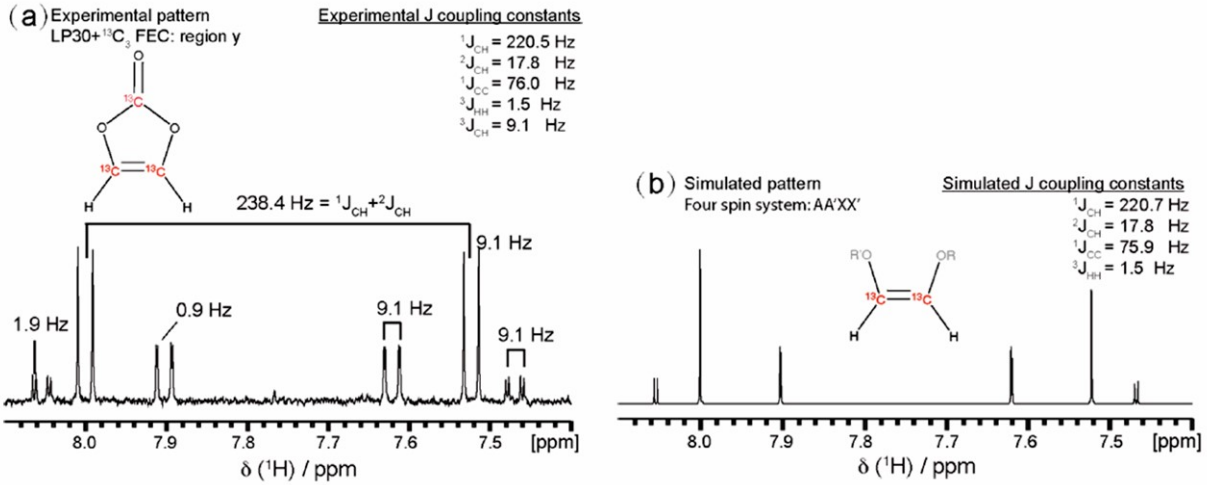


Figure II-313. Multiplet pattern of LP30 + $^{13}C_3$-FEC in region y of an earlier Figure, (a) experimental pattern; (b) simulated pattern of a four-spin system AA'XX' (cis-H-CR=CR-H).

Oligomers with characteristic peaks due to protonated carbons bonded to two adjacent oxygen groups from cross-linking units were also identified. These oligomeric precursors presumably react further to form insoluble polymeric species in the SEI, with similar cross-linking groups (Figure II-314b, peak at 103 ppm). Neither these cross-linking units nor the vinoxyl species are observed in the absence of the FEC additive (Figure II-314a). The vinoxyl species are signatures for the formation of the vinoxyl radicals that are believed to initiate the polymerization that eventually results in a highly cross-linked network. We hypothesize that highly cross-linked polymeric networks are key to the increased stability of SEI formed on Si that is observed the presence of FEC, motivating studies with additives that may promote cross-linking. Further insight into the molecular nature of the SEI and the parameters that impart stability offer the opportunity to tailor the SEI chemistry to maximize performance in LIBs.

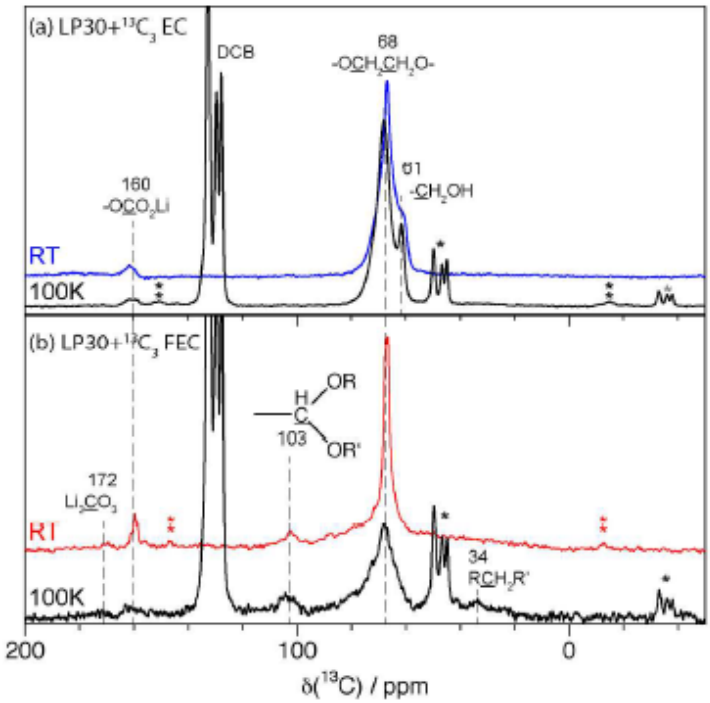


Figure II-314. $^{1}H$-$^{13}C$ cross-polarization (CP) NMR spectra of SiNWs after 30 cycles in (a) LP30 + 25 vol% $^{13}C_3$-EC and (b) LP30 + 10 vol% $^{13}C_3$-FEC electrolytes. The room temperature (RT) spectra were measured by conventional ssNMR, whereas the 100 K spectra were measured with DNP NMR. The DCB was used as the radical solvent for DNP.

## Conclusions

In the first project, we determined how cation substitution of nominally inert ions such as Mg and Li affect the structural transformations and ion mobility in a series of layered Na cathode materials (P2-$Na_{2/3}Mn_{1-y}Mg_yO_2$ ($y$ = 0.0, 0.05, 0.1) at high voltages. We show that Mg substitution leads to smoother electrochemistry, with fewer distinct electrochemical processes, improved rate performance and better capacity retention. These observations are attributed to the more gradual structural changes upon charge and discharge, as observed with synchrotron, powder X-ray, neutron diffraction, and $^{23}Na$ ssNMR. Mg doping reduces the number of $Mn^{3+}$ Jahn–Teller centers and delays the high voltage phase transition occurring in P2-$Na_{2/3}MnO_2$. This study has been complemented by $^{23}Na$ NMR investigations of local structure and electrochemistry of P2-$Na_x[Li_yNi_zMn_{1-y-z}]O_2$ (x,y,z ≤ 1), in which direct evidence for rapid $Na^+$ mobility was observed. The electrochemical performance of the P2-$Na_{2/3}Mn_{1-y}Mg_yO_2$ ($y$ = 0.05) cathode is exceptional, with the material exhibiting very stable electrochemistry upon extended cycling and one of the highest rate performance observed to date for this class of materials.

In a separate project, we performed *in situ* $^{23}Na$ NMR experiments to quantify the high surface area Na metal deposits that form in Na-Na symmetrical cells for comparison to Li dendrite growth. We found that the Na deposits continuously accumulate, even in the case of galvanostatic cycling at low currents (e.g., 0.5 mA cm$^{-2}$). Two regimes for the electrochemical cycling of Na metal are apparent that have implications for the use of Na anodes: at low currents, the Na deposits are partially removed on reversing the current, while at high currents, there is essentially no removal of the deposits in the initial stages. At longer times, high currents show a significantly greater accumulation of deposits during cycling, again indicating a much lower efficiency of removal of these structures when the current is reversed. In general, dendrite formation appears to be more severe for Na metal anodes in comparison to Li metal anodes. We anticipate that differences in the nature of the SEI formed on Na and Li surfaces will be key to elucidating the physical origin of dendrite growth in these systems.

Sn represents a possible anode material in a sodium ion battery with a noticeably higher capacity than a hard carbon. A combination of *ab initio* calculations, *operando* PDF analysis, XRD, $^{23}$Na solid-state nuclear magnetic resonance (ssNMR), and *ex situ* $^{119}$Sn ssNMR was used to identify: (i) the number and nature of the crystalline phase(s) formed during the first electrochemical process; (ii) the structural features of the amorphous phase formed during the second electrochemical process; and (iii) the phase formed during the third process. The first electrochemical process of Na insertion into Sn results in the conversion of crystalline tin into a layered structure consisting of mixed Na/Sn occupancy sites intercalated between planar hexagonal layers of Sn atoms (approximate stoichiometry $NaSn_3$). Following this, $NaSn_2$, which is predicted to be thermodynamically stable by AIRSS, forms; this contains hexagonal layers closely related to $NaSn_3$, but has no tin atoms between the layers. $NaSn_2$ is broken down into an amorphous phase of approximate composition $Na_{1.2}Sn$. Reverse Monte Carlo refinements of an *ab initio* molecular dynamics model of this phase show that the predominant tin connectivity is chains. Further reaction with sodium results in the formation of structures containing Sn–Sn dumbbells, which interconvert through a solid-solution mechanism. These structures are based upon $Na_{5-x}Sn_2$, with increasing occupancy of one of its sodium sites commensurate with the amount of sodium added. ssNMR results indicate that the final product, $Na_{15}Sn_4$, can store additional sodium atoms as an off-stoichiometry compound ($Na_{15+x}Sn_4$) in a manner similar to $Li_{15}Si_4$. The first evidence for significant solid solution behavior and resulting metastability in the sodium−tin system is presented. Overall, this study demonstrates the importance of a complementary suite of characterization techniques to probe both short- and long-range structures, along with a detailed theoretical underpinning of model structures, to comprehensively understand the mechanism of sodium insertion. In addition, our results imply that even in systems under apparent thermodynamic control, the nature of electrochemical alloying means that kinetic considerations are vital.

Finally, to understand how additives influence SEI composition and stability on Si anodes in Li-ion batteries, we performed a detailed electrochemical and multinuclear NMR study. We find that the soluble poly(ethylene oxide)-like linear oligomeric electrolyte breakdown products that are observed after cycling in the standard ethylene carbonate-based electrolyte are suppressed in the presence of 10 vol% FEC additive. FEC is first defluorinated to form soluble vinylene carbonate and vinoxyl species, which react to form both soluble and insoluble branched ethylene-oxide-based polymers. No evidence for branched polymers is observed in the absence of FEC. We speculate that the formation of cross-linked polymers is key to the higher stability of SEI formed on Si in the presence of FEC, motivating studies with additives that promote cross-linking to tailor the SEI chemistry for enhanced performance in Li-ion batteries.

## Key Publications


1. R.J. Clément, D. S. Middlemiss, I. D. Seymour, A. J. Ilott, C. P. Grey, “Insights into the Nature and Evolution upon Electrochemical Cycling of Planar Defects in the beta-$NaMnO_2$ Na-Ion Battery Cathode: An NMR and First-Principles Density Functional Theory Approach” *Chem. Mater.*, **2016**, *28*, 8228.

2. A. J. Ilott, M. Mohammadi, H. J. Chang, C. P. Grey, A. Jerschow “Real-time 3D imaging of microstructure growth in battery cells using indirect MRI” *Proc. Nat. Ac. Sci. USA*, **2016**, *113*, 10779.

3. R.J. Clément, J. Billaud, A.R. Armstrong, G. Singh, T. Rojo, P.G. Bruce, C.P. Grey “Structurally stable Mg-doped P2-$Na_{2/3}Mn_{1-y}Mg_yO_2$ sodium-ion battery cathodes with high rate performance: insights from electrochemical, NMR and diffraction studies” *Energy Environ. Sci.*, **2016,** *9*, 3240.

4. A.L. Michan, B.S. Parimalam, M. Leskes, R.N. Kerber, T. Yoon, C.P. Grey, B.L. Lucht “Fluoroethylene carbonate and vinylene carbonate reduction: Understanding lithium-ion battery electrolyte additives and solid electrolyte interphase formation” *Chem. Mater.*, **2016**, *28*, 8149.

5. Clément, R. J.; Xu, J.; Middlemiss, D. S.; Alvarado, J.; Ma, C.; Meng, Y. S.; Grey, C. P. "Direct evidence for high $Na^+$ mobility and high voltage structural processes in P2-$Na_x[Li_yNi_zMn_{1-y-z}]O_2$ (x,y,z ≤ 1) cathodes from solid-state NMR and DFT calculations" *J. Mater. Chem. A*, **2017**, *5*, 4129.

6. Dally, R.; Clément, R. J.; Chisnell, R.; Taylor, S.; Butala, M.; Doan-Nguyen, V.; Balasubramanian, M.; Lynn, J. W.; Grey, C. P.; Wilson, S. D. "Floating zone growth of $\alpha$-$Na_{0.90}MnO_2$ single crystals" *J. Cryst. Growth*, **2017**, *459*, 203.

7. Ma, C.; Alvarado, J.; Xu, J.; Clément, R. J.; Kodur, M.; Tong, W.; Grey, C. P.; Meng, Y. S. "Exploring oxygen activity in the high energy P2-type $Na_{0.78}Ni_{0.23}Mn_{0.69}O_2$ cathode material for Na-ion batteries" *J. Am. Chem. Soc.*, **2017**, *139*, 4835.

8. Stratford, J. M.; Mayo, M.; Allan, P. K.; Pecher, O.; Borkiewicz, O. J.; Wiaderek, K. M.; Chapman, K. W.; Pickard, C. J.; Morris, A. J.; Grey, C. P. "Investigating Sodium Storage Mechanisms in Tin Anodes: A Combined Pair Distribution Function Analysis, Density Functional Theory, and Solid-State NMR Approach" *J. Am. Chem. Soc.*, **2017**, *139*, 7273.

9. Pell, A. J.; Sanders, K. J.; Wegner, S.; Pintcuda, G.; Grey, C.P., "Low-power broadband solid state MAS NMR of N-14", *J. Chem. Phys.*, **2017**, *146*, 194202.

10. Jin, Y.; Kneusels, N.-J. H.; Magusin, P. C. M. M.; Kim, G.; Castillo-Martinez, E.; Marbella, L. E.; Kerber, R. N.; Howe, D. J.; Paul, S.; Liu, T.; Grey, C. P. "Identifying the Structural Basis for the Increased Stability of the Solid Electrolyte Interphase Formed on Silicon with the Additive Fluoroethylene Carbonate" *J. Am. Chem. Soc.*, **2017**, *139*, 14992.

## References

1. Clément, R. J.; Bruce, P. G.; Grey, C. P., *J. Electrochem. Soc.* **2015,** *162*, A2589.

2. Yabuuchi, N.; Kubota, K.; Dahbi, M.; Komaba, S., *Chem. Rev.* **2014,** *114*, 11636.

3. Irisarri, E.; Ponrouch, A.; Palacin, M. R., *J. Electrochem. Soc.* **2015,** *162*, A2476.

4. Stevens, D. A.; Dahn, J. R., *J. Electrochem. Soc.* **2000,** *147*, 1271.

5. Chandrashekar, S.; Trease, N. M.; Chang, H. J.; Du, L.-S.; Grey, C. P.; Jerschow, A., *Nat. Mater.* **2012,** *11*, 311.

6. Chang, H. J.; Ilott, A. J.; Trease, N. M.; Mohammadi, M.; Jerschow, A.; Grey, C. P., *J. Am. Chem. Soc.* **2015,** *137*, 15209.

7. Ilott, A. J.; Mohammadi, M.; Chang, H. J.; Grey, C. P.; Jerschow, A., *Proc. Natl. Acad. Sci.* **2016,** *113*, 10779.

## II.D.4 Advanced Microscopy and Spectroscopy for Probing and Optimizing Electrode-Electrolyte Interphases in High Energy Lithium Batteries (UCSD)

**Ying Shirley Meng, Principal Investigator**
University of California San Diego
9500 Gilman Drive
La Jolla, CA 92093
Phone: 858-822-4247; Fax: 858-534-9553
E-mail: shmeng@ucsd.edu

**Tien Duong, Technology Manager**
U.S. Department of Energy
Phone: 202-586-7836
E-mail: Tien.Duong@ee.doe.gov

Start Date: April 1, 2017 End Date: March 31, 2021
Total Project Cost: $360,000 DOE share: $360,000 Non-DOE share: $0

### Project Introduction

The energy density and cycling life of state-of-the-art LIBs have to be further improved to meet the performance requirements for transportation applications. However, the relatively low capacity of cathode has become one of the major bottlenecks to achieve higher energy density in LIBs. In principle, the capacity of classical layered transition metal (TM) oxides, the primary commercial cathode materials, is limited to cationic redox activity. Anionic redox has thus emerged as a new paradigm for designing novel cathodes for next generation LIBs. It is recently found and confirmed oxygen redox in lithium-rich layered oxides with composition $xLi_2MnO_3 \cdot (1-x)LiTMO_2$, which enables this group of materials exhibit reversible capacities exceeding 280 mAh $g^{-1}$. Despite its high capacities, this material has several challenges (voltage fading, structural instability, sluggish kinetics, cathode electrolyte interphase instability, etc.) that must be overcome in order to reach commercialization. When the material is charged over TM redox reaction region (above 4.4 V for most of Li-rich material), lattice oxygen removal result in oxygen vacancies formation on the surface, which further triggers surface phase transformation from layered to spinel-like phase. This irreversible phase transformation finally results in voltage degradation and lower Li mobility during extended cycles. By carefully controlling the oxygen activities through the creation of uniform oxygen vacancies, we were able to avoid structural decomposition in Li-excess layered oxides. The modified materials deliver a discharge capacity as high as 306 mAh $g^{-1}$ with an initial coulombic efficiency of 90.6%. Furthermore, they do not exhibit obvious capacity decay, with low voltage degradation and a reversible capacity over 300 mAh $g^{-1}$ after 100 cycles at 0.1 C-rate. Our approach demonstrates the critical needs for advanced diagnosis and characterization. It is through the in-depth understanding of these high voltage cathode materials at atomistic and molecular level and their dynamic changes during the operation of batteries; strategies can be successfully formulated to optimize this class of cathode materials. Although various characterization techniques have been developed in the Li battery research field, some of them fail to properly characterize Li metal because the intrinsic high chemical reactivity and low thermal stability make it difficult to handle the sample without damaging or contaminating. This is evident when observing Li metal by conventional transmission electron microscopy (TEM), with which severe beam damage occurs after short exposure time less then 10s of seconds. The diagnostic tools developed here can also be leveraged to study anode materials such as Li metal anode. We have to apply cryogenic method (low-temperature) and low-dose electron microscopy with specialized camera to enable the reliable and consistent characterization of the lithium metal anode.

## Objectives

The proposed research aims to develop advanced microscopy and spectroscopy tools to probe, understand, and optimize the anion activities that govern the performance limitations such as capacity and voltage stabilities in high energy Li-excess TM (Ni,Co,Mn, etc.) oxides cathode materials. Our approach uniquely combines atomic resolution scanning transmission electron microscopy (STEM), electron energy loss spectroscopy (EELS), operando Bragg Coherent Diffraction Imaging (BCDI), and first principles computation to probe anion redox and oxygen evolutions in Li-excess NMC materials. Furthermore, we will track the lithium and oxygen dynamics under electrochemical testing via operando neutron diffraction which will enhance the understanding of the overall structural changes due to anion activities. Ultimately, this will hone in on the synthesis efforts to produce the modified materials with the optimum bulk compositions and surface characteristics at large scale for consistently good performance. The above-mentioned characterization tools will be extended to diagnose various anode types, such as Li metal anode.

## Approach

This unique approach combines STEM/EELS, operando BCDI, X-ray photoelectron spectroscopy and Ab initio computation as diagnostic tools for probing anion redox and oxygen evolutions in Li-excess NMC materials. This allows for pinning down the atomistic/molecular mechanism of anion oxidation and determining the speciation compositions and surface characteristics for enabling high rate and long life in the proposed materials. Neutron enables the characterization of bulk material properties to enhance and further optimize high energy electrode materials. We also develop novel cryogenic focus-ion-beam and electron microscopy to characterize lithium metal anode. This work funds collaborations on EELS (Miaofang Chi, Oakridge National Lab); neutron diffraction (Ke An, ORNL); soft XAS (Marca Doeff, Lawrence Berkeley National Laboratory). It supports collaborative work with Zhaoping Liu and Yonggao Xia at Ningbo Institute of Materials Technology and Engineering China. It also supports collaboration with Battery500 consortium.

## Results

The following are the key accomplishments:

*Probing the surface transition metal oxidation state and oxygen activities of Li-rich layered oxides*

In order to study the structure and chemistry differences between bulk and surface from the atomic level, STEM/EELS data was collected from the Li-rich electrode ($Li_{7/6}Ni_{1/6}Co_{1/6}Mn_{1/2}O_2$) after one cycle as shown in Figure II-315. Similar to our previous observations, a defect spinel structure that is different from the layered structure in bulk formed on the surface regions (less than 2 nm) due to TM migration from the TM layer to the neighboring lithium layer. Spatially resolved EELS (see Figure II-315b) was also performed using a step size of ~0.6 nm from surface to bulk. The data points are aligned with the STEM image to specify where the specific spectrum was taken. The O K-edge pre-peak, aligned to the onset energy of 532 eV, is associated with the hybridization states between TM 3d and oxygen 2p orbitals in the octahedral unit. There is no O pre-peak detected in the spectra obtained in the surface region. From surface to bulk, the intensity of the pre-peaks increases gradually. The results indicate the reduction of TM ions and oxygen local environment change, which is due to the formation of oxygen vacancy on the surface region where the spinel phase presents after cycling. Mn L-edge EELS was also collected from the identical area. Previous studies have shown that the $L_3/L_2$ ratio is sensitive to the valence state of Mn. In the detailed $L_3/L_2$ ratio analysis shown in Figure II-315c, it is going to lower Mn oxidation state within a ~2 nm region from the surface, which is consistent with XPS result in our previous report. The generation of the reduced Mn can be a direct consequence of the formation of a large number of oxygen vacancies, which once again proves oxygen participates in the electrochemical cycling.

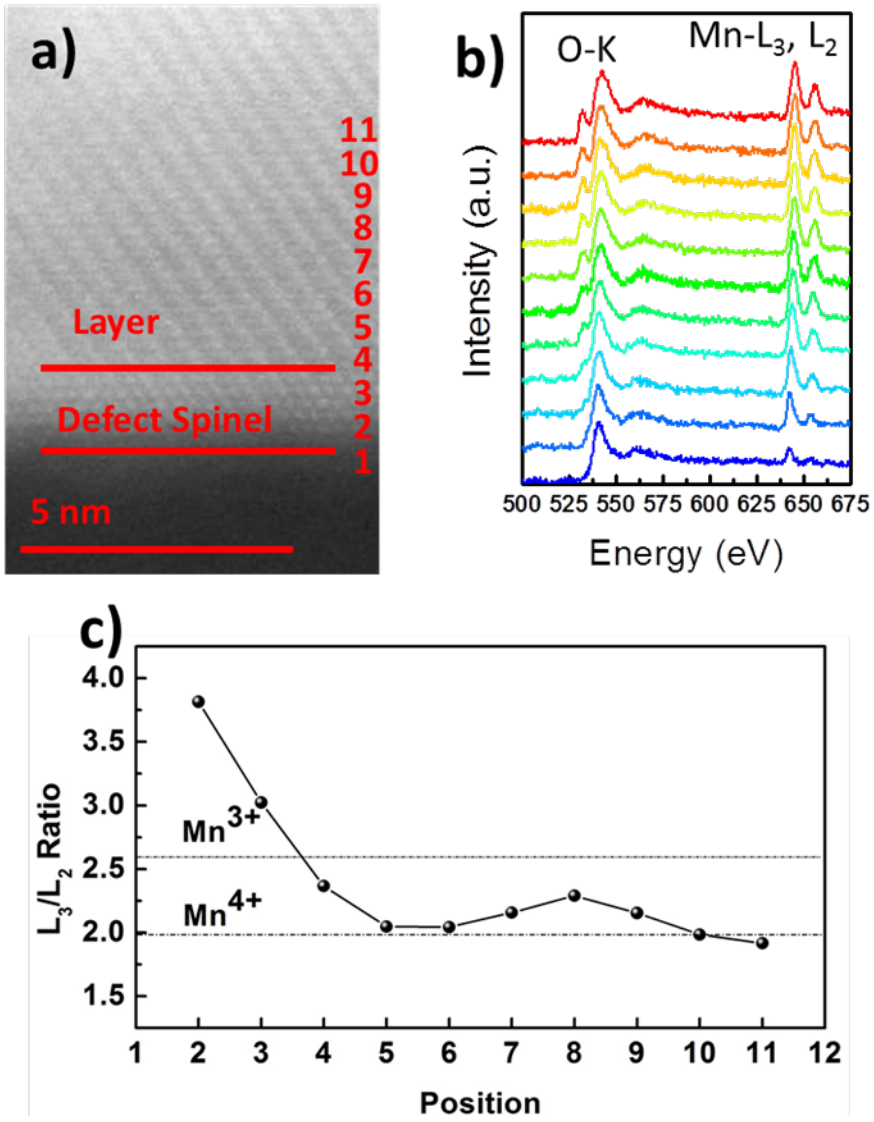


Figure II-315. (a) Aberration corrected high angle annular dark field (HAADF) STEM image; (b) spatially resolved O K-edge and Mn L-edge EELS spectra; (c) Mn $L_3/L_2$ ratio fit results from the EELS spectra.

*BCDI characterization on single particle of Li-rich layered oxide after cycling*

Three-dimensional dislocation network formation was demonstrated in our previous report by BCDI in this group material during the initial charging process under operando conditions. It is also revealed the link between this crystalline defect and voltage decay in this material. To further investigate the dislocation evolution during cycling, BCDI measurement was performed on Li-rich layered oxide electrode after the 1st cycle and the 50th cycle (see Figure II-316a and Figure II-316b). The truncation rod in the diffraction speckle pattern is less symmetric for the sample after 50 cycles compared with that of the sample after only 1 cycle, which typically indicates strain builds up in this material during electrochemical cycling. We have focused on quantitative analysis to reconstruct 3D displacement field as well as strain distribution in the single particle to illustrate crystalline defects influence on cycling performance of Li-rich layered oxide material.

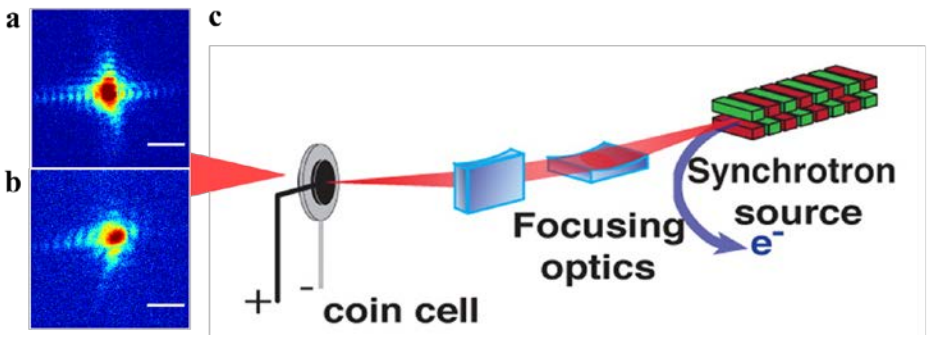


Figure II-316. Diffraction data collected for electrode after the (a) 1st cycle and (b) 50th cycle. (c) Experimental schematic of the in situ BCDI setup. Scale bar is 1e-8 1/Å.

*Structure recovery demonstration of Li-rich layered oxide after electrochemical cycling*

Anion (oxygen) redox in Li-rich layered oxide materials is the main reason for the high reversible capacity over 300 mAh $g^{-1}$ at room temperature. Unfortunately these composites suffer from a poor structural stability and limited cycle life. A large fraction of the TM ions are in under coordinated octahedral sites due to oxygen vacancies formation, which are not stable and spontaneously migrate to the fully coordinated octahedral sites nearby. Li ions in the TM layer migrate to the shared tetrahedral site in the lithium layer. These migrations dramatically alter the cation ordering in the TM layer as well as local lithium environment and thus lead to the structure disorder. The cycled material will be trapped in a metastable state with energetically unfavorable local lithium environment, which finally contributes to the voltage fade during the cycling process. As shown in Figure II-317a, the superstructure peak between 20° and 25° disappears after 50 cycles, which indicates the material becomes partially disordered. A path is designed to re-order the superstructure by high-temperature annealing of the cycled electrode (>150 °C). After the heat treatment, the superstructure peak is partially recovered, which indicates the bulk structure is reordered. Based on the mechanism described above, the superstructure recovery is decisive in restoring the original voltage output of Li-rich layered cathode (see Figure II-317b).

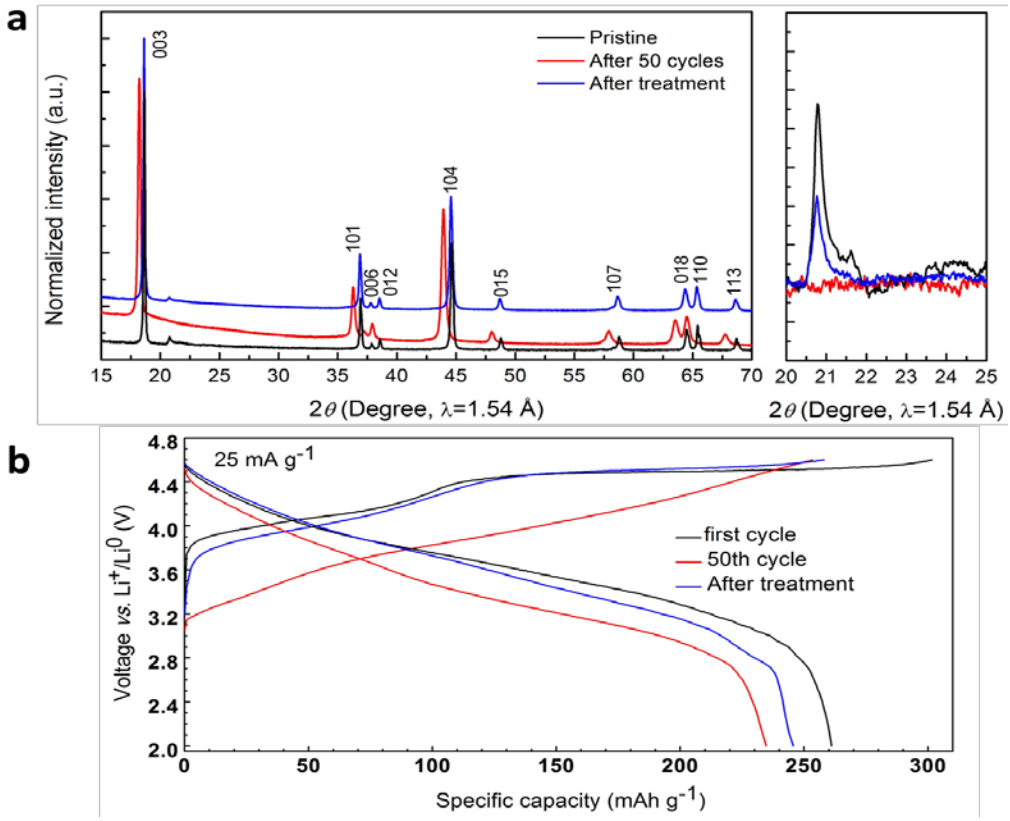


Figure II-317. (a) The evolution of the superstructure peak intensity in the pristine state, after 50 cycles, and after the heat treatment. (b) Charge-discharge voltage curves of Li-rich layered oxide cathode with Li-metal as anode

Neutron diffraction (ND) was applied to investigate the structure transformation of the cycled electrode after heat treatment. Figure II-318a-d shows the as-collected time-of-flight (TOF) ND patterns with 'Rietveld' refinement for Li-rich layered cycled electrodes before and after heat treatment. The lattice parameters of the sample after initial cycle are $a$ = 2.8630(1) Å, and $c$ = 14.3497(9) Å. In comparison, both $a$ and $c$ lattice parameters are reduced after annealing under different temperature. This trend counteracts common effect of material thermal expansion, which indicates structure transformation occurs with strain decrease. In order to illustrate local structure changes in terms of atomic migration induced by heat treatment, lithium occupancy in TM layer and oxygen occupancy are also shown in Figure II-318. After initial cycle, lithium from the TM layer is largely irreversible with only 32% of lithium reinsertion. Oxygen vacancies are also observed in the cycled sample, which results in a large fraction of under-coordinated TM ions. These unstable TM ions can potentially migrate to the fully coordinated octahedral sites nearby. Irreversible lithium insertion together with TM ions migration dramatically alters the cation ordering in the TM layer and thus leads to the structure disorder. Surprisingly, it is found Li occupancy in the TM layer and oxygen occupancy increases for the cycled sample after heat treatment, which is a strong indication of structure ordering recovery.

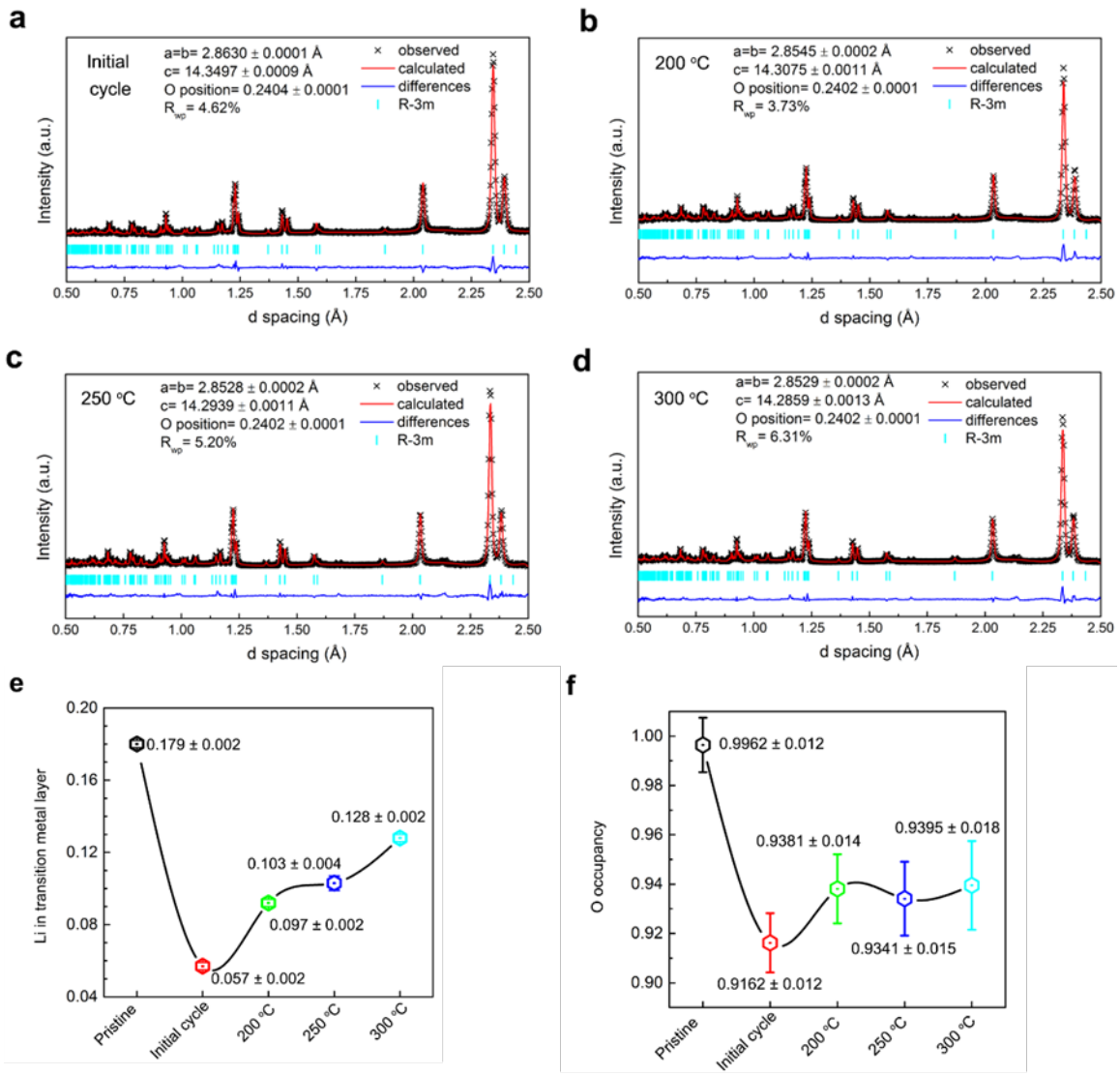


Figure II-318. ND characterization of cycled electrode after heat treatment. (a) Refined ND patterns of the electrode after the initial cycle. (b-d) Refined ND patterns of the initially cycled electrode after heat treatment under 200, 250 and 300 °C, respectively. (e) Lithium occupancy in transition metal layer and (f) Oxygen occupancy for different samples.

*Feasibility of Cryogenic -TEM to characterize Li metal dendrite formation*

Basic understanding of Li growth mechanism is important to prevent the detrimental dendrites formation. Although much work has been done to explore the growth of Li dendrite by various characterizations, such as optical microscopy, scanning electron microscopy (SEM), atomic force microscopy (AFM) etc. Its growth mechanism is still unclear and controversial. Furthermore, little attention is paid on the structure of plated Li metal, especially at the atomic scale. Compared with other characterization tools, TEM provides insight related to both microstructural and chemical evolutions with a superior spatial resolution. The challenge of probing Li metal under TEM is the low dose tolerance (high beam sensitivity) of Li metal. It is difficult to handle Li metal without any contamination and damage. Figure II-319 shows the morphology changes of the Li metal as a function of the beam exposure time under room temperature. At room temperature, the dendritic Li metal is quite unstable: quickly drifted, shrunk and evaporated under TEM beam exposure. Holes are created in the Li metal (Figure II-319c). One of the promising approaches to stabilize the beam-sensitive samples is the Cryo technique. In contrast, Li metal is very stable at 100 K (Figure II-319d-f) and no visible

changes are observed with the same magnification as the room temperature. Therefore, the cryo-TEM allows us to detect the Li metal at the nano scale while avoiding damaging of the sample.

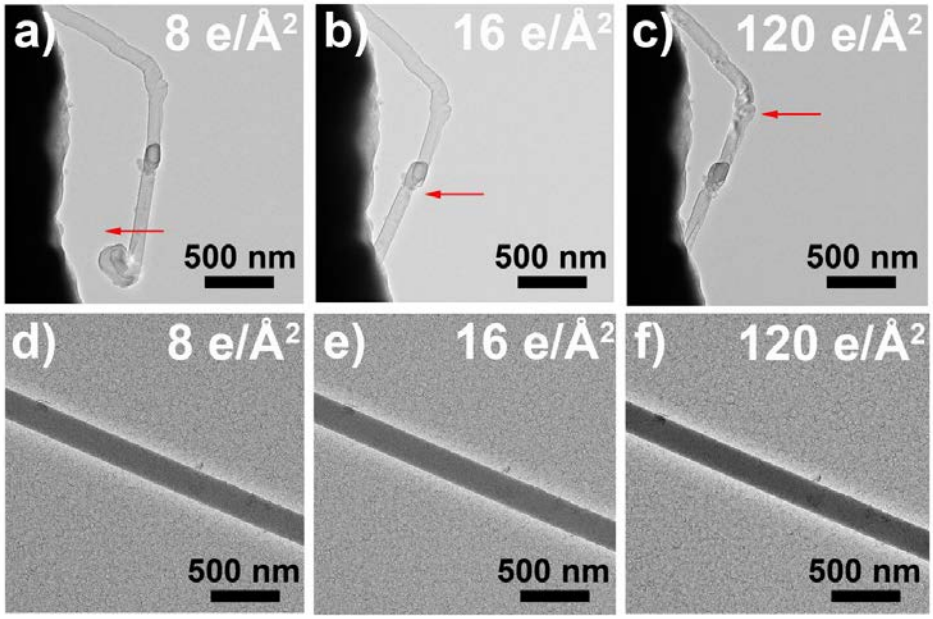


Figure II-319. Morphology changes of the dendritic Li metal as a function of the beam exposure time under: room temperature TEM (a, b, c) and cryo-TEM (d, e, f).

*Structure and chemical composition of electrochemically deposited Li metal at nano scale*

The nanostructure of the electrochemically deposited Li metal (EDLi) is shown in Figure II-320a. The identical contrast in the bulk demonstrates the uniformity of the EDLi. Along the edges of the EDLi an uneven solid electrolyte interphase (SEI) is present with a maximum thickness of ~7 nm. Figure II-320 surprisingly displays lattice fringes present on the surface rather than the bulk, suggesting that the EDLi metal is amorphous while part of the SEI is crystalline. The above results were validated by the area Fast Fourier Transform (FFT) patterns. The absence of characteristic bright rings/spots in the bulk area (red square) shows clearly that the EDLi is amorphous (Figure II-320b). Conversely, two obvious characteristic bright spots appear at the SEI surface (blue square). The ~0.2 nm lattice spacing is consistent with the lattice plane distance of the LiF (200) and cannot be ascribed to any plane distance of the metallic Li, further validating the partially crystalized SEI.

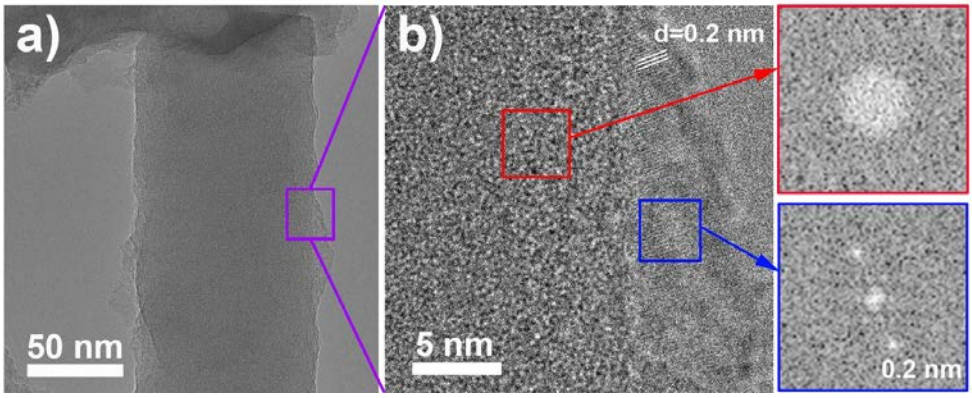


Figure II-320. Cryo-TEM (a) image and (b) its regional zoomed-in image with the bulk and surface FFT results of the EDLi using conventional carbonate electrolyte.

## Conclusions

STEM/ EELS characterization of Li-excess single NMC particle confirms that the layer-to-spinel transformation is largely confined to the surface 2nm, which imply that such surface reconstruction is not the major attributing factor to the voltage fading issue in this class of materials. BCDI measurements on Li-excess single NMC particle demonstrate significantly higher amount of defects such as stacking faults at high voltage (high state of charge), on the contrary the classical layered oxides show much less such defects at high voltage. A path to recover the layer structure and working voltage is designed through annealing. The treatment helps to recover the local environments of the excess Li ions, restore the original oxygen stacking sequence, and eliminates microstrain associated with different defects. Cryogenic (cryo)-electron microscopy is a powerful tool to reveal the detailed chemistry and structure of electrochemically deposited Li and the SEI composition at the nanoscale while minimizing beam damage during imaging. Surprisingly, the results show that the low current density deposited (nucleation-dominated) EDLi is amorphous, while there is some crystalline LiF present in the SEI.

## Key Publications


1. B. Qiu, M. Zhang, Y. Xia, Z. Liu, Y.S. Meng, “Understanding and Controlling Anionic Electrochemical Activity in High-Capacity Oxides for Next Generation Li-Ion Batteries” Chemistry of Materials, 2017, 29, 908.

2. M. Zhang, H.D. Liu, C. Fang, Y.S. Meng, “Minimize the Voltage Degradation in Li-rich Layered Oxide Cathode Materials by Morphology Control” Materials Research Society Meeting, 2016, Boston, U.S., Oral presentation.

3. M. Zhang, H.D. Liu, C. Fang, Y. S. Meng, “Morphological and Surface Structural Changes during Electrochemical Cycling in Li-rich Layered Oxides for Next Generation Li-ion Batteries” Materials Research Society Meeting, 2017, Phoenix, U.S., Oral presentation.

4. Y. S. Meng, “Diagnostic Comparison between Lithium-rich Layered Oxides and Classical Layered Oxides” Materials Research Society Meeting, 2017, Phoenix, U.S., Invited talk.

5. M. Zhang, B. Qiu, Y. S. Meng, “Structural and Voltage Recovery in Li-rich Layered Oxides”, provisional US Patent, in application.

6. X. Wang, M. Zhang, J. Alvarado, S. Wang, M. Sina, B. Lu, J. Bouwer, W. Xu, J. Xiao, J.-G. Zhang, J. Liu, Y. S. Meng, “New Insights on the Structure of Electrochemically Deposited Lithium Metal and Its Solid Electrolyte Interphases via Cryogenic TEM” Nano Letters, 2017, ASAP published online.

## II.D.5 Microscopy Investigation on the Fading Mechanism of Electrode Materials (PNNL)

**Chongmin Wang, Principal Investigator**
Pacific Northwest National Laboratory
902 Battelle Boulevard, Mail Stop K8-93
Richland, WA 99352
Phone: 509-371-6268
E-mail: chongmin.wang@pnnl.gov

**Tien Duong, Technology Manager**
U.S. Department of Energy
Phone: 202-586-7836
E-mail: Tien.Duong@ee.doe.gov

Start Date: October 1, 2015 End Date: September 30, 2018
Total Project Cost: $900,000 DOE share: $900,000 Non-DOE share: $0

### Project Introduction

For layer structured cathode materials based on Ni, Mn and Co transition metal oxide, it can be divided into two categories, one is NMC and the other is the lithium rich and Mn rich NMC (LMR-NMC). Practical use of these two categories of cathodes faces three challenges at the very fundamental level: Voltage fading; capacity fading; and how to increase the packing/tape density. It is generally believed that high Co content in the NMC material enhances the rate performance; high Ni content leads to higher capacity, and the presence of $Mn^{4+}$ improves the structural stability and thermal stability. However, the detailed fundamental roles of each transition metal cation e.g., Ni, Co and Mn, especially at the high voltages are still unclear, not mentioning the possible synergistic effects among these three cations during the electrochemical process. Furthermore, dopants such as Sn, Mg, Al, and Si also strongly affect the fading characteristics of cathode. Understanding the different contributions of Ni, Co, Mn, and their migration during cycling, if any, not only help to optimize the electrochemical performances of NMC at high cutoff voltages, it also unravels the structural and chemical evolution pathway of NMC and LMR-NMC, providing guidance for optimization of these layer structured cathodes for high performance.

To gain insights into the structural information at atomic resolution, aberration-corrected STEM-HAADF imaging combined with EELS/EDX chemical analysis will be used to probe the microstructural and chemical evolution of the NMC and LMR-NMC layered cathode before and after cycling. EELS/EDX mapping, time-of-flight secondary ion mass spectrometry (TOF-SIMS), nano-SIMS, and XPS will be used to explore the elemental distribution and the thickness of SEI layer formed on the surface of the cathode material. Direct correlation of the structural and chemical information with battery properties will provide insight on the capacity degradation mechanism of the layered materials with different compositions and performance improvement mechanism with lattice doping/surface modification/electrolyte additives.

### Objectives

The objective of this work will be using the state of the art in-situ and ex-situ microscopy technique to probe the structural and chemical evolution of electrodes in rechargeable battery. A close collaboration between the synthesis and characterization teams will enable acceleration on the materials optimization process and establishment of a solid knowledge base on the correlation between materials selections and structure evolution in the electrode materials for rechargeable batteries.

### Approach

Using the unique *ex situ* and *in situ* TEM methods to probe the structure of Li-ion batteries, especially a biasing liquid electrochemical cell that uses a real electrolyte in a nano-battery configuration. Use various

microscopic techniques, including *ex situ*, *in situ*, and especially the *operando* TEM system, to study the fading mechanism of electrode materials in batteries. This project will be closely integrated with other research and development efforts on high-capacity cathode and anode projects in the BMR Program to 1) discover the origins of voltage and capacity fading in high-capacity layered cathodes and 2) provide guidance for overcoming barriers to long cycle stability of electrode materials.

## Results

### *1. Does the liquid electrolyte permeate into the boundaries formed by the primary particles in a secondary particle?*

In order to increase the packing density of the cathode particle, it is now a common practice to fabricate the cathode particles into a secondary particle of typically 10-20 micrometer, which is composed of primary particle of several hundred nanometers. One of the critical questions for this type of hard agglomerated particle is whether the electrolyte penetrates into the boundaries formed by the primary particles. To answer this question, the secondary particle of NMC422 as typically shown in Figure II-321a were investigated before and after the battery cycling. Figure II-321a–c show the pristine agglomerated NMC442 particles and cycled electrode from which a TEM sample was prepared using FIB lift-out techniques. Figure II-321d–I are STEM-EDS mapping results; these observations reveal that, within the agglomerated particle, there exists a P-rich SEI layer formed at the grain boundary (GB). This observation conclusively indicates that the electrolyte did indeed penetrate into the inside of the agglomerated particles through the boundaries between the primary particles. Therefore it can be generally concluded that the detrimental solid-liquid electrolyte as observed in the case of primary particle also happens for the secondary particle. To improve the cycling stability, strategy needs to be developed to mitigate this interfacial reaction in the secondary particles.

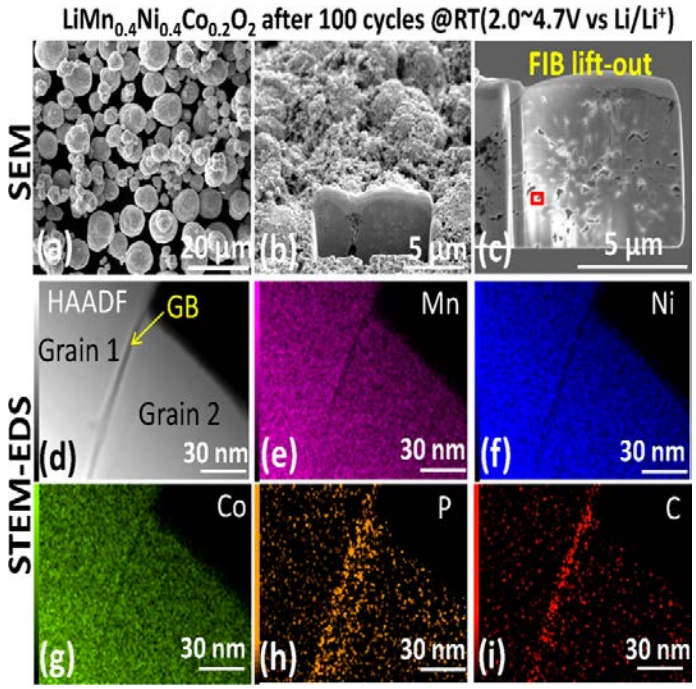


Figure II-321. SEM images of (a) pristine agglomerated particles, (b) and (c) TEM specimen prepared by FIB lift-out techniques from cycled electrode. (d–i) STEM-EDS mapping results from the boxed region in panel (c).

### *2. Intragranular cracking as a critical barrier for high-voltage usage of layer-structured cathode for lithium-ion batteries*

For layered structured transition metal oxides, during charge process, Li ions are extracted from the lattice, which usually causes lattice expansion along *c* direction and shrinkage along *a* and *b* directions, while this

process reverses upon discharging (reversible insertion of Li ions). For example, when NMC333 is delithiated to $Li_{0.5}Ni_{1/3}Mn_{1/3}Co_{1/3}O_2$, the lattice could expand 2.0% along *c* direction and shrink 1.4% along *a* direction, which is a huge strain for oxides with ionic bonds. We found that intragranular cracks in NMC333 cathode can be easily created at high cutoff cycle voltage (Figure II-322), which contributed to the fast degradation of the cell. The comprehensive transmission electron microscopy (TEM) observations unveiled previously unrecognized nature of intragranular cracks from the following four aspects: 1) there are two kind intragranular cracks. One is the normally seen mechanical failure crack with two free surfaces; the other one is termed as premature crack with uniformly sub-nanometer crack width. 2) The premature crack is not empty but with loose materials inside. 3) Many intragranular cracks were initiated from grain interior. 4) Dislocations are acting as crack nucleation sites.

In addition to the real intragranular cracks which have two free surfaces, we also identified tremendous premature intragranular crack whose surfaces are not completely free but with a loose materials in between. Such premature cracks are generated by expanding the neighbored (003) planes (TM slabs) and exhibiting strip contrast while viewing their edge on in TEM. By examining a lot of intragranular cracks, surprisingly, we found many cracks were actually initiated from grain interior, which contradicts the proposed theoretical models as they predicted surface should be the favorite site for crack initiation. Through intensive TEM characterization, we discovered that dislocations could act as nucleation sites of internal cracking. Based on our experimental results, we proposed a mechanism which can fully address the formation process of internal cracking in layered cathode. This study pointed out future directions for mitigating intragranular cracking not only for layered cathode materials but also for other intercalation type cathodes.

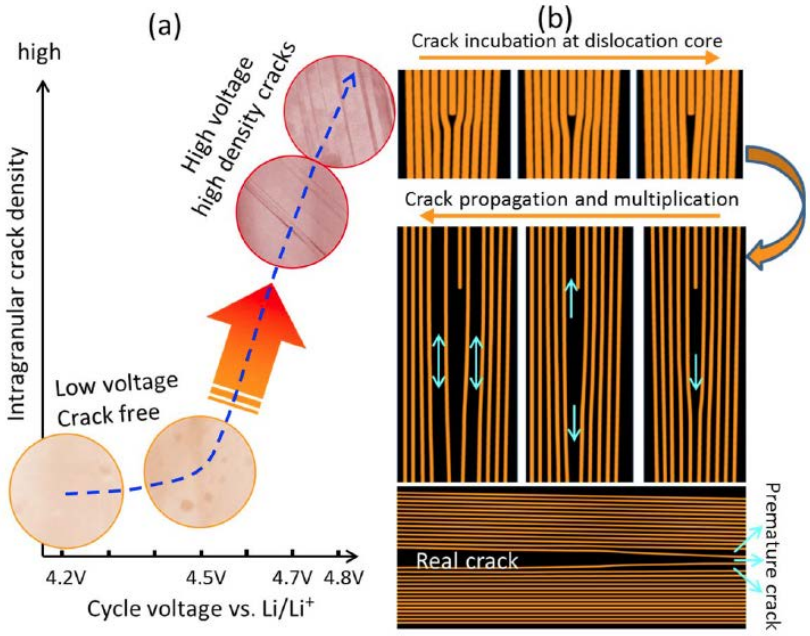


Figure II-322. Cycle voltage governed intragranular cracking and underlying dislocation-based mechanism. (a) HAADF images overlaid diagram shows the apparent dependence of intragranular cracking on the cycle voltage; when cycled below 4.5 V, intragranular crack can be hardly generated, while above 4.7 V, intragranular density shows a drastic increase; and (b) schematic diagrams to illustrate the dislocation-assisted crack incubation, propagation and multiplication process.

### *3. In-situ environmental TEM revealing the reaction mechanism of Li-$O_2$ batteries*

One of the key questions for Li-$O_2$ battery system is why the reaction product shows very unique morphological features, ranging from hollow spheres to toroidal structure. This question is addressed by using

an aberration-corrected in-situ *environmental* TEM under oxygen environment. A solid-state nano-battery was constructed through a two-probe configuration (Figure II-323). The CNTs/$RuO_2$ cathode was loaded on a Pt probe, and brought to a $Li_2O$ covered Li metal anode anchored on the other tungsten probe through precise nano-manipulation inside the ETEM. The electrochemical reaction is driven by external biasing, i.e., a negative bias applied on the Pt end to drive the $Li^+$ to cross the $Li_2O$ layer to react with oxygen, which corresponds to the oxygen reduction reaction (ORR) during the discharging of the Li-$O_2$ battery; a positive bias drives the $Li^+$ ions back to the $Li_2O$/Li end, leading to the decomposition of the discharged product, which is oxygen evolution reaction (OER) during the charging of the battery.

It has been observed that the oxygen reduction reaction on CNTs initially produces $LiO_2$, which subsequently evolves to $Li_2O_2$ and $O_2$ through disproportionation reaction. It is interesting to note that it is just the releasing of $O_2$ that inflates the particles to a hollow structure with a $Li_2O$ outer surface layer and $Li_2O_2$ inner-shell, demonstrating that, in general, accommodation of the released $O_2$ coupled with the $Li^+$ ion diffusion and electron transport paths across both spatial and temporal scales critically governs the morphology of the discharging/charging product in Li-$O_2$ system. This in-situ observation provides insight for understanding as how the toroidal structure forms in Li-$O_2$ system. It would be expected that the determination of Li-$O_2$ reaction mechanisms sets foundation for quantitative understanding/modeling of the electrochemical processes in the Li-$O_2$ system, enabling rational design of both solid-state and aprotic Li-$O_2$ batteries.

## Conclusions

Over the last year, we have made significant progresses on understanding the fading mechanism of layer structured cathode and revealed the reaction mechanism of Li-$O_2$ battery system. For the cathode materials, we concluded that liquid electrolyte penetrates into the boundaries of the secondary particle, where the detrimental solid-liquid reaction will happen. Therefore, new strategy has to be developed to mitigate the detrimental solid-electrolyte reaction for enhancing the performance of the cathode. At the same time, we discovered that a critical barrier for the high voltage operation of layer structured cathode is the formation of intragranular cracks. Qualitatively, the higher of the operating voltage, the higher of the density of the intragranular cracking. To mitigate this intragranular cracking, lattice doping is needed to strengthen the lattice. Using EELS mapping, we reveal that Ni has a high migrating propensity for mixing with Li layer, which in turn will lead to voltage fading. This observation provide insight to the fading mechanism of Ni rich NMC. In addition, we have developed the in-situ environmental TEM, which enables in-situ TEM study of Li-$O_2$ battery. We revealed the reaction mechanism of Li-$O_2$ battery and concluded that the accommodation of the released $O_2$ contributes to the formation of the peculiar morphological feature of the reaction products.

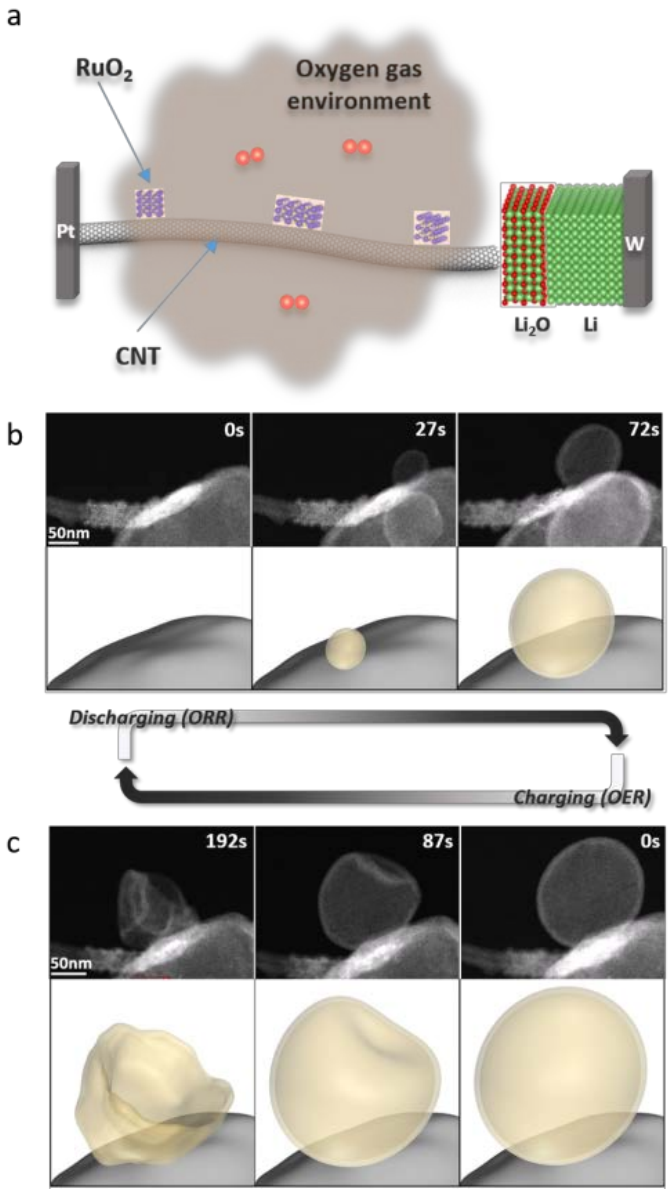


Figure II-323. Experimental set up of the Li-O2 nano-battery and the in situ STEM observation of morphological evolution of the reaction products upon discharge-charge cycling of the Li-O2 battery. a, Schematic drawing to illustrate the configuration of the Li-O2 nano-battery in ETEM chamber. b, The time-resolved HAADF-STEM images depict the morphological evolution of the discharging product (oxygen reduction reaction (ORR)), which is featured by the formation of hollow structure (illustrated by the bottom panel in b. c. The images illustrates the morphological evolution upon charging (oxygen evolution reaction (OER), which is featured by the collapsing of the hollow structure as illustrated by the bottom panel in c.

## Key Publications


1. Pengfei Yan, Jianming Zheng, Meng Gu, Jie Xiao, Ji-Guang Zhang, Chongmin Wang, "Intragranular cracking as a critical barrier for high-voltage usage of layer-structured cathode for lithium-ion batteries", **Nat. Commun. 8, 14101 (2017).**

2. Langli Luo, Bin Liu, Shidong Song, Wu Xu, Ji-Guang Zhang and Chongmin Wang, "Revealing the reaction mechanisms of Li–O2 batteries using environmental transmission electron microscopy", **Nature Nanotechnology, 12, 535-539 (2017).**

3. Pengfei Yan, Jianming Zheng, Ji-Guang Zhang, and Chong-Min Wang, "Atomic Resolution Structural and Chemical Imaging Revealing the Sequential Migration of Ni, Co, and Mn upon the Battery Cycling of Layered Cathode", Nano Lett., 17, 3946−3951 (2017).

4. Xiaotang Lu, Yang He, Scott X. Mao, Chong-min Wang, and Brian A. Korgel, "Size Dependent Pore Formation in Germanium Nanowires Undergoing Reversible Delithiation Observed by In Situ TEM", **J. Phys. Chem. C 2016, 120, 28825−28831.**

5. Pengfei Yan, Jianming Zheng, Xiaofeng Zhang, Rui Xu, Khalil Amine, Jie Xiao, Ji-Guang Zhang, and Chongmin Wang, "Atomic to Nanoscale Investigation of Functionalities of an $Al_2O_3$ Coating Layer on a Cathode for Enhanced Battery Performance", **Chem. Mater., 28, 857−863 (2016).**

6. Yang He, Meng Gu, Haiyan Xiao, Langli Luo, Yuyan Shao, Fei Gao, Yingge Du, Scott X. Mao, and Chongmin Wang, "Atomistic Conversion Reaction Mechanism of $WO_3$ in Secondary Ion Batteries of Li, Na, and Ca", **Angew. Chem. Int. Ed. 55, 6244 –6247 (2016).**

7. Pengfei Yan, Jianming Zheng, Jiaxin Zheng, Zhiguo Wang, Gaofeng Teng, Saravanan Kuppan, Jie Xiao, Guoying Chen, Feng Pan, Ji-Guang Zhang, and Chong-Min Wang, "Ni and Co Segregations on Selective Surface Facetsand Rational Design of Layered Lithium Transition-Metal Oxide Cathodes", **Adv. Energy Mater. 6, 1502455 (2016).**

8. Zhaofeng Gan, Meng Gu, Jianshi Tang, Chiu-Yen Wang,Yang He, Kang L. Wang, Chongmin Wang, David J. Smith, and Martha R. McCartney, "Direct Mapping of Charge Distribution during Lithiation of Ge Nanowires Using Off-Axis Electron Holography", **Nano Lett. 16, 3748−3753 (2016)**

9. Jiangwei Wang, Hao Luo, Yang Liu, Yang He, Feifei Fan, Ze Zhang, Scott X. Mao, Chongmin Wang, and Ting Zhu, "Tuning the Outward to Inward Swelling in Lithiated Silicon Nanotubes via Surface Oxide Coating", **Nano Lett. 2016, 16, 5815−5822 (2016).**

10. Chenfei Shen, Mingyuan Ge, Langli Luo, Xin Fang, Yihang Liu, Anyi Zhang, Jiepeng Rong, Chongmin Wang and Chongwu Zhou, "*In Situ* and *Ex Situ* TEM Study of Lithiation Behaviors of Porous Silicon Nanostructures", **Sci. Rep. 6, 31334 (2016).**

11. Eungje Lee, Joel Blauwkamp, Fernando C. Castro, Jinsong Wu, Vinayak P. Dravid, Pengfei Yan, Chongmin Wang, Soo Kim, Christopher Wolverton, Roy Benedek, Fulya Dogan, Joong Sun Park, Jason R. Croy, and Michael M. Thackeray, "Exploring Lithium-Cobalt-Nickel Oxide Spinel Electrodes for ≥3.5 V Li-Ion Cells", **ACS Appl. Mater. Interfaces, 8, 27720-27729(2016).**

## II.D.6 Characterization Studies of High Capacity Composite Electrode Structures (ANL)

**Michael M. Thackeray, Principal Investigator**
Argonne National Laboratory
9700 South Cass Avenue
Lemont, IL 60439
Phone: 630-252-9184
E-mail: thackeray@anl.gov

**Eungje Lee, Principal Investigator**
Argonne National Laboratory
9700 South Cass Avenue
Lemont, IL 60439
Phone: 630-252-9184
E-mail: eungje.lee@anl.gov

**Peter Faguy, Technology Manager**
U.S. Department of Energy
Phone: 202-586-1022
E-mail: Peter.Faguy@ee.doe.gov

Start Date: October 1, 2015 End Date: September 30, 2018
Total Project Cost: $500,000 DOE share: $500,000 Non-DOE share: $0

### Introduction

Previous studies on the integration of a spinel component into lithium- and manganese-rich oxides to produce $y[xLi_2MnO_3 \bullet (1-x)LiMO_2] \bullet (1-y)LiM_2O_4$ (M=Mn,Ni,Co), layered-layered-spinel (LLS), composite structures have proven promising. Specifically, high first-cycle efficiency, good rate capability, and stable capacity at practical voltages (e.g., ~210 mAh/g at ~4.4 V vs. graphite) can be achieved with these electrode materials. However, critical issues such voltage fade, poor rate performance, and surface stability have yet to be adequately addressed. With respect to voltage fade, complimentary works have shown that Co-based spinels may be interesting options for integrated, stabilizing components in LLS materials, but that their synthesis and properties are not straightforward, especially when integrating into LL compositions. Surfaces of LLS cathode particles are also prone to instabilities, similar to other lithiated oxide materials, including oxygen evolution and transition metal dissolution. Many strategies have been proposed for the protection of particle surfaces but no consensus yet exists as to the efficacy of any given strategy. The difficulty, in part, in identifying specific trends in the literature is the strong dependence of surface modifications on the properties of the underlying cathode particles. For example, composition, morphology, porosity, and the conditions of synthesis under which surface modifications are carried out can all play a role. This chapter deals with efforts in this project to further understand the properties of LLS materials. Specifically, studies of structure, synthesis, and electrochemical properties of end-member and integrated components as well as the stabilization of surfaces are presented.

### Objectives

The primary objective of this project is to explore the fundamental processes that are most relevant to the challenges of next-generation, energy-storage technologies, in particular, high capacity structurally-integrated electrode materials. The goals of this project are to capitalize on a broad range of facilities and collaborations in order to characterize and model structurally-integrated electrode systems, notably those with both layered

and spinel character, and to develop low-cost, high-energy and high-power Mn-oxide-based cathodes for lithium-ion batteries that will meet the performance requirements of PHEV and EV vehicles.

## Approach

A wide array of characterization techniques including X-ray and neutron diffraction (XRD, ND) X-ray absorption (XAS), high resolution transmission electron microscopy (HRTEM), and theory will be brought together to focus on challenging experimental problems. Structural, electrochemical, and chemical mechanisms at play in novel, complex electrode/electrolyte systems will be explored in the pursuit of advancing the properties of state-of-the-art cathode materials.

## Results

*Understanding Synthesis and Structure of Mn- and Ni-doped, $LiCoO_2$-based Spinels via DFT Calculations*

Lithiated-spinel, $LiCoO_2$ materials are of interest as potential stabilizing agents to be incorporated in layered-layered-spinel (LLS) composite cathodes [1]. Previous experimental works have shown that Ni substitution effectively stabilizes the lithiated spinel structure, enhancing electrochemistry. However, Mn substitution results in impurity phases such as $Li_2MnO_3$, $Li_4Mn_5O_{12}$, and $Co_3O_4$. In order to obtain a better understanding of the different effects of Mn and Ni substitution on phase stability, an atomistic simulation of substituted, $LiCoO_2$-based, lithiated-spinels was conducted.

The substitution of Mn or Ni on the Co site of both spinel (Fd-3m) and layered (R-3m) $LiCoO_2$ structures was examined via density functional theory (DFT) calculations. Possible, symmetrically-distinct mixing configurations for $Li_{16}Co_{16-x}M_xO_{32}$ (up to 64 total atoms; M = Mn or Ni; $0 \leq x \leq 16$) were generated using the Enum package [2]. Figure II-324a displays the calculated ground state DFT formation energy ($\Delta H_f$) of $LiCo_xM_{1-x}O_2$ (M = Mn or Ni; and $0 \leq x \leq 1$) sampled uniformly through the composition space. Here, the DFT formation energy of a generic $LiMO_2$ compound is defined as $\Delta H_f(LiCo_xM_{1-x}O_2) = E_0(LiCo_xM_{1-x}O_2) - \mu_{Li} - x\mu_{Co} - (1-x)\mu_M - 2\mu_O$, where $E_0(LiCo_xM_{1-x}O_2)$ is the calculated DFT total energy of $LiCo_xM_{1-x}O_2$ and $\mu_i$ ($i$ = Li, Co, M, O) is the chemical potential of component $i$. Note that the energy difference between Fd-3m and R-3m structures at each composition is almost negligible, as previously reported [3]. Furthermore, the calculated $\Delta H_f$ of $LiCo_xM_{1-x}O_2$ varies almost linearly between the end-members, $LiCoO_2$ and $LiMO_2$ (M = Mn/Ni), in Figure II-324a.

The mixing tendency of two cathode components, $LiCoO_2$ and $LiMO_2$ (M = Mn or Ni), can be obtained using: $\Delta E_{mix} = E_0(LiCo_xM_{1-x}O_2) - \{xE_0(LiCoO_2) + (1-x)E_0(LiMO_2)\}$, where $E_0(LiCo_xM_{1-x}O_2)$, $E_0(LiCoO_2)$, and $E_0(LiMO_2)$ are the calculated DFT total energies of either Fd-3m or R-3m $LiCo_xM_{1-x}O_2$, $LiCoO_2$, and $LiMO_2$ (M = Mn or Ni), respectively. A significantly negative $\Delta E_{mix}$ (i.e., < –25 meV/site) usually leads to the formation of an ordered compound while a significantly positive $\Delta E_{mix}$ (i.e., >25 meV/site) usually results in a two-phase miscibility gap. In contrast, a slightly negative or positive $\Delta E_{mix}$ (i.e., –25 to 25 meV/site) indicates a weak preference for ordering or phase separation, respectively, which could be overcome by configurational entropy at elevated temperatures to form a solid-solution. From Figure II-324b, it can be observed that Mn substitution in either Fd-3m or R-3m $LiCo_xMn_{1-x}O_2$ is only favorable at dilute concentrations of Mn ($x>0.9$). In fact, the mixing of Mn and Co on the Co sublattice in the LCO structure becomes increasingly unfavorable toward equiatomic compositions of Mn and Co. On the other hand, as seen in Figure II-324c, the mixing of Ni and Co on the Co sublattice is generally favorable at all compositions. The energy of mixing becomes increasingly negative (up to ~ –100 meV/site) towards equiatomic compositions of Ni and Co, hence compositions close to $LiCo_{0.5}Ni_{0.5}O_2$ are likely to form ordered compounds. These simulation data are in line with previous experimental results and corroborate the effectiveness of Ni substitution in stabilizing the lithiated spinel structure and improving its electrochemistry.

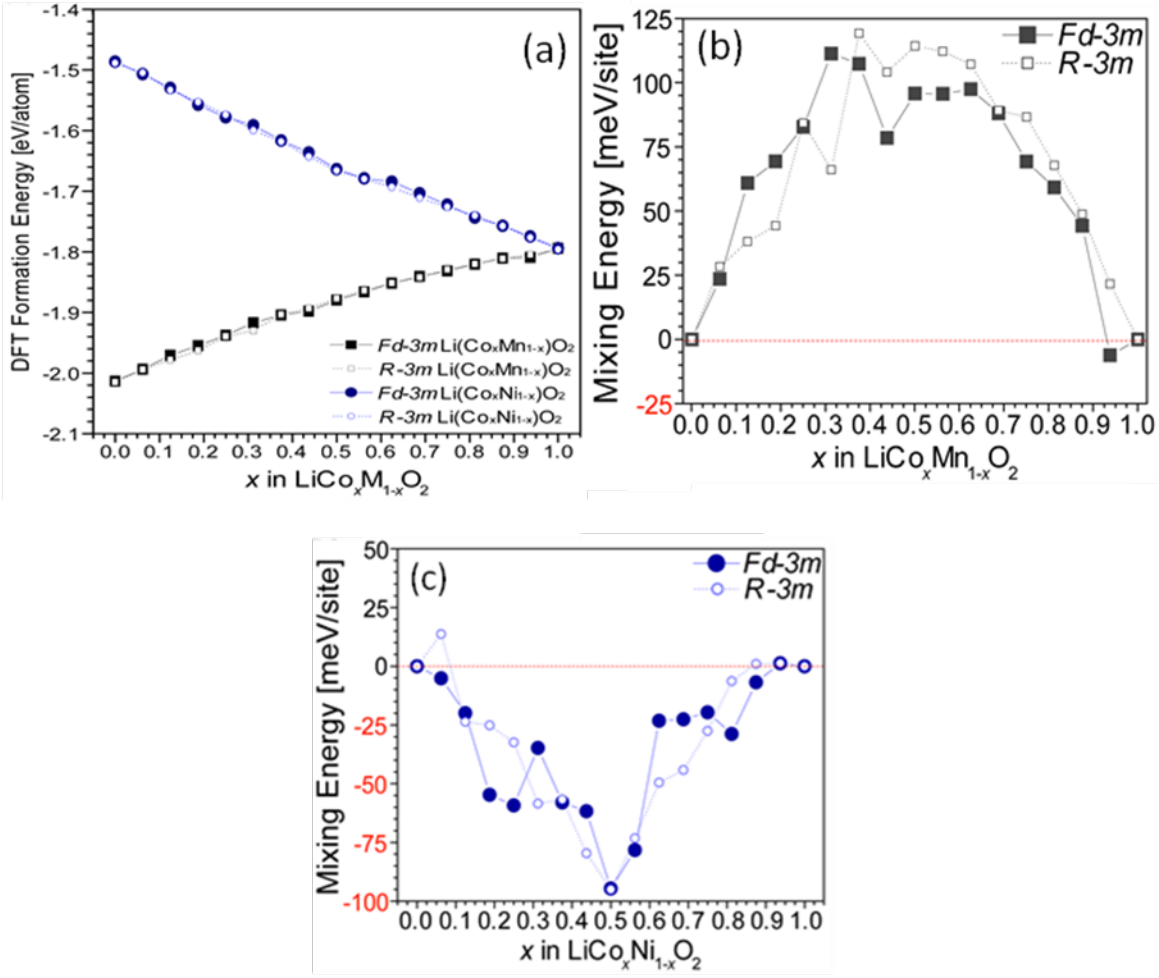


Figure II-324. (a) Calculated DFT formation energies of $LiCo_xM_{1-x}O_2$ (M = Mn or Ni; $0 \le x \le 1$) in both lithiated spinel (Fd-3m) and layered (R-3m) structures. The mixing energies of (b) $LiCo_xMn_{1-x}O_2$ and (c) $LiCo_xNi_{1-x}O_2$. Calculations by S. Kim and C. Wolverton (Northwestern University, IL).

*Synthesis of Complex, Layered-Layered-Spinel Compositions*

The structural integration of a spinel (S) component into a layered (L) electrode structure or a two-component LL system has been demonstrated in model compounds such as $xLi_2MnO_3 \bullet Li_{1-x}M_{2-x}O_4$ ('layered-spinel' (LS)) and $x[Li_2MnO_3 \bullet LiMO_2] \bullet (1-x)LiM_2O_4$ (LLS), where M is typically a transition metal ion, and that these materials have advantages over conventional, layered electrode materials [3]. They can be simply prepared by reducing the amount of lithium in the precursor materials normally used to synthesize stoichiometric L or LL structures. For example, reducing the lithium content of a stoichiometric $0.5Li_2MnO_3 \bullet 0.5LiMn_{0.5}Ni_{0.5}O_2$ compound (alternatively, $Li_{1.5}Mn_{0.75}Ni_{0.25}O_{2.5}$), in which the Mn:Ni ratio is 3:1, drives the composition towards the $LiMn_{1.5}Ni_{0.5}O_4$ spinel apex of the phase diagram, following the L-L-S tie-line in Figure II-325, while maintaining a constant Mn:Ni (3:1) ratio [4]. Note that this is a special case that has been observed experimentally and that the term 'layered-layered-spinel' is used for convenience because it describes the compositions of all compounds within this phase space.

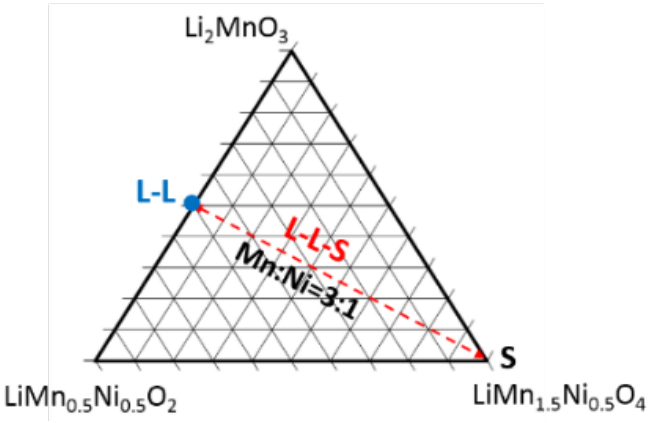


Figure II-325. The compositional phase space of a layered(L)-layered(L)-spinel(S) system.

A question that remains unanswered is: At what lithium deficiency do the transition metal ions start diffusing into the lithium-rich layers during synthesis to provide spinel (or spinel-like) character to predominantly layered structures with complex cation arrangements?

In an attempt to better understand the structural complexity of LLS materials, a series of compounds was prepared by reducing the lithium content in $0.25Li_2MnO_3 \bullet 0.75Li(Ni_{0.375}Mn_{0.375}Co_{0.25})O_2$ by various amounts and analyzed by combined Rietveld refinement analyses of ND and synchrotron XRD data, Figure II-326. For simplicity, the normalized composition and formula, $Li_{1.25-x}(Ni_{0.28}Mn_{0.53}Co_{0.19})O_{2.25-\delta}$ ($0 \le x \le 0.25$), is used for discussion. For $0 \le x \le 0.075$, both ND and XRD patterns could be indexed to compounds with either monoclinic symmetry (C2/m), denoted M-phase or, if the weak ordering peaks associated with the M-phase were ignored, to trigonal symmetry (R-3m), denoted L-phase. For x = 0.1, the XRD pattern showed additional peaks that were tentatively assigned to a spinel component with cubic symmetry, denoted S-phase. These initial refinements and attempts to use a two-phase model to refine both layered and spinel components have not provided conclusive results. The analyses are continuing and HRTEM studies are planned to gather more insight into the structural compositions of these complex electrode materials.

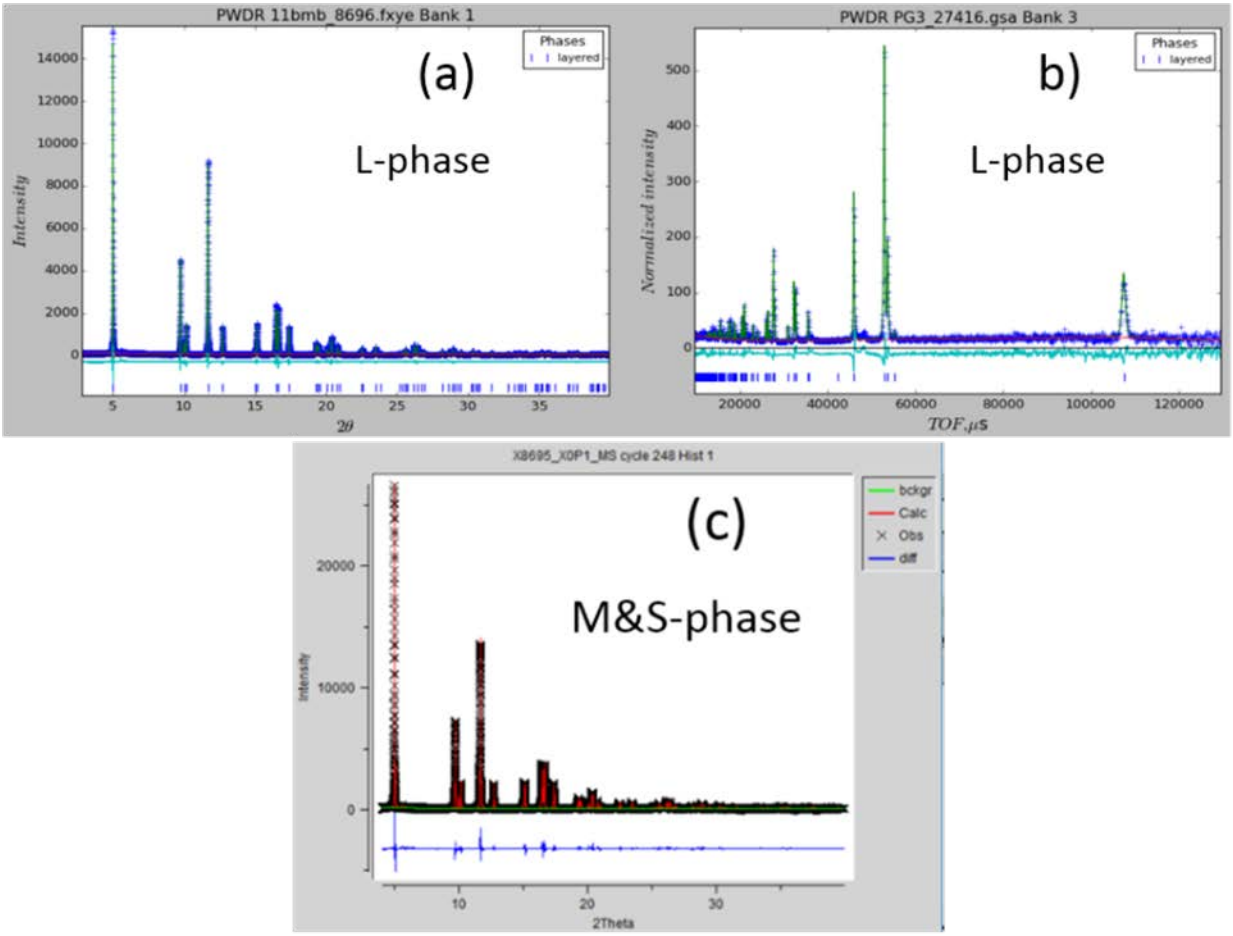


Figure II-326. Rietveld refinement results of (a) synchrotron X-ray and (b) neutron diffraction of the x = 0.75 sample. (c) Synchrotron X-ray diffraction of the x = 1.0 sample. ND by A. Huq (SNS, ORNL), XRD by Y. Ren (APS, ANL)

*Surface-Treated Layered-Layered-Spinel Cathode Particles*

Complementary studies (see II.3.A.x) have found that treatment of LLS particles in an aqueous solution of aluminum nitrate, followed by annealing between 110-750ºC, led to a decrease in performance with increasing temperature. Figure II-327a shows $^{27}Al$ nuclear magnetic resonance (NMR) spectroscopy of LLS particles after Al treatment followed by annealing at 550ºC (blue) and 110ºC (red) along with an $Al_2O_3$/Al(OH) reference (green). At the lowest temperature (110ºC), the aluminum coordination is clearly different than that of $Al_2O_3$/Al(OH), instead resembling a distorted 4-fold coordination environment. By 550ºC (blue) the diamagnetic peak near ~0 ppm completely disappears. This could be due to the presence of lattice aluminum and/or three-coordinate surface/interface aluminum. Figure II-327b shows X-ray photoelectron spectroscopy (XPS) of the un-treated LLS (black) and the Al-treated LLS powders after annealing at 110ºC (red), 400ºC (blue), and 550ºC (green). A small surface impurity (e.g., carbonate) can be seen in the un-treated sample. After Al treatment and annealing at 110ºC, a large peak forms at ~532 eV, in agreement with Al-O bonding. Upon annealing to higher temperature, this feature decreases and virtually disappears by ~550ºC, consistent with the NMR data. Figure II-327c shows the Al content (atomic %) derived from the XPS data as a function of temperature. As shown, increasing annealing temperatures led to less detectable surface Al. These data sets suggest that small amounts of Al might be doped into the bulk of LLS particles after surface treatments and high temperature annealing. This is an important finding considering the observed decrease in electrochemical performance with higher annealing temperatures; an observation that is not consistent with similar studies

reported for Mn-rich, layered materials. These results reiterate the important role of cathode composition with respect to surface modifications.

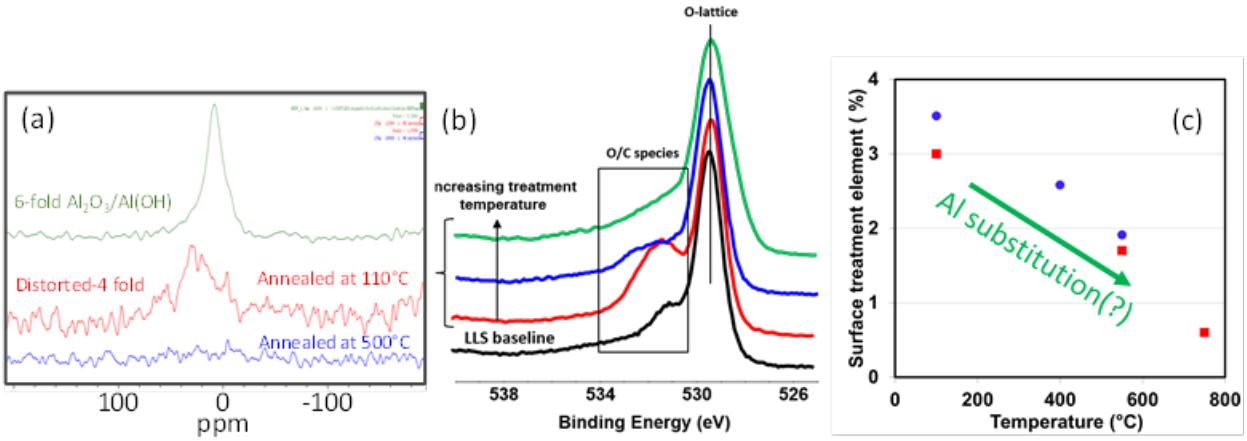


Figure II-327. a) $^{27}$Al MAS-NMR of Al-treated samples annealed at 110°C (red) and 550°C (blue) and an $Al_2O_3$/Al(OH) reference (green). (b) XPS spectra of LLS followed by Al treatment and annealing at 110°C (red), 400°C (blue), and 550°C (green). (c) Al content (at. %) as a function of annealing temperature, determined by XPS. Red squares represent samples that had previously (before Al treatments) been exposed to air, blue circles are samples not exposed to air (similar results were obtained with both sample sets). XPS by R. Ruther and H. Meyer (ORNL).

Figure II-328a shows a scanning electron microscopy (SEM) image of an Al-treated, LLS particle after undergoing a focused ion beam (FIB) lift-out procedure to allow for elemental mapping studies. Figure II-328b shows a HRTEM image of particles including two regions included for Fast Fourier Transform (FFT) analysis. This figure, and similar images, suggest that the Al-treated, LLS particles may have preferentially formed spinel domains at the surface of particles, possibly due to lithium leaching in an acidic environment. Figure II-328c shows energy-dispersive X-ray spectroscopy (STEM-EDX) of an Al-treated, LLS particle. It was found that a thin (~2 nm) Al layer covered the particles in a uniform manner, verifying the efficacy of the treatment conditions. However, some images showed indications of increased concentrations of both Al and Ni on the same surfaces, e.g., top left and bottom right in Figure II-328c. Whether or not this “segregation” is a consequence of the surface treatment itself, or other mechanisms related to the pristine particles is unclear. Additional imaging is underway for both treated and untreated particles to obtain better statistics on the relative formation of surface spinel and any possible tendencies of segregation (e.g., preferential location of Ni/Al) between treated and untreated particles. This information is expected to provide further insight into the structure-property relationships of LLS materials and the dependence of their electrochemical properties on processing conditions.

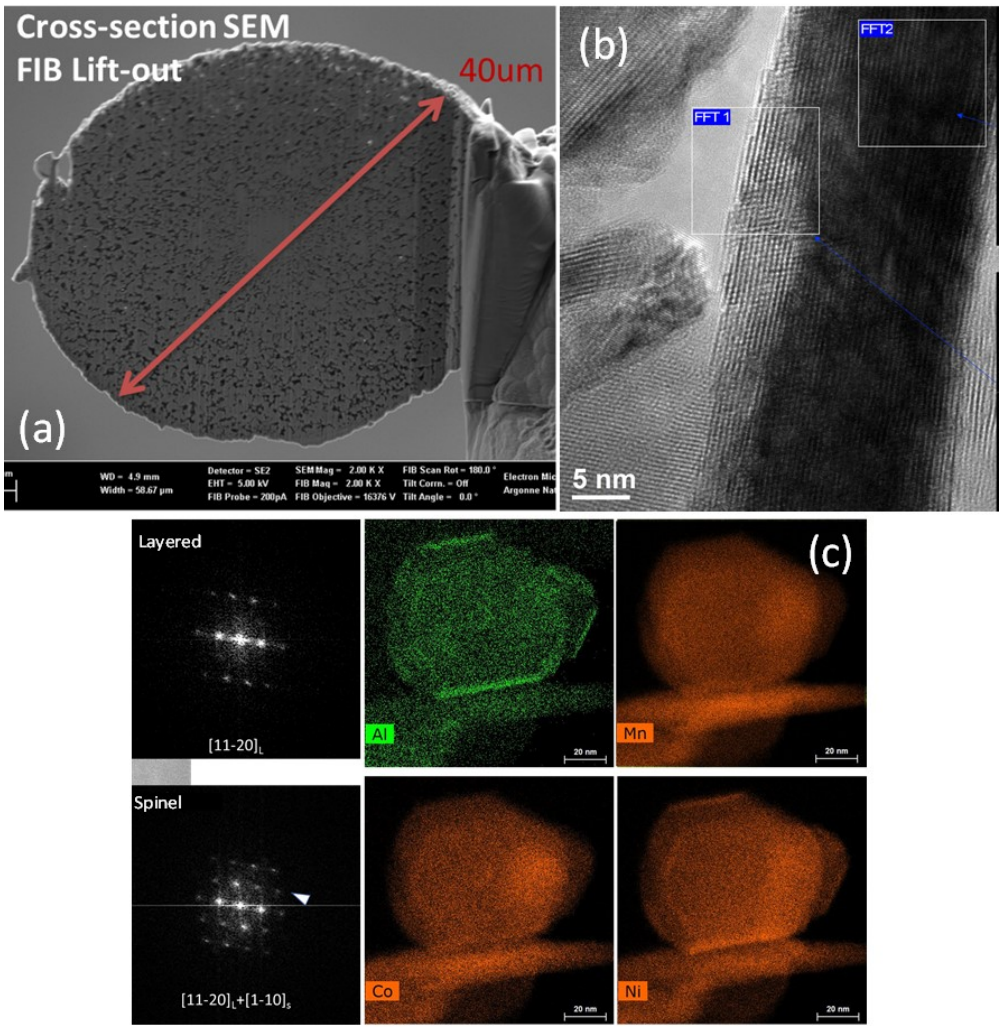


Figure II-328. (a) Cross-sectional SEM image of Al-treated, LLS particle. (b) TEM image and FFT of surface and bulk regions showing spinel integration at the surface of the particle. (c) STEM-EDX analysis of Al-treated LLS particle showing distribution of Al (top left), Mn (top right), Co (bottom left), and Ni (bottom right). HRTEM by J. Wang (ANL).

## Conclusions

- Density functional theory calculations have been used to understand and verify experimental findings showing the effects of Mn and Ni substitution in stabilizing Co-rich spinel structures for integration into complex LLS cathodes

- Synchrotron X-ray and neutron diffraction studies, on a series of $Li_{1.25-x}(Ni_{0.28}Mn_{0.53}Co_{0.19})O_{2.25-\delta}$ ($0 \leq x \leq 0.25$) LLS compositions, are being used to understand the relationships between synthesis and the final structure/electrochemical properties that result as a function of initial lithium content and transition metal composition

- Surface treatment of Mn-rich, LLS particles has shown promise for enhancing electrochemical performance, however, the studies herein show that a complex relationship exists between the cathode particles and processing conditions; importantly, Li- and Mn-rich particles behave differently than their layered counterparts under the similar surface-treatment conditions studied here

## Key Publications


1. Roy Benedek, *Role of Disproportionation in the Dissolution of Mn from Lithium Manganate Spinel*, J. Phys. Chem. C, DOI 10.1021/acs.jpcc.7b05940 (2017).

2. R. Benedek and H. Iddir, *Simulation of First-Charge Oxygen-Dimerization and Mn-Migration in Li-Rich Layered Oxides $xLi_2MnO_3 \cdot (1-x)LiMO_2$ and Implications for Voltage Fade*, J. Phys. Chem. C, 121, 6492 (2017).

3. J.R. Croy and M.M. Thackeray, *Characterization and Modeling of High-Capacity Composite Electrode Structures*, ES235, DOE Vehicle Technologies Program Annual Merit Review (Arlington, VA), 5-9, June (2017).


## References


1. E. Lee, J. Blauwkamp, F. C. Castro, J. Wu, V. P. Dravid, P. Yan, C. Wang, S. Kim, C. Wolverton, R. Benedek, F. Dogan, J. S. Park, J. R. Croy, and M. M. Thackeray, Exploring lithium-cobalt-nickel oxide spinel electrodes for ≥3.5 V Li-ion cells. *ACS Appl. Mater. Interfaces*, **8**, 27720 (2016).

2. G. L. W. Hart and R. W. Forcade, Algorithm for generating derivative structures, *Phys. Rev. B*, **77**, 224115 (2008).

3. C. Wolverton and A. Zunger, Cation and vacancy ordering in $Li_xCoO_2$, *Phys. Rev. B*, **57(4)**, 2242 (1998).

4. B. R. Long, J. R. Croy, J. S. Park, J. Wen, D. J. Miller, and M. M. Thackeray, J. Electrochem. Soc., **161** (14) A2160 (2014).

## II.D.7 *In Operando* Thermal Diagnostics of Electrochemical Cells (LBNL)

**Ravi Prasher, Principal Investigator**
Lawrence Berkeley National Laboratory
1 Cyclotron Road
Berkeley, CA 94720
Phone: 510-486-7291
E-mail: RSPrasher@lbl.gov

**Tien Duong, Technology Manager**
U.S. Department of Energy
Phone: 202-586-7836
E-mail: Tien.Duong@ee.doe.gov

Start Date: October 1, 2015 End Date: September 30, 2019
Total Project Cost: $120,000 DOE share: $120,000 Non-DOE share: $0

### Project Introduction

Effective heat dissipation in batteries is important for many reasons, such as performance, reliability, and safety. Currently, the thermal management of battery cells is provided at the system level by either forced air or liquid cooling. This engineering solution has many shortcomings, such as a reduction in the energy density at the system level and complex system designs to allow for fluid flow. In spite of such high importance, so far no thermal transport measurements or diagnostics have been performed inside electrochemical batteries under operating conditions. An understanding of thermal transport through various interfaces within the electrochemical cell is of particular importance as interfacial thermal transport typically plays the dominant role (up to 90% of the overall thermal resistance according to our preliminary measurements) in determining the internal temperature rise and temperature gradients within various devices. Currently, no thermal model exists that can predict the spatially resolved internal temperature rise within an operating battery, accurate to the true heterogeneous multilayered internal structure of the battery.

### Objectives

We will measure the dominant thermal resistances within the multilayered stack comprising the full battery cell. These measurements will be performed *in-operando* on a fully assembled and functioning battery. This will identify the layer(s) and layer interface(s) that dominate the total thermal resistance to heat flow within an operating battery, even if they are buried deep within the bulk of the battery cell, and quantify their contributions. From these measurements we will build a spatially resolved theoretical thermal model of the internal heat transfer within a battery. This model can then be used to accurately predict the internal temperature rise and temperature profile of a battery under various operating conditions, such as fast charging. This model can also be used to guide the thermal optimization of battery design and battery control software to improve performance, reliability, and safety. Such a model does not currently exist.

### Approach

The thermal measurements will be achieved using a customized derivative of the 3-omega technique. This technique uses microfabricated sensors placed on the outer surfaces of the electrochemical cell stack (see Figure II-329) to launch thermal waves at multiple frequencies into the battery and interrogate the thermal transport properties at various depths within the bulk of the cell. Our technique simultaneously measures thermal transport properties as a function of depth into the cell as well as temperature. Because the measurement is performed in the frequency domain and not the time domain, it is very robust against ambient noise. Our design enables *in-operando* measurement during battery operation because our sensors and measurements are immune to both electrical interference from the battery and thermal interference from any heat generated by the battery's own operation.

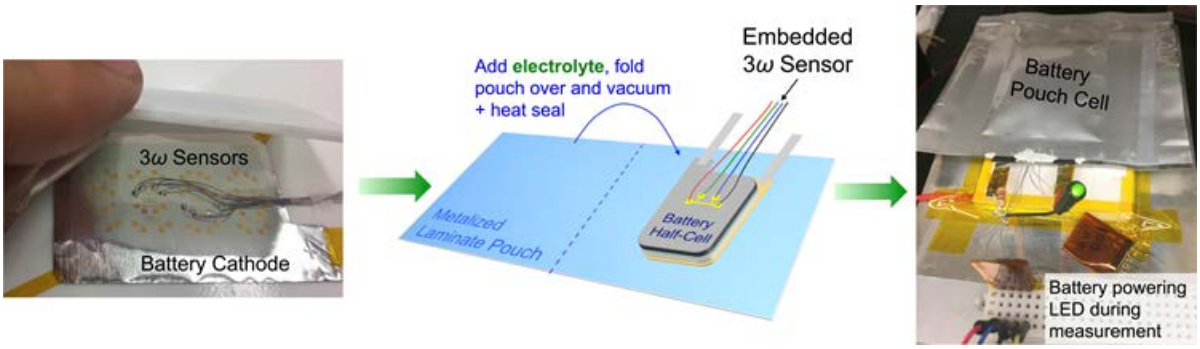


Figure II-329. Design of 3-omega thermal sensors and how they are incorporated into an electrochemical battery pouch cell for *in-operando* measurements.

We are working with the Battaglia group at LBNL in order to make lithium-ion electrochemical pouch cells inside of which we embed our sensors, and to perform electrical measurements on the batteries in addition to our thermal measurements. Because our sensors probe the interior of the battery from the surface of the multilayer stack, the sensors are non-invasive and do not disturb the local environment of the electrochemical multilayer stack. Sending in thermal waves at many different frequencies allows us to separate out the thermal transport properties at different locations throughout the depth profile of the cell.

Prior to performing any measurements, we fully simulate each experiment and numerically optimize the thermal design of the housing of our battery samples so as to maximize sensitivity to the properties of interest and minimize sensitivity to the outside environment and noise. All sensors are designed and fabricated in-house.

## Results

We have designed and constructed the metrology hardware for performing these measurements. We have verified and implemented an analytical solution to the measurement technique physics for our particular geometry. We used this solution to optimize the thermal design of the housing for our battery samples, constructing and testing this housing to confirm that it performs as designed. Based on these tests, we constructed a functioning cathode half-cell with 3-omega sensors and performed *in-situ* measurements on the cell. We found that the thermal transport through the half-cell was dominated by the thermal boundary conductance (TBC) across the cathode-separator interface. Representative fitted raw data is shown in Figure II-330.

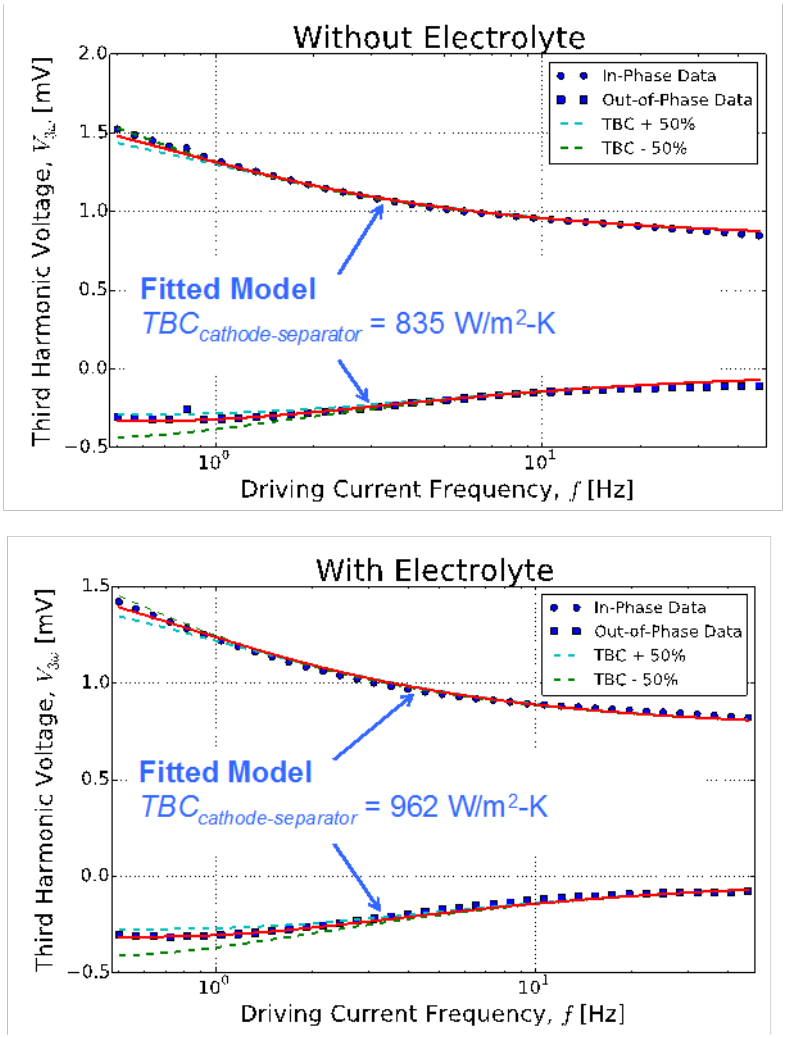


Figure II-330. Representative raw data from a measurement on a li-ion cathode half-cell. Left plot is without the presence of electrolyte; right plot is with electrolyte. Red lines show the best fit to the data. The primary property measured is the thermal boundary conductance (TBC) of the interface between the cathode and the separator. Dashed lines demonstrate fit sensitivity by showing best fit lines where the TBC value has been artificially forced to be +/- 50% as compared to the true best fit value.

Our measurements found the cathode-separator TBC value to be 835 W/m$^2$-K without electrolyte present inside the electrochemical cell, and 962 W/m$^2$-K with electrolyte present. We discovered that this interface dominates the thermal transport within the cell, accounting for over 90% of the total thermal resistance. The multilayer stack of our cathode half cell along with the break down of the relative thermal resistances of each layer and interface are shown in Figure II-331.

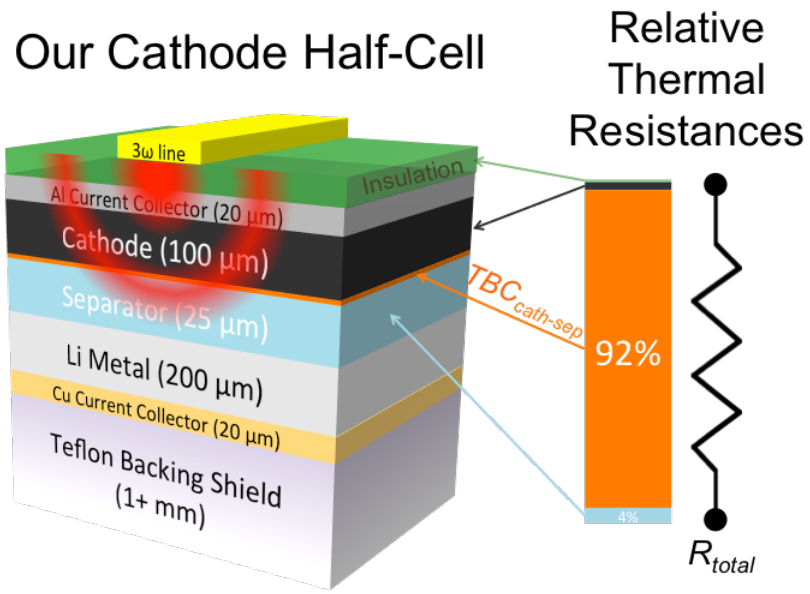


Figure II-331. Left, multilayer stack for the measured cathode half-cell, showing a 3-omega sensor launching a thermal wave. Right, a to-scale breakdown of the relative contributions of each layer and interface to the total thermal resistance. Thermal resistance contributions from the Li and Cu are negligible. Thermal waves did not probe deep enough to be affected by the Teflon, which was only included for mechanical support and is not present in the real battery.

Finally, we have made significant progress toward being able to fabricate and measure the thermal transport within a full li-ion battery pouch cell. We also recently modified our hardware to extend the low-frequency end of our measurement range from 0.5 Hz down to 0.01 Hz, which will increase the sensitivity of our measurements considerably.

## Conclusions

We have designed, characterized, and implemented a technique capable of measuring spatially resolved thermal transport properties within the bulk of an electrochemical cell *in-operando*. We have demonstrated this technique on a functioning cathode half-cell, showing that the total thermal resistance is dominated by the interface between the cathode and separator. We are preparing to measure full battery cells and will measure them under a variety of operating conditions, such as varying levels of externally applied pressure and different charge rates. We have also upgraded our equipment to improve the sensitivity of our measurements by extending the low-frequency capabilities. After completing all measurements, we will use the results to create the first theoretical model capable of accurately predicting the complete internal temperature profile of an operating electrochemical cell, accounting for the full heterogeneous multilayered internal structure of the battery.

## Key Publications

This work has been presented in part at the 2017 International Technical Conference and Exhibition on Packaging and Integration of Electronic and Photonic Microsystems (InterPACK) and the 2017 9th US & Japan Joint Seminar on Nanoscale Transport Phenomena. We are also preparing a manuscript to submit to the 16th International Heat Transfer Conference (IHTC), a section of which will be based on this work.

## II.D.8 Correlative Microscopy Characterization of Oxide Electrodes (SLAC)

**Yi Cui, Principal Investigator**
SLAC National Accelerator Laboratory
2575 Sand Hill Road
Menlo Park, CA 94025
Phone: 650-725-7515
E-mail: wchueh@stanford.edu

**William C. Chueh, Principal Investigator**
SLAC National Accelerator Laboratory
2575 Sand Hill Road
Menlo Park, CA 94025
Phone: 650-725-7515

**Michael F. Toney, Principal Investigator**
SLAC National Accelerator Laboratory
2575 Sand Hill Road
Menlo Park, CA 94025
Phone: 650-725-7515

**Tien Duong, Technology Manager**
U.S. Department of Energy
Phone: 202-586-7836
E-mail: Tien.Duong@ee.doe.gov

Start Date: January 1, 2016 End Date: March 31, 2018
Total Project Cost: $600,000 DOE share: $600,000 Non-DOE share: $0

### Project Introduction

A new cross-technique characterization platform will be developed to track lithiation dynamics at the single-particle level in Lithium- Manganese-rich Nickel Cobalt Oxide (LMR-NMC). Fundamental insights from this new diagnostic capability are expected to increase the power density and cycle life of oxide electrodes by improving electrode utilization, reducing electrochemical hotspots, decreasing capacity and voltage fade, and enhancing safety, which all improve the viability of lithium-ion batteries for vehicle transportation. By understanding lithiation at the single-particle level, this project's success will contribute to improving on-vehicle battery management, such as charging/discharging protocol, state-of-charge and state-of-health monitoring.

Due to the cost of Co, substituting Ni, Mn, Al, Mg, or Cr in the layered oxide cathode $LiCoO_2$ has become the focus of much research. LMR-NMC is of significant interest for use in electric vehicle applications due to its balance of cost and performance, with demonstrated specific capacities of 230- 280 mAh $g^{-1}$. Recharging time, power density, voltage/capacity fade, and thermal stability are important performance matrices for these battery chemistries to grain widespread use in vehicle transportation. Rational engineering of electrode chemistry and microstructure is expected to greatly increase these aspects of battery performance. However, due to the wide range of length scales involved – spanning nanometers to millimeters – a comprehensive understanding of kinetics and degradation in battery electrodes is lacking, especially at the single-primary-particle level. Part of the challenge lies in the characterization of lithiation dynamics across a wide range of length scales of realistic batteries during cycling.

This project is carried out in collaboration with Samsung Advanced Institute of Technology, who provided LMR-NMC materials, as well as scientists at Advanced Light Source and the Molecular Foundry, users facilities at Lawrence Berkeley National Laboratory.

## Objectives

This study aims to develop and utilize a correlative microscopy platform to investigate the lithiation dynamics of LMR-NMC, with the specific goal of understanding factors that determine the rate capability and degradation mechanisms at the single primary particle length scale. By developing a nanoscale and single-particle understanding of lithiation, the project addresses specific engineering problems including electrochemical hotspot, electrode utilization, safety, and capacity/voltage fade. Chemistry-sensitive soft transmission X-ray microscopy, operating in standard and in ptychography mode, will be carried out on cycling electrodes in a liquid electrolyte using a microfluidic cell. A platform to transfer the identical electrode to the transmission electron microscope and Raman microscope will be developed to integrate the X- ray, electron and optical characterization with the goal of achieving a comprehensive understanding of the lithiation dynamics at the single-particle level. Ex-situ spectro- ptychography on electrodes cycled at low (-20 °C) and high (+80 °C) temperatures will be conducted to understand the temperature dependence of lithiation dynamics, hotspots, and degradation in single particles.

## Approach

Chemistry-sensitive soft transmission X-ray microscopy, operating in standard and in ptychography mode, will be carried out on cycling electrodes in a liquid electrolyte using a microfluidic cell while the electrode is cycled between the charged and the discharged state. The expected spatial resolution is 5 nm (ptychography mode) and 50 nm (standard mode). To attain even higher spatial resolution, a platform to transfer the same electrode to the transmission electron microscope will be developed. Finally, Raman microscopy, which is sensitive to the vibrational nature of chemical bonds, will also be used to characterize the same electrode. With the seamless integration the X-ray, electron and optical characterization, the goal is to achieve a complete understanding of the lithiation dynamics at the single-particle length scale.

## Results

To understand the relationship between this structural behavior and the unique redox chemistry of LMR-NMC while decoupling surface and bulk phenomena, we obtain spatially resolved TM $L_3$ and O K edge transmission X-ray absorption spectroscopy (XAS) with ~ 30 nm resolution using scanning transmission X-ray microscopy (STXM). X-ray transparent samples were prepared ex situ through sonication and dispersion of electrodes harvested at various voltages (Figure II-332a) in an Ar glovebox and transported to the microscope with minimal air exposure. We first plot the average spectra during the first cycle in Figure II-332, obtained by averaging the 2D spectral maps obtained from STXM, which allows us to understand the gross changes in the electrode electronic structure. The spatially-averaged transmission XAS spectra obtained through STXM (Figure II-332c-f), which represent the true depth-averaged absorption spectra, show that when charging below the plateau (pristine, ‘P’ → 4.35 V, ‘1’) we observe primarily an inversion in the Ni $L_3$ edge peak ratio and a shift of the Co $L_3$ peak by +0.4 eV, correlated with the simultaneous growth of a peak at 528.5 eV in the O K pre-edge. These changes are well-understood to reflect the depopulation of hybridized $O_{2p}$–$TM_{3d}$ (antibonding) bands, constituting standard hybridized “TM–O redox”. By contrast, when charging through the voltage plateau (4.35 V, ‘1’ → 4.60 V, ‘2’), the TM $L_3$-edge spectra change minimally: the Co and Mn $L_3$ edges exhibit some broadening, and there is a small increase of the low energy peak at the Ni $L_3$ edge, suggesting a surprising reduction of the Ni during charge, which we explain later. By far the most significant change during the voltage plateau is the growth of a sharp and intense peak at 530.8 eV in the O K-edge spectrum, which indicates that predominantly $O_{2p}$ character states are depopulated during the 4.50 V plateau. The differential spectra in Figure II-332c clearly show that this feature is distinct from the peak at 528.5 eV, confirming that the two redox mechanisms are fundamentally different. We therefore refer to the 530.8 eV peak being the signature of “O redox”.

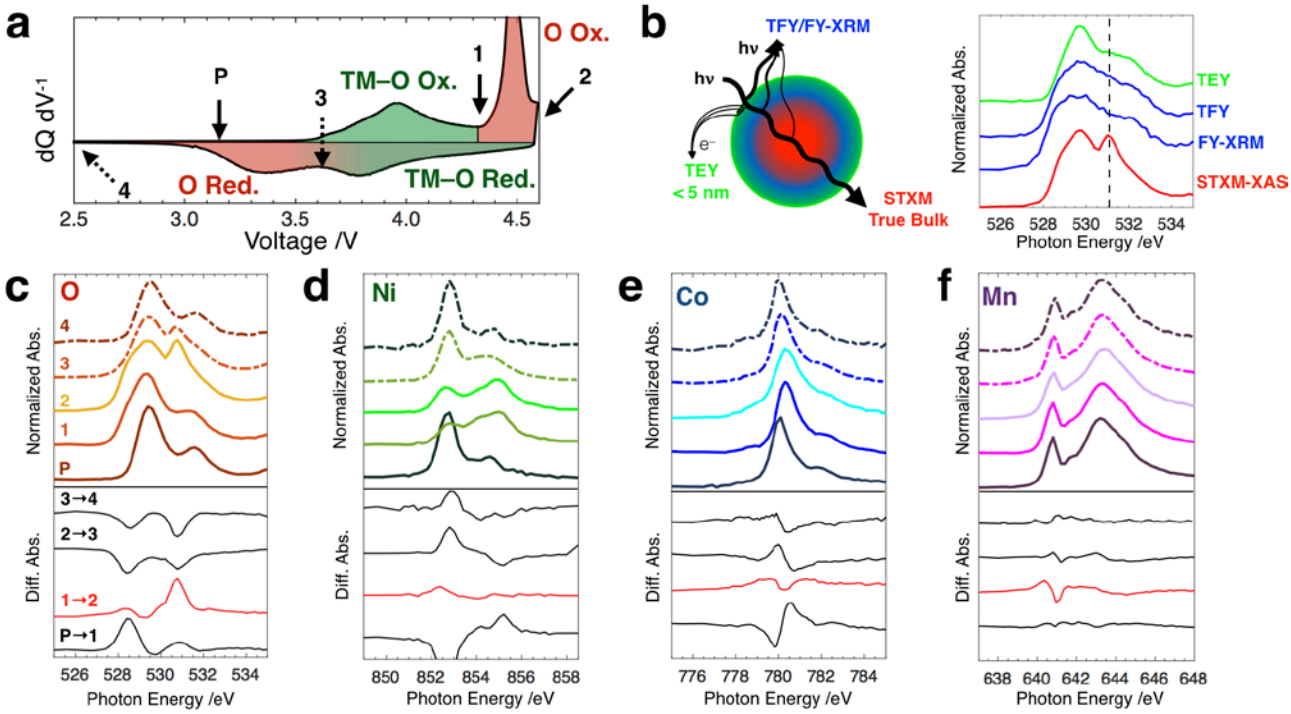


Figure II-332. First Cycle Average STXM-XAS of LMR-NMC. (a) dQ $dV^{-1}$ of the first cycle showing the voltages at which samples were harvested for STXM. The samples are pristine (P), 4.35 V (1), 4.60 V (2), 3.65 V (3), and 2.00 V (4). Regions of the dQ $dV^{-1}$ are shaded to show the hysteresis in the O redox relative to the TM–O redox. (b) Schematic and spectra comparing STXM-XAS to various other XAS detection modes (TEY, FY, and fluorescence yield X-ray microscopy, FY-XRM). (c–f) Spatially averaged transmission soft XAS throughout the first cycle at the (c) O K, (d) Ni $L_3$, (e) Co $L_3$, and (f) Mn $L_3$ edges. Solid traces indicate electrodes harvested during charge, while dashed traces indicate electrodes harvested during discharge. The red and black traces below each plot indicate the differential spectra between the points indicated.

Understanding the spatial distribution of the spectral changes during the voltage plateau can reveal whether O redox is a bulk phenomenon and whether it is correlated to changes in the TM L edges, particularly the Ni reduction, which can in turn give insight into the nature of the oxidized oxygen species. We therefore map the nanoscale distribution of the Ni $L_3$- and O K-edge spectroscopy at the single primary particle length scale during the first-charge voltage plateau. In Figure II-333 we apply principal component analysis (PCA) and non-negative matrix factorization (NMF) to a series of STXM spectro-images taken at six intermediate points along the 4.50 V plateau to identify the end-member spectra that describe the spectroscopic changes. At both the O and Ni edges, two end-member spectra were identified (Figure II-333a): the O spectra are essentially with and without the peak at 530.8 eV, while the Ni spectra resemble $Ni^{4+}$ and $Ni^{2+}$.Using these end-member spectra, we obtain the average fraction (Figure II-333b) and nanoscale map (Figure II-333c) for primary particles throughout the voltage plateau.

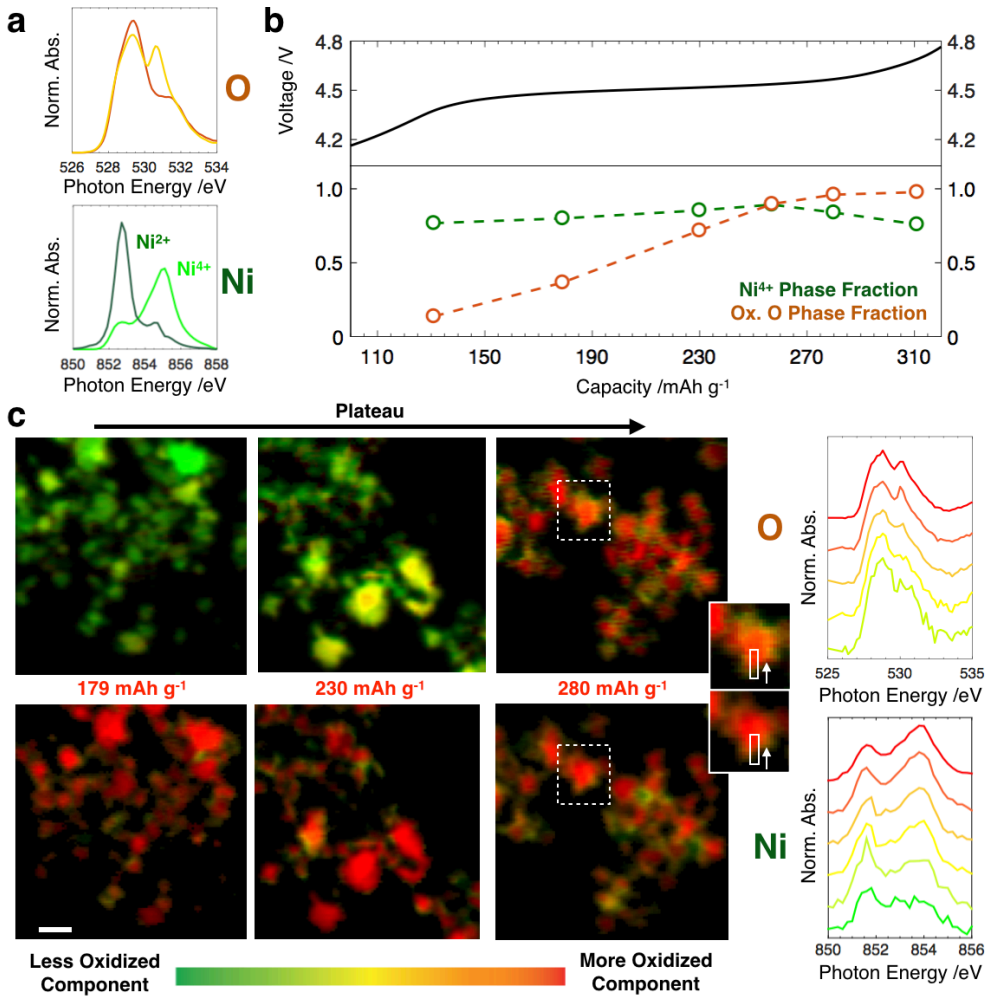


Figure II-333. Spatial Dependence of O and Ni Spectroscopic Response During 4.50 V Plateau. (a) End-member spectra at the Ni $L_3$ and O K edges throughout the first cycle plateau. (b) Total end-member fractions for each sample used in the NMF analysis as a function of capacity through the plateau. (c) Nanoscale distribution of the end-members in (a) for primary particles at different points in the voltage plateau. Scale bar is 500 nm. Right: spectral line-scans of the magnified particle showing the bulk O oxidation and surface Ni and O reduction. The spectra at the bottom correspond to the near-surface region and those at the top correspond to the bulk.

From the nanoscale O component maps (Figure II-333c, top), it is immediately evident that O oxidation occurs throughout the bulk of the primary particles during the voltage plateau, establishing unambiguously that O redox is a bulk process in LMR-NMC. On the other hand, the Ni chemical maps (Figure II-333c, bottom) reveal that bulk Ni ions remain in a 4+ oxidation state during the plateau. The variation observed in the average spectrum in Figure II-332d is in fact due to Ni reduction that is confined mostly to the primary particle surfaces. Spectral linescans in Figure II-333c show that the new peak at 530.8 eV at the O K edge is actually suppressed near the particle surfaces where Ni is reduced. In other words, although Ni reduction and O oxidation occur simultaneously during the voltage plateau, they are spatially separated. Its prevalence near the surface suggests that Ni reduction is more likely due to a steep gradient of oxygen non-stoichiometry due to oxygen evolution or reaction with the electrolyte. This is further confirmed by the redox behavior during the first discharge and second charge which reveals that discharging to 2.00 V reversibly reduces Mn near the surface with no change in the bulk. This is consistent with an electrochemically active but oxygen deficient near-surface structure that approaches the bulk composition within tens of nm. Importantly, oxygen evolution

is only a minor surface phenomenon during the first cycle of LMR-NMC and does not account for the high voltage plateau capacity, which is in fact compensated by reversible oxygen anion redox in the bulk.

Having established that oxygen redox is a major bulk phenomenon in LMR-NMC, we next investigate the nature of the oxidized oxygen species and their role in the unusual electrochemistry and voltage fade of these materials. We note that the O redox peak observed here (530.8 eV) does not appear at the absorption onset (~ 528 eV) but above it. In fact, the O redox state appears above the depopulated TM–O redox state (528.5 eV), suggesting a switch in their relative positioning after O oxidation. Thus, O redox in LMR-NMC is linked to a relative reordering of the anion and cation electronic states that cannot be described by a static $O^{2-}/O^{-}$ redox couple.

The significant change in the $O_{2p}$ states after depopulation is further confirmed in Figure II-334a, which plots the O K-edge resonant inelastic X-ray scattering (RIXS) obtained throughout the first cycle. RIXS maps the fluorescence intensity as a function of both absorption and emission energy, revealing the energy distribution buried in the features observed through STXM-XAS. For the electrode at 4.60 V, however, excitation to the new unoccupied O redox state at 530.8 eV results in a striking new emission feature at 523.75 eV, which is clearly distinct from the broad 522–527 eV emission features from the TM–O hybridized states. The distinct RIXS feature created during the 4.50 V plateau further supports the scenario of reshuffled electron states after O redox, which cannot be explained by a rigid $O^{2-}/O^{-}$ mechanism.

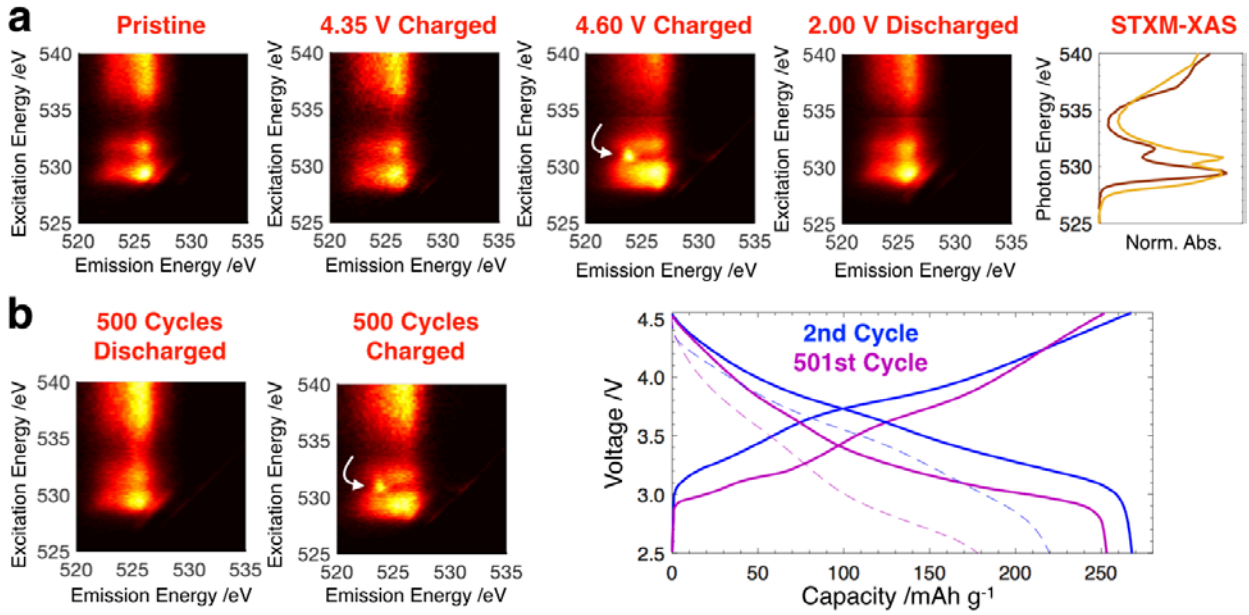


Figure II-334. Probing the Nature and Stability of Oxygen Redox. (a) RIXS maps at the voltages indicated throughout the first cycle. The unique emission signature at 4.60 V indicated by the white arrow supports an electronic restructuring associated with O redox. Right: XAS obtained in the pristine (brown) and fully charged (tan) state during the first cycle for comparison. (b) RIXS maps acquired before and after the 501st charge on an electrode cycled 500 times at 1C/2C charge/discharge rate, showing that the reversible oxygen redox feature persists for hundreds of cycles. The voltage curves for the second and 501st cycles at C/68 (solid) and 2C (dashed) show that most of the capacity fade over 500 cycles is from increased impedance and overpotential, and that the intrinsic capacity is largely retained.

Furthermore, such a mechanism was previously predicted to be unstable against oxygen evolution in 3*d* layered oxides. We therefore investigate the stability of oxygen redox over extended cycling using optimized 18650 cells (Samsung SAIT), which exhibit 94% retention of their low-rate (intrinsic) capacity after 500 cycles at a 1C/2C charge/discharge rate. Figure II-334b plots the O RIXS maps for the 501st cycle in the charged and discharged states. Clearly, a significant fraction of the oxygen anions remains redox active after hundreds of

cycles. These particles were not protected against oxygen evolution through coating. Thus, our result suggests a degree of intrinsic anion redox stability in LMR-NMC, further suggesting that the unstable rigid $O^{2-}/O^{-}$ mechanism is unlikely.

Our RIXS results suggest that O redox can be stabilized against oxygen evolution in LMR-NMC through the electronic restructuring. We now investigate how that electronic restructuring takes place and its implications for mitigating voltage fade. Figure II-333 reveals that the spectra on discharge (4.60 V, '2' → 3.65 V, '3' → 2.00 V, '4') do not follow a simple reversal of the changes observed during charge. Most notably, whereas O oxidation took place exclusively above 4.35 V during charge (after the Ni and Co had been fully oxidized to ~ 4+), during discharge the Ni and Co are almost entirely reduced first in the 4.60 – 3.65 V range ('2 → '3'), with most of the O reduction taking place later in the 3.65 – 2.00 V range ('3' →'4'). This massive > 1 V shift in the O redox voltage is illustrated by the color-coded regions in the dQ $dV^{-1}$ plot in Figure II-332a. Thus the sequence of the redox couples (i.e., the order in which electronic states are (de)populated) is inverted after the 4.50 V plateau, consistent with the altered structure and electrochemistry after the first cycle. This agrees well with our conclusion from XAS that some of the $O_{2p}$ states depopulated during the plateau are shifted from an energy below the $TM_{3d}$–$O_{2p}$ antibonding states to one above them, further confirming the electronic reshuffling associated with O redox.

Figure II-335 reveals a clear correlation between the hysteretic O redox and the fraction of TMs in the Li layer as calculated from Rietveld refinement of synchrotron XRD patterns, suggesting that the electron state reshuffling arises from a strong coupling between O redox and TM migration. To understand this coupling, we perform density functional theory calculations using HSE06 functionals (not shown here). An oxygen that was initially unoxidized and bonded to three TMs can become doubly-coordinated and oxidized, transferring its electrons to another O or a TM. The altered coordination environment of the shifted $O_{2p}$ states due to TM migration is consistent with the distinct RIXS signature, while the shifting to higher energy is consistent with the inverted bulk redox sequence observed by STXM-XAS as well as the strong correlation between oxygen oxidation state and TM migration observed through XRD.

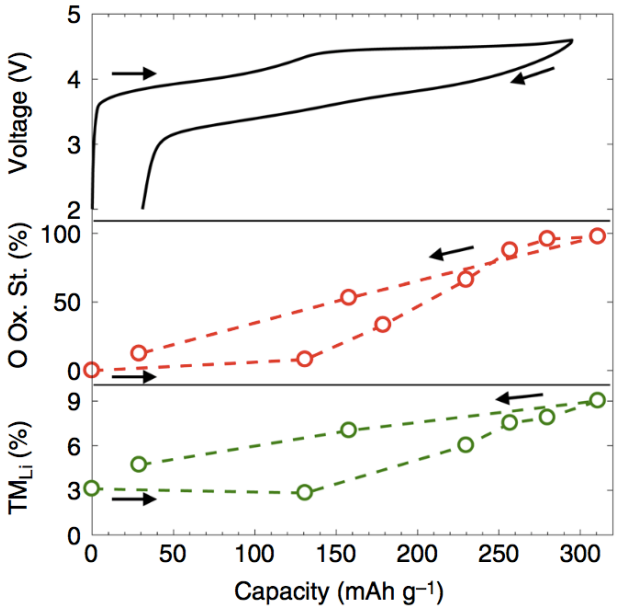


Figure II-335. Plot of the O fractional oxidation state (red) and the migrated TM fraction (green) as a function of capacity, showing the clear link between hysteresis in the TM migration and voltage hysteresis in the O redox. Error bars indicating fitting residual and refinement error for the O oxidation state and TM migration fraction, respectively, are smaller than the data symbols and are therefore not shown.

## Conclusions

We conclude that TM migration is intrinsically coupled to the O redox potential, necessarily causing the reshuffling of the relative O and TM–O redox potentials. Thus, the O redox mechanism in LMR-NMC cannot be described as a static $O^{2-}/O^{-}$ redox couple, but rather as a dynamic $\{O^{2-} + TM\} \rightarrow \{O^{-} + TM_{mig}\} + e^{-}$ process, where $TM_{mig}$ indicates a migrated TM. The substantial change and distribution in the oxygen coordination environments represented by $\{O^{-} + TM_{mig}\}$ modulates the oxygen redox potential and shifts a large fraction to lower voltage (< 3.65 V) after the first charge.

We propose that this structure-redox coupling is involved in stabi- lizing the oxygen redox couple, which we observe to persist for 500 cycles in uncoated LMR-NMC despite predictions of intrinsic instability under the assumption of static structure. Our results suggest that it may be possible to tune the stability and voltage of anion redox through control of the TM migration pathways. Thus, we suggest a new strategy for designing Li-rich layered oxides with improved cycling performance whereby the oxygen redox chemistry is tuned through structural modifications rather than the more common covalency modifications, which typically require substitution with rare 4d and 5d elements. More broadly, we demonstrate that atomic and electronic structural evolution during (de)intercalation need to be considered when assessing anion and cation redox chemistry even in nominally topotactic intercalation electrodes.

## Key Publications

1. W. E. Gent, K. Lim, Y. Liang, Q. Li, T. Barnes, S.-J. Ahn, K. H. Stone, M. McIntire, J. Hong, J. H. Song, Y. Li, A. Mehta, S. Ermon, T. Tyliszczak, D. Kilcoyne, D. Vine, J.-H. Par, S.-K. Doo, M. F. Toney, W. Yang, D. Prendergast, W. C. Chueh. Coupling Between Bulk Oxygen Redox and Cation Migration Explains Unusual Electrochemistry in Lithium-Rich Layered Oxides. *Nature Commun.* (2017). Accepted.

2. W. E. Gent, Y. Li, S. Ahn, J. Lim, Y. Liu, A. Wise, C. B. Gopal, D. N. Mueller, R. Davis, J. N. Weker, J.-H. Park, S.-K. Doo, W. C. Chueh. Persistent State-of-Charge Heterogeneity in Relaxed, Partially Charged Li1-xNi1/3Co1/3Mn1/3O2 Secondary Particles. *Adv. Mater.* **28**, 6631-6638 (2016).

## II.D.9 Understanding and Mitigating Interfacial Reactivity between Electrode and Electrolyte (ANL)

**Khalil Amine, Principal Investigator**
Argonne National Laboratory
9700 S. Cass Avenue
Argonne, IL 60516
Phone: 630-252-7380
E-mail: curtiss@anl.gov

**Larry Curtiss, Principal Investigator**
Argonne National Laboratory
9700 S. Cass Avenue
Argonne, IL 60516
Phone: 630-252-3838
E-mail: amine@anl.gov

**Nenad Markovic, Principal Investigator**
Argonne National Laboratory
9700 S. Cass Avenue
Argonne, IL 60516
Phone: 630-252-5181
E-mail: nmmarkovic@anl.gov

**Tien Duong, Technology Manager**
U.S. Department of Energy
Phone: 202-586-7836
E-mail: Tien.Duong@ee.doe.gov

Start Date: October 1, 2016 End Date: September 30, 2020
Total Project Cost: $1,600,000 DOE share: $1,600,000 Non-DOE share: $0

### Project Introduction

Lithium-ion batteries are dominant energy storage devices in modern portable electronics, and are continuously developed for emerging applications in electric vehicles and smart grids. While lithium-ion batteries have the highest gravimetric and volumetric energy density among all currently available energy storage technologies, emerging applications require longer cycle life, higher energy density and improved safety characteristics. Development of optimal electrochemical interfaces between liquid nonaqueous electrolytes and solid electrodes is needed to successfully extend cycle life and increase energy density.

The challenge for understanding dynamic behavior of solid/liquid interfaces is that many different electrochemical phenomena occur during charge/discharge cycling. These include parasitic interfacial electrochemical reactions that involve electrolyte and dissolution reactions that involve cathode materials.

The team led by Dr. Khalil Amine, Dr. Larry Curtiss and Dr. Nenad Markovic at Argonne National Laboratory (ANL) is developing new approaches to characterize solid/liquid interfaces in lithium ion batteries in order to develop understanding of interface stability during charge/discharge cycling. This will help to correlate electrochemical reactivity with composition and structure of electrolytes and electrodes to enable a rational design of solid/liquid interfaces in lithium ion batteries. This effort will increase energy density, improve safety and stability for this technology for emerging applications.

## Objectives

This project aims to develop an understanding, at atomic/molecular levels, of the stability of electrochemical interfaces during charge-discharge cycling and use the knowledge for stabilizing solid /liquid interfaces in lithium ion batteries. Our goal is to improve the stability of solid/liquid interfaces using insights into the atomic/molecular processes that limit stability during cycling. The core of this proposal is to identify, rationalize and understand the dynamics of the dissolution processes of 3d-TM cations in the cathode materials, the stability of various commercial and highly purified electrolytes comprised of organic solvents, salts and additives, and the evolution of $O_2$ and other gaseous products formed from the electrode material or the electrolyte during the charging-discharging of the Li-ion battery.

## Approach

An integrated program focused on solid-liquid interfaces in Li-ion batteries using state-of-the-art *in situ* characterization tools and computational modeling to understand and design interfaces with enhanced stability. The range of high-end analytical tools include: *A three electrode RDE (rotating disk electrode) setup; Inductively Coupled Plasma with Mass Spectrometry (ICP-MS); Gas Chromatography with Triple Quadrupole Mass Spectrometry (GC-QqQ) in Headspace sampling mode (HS); Differential Electrochemical Mass Spectrometry (DEMS).* High precision electrochemical measurements in combination with *in situ* measurements and characterization are highly suitable to investigate correlation of stability with a number of electrochemical, structural and compositional properties of the interfaces. Computational methods that provide reaction energies and barriers as well as structural information at the atomic level will be used to predict and test possible reactions that affect the stability of solid-liquid interfaces.

Collaborators include Zonghai Chen (ANL), Sanja Tepavcevic (ANL), Pietro Papa Lopes (ANL) and Peter Apol (ANL), as well as Jun Liu (PNNL) and X. He, Tsinghua University.

## Results

*High precision electrochemical system characterization of parasitic electrochemical reactions*

The home-built high precision electrochemical measurement system is used to characterize the kinetics of parasitic reactions occurring at the surface of working electrodes as shown in Figure II-336. In principle, the half-cells are constant-voltage charged/discharged to a desired potential, and the potential is held at the specific value for up to 20 hours. Then, the static leakage current is obtained as the indicator of the rate of parasitic reactions between the working electrode and the electrolyte. In addition, the cells are conditioned in an environmental chamber, which enables us to measure the kinetics of the parasitic reactions.

We demonstrated our newly developed high precision electrochemical measuring system for stability studies by revisiting the corrosion (or anodic dissolution) process of aluminum foils in non-aqueous electrolytes. The measured static leakage current grows roughly exponentially with the applied potential, indicating an ongoing electrochemical oxidation of electrolyte on the carbon coated aluminum foil. The measured parasitic current increased exponentially with the holding potential, indicating an electrochemical oxidation of a certain species as shown in Figure II-336(c).

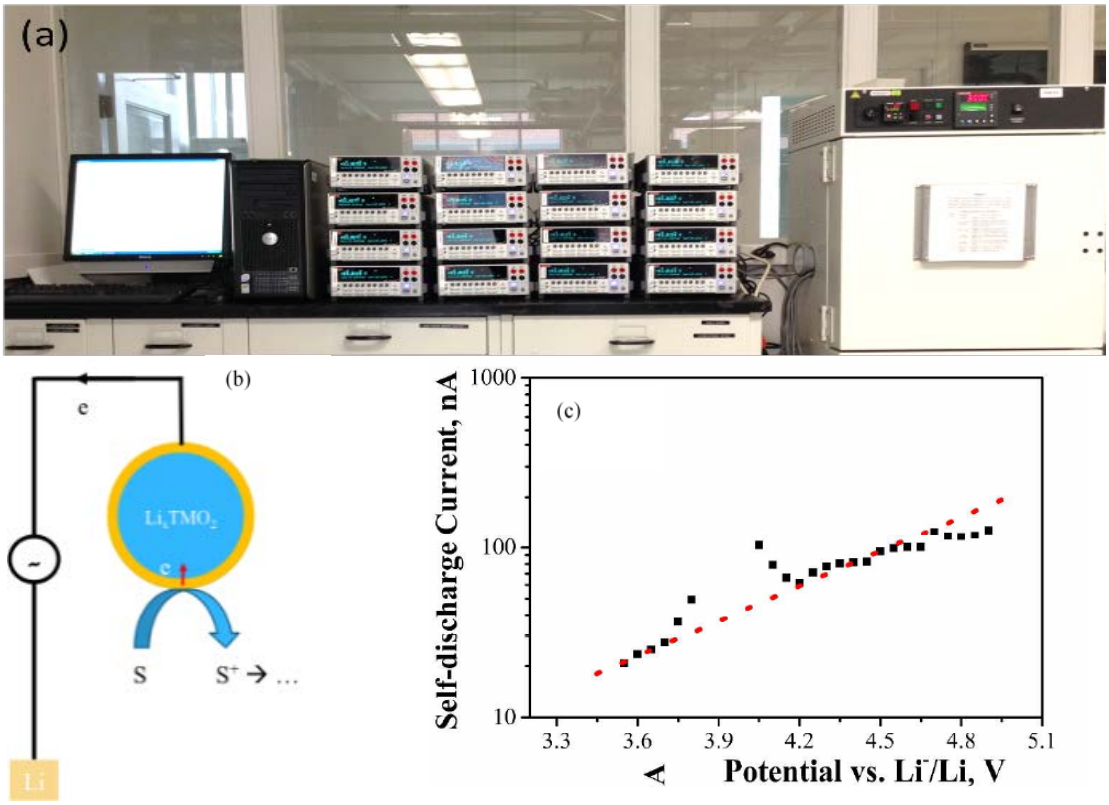


Figure II-336. (a) Picture of a 16-channel high precision leakage current measuring system; (b) schematics showing the connection between the leakage current and the rate of parasitic reactions; (c) evolution of the static parasitic current as a function of the holding potential for the bare aluminum foil. The electrolyte used was 1.2 M LiPF6 in EC/EMC (3:7 by mass). We have shown that that this reaction is related to the oxidation of ethylene carbonate.

*Revisiting corrosion of aluminum current collector*

In order to get insight into the parasitic reactions we carried out XPS analysis for aluminum foils before and after anodic treatment. The control experiment was carried out with bare Al foil and a weak absorption peak was observed at about 73 eV. This corresponds to the binding energy of metallic aluminum. The strong peak at 75.6 eV was assigned to a $Al_2O_3$ thin film on the surface of the aluminum foil. It shows that as-used non-aqueous electrolyte with the presence of possibly a trace amount of moisture was not enough to convert the $Al_2O_3$ layer into a more stable passivation layer of $AlF_3$. After anodic treatment at 3.9 V (20 hours), the absorption peak for $Al_2O_3$ at 75.6 eV disappears and a new peak at 77.2 eV appears. This new peak corresponds to the binding energy of $AlF_3$. A similar result was found for the sample anodized at 4.8 V for 20 h. A depth profile analysis of the XPS results revealed that the sample without anodic treatment was mostly covered by 15−25 nm of $Al_2O_3$; anodic treatment at 3.9 V led to a deposition of about 5 nm of $AlF_3$ on the top of the thinned $Al_2O_3$ layer (10−20 nm). Although a substantially higher parasitic current was measured at 4.8 V, no significant change of the thickness of the $AlF_3$ layer and embedded $Al_2O_3$ was observed. This indicates that the interface of the aluminum foil was stabilized by the $AlF_3$ coating that was electrochemically triggered by the oxidation of solvent to generate protons on the surface. After repeated cycling between 3.4 and 4.9 V for five cycles, it was observed that the open gap at about 3.9 V disappeared, primarily due to stabilization of the aluminum surface. In addition, the open gap associated with the corrosion of $Al_2O_3$ was pushed to a higher potential when EC was replaced with fluorinated EC. Also, the gap almost disappeared when both EC and EMC were replaced with a mixture of fluorinated carbonate and fluorinated ether, indicating that EMC also plays a major role in Al corrosion. These XPS results support the hypothesis that that the degradation of aluminum foil at high potentials is a coupled electrochemical-chemical reaction, i.e., the electrochemical

oxidation of organic solvents such as EC and EMC at high potentials triggers the chemical corrosion of aluminum foils.

Density functional theory calculations using models representative of current collector's surface basic groups indicate that redox potential can decrease even more than that when the proton is transferred to either hydroxyl (by 1.4 to 2.5 V) or thiol group (by 1 to 2 V) coordinated to aluminum. Larger calculations on either hydroxyl group or a bridging oxygen site on amorphous alumina models similarly indicate that the alumina promotes the deprotonation reaction for the radical cation (EC+). We found that the degradation of aluminum foil at high potentials is a coupled electrochemical-chemical reaction; the electrochemical oxidation of organic solvents at high potentials triggers the chemical corrosion of aluminum foils.

The role of carbon was further investigated given that carbon is mostly resistive to chemical corrosion in an acidic environment. A layer of carbon black was deposited on the surface of the aluminum foil. The electrochemical characterization showed that the static parasitic current measured increased almost 10-fold (see Figure II-337a), compared to what was found previously for non-coated aluminum foil. This increase of parasitic current could be a result of either an increase in the active electrochemical surface area or a decrease of charge transfer impedance at the interface of the aluminum foil. Considering the high loading of carbon black physically cast on the sample, the high parasitic current shown in Figure II-336a must be dominated by the reduction of charge transfer impedance across the interface due to the carbon coating, which is intended to protect the aluminum foil from the chemical corrosion in an acidic environment. In addition, graphene with a low out-of-plane electronic conductivity was also deposited on the aluminum foil. The results showed that the measured parasitic current was substantially lower than that for the carbon-coated samples but not better than that for the uncoated sample (see Figure II-337b). Finally, $AlPO_4$, which is an electronic insulator and also resistive to corrosion in an acidic environment, was coated on the surface of aluminum foil, and a dramatic change in the parasitic current was observed with the $AlPO_4$ coating (see Figure II-337c). First, the corrosion window shown at about 3.9 V completely disappeared because the coating layer is really resistive toward reaction with protons, resulting in a constant charge transfer impedance throughout the whole course of the potential sweep. In addition, the maximum parasitic current measured for the $AlPO_4$-coated sample was about 50% that of the non-coated sample, implying that a significantly smaller amount of proton is expected at similar operation conditions. Thus, these results further confirm our hypothesis that the corrosion reaction of aluminum foil at a relatively high potential is a coupled electrochemical−chemical reaction.

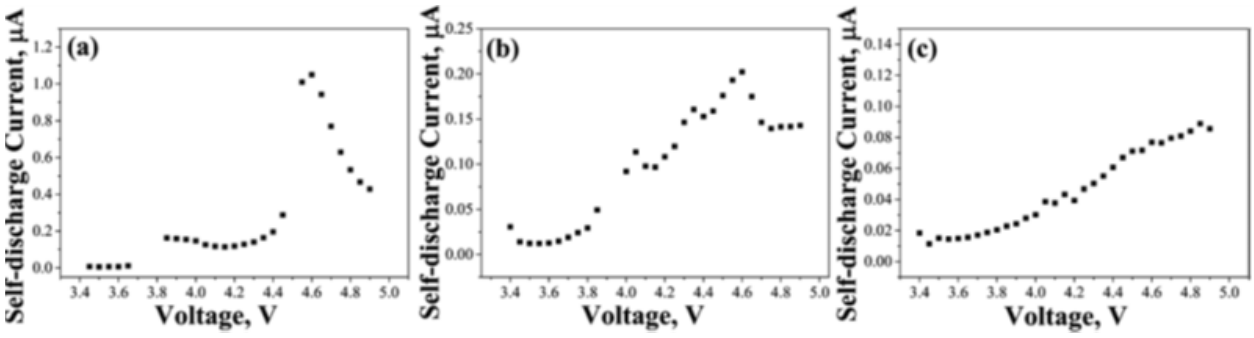


Figure II-337. (a) Potential dependence on the static parasitic current for aluminum foil with surface coating of (a) carbon, (b) graphene, and (c) AlPO4.

*ICP-MS measurements of TM dissolution*

This methodology allows simultaneous monitoring of charge/discharge process arising from Li de-intercalation/intercalation in cathode material and the kinetics of transition metal dissolution as a function of time and potential. Experiments done on a three electrode setup enable identification of electrochemical currents arising solely from the cathode material. To underpin the instabilities of $LiCoO_2$ at higher potentials, the *first-of-its-kind* experiment of *in situ* dissolution of Co monitored by a SPRDE-ICP-MS setup. Our first

experiments already demonstrated the power of such methodology in gaining fundamental knowledge on electrochemical interfaces of high energy cathodes, inaccessible by conventional battery testing. With a *stationary probe* for coupling to ICP-MS, we can probe the kinetics of intercalation/de-intercalation and kinetics of 3d-TM ions dissolution simultaneously as a function of time and potential. For example, while up to 4.2 V de-intercalation of Li is already taking place, we observe significant dissolution of Co only above 4.5 V vs $Li/Li^+$, indicative that interplay between charging/discharging processes to corresponding Co dissolution may occur.

While our first experiments to measure *in situ* dissolution of Co from $LiCoO_2$ under charging as monitored by a SPRDE-ICP-MS setup served to demonstrate the method, the results shown in Figure II-338 provided the first quantitative real-time analysis of cobalt dissolution that happens during charging of $LiCoO_2$ in 1.2M $LiPF_6$ in EC:EMC 3:7 electrolyte. We first explored the dynamics of Co dissolution during potential step transients from 3 V vs $Li/Li^+$ to an upper potential limit (UPL) that lasted 300 seconds per step. At each consecutive step we increased the UPL from 4 V up to 5 V vs $Li/Li^+$ in 0.2 V increments. As observed from Figure II-338, the first potential step to 4 V was enough to trigger a very small transient of Co dissolution that quickly decayed to the same level of signal as in the background. Consecutive steps up to 4.2 and 4.4 showed only this transient behavior as well. However, for potential steps starting at 4.6 V and above it becomes clear that the dissolution current is composed of the initial transient and additional continuous dissolution kinetics. While the charging current is of the order of 1 $mAcm^{-2}$ at 4.6 V, the respective Co dissolution current is 3 orders of magnitude smaller, indicating that any degradation process that involves cobalt dissolution is only happening at the surface of the material and is not a bulk process as intercalation/de-intercalation.

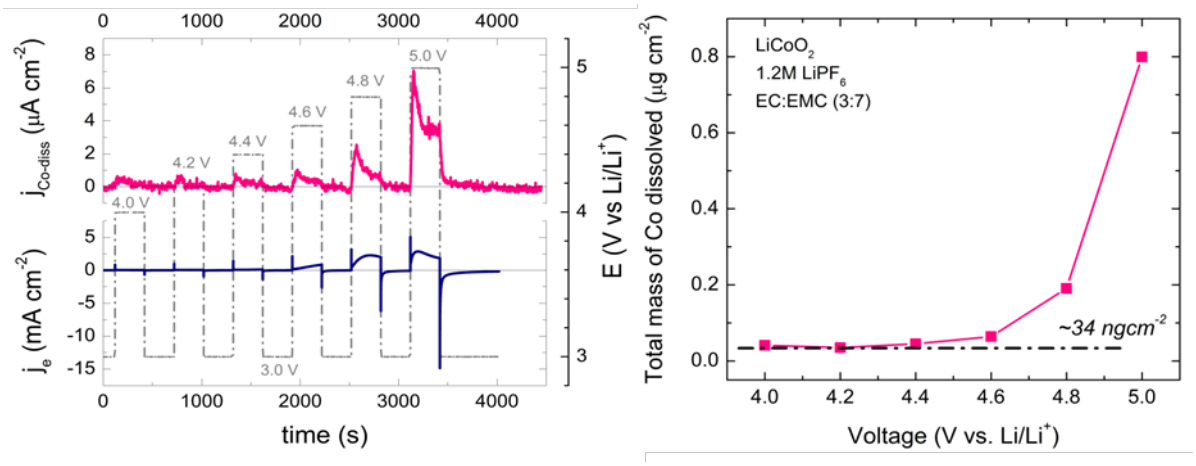


Figure II-338. (left) In Situ ICP-MS results of Co dissolution upon electro-chemical polarization using the SPRDE system. Working Electrode: LiCoO2/C/PVDF. Electrolyte: 1.2M LiPF6 in EC:EMC (3:7 by mass); (right) Total amount of Co dissolution upon electro-chemical polarization using as monitored by the SPRDE-ICP-MS system.

In order to gain deeper insight on how much of Co dissolved after the potential steps, Figure II-338 (left shows the total amount of Co dissolution, obtained as the area under the dissolution curve shown in Figure II-338 (right), as a function of the upper potential limit. While the trend of increasing dissolution with increasing UPL is clear, the amount of Co dissolved reveals the importance of surface processes in battery stability dynamics. Even though the Co dissolution transients that were observed at 4 V are small, the amount of cobalt loss represents a significant portion of the electrode surface (a few percent), which helps to understand why there would be a loss of electrical contact between different particles as their surface are evolving after multiple cycles. Therefore, our unique capability for monitoring in situ dissolution of TM from battery cathodes can provide deeper understanding on the fundamental processes responsible for performance degradation in Li-ion batteries.

## Conclusions

During the past year we have demonstrated use of high precision electrochemical system characterization of parasitic electrochemical reactions by revisiting corrosion of aluminum current collector. We have shown that the corrosion reaction of aluminum foil at a relatively high potential is a coupled electrochemical−chemical reaction. We have also shown that the maximum parasitic current measured for the $AlPO_4$-coated sample was about 50% that of the non-coated sample, implying that significantly smaller amounts of protons are expected at similar operation conditions.

The first-of-its-kind experiment of in situ dissolution of Co monitored by a SPRDE-ICP-MS setup demonstrates simultaneous monitoring of charge/discharge process arising from Li de-intercalation/intercalation in cathode material and the kinetics of transition metal dissolution as a function of time and potential. We have shown that at 4.6 V, any degradation process in $LiCoO_2$ that involves cobalt dissolution is only happening at the surface of the material and is not a bulk process as intercalation/de-intercalation.

## Key Publications

1. “Revisiting the Corrosion of the Aluminum Current Collector in Lithium-Ion Batteries,” Tianyuan Ma, Gui-Liang Xu, Yan Li, Li Wang, Xiangming He, Jianming Zheng, Jun Liu, Mark H. Engelhard, Peter Zapol, Larry A. Curtiss, Jacob Jorne, Khalil Amine, Zonghai Chen, J. Phys. Chem. Lett., **8** (5), 1072-1077, (2017), DOI: 10.1021/acs.jpclett.6b02933

# II.E Next-Gen Lithium-Ion: Modeling Advanced Electrode Materials

## II.E.1 Electrode Materials Design and Failure Prediction (ANL)

**Venkat Srinivasan, Principal Investigator**
Argonne National Laboratory
9700 S. Cass Avenue
Lemont, IL 60439
Phone: 630-252-6003
E-mail: vsrinivasan@anl.gov

**Tien Duong, Technology Manager**
U.S. Department of Energy
Phone: 202-586-7836
E-mail: Tien.Duong@ee.doe.gov

Start Date: October 1, 2016 End Date: September 30, 2017
Total Project Cost: $400,000 DOE share: $400,000 Non-DOE share: $0

### Project Introduction

The next-generation lithium ion batteries are expected to use lithium metal-based anodes, which offer low reduction potential and superior specific capacity. The biggest drawback preventing widespread usage of lithium metal anodes is the formation of dendrites over multiple cycles during operation at higher current densities. Insight gained from this project will provide guidance in designing solid polymer electrolytes (or protective layers) that prevent the growth of dendrites on lithium metal.

At the end of this project, a mathematical model will be developed that can capture the mechanical stress field, concentration and potential profiles around a dendritic protrusion. This model will allow estimation of the propensity for growth of such a protrusion and provide guidance in the design of solid polymer electrolytes (or protective layers) for the prevention of lithium dendrites.

### Objectives

The goal of this project is to develop a continuum-based mathematical model to (i) investigate the impact of mechanical stress on the growth of dendritic protrusions and (ii) elucidate the competition between transport and mechanical means for preventing dendrite growth. Effectiveness of protective layers in preventing the growth of dendritic protrusions will also be studied. The main focus of this project will be to develop a microscale model that can capture the mechanical stresses and transport processes within lithium metal and adjacent electrolyte and/or protective layer. Impact of surface energy on growth of dendrites will be investigated. Possibility of plastic deformation within lithium metal and/or solid electrolyte material will also be elucidated along with its effect on propagation of dendrites. Propensity of fracture within the solid electrolyte interface layer (or the protective layer) and its impact on dendrite growth will be explored.

### Approach

The present work examines the propensity for growth of a dendritic protrusion on a lithium metal electrode. Operation at low as well as high current density has been considered. Elastic-plastic deformations of both lithium metal and PEO-based polymer electrolyte have been taken into account. To capture the correct mechanical deformation of the lithium metal anode, dendritic protrusion and polymer electrolyte, the momentum balance (equilibrium) equation has been solved throughout the system. For estimation of the current distribution, the primary current (due to potential gradient), secondary current (due to electrode

kinetics), and tertiary current (due to concentration gradient) have been calculated. This requires solving the charge and mass conservation equations coupled with the nonlinear Butler-Volmer electrode kinetics relation. During the charging process, lithium gets reduced at the metal anode. Since lithium gets plated on top of the electrode, no lithium transport equation needs to be solved within the lithium metal anode phase. However, charge transport within the electrolyte and the metallic anode phase must be determined. Also, local charge neutrality must be satisfied everywhere to ensure no accumulation of electric charge anywhere within the electrolyte or metallic lithium. This is accomplished by setting the time-dependent accumulation terms to zero within the charge transport equations.

To estimate whether a dendritic protrusion will grow into a complete dendrite or not, the reaction current at the peak ($i_{peak}$) and the valley ($i_{valley}$) is determined. The magnitude of reaction current is calculated using the modified version of the Butler-Volmer equation, which has contributions from both the mechanical-stress and concentration-overpotential induced components:

$$i_{BV}\left(x\right)=\exp\left(\alpha_a\Delta\mu_{e^-}/RT\right)\cdot Fk_a^{\alpha_c}\left(k_c c_e\right)^{\alpha_a}\left[\exp\left(\alpha_a F\eta/RT\right)-\exp\left(-\alpha_c F\eta/RT\right)\right] \quad (1)$$

Here, $k_a$ and $k_c$ are the anodic and cathodic reaction rate constants, and $\alpha_a$ and $\alpha_c$ are the anodic and cathodic transfer coefficients, respectively. Also, $\Delta\mu_{e^-}$ indicates the electrochemical potential change induced by mechanical stresses and surface curvature effects. Moreover, $F$ denotes Faraday's constant, $R$ denotes the universal gas constant and $T$ signifies the local temperature on the Kelvin scale. For the reduction of lithium ions at the lithium metal anode, the anodic and cathodic rate constants are assumed to be equal ($k_a=k_c$). Also, the anodic and cathodic transfer coefficients have been assumed to be equal for reduction of lithium metal by several other researchers, so that $\alpha_a=\alpha_c=1/2$. The magnitude of over-potential at the lithium-electrolyte interface is estimated as $\eta=\phi_s-\phi_e-U_{Li}$, which takes a negative value during the reduction process. Here, $\phi_s$ and $\phi_e$ indicate the solid phase potential and electrolyte phase potential, respectively. The open circuit potential for lithium metal has been denoted by $U_{Li}$, which is taken to be zero.

If the reaction current density at the peak of the protrusion is greater than that at the valley ($i_{peak}>i_{valley}$), dendrites can grow. Otherwise, under the condition that $i_{peak}<i_{valley}$, relatively flat lithium deposits would form. Here, propensity of dendrite growth will be analyzed based on the ratio of current at the peak and the valley.

Since the stress values around the dendritic protrusion appear within the modified Butler-Volmer relation (see Eq. (1)), mechanical deformation of lithium metal and polymer electrolyte must be determined appropriately. Since mechanical equilibration occurs at the speed of sound, it is much faster than the chemical reactions that occur at the lithium-electrolyte interface. Hence the quasi-static equilibrium equation, derived from the momentum balance relation, should be solved to capture the stress field. Also, under the application of sufficiently large tensile or compressive loads, all bulk materials deform in an elastic-plastic fashion. Lithium metal and polymer electrolytes are no exception to that. Hence, to determine the appropriate stress field around a dendritic protrusion, the exact elastic-plastic nonlinear stress-strain constitutive relations must be taken into consideration. To describe the elastic portion, Young's modulus ($E_{Li}$ and $E_{PEO}$) and Poisson's ratio ($\nu_{Li}$ and $\nu_{PEO}$) are sufficient. These are readily available in the literature for both lithium metal as well as PEO-based polymers. Characterizing the plastic deformation of lithium and the polymer electrolyte is more challenging. In the present context, a nonlinear hardening law has been. For both lithium metal and polymer electrolyte, the magnitude of the yield stress changes according to an isotropic strain hardening law.

## Results

It has been observed in several experiments that dendrite growth in lithium metal can be prevented to some extent by the application of mechanical stress. However, how the stress field prevents the growth of dendrites has not been studied extensively. Newman et al., have published two articles investigating the stress state and subsequent deformation of lithium metal and the adjacent electrolyte phase (*JES* (2005) A396 and *JES* (2014) A1350), in which they considered lithium electrodes in a *pre-stressed* state. They found that prevention of dendrite growth by mechanical means is only possible by using electrolytes with shear modulus at least two times larger than that of lithium metal. The *pre-stressed* condition led to severe dendrite growth even during operation at extremely low current densities. The present study assumed that the lithium metal begins in a *relaxed* state. A schematic diagram of the *pre-stressed* and *relaxed* condition is shown in Figure II-339.

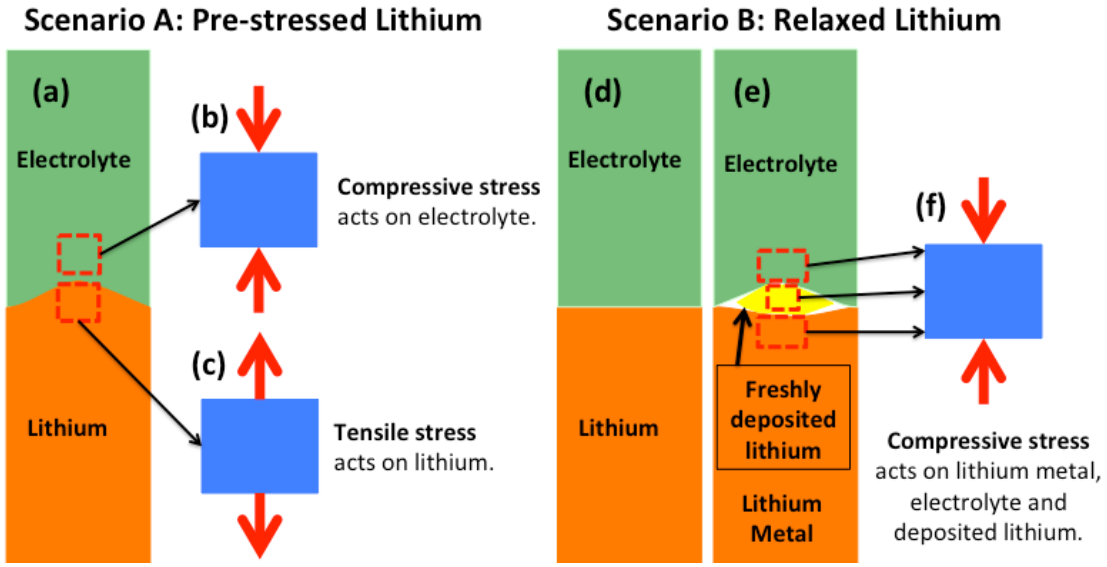


Figure II-339. (a-c) According to the *pre-stressed* lithium scenario, tensile stresses act within lithium metal and compressive stresses act inside electrolyte. (d-f) *Relaxed* lithium assumes stress-free condition for lithium metal and electrolyte. When fresh lithium gets deposited, bulk lithium metal, electrolyte and the newly deposited lithium experience compression.

Detailed simulations have been conducted to estimate the deformation and stress generation in a lithium metal protrusion and adjacent electrolyte for different shear modulus of the electrolyte phase. An electrochemical potential term has been defined that incorporates the impact of mechanical stress and surface tension into the effective exchange current density. Figure II-340(a-c) demonstrates that during operation at low current density, initially *relaxed* lithium does not lead to any dendrite growth, whereas the *pre-stressed* lithium leads to severe dendrite formation, which is not typically observed experimentally. Hence, for all subsequent analysis, lithium metal in an initially *relaxed* condition will be considered.

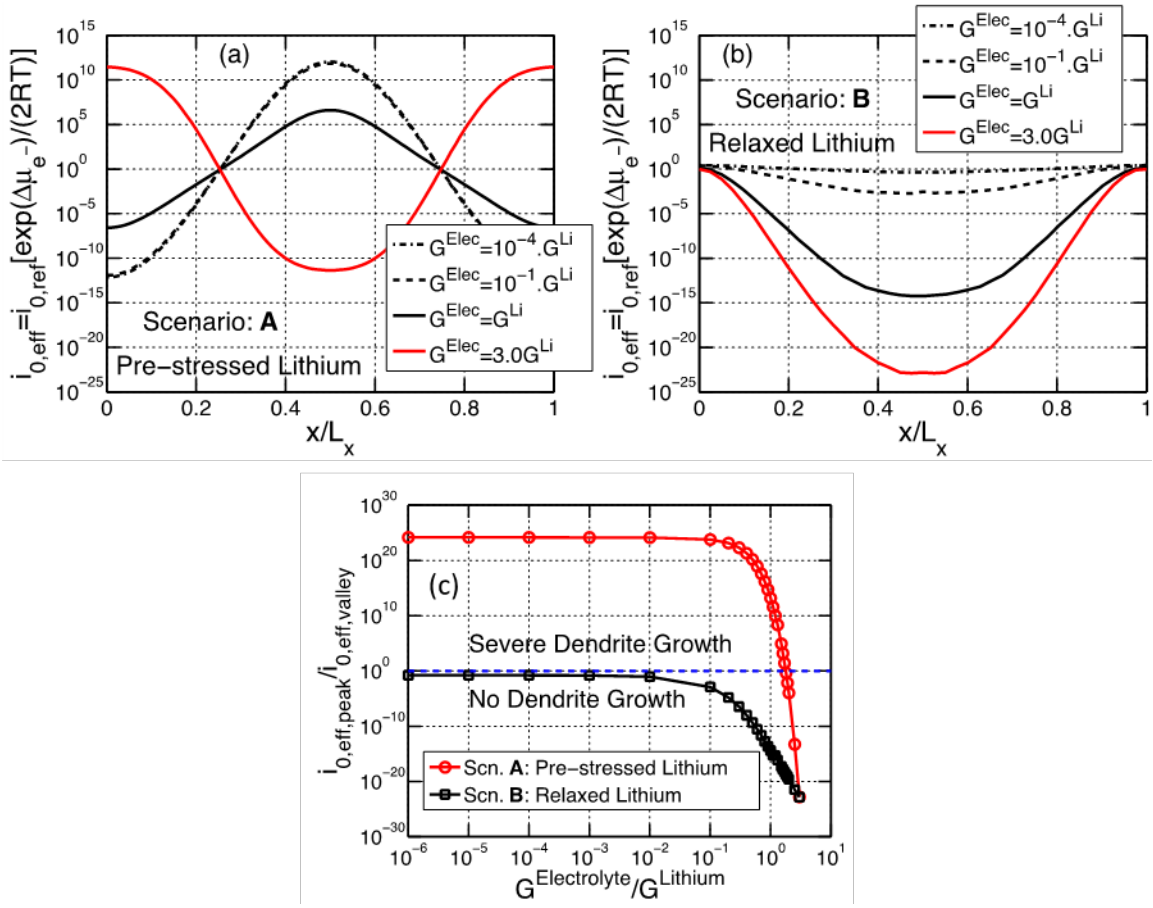


Figure II-340. (a-b) Variation in effective exchange current density around the dendritic protrusion. If the current at the peak is greater than that at the valley, dendrites grow. (a) For pre-stressed lithium. (b) For initially relaxed lithium.(c) Ratio of the effective exchange current density at the protrusion peak over that at the valley. For initially relaxed lithium, dendrite growth never occurs at low current operation.

Several researchers have argued that growth of dendritic protrusions during deposition of lithium metal can be prevented by the application of externally applied mechanical stress. This possibility is explored in the present project. In the first quarter, it was determined that the components of typical Li/solid electrolyte/Li cells are in stress-free states prior to assembly, which has significant implications for the evolution of tensile and compressive stress at the lithium-electrolyte interface. Work in the second quarter has built on this finding to investigate the effectiveness of a PEO-type polymer-based electrolyte in preventing the growth of dendritic protrusions. This has demonstrated that plastic deformation of lithium metal and polymer electrolyte must also be considered. Figure II-341(a) depicts the computational mesh for lithium metal with a dendritic protrusion and a PEO-based electrolyte, before and after cell assembly. Figure II-341(b) demonstrates that, under the assumption of only elastic deformation, the compressive stress that evolves within the lithium and polymer greatly exceeds the yield limits in both regions, over much of the interfacial region. Hence, proper elastic-plastic stress-strain constitutive relations must be used to correctly predict the hydrostatic and deviatoric stresses within the lithium and polymer regions.

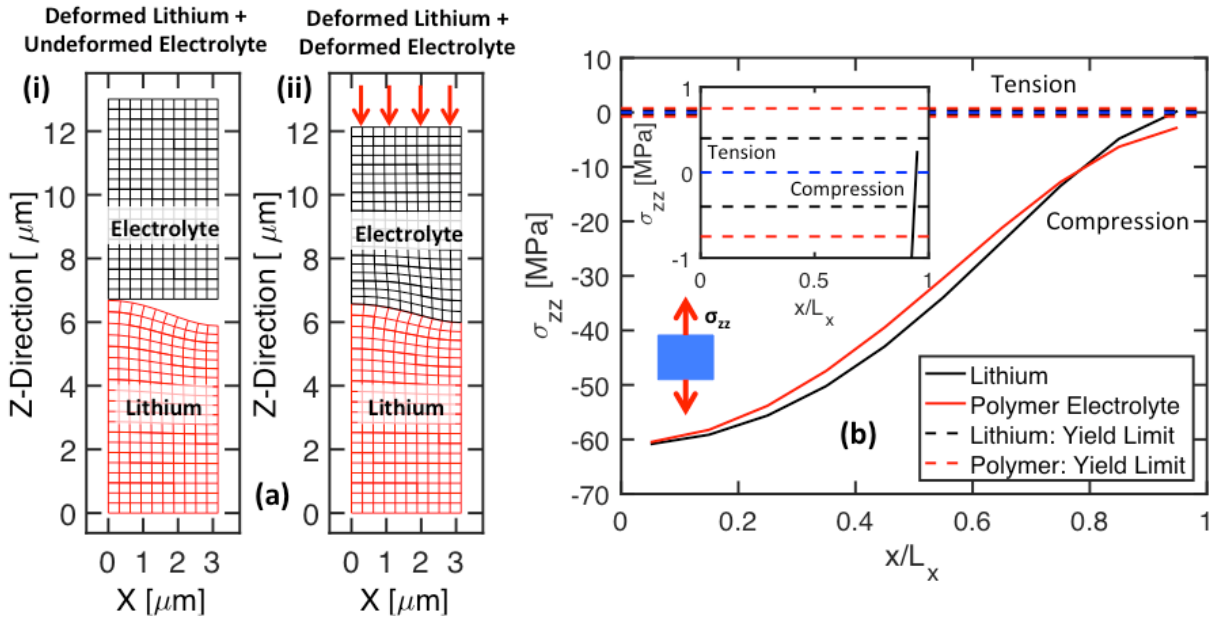


Figure II-341. (a) Lithium and polymer electrolyte regions (i) before assembly and (ii) after the regions are fully in contact. Both lithium and polymer have deformed plastically. (b) Stresses within lithium metal and polymer electrolyte regions under the assumption of only elastic deformation. The stresses exceed the elastic limits across much of the domain.

Nonlinear, isotropic elastic-plastic constitutive models including strain-hardening have been adopted to capture the stress-strain relationships observed in lithium metal and PEO-based polymers. Comparisons between the experimental data (obtained from literature) and the computational models for lithium and pure PEO are shown in Figure II-342(a) and Figure II-342(b), respectively. The ratio of effective exchange current densities at the protrusion peak and valley as a function of the electrolyte shear modulus is shown in Figure II-342(c), with the model including plasticity clearly predicting a much smaller current ratio.

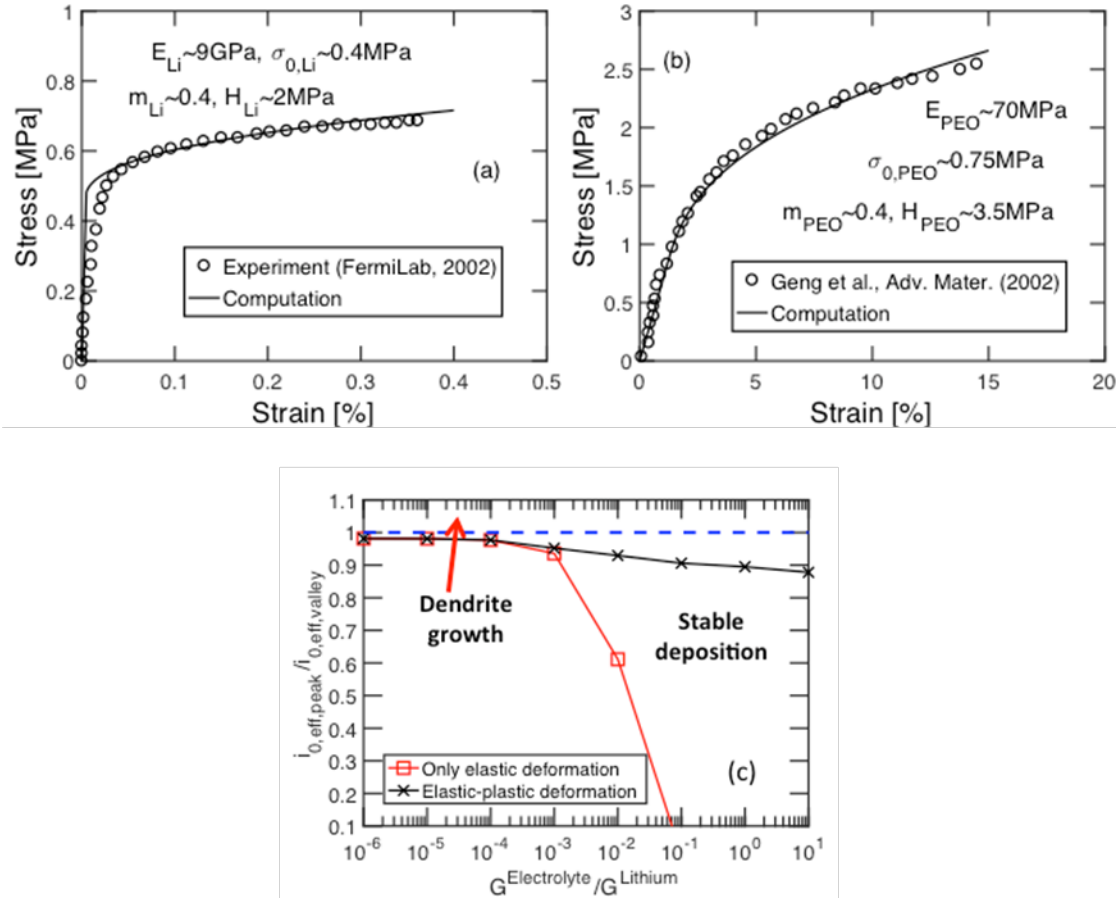


Figure II-342. (a) Computational model compared with elastic-plastic stress-strain experimental data. (b) Experimental stress-strain curve for PEO polymer and corresponding numerical model. (c) Ratio of effective exchange current density at the protrusion peak over that at the valley using purely elastic (squares) or elastic-plastic (crosses) models.

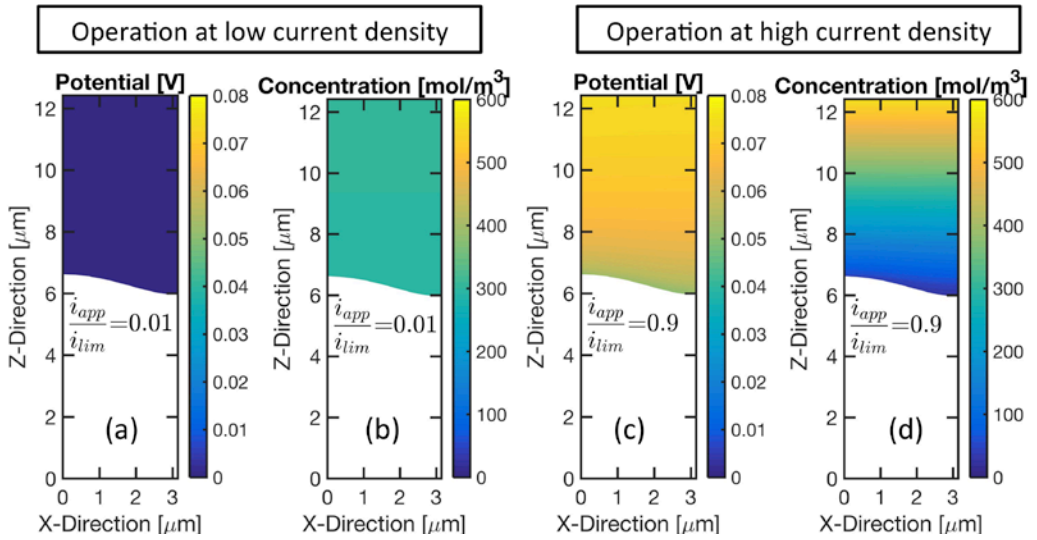


Figure II-343. Concentration and potential contour within the electrolyte around the dendritic protrusion at high and low rates of current. Potential in lithium metal remains extremely close to zero. (a) Potential contour for $i_{app} = 0.01 i_{lim}$. (b) Concentration contour for $i_{app} = 0.01 i_{lim}$. (c) Potential contour for $i_{app} = 0.9 i_{lim}$. (b) Concentration contour for $i_{app} = 0.9 i_{lim}$.

In a lithium ion battery, formation of lithium dendrites depends significantly on the distribution of potential and salt concentration within the electrolyte, which is again affected by the applied current density. The total reaction current around the dendritic protrusion should be estimated according to the Butler-Volmer equation. As shown in Eq. (1), The first exponential term is the mechanical-stress factor and the remaining portion is the conventional Butler-Volmer expression. Mass transport and charge balance equations have been solved in the electrolyte and the lithium metal. Figure II-343(a-d) shows the potential and concentration contours observed at low and high current density operations within electrolyte around the dendritic protrusion.

Variation in reaction current density from protrusion peak to valley has been shown in Figure II-344(a), by the black lines, for two different applied current densities (circle – high current, and square – low current). The reaction currents have been normalized with respect to the current density at the protrusion peak. Relative contribution from the mechanical-stress factor (blue line) and the concentration-overpotential factor (red line) has also been demonstrated. Figure II-344(b) depicts the reaction current ratio between protrusion peak and valley for different applied current densities. Present analysis indicates that, with polymer electrolytes, no dendrite growth should occur for applied current less than 40% of the limiting current. Model predictions are also consistent with experimental observations adopted from Brisot et al. (*Journal of Power Sources* (1999) 81-82 925-929).

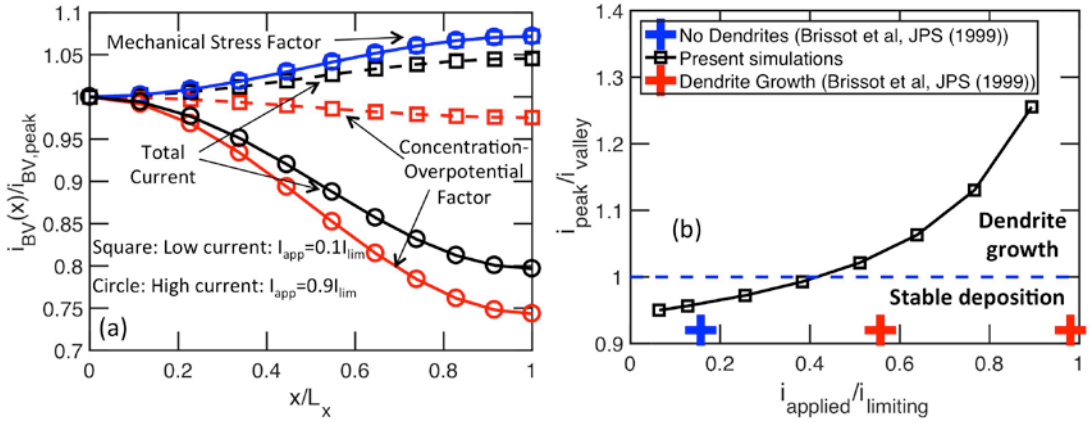


Figure II-344. (a) Distribution of reaction current from the peak to the valley at two different applied current densities. (b) Reaction current ratio between protrusion peak and valley for different applied current densities. Model predictions are consistent with experiments.

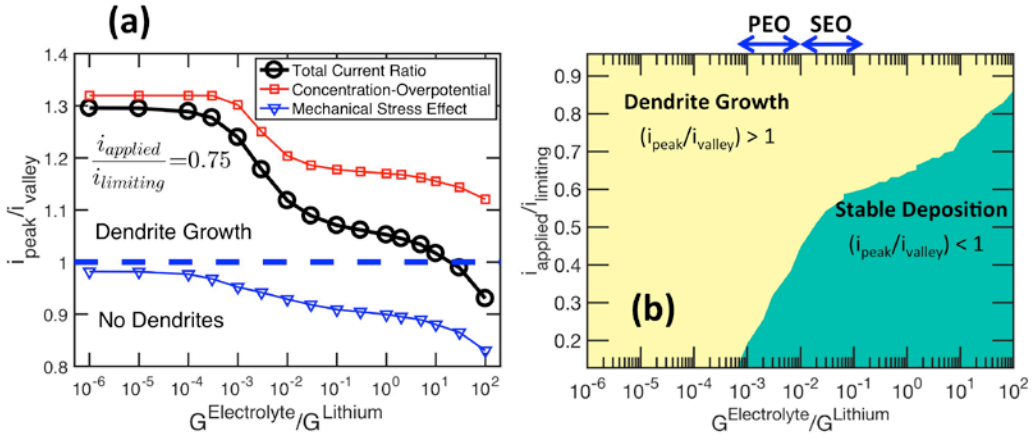


Figure II-345. (a) Impact of stress -factor and current – distribution -factor on the overall reaction current density. Electrolytes with shear modulus 20 times larger than that of lithium may prevent dendrite growth. (b) Phase map demonstrating the correlation between applied current density and electrolyte shear modulus on lithium stabilization.

In the fourth quarter, we investigated the impact of electrolyte modulus on dendrite growth by incorporating elastic-plastic deformation of both metallic lithium and polymer electrolyte. A modified version of the Butler-Volmer equation has been adopted from existing literature that takes into account the impact of mechanical deformation induced strain energy. This expression has been used to determine the reaction current at the lithium/electrolyte interface. The two components of the Butler-Volmer equation are as follows: (i) The "mechanical stress factor" that takes into accounts the impact of strain energy and surface curvature effects, and (ii) The "current distribution factor" that takes into accounts the effect of concentration and potential distribution within the electrolyte. Figure II-345(a) compares the impact of mechanical stress induced component and the current distribution induced component of the Butler Volmer equation on the ratio of total reaction currents between the protrusion peak and the valley. Mechanical stress always tries to prevent the dendrites, whereas, the current distribution helps in growth of the dendritic protrusion. The combined effect clearly indicates that electrolytes with shear modulus 20 times larger than that of lithium, may be able to prevent the growth of dendritic protrusions. Figure II-345(b) shows a phase map between applied current density and electrolyte shear modulus, where the domain of stable lithium deposition has been clearly pointed out.

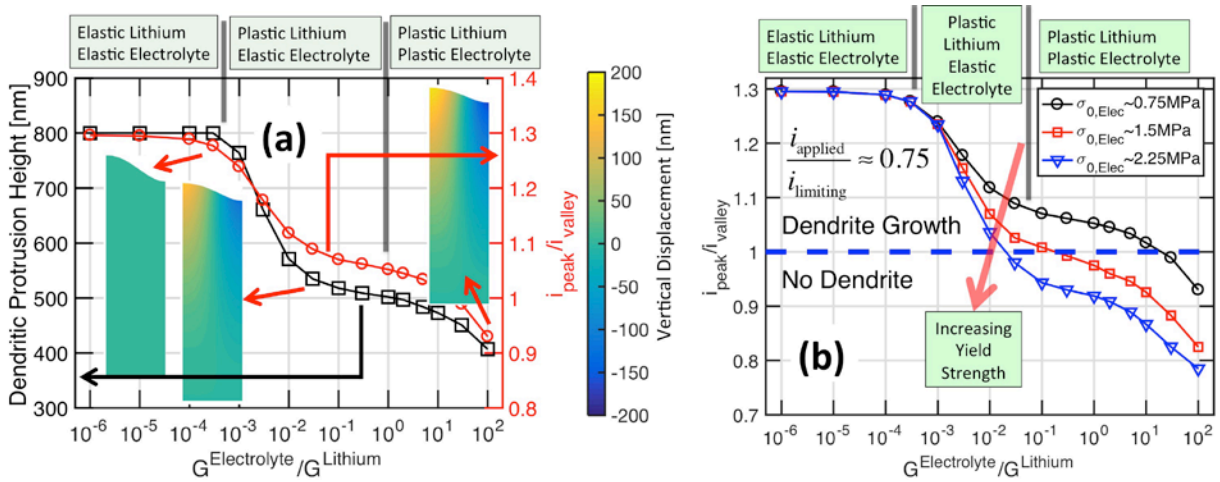


Figure II-346. (a) Effect of elastic-plastic deformation of both lithium metal and electrolyte on the overall suppression of the dendritic protrusion. (b) Increasing yield strength of the electrolyte may help to prevent dendrite growth even with present day polymer electrolytes.

Impact of elastic-plastic deformation experienced by both lithium metal and polymer electrolyte on the suppression of dendritic protrusion has been demonstrated in Figure II-346(a). For intermediate modulus electrolytes, where plastic flow of lithium occurs along with elastic deformation of the electrolyte provides the maximum suppression of dendritic protrusion. Following this realization, if we can improve the yield strength of the present day polymers by approximately three times, prevention of dendritic protrusion may be possible (see Figure II-346(b)).

## Conclusions

A detailed computational methodology have been developed as part of the present research effort that can predict the elastic-plastic deformation and subsequent stress evolution within both lithium metal and adjacent solid electrolyte. Corresponding impact on the protrusion height (due to plastic flow of lithium) and reaction current density at the peak and the valley have been investigated. The mass transport and charge conservation equations have been successfully solved to determine the propensity of lithium dendrite growth under the influence of mechanical stress. It has been realized that there should exist critical current densities below which dendrite growth in polymer electrolytes will not occur. Also, yield strength of lithium metal and solid electrolyte (polymer in the present case) has significant impact on the overall growth of dendritic protrusions. Increasing the yield strength of present day low modulus polymer electrolytes can potentially lead to dendrite

free lithium deposition. The developed computational model can be easily extended to understand the impact of external pressure on the overall lithium dendrite growth process. Also the impact of transport parameters, such as, electrolyte conductivity, diffusivity and transference number, on the propensity of dendrite growth can be estimated using the developed computational model. One major drawback of the present model is the inherent assumption of homogeneous material parameters. Propensity of dendrite growth in solid state electrolytes with inhomogeneous grain-interior/grain-boundary microstructure cannot be captured using the present model.

## Key Publications

1. P. Barai, K. Higa and V. Srinivasan. Effect of Initial State of Lithium on the Propensity for Dendrite Formation: A Theoretical Study. *Journal of the Electrochemical Society*. **164** (2) (2017) A180 – A189.

2. P. Barai, K. Higa and V. Srinivasan. Lithium Dendrite Growth Mechanisms in Polymer Electrolytes and Prevention Strategies. *Physical Chemistry Chemical Physics.* **19** (2017) 20439 – 20505.

# II.E.2 Predicting and Understanding Novel Electrode Materials from First Principles (LBNL)

**Kristin A. Persson, Principal Investigator**
Lawrence Berkeley National Laboratory
1 Cyclotron Road
Berkeley, CA 94720
Phone: 510-486-7218
E-mail: KAPersson@lbl.gov

**Tien Duong, Technology Manager**
U.S. Department of Energy
Phone: 202-586-7836
E-mail: Tien.Duong@ee.doe.gov

Start Date: October 1, 2016 End Date: September 30, 2017
Total Project Cost: $350,000 DOE share: $350,000 Non-DOE share: $0

## Project Introduction

This project supports VTO's programmatic goal by developing next-generation, high-energy cathode materials and enabling stable cathode operation at high voltages through target particle morphology design, functional coatings and rational design of electrolytes.

During the last two years, we have focused on understanding the origin of performance limitations of Li-excess Mn-rich layered cathodes which have attracted the attention of the community due to their high capacity. We choose the end-member $Li_2MnO_3$ as a representative, 'worst-case' Li-rich and Mn-rich phase for our modeling work. In previous years, we investigated the bulk structure and the Li intercalation mechanisms, which in these materials includes inter-layer as well as intra-layer migration pathways. Interestingly, we found evidence of excellent Li mobility in these materials, which points to other mechanisms for the overall observed poor rate capability. Seeking the diffusion bottleneck elsewhere, we charted the particle morphology for pristine $Li_2MnO_3$ and found that all majority surfaces are prone to spontaneous, increasingly drastic oxygen evolution as a function of delithiation. This oxygen release is likely strongly related to surface phase transformation, surface densification and resulting impedance of Li intercalation into the material. Hence, in 2017, our research efforts focused on protecting the $Li_2MnO_3$ particle surface from oxygen release, which can be achieved e.g., by coatings or surface dopants. As a first attempt, we examined the possibility of using surface doping to enhance oxygen retention at the particle surface, using high-throughput first-principles calculations covering 38 elements spanning all transition metal, the post-transition metal, and metalloid elements.

## Objectives

- New fundamental understanding of the cathode/electrolyte interface and the factors that control the interfacial chemistry and interfacial impedance
- Critical surface and coating design and optimization strategies that will improve cycling of LIB cathodes
- Understanding the factors that govern stability in non-aqueous electrolytes for Li-ion and Li-S systems

## Approach

- Determine matrix of candidate surface dopants for improved oxygen stability through literature search and first principles calculations.
- Evaluate dopant affinity within the surface and bulk $LiMnO_3$.

- Screening a range of dopants on the dominant and sub-dominant surfaces.
- Identify most promising dopants.

This research used resources of the National Energy Research Scientific Computing Center, a DOE Office of Science User Facility supported by the Office of Science of the U.S. Department of Energy under Contract No. DE-AC02-05CH11231.

## Results

To identify the most efficient dopant, we investigated 38 elements containing all transition metal, the post-transition metal, and metalloid elements. We assume, for efficiency, that the dopant element would be added during the synthesis of the cathode material. We designed our screening following three selection Tiers:

1. Promotion of dopants that preferentially segregate towards the surface comparing defect formation energies between the surfaces and bulk (Figure II-347).
2. Elimination of dopants that have a strong driving force to form secondary impurity phases instead of residing within the cathode material (Figure II-348).
3. Promotion of dopants that increase oxygen retention at the surface of the cathode particle, by calculating the oxygen release energy difference between the doped surface and the pristine surface (Figure II-349).

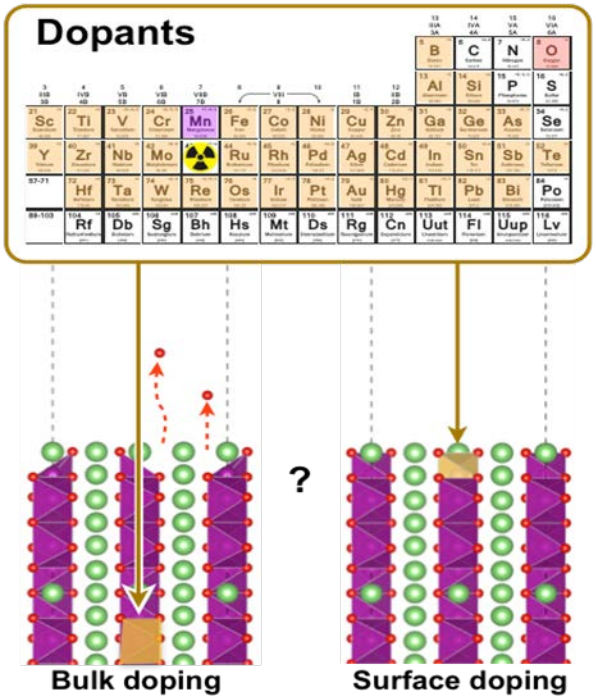


Figure II-347. Illustration of the initial screening process including the range of considered elements and the preference of surface dopant occupancy to enhance oxygen retention at the surface.

All stable facets including two dominant surfaces ((001) and (010) and two sub-dominant surfaces ((100), (110), and (111)) of $Li_xMnO_3$ were included in each calculation. In the first Tier, we examine the defect segregation energy defined as:

$$E_S = \Delta E^{bulk} - \Delta E^{surface}$$

Where $\Delta E^{bulk}$ represents the energy difference between the doped and undoped bulk, and $\Delta E^{surface}$ shows the equivalent quantity for surface. Hence, a positive $E_S$ indicates a dopant which preferentially occupies the surface. Our calculations show that the defect preferences depend somewhat on the specific surface chemistry and morphology. For example, Co generally prefers to reside in the bulk as compared to the surface, yet the (001) surface is less preferred than e.g., the (110) surface. Therefore, optimal candidate dopants segregate to the surface for all dominant facets.

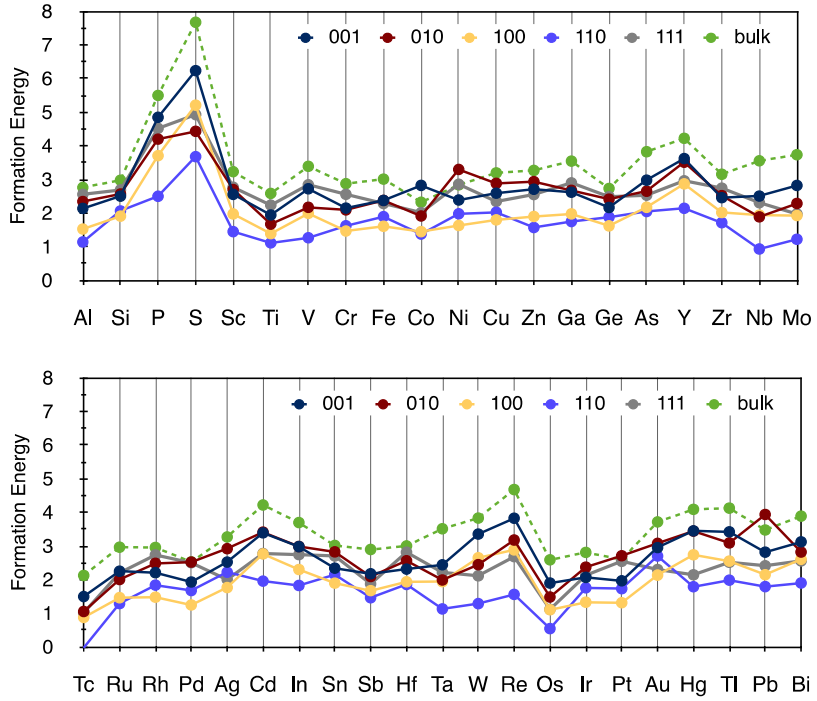


Figure II-348. The defect formation energy of each stable surface facet as compared to the bulk, covering defect transition metal, post-transition metal, and metalloid elements.

To eliminate dopants that have a strong preference towards forming undesirable impurity phases, the dopant defect formation energy is examined as;

$$E_D^S = \left(\Delta E^{target} + E^{bulk}\right) - E_{hull}^{MP}$$

where $\Delta E^{target}$ represents the energy difference between the doped and undoped target system, $E^{bulk}$ the bulk energy of $Li_2MnO_3$, and $E_{hull}^{MP}$ the energy above the convex hull of the composite system. The $E_{hull}^{MP}$ values are listed in the public open database (MaterialsProject.org) and represent the most likely impurity phases that would form under the conditions where $Li_2MnO_3$ is formed. All surface defect formation energies exhibit positive numbers which indicate a metastable surface doping process. Consistently, most of the surface defect formation energies are lower than the comparative bulk (green dashed line in Figure II-348). Dopants with limited tendency to form impurity phases are those with lower positive defect formation energies.

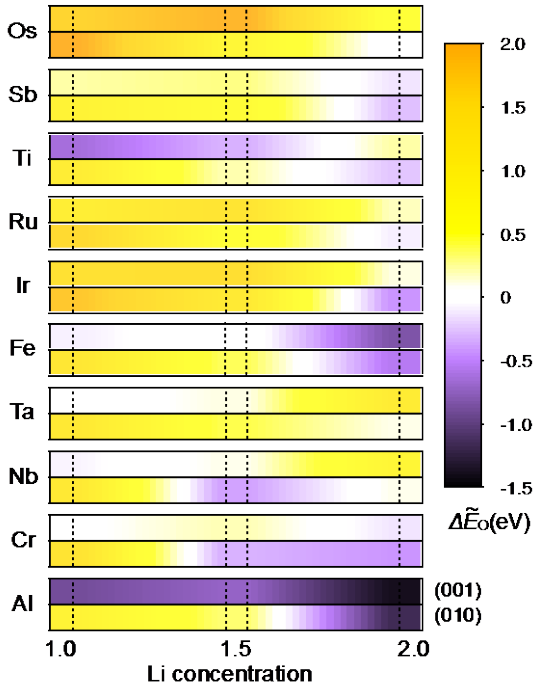


Figure II-349. The relative surface oxygen release energy for the top 10 candidate dopants as compared to the pristine systems shown for representative (001) and (010) surface facets. A dark yellow color indicates stronger oxygen retention, while a purple color indicates less protection against oxygen release as compared to the pristine, undoped surface.

The top 10 candidate dopants selected through Tier 1 and 2, are Os, Sb, Ti, Ru, Ir, Fe, Ta, Nb, Cr, and Al. In the final Tier 3, we calculate the oxygen evolution energy difference between the doped surface and the pristine surface. We define the relative oxygen release energy as;

$$\Delta\tilde{E}_O = \tilde{E}_O^{doping} - \tilde{E}_O^{pristine}$$

Figure II-349 shows $\Delta\tilde{E}_O$ of the top 10 candidate dopants obtained from the two first selection criteria. Here, $\Delta\tilde{E}_O$ is provided for the (001) and (010) surfaces as the two dominant surfaces of $Li_xMnO_3$. The oxygen evolution energy of the pristine surface $\tilde{E}_O^{pristine}$ was defined in our previous work using the slab vacuum mode. Each color in Figure II-349 represents the relative oxygen evolution energy as compared to the pristine surface, therefore, yellow (purple) colors indicates an improved (decreased) oxygen retention relative to the pristine surfaces. The underlying atomistic reason for the improved the oxygen retention can be understood by elucidating the influence of the dopant on the local electronic structure at the specific surface facet. We found that a strong hybridization between the oxygen p-orbitals on the surface and the surface defect d-orbitals promotes strong binding and hence oxygen retention. In Figure II-349, yellow colored elements exhibit strong electron energy hybridization.

In summary, our 3-Tier screening identified Os, Sb, Ru, Ir and Ta as optimal candidate dopants to be added during synthesis of Li-excess, Mn-rich cathode materials for improved surface oxygen retention. It should be noted that the higher concentration of the dopant at the surface, the better oxygen retention is expected. Exciting recent results from LBNL BMR co-PIs Chen and McCloskey confirm the ability of Ta doping to enhance oxygen retention of Li-excess, Mn-rich cathode materials.

## Conclusions

Early cycle cathode degradation in Li excess cathode materials is correlated with spontaneous surface oxygen evolution, which causes densification of the surface and deteriorated transport. Hence, to address this issue, we computationally screened the periodic table for surface dopants to enhance surface oxygen-retention in Li-excess Mn-rich cathode materials. Using our three-tier screening process, we identified Os, Sb, Ru, Ir, Ta as optimal candidate dopants in representative, model material $Li_xMnO_3$. As validation and verification, Ta-doped disordered Li-excess cathodes are being evaluated by co-PI Chen and McCloskey.

## Key Publications

1. Yongwoo Shin and Kristin A. Persson, “Surface Morphology and Surface Stability against Oxygen Loss of the Li-excess Layered Cathode Material”, MRS Fall Meeting November 30th 2016, Boston MA

2. Predicting and Understanding Novel Electrode Materials From First-Principles, by Yongwoo Shin and Kristin A. Persson, AMR 2017, Washington

## II.E.3 First Principles Calculations of Existing and Novel Electrode Material (LBNL)

**Gerbrand Ceder, Principal Investigator**
Lawrence Berkeley National Laboratory
1 Cyclotron Road, MS: 33-146
Berkeley, CA 94720
Phone: 510-486-7193
E-mail: gceder@berkeley.edu

**Tien Duong, Technology Manager**
U.S. Department of Energy
Phone: 202-586-7836
E-mail: Tien.Duong@ee.doe.gov

Start Date: October 1, 2015 End Date: September 30, 2019
Total Project Cost: $692,616 DOE share: $692,616 Non-DOE share: $0

### Project Introduction

It was recently demonstrated that cathode materials based on Li-excess disordered transition metal oxides (LEX-RS) can deliver high capacities and sustain efficient Li transport provided Li is in an excess of at least 10% with respect to the transition metal concentration, creating a network of 0-TM channels through which Li can diffuse [1,2]. While only a small subset of TM species (Mn, Ni, Co) stabilizes the conventional layered oxide structure, compositions that form cation-disordered compounds comprise a larger TM compositional space, including Ti, V, Cr, Fe, Zr and Nb. Besides the increased design space, cation disorder is also beneficial for structural stability upon extended electrochemical cycling, as disordered structures undergo smaller volume changes upon Li extraction than layered structures [1]. The high capacity generally observed for LEX-RS oxide cathodes relies on oxygen redox processes which can cause oxygen loss near the surface of the particles. This results in the creation of high impedance surface layers and large polarization of the voltage profile, leading to poor cycling performance [3]. By contrast, reversible oxygen redox processes have the potential to enable high energy density by delivering excess capacity beyond the theoretical transition metal redox capacity at a high voltage. We have found that specific chemical and structural features in Li-excess metal oxides introduce labile oxygen electrons that can be easily extracted and participate in the practical capacity of these materials [4].

The development of percolation theory for LEX-RS has proven to be powerful for finding novel Li-ion cathode materials with high capacity and energy density. Recently, we succeeded in designing a new class of Li-excess cation disordered Li-Ni-Ti-Mo oxides that delivers up to 250 mAh/g and 750 Wh/kg at 10 mA/g [5].

### Objectives

Develop very high capacity layered cathodes with high structural stability (>250 mAh/g) and high surface stability. Clarify the role of the initial structure as well as that of structural changes upon first charge and discharge. Clarify the role that Li-excess and cation disordered play in capacity and structural stability. Develop predictive modeling of oxygen charge transfer and oxygen loss and find ways to make oxygen redox beneficial in terms of increasing capacity. Develop materials with engineered surface passivation which does not lead to impedance increase. Study the effect of fluorination on electrochemical performance.

### Approach

A combination of first-principles computations and experimental synthesis/characterization are used to evaluate existing and novel materials. Voltages and intercalation curves are calculated with GGA+U, and if highly accurate results are required hybrid functionals (HSE) are used. Phase diagrams are calculated with the Materials Project infrastructure based on high-throughput computations. Configurational disorder for elevated

temperature and off-stoichiometry is modeled with either point defect models (when off-stoichiometry is small) or with the cluster expansion for larger disorder. Ion mobility is evaluated with the Nudged Elastic Band Method or with direct Molecular Dynamics Simulations. Thermal stability is investigated with the approach developed previously under this program. Some of the computational work is performed in collaboration with Persson and with the Materials Project. Work on Li-excess layered materials is done in coordination with Persson (computational) and with the experimental efforts in the BMR Program (e.g., Chen).

## Results

*Computational approach to predict cation disorder and synthesis temperature*

Owing to the large number of possible constituents it is practically infeasible to scan all possible compositions for their stability, and thus concrete design guidelines are required. We have recently demonstrated that high-throughput computations allow for the systematic screening of select composition spaces [6], but a qualitative understanding of the origin of cation disorder is desirable.

According to the Hume-Rothery rules, a species is likely soluble in a metal if the atomic sizes are within about 15%. We find that, in Li-TM oxides, similar cation radii are also a requirement for stable cation-disordered structures, but this alone is not a sufficient criterion. Even small ionic radius differences give rise to distortions of the octahedral TM sites that affect the stability.

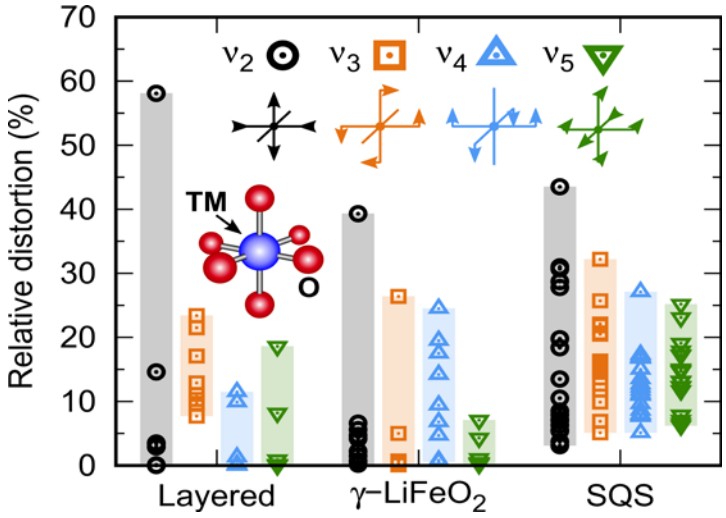


Figure II-350. Maximal TM site distortion relative to the original bond lengths in ordered $LiTMO_2$ ground state structures and in cation-disordered $LiTMO_2$ structures. Contribution of the four symmetry-breaking normal modes, $v_2$ through $v_5$, to the site distortions are shown.

Figure II-350 shows the magnitude of the maximal TM site distortions in ordered LiTMO2 ground state structures and special quasi-random structures (SQS) for all first- and second-row TMs except Mn and Tc. The site distortions are decomposed in contributions from the four symmetry-breaking normal modes of the octahedral point group. As seen in the figure, disordered structures generally exhibit distortions in all four modes whereas distortions of types v2 and v5 are small in most of the ordered structures. Depending on the electronic configuration of the TM species, these additional distortions may give rise to large energy penalties. In fact, it can be shown that only TM cations with $d^0$ configuration are insensitive with respect to the mode of distortion. As a consequence, in compositions containing at least one $d^0$ TM species ($Ti^{4+}$, $Nb^{5+}$, $Mo^{6+}$, etc.), sites occupied by the $d^0$ species may absorb the distortions required to stabilize the structure (Figure II-351). This conceptual understanding takes us one step closer to the rational design of new cation-disordered cathode materials for Li-ion batteries.

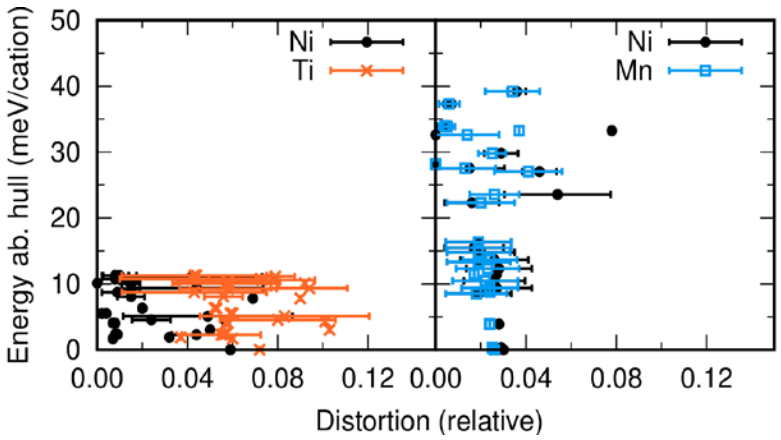


Figure II-351. Energy and relative TM site distortion in $LiNi_{0.5}Ti_{0.5}O_2$ and $LiMn_{0.5}Ni_{0.5}O_2$. Each data point corresponds to a single atomic structure. The error bars indicate the range of distortions for all sites of one TM species within that structure.

*Investigate O K-edge XAS for cation disordered $Li_{1.25-x}Mn_{0.5}Nb_{0.25}O_2$*

Our theoretical study shows that specific chemical and structural features in Li-excess metal oxides introduce labile oxygen electrons that can be easily extracted and participate in the practical capacity of these materials. In this project, we investigated O K-edge XAS for cation-disordered $Li_{1.25-x}Mn_{0.5}Nb_{0.25}O_2$ using first principles calculation.

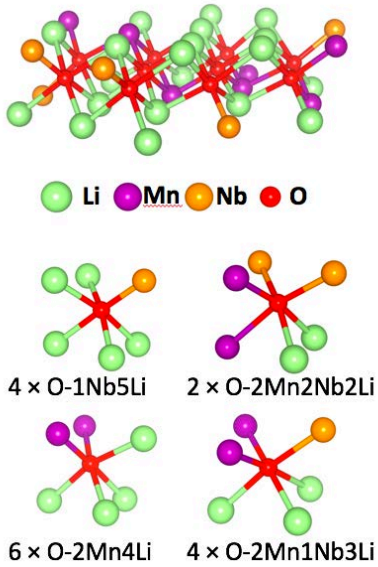


Figure II-352. Atomic structure of $Li_{1.25-x}Mn_{0.5}Nb_{0.25}O_2$ and its various oxygen local environments.

To prepare the atomic structure of cation-disordered $Li_{1.25}Mn_{0.5}Nb_{0.25}O_2$, all possible cation arrangements within the primitive unit cell of $Li_3NbO_4$ were created by an enumeration method. The lowest energy structure of this material was determined from the GGA+U energies of fifty cation arrangements with low electrostatic energies. Figure II-352 represents the atomic structure of the most stable structure of $Li_{1.25}Mn_{0.5}Nb_{0.25}O_2$, showing that it has various oxygen local environments.

The HSE06 hybrid functional was adopted to describe the relative energy level of metal and oxygen states accurately. The Z+1 approximation was employed to treat the core hole effect of XAS. O K-edge XAS of all individual oxygen atoms in $Li_{1.25}Mn_{0.5}Nb_{0.25}O_2$ and $Li_{0.75}Mn_{0.5}Nb_{0.25}O_2$ were calculated and summed to obtain

the total O K-edge XAS. The resolution of the computed spectra was reduced by convolution with Gaussian distribution and 1 eV of full width at half maximum (FWHM) to consider instrumental broadening of XAS. Computed and experimental spectra were aligned at the first peak to be comparable. Computed O K-edge XAS of $Li_{1.25}Mn_{0.5}Nb_{0.25}O_2$ and $Li_{0.75}Mn_{0.5}Nb_{0.25}O_2$ are in a good agreement with experimental ones, as shown in Figure II-353, validating the method used for computing O K-edge EELS spectra. The small discrepancy between computed and experimental XAS may be attributed to a slightly different composition.

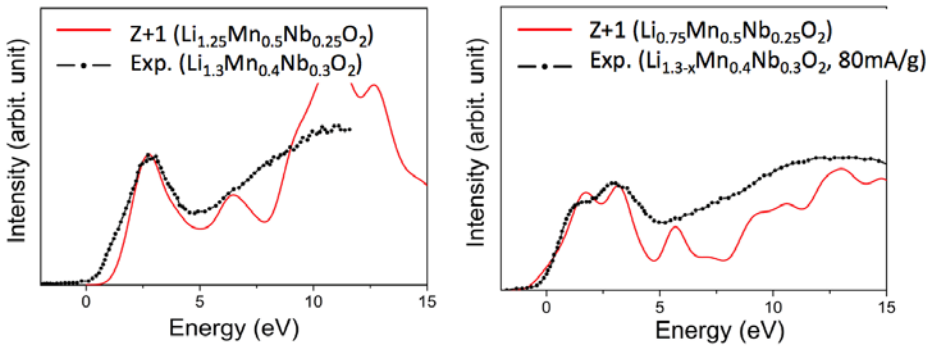


Figure II-353. Computed O K-edge XAS of $Li_{1.25-x}Mn_{0.5}Nb_{0.25}O_2$ (x = 0 and 0.5).

*Design of Li-excess cation disordered Li-Ni-Ti-Mo oxides*

We have designed a new class of Li-excess cation disordered Li-Ni-Ti-Mo oxides that delivers up to 250 mAh/g and 750 Wh/kg at 10 mA/g. To understand the origin of this remarkable performance, we applied a combination of *in-situ* X-ray diffraction (XRD), X-ray absorption near edge spectroscopy (XANES), electron energy loss spectroscopy (EELS) and electrochemistry, to elucidate the oxidation mechanism for a representative compound of that class, the $Li_{1.2}Ni_{1/3}Ti_{1/3}Mo_{2/15}O_2$ composition. Based on this detailed characterization, we were able to distinguish between $Ni^{2+}/Ni^{3+}$ oxidation, oxygen loss, and oxygen oxidation as separate redox processes, demonstrating the relationship of oxygen loss and capacity fading.

We obtained $Li_{1+x/100}Ni_{1/2-x/120}Ti_{1/2-x/120}Mo_{x/150}O_2$ ($x$ = 0, 5, 10, 15, 20) compounds, in the following referred to as LNTO and LNTMO$x$ ($x$=5, 10, 15, 20), by traditional solid state synthesis. Figure II-354 shows the cycling performance of these materials (1.5-4.5 V, 20 mA/g), showing an increasing capacity with Li content. As seen in Figure II-354a, LNTMO20 delivers much higher capacity (~230 mAh/g) and energy density (~680 mAh/g) compared to LNTO (~110 mAh/g, ~350 Wh/kg). More importantly, we note that the capacity of LNTMO20 significantly exceeds the theoretical $Ni^{2+}/Ni^{4+}$ capacity (=201.6 mAh/g), indicating other active redox couples in LNTMO20. The material also exhibits some capacity fading upon cycling, as shown in Figure II-354b. Motivated by these observations, we studied the oxidation mechanism and capacity fading with *in-situ* XRD, XANES, and EELS.

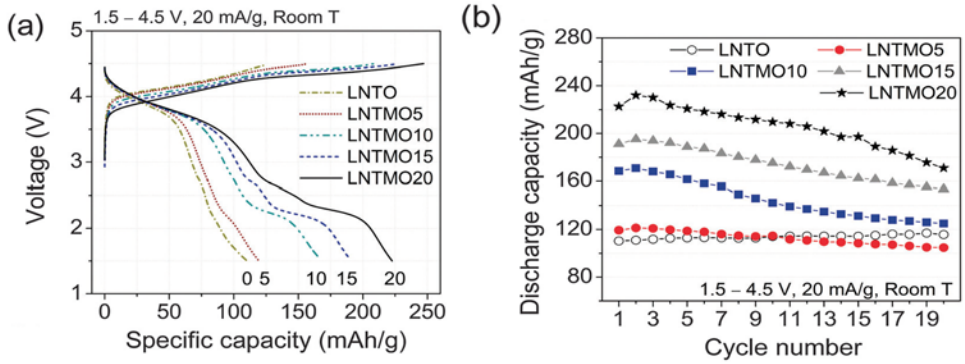


Figure II-354. (a) The first-cycle voltage profiles of LNTMO compounds. (b) Capacity evolution over 20 cycles.

Surprisingly, our XANES results show that only the $Ni^{2+}/Ni^{3+}$ redox couple is accessed, and $Ni^{3+}$ is not oxidized further to $Ni^{4+}$, which accounts for around 110 mAh/g of the charge capacity. The remaining capacity has to originate from oxygen activity, i.e., either from oxygen loss or from reversible oxygen oxidation. As shown in Figure II-355a, charged to ~ 215 mAh/g, i.e., beyond $Ni^{2+}/Ni^{3+}$ oxidation, the lattice constant barely changes, indicating oxygen loss from the electrode surface. Finally, charging beyond ~215 mAh/g gives rise to a decrease of the lattice parameter, as oxygen oxidation contracts the oxygen framework by reducing the size of the oxygen ions.

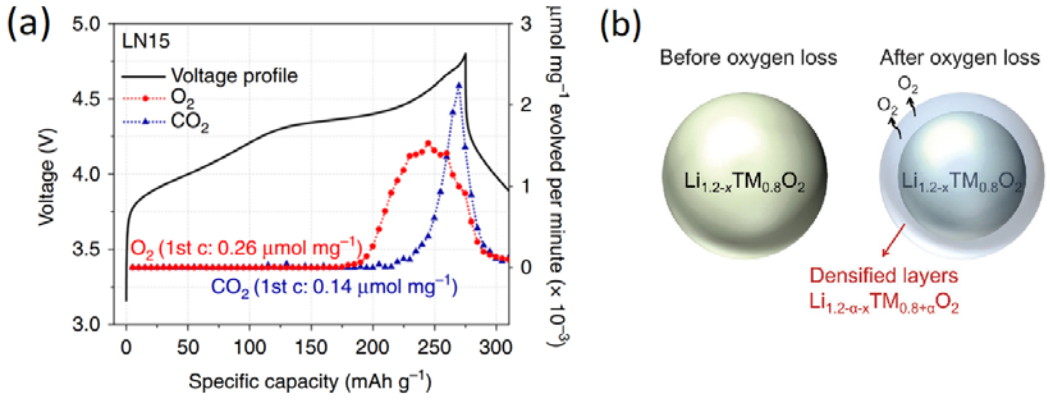


Figure II-355. (a) DEMS study of LN20 when charged to 4.8 V and discharged to 1.5 V at 20 mA $g^{-1}$, along with the DEMS results on $O_2$ (red circle) and $CO_2$ (blue triangle). (b) Illustrations of a LNTMO20 particle before and after oxygen loss.

With this insight, the capacity fading on discharge can be attributed mainly to irreversible oxygen loss. From the differential electrochemical mass spectroscopy (DEMS) results shown in Figure II-355a, we can observe some amount of oxygen gas evolution at highly charged state (above 4.2 V). When oxygen is released from the particle surface, either oxygen vacancies or under-coordinated TM ions at the surface may diffuse into the bulk, creating new surface phases rich in TM. After such surface densification, the Li content drops below the percolation threshold (~9% excess), and Li diffusion through the surface is no longer facile, causing the capacity fading. Currently, we are working on fluorination to reduce the irreversible oxygen loss so that capacity retention can be enhanced.

*Fluorination of Li-excess disordered (rocksalt) transition metal oxides*

Our comparative study of the disordered oxides $Li_{1.15}Ni_{0.375}Ti_{0.375}Mo_{0.1}O_2$ (LN15) and $Li_{1.2}Ni_{0.333}Ti_{0.333}Mo_{0.133}O_2$ (LN20), with fluorine-substituted $Li_{1.15}Ni_{0.45}Ti_{0.3}Mo_{0.1}O_{1.85}F_{0.15}$ (LNF15) [3] showed that, since fluorine substitution allows for more $Ni^{2+}$ in the as-prepared material, it increases the metal-based redox reservoir of the cathode, reducing oxygen (O) redox and therefore O loss from the lattice on charge, and leading to significant improvements in electrochemical performance.

We performed TEM energy dispersive spectroscopy (TEM-EDS) to prove that fluorine is substituted in the bulk disordered lattice instead of forming secondary phases at the surface of the particles. As shown in Figure II-356 a, EDS mapping reveals a uniform distribution of fluorine in the LNF15 particle.

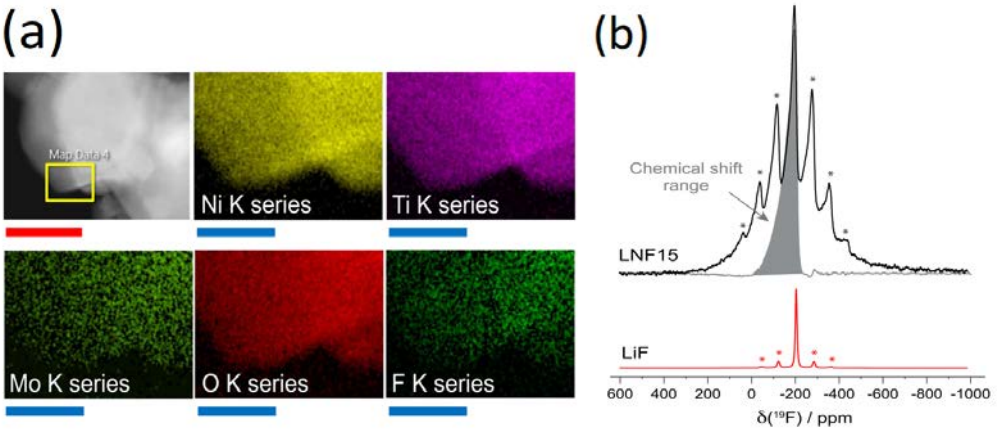


Figure II-356. (a) EDS mapping on one area of a LNF15 particle. Scale bars, red: 100 nm, blue: 25 nm. (b) $^{19}F$ spin echo NMR spectra obtained at 30 kHz MAS for LNF15 and LiF.

We also carried out $^{19}F$ solid-state nuclear magnetic resonance spectroscopy (ssNMR) to confirm that the fluorine distribution observed with TEM-EDS is not due to LiF on the surface of the particles. The $^{19}F$ NMR data presented in Figure II-356b show the presence of multiple broad fluorine local environments in LNF15, in contrast to the single fluorine site observed for LiF, confirming that F is doped into the bulk Li–Ni–Ti–Mo oxide lattice.

Figure II-357a&b are showing electrochemical properties of LN15 and LNF15 when cycled between 1.5 V and 4.6 V at 20 $mAg^{-1}$ at room temperature. We can see obvious improvement of both discharge capacity and energy density (from 194 mAh/g, 587 Wh/kg to 210 mAh/g, 681 Wh/kg). Differential electrochemical mass spectroscopy (DEMS) results show that LNF15 has less oxygen loss compared to LN15 (Figure II-355a), indicating less irreversible oxygen oxidation.

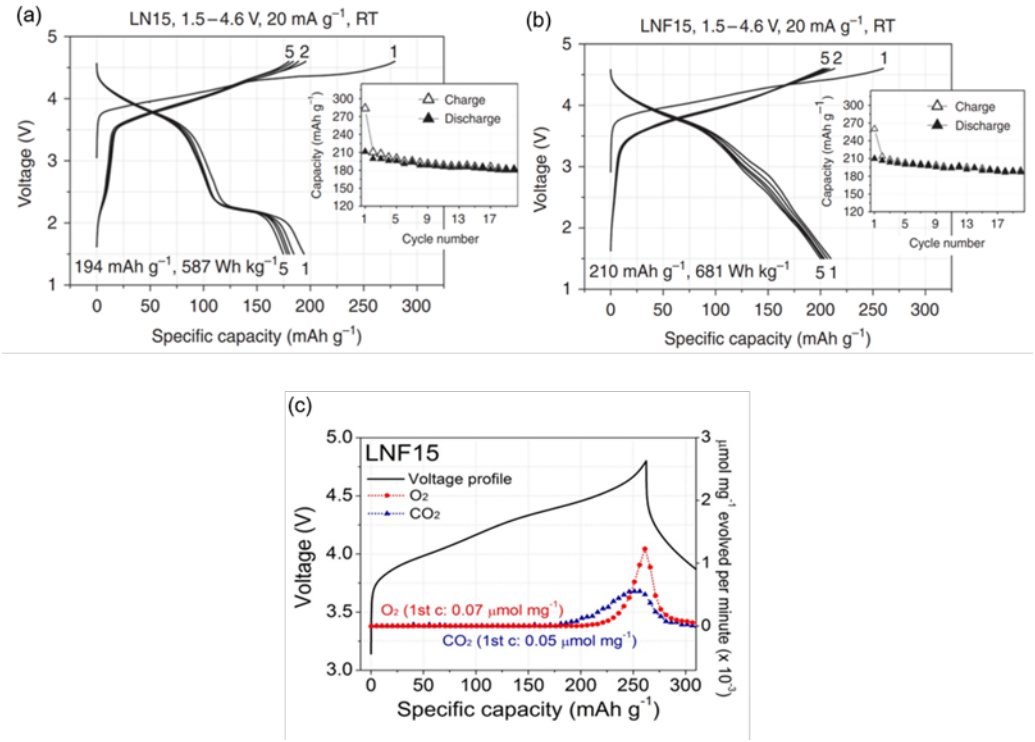


Figure II-357. (a) & (b) Cycling performance of LN15 and LNF15. (c) DEMS study of LNF15.

## Conclusions

The work carried out over the past year has resulted in important progress in our understanding of ordered and cation-disordered Li-excess cathode materials. Using rigorous electronic structure theory, we demonstrated that $d^0$ transition metal species ($Ti4^+$, $Nb^{5+}$, $Mo^{6+}$, etc.) promote cation disorder, thereby providing a straightforward design criterion for novel disordered compositions. To investigate oxygen redox in Li-excess cathodes, we developed and benchmarked a first-principles methodology for the calculation of oxygen K-edge X-ray absorption spectra. This approach will aid the interpretation of experimentally measured spectra in the future. We further succeeded in designing a new class of Li-excess cation disordered Li-Ni-Ti-Mo oxides (LNTMO) that delivers up to 250 mAh/g and 750 Wh/kg at 10 mA/g. Based on results from various characterization methods (*in-situ* XRD, XANES, EELS and electrochemistry), we showed that the redox mechanism in LNTMO is highly complex and involves $Ni^{2+}/Ni^{3+}$ oxidation, oxygen loss, and oxygen oxidation as separate redox processes, demonstrating the relationship of oxygen loss and capacity fading. Finally, we found that fluorine doping of the LNTMO materials is feasible and results in a reduction of oxygen release as measured by differential electrochemical mass spectrometry. This finding demonstrates that oxygen loss can be prevented in Li-excess disordered cathodes with very high capacities, pointing to an exciting new direction for the development of high energy-density Li-ion batteries.

## Key Publications


1. W. D. Richards, S. T. Dacek, D. A. Kitchaev, G. Ceder, Adv. Energy Mater. 2017, 1701533. https://doi.org/10.1002/aenm.201701533
2. Lee, J., Papp, J.K., Clément, R.J., Sallis, S., Kwon, D.H., Shi, T., Yang, W., McCloskey, B.D. and Ceder, G., 2017. Mitigating oxygen loss to improve the cycling performance of high capacity cation-disordered cathode materials. *Nature Communications*, *8*(1), p.981.
3. Urban, A., Abdellahi, A., Dacek, S., Artrith, N. and Ceder, G., 2017. Electronic-Structure Origin of Cation Disorder in Transition-Metal Oxides. *Physical Review Letters*, *119*(17), p.176402.
4. Lee, J., Seo, D. H., Balasubramanian, M., Twu, N., Li, X., & Ceder, G. (2015). A new class of high capacity cation-disordered oxides for rechargeable lithium batteries: Li–Ni–Ti–Mo oxides. *Energy & Environmental Science*, *8*(11), 3255-3265.


## References


1. J. Lee, A. Urban, X. Li, D. Su, G. Hautier, G.Ceder, *Unlocking the potential of cation-disordered oxides for rechargeable lithium batteries*, Science, 343, 519-522 (2014).
2. A. Urban, J. Lee, G. Ceder, *The Configurational Space of Rocksalt-Type Oxides for High-Capacity Lithium Battery Electrodes*, Advanced Energy Materials, 4, 1400478 (2014).
3. Lee, J., Papp, J.K., Clément, R.J., Sallis, S., Kwon, D.H., Shi, T., Yang, W., McCloskey, B.D. and Ceder, G., 2017. Mitigating oxygen loss to improve the cycling performance of high capacity cation-disordered cathode materials. *Nature Communications*, *8*(1), p.981.
4. Seo, D. H., Lee, J., Urban, A., Malik, R., Kang, S., & Ceder, G. (2016). The structural and chemical origin of the oxygen redox activity in layered and cation-disordered Li-excess cathode materials. *Nature chemistry*, *8*(7), 692-697.
5. Lee, J., Seo, D. H., Balasubramanian, M., Twu, N., Li, X., & Ceder, G. (2015). A new class of high capacity cation-disordered oxides for rechargeable lithium batteries: Li–Ni–Ti–Mo oxides. *Energy & Environmental Science*, *8*(11), 3255-3265.
6. Urban, A., Matts, I., Abdellahi, A., & Ceder, G. (2016). Computational Design and Preparation of Cation Disordered Oxides for High Energy Density Li Ion Batteries. *Advanced Energy Materials*, *6*(15).

## II.E.4 First Principles Modeling of SEI Formation on Bare and Surface/Additive Modified Silicon Anodes (TAMU)

**Perla B. Balbuena, Principal Investigator**
Texas A&M University
3122 TAMU
College Station, TX 77843
Phone: 979-845-3375
E-mail: balbuena@tamu.edu

**Jorge M. Seminario, Co-Principal Investigator**
Texas A&M University
3122 TAMU
College Station, TX 77843
Phone: 979-845-3301
E-mail: seminario@tamu.edu

**Tien Duong, Technology Manager**
U.S. Department of Energy
Phone: 202-586-7836
E-mail: Tien.Duong@ee.doe.gov

Start Date: April 1, 2013 End Date: March 31, 2017
Total Project Cost: $714,128 DOE share: $714,128 Non-DOE share: $0

### Project Introduction

The focus of this project is on SEI layer formation and evolution during cycling and subsequent effects on capacity fade through two concatenated problems: 1) SEI layers formed on lithiated Si surfaces, and 2) SEI layers formed on coated surfaces. Key issues that this project addresses include the dynamic evolution of the system and electron transfer through solid-liquid interfaces.

### Objectives

This project aims to develop fundamental understanding of the molecular processes that lead to the formation of a solid electrolyte interphase (SEI) layer due to electrolyte decomposition on Si anodes, and to use such new knowledge in a rational selection of additives and/or coatings.

### Approach

Investigating the SEI layer formed on modified Si surfaces involves analysis of the interfacial structure and properties of specific coating(s) deposited over the Si anode surface, characterization of the corresponding surface properties before and after lithiation, especially how such modified surfaces may interact with electrolyte systems (solvent/salt/additive), and what SEI layer structure, composition, and properties may result from such interaction. This study will allow identification of effective additives and coatings able to overcome the intrinsic deficiencies of SEI layers on bare surfaces. Once the SEI layer is formed on bare or modified surfaces, it is exposed to cycling effects that influence its overall structure (including the anode), chemical, and mechanical stability.

### Results

*Stability of growing solid-solid interfaces*

At the onset of nucleation of new phases, one important property is the mechanical stability of the interface between the growing nuclei and the support. One possible test includes the evaluation of the electrostatic

potential of the system including the support phase in contact with the nucleating phase. At the interface, there is a discontinuity in this potential, the magnitude of which is an indicator of the degree of instability of the interface. The TAMU team has computed this indicator for various relevant interfaces as a nucleation advances. The interfacial electrostatic potential is illustrated in Figure II-358 for the nucleation of $Li_2CO_3$ over a graphite surface. Initially, $CO_3$ radical anions, products of decomposition of the solvent are adsorbed on the graphite edges, and generate the sites where the nucleation of $Li_2CO_3$ may take place. The potential shown at the top corresponds to that of the electrode surface; the first red arrow points to the potential of the exposed graphite edges. After that, there is a clear discontinuity in the potential which corresponds to the incipient nucleation of the $Li_2CO_3$ phase. The difference between the two peaks shown with the red arrows is the indicator of the stability of the interface. As the difference reduces, the interface is more stable. The idea can be extended to evaluate nucleation of a heterogeneous film on the electrode. K. Leung (Sandia) has modeled grain boundaries in a LiF film coating a Li metal surface. It was found that a substantial over-potential is needed to insert a Li atom ($Li^+ + e^-$) into the grain boundary core regions. As shown previously by this team, such Li atoms can carry an undesirable electric current and degrade the electron-blocking passivation function of SEI films; therefore it is important that they are minimized.

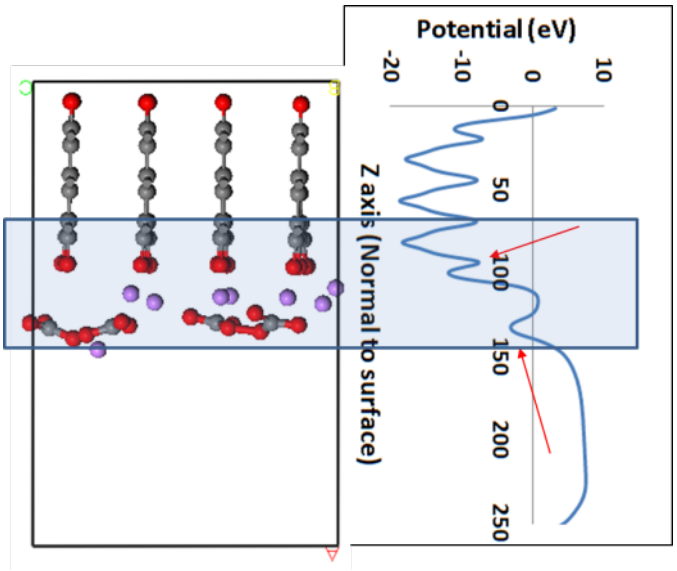


Figure II-358. Left: Nucleation of $Li_2CO_3$ over graphite electrode. Li ions interact with adsorbed O atoms at the graphite edge. Right: Electrostatic potential (eV) of the nucleating phase on the solid electrode. Note the discontinuity at the interface (highlighted).

*Li ion transport through SEI layer*

Rempe's group (Sandia) is using non-polarizable force fields to study $Li^+$ ion transport in SEI layers. They focus on the well-known component of SEI layers, di-lithium ethylene dicarbonate ($Li_2$-EDC). For fluids like EC, the Gaussian behavior of the self-part of the Van Hove function obtained from MD simulations is exact (Figure II-359, right). The non-Gaussian behavior of the "self" part in SEI layers further confirms that the SEI layer is glassy. To understand transport properties in this glassy SEI layer, the group next will use mode-coupling theory on the "self" part.

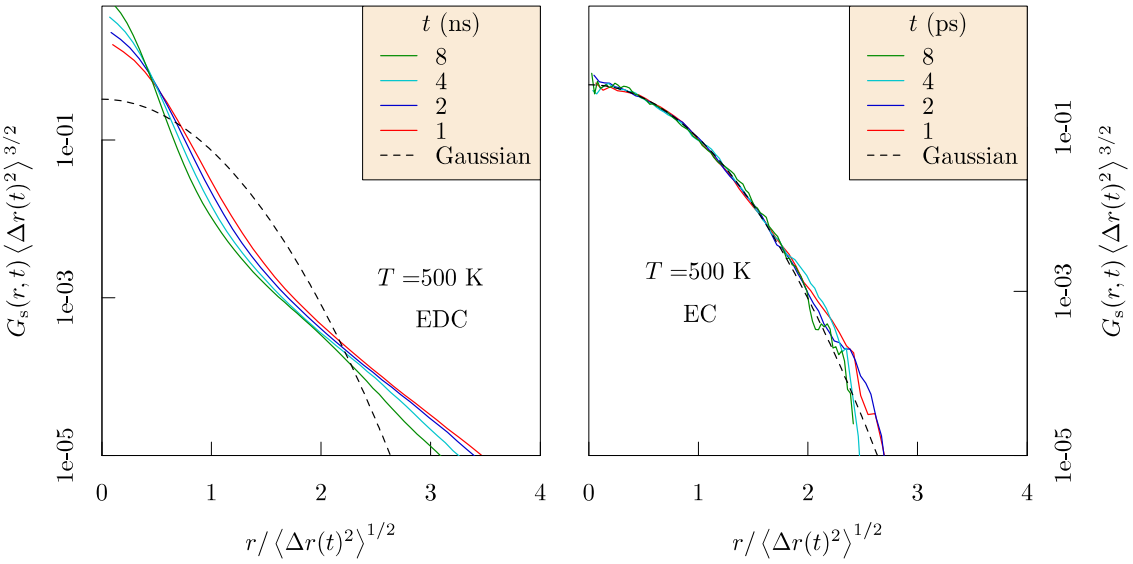


Figure II-359. Gaussian fit to the "self" part of van Hove function suggests $Li_2EDC$ (left) is crystalline compared to pure EC (right). Correlations are calculated for ps compared to ns in the $Li_2EDC$ case.

*Electron transfer at the anode/SEI/electrolyte interface*

We investigated the electron transport on various SEI products and oxides in four lithiation stages of the anode using a DFT-GF approach to understand early stages of SEI nucleation and growth. Results shown in Figure II-360 indicated that, in all $Li_xSi_y$ cases, the current is significantly reduced with the addition of the SEI components as compared with the systems where no SEI element is present. Moreover, increasing the thickness of the SEI layer also resulted in a reduction of the electron transfer. Our results also indicate that at high voltages of ~5 V, $Li_2Si_2O_5$ presents a much higher resistance to electron transfer than $Li_2CO_3$ and $SiO_2$. The current decreases exponentially as the SEI layer thickness increases, thus implying higher electron transport at initial SEI formation stages and then significantly slower steady growth.

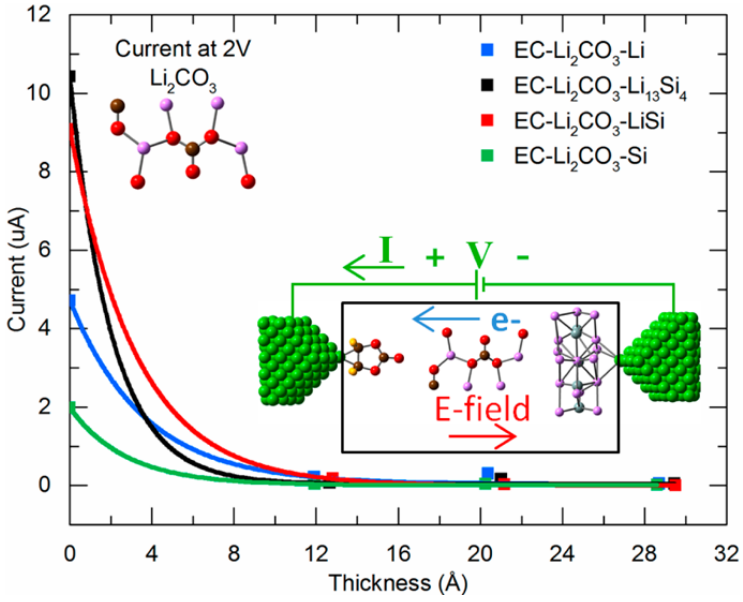


Figure II-360. Leakage current from the anode to the solvent through the SEI under an external voltage between two nanotips (green).

*Ion transport from the cathode through the electrolyte to the anode*

We investigated Li ion transport in a model nanobattery containing all the main elements: from the cathode through the electrolyte to a graphite anode, using classical molecular dynamics simulations. Figure II-361 illustrates the interaction energy experienced by one Li ion traveling under an applied potential through all the phases.

Region 1 (cathode) shows the Li-ion in the $LiCoO_2$ crystal with a potential energy average of −255 kcal/mol. After 4.62 ps the Li-ion has moved to the interface between regions 1 and 2 (electrolyte). An average energy of −36.7 kcal/mol is calculated in region 2, which represents the binding of the Li-ion with the electrolyte solution. The energy for the Li-ion to leave the cathode-electrolyte interface is 218.3 kcal/mol; this energy is supplied by the applied electric field. After the Li-ion has gone through the electrolyte, entered the anode, and has been reduced; its potential energy average in region 3 is 2.1 kcal/mol and the binding energy of the Li-ion at the anode−electrolyte interface is 38.8 kcal/mol. Notice that this is the energetics for one particular Li-ion, these energies are not representative averages as they simply allow us to obtain typical geometric structures of the Li-ion local environment.

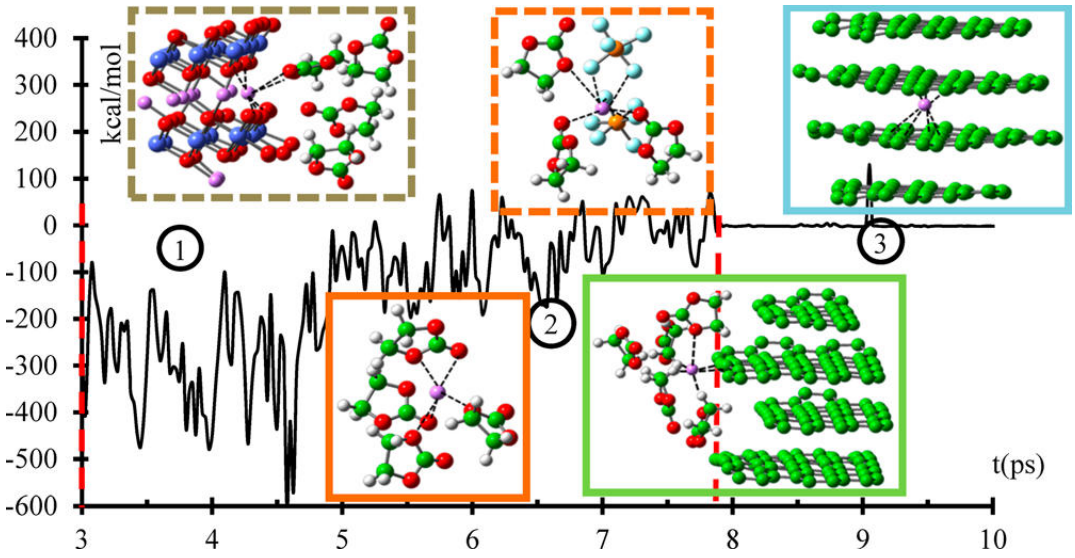


Figure II-361. Interaction energy (E) of one Li-ion with its nearest neighbors within a sphere of 6 Å radius during charging with E = 1.0 V/Å. This is one particular trajectory of a Li-ion from the cathode (1) through the electrolyte (2) to the anode (3). From Ponce et al., JPCC, 121, 12959, (2017).

*Alucone bonding and coordination*

Current work in collaboration with NREL focuses on the reactivity behavior of an alucone coating deposited on a silicon anode. We studied the reactivity of the film using ab initio molecular dynamics (AIMD) simulations and were able to detect changes in the oxidation state of Al in the film, as well as changes in its coordination number, and structural changes inside the film. All of these properties are also being studied experimentally at NREL.

Some of the questions that we want to answer are: i) what is the coordination of Al?; ii) what changes occur to the structure of the film?; iii) what are the changes in oxidation state of Al?

Analyses based on AIMD simulations yield the following answers: i) Al coordination evolves with time, the most common is coordination 4. However higher coordination (e.g., n = 5, 6) tends to be observed at higher Li loading of the film. Kinetics of this process may be slow to be captured in the timeframe of the simulations. Also, 80+% Al atoms coordinate with O, and a few Al atoms coordinate with Si, C and H due to bond re-arrangement; ii) Transformations of structure inside the film include some H atoms from OH groups in alucone

may bond to Al; Al-hydride bonds may form in alucone when H from OH breaks and bonds to Al; iii) The dominant charge is +3, with very few Al atoms having charges of +2.

*Passivation breakdown at Li metal anode interfaces with SEI layer*

Effective passivation of lithium metal surfaces and prevention of battery-shorting lithium dendrite growth are critical for implementing lithium metal anodes for batteries with increased power densities. Nanoscale surface heterogeneities can be "hot spots" where anode passivation breaks down. Motivated by the observation of lithium dendrites in pores and grain boundaries in all-solid batteries, we examine lithium metal surfaces covered with $Li_2O$ and/or LiF thin films with grain boundaries in them. Electronic structure calculations show that at >0.25 V computed equilibrium overpotential $Li_2O$ grain boundaries with sufficiently large pores can accommodate $Li^0$ atoms which aid $e^-$ leakage and passivation breakdown. Strain often accompanies Li insertion; applying a ~1.7% strain already lowers the computed overpotential to 0.1 V. Lithium metal nanostructures as thin as 12 Å are thermodynamically favored inside cracks in $Li_2O$ films, becoming "incipient lithium filaments". LiF films are more resistant to lithium metal growth. The models used in Leung's group should in turn inform passivating strategies in all-solid-state batteries.

## Conclusions

This work has provided several new insights into the nucleation and growth of SEI layers. During this year, the main findings were related to the analysis of the stability of the solid-solid interfaces inside the SEI. Moreover, such analysis was also extended to interfaces between electrode and solid electrolyte, where cracks or simply defects at the interfaces are potential places where Li metal can grow initially as thin wires and then propagate in dendritic growth. Solvation effects in liquid electrolytes were also examined. In particular atomistic details regarding the motion of Li ion through the electrolyte have been clarified. Finally, work is in progress for the characterization of artificial coatings modified by the formation of natural SEI layers.

## Key Publications

1. L. Benitez and J. M. Seminario, "Electron Transport and Electrolyte Reduction in the Solid-Electrolyte Interphase of Rechargeable Lithium Ion Batteries with Silicon Anodes," J. Phys. Chem. C, 120, 17978-17988, (2016).

2. K. Leung and K. L. Jungjohann, "Spatial Heterogeneities and Onset of Passivation Breakdown at Lithium Anode Interfaces," J. Phys. Chem. C, 121, 20188-20196, (2017).

3. V. Ponce; D. E. Galvez-Aranda; J. M. Seminario, "Analysis of a Li-Ion Nanobattery with Graphite Anode Using Molecular Dynamics Simulations," J. Phys. Chem. C, 121, 12959-12971, (2017).

## II.E.5 Addressing Heterogeneity in Electrode Fabrication Processes (BYU)

**Dean Wheeler, Principal Investigator**
Brigham Young University
Department of Chemical Engineering
350 Clyde Building
Provo, UT 84602
Phone: 801-422-4126; Fax: 801-422-0151
E-mail: dean_wheeler@byu.edu

**Brian Mazzeo, Co-Principal Investigator**
Brigham Young University
Department of Electrical and Computer Engineering
459 Clyde Building
Provo, UT 84602
Phone: 801-422-1240; Fax: 801-422-0201
E-mail: bmazzeo@byu.edu

**Tien Duong, Technology Manager**
U.S. Department of Energy
Phone: 202-586-7836
E-mail: Tien.Duong@ee.doe.gov

Start Date: October 1, 2017 End Date: September 30, 2018
Total Project Cost: $700,000 DOE share: $700,000 Non-DOE share: $0

### Project Introduction

A lack of fundamental understanding about the relationships between fabrication parameters, microstructure, and performance prevents appropriate feedback and hurts the development of next-generation battery materials and process improvement in battery manufacturing. For instance, one problem with large-format batteries is ensuring uniformity in the manufacturing process, so that all components perform equally well and no component contributes unduly to performance limitations and failure. This improvement in manufacturing will not be possible without additional information on the nature of heterogeneities and how they relate to electrode fabrication steps. Even more beneficial is if the information is made available in a timely manner through the use of convenient and reliable experimental and modeling tools.

### Objectives

The goal of this work is to better understand connections between fabrication conditions and undesired heterogeneity of thin-film electrodes by means of new non-destructive inspection techniques and computer models. This work will result in new diagnostic and modeling tools for rapidly and conveniently interrogating how well homogeneity has been maintained in electrodes during fabrication and in subsequent cycling. Real-time measurement of heterogeneity will enable manufacturer quality control improvements. The measurement and modeling tools will further enable researchers to compare different electrodes, improve formulations and processes, and anticipate cell performance of new designs.

### Approach

Two non-destructive inspection techniques will be developed or improved which will characterize electrochemical and mechanical uniformity of the electrodes. The first tool will be a flexible contact probe on a polymer substrate for rapidly measuring local electrical conductivity across electrodes of any geometry. The second tool will be a new acoustic probe that measures local elasticity and density of the composite film. These

two prototyping efforts will be tied together by a particle-based microstructure model that allows prediction and correlation of electrode conductive and mechanical properties with fabrication conditions. Each of these tools involved one or more quarterly milestones.

In addition to model and tool development, the tools were used to begin examining electrodes sourced from other researchers, including from industry, in order to assess the effects of mixing and composition changes, and the effects of cycling. Partners in this effort included Ram Subbaraman (Bosch), Daniel Abraham (ANL), Kandler Smith (NREL), Bryant Polzin (ANL), Chisu Kim (Hydro-Québec), and Henning Dreger (TU Braunschweig). Other collaborations and the transfer of this technology to interested parties are being pursued.

## Results

*Milestone 1*

Milestone 1 of FY 2017 and of the project as a whole was to demonstrate that the micro-flex-line probe (µFLP), which is the flexible variant of the micro-N-line probe (µNLP), obtains valid measurements of electrode-film electronic conductivity. Specifically the flex probe results were compared to those obtained for the previously validated µNLP. Figure II-362 shows a side-by-side comparison of the geometry of the completed µNLP and the µFLP probes. In this case N = 6; that is, there are 6 parallel lines on the devices, 4 of which are used for any particular electrical measurement.

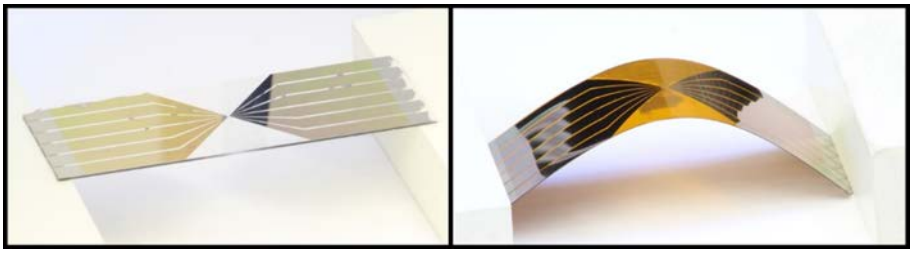

Figure II-362. Side by side comparison of the rigid µNLP consisting of metal deposited on a glass substrate (left), and the flexible µFLP consisting of metal deposited on a polyimide substrate (right).

The design and materials used to construct the µFLP were iterated and improved to increase reliability of the measurements. Nevertheless, this should still be considered the first-generation design and further improvements are anticipated. For this report, the primary test material used is an anode provided by an undisclosed commercial battery manufacturer.

To obtain the results found in Table II-10, tests were performed as follows. Using a µNLP, an electrical sample of the electrode film was collected in 9 independent locations and used with the inversion model to obtain average conductivity with 95% confidence interval. The process was then repeated on the same sample using the µFLP.

**Table II-10: Experimental conductivity results (with 95% confidence intervals) from using µNLP and µFLP on the same electrode sample.**

| | Rigid probe | Flex probe |
|---|---|---|
| Conductivity (mS/cm) | 1421±33 | 1496±182 |

These results show that the µFLP measures conductivity that is largely consistent with measurements of the rigid probe, though the significance level is not as high as ultimately desired. Through these and other results there are indications of a modest bias of the flex probe toward measuring larger conductivity values than does the rigid probe. This may be caused by a small amount of current leakage between lines on the flex probe.

Work will continue on the flex probe to confirm this hypothesis and reduce the problem so as to improve accuracy relative to other methods. It is anticipated that as the flexible probe becomes a more mature technology as a result of this project, it will allow conductivity measurements on thin-film electrodes in new geometries.

*Milestone 2*

Milestone 2 was to further demonstrate that the micro-flex-line probe (µFLP), which is the flexible variant of the micro-N-line probe (µNLP), can be used to make measurements of electrode-film electronic conductivity. The primary value of the flex probe is that it can be used to test much larger samples than the previous design, which will allow extension of this testing technology eventually to on-line measurement during the electrode manufacturing process.

Specifically for this milestone, the flex probe results are to be performed for three different electrode samples while the probe is mounted on the high-precision positioning system. Table II-11 shows results for three different commercial-grade electrodes provided by Argonne National Laboratory. The first two are cathodes while the last is an anode. At least 9 spatially separated points were used to obtain the averages and confidence intervals.

**Table II-11: Experimental conductive property results (with 95% confidence intervals) from using µFLP on the three electrode samples.**

| | AC005 | C015 | AA002 |
|---|---|---|---|
| **Conductivity (mS/cm)** | 241±15 | 198±5 | 3962±681 |
| **Contact Resistance (Ω cm²)** | 0.146±0.021 | 0.198±0.010 | 0.053±0.011 |

As during the previous quarter, the design and materials used to construct the µFLP were iterated and improved to increase reliability of the measurements, and further improvements in future quarters were likewise realized. As further validation of the results, the values in Table II-10 have been compared to previous measurements using other methods (such as 4-line probe and the van der Pauw method) where available. The comparative results are consistent, though additional investigations are planned for ongoing validation.

During this and the prior quarter, additional samples were obtained from other researchers. Investigations were begun to use the current suite of tools to assess effects of formation and cycling on changes in electronic and ionic conductivity of electrodes. Additional work was begun to study the effect of different mixing processes on resulting electrode conductivities. It is anticipated that these studies will provide insight into what manufacturing practices can most efficiently increase needed conductivities and increase power and accessible energy of Li-ion batteries.

*Milestone 3*

Milestone 3 was to make improvements to the dynamic particle packing (DPP) microstructural model and validate that it can match experimental values of conductivity for one anode and two cathode films. A significant part of VTO-funded efforts at BYU has been to develop a versatile and accurate electrode microstructure prediction model. The model uses fundamental forces and interactions to determine particle dynamics and packing during all electrode-fabrication steps: mixing, coating, drying, and calendering. The previous iteration of the model (FY15-16) was reasonably successful at predicting microstructure and transport and mechanical properties of dried films, but exhibited a few physical deficiencies. Thus a major overhaul was begun during the last year to incorporate smoothed-particle hydrodynamics (SPH) into the model to better describe slurry and solid bulk behavior and interfaces.

The model uses spheres with diameter ~2 µm to represent the carbon-binder domain and solvent. Active material particles were constructed from overlapping combinations of spheres; the technique allows different shapes such as bumpy spheroids and flattened discs that approximate the observed shapes of active-material particles. For this milestone there was an emphasis on the drying and calendering steps with the new SPH framework, because these steps lead to substantial particle rearrangements that that directly affect the electrode structure and therefore conductivity. Ionic conductive properties are compared in Table II-12, in which tortuosity can be considered a dimensionless resistance to ion movement. The results show that the model is semi-quantitatively correct for 3 different active materials (each having different particle shapes). Further refinement of the model parameters will be undertaken to achieve quantitative agreement with experiment for a range of physical properties. A comparison of modeled microstructures is likewise shown in Figure II-363, illustrating the complex pore structures able to be simulated by the model.

**Table II-12: Simulated and experimental effective ionic transport results, following drying and calendering steps.**

| Electrode | Simulation | | Experiment | |
|---|---|---|---|---|
| | Porosity (%) | Tortuosity | Porosity (%) | Tortuosity |
| CPG-A12 | 43.9 | 4.3 | 36.1 | 3.4 |
| Toda 523 | 44.3 | 5.4 | 30.0 | 3.1 |
| Toda HE5050 | 49.4 | 3.6 | 36.1 | 2.9 |

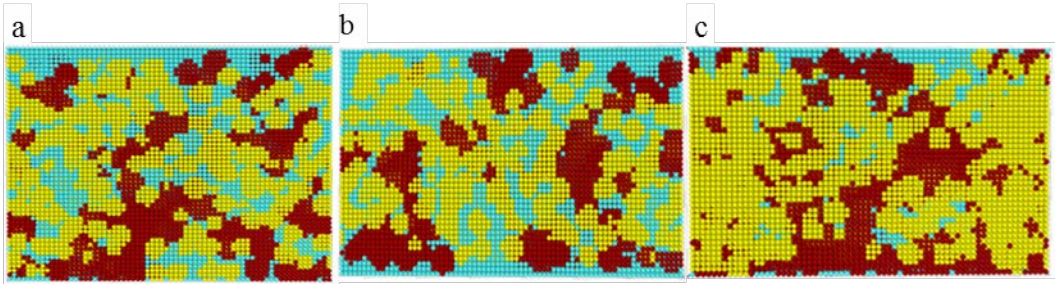


Figure II-363. Cross-section images from models of (a) CPG-A12, (b) Toda 523 (B), and (c) Toda HE5050; carbon-binder domain is red, active material is yellow, and larger pores are blue.

*Milestone 4*

Milestone 4 was to develop preliminary results for a new acoustic probe and associated model, with an associated Go/No-Go decision. Based on a successful outcome, the decision was made to continue developing the acoustic method of interrogating battery electrode films. The ultimate purpose of this type of test is to rapidly determine if there are mechanical variations in an electrode that would lead to poor electrochemical performance. This will allow improvement of the manufacturing process.

There are multiple means of using sound waves to analyze mechanical behavior of thin films. One method was to examine resonance frequencies. Figure II-364 depicts that the resonances of three cathodes with a 20 µm aluminum current collector are seen to occur at different fundamental frequencies. Each of the cathodes had coating layers of different thicknesses (42 µm, 38 µm, and 26 µm coatings on top of the current collector) and densities. The purple line labeled “laser off” is a baseline reading to ensure that the peaks seen by the probe are not due room noise. The tendency of the resonance frequency showed in Figure II-362 demonstrates that the battery film acted more like a membrane, with $h^{-0.5}$ dependence, where $h$ is the film thickness. The results were also confirmed by comparing the resonance frequencies obtained from a scanning laser doppler vibrometer (SLDV).

By fitting the acoustic measurements to the results of a numerical model, the Young's modulus was found in Table II-13. The thickness is the reported value from the manufacturer (of the coating only, not including the 20-µm-thick aluminum current collector), and the Young's modulus values are obtained from a combination of simulated experimental results.

Based on these results, the acoustic method exhibits enough sensitivity to distinguish different values of Young's modulus from different coating layers. It is anticipated that refinement of the method is required to give more accurate results and to enable more robust sampling in an industrial environment.

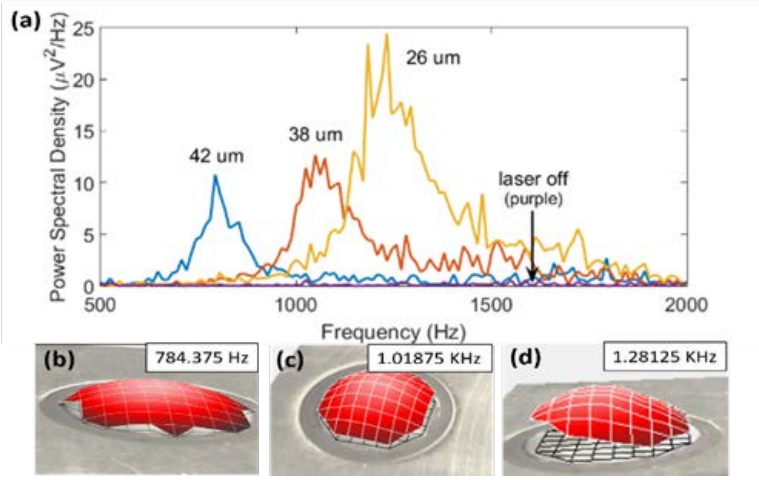


Figure II-364. (a) Power spectral density for various battery films. SLDV results of various battery films with thicknesses of (b) 42 µm (c) 38 µm (d) 26 µm

**Table II-13: Measured and calculated properties of the battery films coated layer.**

| Coating | *h* (µm) | ρ (g/cm³) | *E* (GPa), SLDV | *E* (GPa), peaks | ν |
|---|---|---|---|---|---|
| **1** | 42 | 2.760 | 0.344 | 0.412 | 0.3 |
| **2** | 38 | 3.055 | 1.71 | 2.01 | 0.3 |
| **3** | 26 | 2.479 | 5.04 | 4.13 | 0.3 |

## Conclusions

To date this work has led to

1. A redesign and manufacture of a flexible conductivity probe that improves accuracy and allow sampling of larger electrode films.
2. Electronic and ionic conductivity measurements comparing pristine and cycled commercial electrodes to quantify effects of cycling on microstructure and transport performance.
3. An improved dynamic particle packing (DPP) model to allow predictive insight into the slurry coating process.
4. A successful proof-of-concept acoustic probe used to determine electrode film stiffness.

In the next fiscal year, further improvements are anticipated, including work to adapt the probe technology to assessment of large or continuous samples, consistent with how Li-ion battery electrodes are made commercially.

## Key Publications

The following publications were made during FY 2017 under VTO support. Additional manuscripts based on this work are under preparation.

1. D.R. Nevers, F.R. Brushett, and D.R. Wheeler, "Engineering radical polymer electrodes for electrochemical energy storage," J. Power Sources 352, 226-244 (2017).

2. M.M. Forouzan, M. Wray, L. Robertson, and Dean R. Wheeler, "Tortuosity of composite porous electrodes with various conductive additives in an alkaline system," J. Electrochem. Soc., 164, A3117-A3130 (2017).

The following presentations at scientific conferences were made.

1. M. Mehdi Forouzan, Anthony Gillespie, Nicholas Lewis, Brian A. Mazzeo, and Dean R. Wheeler, "A Predictive Model of Lithium-Ion Electrode Fabrication, including Mixing, Coating, Drying, and Calendering," ECS/PRiME Meeting, Honolulu, Hawaii, October 2016.

2. John E. Vogel, William Lange, Derek Clement, Brian A. Mazzeo, and Dean R. Wheeler, "Correlation of Local Conductivity to Microstructure for Li-Ion Battery Electrodes by Use of a Contact Probe and SEM/FIB," ECS/PRiME Meeting, Honolulu, Hawaii, October 2016.

3. D.R. Wheeler and B. A. Mazzeo, "Addressing heterogeneity in electrode fabrication processes," U.S. Department of Energy 2017 Annual Merit Review Meeting, Washington, DC.

4. F. Pouraghajan, H. Knight, B. A. Mazzeo, and D. R. Wheeler, "Quantifying tortuosity of porous Li-ion battery electrodes: Comparing polarization-interrupt and AC impedance (blocking-electrolyte) methods," 231st Meeting of the Electrochemical Society, New Orleans, LA, 2017.

5. K. L. Dallon, M. Wray, D. R. Wheeler, and B. A. Mazzeo, "Determination of mechanical properties of battery films from acoustic measurements," 231st Meeting of the Electrochemical Society, New Orleans, LA, 2017.

6. H. Knight, F. Pouraghajan, M. Wray, D. R. Wheeler, and B. A. Mazzeo, "The effects of aging on the tortuosity of Li-ion battery electrodes," 231st Meeting of the Electrochemical Society, New Orleans, LA, 2017.

7. E. E. Hardy, J. E. Vogel, D. V. Clement, D. R. Wheeler, and B. A. Mazzeo, "Flexible probe for measuring local conductivity variations in Li-ion electrode films," 231st Meeting of the Electrochemical Society, New Orleans, LA, 2017.

8. J. E. Vogel, D. V. Clement, E. Hardy, B. A. Mazzeo, and D. R. Wheeler, "Local variation in microstructure causes heterogeneity in the conductivity of commercial lithium-ion cathode films," 231st Meeting of the Electrochemical Society, New Orleans, LA, 2017.

9. K.L. Dallon, J. Yao, D.R. Wheeler, and B.A. Mazzeo, "Determination of mechanical properties of battery films from acoustic resonances," Review of Progress in Quantitative Nondestructive Evaluation, Provo, UT, 2017.

10. E. Hardy, D. Clement, J. Vogel, D.R. Wheeler, and B.A. Mazzeo, "Flexible probe for measuring local conductivity variations in Li-Ion electrode films," Review of Progress in Quantitative Nondestructive Evaluation, Provo, UT, 2017.

## II.E.6 Large Scale *Ab Initio* Molecular Dynamics Simulation of Liquid and Solid Electrolytes (LBNL)

**Lin-Wang Wang, Principal Investigator**
Lawrence Berkeley National Laboratory
One Cyclotron Road, MS-66
Berkeley, CA, 94760
Phone: 510-486-5571
E-mail: lwwang@lbl.gov

**Tien Duong, Technology Manager**
U.S. Department of Energy
Phone: 202-586-7836
E-mail: Tien.Duong@ee.doe.gov

Start Date: October 1, 2016 End Date: September 30, 2017
Total Project Cost: $225,000 DOE share: $225,000 Non-DOE share: $0

### Project Introduction

One major obstacle for lithium sulfur battery is the dissolution of the lithium polysulfur in the electrolytes. The dissolution mechanism, the bonding structure of the dissolved lithium polysulfur (e.g., whether they cluster or are dissociated) are not well understood. The goal of this project is to use large scale ab initio calculation and molecular dynamics simulations to study the discharge mechanism in Li sulfur battery, especially for polysulfur interaction with liquid electrolyte solvent molecules, and cathode materials, as well as Li diffusion mechanism in superionic crystal solid electrolytes. We also like to search for cathode materials to prevent the dissolution based on thermodynamic principles. The long term goal is to use such theoretical understanding to provide guidance to develop better electrolyte and cathode systems to overcome the bottlenecks which currently prevent the commercialization of the Li/S battery.

### Objectives

For the first year, we will focus on the study of polysulfur interaction with substrate cathode materials, and to find such substrates to bind the polysufur with sufficient binding energies to overcome their dissolution. One objective is to screen a few cathode materials for their feasibilities for Li-S battery applications through ab initio calculation. We will also study solid electrolytes for the lithium diffusion in such systems. One long term objective is to study the actual lithium polysulfur thermodynamic properties and morphology in the electrolyte. For this goal, we also need to develop the proper ab initio calculation methods to study such thermodynamic properties in liquid.

### Approach

Several ab initio calculation methods will be used, and new methods will be tested and developed. Most of our calculations will be based on density functional theory (DFT). One approach is to use genetic algorithm to search for the minimum energy structure. This is a particularly important for Li-S battery since the cathode material and the binding morphology might be complicated, an efficient algorithm is needed to search for the minimum energy structure. Another method is the dealing with the solvent effects. First, we will use implicit solvent model to deal with this solute-solvent interaction energy. The uncertainty of the interaction parameters will be fixed through the comparison with the experimental voltages in the dissolved $Li_2S_n$ cases. In the following years, however, we will test a molecular dynamics (MD) based method to study the solute-solvent interaction energy. This will include two aspects, one is the configuration average between the solute-solvent binding configurations, and another is a way to calculate the solute-solvent interaction energy avoiding big thermodynamics fluctuation caused by the rest part of the system. For the configuration average, we will test

an approach using force field method to carry out MD, then take snapshots from the MD trajectories to carry out ab initio calculations. The force field MD will enable us to explore different configurations, while ab initio calculation will give us energy correction upon the force field energy. To avoid thermodynamic fluctuation, two approaches will be tested. One is the thermodynamic integration method (e.g., umbrella sampling), which will be done coupling the force field simulation with ab initio calculation. Another is a new method we proposed to calculate the interaction energy directly. Finally, to study the solid electrolyte, especially the collective lithium ion movements, we will use the nudged elastic band (NEB) method as well as metadynamics method. NEB will be useful to calculate the transition barrier when the initial and final stages are known, and the path is relatively clear. Metadynamics will be useful if a general reaction coordinate can be defined, for example, the direction of the lithium migration.

## Results

We have studied the use of $C_2N$ nanosheet as a Li-S cathode material. $C_2N$ has been recently synthesized as another carbon nitride 2D system besides the well-known g-$C_3N_4$ polymeric carbon nitride. Compared to the g-$C_3N_4$, $C_2N$ could be mechanically more stable. Recently, nitrogen doped graphene or black carbon systems have shown promise as Li-S cathode materials to prevent the dissolution of the polysulfur. However, such doped systems have low capacity due to the limited amount of nitrogen compared to the compound systems. We have thus investigated the use of $C_2N$ as a cathode material. We find that the lithium atoms like to bind strongly with the two coordinated N atoms, while there is no binding between N and S atoms. Although the $C_2N$ itself (without sulfur) can be used as an cathode material, its binding is weak and the energy capacity is low. Thus it is essential to have the sulfur in the system. Thus the binding topology is that, the Li binding to the substrate N, and an upper layer S atoms, while the S atoms can bind with more additional lithium away from the substrate to form a lithium polysulfur. We found that the binding of the lithium polysulfur to the substrate can prevent its dissolution. In particular, at the beginning of lithiation process, a $Li_2S_8$ can be anchored within one hole of the $C_2N$ substrate. At the end of the lithiation, a $Li_{10}S_8$ cluster will be attached to one hole of the $C_2N$ substrate. The binding of the cluster to the substrate is strong enough to prevent its fragmentation or dissolution. The lithiation processes have voltages from 3.9 V to 1.6 V, and an average voltage of 2.02 V at the end step of $Li_{10}S_8$. The total energy capacity will be 1122 Whkg$^{-1}$. Although this is only half as the original LiS battery due to the added weight of the substrate and the limited sulfur reduced stage ($Li_{10}S_8$, instead of $Li_2S$), nevertheless, it is much higher than the current Li ion battery based on intercalations. Finally, we also show that the $Li_mS_8$_$C_2N$ system is metallic throughout the whole process, which solves another problem of the Li-S battery (the insulating natures of $Li_2S$ and $S_8$).

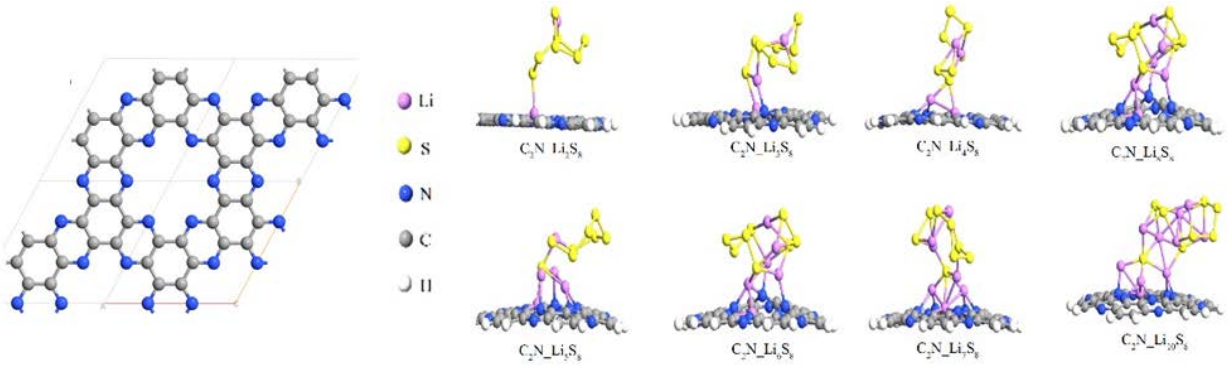


Figure II-365. The $C_2N$ nanosheet (left) and the binding configurations of C2N_$Li_mS_8$ (right). These binding configurations are searched through genetic algorithms based on DFT calculations.

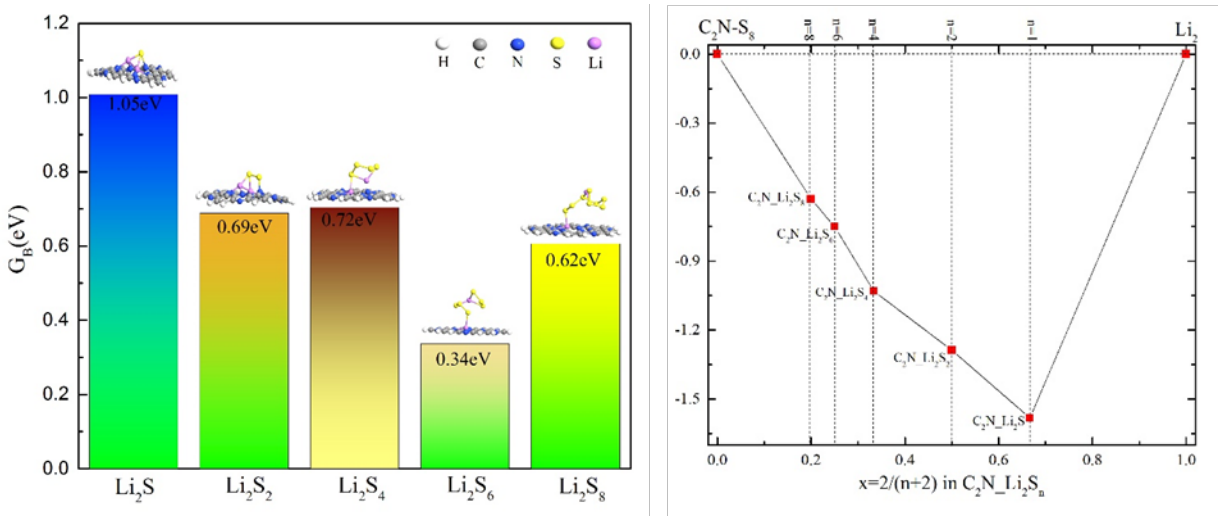


Figure II-366. The binding energy between the Li2Sn polysulfur and the C2N substrate (left), and the formation energy diagram (left) of $C_2N\_Li_2S_m$.

Figure II-365 shows the basic structure of $C_2N$ and the binding configurations of $C_2N\_Li_mS_8$ systems, while Figure II-366 shows the binding energy between Li2Sm polysulfur and the $C_2N$ substrate, as well as the formation energies of $C_2N\_Li_2S_m$. The formation energy of a general formula $C_2N\_Li_mS_n$ is defined as: $G_{form}^{Li_mS_n\_C_2N} = (G_{Li_mS_n\_C_2N} - mG_{Li} - nG_{S_8}/8 - G_{C_2N})/(n+m)$, with the alloy style composition x defined as x=m/(n+m). However, in the right hand panel of Figure II-366, what actually shown is $\Delta G_{form}(x) = G_{form}(x) - (1-x)G_{form}(0) - xG_{from}(1)$ for the $C_2N\_Li_2S_m$ system. Table II-14 lists the voltages of the different reaction steps for the products based on $C_2N\_Li_2S_n$ and $C_2N\_Li_mS_8$ respectively.

**Table II-14: The lithiation reactions and their corresponding voltages for Li-S battery cathodes based on $Li_2Sn\_C_2N$ and $Li_mS_8\_C_2N$.**

| Label | Category | Reactions (DME/DOL(1:1, v/v)) | Voltage(V) | Feasibility |
|---|---|---|---|---|
| $R_{10}$ | $Li_2S_n\_C_2N$ | $S_8\_C_2N + 2Li = Li_2S_8\_C_2N$ | 3.03 | √ |
| $R_{11}$ | | $3Li_2S_8\_C_2N + C_2N + 2Li = 4Li_2S_6\_C_2N$ | 2.36 | √ |
| $R_{12}$ | | $2Li_2S_6\_C_2N + C_2N + 2Li = 3Li_2S_4\_C_2N$ | 3.26 | √ |
| $R_{13}$ | | $Li_2S_4\_C_2N + C_2N + 2Li = 2Li_2S_2\_C_2N$ | 2.05 | √ |
| $R_{14}$ | | $Li_2S_2\_C_2N + C_2N + 2Li = 2Li_2S\_C_2N$ | 2.17 | √ |
| $R_{15}$ | $Li_mS_8\_C_2N$ | $Li_2S_8\_C_2N + Li = Li_3S_8\_C_2N$ | 3.95 | √ |
| $R_{16}$ | | $Li_3S_8\_C_2N + 2Li = Li_5S_8\_C_2N$ | 2.34 | √ |
| $R_{17}$ | | $Li_5S_8\_C_2N + 2Li = Li_7S_8\_C_2N$ | 2.65 | √ |
| $R_{18}$ | | $Li_7S_8\_C_2N + 3Li = Li_{10}S_8\_C_2N$ | 1.55 | √ |

We have also studied using oxidized black phosphorene as lithium battery cathode. This is under the generation direction of using light elements from upper right corner of periodic table as Li cathodes, in contrast

with the transition metal oxides as the lithium ion battery cathodes. The light weights of these elements and the strong chemical bonding with the Li ion can lead to high energy capacity of such battery materials. One two examples are the Li-S battery and Li air battery. Both batteries are based on chemical reactions, which however cause many other issues like the mechanical stability, large volume change, and the electric conductivity of the cathode. To overcome such issues, 2D materials can be used. The 2D material can form the framework, which provides the mechanical stability and electric conductivity. As such 2D materials can be made monolayer thick, they provide ample surface area to bind the Li, which can also improve the kinetic of the charging/discharging process. To have high energy capacity however, one needs strong binding energy of Li and the 2D material. People have tried to use black phosphorene as lithium cathode, but the binding energy is too small. Here we found that the phosphorene oxide can provide large binding energy. The Li atom will bind with the oxygen atom at the surface of phosphorene oxide. In this aspect, this is like the Li air battery, except the oxygen is provided in a solid form, instead of in the gas phase, and the whole battery can be sealed. Since there is no air coming in and out of the system, the whole device should be mechanically stable. We found that each surface O can bind with one Li atom. If more Li atom is bond with one O atom, the structure can become unstable. For the fully oxidized black phosphorene: $P_4O_4$, 4 Li atom can be bonded, with a final product as $Li_4P_4O_4$. This will have a theoretical energy capacity of 1457 Wh/Kg. Ab initio molecular dynamics is carried out, showing that the system is vibrationally stable. The solvent effect is taken into account by implicit solvent model.

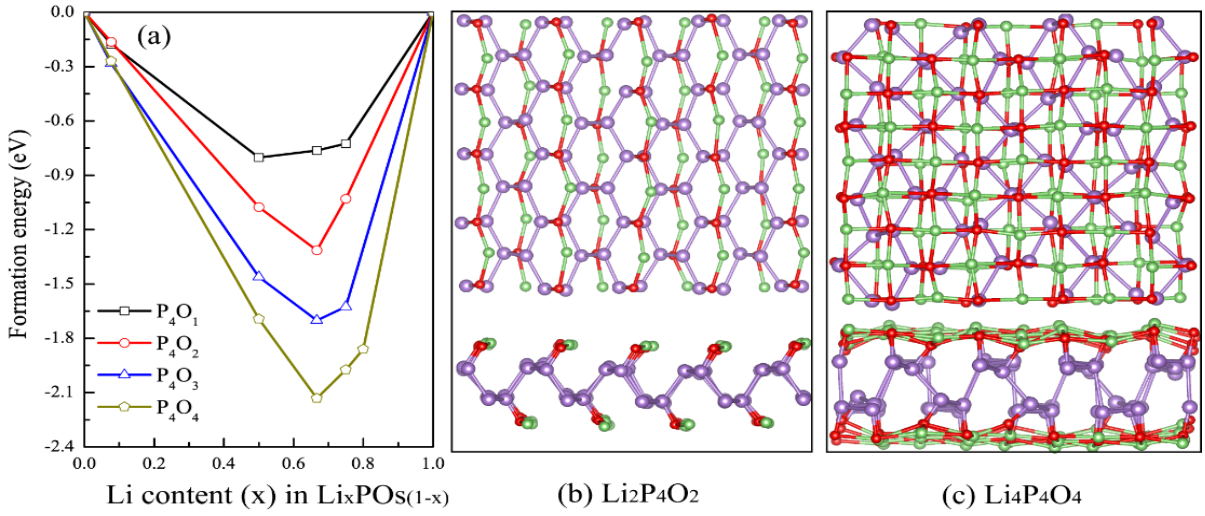


Figure II-367. The formation energy (a), the Li2P4O2 configuration (b) and Li4P4O4 configuration (c). In (b) and (c), the blue ball is P, red ball is O, and green ball is Li.

Figure II-367 show the formation energy and binding configurations of different phosphorene oxides. We have also calculated the band structure of the system (Figure II-368), and showing that the oxidized phosphorene absorbed with Li are metallic, thus should be electric conductive.

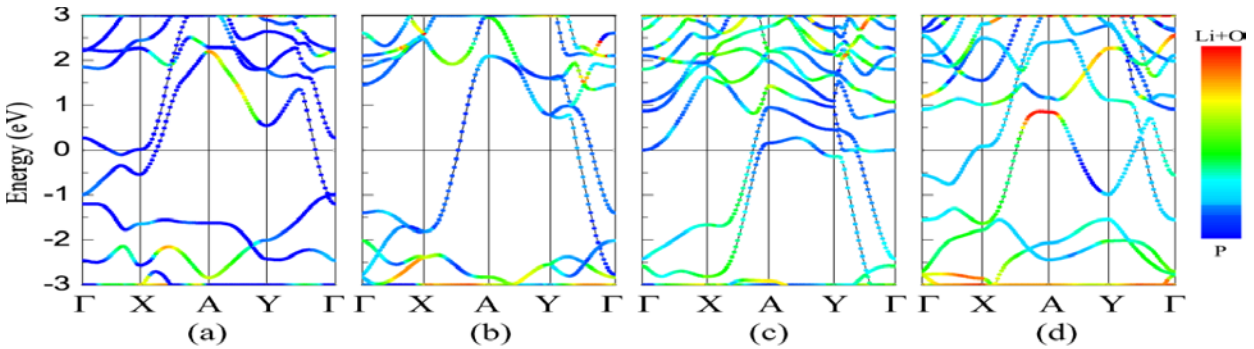


Figure II-368. Projected band structures of (a) $Li_1P_4O_1$, (b) $Li_2P_4O_2$, (c) $Li_3P_4O_3$ and (d) $Li_4P_4O_4$.

## Conclusions

In conclusion, we found that $C_2N$ can be a very good Li-S cathode material, which can provide sufficient energy capacity, meanwhile can solve the problems of polysulfur dissolution, insulating of $Li_2S$ and $S_8$, as well as mechanical stabilities. We also find that oxidized phosphorene can be used as a Li battery cathode. This is alike the Li air battery but with the oxygen provided by the solid form O binding with the phosphorene framework. This system is also mechanically stable and can provide relatively high energy capacity of 1457 Wh/Kg.

## Key Publications

1. Y. Duan, B. Zhang, J. Zheng, J. Hu, J. Wen, D.J. Miller, P. Yan, T. Liu, H. Guo, W. Li, X. Song, Z. Zhuo, C. Liu, H. Tang, R. Tan, Z. Chen, Y. Ren, Y. Lin, W. Yang, C.M. Wang, L.W. Wang, J. Lu, K. Amine, F. Pan, "*Excess Li-ion storage on nanocrystal reconstructed surface to boost battery performance*", Nano Lett, 17, 6018 (2017).

2. J. Wu, L.W. Wang, "*2D frameworks C2N as a potential cathode for lithium sulfur batteries: an ab initio density functional study*" (submitted).

3. Y. Li, F. Ma, L.W. Wang, "*Phosphorene oxides as a promising cathode material for sealed non-aqueous Li-oxygen battery*" (submitted).

## II.E.7 Dendrite Growth Morphology Modeling in Liquid and Solid Electrolytes (MSU)

**Yue Qi, Principal Investigator**
Michigan State University
3509 Engineering Building
East Lansing, MI 48824
Phone: 517-432-1243; Fax: 517-432-1105
E-mail: yueqi@egr.msu.edu

**Tien Duong, Technology Manager**
U.S. Department of Energy
Phone: 202-586-7836
E-mail: Tien.Duong@ee.doe.gov

Start Date: January 1, 2017 End Date: December 31, 2019
Total Project Cost: $1,135,125 DOE share: $999,943 Non-DOE share: $135,182

### Project Introduction

In this project, we will first develop a phase-field model to incorporate the electrochemical driving forces predicted from first principles simulations in liquid electrolytes and then incorporate mechanical driving forces to simulate dendrite growth in solid electrolytes with resolved microstructures. The μm-thick solid electrolytes will allow easier, direct comparison of modeling and experimental results, thus facilitating the validation of the electrochemical-mechanically driven Li-dendrite growth model. Last but not the least, the computational model for solid electrolytes can also be applied to study and design nm-thin artificial SEI on Li metal surface. Therefore, this atomically-informed phase-field model will allow us to design the desired properties of artificial SEI coating to suppress dendrite growth in liquid-electrolyte and the microstructure of a solid-electrolyte to be dendrite-resistant during cycling. This model will enable the design of durable and safe Li-anodes for Li-S, Li-air, all-solid Li-ion batteries, as well as high energy density Li-ion batteries, lead to batteries that meet DOE's target for the high energy batteries cell density (>350 Wh/kg) for EV applications and cost below $100/kWh$_{use}$.

### Objectives

The ultimate goal of this project is to develop a validated model to predict Li dendrite morphology evolution in both liquid and solid electrolytes during electrodeposition and stripping, in order to accelerate the adoption of Li metal electrodes in current and emerging battery technologies. To achieve this goal, the project has four objects:

1. formulate a general framework that captures the electrochemical-mechanical driving forces for Li morphology evolution;
2. consider the role of the nm-thin SEI in liquid-electrolytes as well as the microstructures of mm-thick solid-electrolytes for Li morphology evolution;
3. connect micron-scale phase-field models and atomic-scale DFT-based simulations via parameter- and relationship-passing in order to predict Li dendrite nucleation and growth kinetics and morphology; and
4. validate the key input parameters and main conclusions of the multi-scale model as new capabilities being developed step-by-step.

### Approach

This project will develop a multi-scale model that connects micron-scale phase-field models and atomic-scale DFT-based simulations via parameter- and relationship-passing in order to predict Li-metal dendrite morphology evolution, in both liquid and solid electrolytes. The key innovation of this project is to capture the

electrochemical-mechanical driving forces and incorporate the roles of an nm-thin solid electrolyte interphase (SEI) in liquid electrolytes as well as of the microstructures of μm-thick solid electrolytes for all-solid-state batteries. Our strategy to study Li dendrite morphology in both liquid and solid electrolytes allows us to share many similar governing equations and common mechanisms, gradually increase the complexity of the model, and validate the model step-by-step for its key input parameters and main conclusions through tailored experiments

## Results

*Task 1: Illuminate the role of SEI kinetics in Li dendrite growth in liquid electrolytes*

**Subtask 1.1 A new set of DFTB parameters for Li, H, C, and O interactions were developed and verified**
This set of DFTB parameters were obtained by fitting to DFT results of a broad range of structures (bcc and fcc Li metal, $Li_2O$, LiOH, LiH, $LiCH_3$, and $LiC_6$) and properties (surface energy, adsorption energy, band structures). This set of DFTB parameters were then used to predict additional properties, such as $Li^+$ ion solvation energy, interface energy, $Li^+$ ion diffusivity in liquid EC, *et al.* to validate the accuracy and transferability of the parameters. The agreement of DFTB and DFT results (shown in Table II-15) suggests the reliability of this set of parameters.

Table II-15: Key Properties not used for DFTB parameterization, but compared with DFT (GGA/PBE) for validation

| Property | System | DFTB | DFT |
|---|---|---|---|
| Li surface energy ($J/m^2$) | (001) | 0.5 | 0.46 |
| | (011) | 0.49 | 0.49 |
| | (111) | 0.58 | 0.53 |
| Li adsorption energy on Li(001) (eV) | hollow | 1.49 | 1.37 |
| | bridge | 1.30 | 1.28 |
| | top | 1.08 | 1.07 |
| Interface energy ($J/m^2$) | Li(001)/$Li_2CO_3$(001) | 0.64 | 0.5 |
| HOMO and LUMO gap (eV) | EC | 6.5 | 6.8 |
| Solvation energy (eV) | $Li^+$ in EC | 5.4 | 5.2-5.5 |
| Diffusivity ($cm^2/s$) | $Li^+$ in EC at 450K | $2.4x10^{-5}$ | $1.1x10^{-5}$ |

*DFTB method along with this set of parameters was used to compute the charge transfer reaction energetics on an SEI covered Li metal surface, under an applied potential.*
Figure II-369 shows the $Li^+$ ion energy change when it de-solvates from the EC solvents, diffuses through the 4 layers of $Li_2CO_3$ (a model SEI layer), and gets reduced by the electrons on the Li-metal slab. The reduced state is considered to be the reference state. Three oxidized states with varying electron $xe^-$ at x = 1 to 3, corresponding to electron density of 0.002 to 0.006 e/Å$^2$ on Li-metal surface were simulated. To verify the reliability of calculated charge transfer reaction energy from minimization, molecular dynamics (MD) simulations were performed. The results show that the calculated average energy from MD is close to that from minimization with the maximum deviation of 0.1eV.

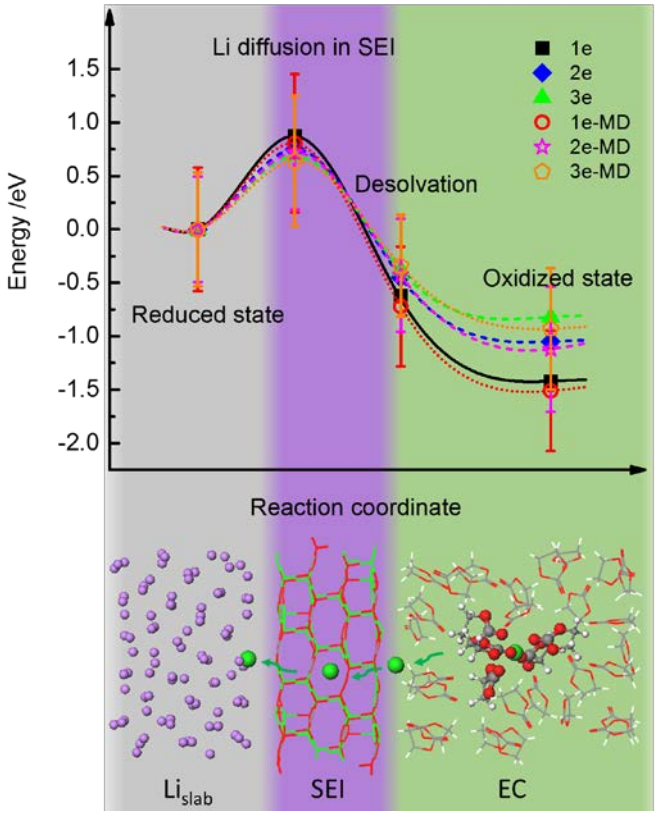


Figure II-369. Energy landscape for $Li^+$ transport from electrolyte to Li-metal slab under different potential.

For the atomic simulations of the Li/$Li_2CO_3$/EC interface, the experimentally defined zero voltage of $Li^+/Li^0$ was calibrated with DFTB and DFT calculations. The zero voltage of electrode is the important reference state in the Li-ion batteries. We have considered a typical electrochemical reaction

$$Li^+(sol) + e^- \leftrightarrow Li^0 \quad (1),$$

where the $Li^+$ ions in the electrolyte solution react with electrons $e^-$ in the electrode to produce the electrode $Li^0$ atoms. The thermodynamic driving force is given by

$$\Delta G = \Delta G^o + F\varphi - RT \ln a_{Li^+} \quad (2),$$

where $\Delta G^0$ is the standard free energy change for the electrode reaction (1), $F$ is the Faraday constant, $\phi$ is the potential on the Li metal electrode, and $a_{Li^+}$ is the activity of $Li^+$ in the electrolyte, which depends on temperature and on the concentrations of other ions. At equilibrium,

$$\Delta G^o + F\phi^o - RT \ln a_{Li^+} = 0 \quad (3)$$

where $\phi^0$ is the equilibrium potential of the Li metal electrode. Therefore, by subtracting Eq. (3) from Eq. (2), the thermodynamic driving force can also be expressed in experiment as,

$$\Delta G = F(\phi - \phi^o) = F\eta, \quad (4)$$

where $\eta$ is the overpotential. If $\eta < 0$, the $Li^+$ is reduced (plating); whereas if $\eta > 0$, the $Li^0$ is being oxidized to $Li^+$ (stripping).

In fact, the potential $\phi$ on the Li metal electrode supplies electrical energy and possesses the electron density on Li metal surface. Therefore, $\phi$ is related to the Fermi level and the work function shift on the Li metal. In addition, as the atomic simulation shows, as the applied voltage increases, the $Li^+$ concentration near the electrode surface will increase, which would change the activity $a_{Li^+}$. In our model, the temperature is

unchanged and only $Li^+$ ion concentration changes, thus the 3rd term in eq (2) can be linked to $Li^+$ solvation energy change with $Li^+$ concentration. Therefore, the thermodynamic driving force can be expressed in our model as

$$\Delta G = \Delta G^o + \Delta W_f + \Delta E_{sol} \qquad (5),$$

where $\Delta W_f$ is the work function shift with excess electron density on Li metal surface, and $\Delta E_{sol}$ is $Li^+$ solvation energy change with $Li^+$ ion concentration in the EC-electrolyte.

To find the zero voltage of $Li^0/Li^+$, according to eq (5), it is necessary to obtain the $\Delta G^0$, $\Delta W_f$, and $\Delta E_{sol}$. We used the case of one electron in eq (1) as a reference, which corresponds to an electron density of 0.002 e/Å$^2$ on the Li-metal surface. The predicated $\Delta G^0$ is 1.42 eV from DFTB method. Also, we used the DFT (with GGA/PBE functional) method to compute the work function as a function of excess electron density on Li metal surface by the slab model. As shown in Figure II-370, when the potential decreases, the excess electron density increases on the Li-metal, the work function will then decrease due to the rise of Fermi level. In addition, we considered a set of bulk models including 32 EC liquid molecules and n (n=1-6) $Li^+$ ions, using DFTB MD method with NVT ensemble at 450 K, to predicate the $Li^+$ solvation energies in EC-electrolyte. The results show that $Li^+$ solvation energies in EC-electrolyte decrease with $Li^+$ concentration (Figure II-370). When the applied potential decreases, the negative charge density increases on Li metal surface, $\Delta W_f$ and $\Delta E_{sol}$ then decrease, and thus $\Delta G$ will decrease accordingly. The values are in good agreement with that of direct predictions from DFTB method.

At excess negative charge density of 0.012e/Å$^2$ on Li metal surface, $\Delta G$=0, corresponding to the experimentally defined zero voltage of $Li^0|Li^+$. When the electron density is larger than this (more negative potential) Li plating occurs; while when the electron density is lower than this (more positive potential), Li stripping occurs. The excess electrons on Li surface will trigger more electrolyte decomosition when SEI fractures.

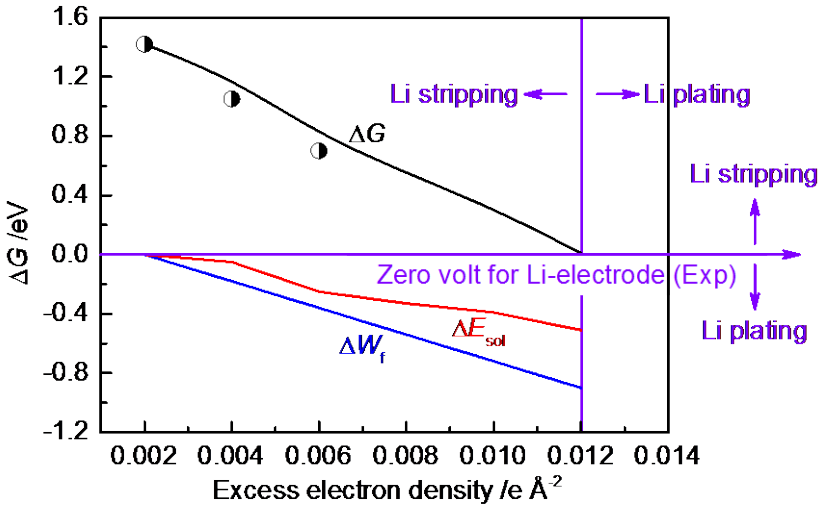


Figure II-370. The thermodynamic driving force of the electrochemical reaction at the Li|$Li_2CO_3$|EC-electrolyte interface, work function shift and $Li^+$ solvation energy change with $Li^+$ ion concentration in the EC-electrolyte as a function of excess electron density on Li metal surface. The circle denotes the directly predicated $\Delta G$ by DFTB method.

**Subtask 1.2, 1.3 Coupled Morphology Evolution Model**

The previously developed dendrite growth model was extended to implicitly include the effect of SEI by the parametric study of the metallic Li/liquid electrolyte binary phase field model. The governing equations for phase field model are diffusion and phase evolution equations.

$$\frac{\partial c_+}{\partial \mathrm{t}} = \nabla \cdot \left[ D^{eff} \nabla c_+ + \frac{D^{eff} c_+}{RT} nF \nabla \phi \right] - \frac{c_s}{c_0} \frac{\partial \xi}{\partial t} \quad (6)$$

$$\frac{\partial \xi}{\partial t} = -L_\sigma (g'(\xi) - \kappa \nabla^2 \xi) - L_\eta h'(\xi) \left\{ exp\left[ \frac{(1-\alpha) nF \eta_\alpha}{RT} \right] - c_+ exp\left[ \frac{-\alpha nF \eta_\alpha}{RT} \right] \right\} \quad (7)$$

The key parameters closely associated with Li plating behavior in the model are: interfacial energetics and anisotropy (formulated in $\kappa$), Li ion diffusion coefficients ($D^{eff}$), charge transfer rate (normalized in $L_\eta$) and double-well energy profile ($g'(\xi)$). These information were obtained from previous DFT results and current DFTB calcautlions.

The implicitly Li morphology model was used to investigate the impact of four major SEI properties, namely interfacial energy, anisotropy, diffusion coefficient and reaction rate constant. The non-linear phase-field model simulation of the Li electrodeposition process revealed that higher Li/SEI interface energy, faster Li-ion diffusion in SEI, and slower reaction rate constants favor less branched Li morphology (as shown in Figure II-371), leading to higher Coulombic efficiency compared to more branched morphology.

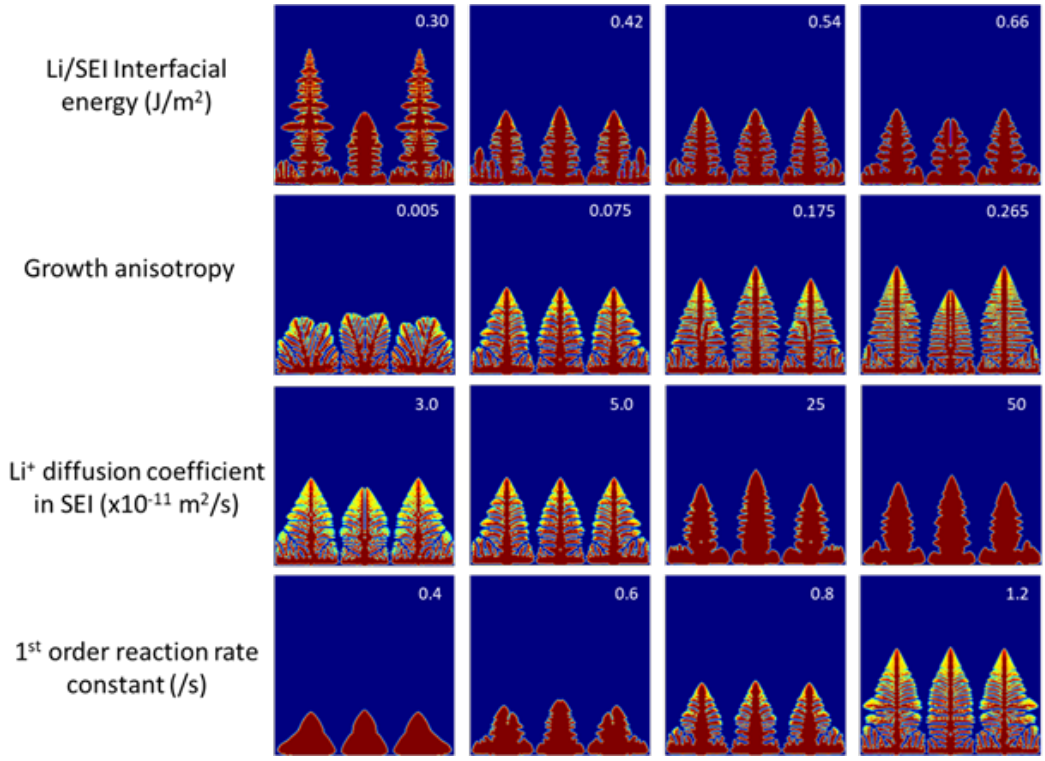


Figure II-371. SEI properties-Li dendrite morphology map from phase field simulation.

**Subtask 1.4 *in situ* Observation Li Dendrite Morphology in Liquid Electrolyte**

Experimental protocol has been established. Our preliminary *in-situ* electrochemical optical observation (Figure II-372) shows the Li plating and stripping process which involves dendrite and mossy structure formation.

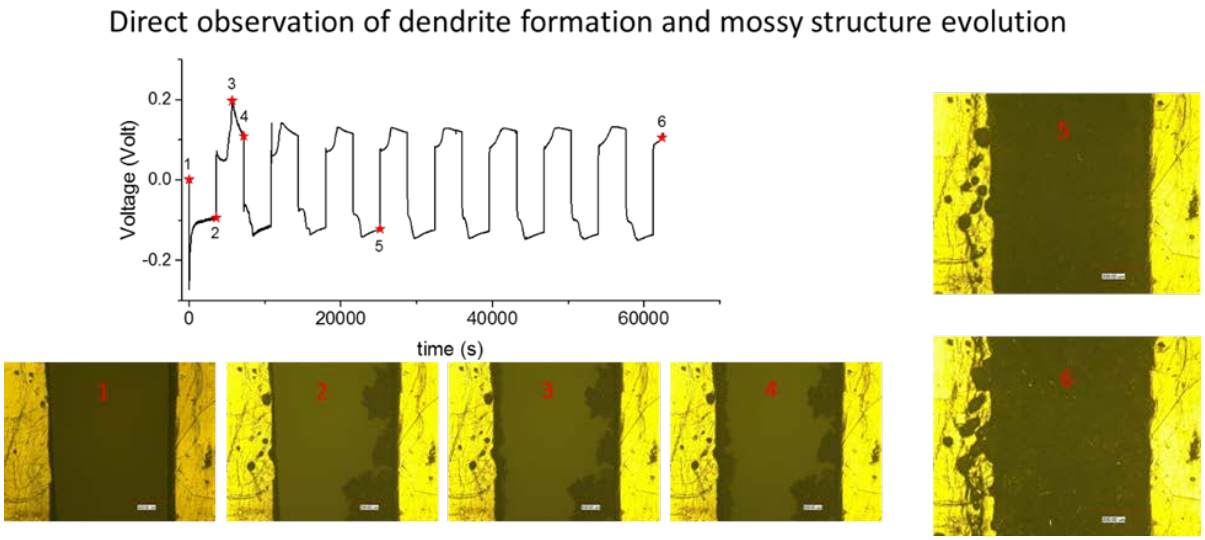


Figure II-372. *in-situ* electrochemical optical observation of Li dendrite growth morphology

A large amount of dead Li formed, which cannot further participate the plating and stripping. Due to the electrical insulating SEI layer, it did not show the shorting. The impact of current density, protective coating, and different electrolyte additives will be further explored. It will be correlated with the cycle efficiency and phase-field modeling.

*Task 2: Model the metallic Li precipitation in solid electrolytes of all-solid batteries*

**Subtask 2.1 DFT Calculations revealed Li nucleation mechanism on LLZO surface**

DFT calculations were performed to address the nucleation mechanism of metallic Li inside LLZO. Both tetragonal and cubic phases LLZO were investigated. It was found the excess electrons in LLZO can be trapped to the La atoms at/near the surface in LLZO. Figure II-373 shows the localized electrons clouds on La. Thermodynamics calculations confirmed that metallic La can be more stable than metallic Li with the excess electrons, providing the nucleation mechanism of metallic Li phase in LLZO. This mechanism is being investigated for LLZO grain boundaries as well.

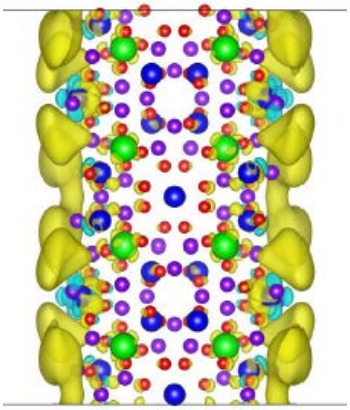

Figure II-373. The excess electrons located on La atoms on LLZO surface.

This mechanism was introduced as a non-uniform, structure-dependent electron activity ($a_e(r)$) in the phase field model. An intergranular Li dendrite growth has been simulated in 2D microstructures. The results showed

that the Li-dendrite growth rate was higher inside wider grain boundaries ore pores than the narrow ones, indicating larger growth resistance at narrower grain boundaries or pores.

**Subtask 2.2 Phase Field Model of Li Dendrite Growth in Solid Electrolyte**

It has been reported that Li dendrites tend to grow into pores and along the grain boundaries (GBs) of the solid electrolytes. A general non-linear phase-field model for Li dendrite growth in a solid electrolyte (e.g., LLZO, LLZTO, etc.) were formulated and implemented. The microstructure of LLZO was resolved and three-phase fields were defined to describe the solid-state battery system as $\{\phi_1(r) = 1, \phi_2(r) = 0, \phi_3(r) = 0\}$ for pure Li-metal anode, $\{\phi_1(r) = 0, \phi_2(r) = 1, \phi_3(r) = 0\}$ for solid electrolyte, and $\{\phi_1(r) = 0, \phi_2(r) = 0, \phi_3(r) = 1\}$ for pores, cracks and GBs. The phase-field equations were reformulated with Butler-Volmer kinetics for the three-phase system. Currently, the solid-electrolyte phase was considered to be non-evolving during electrodeposition, and the Li diffusion coefficients were assumed to be: $D_{GB} > D_{Grain} >> D_{pore}$. Numerically, phase field governing equations were solved together with diffusion and charge conservation equations via finite element method.

An intergranular Li dendrite growth has been simulated in 2D by the as-developed phase field model for solid electrolyte system, as shown in Figure II-374c. The electrodeposited Li metal tends to grow along and fill in the GBs of the solid electrolyte, which is in agreement with the SEM image of dendrite morphology from cycled LLZO battery, as shown in Figure II-374a. The Li-ion concentration distribution profile from phase field simulation is also provided in Figure II-374b, which demonstrated that the isolated grains by encircled Li dendrites have slightly lower local Li-ion concentration. It also shows that the intergranular ion diffusion was impeded by the Li dendrite growth, leading to degraded local Li conductivity in the solid electrolyte region where dendrites form.

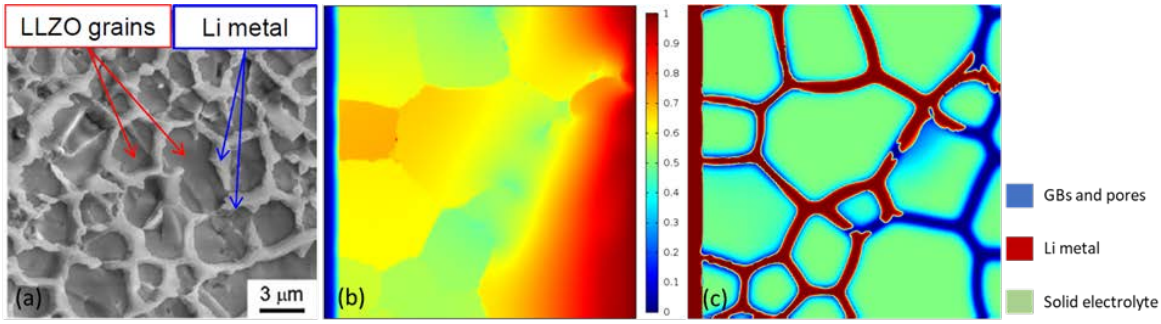


Figure II-374. Preliminary phase-field simulation of Li dendrite growth in solid electrolyte results with experimental results as comparison: (a) SEM observation of intergranular Li dendrite growth in LLZO [Cheng E. J., Sharafi A. and Sakamoto J., Electrochimica Acta 223, 85-91 (2017).]; and phase field simulation results: (b) Li-ion concentration distribution in the solid electrolyte battery system; (c) morphology of Li dendrites growth in solid electrolyte.

## Conclusions

A phase-field model was developed to capture the electrochemically driven dendrite morphology evolution in a liquid electrolyte. The role of SEI was modeled implicitly. The kinetic properties, as well as Li diffusion coefficient along the Li/SEI interface, was directly computed from DFT and DFTB-based atomic simulations. The DFTB calculations have revealed that delithiation generates voids at the Li/SEI interface and the charge transfer reaction occurs underneath the SEI layer. More importantly, the Li metal is negatively charged at the zero voltage (consequences for Li-plating and dendrite growth). The non-linear phase-field model simulation of the Li electrodeposition process revealed that higher Li/SEI interface energy, faster Li-ion diffusion in SEI, and slower reaction rate constants favor less branched Li morphology, leading to higher Coulombic efficiency compared to more branched morphology.

# II.F Next-Gen Lithium-Ion: Processing Science R&D

## II.F.1 Advanced Active Battery Materials: Non-traditional Approaches to Synthesizing Active Cathode Materials (ANL)

**Gregory K Krumdick, Principal Investigator**
Argonne National Laboratory
9700 South Cass Avenue
Argonne, IL, 60439-4837
Phone: 630-252-3952
E-mail: gkrumdick@anl.gov

**Peter Faguy, Technology Manager**
U.S. Department of Energy
Phone: 202-586-1022
E-mail: Peter.Faguy@ee.doe.gov

Start Date: October 1, 2016 End Date: September 30, 2017
Total Project Cost: $1,000,000 DOE share: $1,000,000 Non-DOE share: $0

### Project Introduction

To enable lower cost and higher performing active battery materials, advanced synthesis approaches are needed. This work focuses on establishing non-traditional synthesis capabilities at Argonne's Materials Engineering Research Facility (MERF) for the assessment of the technology and producing materials for evaluation.

### Objectives

The objectives of this project are to augment the MERF's synthesis capabilities to establish and evaluate advanced non-traditional approaches for active material synthesis. Specifically, we intend to establish advanced flame spray pyrolysis and hydrothermal synthesis capabilities at the MERF. These capabilities will be used to synthesize advanced active battery materials which will be evaluated and distributed to the basic R&D battery community for further research.

In addition, a CRADA with the equipment manufacturer Laminar was established and they have provided a 40L Taylor Vortex Reactor that will be used for a comparison study between existing 1L and 10L reactors in FY18.

### Approach

Flame and hydrothermal made nano- and micro-powders are viable competitors for powders made by other means but carry the potential for lowest-cost largest-scale production. Flexible, highly instrument synthesis systems are being designed, fabricated and commissioned for the DOE-VTO battery program. Collaborations with companies such as Cabot and Praxair are being established for technical guidance and to enable a commercialization pathway for the technology.

The Taylor Vortex Reactor (TVR) is a candidate commercially available synthesis technology to commercially utilize continuous stirred tank reactors (CSTR's). Establishing a CRADA with equipment vendor Laminar which places a 40L pre-pilot reactor in the MERF enables an unbiased evaluation of the scalability of the technology.

## Results

*Flame Spray Pyrolysis Synthesis*

The MERF FSP facility was designed and constructed at a greenfield location in the MERF high bay W162. This effort required: (a) selecting a material production target (b) selecting a burner strategy (c) establishing the engineering and safety protocols necessary to allow for combustion synthesis of nano-micron powders in the national laboratory system (d) integrating in-situ annealing (high-temperature-residence-time: HTRT) as a fundamental part of the FSP process and (e) developing a material collection system along with a clean-in-place fixture that will allow for efficient collection and system cleaning aimed at allowing for a daily turnover of synthesis operation.

The FSP burner, HTRT section, filter box, Spencer blower and combustion exhaust is a closed system that is provided with controls to maintain a negative pressure of 0.5-1.0 inches $H_2O$ with respect to the room. This assures that nanomaterials cannot leak out of the system and into contact with personnel while allowing some flexibility to service or adjust the burner when needed. The maintenance of negative pressure is provided by a variable frequency drive to adjust the Spencer Blower speed as need to keep the combustion duct at a specified negative pressure setpoint between 0.5-1.0 inches $H_2O$.

The filter box (see Figure II-375) was designed to provide 2 $ft^2$ of normal filter surface area allowing for a minimum of 100g of material collection while staying within the delta-P provided by the Spencer Blower. The filter box fits entirely within the Powder Hood. The interior of the filter box is accessed by glove-box style gloves that permit the easy harvesting of any nano-powder without breaking quarantine for these health hazard materials. This feature greatly simplifies PPE for the daily harvesting of produced materials. In addition, a ULPA vacuum cleaner accessed by the gloves allows for daily cleanup of the filter box to allow for efficient collection and preparation for the next experiment.


Figure II-375. Filter Box and glove box style PPE for material collection

The burner design is similar to many common configurations found in other research labs. The powder product originates from the combustion of the sprayed liquid precursor. The precursor liquid is atomized by a 2-fluid nozzle. Oxygen or air is used as the atomization gas using a Schlick atomizing nozzle. A sheath flow of oxygen or air provides additional combustion air as the atomizing nozzle does not provide a lot of flexibility in the atomizing gas to liquid ration so that the sheath gas is used to control the excess air parameter. A ring of pilot flames using premixed methane-oxygen gas is used to ignite and support the spray combustion. Nitrogen gas is also provided which is at least used to purge the combustion exhaust duct before ignitions attempts are made as required by NFPA 86. The nitrogen also provides another source of gas to control the post-combustion gas temperature. The burner is fitted on a sliding mount that can be retracted into the burn hood for service under the protection of the fume hood exhaust (see Figure II-376, Figure II-377).

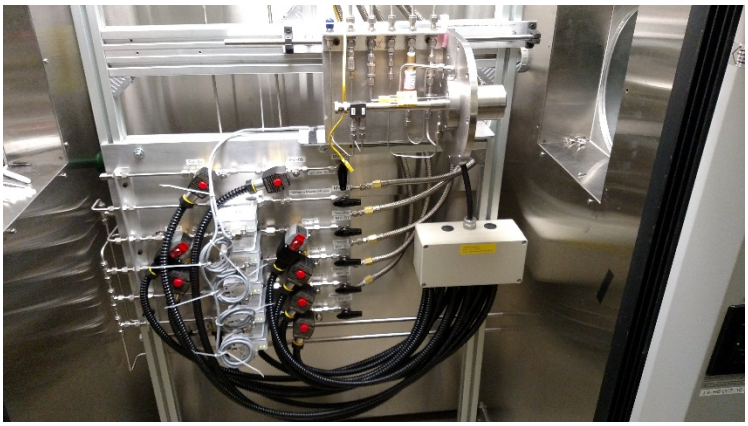

Figure II-376. Burner Hood with Cabot Inspired Burner

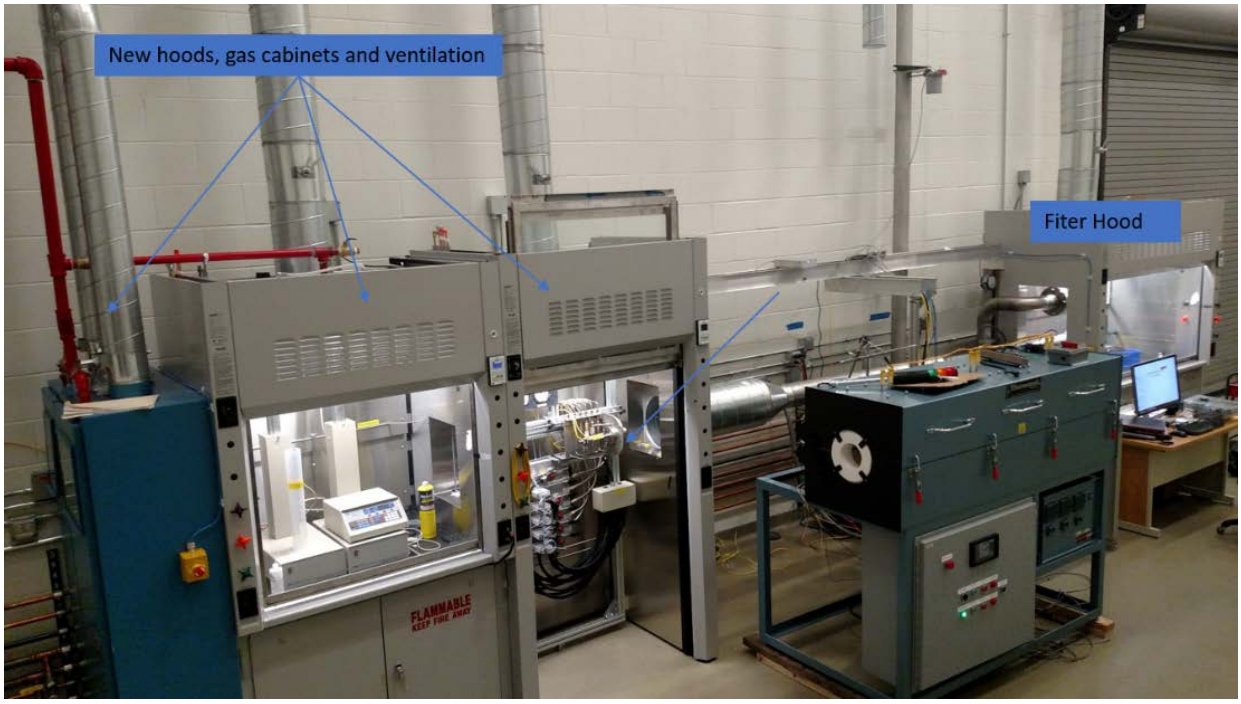


Figure II-377. New Hoods and Ventilation

A flame supervision and control system panel was specified and procured from an industrial furnace controls contractor. This system was specified to adhere as strictly as possible to the guidance of NFPA 86 which provides a framework for the safe operation of burners (see Table II-16). NFPA 86 prescribes the use of pressure switches, safety solenoid valves, flame sensors and operational protocols to assure that fuel is delivered only when it is safe and to prevent the accumulation of large amounts of un-combusted flammable materials. The control panel provides for two independent burners for the pilot and the spray flames. Electively, the spray flame can be operated if the pilot flame is off but the pilot flame must be on to ignite the spray flame.

Table II-16: MERF FSP System Parameters

| | |
|---|---|
| **Material Production Rate** | 20 g/hour or 100 g/day (leaving 3 hours for system turnaround: collection and cleaning) |
| **Basic Burner Design** | Adapted from engineering provided by Cabot Corp under NDA. |
| **Combustion Stream** | Fully enclosed 5" diameter duct(no air entrainment with independent control of $N_2$ and $O_2$ for excess air control) |
| **Pilot Flame Rate** | 25,000 Btu/hr |
| **Spray Flame Rate** | 25,000 Btu/hr |
| **$O_2$ Sheath Flow Rate** | 50 LPM max |
| **$N_2$ Excess Air/Purge Flowrate** | 50 LPM max |
| **Combustion Safety – Flame Supervision** | NFPA 86 flame supervision control panel (Honeywell SLATE) |
| **Combustion Safety - Containment** | Individual Flammable Gas Cabinets for solutions and pilot combustion gas (methane) |
| **Combustion Safety – Segregation** | 8-cylinder $O_2$ manifold located in service corridor |
| **Liquid Precursor Delivery** | Dual ISCO syringe pump |
| **High Temperature Residence Time (HTRT) Section** | 72" Tube furnace up to 1000 C |
| **Gas/Solid Cooling** | N2 gas quench in 72" section between HTRT section and filter box |
| **Material Collection** | 16"x25" glass-fiber filter accessed by pseudo-glove box design to minimize PPE burden during material collection |
| **Filter Blower** | Spencer Blower 100 cfm @40 inches $H_2O$ |
| **Clean-In-Place Fixture** | Custom design to allow cleaning of the system ducts without requiring disassembly. Daily cleaning within the 100 g/day target is feasible |
| **System Integration** | National Instruments/Labview control System |

The pilot flame was tested along with all of the NFPA 86 protocol functions. The pilot flame provides stable premixed flames in the 1-3 LPM methane range. Next, a spray of pure ethanol was used to test the spray flame. Stable spray flames were obtained in the 2-5 ml/min ethanol range. Figure II-378 shows the combined pilot and spray flame operation

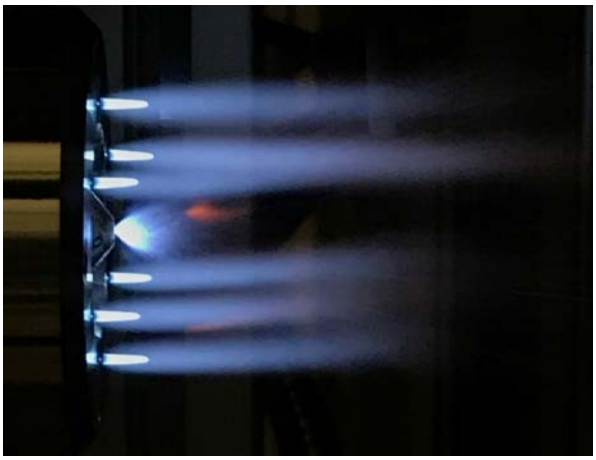

Figure II-378. Pilot and Ethanol Spray Flame Operation at the MERF FSP

*Hydrothermal Synthesis*

The Materials Engineering Research Facility (MERF) in the Engineering Systems Division at Argonne National Laboratory proposes to incorporate a new materials synthesis platform into the facility. The synthetic capability to be developed would be based on the design and construction of a turnkey hydrothermal synthesis (HyTS) reactor system capable of batch production of 20 to 50 g of nanoparticles per run. The immediate objective of this project is to develop and set up an advanced bench scale HyTS process for the production and evaluation of high-capacity engineered silicon nanoparticles and composites used as the active anode material in advanced Li-ion batteries.

HyTS is generally defined as crystal synthesis or crystal growth under high temperature and high pressure with water as the solvent / reaction medium and utilizing precursors that are ordinarily insoluble in water. As temperature and pressure approach the critical point of water, 374°C and 22.1 MPa (218 atm), the reactive and energetic nature of water changes dramatically. Characteristics such as density, ionic product, and dielectric constant, are strongly perturbed; thus supercritical water and subcritical water become useful new reaction media. The synthesis of single crystals and their growth is achieved in a hydrothermal reactor depending on the solubility of the precursors in hot water under high pressure. Especially for supercritical HyTS, around the critical point of water, the solubility of metal ionic species decreases dramatically because the density and dielectric constant of water decrease rapidly. The decrease in solubility leads to a higher degree of supersaturation. The formation of nanosized materials can be achieved in supercritical water (SCW) and subcritical water (SbCW) because of the high reactant diffusivity, fast reaction rates, and extremely high nucleation rate of these novel reaction media. Hydrothermal reactors can generate highly crystalline nanosized particles with well-defined morphology superior to competing reaction technologies, such as solid-state, co-precipitation, sol-gel, spray pyrolysis and emulsion drying. In addition, the nanoparticle size and size distribution can be controlled by adjusting the reaction conditions between subcritical and supercritical regimes depending on the reaction temperature and pressure as schematically shown in Figure II-379.

HyTS utilizes water at high temperature (200 ~ 400 °C) and high pressure (10 ~ 24 MPa) as the reaction media. The HyTS reactor will be constructed at a lab-bench scale where the reactor volume of one liter determines the typical batch size and reaction energetics.

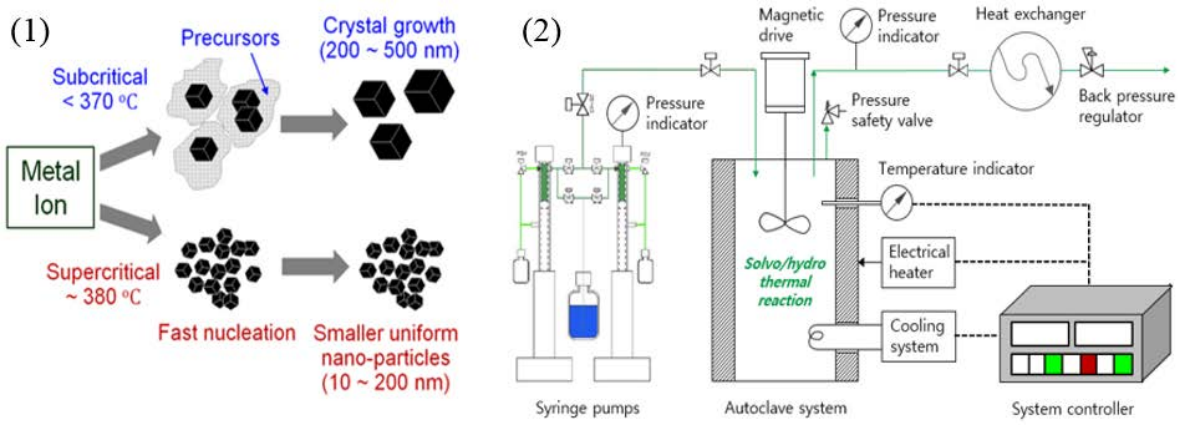


Figure II-379. (1) Hydrothermal Reaction Mechanism, (2) Schematic Diagram of Bench Scale Hydrothermal Synthesis System

*Taylor Vortex Synthesis*

The Taylor Vortex Reactor (TVR) is one of the commercially available emerging manufacturing technologies we are evaluating (see Figure II-380). This reactor has cylindrical rotor inside and provides tremendous Taylor Vortices in the annulus. This produced homogenous micro mixing, high mass and heat transfer enabling a high degree of uniform super saturation. This results in faster kinetics and denser particles. The TVR continuously

produces spherical precursors with narrow particle size distribution, which is critical to achieve high quality battery material.

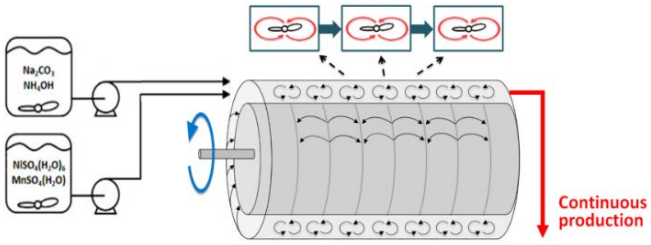


Figure II-380. Taylor vortex flow enabling micro mixing zones.

As part of a CRADA with Laminar, a 40L TVR pre-pilot reactor was delivered and is being installed. (Figure II-381). This 40L TVR will be used in the process scale-up study in conjunction with 1L and 10L reactors. We are planning to conduct a systematic TVR scale-up research for mass production of active cathode materials in FY18.

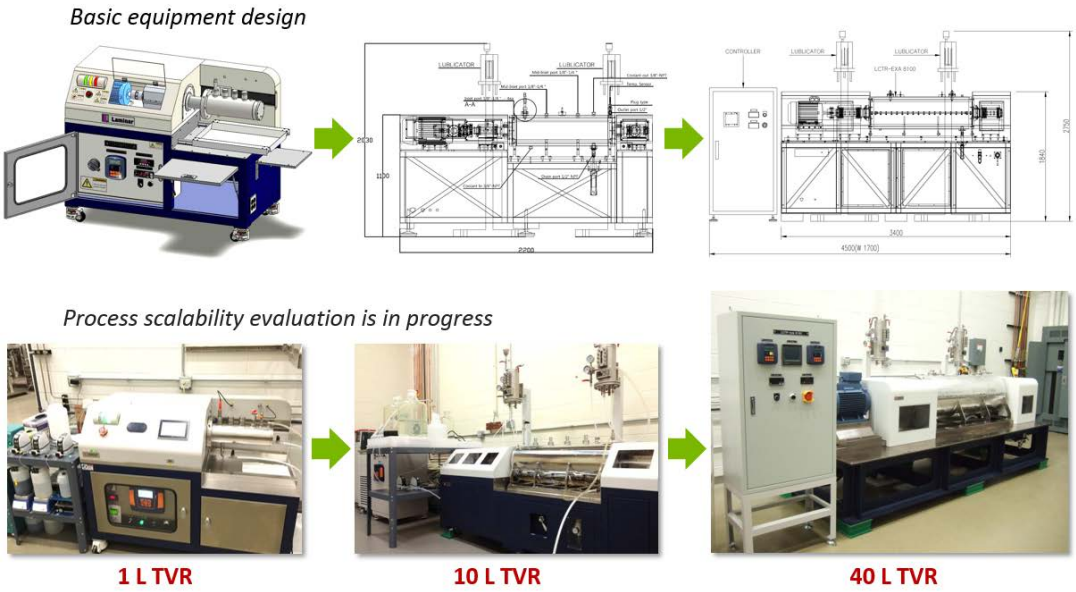


Figure II-381. 1L, 10L and 40L TVRs for Process Scalability Evaluation.

## Conclusions

The flame spray pyrolysis facility has been installed and commissioned. Additional analytical equipment has been added to the facility from a catalyst synthesis project but will be able to be utilized for battery material synthesis.

The hydrothermal synthesis facility has been designed and equipment has been ordered.

A CRADA with Laminar has been established and a 40L TVR was been delivered and installed. The unit will be fully commissioned in early 2018.

## Key Publications

1. Y. Shin*, O. K. Feridun and G. Krumdick, Scalable Advanced Chemical Reactor, Taylor Vortex Reactor, for Producing Li-ion Cathode Precursors, Argonne Battery Industry Day, June 2017

## II.F.2 Advanced Active Battery Materials: Active Cathode Materials with Component Concentration Gradient Structures (ANL)

**Gregory K Krumdick, Principal Investigator**
Argonne National Laboratory
9700 South Cass Avenue
Argonne, IL, 60439-4837
Phone: 630-252-3952; Fax: 630-252-1342
E-mail: gkrumdick@anl.gov

**Peter Faguy, Technology Manager**
U.S. Department of Energy
Phone: 202-586-1022
E-mail: Peter.Faguy@ee.doe.gov

Start Date: October 1, 2010 End Date: September 30, 2018
Total FY17 Project Cost: $1,600,000 DOE FY17 share: $1,600,000 Non-DOE share: $0

### Project Introduction

Newly-invented active battery materials that are not yet commercially available are being synthesized in gram quantity at bench-scale without quality control and reproducibility. These chemistries need to be tested and validated in large format prototype cells before going to high-volume manufacturing which needs a fair amount of material. Moreover, for in-depth material characterizations and further material modification such as surface coating, kilogram scale stocks of these materials are necessary as baseline materials. Therefore, the supplement of newly-invented materials with high quality and large quantity is critical for both fundamental research and industrial validation for commercialization.

From material engineering perspective, the development of a tailored synthesis process and composition optimization are the key issues to produce sufficient quantities of these newly-invented materials with high quality and reproducibility. But they are challenging. Barriers addressed are synthesis route selection, process and composition optimization, quality control with reproducibility and manufacturing cost reduction. The systematic material engineering and customized scaled process that we develop, will resolve the scale-up constraints of these materials and bridge the gap between basic material research and commercialization.

### Objectives

The program is a key missing link between discovery of advanced active battery materials, market evaluation of these materials and high-volume manufacturing to reduce the risk associated with their commercialization. We provide systematic process and material engineering researches to develop cost-effective customized processes and to produce sufficient quantities of target materials with high quality by optimizing synthesis process and material composition, evaluating material purity profile and applying emerging manufacturing technologies. The technical targets of this program are developing customized synthesis processes for each material selected, scaling up multi-kilogram material with reproducibility under rigorous quality control and evaluating emerging manufacturing technologies to assist the fundamental research of R&D groups and reduce the commercialization risk of newly-invented active battery materials.

## Approach

Advanced active battery materials with component concentration gradient structures were selected as target materials which are composed of Ni-rich central bulk together with Mn-rich outer layer. This type of material has been reported to have the potential to have a high capacity of more than 200 mAh/g together with improved thermal stability. We first performed preliminary synthetic studies on one of these materials to evaluate whether it can have both high capacity and thermal stability. In order to verify the electrochemical performance of the synthesized materials, the coin half cell evaluation was carried out. Through a collaboration with BNL, advanced structural analysis and thermal stability evaluation are being carried out. At the same time, as shown in Figure II-382, a tailored synthesis process is being developed to enable mass production of this material using various synthesis process equipment installed in Material Engineering Research Facility (MERF) at ANL.

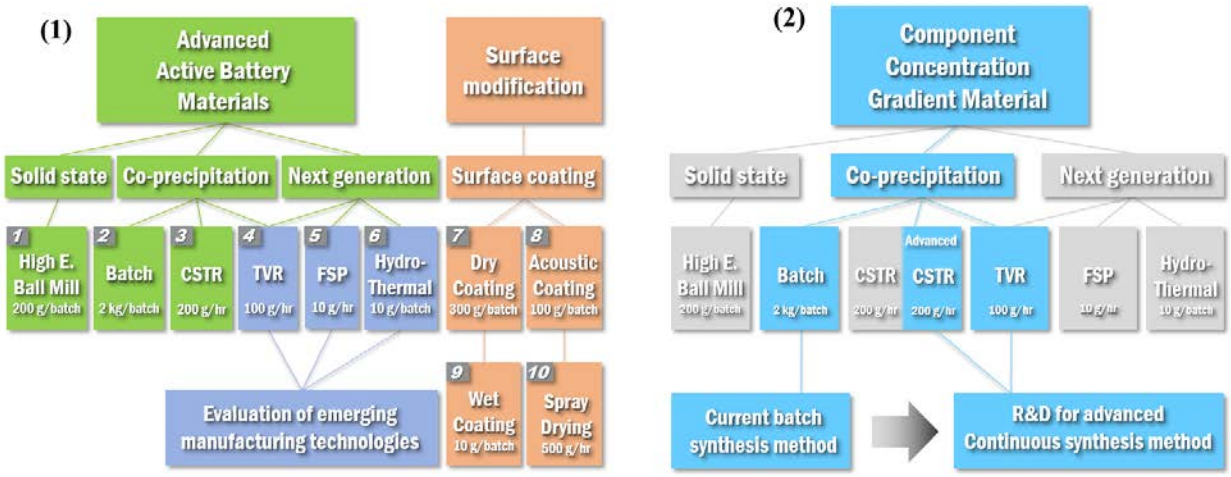


Figure II-382. Material Synthesis and Optimization Approach: (1) Process Capability Established at MERF and (2) Development of a Customized Synthesis Process for Advanced Cathode Material with Component Concentration Gradient Structure

## Results

Layered Ni-rich NMC material exhibits high specific capacity of approximately 210 and shows significant interest for use in electric vehicles due to its high reversible capacity, good rate capability and low cost. However, many challenges remain to improve the capacity retention during cycling and thermal-abuse tolerance of this material. To stabilize this high-capacity Ni-rich cathode material, as an approach, particle shape with component concentration gradient structures has been implemented.

For preliminary synthesis and evaluation of these types of materials, one can see the schematic particle drawing in Figure II-383, we selected NMC811 as core composition, NMC442 as surface composition and we prepared two kinds of core-gradient materials by controlling the thickness of gradient layer which shows same initial discharge capacity at C/10-rate and improved cycling performance at 1C-rate. To investigate the particle structure and thermal stability of this 622 gradient material, we set up a collaboration with Dr. Yang's group at BNL. Figure II-384 is the X-ray absorption spectroscopy result. Ni, Co, and Mn K-edge XANES data of the commercial NMC622 and 622 gradient materials are almost identical, which indicates that 622 gradient material was well-synthesized. We can see the peak broadening of 622 gradient which indicates more structural inhomogeneity compared to the commercial NMC622 in Figure II-385. This unique phase transition behavior of 622 gradient is related to broadened oxygen release which is much safer than sharp oxygen release of commercial NMC622 shown at this oxygen release graph in Figure II-385.

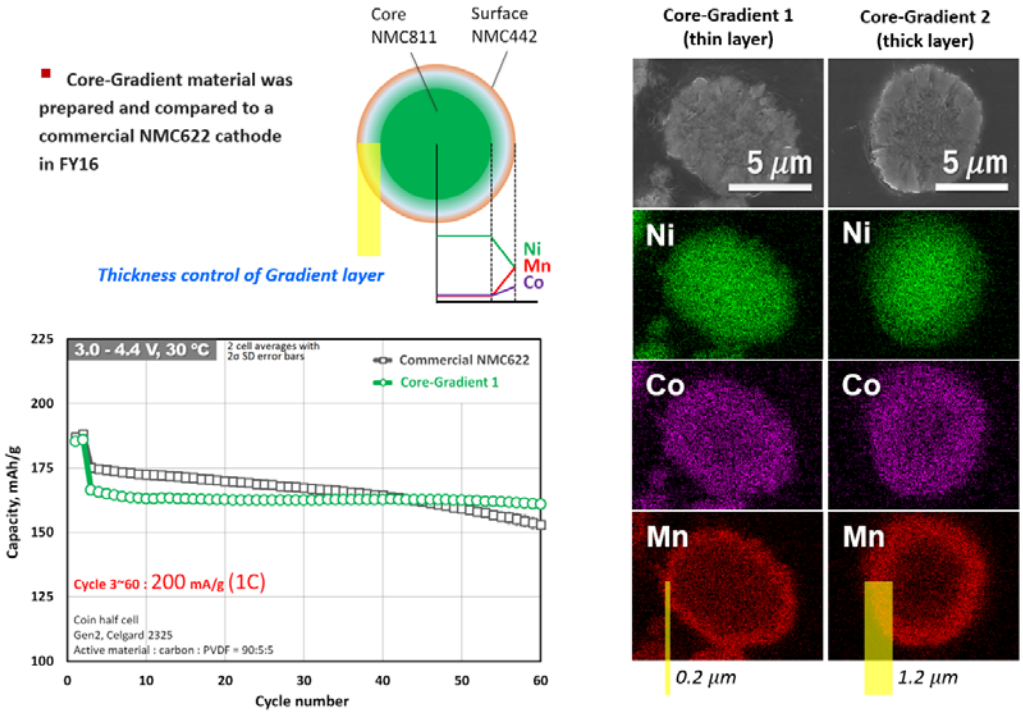


Figure II-383. Preliminarily Synthesized 622 Gradient Material with Component Concentration Gradient Structures

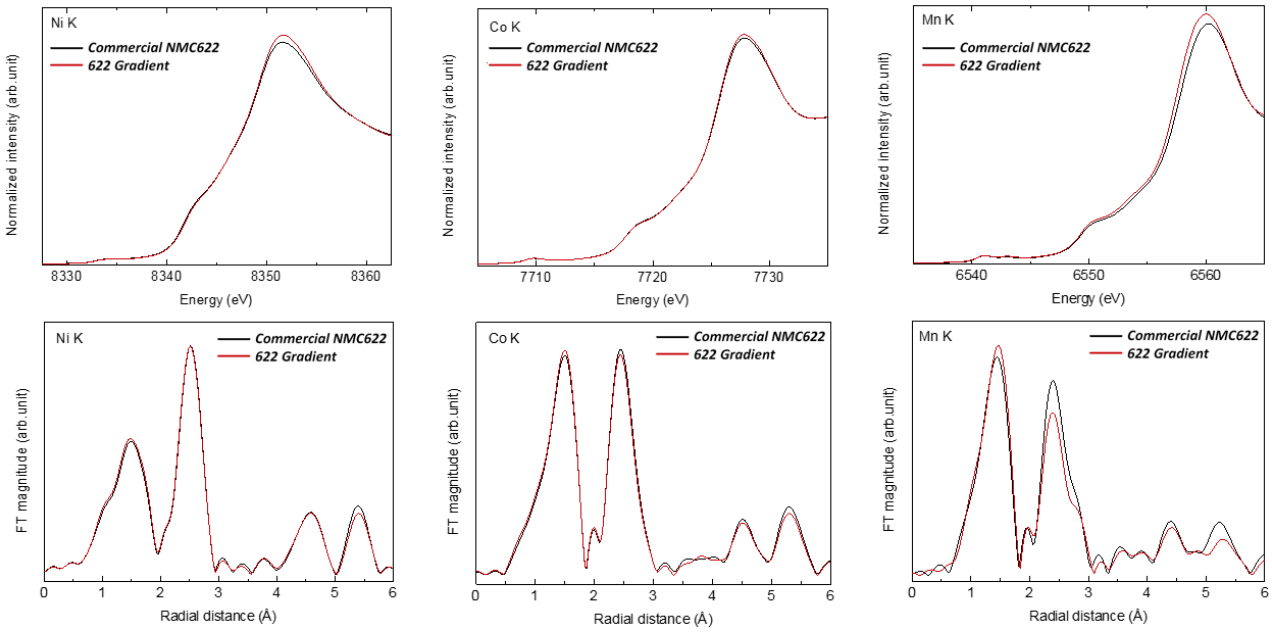


Figure II-384. X-ray Absorption Spectroscopy on 622 Gradient and Commercial NMC622 Materials (BNL)

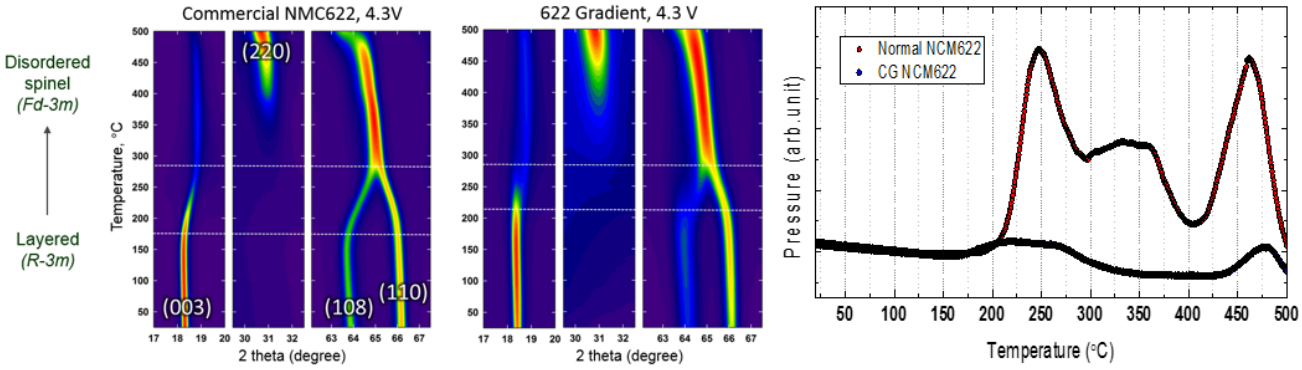


Figure II-385. Thermal Stability of Charged 622 Gradient and Commercial NMC622 Materials using Time Resolved XRD (BNL)

To achieve higher-capacity gradient material with better stability, NMC90/5/5 was selected as a core composition and NMC333 as a surface composition to make overall composition like NMC811. We prepared two types of gradient materials. 811 core-gradient and 811 core-shell as you can see at Figure II-386.

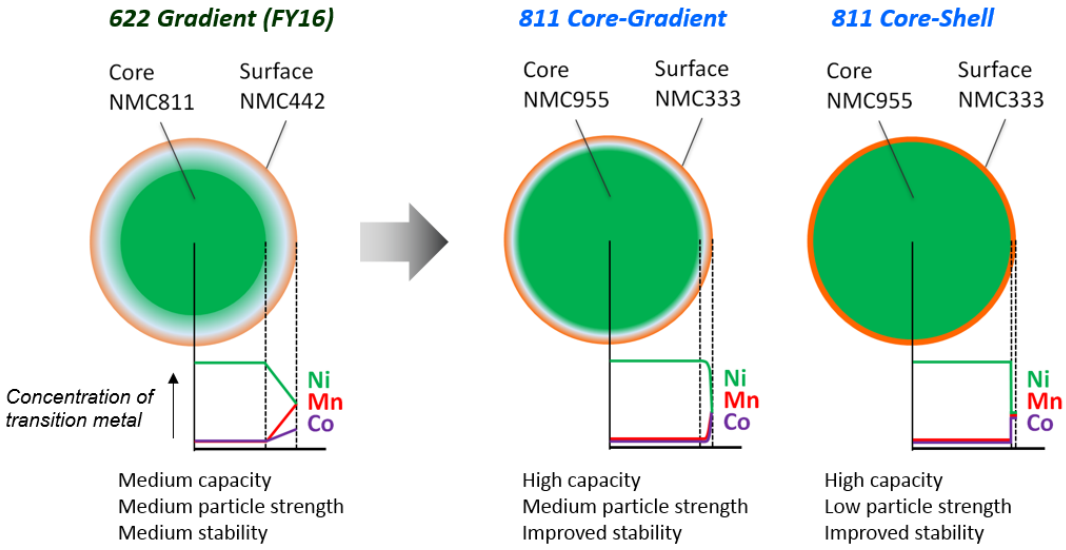


Figure II-386. Particle Structure Design for 811 Gradient Materials to Achieve Higher Capacity with Stability

Figure II-387 is the cross-sectional elemental mapping of the prepared materials. For 811 core-gradient particle, Ni concentration decreases from 90% to 33% as it approaches to the particle surface. On the other hand, Co and Mn concentrations increase from 5% to 33%. For 811 core-shell particle, Ni concentration decreases stepwise from 90% to 33% as it approaches to the particle surface. Co and Mn concentrations also increase stepwise from 5% to 33%. The prepared 811 core-gradient and core-shell materials exhibit similar physical properties and initial discharge capacity, compared to the commercial NMC811 as shown in Figure II-388.

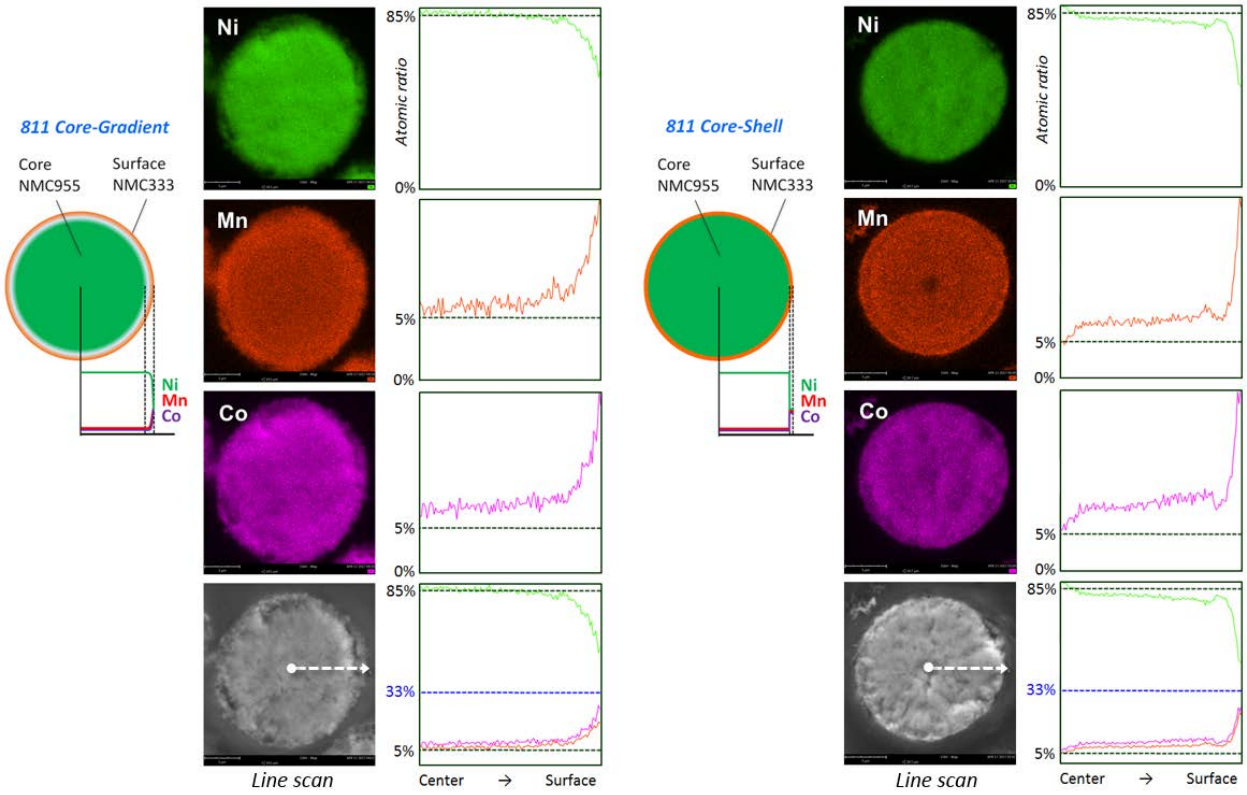


Figure II-387. SEM with EDS on Synthesized 811 Core-Gradient and Core-Shell Material

| Material | NMC 811 | NMC 333 | 811 Core-Gradient | 811 Core-Shell |
|---|---|---|---|---|
| Scale / status | Commercial product | | MERF pre-pilot preliminary product | |
| SEM | 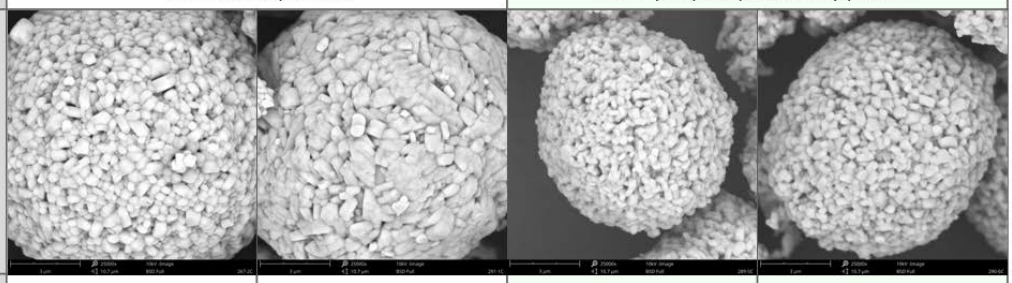 | | | |
| Composition | NMC 811 | NMC 333 | ~ NMC 811 | ~ NMC 811 |
| ICP-MS analysis | $Li_{1.04}Ni_{0.80}Mn_{0.10}Co_{0.10}O_y$ | $Li_{1.07}Ni_{0.34}Mn_{0.33}Co_{0.33}O_y$ | $Li_{1.00}Ni_{0.76}Mn_{0.12}Co_{0.12}O_y$ | $Li_{1.00}Ni_{0.76}Mn_{0.12}Co_{0.12}O_y$ |
| Particle size $D_{50}$ [µm] | 13.7 | 11.7 | 8.0 | 8.0 |
| BET [$m^2/g$] | 0.37 | 0.34 | 0.55 | 0.57 |
| * FCE [%] | 90.0 | 90.5 | 88.1 | 86.7 |
| * Avg. working voltage | 3.86 | 3.88 | 3.87 | 3.87 |
| * Discharge capacity @ 5 cycle [mAh/g] | **210.0** | **171.6** | **209.1** | **205.4** |

* At C/10, 2.7 – 4.4 V and 30°C

Figure II-388. Comparison of the Prepared 811 Core-Gradient and Core-Shell Materials with Commercial Products

We compared the electrochemical performance of the 811 core-gradient and core-shell materials with commercial NMC811 and NMC333 materials using coin half cell. Figure II-389 is the C/2 cycling and rate performance comparison between 2.7 and 4.4 voltages at 30ºC and Figure II-390 is the C/2 cycling and rate performance comparison between 2.7 and 4.4 voltages at 55ºC. At both 30 and 55 degrees, 811 core-gradient and core-shell materials show similar initial discharge capacity but improved high C-rate performance and capacity retention, compared to the commercial NMC811 material.

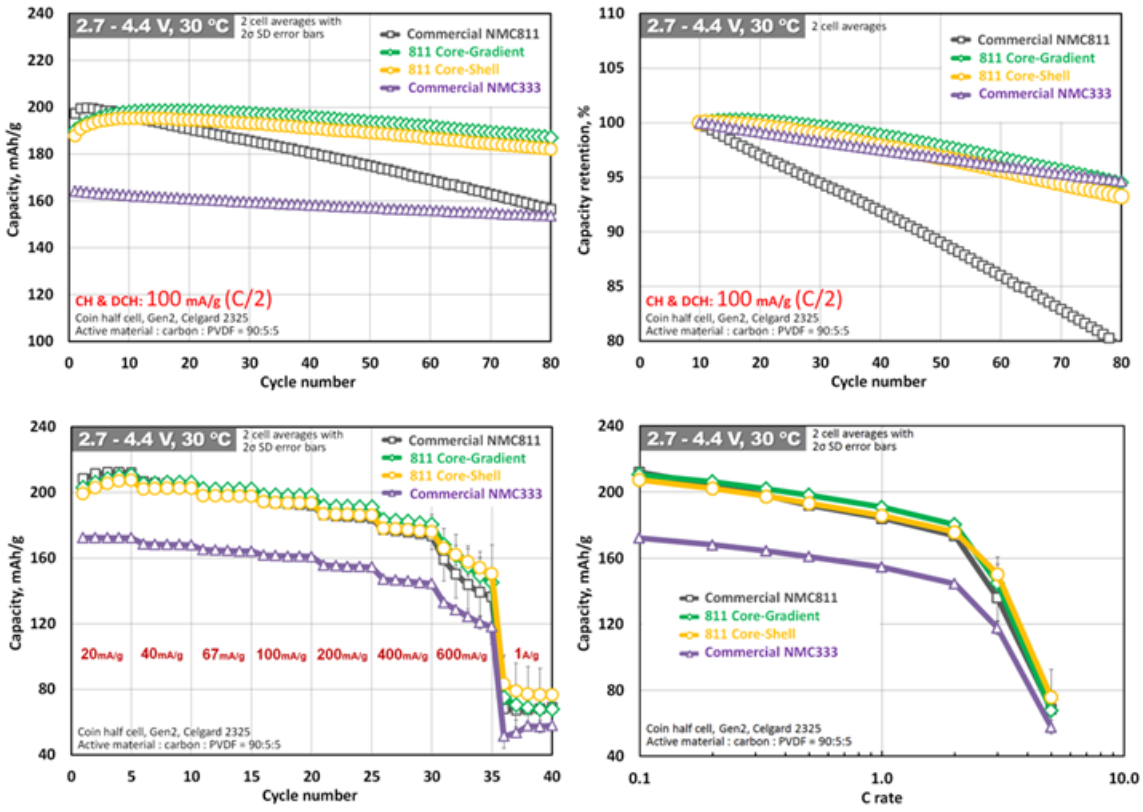


Figure II-389. C/2 Cycling and Rate Performance Comparison at 30ºC

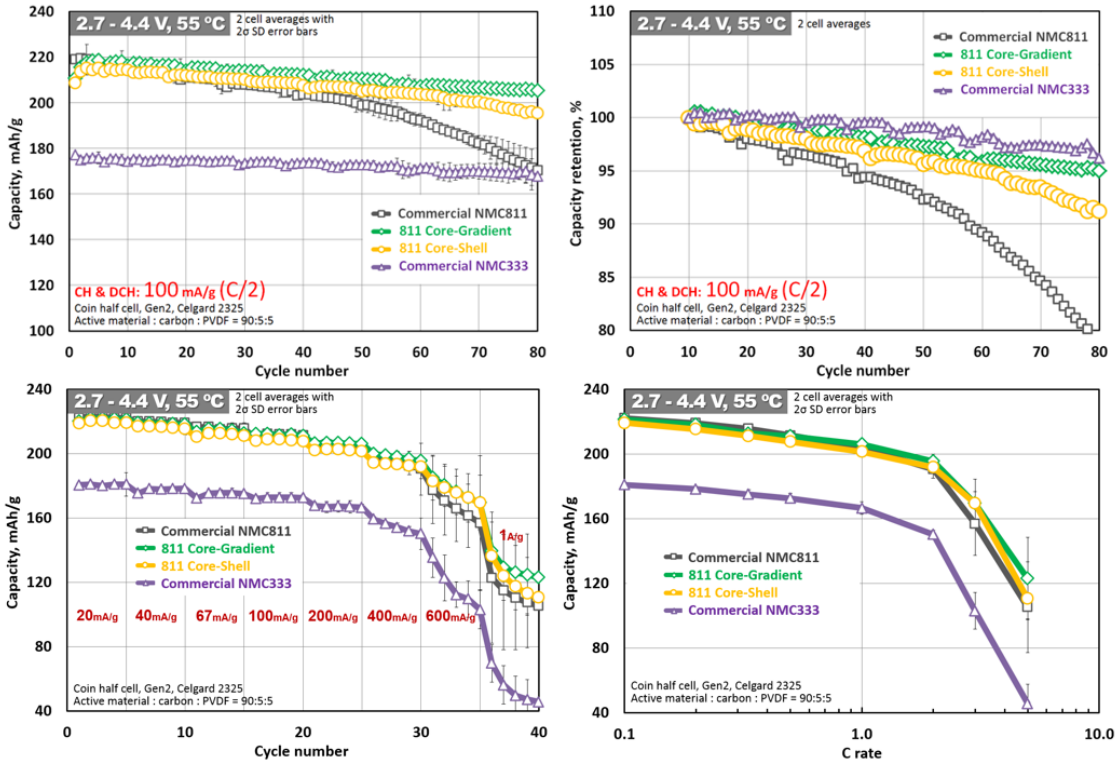


Figure II-390. C/2 Cycling and Rate Performance Comparison at 55°C

Two radar maps in Figure II-391show overall electrochemical performance comparisons of the 811 core-gradient, core-shell and commercial NMC811 materials at 30 and 55ºC. First cycle efficiency, average working voltage and initial discharge capacity are almost similar but 811 core-gradient and core-shell materials shows 20% improved capacity retention together with better rate capability compared to the commercial NMC811.

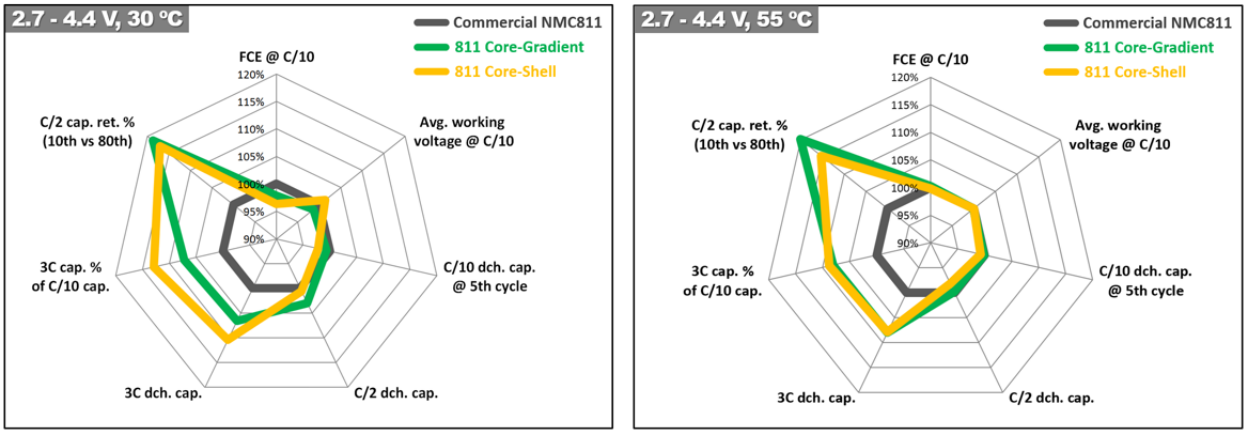


Figure II-391. Radar Map Comparison of the Prepared 811 Core-Gradient and Core-Shell Materials with Commercial NMC811

## Conclusions

As an approach to improve the cycling and thermal abuse tolerance of layered nickel-rich NMC materials, cathode particle with component concentration gradient structures has been implemented. First, the particle structure and characteristics of the preliminarily-synthesized 622 core-gradient material were analyzed through the X-ray absorption spectroscopy and time-resolved XRD analysis in collaboration with BNL. The results confirmed that the prepared 622 core-gradient material showed improved thermal stability than the commercial NMC622 material.

In order to achieve more than 200mAh/g with stability, 811 core-gradient and core-shell materials were synthesized and evaluated. 811 core-gradient, core-shell and commercial NMC811 materials have similar first cycle efficiencies, average working voltages and initial discharge capacities, but 811 core-gradient and core-shell materials have about 20% better capacity retention and better rate capacity than commercial NMC811. Based on the obtained electrochemical data, we can conclude that cathode particle with component concentration gradient structures is a good approach to stabilize high-capacity nickel-rich cathode materials for longer cycle life. To achieve higher capacity together with longer cycle life, combinations of various particle structures and component concentrations have been attempted. As part of these efforts, we are producing samples to assist basic research groups and conducting new process development studies to promote the commercialization of these kinds of materials with component concentration gradient structures.

## Key Publications

1. Y. Shin, O. K. Feridun and G. Krumdick, IV.E.2 Process Development and Scale up of Advanced Active Battery Materials (ANL), US Department of Energy (DOE), November 2016

2. J. R. Croy, J. S. Park, Y. Shin, B. T. Yonemoto, M. Balasubramanian, B. R. Long, Y. Ren and M. M. Thackeray, Prospects for spinel-stabilized, high-capacity lithium-ion battery cathodes, Journal of Power Sources, December 2016

3. G. Krumdick, Y. Shin and O. K. Feridun, Manufacturing Research on Advanced Cathode Materials, 2017 United States Drive Advanced Engine Crosscut Team Meeting, May 2017

4. Y. Shin, O. K. Feridun and G. Krumdick, Scalable Advanced Chemical Reactor, Taylor Vortex Reactor, for Producing Li-ion Cathode Precursors, Argonne Battery Industry Day, June 2017

5. Y. Shin, O. K. Feridun and G. Krumdick, Process Development and Scale up of Advanced Active Battery Materials –Gradient Cathode Materials, US Department of Energy (DOE), June 2017

6. Y. Shin, How to Stabilize High-capacity Nickel-rich Cathode Materials for Longer Cycle Life, 2017 The Battery Show, September 2017

## II.F.3 Integrated Flame Spray Process for Low Cost Production of Battery Materials for Lithium Ion Batteries and Beyond (University of Missouri)

**Yangchuan Xing, Principal Investigator**
University of Missouri
Department of Chemical Engineering
Columbia, MO 65211
Phone: 573-884-1067
E-mail: xingy@missouri.edu

**Peter Faguy, Technology Manager**
U.S. Department of Energy
Phone: 202-586-1022
E-mail: Peter.Faguy@ee.doe.gov

Start Date: January 1, 2016 End Date: December 30, 2018
Total Project Cost: $2,526,250 DOE share: $2,215,556 Non-DOE share: $310,694

### Project Introduction

Flame (combustion) processes have been proven to be the most economical way to produce fine powders. Pigment titanium oxide and fused silica are produced in millions of tons per year worldwide using flame processes. One of the challenges in these gaseous flame processes is that multiple metal oxides, like those used for lithium ion batteries, are difficult to produce due to the lack of appropriate gasified chemical precursors. Oxides of multiple metals are often produced in flame spray pyrolysis processes in which liquid precursors (mostly dissolved metal salts) are used. Precursor salt solutions are atomized and sprayed into a flame to make metal oxide powders. Unfortunately, the current flame spray technologies have problems in high throughput manufacturing. They also use a large amount of water and are prone to producing pollutants.

This project is to develop a battery material manufacturing technology using an integrated flame spray process (iFSP). It is a green chemical process and has the potential to significantly reduce manufacturing cost of battery materials. The technology is based on our innovations in spray processes, chemical precursors, and process integrations. The R&D project is a collaborative effort with EaglePicher Technologies, and will take the proposed iFSP to a new technology readiness level, with a goal to achieve a 25% cost reduction for the cathode active materials. Further full-scale production development beyond the performance period is expected to reduce the cost by 50% by 2020.

### Objectives

The overall objective of this project is to develop an advanced technology for battery materials production at low cost and in a green chemical process. The specific objectives for 2017 include reactor development and powder synthesis, materials testing, and battery cell development with desired chemistry.

### Approach

The main approach is to develop an integrated flame spray process in the manufacturing of transition metal oxide powder materials for batteries. The innovations of the proposed R&D include (1) using deep eutectic solvents (DES) as novel chemical precursors; (2) developing an innovative flame spray process; (3) integrating downstream powder processing; (4) leveraging with first class battery cell design and fabrication facilities (at EaglePicher Technologies).

## Results

*(1) DES Flame Spray Process R&D*

A Gen 3.0 flame reactor has been developed and fabricated to spray the deep eutectic solvent precursors and produce transition metal powders at a capacity of 3 kg/day or more. New developments include flow field control, temperature control, and precursor feeding in the flame reactor. Efforts have been made and will continue to be made on testing the new reactor and improving its performance in the production of powder materials.

*(2) NMC Powders and Performance*

NMC (333) powders were produced in the flame reactor. The newly produced powders (Figure II-392) showed much better performances (Figure II-393) than powders produced previously. The significant improvement in capacity was attributed to the increase of lithium content in the powders to form stoichiometric compound of $LiNi_{1/3}Mn_{1/3}Co_{1/3}O_2$.

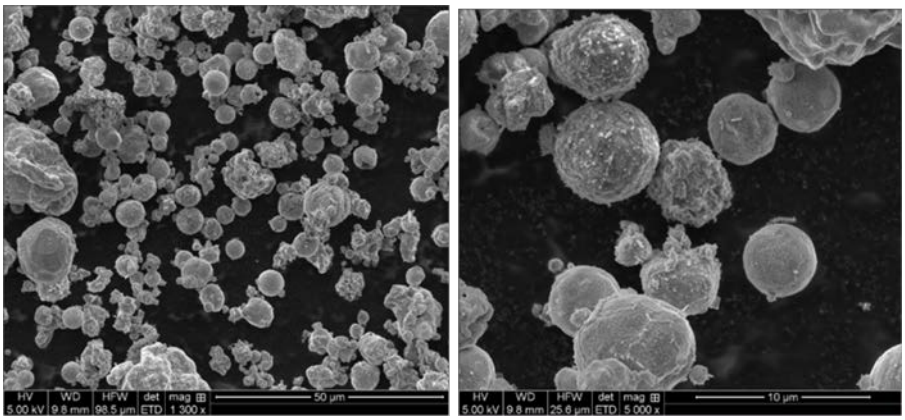

Figure II-392. Powders produced from the flame spray process, showing average size of 3 microns, much smaller than those obtained from last quarter at 50 microns. The powders also appear to be solid, not porous as before.

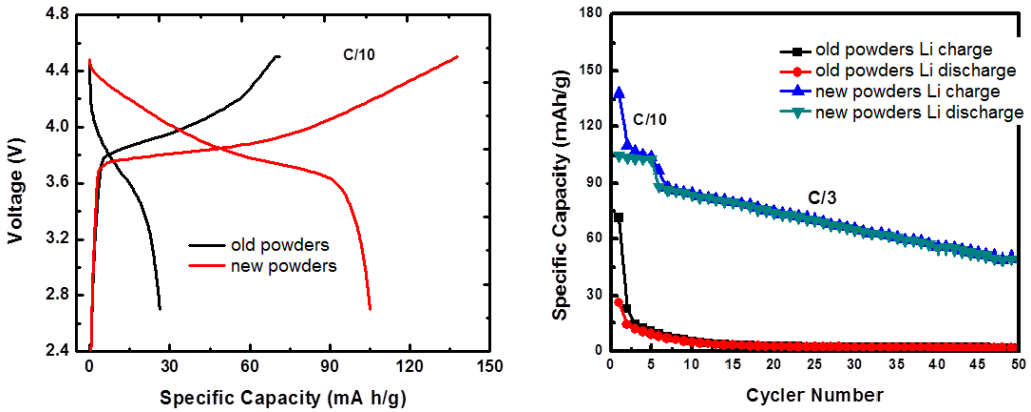


Figure II-393. Coin cell test of the new powders as compared to the old powders, showing much improved performance.

*(3) Nanocoatings on Powders*

Nanocoatings on active powders are intended to protect the powders from degradation and maintain their performance. Studies were conducted in two cases: one is carbon coating in a CVD process and the other is metal oxide (e.g., $Al_2O_3$, $Nb_2O_5$) coating in a proprietary process. For the CVD coating of carbons, a preliminary work was conducted to coat carbon on metal oxide nanowires. A carbon nanocoating was successfully made on sodium titanate nanowires in the CVD process (Figure II-394). The accomplishment lies in the uniformity of the nanoscale thickness of the carbon coating that conformably covers the whole fiber. The carbon coatings improved the performance of the material, ascribed to increase in electrical conductivity and surface protection.

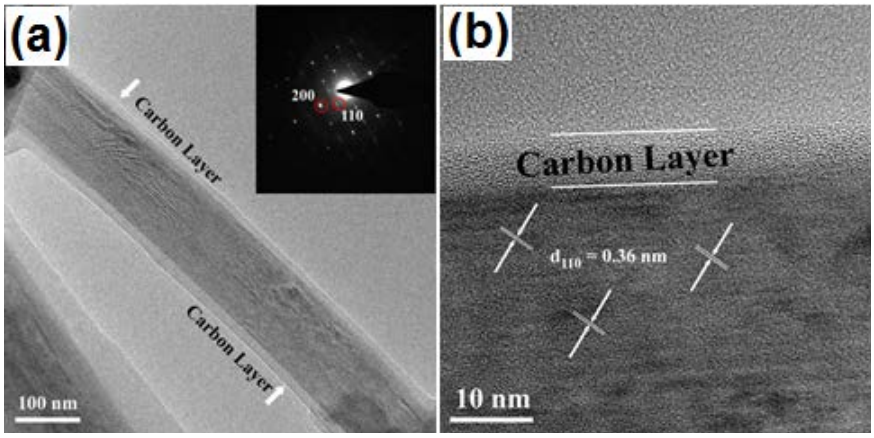


Figure II-394. Carbon coating on a sodium titanate fibrous battery material, showing a uniform, nanoscale carbon coating. The carbon coating is dense without holes.

Metal oxide nanocoatings were made on NMC powders that were made in a solution-based process. Preliminary studies showed that the NMC powders can be coated with metal oxide nanocoatings (Figure II-395), evidenced by the stability of the powder performances that are shown in Figure II-396. The charge-discharge curves are from the 1st cycle to 100th cycle. The powder as prepared showed large capacity loss after 50 cycles, but the coated powders showed much less loss. The stability of the NMC powders is obviously improved after a metal oxide coating.

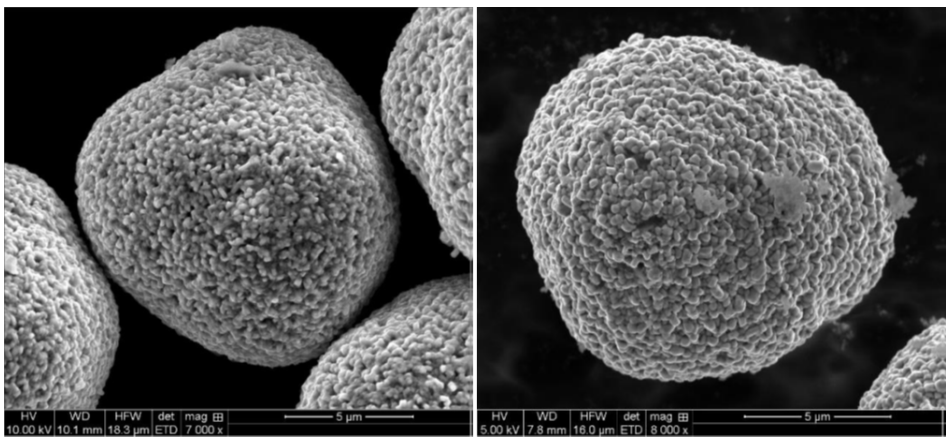

Figure II-395. (Left) Bare NMC powders as prepared; (Right) after a metal oxide coating.

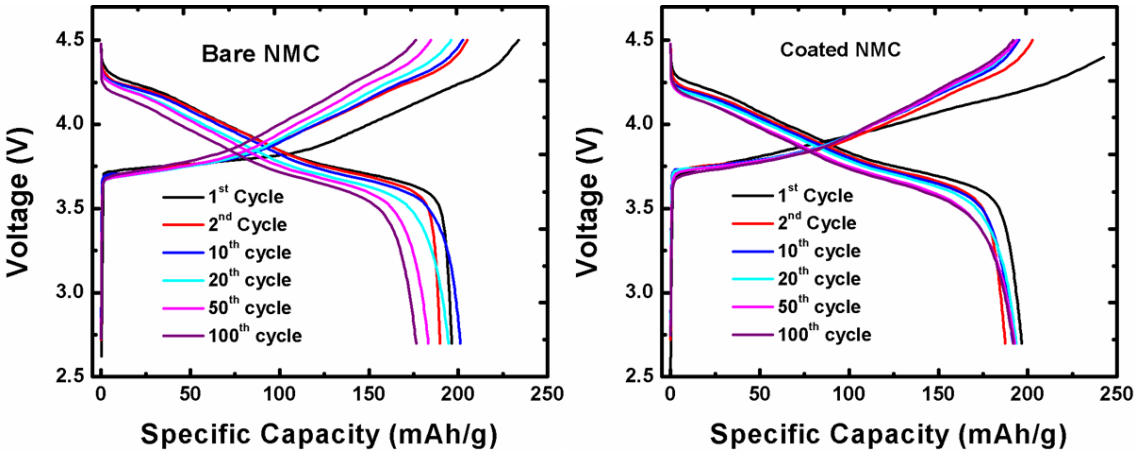


Figure II-396. Charge-discharge profiles on bare and coated NMC electrodes. The coated NMC shows much improved cycling stability (less polarization).

*(4) Cell Design to Achieve Energy Density*

Initial cell design work was conducted at EaglePicher. To achieve energy density of 250Wh/kg Li-ion cell the work was started with an establishment of baseline cell design template. A baseline cell design template serves as a design guideline for screening suitable chemistry and determining electrode design parameters such as optimal compositions and physical configuration. Establishment of baseline cell design template could reduce extensive optimization works for identifying suitable electrode chemistry, electrode designs, and a final cell design. Some commercial battery powders were used to establish the baseline in our battery cell design. The goal is to search for suitable battery chemistries that will guide the synthesis of powder compositions in the flame spray process.

High loading cathodes have initially been processed with several commercial cathode active materials. Lithium cobalt oxide ($LiCoO_2$, LCO), lithium nickel cobalt manganese oxide ($LiNi_{0.6}Co_{0.2}Mn_{0.2}O_2$, NCM622) and lithium nickel cobalt aluminum oxide ($LiNi_{0.8}Co_{0.15}Al_{0.05}O_2$, NCA9152) were selected as candidate cathode materials for the study. Through cell fabrications and testing, electrochemical tests of these electrodes have been carried out under different rates in coin cells with cut-off voltage 4.3 V vs $Li/Li^+$. The initial results for validating the cathode materials are shown in Table II-17.

**Table II-17: The cell capacities of high loading electrodes using NCA9152, NCM622 and LCO.**

| Cathode Material | NCA9152 | NCM622 | LCO |
|---|---|---|---|
| Columbic Eff (%) | 89.2% | 91.0% | 98.4% |
| C rate | Specific Discharge Capacity (mAh/g) | | |
| C/20,C/20 | 195.4 | 184.5 | 160.0 |
| C/10,C/10 | 190.2 | 180.3 | 157.6 |
| C/5,C/5 | 183.0 | 176.5 | 157.9 |
| C/5,C/2 | 173.0 | 166.8 | --- |

Based on the electrochemical tests above, the energy densities of the cathode in coin cells have been summarized in Table II-18, which will be used for the cell design to reach the energy density of 250 Wh/kg when matched with a suitable anode material. The maximum energy density with the current design is from the cathode with NCA9512. NCA powder is a material to be produced in the flame spray process in our next step.

Table II-18: Energy densities using NCA9152, NCM622 and LCO, with discharge voltages of 3.81, 3.82, and 3.96 V vs $Li/Li^+$, respectively.

| Cathode Material | NCA9152 | NCM622 | LCO |
|---|---|---|---|
| C rate | Energy density (Wh/kg)* | | |
| C/20,C/20 | 746.6 | 706.4 | 636.4 |
| C/10,C/10 | 726.6 | 690.4 | 626.1 |
| C/5,C/5 | 699.2 | 677.1 | 625.9 |
| C/5,C/2 | 656.8 | 633.6 | --- |

* based on cathode material.

## Conclusions

1. A Gen 3.0 flame reactor was fabricated and tested that can achieve a high throughput rate of 3 kg/day or more of active material NMC powders.

2. The NMC powders produced in the reactor showed mostly spherical powders with much improved capacity that can be increased when further tailored in morphology and size.

3. Surface coating processes have shown promising results. They will be further developed and integrated into the flame spray process.

4. Baseline battery cell design shows that NMC material with a different composition and an NCA material could be targeted cathode powder materials to achieve the energy density of 250 Wh/kg. They will be further pursued in our future work.

## Key Publications

*Presentations*

1. Liao, J.-Y., Smith, T.W., Hamad, K.I. and Xing Y., "Transition Metal Oxide Powders Made from Flame Spray Pyrolysis for Li-Ion Batteries", 2017 AIChE Annual Meeting, Minneapolis, MN, Oct. 29-Nov. 3, 2017.

2. Smith, T.W., Liao, J.-Y., Hamad, K.I. and Xing Y., "Transition Metal Oxide Powders Made from Flame Spray Pyrolysis for Li-Ion Batteries", 232nd ECS Meeting, National Harbor, MD, Oct. 1-5, 2017.

3. Liao, J.-Y., Smith, T.W. and Xing Y., "Hydrogenated and Carbon-coated $Na_2Ti_6O_{13}$ Nanowires as High-Rate Anode Materials for Lithium Ion Batteries", 232nd ECS Meeting, National Harbor, MD, Oct. 1-5, 2017.

*Journal Papers*

1. Hamad, K.I., Liao, J.-Y., Smith, T.W. and Xing, Y., "Synthesis of layered $LiMn_{1/3}Ni_{1/3}Co_{1/3}O_2$ oxides for Li-ion batteries using biomass glycerol as solvent", *Energy Technology*, ASAP 2017. DOI: 10.1002/ente.201700646. (Work related to DES precursors.)

2. Liao, J.-Y., Smith, T.W., Pandey, R.R., He, X., Chusuei, C.C. and Xing, Y., "$Ti^{3+}$ Self-doped and Carbon-coated $Na_2Ti_6O_{13}$ Nanowires as High Rate Anode Materials for Lithium Ion Batteries', under review at *ACS Applied Materials & Interface*, 2017. (Work related to carbon coating.)

## II.F.4 High Performance Li-Ion Battery Anodes from Electrospun Nanoparticle/Conducting Polymer Nanofibers (Vanderbilt University)

**Peter N. Pintauro, Principal Investigator**
Vanderbilt University
Department of Chemical and Biomolecular Engineering
Nashville, TN 37235
Phone: 615-343-3878;
E-mail: pn.pintauro@vanderbilt.edu

**Peter Faguy, Technology Manager**
U.S. Department of Energy
Phone: 202-586-1022
E-mail: Peter.Faguy@ee.doe.gov

Start Date: October 1, 2015 End Date: September 20, 2019
Total Project Cost: $707,062 DOE share: $590,000 Non-DOE share: $117,062

### Project Introduction

Si is an attractive replacement for graphite in Li-ion battery anodes due to its high theoretical capacity (3,600 mAh/g for $Li_{15}Si_4$ vs. 372 mAh/g for $LiC_6$) and low operating potential (< 0.5 V *vs.* $Li/Li^+$). However, Si-based anodes often exhibit poor cycling stabiity due to large volume changes, particle pulverization, and instablities associated with the solid electrolyte interphase (SEI) layer. The use of Si nanoparticles and nanowires has shown promise, but the active material loading in such nano-Si anodes is low, resulting in low areal and volumetric capacities. Thus, there is a need for new anode designs which can tolerate Si volumetric changes while maintaining high gravimetric, areal, and volumetric capacities over many charge/discharge cycles at low and high C-rates.

### Objectives

The objectives of this project are to fabricate an electrospun Li-ion battery nanofiber anode and demonstrate its superior performance in half-cell and full-cells. The fiber mat anode is expected to outperform current state-of-the-art thin film slurry anodes, in terms of volumetric capacity and rate capability, and could enable a substantial reduction in the weight and size of an electric vehicle battery. The project will also demonstrate that the fiber mat anode can be manufactured in large scale at a commercial electrospinning facility. Experiments will focus on optimizing the composition and morphology of Si-based nanofiber anodes with/without a conducting polymer binder for lithium ion batteries. Such anodes will designed for high gravimetric and volumetric energy densities, e.g., an initial capacity of 1,200 mAh/g and 1-2 mAh/cm$^2$ with 90% capacity retention after 200 cycles at 0.1C and a capacity of 500 mAh/g after 200 cycles at 2C which is recoverable to at least 1,000 mAh/g at the lower charge rate of 0.1C. The project will also generate useful correlations and insightful understandings regarding the electrospun anode composition/structure and its performance.

### Approach

This project is an extension of the PI's prior successes in using neat polymer and polymer/particle nanofiber electrospinning for membranes and electrodes in electrochemical devices. In prior studies, electrospun Li-ion battery electrodes were prepared by carbonizing polymer fiber precursors at high temperature. In particle/polymer electrospinning, there is no fiber pyrolysis; the electrospinning and post-processing are performed at room temperature to preserve the beneficial properties of the polymer binder and to ensure an electrode with a high fiber volume fraction. High gravimetric, areal, and volumetric capacities are achieved at fast charge/discharge rates through the use of thick, densely packed particle/polymer nanofiber mats. Four key tasks will be performed: (1) Synthesis, optimization and testing of conducting polymer binders;

(2) Electrospinning and post-processing of composite nanofiber mat anodes of Si nanoparticles with a conducting binder or with electrically conducting carbon powder and a non-conducting binder; (3) Evaluation of short-term and long-term performance of electrospun anodes in half-cells and full-cells (with a NMC cathode) followed by post-mortem characterization; and (4) Preliminary scale-up of anode fiber mat manufacturing at a commercial electrospinning facility, where the resultant materials meet the project performance targets. Experiments during this reporting period focused on: (a) single fiber mats composed of Si and carbon particles in a suitable polymer binder; (b) dual fiber mat anodes, where one fiber type contains Si nanoparticles and binder and the second fiber is composed of carbon powder and binder; and (c) an electrosprayed anode composed of Si nanoparticles and carbon powder with a new thermally crosslinked polymer binder. National laboratory partners on this project are Dr. Gao Liu at Lawrence Berkeley National Laboratory (LBNL), who has been providing electrically conductive polymer binders and Dr. Jagjit Nanda at Oak Ridge National Laboratory (ORNL) who is overseeing electrode characterization experiments. eSpin Technologies, Inc. is a subcontractor on the project and will be responsible for making fiber mat anodes on their commercial electrospinning equipment.

## Results

### *Single Fiber Anodes*

Experiments were carried out to optimize the composition of single fiber Si/C/poly(acrylic acid) (PAA) electrospun anode mats. Specifically, we sought to better understand how a fiber mat anode performs when the PAA binder content is increased at a constant Si loading. Three fiber mat electrodes were prepared and tested in CR2032 half-cells (with a Li metal anode) at Si/C/PAA compositions of 40/15/45, 40/25/35, and 40/35/25. The charge/discharge cycling results at 0.1C are shown in Figure II-397. Increasing the PAA content leads to a dramatic improvement in cell performance after 20 charge/discharge cycles, with an increase in capacity retention from 40% retention at 25 wt.% PAA to 80% retention at 45 wt.% PAA.

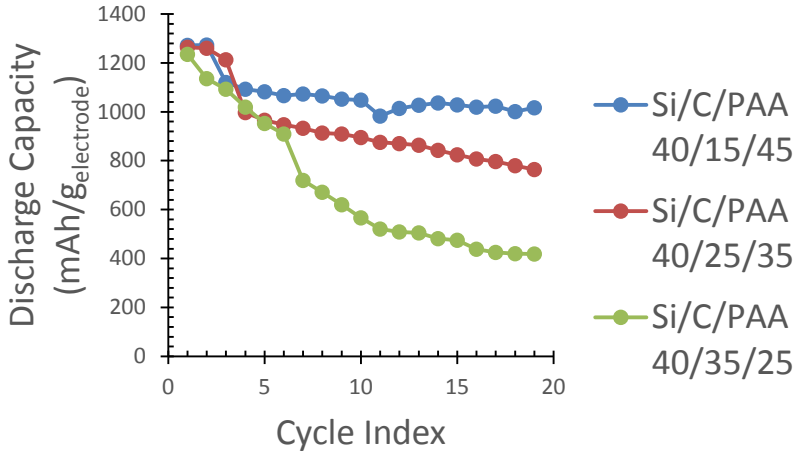


Figure II-397. Cycling results of anodes fabricated from electrospun single fiber mats containing 40 wt.% Si and varying content of C and PAA binder.

Research activities at ORNL focused on using x-ray diffraction (XRD), energy dispersive x-ray spectroscopy (EDX), and Raman spectroscopy to characterize the structure of electrospun single fiber anodes with a Si/C/PAA weight ratio of 40/25/35. An X-ray diffraction (XRD) pattern of the Si/C/PAA fiber mat is shown in Figure II-398. Peaks associated with crystalline Si were observed. The broad peaks near $2\theta = 20°$ are attributed to the carbon powder and PAA binder. An energy-dispersive X-ray spectroscopy (EDX) analysis of the same fiber mat (Figure II-399) shows that Si and C particles were uniformly distributed throughout the fiber structure.

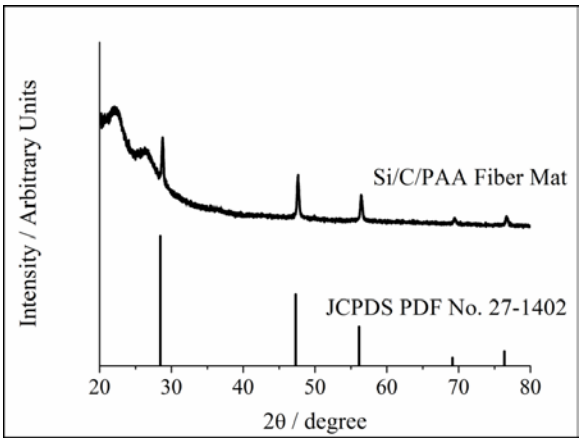


Figure II-398. XRD pattern of an as-spun Si/C/PAA fiber mat and a reference pattern for Si (PDF No. 27-1402)

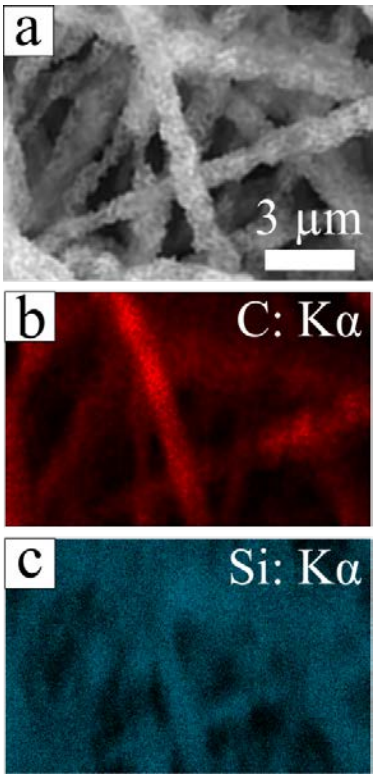


Figure II-399. (a) SEM image of a Si/C/PAA fiber mat and the corresponding EDX maps showing the (b) carbon and (c) silicon distributions.

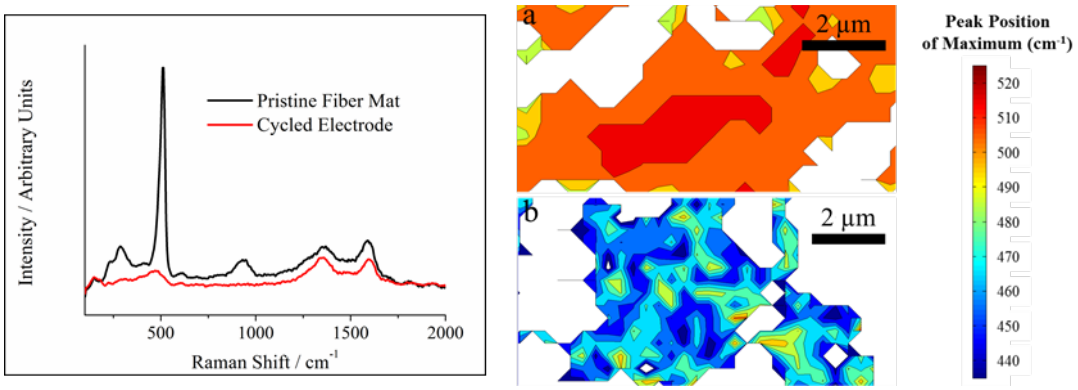


Figure II-400. (a) Average Raman spectra for a Si/C/PAA fiber mat containing 35 wt% PAA before and after 50 cycles. (b-c) Raman maps over an area of ~ 4.5 x 9.0 µm² showing the Raman shift of the maximum peak for these electrodes (b) before cycling and (c) after 50 cycles at 0.1C.

Figure II-400 shows Raman spectra for a pristine (i.e., uncycled) fiber mat anode (Si/C/PAA ratio of 40/25/35) and an electrode after 50 cycles at 0.1C. The pristine electrode had a large peak near 520 $cm^{-1}$, associated with the presence of crystalline Si. This peak was absent in the cycled electrode which contained a broad peak near 475 $cm^{-1}$, indicating a crystalline to amorphous transformation of Si during cycling. This change was mapped over an area ~4.5 x 9.0 $\mu m^2$ as shown in Figure II-400; these results indicate that the transformation occurred uniformly throughout the fiber mat. Note that portions of the electrode surfaces were out of focus during Raman mapping, and the white pixels in Figure II-400 represent regions where the data were omitted due to low spectral intensities (i.e., counts < 10).

*Electrospinning Electrically Conductive Polymers*

A new conducting binder, PEFM, was synthesized by G. Liu at LBNL for possible use as the binder in electrospun nanofiber mat Si anodes. The polymer is comprised of four subunits: (P) polyfluorene with octyl side chains, (E) fluorine with trietyleneoxide monomethylether side chains, (F) fluorenone, and (M) methyl benzoate ester. The synergistic functionalities of the subunits should provide PEFM with an acceptable balance of electronic conductivity, electrolyte uptake, mechanical strength and Si adhesion. Well-formed polymer fibers (with no Si particles) were electrospun from a solution a 5.5 wt.% PEFM in chlorobenzene. Unfortunately, after extensive experimentation, it was concluded that Si/PEFM fibers could not be made via electrospinning.

*Dual Fiber Mat Anodes*

Several dual fiber mats were prepare using a custom built setup with a rotating and oscillating drum collector onto which a Cu foil was wrapped prior to electrospinning. The spinning inks consisted of: (i) 0.3g Si, 0.3g PAA, 2g isopropanol (IPA) and 2g methanol (MeOH), and (ii) 0.34g C, 0.2g polyacrylonitrile (PAN) and 2.75g dimethylformamide (DMF). The inks were sonicated for 30 min and then mixed using magnetic stirrers for 2 days. The electrospinning conditions for fiber mat formation were as follows: (i) C/PAN ink – bias voltage 9 kV, distance to collector 9.4 cm, flowrate 0.25 ml/h and (ii) Si/PAA ink – bias voltage 8 kV, distance to collector 7.5 cm, flowrate 0.85 ml/h. Electrospinning was carried out in a controlled environment chamber at a relative humidity of 30% and a temperature of 24ºC. Only the central section of the mat, where the two fiber types were uniformly deposited and well mixed, was used for further processing. The selected mat section was pressed for 60 sec at 10 MPa followed by 30 min exposure to MeOH and then 30 min exposure to DMF (these steps were performed to increase the fiber volume fraction and to create interfiber welds). The mat was dried in a vacuum oven at 70ºC for 1 hour and then at 110ºC overnight. The final anode mat composition was as follows: 70 wt.% Si/PAA (50/50 weight ratio) fibers and 30 wt.% C/PAN fibers (63/37 weight ratio). The Si areal loading in the dual fiber mat was 0.70 $mg/cm^2$. A coin cell was assembled as in previous

experiments with a Li metal anode and an electrolyte of 1.2 M $LiPF_6$ in a mixture of ethylene carbonate and diethyl carbonate (3/7 by volume, BASF Corp.) with 30 wt. % fluoroethylene carbonate (BASF Corp.).

Scanning electron microscope surface images of a dual fiber mat, at various levels of magnification are shown in Figure II-401. Thinner C/PAN fibers can be clearly distinguished from the much thicker Si/PAA fibers. The C/PAN fibers appear to be well formed, whereas some droplets (with an average diameter 20 μm) and beading can be observed in the Si/PAA fibers. Although the overall fiber mat quality is far from ideal, the Si nanoparticles are well distributed within the PAA fibers and intra-fiber pores can be detected in these fibers (the inter-fiber volumetric porosity was estimated to be 50%).

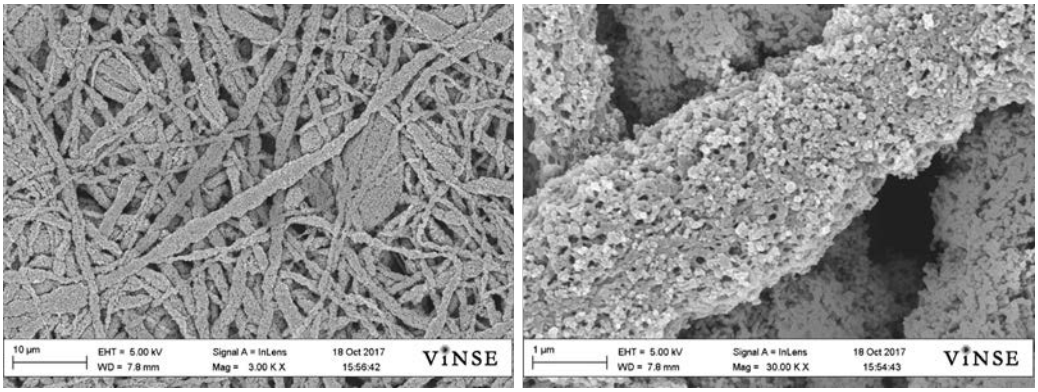


Figure II-401. SEM image of the surface of the electrospun dual fiber mat containing 70 wt.% of Si/PAA (50/50) and 30 wt.% of C/PAN (63/37) fibers.

A charge/discharge cycling plot for a half-cell with a dual fiber anode is shown in Figure II-402. Capacity data were collected by first cycling the cell at 0.1C for 35 cycles and then cycling the same cell at 1.3C for 50 cycles. At 0.1C, the capacity retention after 35 cycles was 87.4%. The theoretical capacity calculated from the electrospinning ink composition and flowrate was 1311 mAh/g, which is very close to the recorded first cycle charging capacity. The coulombic efficiency was above 98% during 0.1C cycling. After 50 cycles at 1.3C, the gravimetric capacity was 671 mAh/g (a capacity retention of 93.4%) with a coulombic efficiency of 99.4%. This capacity exceeds the 500 mAh/g Year 3 Go/No-Go target for this project. The excellent capacity and capacity retention is attributed to the use of PAN for the carbon fibers, improved intermixing of the Si/PAA and C/PAN fibers in a dual fiber mat, and the use of the Cu foil current collector (depositing fibers directly onto the Cu foil may be providing additional mechanical strength to the anode mat). Cycling experiments at high C-rates were also performed; for 50 cycles at 3C, the gravimetric capacity was essentially constant at 533 mAh/g, with a coulombic efficiency of 99.6%. The results clearly show that the C/PAN fibers are acting as electrically conducting pathways in the Si/PAA fiber mat, with electrons migrating between the two fiber types during electrode charging and discharging.

*Examination of a New Crosslinkable Binder for a Si + C Anode*

A new polymeric crosslinkable binder based on blends of poly(vinyl alcohol-co-ethylene) (PVAE) and PAA was investigated. In preliminary solution cast thin film experiments, it was found that PVAE/PAA mixtures could be thermally crosslinked (via ester formation) at 110°C, i.e., a thermally treated film did not dissolve in the casting solution solvent. Initial attempts to electrospin a Si/C/PVAE-PAA ink to make a single fiber mat anode, however, were unsuccessful. Nevertheless, an electrosprayed droplet anode was produced directly on a Cu foil current collector, where the Si/C/PVAE-PAA content was 40/25/35. This sprayed film was thermally crosslinked (110°C for ca. 12 hours) and then tested as the anode in a CR2032 half-cell cycling experiment.

SEM micrographs of the anode surface after overnight annealing are shown in Figure II-403. A uniformly porous structure is observed with no significant Si or C nanoparticle clustering. The results of a coin cell

cycling experiment are shown in Figure II-404. The first charging capacity at 0.1C was 1508 mAh/g, which is close to the expected value of 1515 mAh/g (assuming 3600 mAh/g for Si and 300 mAh/g for carbon). Charge/discharge cycling at 0.1C was continued for 10 cycles (to stabilize the SEI) and then the charge/discharge rate was increased to 1.3C. At this higher C-rate, the initial capacity was 1003 mAh/g, which decreased to 815 mAh/g after 50 cycles (the capacity retention was 81.3%), with a final coulombic efficiency of 98.9%. When the C-rate was further increased to 3C, the gravimetric capacity decreased from 623 mAh/g at cycle 2 to 574 mAh/g at cycle 50 (a capacity retention of 92%, with a coulombic efficiency of 99.5% at cycle 50). It is not known if the excellent cycling stability of this sprayed electrode, as compared to a single fiber Si/C/PAA anode, is due to the new binder or to the sprayed droplet morphology. We will continue to investigate PVAE-PAA binders next quarter, in an effort to answer this important question.

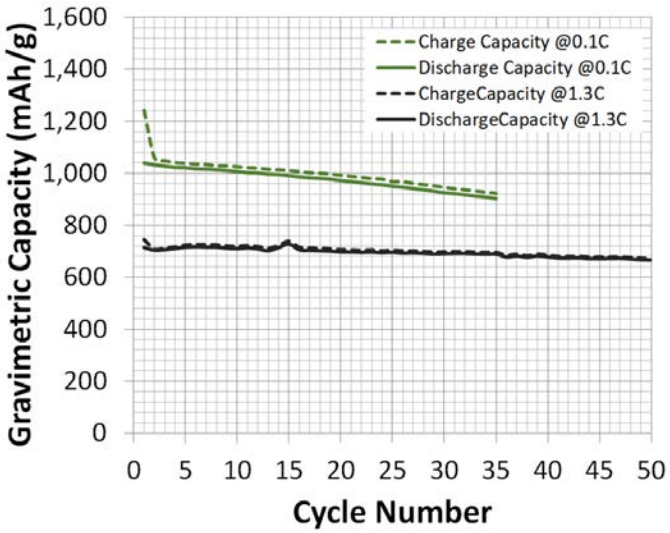


Figure II-402. Cycling results of an anode fabricated from electrospun dual fiber mat containing 70 wt.% of Si/PAA (50/50) and 30 wt.% of C/PAN (63/37) fibers.

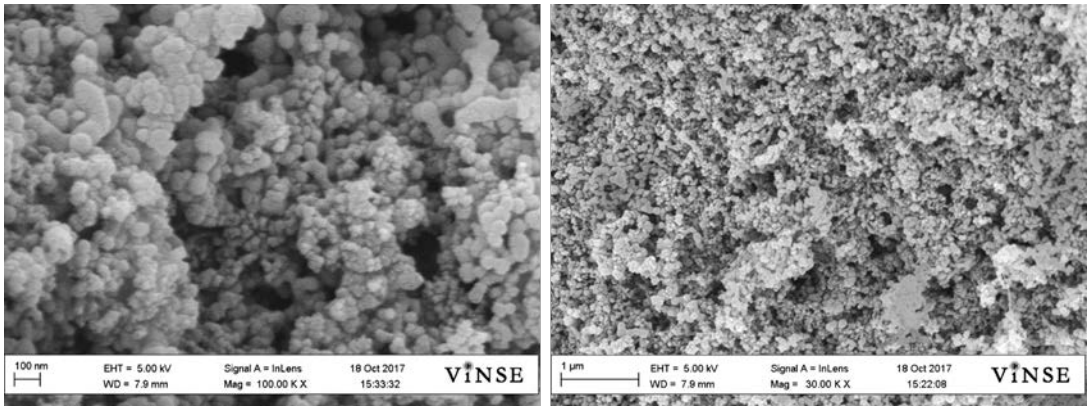


Figure II-403. SEM image of the surface of the electrosprayed Si/C/PVAE-PAA 40/25/35 anode annealed at 110°C and supported on Cu foil.

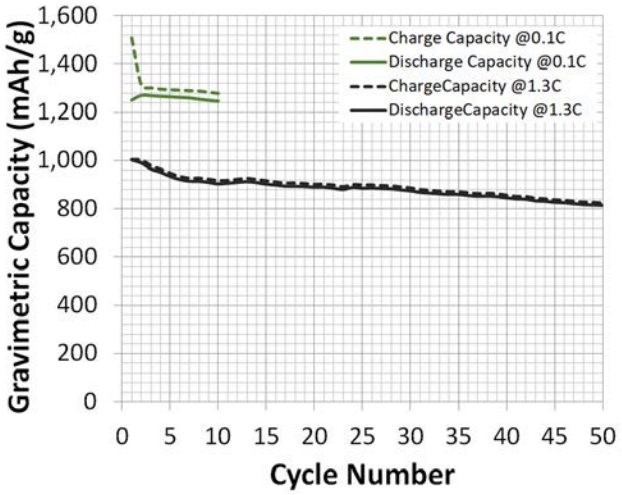


Figure II-404. Cycling results of an anode fabricated from electrosprayed ink containing new PVAE-PAA crosslinkable binder.

## Conclusions

A new dual fiber electrospun anode mat was created and successfully tested, with separate fibers for Li storage (Si/PAA fibers) and for electrical conduction (C/PAN fibers), where PAA denotes poly(acrylic acid) and PAN denotes poly(acrylonitrile). Good charge/discharge behavior was observed (essentially complete utilization of Si during the first cycle). The results show that: (i) 33% carbon fibers in a dual fiber mat is sufficient for good electron conduction and (ii) there are sufficient contact points between Si/PAA fibers and C/PAN fibers in a dual fiber mat for isotropic electron flow throughout the dual fiber anode mat, with good electrolyte infusion between fibers. The gravimetric capacity retention was excellent (87.4% after 35 cycles at 0.1C and 81.8% retention after 50 cycles at 1.3C).

A new thermally crosslinkable blended polymer binder was utilized in an electrosprayed droplet morphology anode, where the binder was a blend of poly(vinyl alcohol-co-ethylene) and PAA. The anode composition was 40/25/35 (Si/C/binder weight ratio). At 1.3C, the anode exhibited a high initial gravimetric capacity of 1003 mAh/g and excellent cycling stability, with a capacity retention of 81.8% after 50 cycles.

## Key Publications

1. E. C. Self, M. Naguib, R. E. Ruther, E. C. McRen, R. Wycisk,G. Liu, J. Nanda,and P. N. Pintauro, “High Areal Capacity Si/$LiCoO_2$ Batteries from Electrospun Composite Fiber Mats”, *ChemSusChem*, **10**, 1823–1831 (2017). DOI : 10.1002/cssc.201700096.

## II.F.5 Process R&D and Scale up of Critical Battery Materials (ANL)

**Gregory Krumdick, Principal Investigator**
Argonne National Laboratory
9700 S Cass Avenue
Lemont, IL 60439
Phone: 630-252-3952
E-mail: gkrumdick@anl.gov

**Peter Faguy, Technology Manager**
U.S. Department of Energy
Phone: 202-586-1022
E-mail: Peter.Faguy@ee.doe.gov

Start Date: October 1, 2016 End Date: September 30, 2017
Total Project Cost: $1.500,000 DOE share: $1,500,000 Non-DOE share: $0

### Project Introduction

New, experimental materials are being constantly invented to improve the safety, energy density, cycle, and calendar life of lithium ion batteries for HEV and PHEV applications. These materials are typically synthesized in discovery laboratories in small batches providing amounts sufficient only for limited basic evaluation but not in quantities required for full scale validation and prototyping. In addition, bench-scale processes are often un-optimized, not validated, and generate materials with inconsistent purity and yield. The project is aim to assist battery community by enabling access to larger quantities of high quality innovative materials.

### Objectives

The objective of this project is to conduct research toward scaling up production of advanced materials for Li-ion batteries originally created in small quantities by discovery scientist. Scaling up the original route used by discovery scientists requires sometimes extensive modification of the bench-scale chemistry and scientific-based process R&D to allow for safe and cost effective production, development of an engineering flow diagram, design of a mini-scale system layout, construction of the experimental system, and validation of the optimized process. The experimental system will be assembled and the materials will be manufactured in quantities sufficient for full scale industrial evaluation. The materials produced by the program will be fully characterized to confirm chemical identity and purity. Analytical methods will be developed for quality control. The electrochemical performance of the materials will be validated to confirm that the properties match the original sample generated by the discovery scientist. Sample of the materials produced by the project will be available to LIBs community to support basic research and large scale performance validation.

### Approach

A comprehensive, systematic approach to scale-up of advanced battery materials has been defined. This approach starts with the original route the new material was first made in the discovery lab and initial electrochemical evaluation. This determines if the material is to be added to the inventory database, ranked, prioritized and selected for scale up. MERF prioritize new materials based on level of interest, validated performance and scale up feasibility. The new candidate materials for scale up are discuss with DOE for final approval. MERF evaluates several approaches, including new emerging manufacturing technologies, to determine the best approach to scale up each particular material. One of such technology is Continuous Flow Chemical Reactor that enables the continuous synthesis of materials from discovery through process development and production scale. Continuous flow reactor can be used for rapid screening of reaction condition to better understand fundamentals of process kinetic and thermodynamic. The technology offers

cost-effective alternative to traditional batch processes by improving material and energy usage and minimize environmental impact of the manufacturing operation.

At this point, the scale-up process begins with a feasibility study, followed by proof of concept testing, 1st stage scale-up and final 2nd scale scale-up. Several Go/No Go decisions are located after feasibility determination and electrochemical validation testing.

For each material, we will develop a scalable manufacturing process, analytical methods and quality control procedures. We will also prepare a "technology transfer package" which includes detailed procedure of the revised process for material synthesis, materials balance, analytical methods and results (Certificate of Analysis) and SDS for the material. The detailed process description allows for preliminary estimates of production cost, an important factor for decision making in industry.

We apply the newly developed process to make kilogram quantities of the material. We will fully characterize chemically each material and make samples available for industrial evaluation and to the research community. We will also provide feedback to discovery chemist helping guide future research.

## Results

*1. Binder for Advanced Anode*

MERF contributes to the Advanced Anode Program by developing binary polymeric systems able to in-situ crosslinking during the process of electrode laminate manufacturing. The two components of the system need to be stable and non-reactive during aqueous slurry preparation process to allow for casting but should undergo rapid thermally induced crosslinking during laminate drying. The selection of proper components for the binary system needs to take under consideration several criteria required for binder for LIBs electrode. The components of the binary system need to be soluble or forming stable emulsion in water, the cross- linked polymer needs to be chemically compatible with electrolyte and other electrode materials and electrochemically stable during cycling of the batteries. The polymer needs to be characterized by good adhesion to the current collector and good cohesion between particles of the composite anode.

The intra- and extra-molecular crosslinking will result in a flexible 3D mesh holding silicon and graphite particles together preventing loss of electrical contact and mechanical degradation of the electrode during cycling (Figure II-405). Interaction of the backbone polymer with Si surface may further strengthen the structure and improve performance.

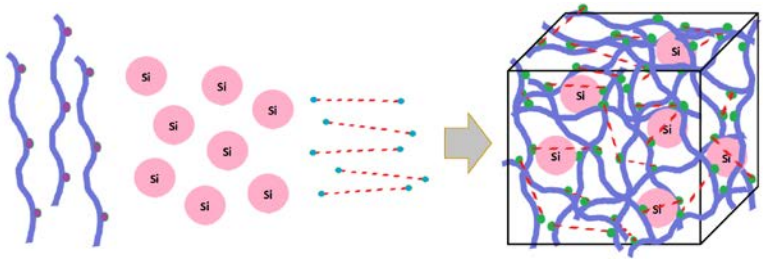


Figure II-405. Schematic of 3D mesh formation by in-situ cross-linking offunctionalized backbone polymer and small molecules.


Figure II-406. Poly(ethylene-alt-maleic anhydride) and poly(methyl vinyl ether-alt-maleic anhydride)

We selected inexpensive, commercially available poly(ethylene-alt-maleic anhydride) and poly(methyl vinyl ether-alt-maleic anhydride) as starting materials for syntheses of backbone polymers (Figure II-406).

The anhydride moiety in the starting materials were hydrolyzed to the corresponding poly(ethylene-alt-maleic acid) and poly(methyl vinyl ether-alt-maleic acid), respectively. Both backbone polymers containing maleic acid moieties were used in model cross-linking reactions with the following bi-functional small molecules: triethylene glycol, PEG400, PEG1000, 1,4-butanediol, and 4-aminobutan-1-ol.

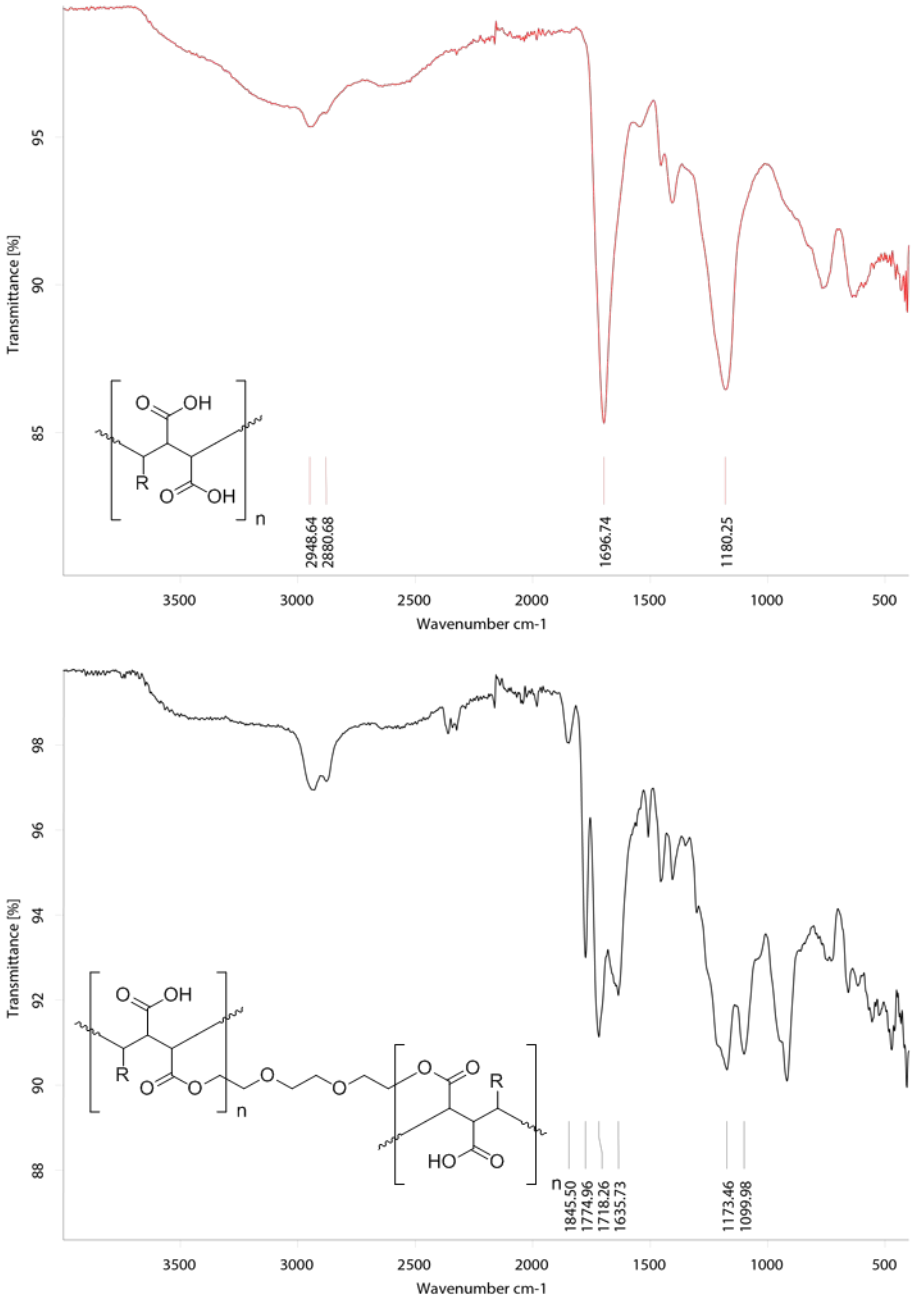


Figure II-407. FT-IR of poly(ethylene-alt-maleic acid) and material cross-linked with 20% molar of triethylene glycol.

FTIR analyses of the resulting materials revealed, in each case, formation of the expected crosslinks as evident by presence of ester or/and amide bonds (Figure II-407). Small amount of anhydride in the product was also observed.

*2. Scale up of Trifluoromethyl Sulfone Solvents*

Ethyl and propyl trifluoromethyl sulfones (Figure II-408) are promising solvents for high voltage LIBs electrolyte.

Figure II-408. Ethyl and propyl trifluoromethyl sulfones

The materials although known (12 references for Et and 4 references for Pr in SciFinder including patents for electrolyte formulations [1-2]) are purely described in the literature. There are only a very few references to the synthesis of the compounds [3]. (See Figure II-409.)

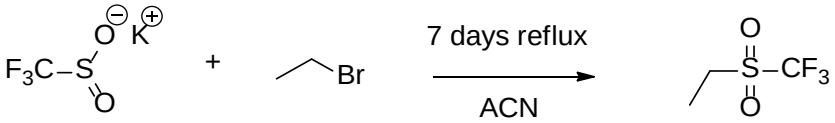


Figure II-409. Published synthesis of ethyl trifluoromethyl sulfone

The above reaction run at MERF at various conditions did not provide the desired product in an appreciable amount. Xu et al., [4] described multi-step synthesis procedure in 2002 publication without providing any experimental details. The synthesis route described by Argonne researches [5] utilizes Grignard reagent and trifluoromethanesulfonic anhydride (triflic anhydride). (See Figure II-410.)

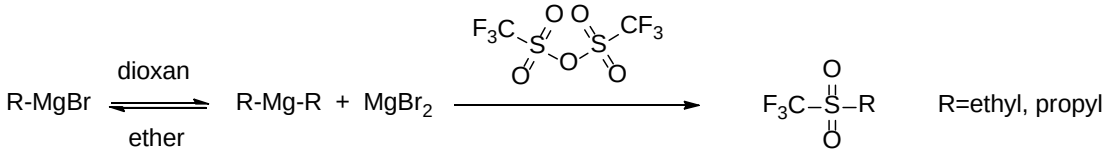


Figure II-410. Published synthesis of ethyl and propyl trifluoromethyl sulfones

The reported yield is low (~40%) and isolation of the desired product in a pure form is difficult due to complexity of the post-reaction mixture. Additionaly, the process involves centrifugal separation of moisture sensitive intermediate (diethyl or dipropylmagnesium) that makes it impractical in a larger scale production.

MERF run several experiments in an attempt to simplify the process, enhance material purity and to improve overall yield (for example using organozinc instead of organomagnesium compound and copper catalysis).

We found out that the process can be reduced to one-step (Grignard equilibrium shift by addition of dioxane is not necessary) if chloromagnesium instead of bromomagnesium Grignard compound is used. (See Figure II-411.)

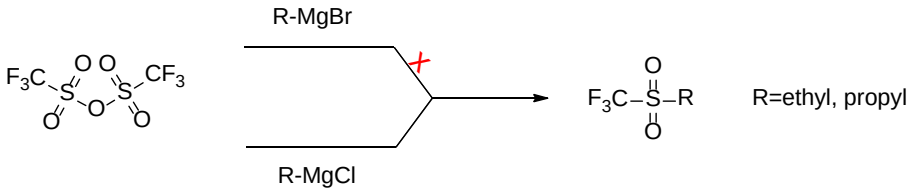


Figure II-411. Improved synthesis of ethyl and propyl trifluoromethyl sulfones

Although small amount of the materials can be made in batches, the current process that is extremely exothermic is not suitable for larger scale production. We currently investigate continuous flow reactor process as a technology platform to manufacture ethyl and propyl trifluoromethyl sulfones.

*3. Scale-up of Pre-Lithiation Compounds - $Li_5FeO_4$ and $Li_6CoO_4$.*

Scaled-up synthesis of $Li_5FeO_4$ and $Li_6CoO_4$ is completed. The material, a pre-lithiation additive was developed and requested by Argonne's CSE Division (Chris Johnson). The material is made via solid state synthesis by step-wise heating following grinding in temp range from r.t. to 450 to 600°C to 800°C. The entire process needs to be done in a moisture free atmosphere. Several reactions (muffle furnace and tube furnace, outside and inside glovebox) have been run to optimize condition and validate reproducibility. The quality of the material seems not be scale-dependent (3g, 11g and 35g all appear the same if the process is run in muffler furnace that was located inside glovebox) and it material is phase pure (XRD). Several samples of $Li_5FeO_4$ were provided to Argonne's CSE researchers for electrochemical evaluation. Lithium cobalt oxide ($Li_6CoO_4$) were scaled up to 12 g and the material was forwarded to CSE researchers.

*4. Novel silicon-containing carbonate solvents with improved safety profile.*

In the quest for materials that offer improved safety without sacrificing performance we synthesized and investigated series of electrolyte carbonate solvents containing silicon atoms. Single literature reference [6] suggested potential flame retardant ability of methyl (trimethylsilyl)methyl carbonate (MTMSMC). The above reference did not disclosure source or technique used to obtain the material.

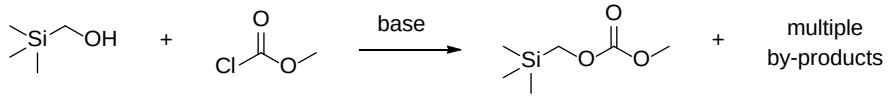


Figure II-412. Standard method for synthesis of unsymmetrical carbonates

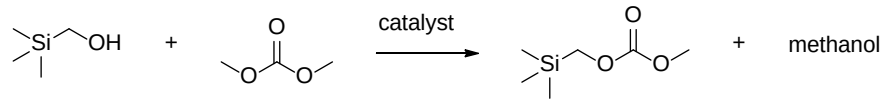


Figure II-413. Transesterification method for synthesis of unsymmetrical carbonates

Standard reaction procedure (Figure II-412) for synthesis of MTMSMC failed to produce battery grade materials. The reaction produced multiple by-product difficult to separate from the desired material.

Transesterification of dimethyl carbonate with (trimethylsilyl)methanol (Figure II-413) was proposed as an attractive alternative and possible candidate for a continuous flow manufacturing process.

Screening of several catalysts and various reaction conditions in batch and continuous flow mode revealed that the material can be made in continuous flow reactor in more feasible manner than in batch. The reaction has been successfully scaled up in continuous mode to work out 250 mL reactants in 4 mL solid catalyst reactor in several hours. The product (MTMSMC) has been isolated by simple distillation with excellent yield and purity greater than 99.8%.

Several other silicon-containing carbonate solvents have been invented and synthesized at MERF (Figure II-414, compounds 2,3,4,5 and 6). Sample of the new materials are available to research community for further evaluation.

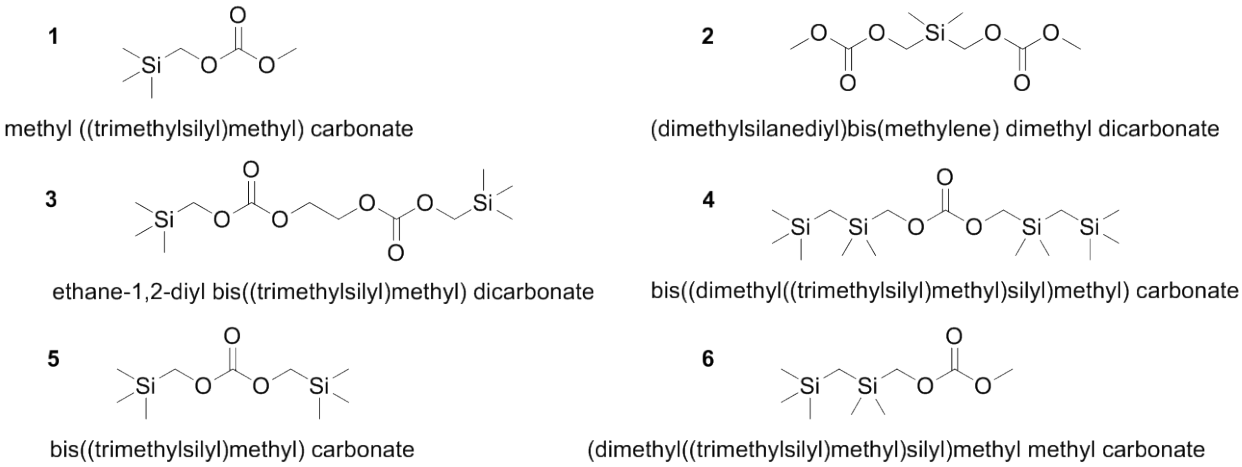


Figure II-414. Structures of some novel silicon-containing carbonates invented and produced by MERF

Preliminary investigations of electrochemical performance of ethyl (trimethylsilyl)methyl carbonate (ETMSMC) revealed that replacement of up to 20% EMC with ETMSMC in Gen2 electrolyte formulation does not decrease performance of the cell. (See Figure II-415.)

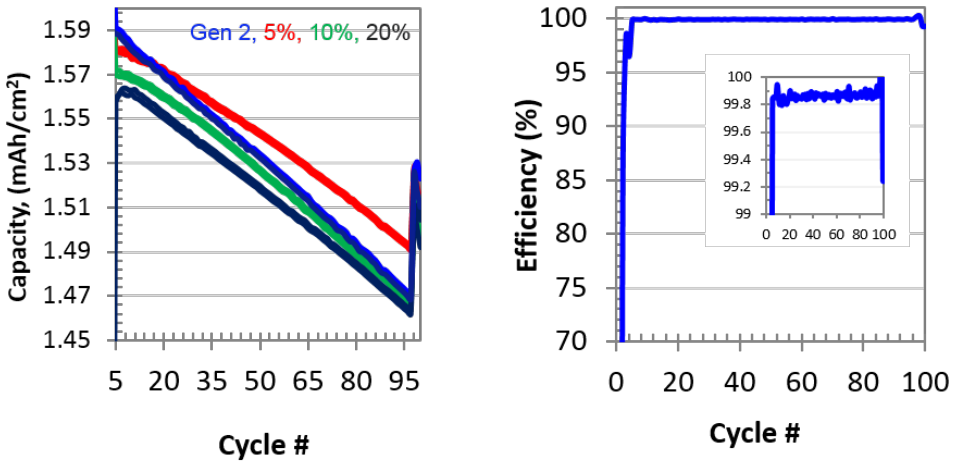


Figure II-415. 5, 10, 20% w/w ETMSMC in Gen2, graphite//NCM523, 3.0 - 4.4 V cycling (Ch/DCh at C/3), 30ºC.

Sample of selected electrolyte formulations containing the new materials were provided to Argonne's CAMP facility for throughout evaluation. Materials (electrolyte formulations) with acceptable electrochemical performance will be used to manufacture larger cell formats for safety and abuse tolerance tests.

## Conclusions

MERF's experimental materials scale-up program assists the battery research community and allows for a comprehensive evaluation of new materials by industrial laboratories as well as supports basic research.

In FY17 the program provided several new, not commercially available materials. Sample of high, uniform quality materials were distributed for further evaluation and research. Over 130 samples, ranging from grams

to hundreds of grams of experimental battery materials have been provided to researches since the program inception.

MERF contributes to Advanced Anode Program by designing, synthesizing, and evaluating new class of binder for silicon-graphite composite anodes. MERF's ability for rapid synthesis and evaluation of large number of materials permits for developing structure - properties database. Such a database allows for better understanding of binder's performance requirements and assists in science-based rationale design of a new materials.

MERF successfully investigated scale up process for making two sacrificial lithium source additives for cathode materials. Several samples of the two materials, lithium iron oxide and lithium cobalt oxide, were produced and provided to researches for electrochemical evaluation.

MERF invented and synthesized series of silicon-containing carbonate solvents. The materials have significantly higher flash point than solvents commonly used to formulate LIBs electrolytes. Preliminary electrochemical evaluation revealed that the materials can improve safety of LIBs without performance degradation.

Evaluate emerging manufacturing technologies such as continuous flow reactors, microwave assisted reactions or reactive distillations to improve product quality while lowering manufacturing costs are all under consideration. MERF utilized recently acquired customized Syrris ASIA320 flow reactor to develop expedient manufacturing processes for new electrolyte solvents by improving safety, minimize waste stream and lower material and energy cost.

## Key Publications

*Publications*

1. Layered Oxide, Graphite and Silicon-Graphite Electrodes for Lithium-Ion Cells: Effect of Electrolyte Composition and Cycling Windows, Klett, Matilda; Gilbert, James A.; Pupek, Krzysztof Z.; Trask, Stephen E.; Abraham, Daniel P., Journal of the Electrochemical Society (2017), 164(1), A6095-A6102.

2. Chemical Stability of Lithium 2-Trifluoromethyl-4,5-dicyanoimidazolide, an Electrolyte Salt for Li-Ion Cells, Shkrob, Ilya A.; Pupek, Krzysztof Z.; Gilbert, James A.; Trask, Stephen E.; Abraham, Daniel P., Journal of Physical Chemistry C (2016), 120(50), 28463-28471.

*Presentations*

1. Battery Materials Scale-Up and Manufacturing Research, Gregory Krumdick, International Battery Seminar, March 23, 2017

2. Matching Electrolyte Formulation with Cathode Chemistry, Krzysztof Pupek, Daniel Abraham, Trevor Dzwiniel, Gregory Krumdick, Electrochemical Society 231st Meeting, May 2017.

*Patent Applications*

1. Process for Manufacturing Fluorinated Electrolyte Solvent, Trevor Dzwiniel, Krzysztof Pupek and Gregory Krumdick, US Patent Application 15/270,256, Filed 9-20-2016

2. Improved and Practical Process for the Synthesis of Lithium bis(2-methyl-2 fluoromalonato)borate, Trevor Dzwiniel, Krzysztof Pupek and Gregory Krumdick, US Patent Application 15/272,955, Filed 9-22-2016

*Technical Report*

1. Pupek, Krzysztof, Trevor Dzwiniel and Gregory Krumdick. "Li-FSI Impurity Impact Study: Final CRADA Report." Argonne National Laboratory, ANL/ES-C1401001, 2017.

## References


1. Xu, Wu, U.S. Pat. Appl. Publ. (2009), US 20090017386 (Ferro).
2. Li, Wentao, U.S. Pat. Appl. Publ. (2015), US 20150140446 (BASF).
3. Hendrickson, James B. et al., Accounts of Chemical Research, 10(8), 306-12; 1977.
4. Xu, Kang at al., J. Electrochem. Soc., 2002, 149, A920–A926.
5. Zhang, Z. at al, Energy and Environ. Sci. 2017, 10, 900.
6. Miura, Hitoshi; Sakano, Fumihiro; Yahagi, Akira; Yamamoto, Taketsugu; Jpn. Kokai Tokkyo Koho (1998), JP 10172610 A 19980626.

# II.G Next-Gen Lithium-Ion: Core and Enabling Support Facilities

## II.G.1 Cell Analysis, Modeling, and Prototyping (CAMP) Facility Research Activities (ANL)

**Andrew N. Jansen, Principal Investigator**
Argonne National Laboratory
9700 S. Cass Avenue
Lemont, IL 60439
Phone: 630-252-4956
E-mail: Jansen@anl.gov

**Peter Faguy, Technology Manager**
U.S. Department of Energy
Phone: 202-586-1022
E-mail: Peter.Faguy@ee.doe.gov

Start Date: October 1, 2014 End Date: September 30, 2018
Total Project Cost: $1,900,000 DOE share: $1,900,000 Non-DOE share: $0

### Project Introduction

The “valley of death” is a phrase often used to describe the path a new discovery must traverse to become a commercial product. This is especially true for novel battery materials invented in research laboratories around the world. Often researchers are resource limited and are only able to make gram quantities of their new material. The CAMP Facility is appropriately sized to enable the design, fabrication, and characterization of high-quality prototype cells using just a few hundred grams of the latest discoveries involving high energy battery materials. Prototype cells made in the CAMP Facility generally have near 400-mAh capacity, which straddles the gap between coin cells and industrially-sized cells nicely – two orders of magnitude from each end point. Thus, a realistic and consistent evaluation of candidate chemistries is enabled in a time-effective manner with practical quantities of novel materials in cell formats commonly used in industry.

The CAMP Facility is an integrated team effort designed to support the production of prototype electrodes and cells, and includes activities in materials validation (benchmarking), modeling, and diagnostics. It is not the aim of this facility to become a small battery manufacturer, but instead to be a laboratory research facility with cell production capabilities that adequately evaluate the merits and limitations of new lithium-ion chemistries in a close-to-realistic industrial format. The source of these materials (anodes, cathodes, electrolytes, additives, separators, and binders) may originate from the ABR and BMR Programs, as well as from other domestic and foreign organizations such as universities, national labs, and industrial vendors. Electrochemical couples with high power and energy density are given extra priority. Lately efforts have focused on silicon-based anodes, and nickel-manganese-cobalt (NMC) cathodes that are high in nickel and operating at higher potentials.

The CAMP Facility has the capability to make three prototype cell formats in their 45 m² dry room: pouch cells (xx3450 format, with capacity around 0.5 Ah; and xx6395, with capacity around 2 Ah) and 18650 cells (with capacity around 2 Ah). Pouch cells are generally easier to assemble, but they may suffer from bulging if gases are evolved during cell aging and cycling. 18650s, which are rigid containers, may be used if the pouch cell format is deemed unreliable due to gassing. Central to this effort is a pilot-scale coating machine that operates with slurry sizes that range from 20 grams to a couple kilograms. This is a key feature of the CAMP Facility that enables a professional evaluation of small quantities of novel materials. If needed, the Materials Engineering Research Facility (MERF) is available for scaling up materials for these prototype cell-builds.

## Objectives

The objective of this core-funded effort is to design, fabricate, and characterize high-quality prototype electrodes and cells that are based on the latest discoveries involving high energy anode and cathode battery materials. Using this multi-disciplined facility, analytical diagnostic results can be correlated with the electrochemical performance of advanced lithium-ion battery technologies for plugin electric vehicle (PEV) applications.

- Link experimental efforts through electrochemical modeling studies.
- Identify performance limitations and aging mechanisms.
- Support lithium-ion battery projects within the DOE-EERE-VTO

## Approach

The general approach used in this effort is to start small and grow large in terms of cell size and amount of resources devoted to each novel battery material. At various points in the development process, decisions are made to either advance, modify, or terminate studies to maximize utilization of available resources.

Coin cells (2032 size) are used for materials validation purposes with initial studies performed at room temperature or 30°C. After formation cycles, the coin cells go through rate capability testing, HPPC testing, and limited cycle life testing. Additional temperatures and test conditions are employed if warranted.

Using the results obtained by the materials validation of promising materials, single-sided electrodes are fabricated on the larger dry-room coater for diagnostic study. The new cell chemistries are studied in detail using advanced electrochemical and analytical techniques, including the employment of micro-reference electrode cells. Factors are identified that determine cell performance and performance degradation (capacity fade, impedance rise) on storage and on extensive deep-discharge cycling. The results of these tests are used to formulate data-driven recommendations to improve the electrochemical performance/life of materials and electrodes that will be incorporated in the prototype cells that are later fabricated in the dry room. This information also lays the foundation for electrochemical modeling focused on correlating the electrochemical and analytical studies, in order to identify performance limitations and aging mechanisms.

If the results from diagnostics and modeling still look promising, full cell-builds are conducted using double-sided electrodes. The electrodes are then either punched in the case of pouch cells, or slit in the case of 18650 cells and assembled into full cells in the dry room using semi-automated cell assembly equipment. Formation procedures are conducted on the cells to encourage electrolyte wetting and uniform solid-electrolyte-interface (SEI) formation. These cells undergo rigorous electrochemical evaluation and aging studies under the combined effort of the CAMP Facility team, and Argonne's Electrochemical Analysis and Diagnostic Laboratory (EADL) and Post-Test Facility. After testing, select cells are destructively examined by the Post-Test Facility to elucidate failure mechanisms. This information is then used to further improve the new chemistry, as well as future electrode and cell-builds.

## Results

The CAMP Facility is designed to work closely with materials researchers across the many electrochemical energy storage programs throughout the DOE-EERE-VTO. In addition to its own yearly R&D tasks, it actively coordinates its efforts to provide support to other national lab teams such as: the High-Energy High-Voltage deep dive, the Next Generation Anodes deep dive, and the CAEBAT programs. The Materials Benchmarking Activities (Section IV.B.2) is a segment of the CAMP Facility. The CAMP Facility also complements the capabilities of other DOE support facilities such as: the Materials Engineering Research Facility (MERF - ANL), the Post-Test Facility (PTF - ANL), the Battery Abuse Testing Lab (BATLab - SNL), and the Battery Manufacturing Facility (BMF - ORNL).

In particular, key deliverables that were met in FY17 for these programs include:

- Over 20 meters of advanced double-sided anode and cathode matching electrodes were produced and delivered for the SilLion SBIR Phase II project.
- Over 10 meters of alumina-coated NMC532 single-sided electrodes were produced and distributed to the "High Energy/High Voltage" project
- 30 pouch cells with >400 mAh capacity using Si-Graphite anode and NMC cathode for NREL CAEBAT studies were fabricated and delivered

More information about these projects can be found in the relevant chapters and sections of this annual report. The remainder of this CAMP Facility section will discuss the results of the remaining CAMP Facility deliverables for FY17, and include results of related topics.

*Deliverable: Deliver to "Next Generation Anodes" Project at Least 10 meters of Single-Sided Negative Electrode Based on 30% Silicon-Graphite with ~ 2 mAh/cm² Loading for FY17 Baseline*

Using our knowledge of the challenges that silicon can present for slurry making and coating, we have implemented effective strategies to help mitigate dispersion issues. New preparation processes were developed for the fabrication of both the 15 wt.% Si electrode (15 wt.% silicon, 73 wt.% graphite, 2 wt.% carbon black, and 10 wt.% LiPAA in $H_2O$) and the 30 wt.% Si electrode (30 wt.% silicon, 58 wt.% graphite, 2 wt.% carbon black, and 10 wt.% LiPAA in $H_2O$) in this section from silicon suppliers: Nanostructured and Amorphous Materials, Inc. from Houston, TX and Paraclete Energy from Chelsea, MI.

The initial observations of pressure building during the aqueous slurry processing add to the challenges that silicon already has on the electrochemical front. Gas generation suggests there is an uncontrolled reaction changing the chemistry and properties of the silicon material. Gas generation during slurry processing is not typical in NMP+PVDF-based slurries or $H_2O$+CMC+SBR (no Si)-based slurries. To demonstrate the gas generation of slurries containing silicon, we sealed pouch laminate foil with a pocket for slurry contents. This laminate serves only as a container and is not an actual electrochemically active pouch cell. We observed that high surface area silicon (30-50 nm particles), when combined with the binder solution LiPAA in $H_2O$ (pH ~6), produced a significantly higher amount of gas generation than the other combinations. $H_2O$ with silicon and $H_2O$+PAA with silicon showed minimal gas generation. All pouches using NMP as the solvent, either alone or in solution with PAA, showed no signs of gas generation. LiPAA does not dissolve in NMP, therefore this was not part of the test matrix. A baseline of LiPAA in $H_2O$ (pH ~6) with graphite and carbon additives showed no gassing.

Early 15 wt.% silicon coatings using the larger 70 to 130 nm silicon from NanoAmor showed a reappearance of coating brittleness and stresses on the copper foil as the electrode dried that plagued early development silicon electrodes. These undesirable properties were somewhat apparent in coatings at ~2 mAh/cm², but calendering helped improve the flexibility and avoidance of electrode cracking to extent that made them acceptable for the Electrode Library. However, achieving >3 mAh/cm² with 15 wt.% silicon proved to be very challenging with this material, which prevented this material from being fully adopted as the new baseline. SEM images revealed that the previously used 50-70 nm silicon had a smooth spherical grown shape morphology with secondary particles measuring around 50-70 nm, while the 70-130 nm powder showed jagged edges that appeared to be milled resulting in a more broad particle size distribution with some secondary particles micron sized. This result demonstrated that switching silicon particle size and morphology can have drastic changes in coating behavior and can slow the development of obtaining high quality, flexible, and robust electrodes.

A variety of coatings were made with different electrode compositions, solvent blends, and mixing procedures. NMP produced a high quality electrode but showed a decrease in mAh/g compared to the aqueous produced electrode. The NMP made electrode also took more cycles to reach the coulombic efficiency of ~99.5% that a

typical aqueous electrode achieves. For this reason, it was decided to use the slurry process based on aqueous LiPAA. The efforts in experimental coatings of 70-130 nm silicon from NanoAmor eventually resulted in coating a single-sided high-quality 30 wt.% Si electrode at ~2 mAh/cm² (A-A011). This electrode (see Figure II-416) was entered into the CAMP Facility Electrode Library and also provided to the Next Generation Anodes Project (Silicon Deep Dive).

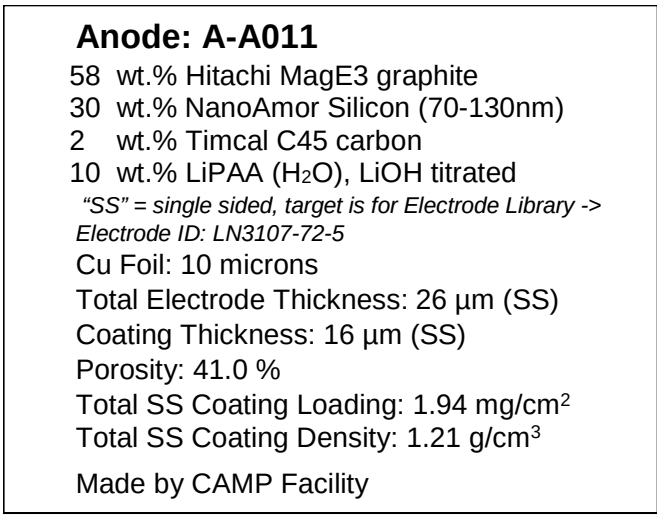


Figure II-416. Electrode information for A-A011 containing 30 wt.% 70-130 nm silicon from NanoAmor.

Efforts were also expended to develop 15 wt.% Si electrodes using silicon from Paraclete Energy, which is their non-surface-modified silicon metal powder with oxide on the surface. These electrodes had better physical properties than the 70-130 nm Si from NanoAmor and was capable of making electrodes with > 3 mAh/cm². This Paraclete Si was then used in a study to better understanding the impact n:p ratio may have for the silicon-graphite composite electrode system. Two electrodes were made with 15 wt.% Si: one with a n:p ratio near 1.5 [electrode A-A012], and one with a n:p ratio near 1.15 [electrode A-A013]. Full cells were then made using these new baseline materials paired against the same cathode [A-C013A] using the Silicon Deep Dive Protocol to evaluate the cycling performance. These results are shown in Figure II-417. The higher n:p ratio cell couple has a slight advantage over the lower n:p ratio cell, most likely because the Si in the higher n:p ratio is not cycled as deeply. Based on the results of using the Si material from Paraclete Energy, it was decided to use this Si material as the baseline Si going forward.

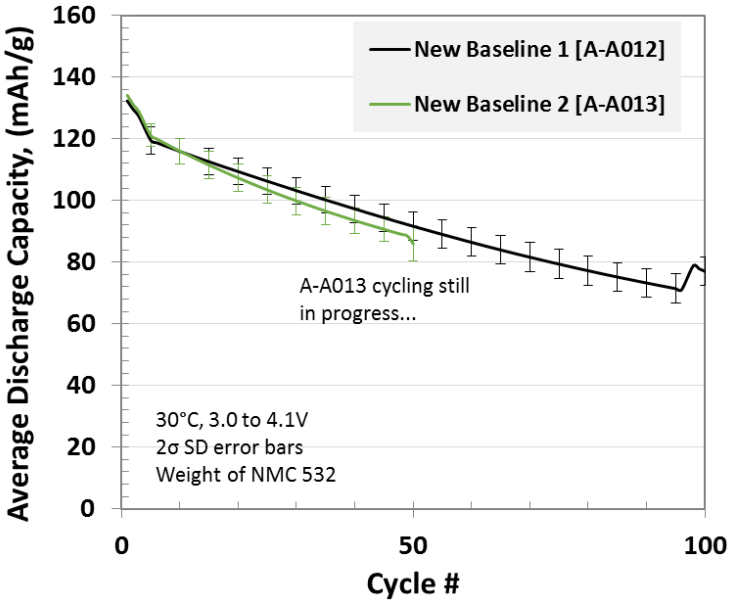


Figure II-417. Full-cell coin-cell results showing cycle number vs. average discharge capacity of the new Silicon Deep Dive baseline electrodes (Paraclete Energy silicon) vs. NMC532 [A-C013A]. Data shows the average values based on 4 coin cells for each electrode pair. The capacity values are normalized to the weight of NMC532.

*Deliverable: Developing Techniques for In-Operando Detection of Lithium Plating During Fast Charging*

A major effort is underway to enable fast charging of lithium-ion battery cells at rates greater than 6C, i.e., complete battery charging in 10 minutes or less. A key limitation at high charge rates is the plating of lithium on the graphite-based negative electrodes used in conventional, high-energy lithium-ion battery cells. This plating has consequences that include the following: (a) the plated lithium reacts with the electrolyte, reducing the inventory of lithium-ions and electrolyte, and causing a rapid decline in cell life; and (b) the plated lithium may form dendrites, which create short-circuits in the cell resulting in hazardous outcomes such as cell fires and/or explosions. We have been exploring various techniques to detect lithium plating during cell cycling. These techniques are under various stages of development and include (a) reference electrode cells that provide reliable data during high-rate cycling, (b) operando energy dispersive X-ray diffraction, and (c) operando radiography and tomography techniques.

As mentioned above, various techniques to detect lithium plating during cell cycling are under development. The reference electrode cells provide information on the positive and electrode potentials; lithium-plating becomes likely when the graphite-based negative electrode potential goes below 0.0 V vs. Li/Li+. Our typical setup includes a Li-metal reference electrode (RE) that is external to the electrode stack; the electrode potentials measured by this arrangement are affected by the distance of the RE from the electrodes, and are not reliable at high cycling currents. We are examining alternative approaches, including the use of an RE that is placed within the electrode stack; initial results are promising and more details will be provided in future reports. The operando energy dispersive X-ray diffraction (XRD) measurements are conducted with a conventional 2032-type coin cells at the 6BM-A beamline of Argonne's Advanced Photon Source (APS). The high-energy X-ray from the synchrotron source penetrates the stainless casing of the coin cell to allow for the operando measurements. Initial experiments show that lithium-metal foil can be identified in the XRD spectra collected on the coin cells. Future experiments will identify the cycling conditions (cell voltage, nature of the electrode, electrolytes, etc.) under which lithium-plating on graphite becomes most likely. For the operando micro-tomography work, a custom cell has been designed and fabricated to image dendrite formation during electrochemical cycling. Tomographic scans collected on symmetric lithium-lithium cells during a recent study indicate that lithium dendrites can be imaged in operando. Future experiments will include the study of lithium

plating on graphite electrodes; further modification of the cell and data acquisition conditions may be needed to achieve this challenging goal.

*Deliverable: Determine Effect of Cycle Life/Calendar Life/Cell Pressure on Silicon-Graphite vs. NMC532 Pouch Cells*

Silicon particles in lithium-ion batteries are known to grow up to 300% of their original size when lithiated. The current standard negative electrode active material, graphite, will expand only around 10%. While silicon-containing electrodes volumetrically expand when lithiated (full cell charging), they also deflate to a thickness above the original thickness when de-lithiated (full cell discharging). The destructive nature of the significant expansion and contraction during each charge and discharge cycle that silicon-containing electrodes exhibit is thought to be one cause of the poor cycle life performance. In FY 2017, we evaluated the effects of applied pressure on the cell stack for silicon-graphite composite and graphite-only electrodes. The CAMP Facility fabricated xx3450 pouch cells with silicon-containing and baseline graphite negative electrodes against the same NMC532 positive electrode and evaluated the formation, rate, impedance, and cycling performance under a relatively low stack pressure (2 psi) and a high stack pressure (76 psi). Two additional pressures will be selected in the second round of testing depending on these results.

| Anode: **Si-Gr** | Anode: **Gr** | Cathode: **NMC532** |
|---|---|---|
| 15 wt% NanoAmor Silicon (70-130nm)<br>73 wt% Hitachi MagE3<br>5 wt% Timcal C45<br>10 wt% LiPAA | 91.83 wt% Hitachi MagE3<br>2 wt% Timcal C45<br>6 wt% Kureha 9300 PVDF<br>0.17 wt% oxalic acid | 90 wt% Toda NMC532<br>5 wt% Timcal C45<br>5 wt% Solvay 5130 PVDF |
| *Matched for 4.1V full cell cycling*<br>Cu Foil Thickness: 10 µm<br>Total DS Electrode Thickness: 94 µm<br>SS Coating Thickness: 42 µm<br>Porosity: 44.0 %<br>Total Coating Loading: 4.80 mg/cm²<br>Total Coating Density: 1.14 g/cm³<br>Estimated Capacity: 2.85 mAh/cm²<br>(0.050 to 1.5V vs. Li metal, C/10) | *Matched for 4.1V full cell cycling*<br>Cu Foil Thickness: 10 µm<br>Total DS Electrode Thickness: 130 µm<br>SS Coating Thickness: 60 µm<br>Porosity: 32.0 %<br>Total Coating Loading: 8.85 mg/cm²<br>Total Coating Density: 1.47 g/cm³<br>Estimated Capacity: 2.73 mAh/cm²<br>(0.000 to 1.5V vs. Li metal, C/10) | *Matched for 4.1V full cell cycling*<br>Al Foil Thickness: 20 µm<br>Total DS Electrode Thickness: 136 µm<br>SS Coating Thickness: 58 µm<br>Porosity: 33.6 %<br>Total Coating Loading: 15.64 mg/cm²<br>Total Coating Density: 2.70 g/cm³<br>Estimated Capacity: 2.27 mAh/cm²<br>(3.0 to 4.2V vs. Li metal, C/10) |

Figure II-418. Electrode design for Si-Gr//NMC532 and Gr//NMC532 xx3450 pressure study pouch cells. "SS" = single side, "DS" = double side. All electrodes were fabricated at the CAMP Facility and designed for 3.0 to 4.1 V full-cell cycling.

Details of the fabricated electrodes are provided in Figure II-418. Single and double side electrodes were made to enable multilayer pouch cell stacking. The coating loadings targeted were based on each of the electrode active materials' half-cell 1st cycle performance, reversible C/10 capacity, and reversible 1C capacity, the n:p ratios for the Si-Gr//NMC532 and Gr//NMC532 cells were calculated to be 1.10-1.19 and 1.15-1.17, respectively, for cycling from 3.0 to 4.1 V in a full cell. Weight normalization of the data within this section is based on the total active material weight in the cathode (namely NMC532). The xx3450 cells each contain 2.779 grams of NMC532 per pouch cell.

The electrodes were calendered, stamped to xx3450 electrode pouch cell dimensions, and z-fold wound with 15 total layers (7 double-sided anode, 6 double-sided cathode, and 2 single-sided cathode for the outside layers). Celgard 2325 PP/PE/PP was used as the separator. Area normalization of the data within this section is based on the total cathode area in a cell. Each xx3450 cell has a total cathode area of 197.4 cm². After the cells completed assembly, all cells were filled with 3.0 mL of 90 wt.% (1.2 M $LiPF_6$ in EC:EMC 3:7 wt.%, "Gen2", Tomiyama) + 10 wt.% (FEC, Solvay) electrolyte and vacuum sealed. The electrolyte volume to available pore volume (anode, cathode, and separator porosities) factor was calculated to be ~2.8 for all the cells. The cells were then placed in rigid fixtures for electrochemical testing. The chosen stack pressures per pouch cells of 2 psi and 76 psi are examples of a modest stack pressure and relatively extreme stack pressure, respectively. Stack pressure per cell was calculated by accounting for the number of cells per layer, cell dimensions, spring constant, length of spring before and after compression, number of springs, and weight of the top steel plate

above the cells. Four cells were put on test for each of the four variables based on the anode and pressure applied to each cell: (Si-Gr, 2 psi), (Si-Gr, 76 psi), (Gr, 2 psi), and (Gr, 76 psi).

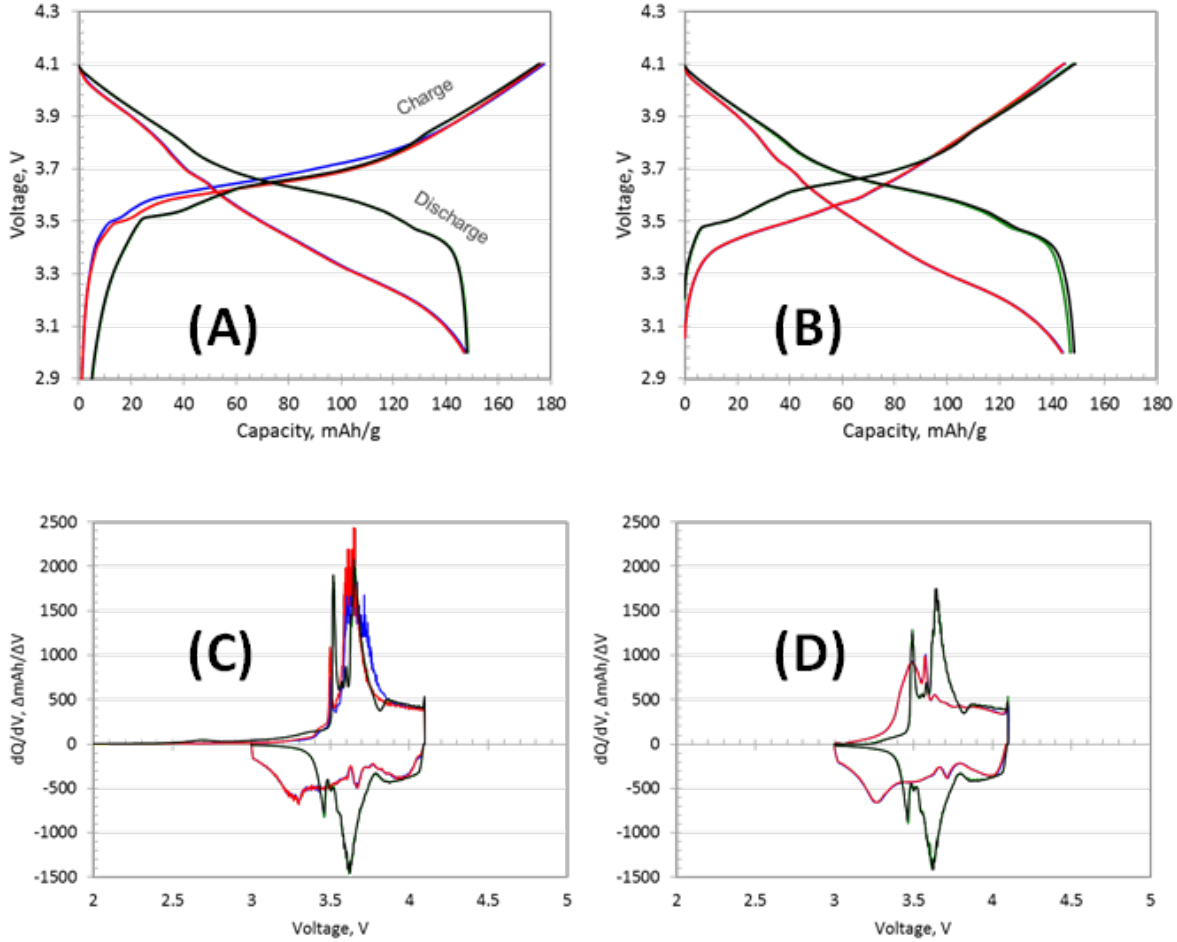


Figure II-419. Representative individual cycle voltage (a,b) and dQ/dV (c,d) profiles of Si-Gr//NMC532 pouch cells at 2 psi per cell (blue), 76 psi per cell (red), and Gr//NMC532 pouch cells at 2 psi per cell (green), 76 psi per cell (black) of the 1st (a,c) and 3rd (b,d) cycles during formation. (The green and black curves are often on top of each other, as are the blue and red - indicating little influence of pressure during formation.)

The 1st and 3rd cycles for each of the cell-builds and corresponding stack pressures are shown in Figure II-419. The initial charge and discharge capacities are similar to each other, however as seen previously, the lower cell voltage (and hysteresis) upon silicon delithiation is visible in these full cell discharge curves. The 3rd cycle plots show the early stages of capacity loss and a lower charge energy in the first 50% state of charge for the Si-Gr//NMC532 cells. While the impact of silicon in the system has been highlighted thus far, the low and high stack pressures placed on the cells had minimal impact on the formation process for both the Si-Gr//NMC532 and Gr//NMC532 cell-builds. The cells were then removed from their testing fixtures, degassed, vacuum sealed, and put back on the testing fixtures to move on to the rate performance study.

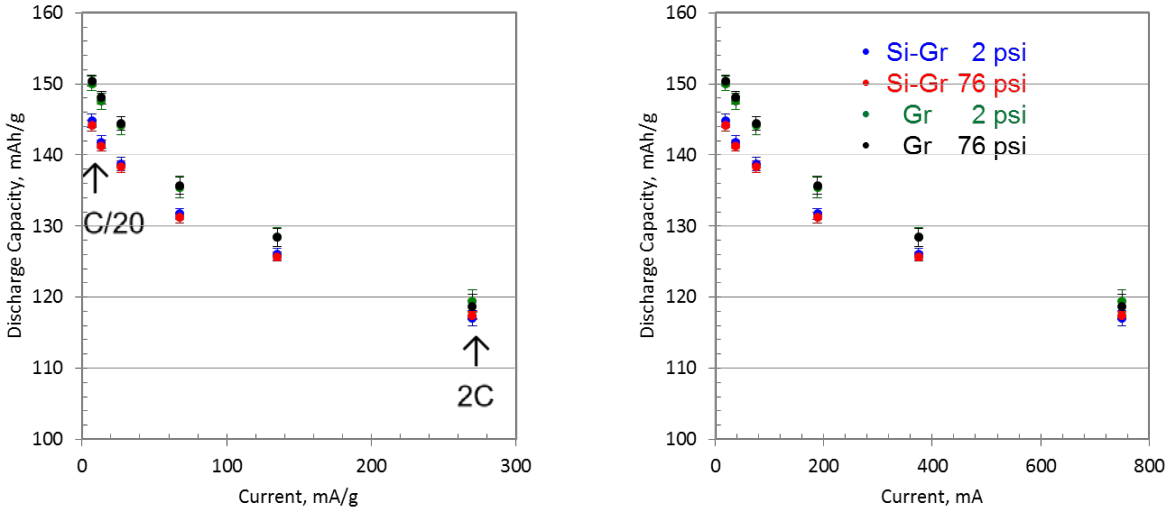


Figure II-420. Average rate study performance of Si-Gr//NMC532 pouch cells at 2 psi per cell (blue), 76 psi per cell (red), and Gr//NMC532 pouch cells at 2 psi per cell (green), 76 psi per cell (black) specific discharge capacities as a function of current, mA/g (left) and mA (right). The cells were cycled at 30 °C between 3.0 and 4.1 V. The plots show the discharge performance from the 2nd cycle at C/20 and 3rd cycle at C/10, C/5, C/2, 1C, and 2C rates.The error bars represent 2σ standard deviation.

The cells underwent identical rate testing in the following order: 2 cycles at C/20, 3 cycles at C/10, 3 cycles at C/5, 3 cycles at C/3 charge and C/2 discharge, 3 cycles at C/3 charge and 1C discharge, and 3 cycles at C/3 charge and 2C discharge. The rate performance of the 4 test variables is shown in Figure II-420. The Si-Gr//NMC532 have slightly lower capacities at slower rates but converge with the Gr//NMC532 capacities at the faster rates. Similar to the formation performance, the low and high stack pressures do not appear to have an impact on the rate capabilities for either of the cell chemistries.

The Hybrid Pulse Power Characterization (HPPC) testing protocol was then performed on these cells with 10 s discharge pulses at a 5C rate (1.75 A, 629.7 mA/g, 8.87 mA/cm²) and 10 s charge pulses at a 3.75C rate (1.31 A, 472.3 mA/g, 6.45 mA/cm²). The differences between the Si-Gr//NMC532 and Gr//NMC532 systems are again seen in this initial HPPC test (Figure II-421). While the overall Area Specific (ASI) values are on average slightly higher for the Si-Gr//NMC532 cells, the operating voltages extend 300 mV lower than the Gr//NMC532 cells. In addition, the right side of Figure II-421 shows that ~50 % of the ASI occurs in the beginning of the pulse. Consistent with the formation and rate performance, the HPPC results suggest there are minimal differences in the ASI results between the low and high stack pressures.

Figure II-422 shows the cycle life performance of the cells, which consisted of a repeating loop: a slow rate cycle (C/20), HPPC, then cycling 48 cycles with C/3 charging (C/5 trickle charge) and C/2 discharging testing at 30°C. The Si-Gr//NMC532 cells perform consistent to previous 15 wt.% silicon-containing cell-builds, that is, short cycle life to 80 % capacity retention, while the Gr//NMC532 cells perform as expected with having minimal capacity fade. Low or high stack pressure on either of the cell-builds does not seem to change the performance. The Gr//NMC532 cells are still under test at the time of this writing.

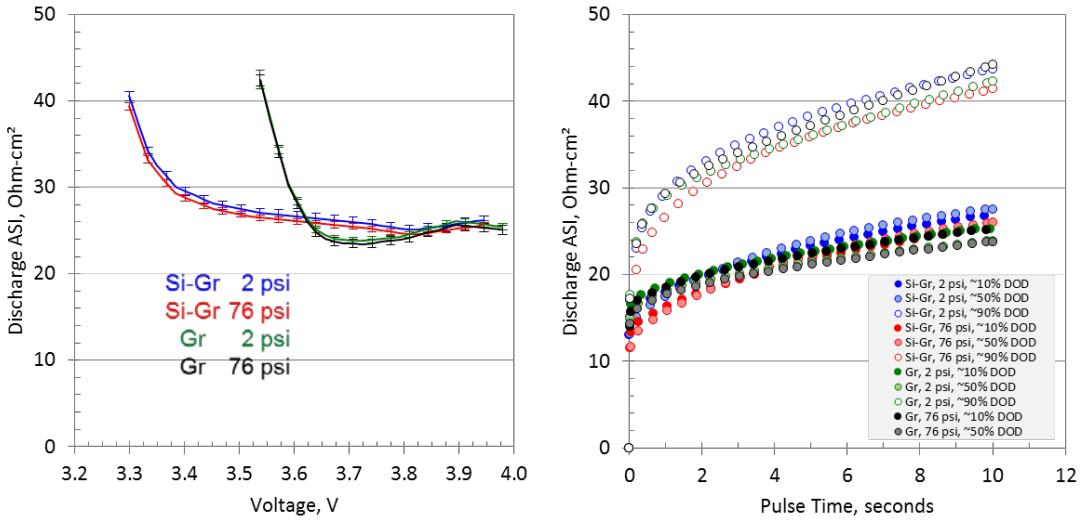


Figure II-421. Average initial discharge interpolated ASI as a function of open circuit voltage (left) and individual ASI discharge pulse voltages at 10, 50, and 90 % depth of discharge (right) as a function of pulse time for Si-Gr//NMC532 pouch cells at 2 psi per cell (blue), 76 psi per cell (red), and Gr//NMC532 pouch cells at 2 psi per cell (green), 76 psi per cell (black) from initial HPPC testing at 30 °C. The error bars represent 2σ standard deviation.

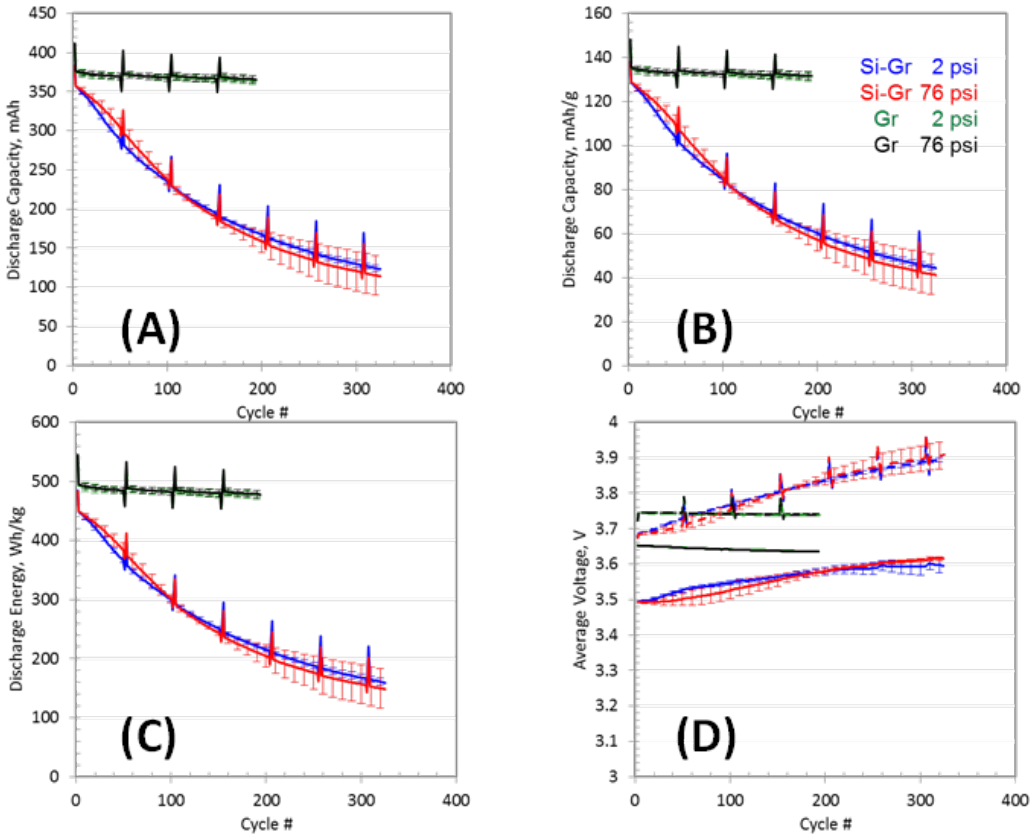


Figure II-422. Average cycle life plots showing discharge capacity (a), specific discharge capacity (b), specific discharge energy (c) and average voltage (d) performance (solid line = discharge, dashed line = charge) for Si-Gr//NMC532 pouch cells at 2 psi per cell (blue), 76 psi per cell (red), and Gr//NMC532 pouch cells at 2 psi per cell (green), 76 psi per cell (black). The error bars represent 2σ standard deviation.

The continual theme in our stack pressure study evaluation of formation, rate characterization, HPPC impedance, and cycling life testing suggests there are minimal differences in electrochemical performance between 2 psi and 76 psi per cell for either of the cell-build chemistry systems. The results imply that using linear physical extreme stack pressure does not improve electrochemical performance for electrodes that contain silicon. Potential further studies may include post-mortem analytical analysis of the disassembled pouch cells to see if there are obvious differences in electrode appearance that the high pressure influenced on the relentless silicon expansion and contraction.

*Deliverable: Fabricate Pouch Cells with at Least 1 Ah Capacity Based on Latest Improvements to Composite Negative Electrode Developed in CAMP and High-Nickel NMC Positive Electrode*

In FY17, the CAMP Facility acquired the ability to wind z-fold pouch cells in both the xx3450 and xx6395 formats with state-of-the-art equipment from MEDIA TECH Co., Ltd. The term xx3450 refers to the nominal pouch cell dimensions of a 34 mm width, 50 mm length, and varying "xx" thickness based on the number of layers in the pouch stack. The xx3450 has been a dependable format for the CAMP Facility that is well suited when limited quantities of novel active materials are provided. However, while the xx3450 format demonstrates a large capacity increase over a coin cell, the dimensions limit the capacity range to ~0.5 to 1.0 Ah. In addition, the original CAMP Facility winding equipment used an older method of winding the cell starting at the center and building outward. Z-fold winding is today's current industry standard method for stacked pouch cell assembly. Depending on the requirements for a project, capacities on the order of 2 Ah could be needed. 18650 cells reach this capacity range, however, they have their limitations that could be critical for evaluating R&D materials (such as easily identifying gassing issues, controllable stack pressure, high impedance without additional tabbing, etc.). Thus, having xx6395 formats enables us to achieve larger capacities while still having the inherent advantages of being a pouch cell (Figure II-423).

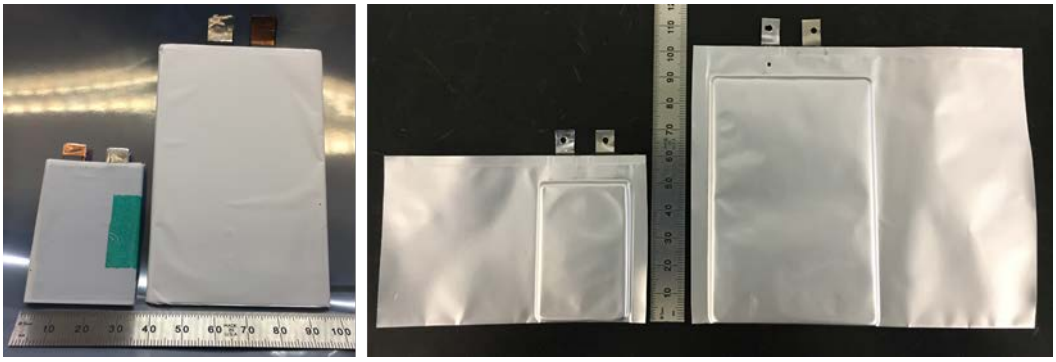

Figure II-423. Images of xx3450 and xx6395 partially assembled before pouching (left), and before electrolyte filling (right).

To demonstrate the xx6395 pouch cell format, we decided to evaluate the cells against xx3450 pouch cells using the same z-fold winding equipment, electrode couples, electrolyte, separator, width of tabbing/welding, and number of layers inside the cell. Our aim was to create two sets of cells with the only difference being the planar electrode dimensions and evaluate the formation, rate capability, impedance (HPPC), and cycle life performance between the two builds.

Electrode properties are provided in Figure II-424. The materials used for this study are frequently used at the CAMP Facility and were thus chosen to evaluate the impact of cell geometry without compounded complexities that novel chemistries may introduce. The electrode slurries were prepared via traditional NMP methods with each of their specific stepwise mixing processes to achieve the desired dispersion and rheological properties for high quality coatings. With the exception of slurry preparation, all processing steps took place in the CAMP Facility dry room. Single and double side cathode electrodes were made to enable multilayer pouch cell stacking. The coating loadings targeted were based on each of the active materials half-

cell 1st cycle performance, reversible C/10 rate, and reversible 1C rate. The n:p ratio for these graphite//NMC532 cells is calculated to be 1.13-1.25 for a full-cell cycling window of 3.0 to 4.1 V.

| Anode: **Graphite** | Cathode: **NMC532** |
|---|---|
| 91.83 wt% Hitachi MagE | 90 wt% Toda NMC532 |
| 2 wt% Timcal C45 | 5 wt% Timcal C45 |
| 6 wt% Kureha 9300 PVDF | 5 wt% Solvay 5130 PVDF |
| 0.17 wt% oxalic acid | |
| *Matched for 4.1V full cell cycling* | *Matched for 4.1V full cell cycling* |
| Cu Foil Thickness: 10 µm | Al Foil Thickness: 20 µm |
| Total DS Electrode Thickness: 162 µm | Total DS Electrode Thickness: 176 µm |
| SS Coating Thickness: 76 µm | SS Coating Thickness: 78 µm |
| Porosity: 31.2 % | Porosity: 33.4 % |
| Total Coating Loading: 11.33 mg/cm² | Total Coating Loading: 21.10 mg/cm² |
| Total Coating Density: 1.49 g/cm³ | Total Coating Density: 2.71 g/cm³ |
| Estimated Capacity: 3.50 mAh/cm² (0.000 to 1.5V vs. Li metal, C/10) | Estimated Capacity: 2.98 mAh/cm² (3.0 to 4.2V vs. Li metal, C/10) |

Figure II-424. Electrode design for xx6395 and xx3450 graphite//NMC532 pouch cells. “SS” = single side, “DS” = double side. All electrodes were fabricated at the CAMP Facility.

Following the electrode fabrication, the electrodes were calendered to their respective calculated porosities in Figure II-424. The electrodes were cut into sheets and stamped to xx3450 and xx6395 pouch cell dimensions using steel rule dies and cleaned to remove any loose coating along the edges and tabbing area. The xx3450 stamped cathode and anode dimensions are 31.3 mm by 45.0 mm and 32.4 mm by 46.0 mm, respectively. The xx6395 stamped cathode and anode dimensions are 55.5 mm by 83.5 mm and 57.45 by 85.45 mm, respectively. The xx3450 and xx6395 anodes are dimensionally larger than the cathodes by 5.8 % and 6.0 %, respectively. Area normalization of proceeding data referred to in this section is based on the total cathode area in a cell. Each xx3450 cell has a total cathode area of 169.2 cm². Each xx6395 cell has a total cathode area of 555.6 cm². The punched electrodes were then wound with Celgard 2325 PP/PE/PP separator using the z-fold winder to 13 total layers per cell (6 double-sided anode, 5 double-sided cathode, and 2 single-sided cathode for the outside layers). The xx3450 cells were wound using 48 mm wide separator. The xx6395 cells were wound using 90 mm wide separator.

After the cells completed assembly, they were vacuumed dried and filled with electrolyte. The xx3450 and xx6395 cells were filled with 3.11 mL and 10.20 mL, respectively, of 1.2 M $LiPF_6$ in EC:EMC 3:7 wt.% “Gen2” (Tomiyama) electrolyte and vacuum sealed. The electrolyte volume to available pore volume factor for each cell-build were calculated to be 2.77 for all the cells. The cells were then placed in stainless steel fixtures for electrochemical testing. For all cells, 2 psi was chosen to be the stack pressure per pouch cell. Four cells were put on test for each of the cell sizes, for a total of eight cells, and are referred to as xx6395 and xx3450 in the plots below. Weight normalization of the data within this section is based on the total active material weight in the cathode (namely NMC532). The xx3450 cells each contain 3.213 grams of NMC532, and each xx6395 cell contained 10.551 grams of NMC532.

The xx6395 and xx3450 cells underwent identical formation, rate characterization, impedance (HPPC), and cycle life testing with appropriately scaled current values with respect to the capacity of the cell-builds. All of the cells underwent an initial tap charge limited to 1.5 V, held there for 15 minutes, and then left open circuit for 24 hours to allow for electrolyte wetting of the electrode. They were then cycled between 3.0 to 4.1 V at a C/10 rate for 3 cycles, followed by 3 cycles at a C/3 rate, and finally left in an open circuit to observe any voltage changes that could indicate soft shorting. The formation protocol listed above is a typical process used by the CAMP Facility. Initial results suggest that no added modifications to the formation protocol would likely be needed for the xx6395 cells as the current protocol over estimates the time and break-in features needed for proper electrode wetting for these size cells.

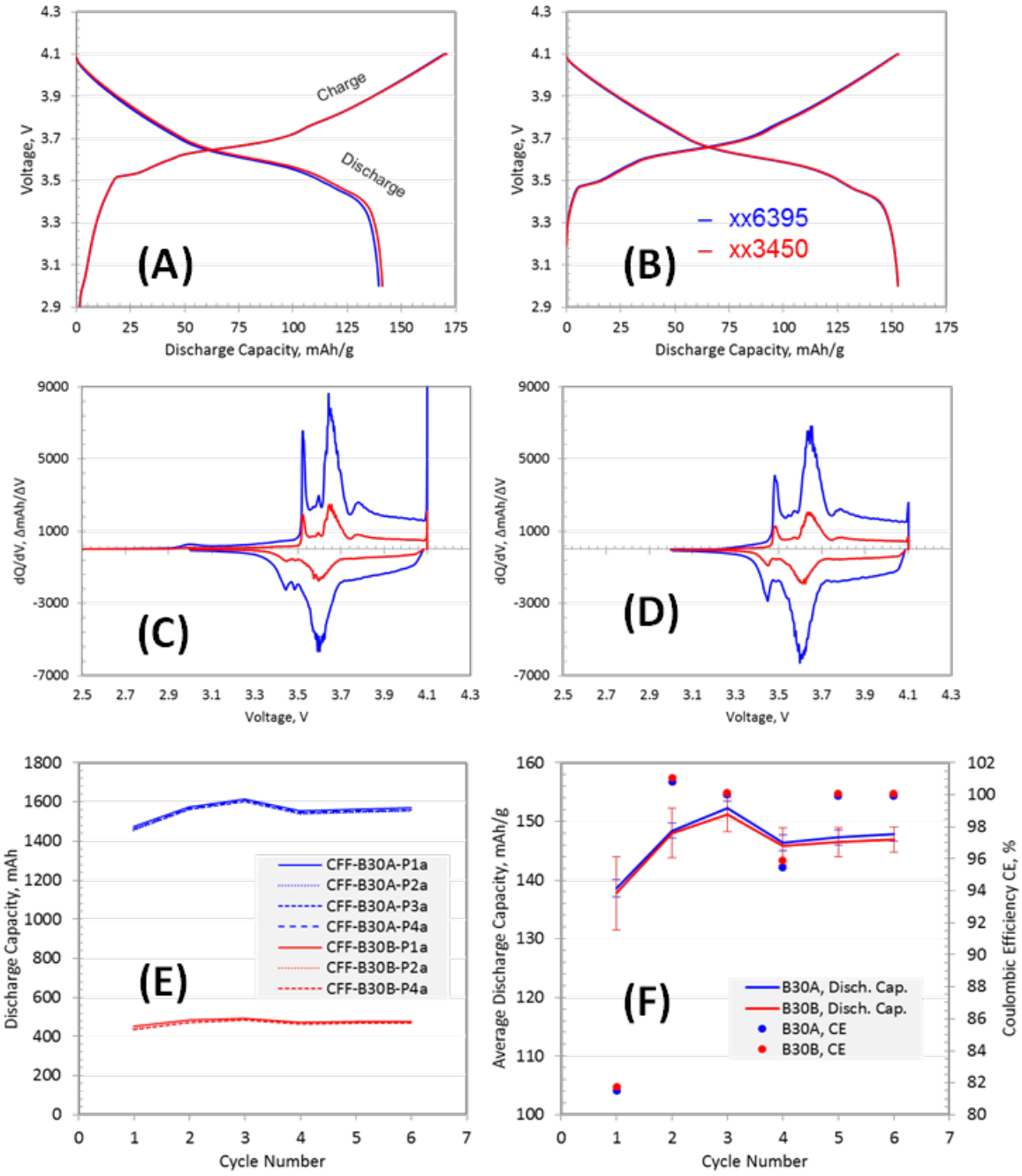


Figure II-425. Representative individual cycle voltage (a,b) and dQ/dV (c,d) profiles of graphite//NMC532 xx6395 (blue) and xx3450 (red) pouch cells of the 1st (a,c) and 3rd (b,d) cycles during formation. Individual formation discharge capacity performance (e). Average discharge specific capacity and coulombic efficiency performance (f). The cells were cycled between 3.0 and 4.1 V at 30 °C. The error bars represent 2σ standard deviation.

The 1st and 3rd cycles for the xx6395 and xx3450 cell-builds, seen here in Figure II-425a-b, show very similar individual charge and discharge voltage profiles. The corresponding similar capacities seen in Figure II-425, demonstrate that the different cell geometries are performing similar to one another. The cell capacity in mAh is shown in Figure II-425e, which highlights the size differences.

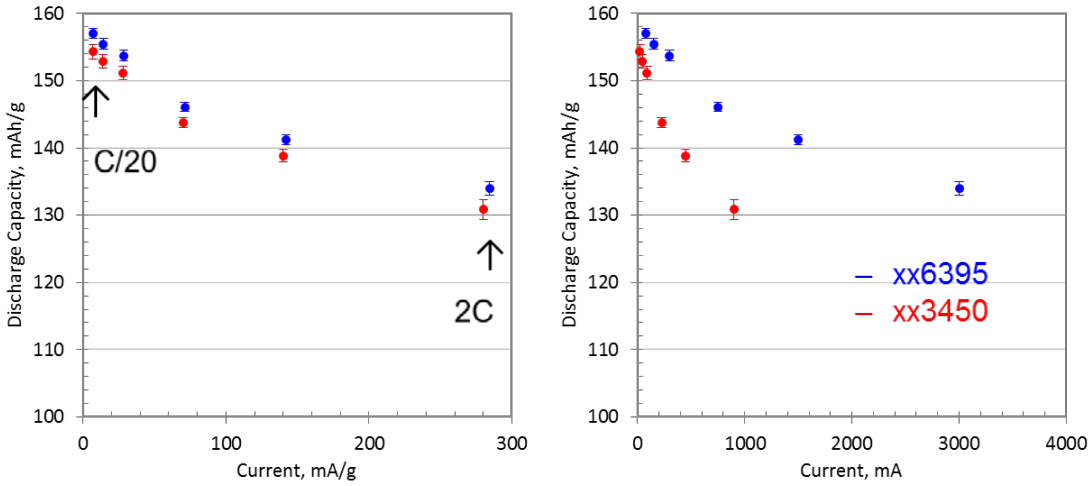


Figure II-426. Average rate study performance of graphite//NMC532 xx6395 (blue) and xx3450 (red) with specific discharge capacities as a function of current, mA/g (left) and mA (right). The cells were cycled at 30°C between 3.0 and 4.1 V. The plots show the discharge performance from the 2nd cycle at C/20 and 3rd cycle at C/10, C/5, C/2, 1C, and 2C rates. The error bars represent 2σ standard deviation.

The rate study consisted of the following conditions: 2 cycles at C/20, 3 cycles at C/10, 3 cycles at C/5, 3 cycles at C/3 charge and C/2 discharge, 3 cycles at C/3 charge and 1C discharge, and 3 cycles at C/3 charge and 2C discharge. The rate performance of the two cell sizes is shown in Figure II-426. In the rate study, the xx3450 cells have consistently slightly lower capacities (2 or 3 mAh/g) than the xx6395 cells. These encouraging results suggest that the rate performance, even up to 2C discharge, is very similar between the xx6395 and xx3450 cell formats.

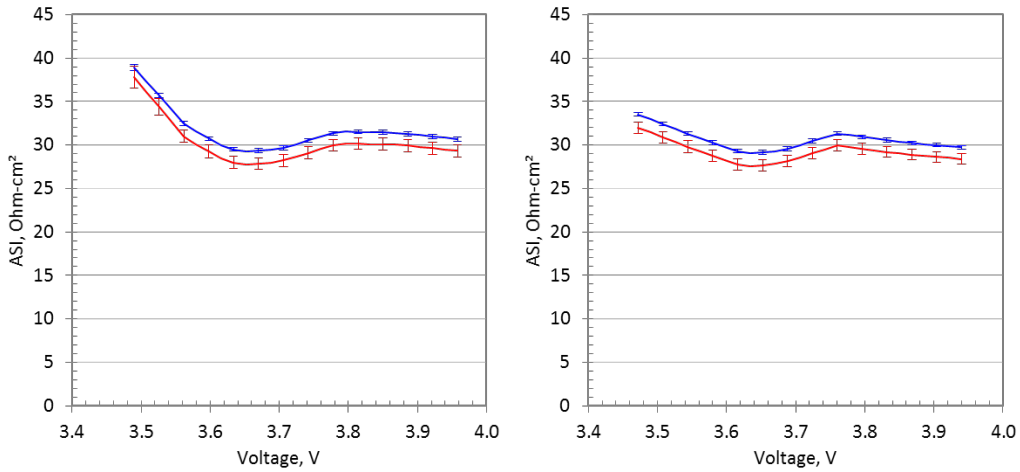


Figure II-427. Average interpolated discharge (left) and charge (right) ASI performance for graphite//NMC532 xx6395 (blue) and xx3450 (red) from initial HPPC testing at 30°C. The error bars represent 2σ standard deviation.

The HPPC protocol was performed by charging the cells to 4.1 V, then discharging in 10% capacity increments while collecting voltage information during pulsing at each 10% DOD. The discharge pulses were 10 seconds at 3C (4.5 A, 426.5 mA/g, 8.1 mA/cm² for xx6395 and 1.35 A, 420.2 mA/g, 8.0 mA/cm² for xx3450) and charge pulse were 10 seconds at 2.25C (3.375 A, 319.9 mA/g, 6.1 mA/cm² for xx6395 and 1.0125 A, 315.1 mA/g, 6.0 mA/cm² for xx3450). The HPPC protocol was modified to use 3C discharge and 2.25C charge pulses due to the 5 A per channel limit of the MACCOR Series 4000 Test System. The ASI curves follow a similar trend to one another (Figure II-427), with slightly lower values obtained from the

xx3450 cells. This result further demonstrates that the xx6395 and xx3450 cells are similar in terms of capacity and impedance over the initial 150 cycles tested so far.

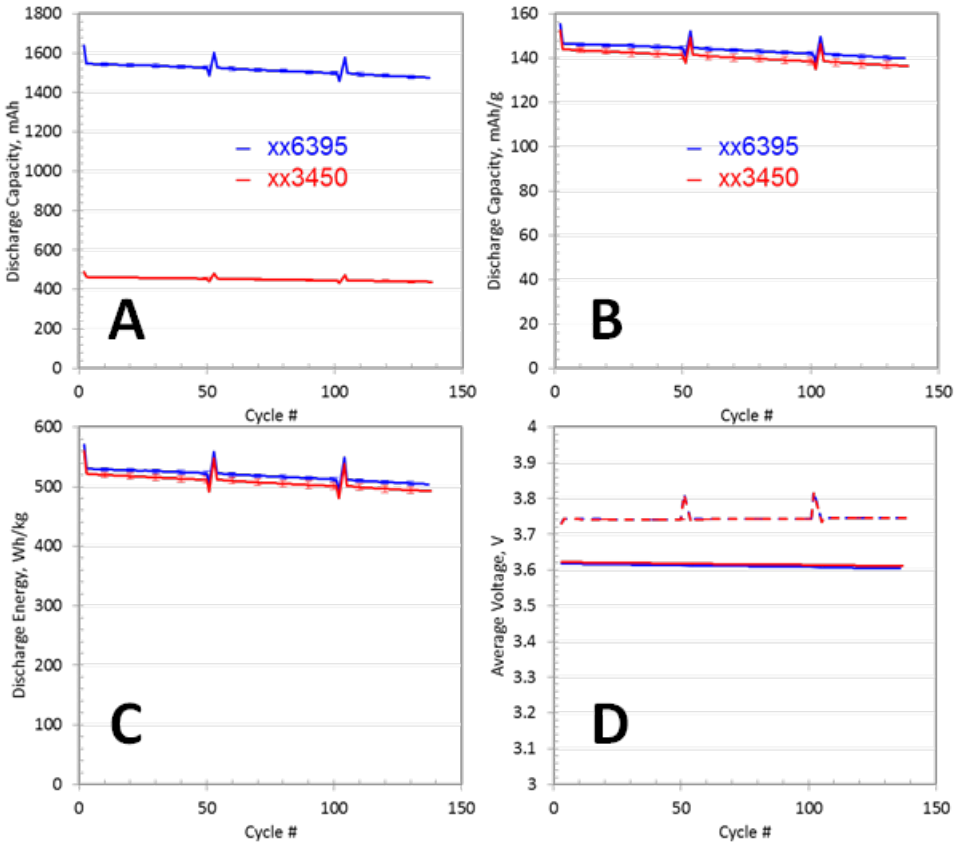


Figure II-428. Average cycle life plots showing discharge capacity (a), specific discharge capacity (b), specific discharge energy (c) and average voltage (d) performance (solid line = discharge, dashed line = charge) graphite//NMC532 xx6395 (blue) and xx3450 (red) from cycle life testing. The error bars represent 2σ standard deviation.

Figure II-428 shows the cycle life performance of these cells, which consists of a repeating loop: a slow rate cycle (C/20), HPPC, then cycling 48 cycles with C/3 charging (C/5 trickle charge) and C/2 discharging testing at 30°C. The xx3450 and xx6395 cells perform consistent to previous graphite//NMC532 cell-builds with relatively stable capacity during cycling in the 3.0 to 4.1 V window. The size difference of these cells does not appear to change the specific capacities, capacity retention, and average operating voltages.

Thus far our evaluation of the formation, rate characterization, HPPC impedance, and initial 100 life cycles suggests there are minimal differences in electrochemical performance between our xx6395 and xx3450 pouch cells under the tested conditions. The performance similarities between the xx6395 and xx3450 also gives us an even higher degree of confidence that our xx3450 (~0.5 Ah) format offers high quality and relevant results when only small amounts of novel material quantities are provided to the CAMP Facility for cell-building, which would otherwise inhibit the fabrication of xx6395 (~2 Ah) cells.

*Deliverable: Summary of Electrode Library Activities*

Table II-19 shows the distribution of electrodes from the Electrode Library, which is maintained by the CAMP Facility. In FY17, 1548 sheets of electrode were fabricated and distributed by the CAMP Facility, which is 38 square meters of electrodes. Many of these electrode were supplied by the CAMP Facility in support of DOE's High-Energy High-Voltage Program as well as the Next Generation Anodes Program, among others. Since these programs are consortiums of the various national laboratories, the CAMP Facility is supplying all of the

baseline electrodes for these DOE programs. In addition to the electrodes, the CAMP Facility has distributed 16 kg of active materials, carbon additives, binders, and electrolytes.

Table II-19: Summary of Electrode Library distributions

| Electrodes Delivered | FY14 | | FY15 | | FY16 | | FY17 | |
|---|---|---|---|---|---|---|---|---|
| Argonne | 116 | 13 % | 206 | 12 % | 174 | 8 % | 142 | 9 % |
| Other National Labs | 213 | 24 % | 373 | 22 % | 726 | 36 % | 172 | 11 % |
| Universities | 119 | 14 % | 83 | 5 % | 117 | 6 % | 151 | 10 % |
| Industry | 423 | 49 % | 1028 | 61 % | 1004 | 50 % | 1083 | 70 % |
| **Total:** | **871** | | **1690** | | **2021** | | **1548** | |

*Examining Effect of Moisture on Performance of Lithium-Containing Layered Oxide Electrodes*

In recent years there has been a shift to processing of electrodes using aqueous slurries containing water-based polymer binders. The technological drivers that necessitate reliance on aqueous processing include the use of electrophoretic methods and the application of protective coatings, which frequently involve using aqueous solutions or water vapor as a reagent during atomic layer deposition. All these methods expose the layered oxides to gaseous and/or liquid water, which can potentially have adverse effects on cell operation. We have studied the electrochemical performance of cells exposed to moist air (100% humidity) at 30 °C, for time periods of up to two months. These data were complemented by results from X-ray diffraction, X-ray photoelectron spectroscopy, and electron microscopy measurements to examine the relationships between oxide structure changes and electrochemical performance.

The effects of moisture were studied on CAMP-made electrodes containing 90 wt.% NMC532 oxide, 5 wt.% Timcal C45 carbon black and 5 wt.% PVdF binder on a 20 μm thick aluminum foil. Electrochemical performance data were collected on these electrodes in 2032-type coin cells using Li foil as the counter electrode and in an electrolyte solution with 1.2 M $LiPF_6$ in a 3:7 w/w EC:EMC mixture. In Figure II-429a we compare the first cycle capacity-voltage profiles, from half cells assembled using the pristine electrode and two humid-air exposed electrodes, obtained on cycling with a ~11 mA/g (~C/18) current between 3.0 and 4.5 V at 30°C. The pristine electrode shows the expected cycling behavior, displaying charge and discharge capacities of 219 mAh/$g_{oxide}$ and 198 mAh/$g_{oxide}$, respectively. Cells with the humid-air exposed electrodes show behaviors that are distinctly different from that of the pristine electrode cell. The charge and discharge capacities are 191 mAh/$g_{oxide}$ and 166 mAh/$g_{oxide}$ respectively, for the 1-month exposure electrode and 179 mAh/$g_{oxide}$ and 155 mAh/$g_{oxide}$ respectively, for the 2-month exposure electrode. The voltage profiles of both electrodes indicate the effects of moisture exposure; the higher charge voltages, suggest the presence of species at the oxide particle surfaces that impedes the motion of $Li^+$ ions. The lower charge capacities, and the uneven rise in voltage on further removal of $Li^+$ ions, indicate changes within the oxide bulk. An example of these changes is shown in Figure II-429b, which is a scanning transmission electron microscopy (STEM) image of the two-month exposure electrode. The thin amorphous coating observed on the particle surface is either $Li_2CO_3$ (or $LiHCO_3$), which was suggested by the X-ray photoelectron spectroscopy (XPS) data. Crystal structure changes are observed at the particle surface, which indicates the presence of a new phase that extends from 5-20 nm into the oxide bulk. From an analysis of high-resolution synchrotron X-ray diffraction data we concluded that this new cubic phase has a rock salt structure in which some of the transition metal (TM) ions are substituted by lighter ions such as protons and/or TM vacancies, which will both contract the unit cell.

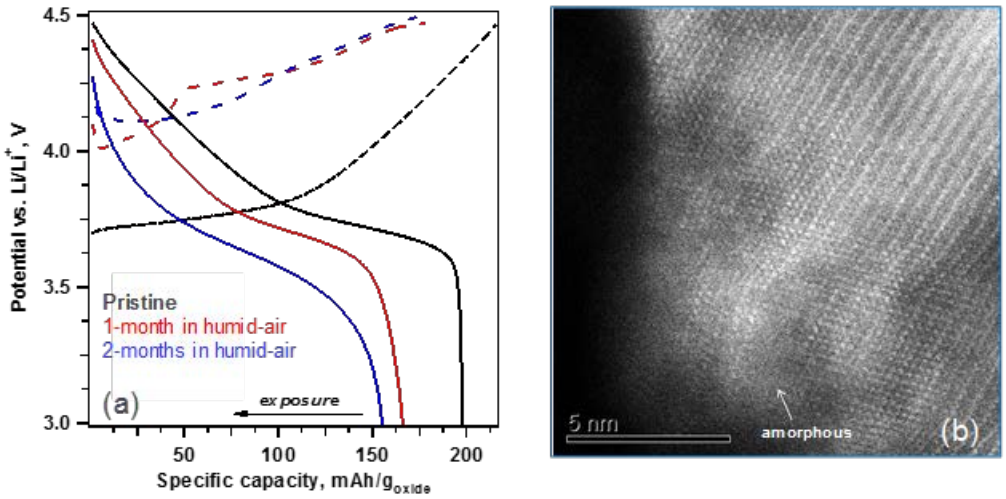


Figure II-429. Effects of moisture exposure on (a) electrochemical performance and (b) oxide structure, imaged by scanning transmission electron microscopy (high angle annular diffraction mode).

*Separator Study*

A variety of commercial separator products are available that are designed with unique safety functions. This study explores the impact separator choice can have on cell performance at the higher voltages and rates sought by the HEHV program and battery developers. For high voltage, high energy density battery systems, the goal is to have a separator that is thin, flexible, highly porous, thermodynamically stable, temperature resistant, mechanically strong, and inexpensive. Each material currently on the market has some but not all of these properties. Polyethylene (PE) is inexpensive, but has a lower melting point, and may have trouble withstanding higher voltages. Polypropylene (PP) has a slightly higher melting point, is mechanically strong, and is also fairly inexpensive. When PP is paired with PE to make a trilayer microporous membrane, PP:PE:PP, the separator has a more robust exterior, while the interior has the ability to melt before thermal runaway occurs. However, with a little extra heat, the PP will also melt and the electrodes will touch. Since, the PP isn't fully protective, another avenue had been approached - ceramic and polyolefin combinations have been created to provide that extra thermodynamic stability. Ceramics can withstand high voltages and temperature, and can be chemically inert and porous - but they are more difficult to incorporate into a thin flexible separator.

For initial testing, nine different separators from five different suppliers were chosen and tested in NMC532 half-cells: 3 monolayer polyolefins at various thicknesses (16, 20, 25µm), 3 trilayer PP:PE:PP at various thicknesses (16, 20, 25µm), one single-sided ceramic-coated polypropylene, one double-sided ceramic-coated polyethylene, and one $Al_2O_3$ embedded into a nonwoven polyethylene terephthalate (PET). (See Table II-20.)

In preparation for the half cell-builds, all the separators were punched with a 5/8" diameter punch and dried at 60°C. Eight cells per separator configuration were assembled using a 1.54 $cm^2$ NMC532 electrode disk (90 wt.% active material, 5 wt.% Timcal C45, 5 wt.% Solvay 5130 PVDF binder) from the CAMP Electrode Library with a 11.32 $mg/cm^2$ loading, which was paired against a 1.91 $cm^2$ Li metal electrode disk. Each cell was flooded with 9 drops of 1.2 M $LiPF_6$ in EC:EMC (3:7 wt.%) during assembly. After which, each cell went through a Formation and a Rate testing protocol. Formation consisted of 3 cycles with a C/10 charge and discharge. The Rate Study started with 2 cycles of C/20 charge and discharge and with 3 cycles of C/10 charge and discharge. It then continued with 12 C/5 charges, where every three cycles had the discharge rate increasing (C/5 to C/2 to 1C to 2C). Each separator configuration had four cells tested at a 3.0-4.3 V window to see its standard performance, and had four cells tested at a 3.0-4.7 V window to see how it performs in a high voltage window.

Table II-20: Commercial separators used in this study

| Separator Supplier | ID Name | Total Thickness (µm) | Separator Material | Porosity (%) | Air Permeability (Gurley) |
|---|---|---|---|---|---|
| | | | Microporous Membrane Category | | |
| IV | 20µm_UHMW PE | 20 | UHMW PE (Microporous Monolayer Membrane) | 83 | 1.4 s/50mL |
| II | 16µm_PP | 16 | PP (Microporous Monolayer Membrane) | 50 | 125 s/100cc |
| I | 25µm_PP | 25 | PP (Microporous Monolayer Membrane) | 41 | 620 (s) JIS |
| I | 16µm_PP:PE:PP | 16 | PP/PE/PP (Microporous Trilayer Membrane) | 44 | 250 (s) JIS |
| I | 20µm_PP:PE:PP | 20 | PP/PE/PP (Microporous Trilayer Membrane) | 45 | 320 (s) JIS |
| I | 25µm_PP:PE:PP | 25 | PP/PE/PP (Microporous Trilayer Membrane) | 39 | 620 (s) JIS |
| | | | Ceramic Category | | |
| II | 3µm_SS_Ceramic_on_16µm_PP | 19 | Single Side Ceramic Coated on 16µm PP | 51 | 145 s/100cc |
| III | 4µm_DS_Al2O3_on_12µm_PE | 16 | Double Sided $Al_2O_3$ Coating on 12µm PE | 40 | unknown |
| V | 28µm_Al2O3 Embedded in PET | 28 | $Al_2O_3$ Embedded in PET - Non woven | 46 | 22 s |

When discussing single-sided ceramic-coated separators, the question arises as to which electrode the ceramic side should be facing: anode or cathode? In pursuit of this question, the single-sided separator with 4-µm thick ceramic-coating on 16-µm thick PP was tested where 8 cells had the ceramic side facing the anode and 8 cells had the ceramic facing the cathode. These cells were also tested in the 3-4.3 V and 3-4.7 V windows.

After the initial 3-4.3 V formation cycles, one separator stood out against all the rest. All four cells with the $Al_2O_3$ embedded in PET (non-woven) separator failed their formation cycles. This was surprising, since this separator was used previously in full cells without a problem. It was decided to retry this separator in half cells, but to increase the drying temperature to 150°C. Eight more cells were assembled, 4 cells tested with the 3-4.3 V window, and 4 cells tested at the 3-4.7 V. All eight of these new cells also failed their formation tests. This suggests that this separator system could not withstand the reductive potential of lithium metal. No further testing was done with this separator system (it is not shown in the summary graph below).

The rate performance study of the remaining (non-PET) half cells indicated there was no significant statistical difference in 3-4.3 V window for any of the separators regardless of the discharge rate (up to 2C). Advancing on to the 3.0-4.7 V rate study, some of the separators began to show differences in performance. In particular, for the 3.0-4.7 V high voltage tests, the NMC532 half-cells using the Ultra High Molecular Weight Polyethylene (UHMW PE) separator underwent a sudden and significant loss of capacity at the discharge rate of C/5. This suggests that UHMW PE separators may suffer from eventual oxidation at higher potentials. The three trilayer PP:PE:PP and the two monolayer PP separator cells, on the other hand, showed no significant differences in the 3.0-4.7 V rate study.

Aside from the $Al_2O_3$ embedded in PET separator and the UHMW PE separator, there was no significant difference in the formation and rate performance of the remaining separators (see Figure II-430). This result is regardless of separator thickness, trilayer vs. monolayer PP, ceramic coating, and orientation of the ceramic coating. This is also true for the double-sided ceramic-coated monolayer PE separators. Full cells will be tested in FY18 using the aggressive HEHV testing protocol to see if there might be any further problem areas when using certain separators. It is anticipated that the performance of some of the various separators will differentiate from each other based on cycle life and HPPC ASI.

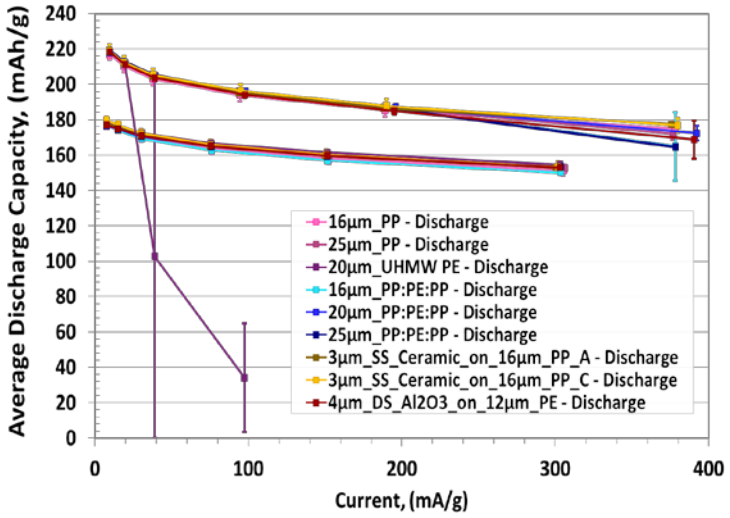


Figure II-430. Summary of the rate capabilities for the separators in this study in the 3.0-4.3 V and 3.0-4.7 V voltage windows. The data for the $Al_2O_3$ embedded in PET separator were omitted in this plot.

*High Voltage Evaluation of Industrially Applied ALD of $Al_2O_3$ Coating on NMC532 Powder*

The CAMP Facility was tasked with providing an evaluation of $Al_2O_3$ coated onto NMC532 powders via Atomic Layer Deposition (ALD). We partnered with Forge Nano (Louisville, CO), who provided ANL with four samples of $Al_2O_3$ ALD coated on Toda NMC532. These samples were: Pristine, Sample A (2 ALD cycles), Sample B (4 ALD cycles) and Sample C (8 ALD cycles). Electrodes were made of each powder with a 90 wt.% active material (NMC532), 5 wt.% Timcal C45 carbon black, and 5 wt.% Solvay 5130 PVDF binder composition with a target total electrode loading of 10.9 mg/cm$^2$. In this testing, we focused on the 3-4.5 V (half-cell) and 3-4.4 V (full-cell) performance.

Half-cells (vs. Li metal) were assembled using the above electrodes and tested in the 3-4.5 V window via a Formation Protocol and Rate Study Protocol. The formation protocol consists of three cycles at a C/10 rate. Four coin cells were made from each electrode, which used a 14 mm diameter cathode electrode and a 15.6 mm diameter lithium metal disk. The separator used in the coin cells was Celgard 2325 and the electrolyte used was 1.2 M $LiPF_6$ in EC:EMC (3:7 wt.%). From the half cell data, we were able to design new cathode electrodes that would match to a graphite anode (A-A002A - Phillips 66 CPG-A12 graphite) that was in the Electrode Library. The new cathodes that were produced also had the 90/5/5 composition and their loadings were as follows; Pristine = 8.98 mg/cm$^2$, Sample A = 9.26 mg/cm$^2$, Sample B = 9.15 mg/cm$^2$, and Sample C = 9.17 mg/cm$^2$. Each of these electrodes were matched to the selected anode (A-A002A) resulting in an n:p ratio of ~1.1-1.2. Four CR2032 full-cell coin-cells were made with each of the above electrodes, and a total of 25 microliters of 1.2 M $LiPF_6$ in EC:EMC (3:7 wt.%) electrolyte was used for each cell. These full-cell coin-cells went through Formation, Rate Study, HPPC, and Cycle Life Testing.

There was little change in the first charge capacity between all the coated samples and the pristine material. Following the Formation and Rate Study testing, Cycle Life testing was performed. Literature [1] has suggested that coatings of $Al_2O_3$ can improve cycle life and rate performance of cells at various voltages. Two sets of coin cells were used to evaluate two slightly different cycle life conditions: Set 1 of cells went through the following Cycle Life Protocol: 1 cycle at C/20, 47 cycles at C/3 charge and C/3 discharge, and HPPC with 3C discharge and 2.25C charge; this was looped 10 times to give approximately 500 cycles on the cells. Set 2 of cells went through the following Cycle Life Protocol: 1 cycle at C/20, 47 cycles at C/3 charge and 1C discharge, and HPPC with 3C discharge and 2.25C charge; this was looped 10 times to give approximately 500 cycles on the cells. By doing this testing we were looking to see if the ALD coatings would have any performance improvements under typical cycling conditions (C/3) at high voltage as well at higher current

discharge rates (1C) at high voltages. Since similar conclusions were reached with both sets, only Set 1 results will be discussed below.

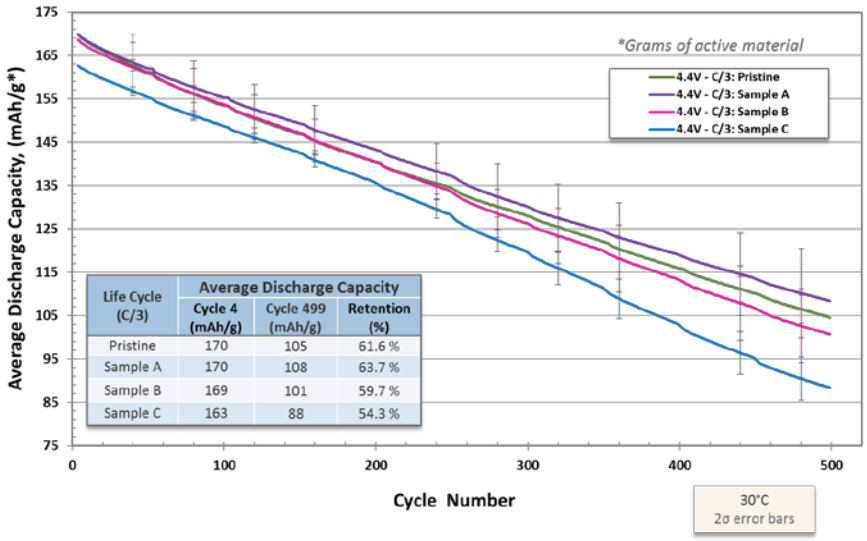


| Life Cycle (C/3) | Average Discharge Capacity | | |
|---|---|---|---|
| | Cycle 4 (mAh/g) | Cycle 499 (mAh/g) | Retention (%) |
| Pristine | 170 | 105 | 61.6 % |
| Sample A | 170 | 108 | 63.7 % |
| Sample B | 169 | 101 | 59.7 % |
| Sample C | 163 | 88 | 54.3 % |

Figure II-431. Cycle life plot of Set 1 full-cell coin-cells – C/3 Charge and C/3 Discharge cycling.

As seen in Figure II-431, the Pristine, Sample A, and Sample B full cells all started with approximately the same capacity. Sample C full cells, in both cases, started at a lower capacity. The C/3 cycling data (Set 1) suggest that there was minimal statistical difference in the performance of the Pristine, Sample A and Sample B cells. They all ended at 500 cycles with a capacity retention around 61 % capacity and were within the error bars of each other. Sample C did show worse cycling performance than the other samples and was outside the error bars of the other cells. To further analyze these cells during the cycle life testing, we have charted the HPPC data as a function of the Depth of Discharge to monitor the change in impedance (ASI) as the cells age.

Figure II-432 summarizes the HPPC data that was collected every 50 cycles during the cycle life testing for the Set 1 C/3 cycling cells. The starting ASI for the Pristine material was around 25 ohm-cm$^2$, while the ALD coated samples had slightly higher initial ASI of around 35 ohm-cm$^2$. Sample A cells had the lowest ASI rise, going from ~35 to 55 ohm-cm$^2$. The Pristine cells had the next lowest rise; Sample B and Sample C had the highest rise of these samples. This impedance rise correlates with the capacity fade for Sample C cells. We postulate that the $Al_2O_3$ coating on the NMC532 particles reached a thickness that inhibited efficient lithium ion transport and/or decreased the electrical conductivity of the particle.

Future investigations may include analyzing the coated materials and cycled cells under spectroscopic, as well as other analytical techniques to better understand these observations. We may additionally repeat this study with NMC622 and NMC811 materials to probe the electrochemistry of ALD coated samples. Literature [1] has shown that these higher nickel content materials are more influenced by coatings then the NMC532.

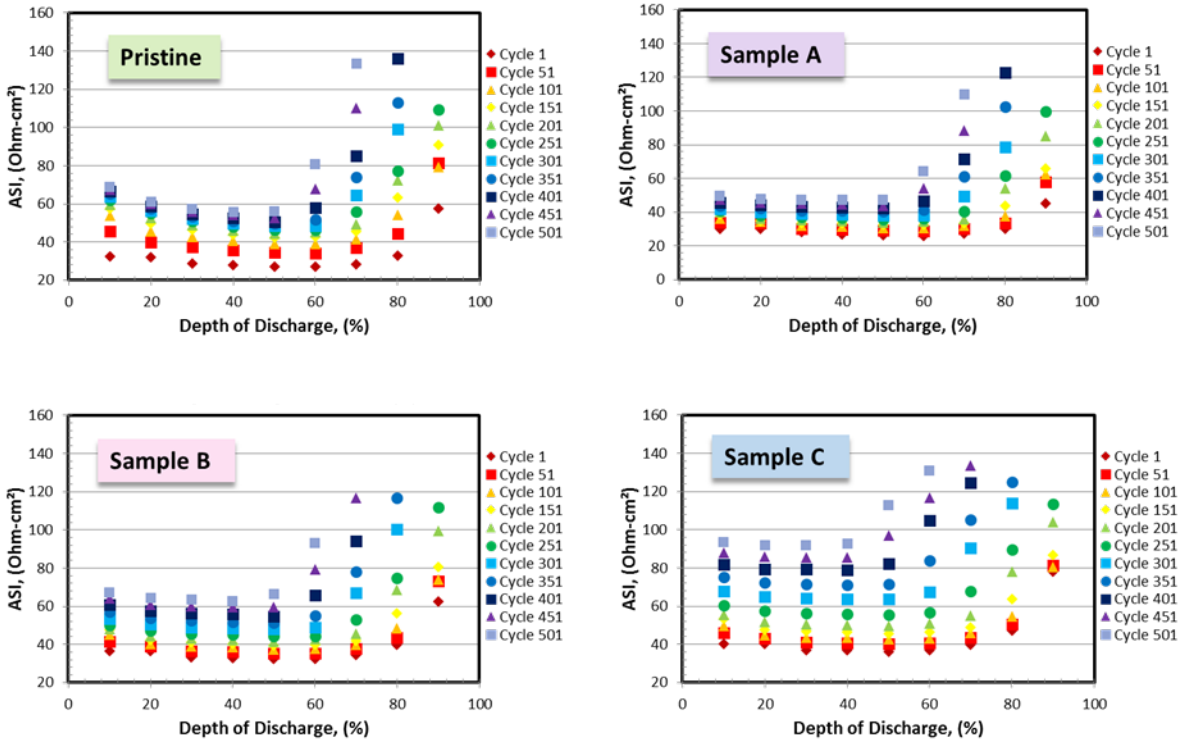


Figure II-432. Full cell HPPC ASI (averaged discharge) data for full cells of graphite vs. Pristine, Sample A, Sample B, and Sample C in Set 1 (C/3 C: C/3 D).

## Conclusions

The CAMP Facility has had another very productive year in the R&D of advanced lithium-ion electrochemical energy storage systems. We were also critical to the support of other numerous DOE-EERE programs, much of which was performed through the CAMP Facility's Electrode Library. A summary of some of the key successes in FY17 are as follows:

- The influence of stack pressure on silicon-graphite//NMC532 and baseline graphite//NMC532 pouch cells was determined to not be a significant factor. It was previously hoped that the extra high pressure (~76 psi) would help minimize the damage to the electrode structure caused by the excessive expansion of silicon during lithiation.

- We now have the capability to make multi-stack pouch cells in a Z-fold separator configuration with two cell sizes: xx3450 and xx6395. This enable the fabrication of cells with capacities from 20 mAh to over 2 Ah. A direct comparison of these two cell sizes determined that nearly identical results are obtained from either cell size.

- Single-sided negative electrode based on 30% silicon-graphite with ~ 2 mAh/cm² loading were developed as a FY17 baseline. Even higher loadings of silicon will be explored in FY18 with the idea to extend the cycle life of silicon systems by using shallower levels of lithiation. This should limit the drastic volume expansion of silicon, which occurs during full lithiation. In addition, a new source of domestic silicon powder was identified (Paraclete Energy), which is now the preferred silicon material going forward.

- We have shown that the lithiated layered NMC oxides undergo changes, when they are stored in humid air or exposed to moisture, that adversely affect their electrochemical performance. By using a combination of X-ray diffraction, electron microscopy, and X-ray photoelectron spectroscopy measurements we identified the chemical mechanisms which cause these changes. We suggest that the

proton – lithium exchange that occurs during the moisture exposure trigger these transformations. We show that such an exchange provides a simple, comprehensive rationale for our observations, which include contraction of the c-axis (unit cell) lattice parameter, rock salt phase formation in the subsurface regions, presence of amorphous surface films, and the partial recovery of oxide capacity during electrochemical relithiation. The detrimental effects of water exposure need to be mitigated before aqueous processing of the positive electrode can find widespread adoption during cell manufacturing.

- Techniques to enable for detection of lithium-plating during cell cycling after under development. The most promising advances are in the area of reference electrode cell measurements. X-ray techniques to detect lithium metal show promise and efforts are underway to improve resolution and accuracy of the measurements.

- $Al_2O_3$ ALD coatings on the NMC532 powder did not show any significant performance improvements over the pristine material when tested in the 3-4.4 V window. It was observed that the performance of this material is highly dependent on the ALD coating thickness. The trend suggests there is a negative performance impact as the thickness of $Al_2O_3$ layer approaches ~1nm.

- Preliminary study of commercial separators indicate that trial studies are warranted when developing new electrochemical systems with high reductive power (*e.g.*, lithium metal) or high oxidative power (*e.g.*, high voltage). Under normal conditions, many separators have nearly identical rate performance (up to 2C).

## Key Publications


1. S. Ahmed, I. Bloom, A.N. Jansen, T. Tanim, E.J. Dufek, A. Pesaran, A. Burnham, R.B. Carlson, F. Dias, K. Hardy, M. Keyser, C. Kreuzer, A. Markel, A. Meintz, C. Michelbacher, M. Mohanpurkar, P.A. Nelson, D.C. Robertson, D. Scoffield, M. Shirk, T. Stephens, R. Vijayagopal, and J. Zhang, "Enabling fast charging–A battery technology gap assessment", *J. Power Sources* **367** (2017) 250-262.

2. J.A. Gilbert, J. Bareno, T. Spila, S.E. Trask, D.J. Miller, B.J. Polzin A.N. Jansen, D.P. Abraham, "Cycling Behavior of NCM523/Graphite Lithium-Ion Cells in the 3-4.4 V Range: Diagnostic Studies of Full Cells and Harvested Electrodes", *J. Electrochem. Soc.* **164** (2017) A6054-A6065. [DOI: 10.1149/2.0081701jes]

3. I.A. Shkrob, J.A. Gilbert, P.J. Phillips, R. Klie, R.T. Haasch, J. Bareno, D.P. Abraham, "Chemical Weathering of Layered Ni-Rich Oxide Electrode Materials: Evidence for Cation Exchange", *J. Electrochem. Soc.* **164** (2017) A1489. [DOI: 10.1149/2.0861707jes]

4. N.R. Vadivel, S. Ha, M. He, D. Dees, S. Trask, B. Polzin, K.G. Gallagher, "On Leakage Current Measured at High Cell Voltages in Lithium Ion Batteries", *J. Electrochem. Soc.* **164** (2017) A508-A517. [DOI:10.1149/2.1341702jes]

5. J.A. Gilbert, I.A. Shkrob, D.P. Abraham, "Transition Metal Dissolution, Ion Migration, Electrocatalytic Reduction and Capacity Loss in Lithium-Ion Full Cells", *J. Electrochem. Soc.* **164** (2017) A389-399. [DOI: 10.1149/2.1111702jes]

6. J. Zheng, M.H. Engelhard, D. Mei, S. Jiao, B.J. Polzin, J. Zhang, W.Xu, "Electrolyte Additive Enabled Fast Charging and Stable Cycling Lithium Metal Batteries" *Nature Energy* **2** (2017) 17012, [DOI: 10.1038/nenergy.2017.12]

7. I.A. Shkrob, K.Z. Pupek, J.A. Gilbert, S.E. Trask, D.P. Abraham, "On the Chemical Stability of Lithium 2-Trifluoromethyl-4,5- Dicyanoimidazolide (LiTDI), an Electrolyte Salt for Li-Ion Cells" *J. Phys. Chem. C* **120** (2016) 28463-28471. [DOI: 10.1021/acs.jpcc.6b09837]

8. J. Bareño, I.A. Shkrob, J.A. Gilbert, M. Klett, D.P. Abraham, "Capacity Fade and Its Mitigation in Li-ion Cells with Silicon-Graphite Electrodes", *J. Phys. Chem. C* **121** (2017), pp 20640-20649. [DOI: 10.1021/acs.jpcc.7b06118]

9. C.D. Malliakas, K. Leung, K.Z. Pupek, I.A. Shkrob, D.P. Abraham, "Spontaneous aggregation of lithium ion coordination polymers in fluorinated electrolytes for high-voltage batteries", *Phys. Chem. Chem. Phys.* **18** (2016) 10846-10849.

10. I.A. Shkrob, K.Z. Pupek, D.P. Abraham, "Allotropic Control: How Certain Fluorinated Carbonate Electrolytes Protect Aluminum Current Collectors by Promoting the Formation of Insoluble Coordination Polymers", *J. Phys. Chem. C* **120** (2016) 18435–18444.

11. J. Zheng, P. Yan, D. Mei, M.H. Engelhard, S.S. Cartmell, B.J. Polzin, C. Wang, J. Zhang, W. Xu "Highly Stable Operation of Lithium Metal Batteries Enabled by the Formation of a Transient High-Concentration Electrolyte Layer" *Adv. Energy Mater.* **6** (2016) 1502151 [DOI: 10.1002/aenm.201502151]

## References

1. Han et al., "Understanding the Role of Temperature and Cathode Composition on Interface and Bulk: Optimizing Aluminum Oxide Coatings for Li-Ion Cathodes", *ACS Applied Materials and Interfaces*, 2017, 9 (17), 14769-14778

## II.G.2 Materials Benchmarking Activities for CAMP Facility (ANL)

**Wenquan Lu, Principal Investigator**
Argonne National Laboratory
9700 S. Cass Avenue
Lemont, IL 60439
Phone: 630-252-3704
E-mail: luw@anl.gov

**Peter Faguy, Technology Manager**
U.S. Department of Energy
Phone: 202-586-1022
E-mail: Peter.Faguy@ee.doe.gov

Start Date: October 1, 2014 End Date: September 30, 2018
Total Project Cost: $400,000 DOE share: $400,000 Non-DOE share: $0

### Project Introduction

High energy density electrode materials are required in order to achieve the 40-mile all electric range within the weight and volume constraints established by DOE and the USABC. One would need a combination of anode and cathode materials that provide 420mAh/g and 220mAh/g, respectively, as predicted by Argonne's battery design model (BatPac), if one uses a 20% margin for energy fade over the life of the battery assuming an average cell voltage of 3.6 volts. Therefore, the search for new high energy density materials is the focus of this material benchmarking project. In addition to electrode materials, other cell components, such as separators, binders, current collectors, etc., are evaluated to establish their impact on electrochemical performance, thermal abuse, and cost.

This benchmarking effort is conducted as part of the Cell Analysis, Modeling, and Prototyping (CAMP) Facility (Refer to IV.B.1) to identify and support promising new materials and components across the "valley of death", which happens when pushing a new discovery towards a commercial product. The CAMP Facility is appropriately sized to enable the design, fabrication, and characterization of high-quality prototype cells, which can enable a realistic and consistent evaluation of candidate chemistries in a time-effective manner.

However, the CAMP Facility is more than an arrangement of equipment, it is an integrated team effort designed to support the production of prototypes electrodes and cells. In order to utilize the facility more efficiently and economically, cell chemistries are validated internally using coin type cells to determine if they warrant further consideration.

### Objectives

- The primary objective is to identify and evaluate low-cost materials and cell chemistries that can simultaneously meet the life, performance, and abuse tolerance goals for batteries used in PHEV and EV applications.
- A secondary objective is to enhance the understanding of the impact of advanced cell components and their processing on the electrochemical performance and safety of lithium-ion batteries.
- To support the CAMP Facility for prototyping cell and electrode library development, also the MERF facility for material scale up.

## Approach

Under materials benchmarking activities, we constantly reach out to material developers to seek opportunities to test their advanced or newly released products. By leveraging ANL's expertise in electrode design and cell testing, we can provide not only a subjective third opinion to material suppliers, but also deeper understanding on their materials, which can aid their material development. This deep understanding becomes even more important when the material developers are small companies or new players, who often overlook overall requirements of battery materials.

In addition to industrial partners, we also work closely with scientists from various research institute, such as universities and research laboratories. They often come up with novel materials with advanced electrochemical performance, but small quantities, which is only enough for validation purpose. These test results help us to determine how much effort should be expanded to explore the material potential.

For any potential cell material, which has impact on the cell performance, we validate its performance, mainly in terms of electrochemical performance, electrode optimization, and thermal stability. The electrochemical performance is the centerpiece of the materials benchmarking activities, which will be tested using 2032 coin type cells under test protocol derived from USABC PHEV 40 requirements [Battery Test Manual For Plug-In Hybrid Electric Vehicles, Idaho National Laboratory]. In general, three formation cycles are tested at a C/10 rate. After the formation cycles, the cells are then tested for the rate performance. For the rate test, the charging rate is set at C/5, while the discharge rate varies from C/5, C/3, C/2, 1C to 2C. Three cycles are performed for each discharge rate. After the rate test, the cells then undergo cycling test at C/3 rate. During the cycling test, we change the current rate to C/10 every $10^{th}$ cycle to check the rate effect. Also, Hybrid Pulse Power Characterization (HPPC) is conducted every $10^{th}$ cycle. Area Specific Impedance (ASI) can be calculated from HPPC test.

This fiscal year, electrochemical characterization of nickel-rich high energy cathode materials were carried out. Two $LiNi_{0.5}Mn_{0.3}Co_{0.2}O_2$ (NMC532) materials were received from Guizhou ZhenHua E-Chem Co. LTD. Those two NMC532 possess difference morphologies, whose effect on electrochemical performance was investigated.

Furthermore, we studied coating effect on NMC532. It has been well reported that $Al_2O_3$ coating will generally improve the electrochemical performance of cathode materials. In this work, we studied $Al_2O_3$ coated NMC532 using two different coating approaches, wet method and atomic layer deposition (ALD). The $Al_2O_3$ coated NMC532 using wet method is presented in this work. The test results for $Al_2O_3$ coated NMC532 using ALD method can be seen in the previous section: IV.B.1.

Continued from previous year's work on conductive additive, we investigated Carbon Nano Tube (CNT) as an additive. Other cell components, such as silicon and metal alloy materials, electrolytes and additives, separators, binders, etc. have also been investigated. These test results have been shared with material providers, but not included in this report.

## Results

### *Nickel-Rich High Energy Cathode Materials (NMC)*

Nickel-rich $LiNi_xMn_yCo_zO_2$ (NMC) is gaining momentum as high energy cathode materials for electric vehicle applications. NMC532 is penetrating the market due to its balance of good electrochemical performance, low cost, and reasonable thermal safety. Compared to $LiCoO_2$, NMC particles consist of small primary particles, which tend to separate from each other during cycling. Meanwhile, the secondary particles have less mechanical strength, which can results in particle cracks during the calendering process.

We received two different commercial available NMC532 samples with different morphologies from Guizhou ZhenHua E-Chem Co. LTD. SEM images were taken for these two NMC532 samples (S1 and S2) and are shown in Figure II-433. As you can see from Figure II-433, sample 1 is a typical secondary NMC particle

consisting of small primary particles with voids between primary particles. As for sample 2, the primary particle is larger than that of sample 1. In addition, the primary particle of sample 2 appears to be very smooth.

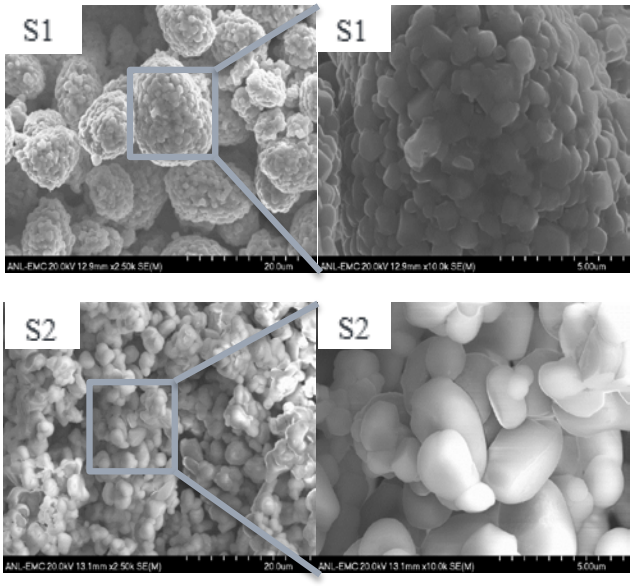


Figure II-433. SEM images of NMC523 sample 1 (S1) and sample 2 (S2). The right two figures are enlarged views of S1 and S2

These two cathode materials were made into laminates with 90 wt.% active material, 5 wt. % PVDF binder and 5 wt.% carbon black. The 2032 coin type cells were fabricated and electrochemically tested between 3.0 V and 4.5 V. The voltage profiles of half cells (vs. lithium metal) of these two samples during the third formation cycle are shown in Figure II-434. The similar voltage profiles suggest that these two NMC532 materials have almost the same chemistry. However, less capacity was obtained from samples 2, which can be attributed to the larger over-potential resulting from the larger primary particle size of sample 2.

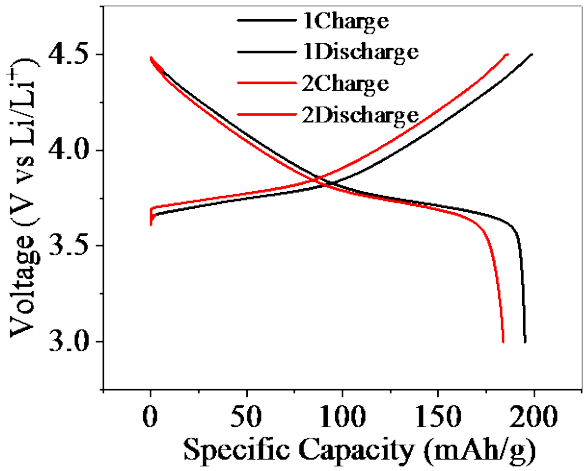


Figure II-434. Voltage profiles of NMC532: sample 1 (black) and sample 2 (red)

After 3 formation cycles and 15 rate cycles, the half cells were cycled under C/3 rate for 50 cycles. The specific capacity as a function of cycle number is shown in Figure II-435 for a total of 68 cycles. Clearly, the specific capacity of sample 2 is less than that of sample 1. However, better capacity retention was obtained for sample 2.

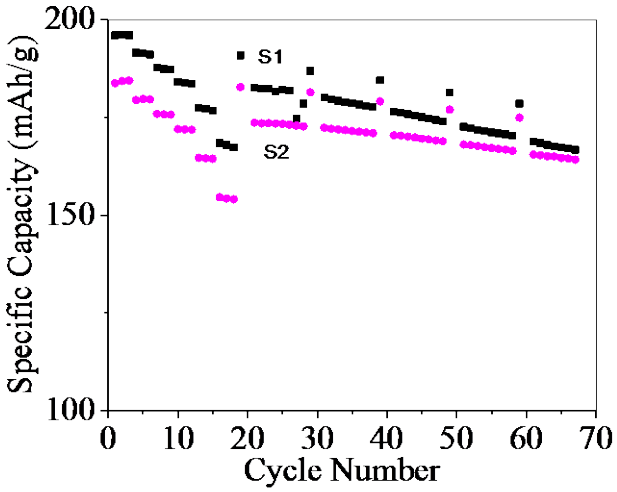


Figure II-435. Specific capacity as a function cycle number: sample 1 (black) and sample 2 (red)

*Coating Effect on NMC Cathode Material*

Surface modification on cathode materials is generally considered an effective approach to prevent the parasitic reaction between the active material and electrolyte, especially when high voltage is applied on the cathode to improve the energy density of LIBs. However, the coating effect is sensitive to the chemistries of transition metal oxides. Previous studies show various coating effects, especially when the coating is applied to NMC cathode materials. At Argonne, a wet coating process was developed, which can mitigate the process effect on transition metal oxides.

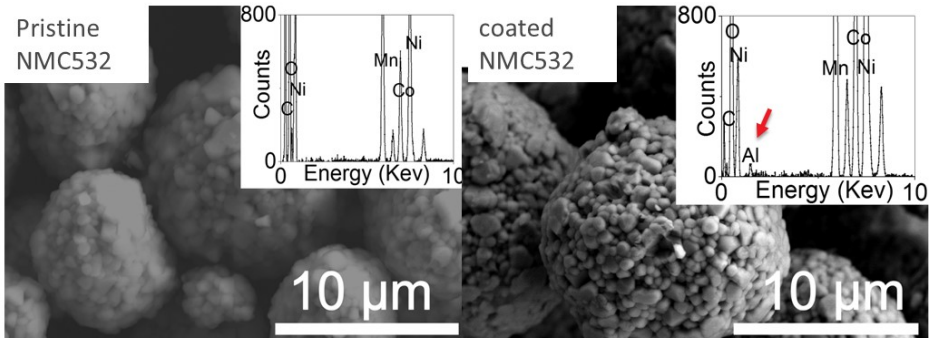


Figure II-436. SEM image of pristine NMC532 (left) and coated NMC532 (right). The insets are the EDS for two particle.

In this work, as low as 0.5% $Al_2O_3$ was coated on NMC532 (Toda, Japan). SEM images for both pristine and coated NMC532 powders are shown in Figure II-436. There is no clear morphology change observed between the pristine and 0.5 % $Al_2O_3$ NMC532. Also, a small aluminum signal was observed from EDS results, which suggests that $Al_2O_3$ was coated on the NMC532 particles.

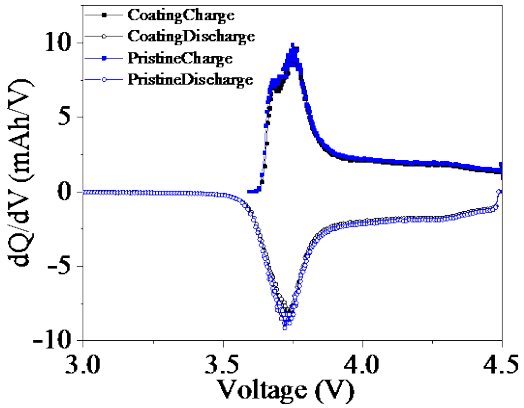


Figure II-437. Differential capacity plots of pristine (black) and coated (blue) NMC532.

Similar to the above electrochemical characterization experiment, the pristine and coated NMC532 powders were made into laminates and the 2032 coin type cells were fabricated and electrochemically tested. Figure II-437 shows the differential capacity plot of the NMC532 with and without coating. No difference in redox reaction for these two materials was obtained, indicating no chemical and structural change after coating.

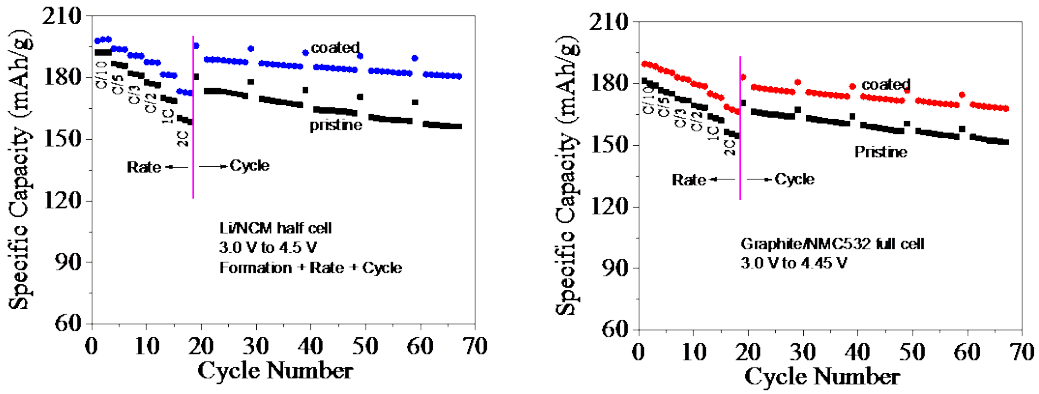


Figure II-438. Specific capacity of NMC532 versus cycle number for half cell (left) and full cell (right)

Figure II-438 shows the specific capacity of pristine and coated NMC532 as a function cycles in both half cells (left) and full cells (right). The cycle numbers include a total of 3 formation, 15 rate test, and 50 life cycles. Surprisingly, as high as 199 mAh/g specific capacity was observed for coated NMC532 from the half cell test, which is higher than 192 mAh/g of pristine NMC532 according to 3rd formation cycle. Furthermore, the capacity retention in half cells is also improved for coated NMC532 from 93% to 96% between cycle number 67 and 21. Similarly, the higher specific capacity and better capacity retention were also obtained from the graphite/NMC532 full cells.

The better performance of coated NMC532 could be attributed the lower impedance of coated NMC532 electrode as shown in Figure II-439. Figure 7 shows the ASI change of pristine (left) and coated (right) NMC532. Firstly, ASI values of pristine NMC532 increase with cycles. However, the ASI increase is very minor for coated NMC532. Secondly, the ASI value of the full cell with coated NMC532 is lower. $Al_2O_3$ coating is generally considered an insulating material. The lower impedance for the cells with coated NMC532 can be attributed to the better ionic conductivity. This improved ionic conductivity was also observed for $Al_2O_3$ coated separator due to its better wettability. Another possibility is that the coating on NMC532 could prevent the side reaction between cathode material and electrolyte, leading to less transition metal dissolution and solid electrolyte interphase (SEI) formation.

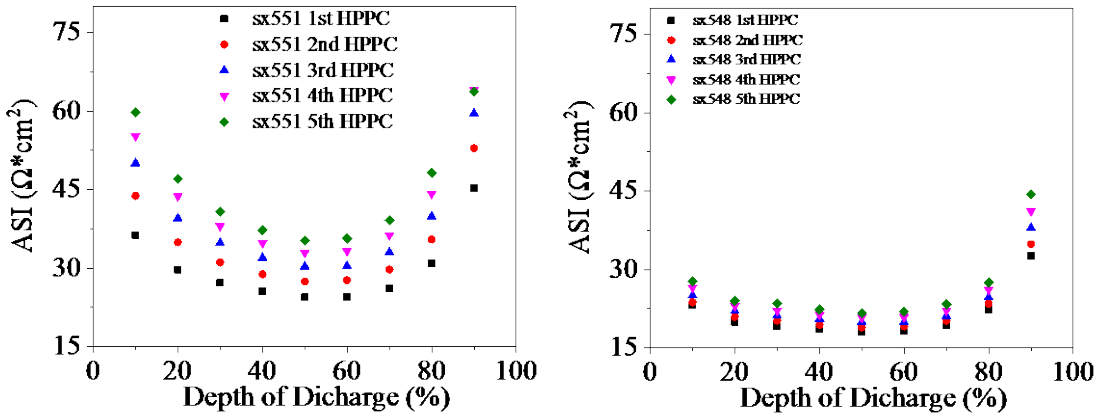


Figure II-439. ASI of full cells with pristine (left) and coated (right) NMC532

## Conclusions

In this fiscal year, materials benchmarking activities focus on high energy nickel-rich nickel manganese cobalt oxide cathode materials. The morphology effect on the electrochemical performance was observed. Also, improved high voltage performance was obtained for wet-coated NMC532.

In the future, we will continue to work on the high energy nickel rich cathode materials. We will also work on high capacity anode materials, such as silicon and other metal alloys. We will continue to work closely with research institutions and industrial suppliers to enable the LIB technology for EV applications.

## Key Publications

1. Mechanisms for lithium nucleation and dendrite growth in selected carbon allotropes, Su, Xin; Dogan, Fulya; Ilavsky, Jan; Maroni, Victor; Gosztola, David; Lu, Wenquan, Chem. Mater., 2017, 29, 6205-6213.

2. High-Performance high-loading Lithium-sulfur Batteries by low temperature atomic layer deposition of aluminum oxide on nanophase S cathode, Xiangbo Meng, Yuzi Liu, Yanqiang Cao, Yang Ren, Wenquan Lu and Jeffery W. Elam, Adv. Mater. Interfaces, 2017, 1700096

3. Nonlinear conductivities and electrochemical performances of $LiNi_{0.5}Co_{0.2}Mn_{0.3}O_2$ electrodes utilizing novel carbon nanoparticles, Xin Su, Seonbaek Ha, Manar B. Ishwait, Hanwei Lei, Miki Oljaca, Berislav Blizanac, Dennis Dees, Wenquan Lu, J. Electrochem. Soc., 163 (13) A2720-A2724 (2016).

4. Optimization of Inactive Material Content in Lithium Iron Phosphate Electrodes for High Power Applications, Seonbaek Ha, Vijay K. Ramani, Wenquan Lu, Jai Prakash, Electrochimica Acta, 191 (2016), 173-182.

5. High rate lithium ion battery development, Wenquan Lu, Xin Su, Andrew Jansen, and Dennis Dees, 34th International Battery Seminar and Exhibit - (Fort Lauderdale, FL, US, 03/20/17-03/23/17)

6. The energy and power density of $LiNi_{0.5}Co_{0.2}Mn_{0.3}O_2$ electrodes promoted by optimizing the carbon additive, Xin Su, Seonbaek Ha, Manar Ishwait, Dennis Dees, and Wenquan Lu, 2017 Gordon Research Conference on Nanomaterials for Applications in Energy Technology, Ventura, CA, US, 02/26/17-03/03/17

7. $Li_5FeO_4$ Li Source Additive: Fixing Irreversibility in LIBs, Chi-Kai Lin, Xin Su, Wenquan Lu, Xiaoping Wang, and Christopher S. Johnson, 230th Electrochemical Society Meeting, October 2-7, 2016, Honolulu, HI

## II.G.3 Post-test Analysis of Lithium-Ion Battery Materials (ANL, ORNL, SNL)

**Ira Bloom, Principal Investigator**
Argonne National Laboratory
9700 South Cass Avenue
Argonne, IL 60439
Phone: 630-252-4516
E-mail: ira.bloom@anl.gov

**David L. Wood III, Principal Investigator**
Oak Ridge National Laboratory
P.O. Box 2008
Oak Ridge, TN 37831
Phone: 865-574-1175
E-mail: wooddl@ornl.gov

**Kyle R. Fenton, Principal Investigator**
Sandia National Laboratories
P.O. Box 5800
Albuquerque, NM 87185
Phone: 505-284-3377
E-mail: krfento@sandia.gov

**Peter Faguy, Technology Manager**
U.S. Department of Energy
Phone: 202-586-1022
E-mail: Peter.Faguy@ee.doe.gov

Start Date: October 1, 2015 End Date: September 30, 2018
Total Project Cost: $3,375,000 DOE share: $3,375,000 Non-DOE share: $0

### Project Introduction

Battery technologies are routinely characterized by measuring the initial electrochemical performance and how it changes with age and use. These characterization methods and tests provide valuable information, from which degradation mechanisms can be inferred by modeling or curve fitting. However, these results do not have the benefit of direct, experimental observation of the underlying causes of the change in electrochemical behavior. There is much still left to be learned by the systematic investigation of the effects of manufacturing variables on the materials changes in the cell responsible for aging. Because of the serious hazardous consequences of overcharge, particularly in modular systems where failure can propagate from cell to cell, understanding the physical and chemical changes of overcharging the cell is extremely important for the development of safe batteries that can be used in an EV. With a materials level understanding of these changes, the abuse response may be mitigated by the development of new strategies that may lead to mass-produced, long-lived cells with minimal abuse response. Additionally, this information would be valuable in confirming that the mechanistic hypotheses employed to develop these strategies corresponds to the actual aging processes at operation.

With this information, battery developers may be able to improve the life and performance of batteries. Improved performance and life would be important to accelerate consumer acceptance of electrified vehicles. In turn, with more electrified vehicles on US roads, electricity generated from both renewable and domestic fossil fuel sources would lessen the importance of imported oil as a source of energy for transportation, contributing to the nation's energy independence. Additionally, a decrease in air pollution due to automobile exhaust would be a direct result.

## Objectives

- The main objective of this project is to understand the materials-level effects of overcharging and overheating on the chemistry and physical properties of the cell components in small (~1.5 Ah) lithium-ion cells.
- Other objectives include characterizing the impact of electrode processing conditions on the performance and abuse response of lithium-ion cells.

## Approach

Cell components harvested from abuse-tested cells will be characterized to determine the changes produced by differences in cell chemistry and processing variables. The characterization data will be compared to pristine materials to help delineate changes. The materials will be characterized, at first, by many techniques to determine which ones yield data that responds to the given perturbation of the system. Those techniques will then be the first ones used thereafter to track changes. The techniques available include EIS, SEM, XPS, XRD, NMR, Raman, FT-IR and HPLC methods.

## Results

*Effect of binder on overcharge response*

Argonne, ORNL, and SNL are collaborating to understand the physical and chemical changes on and in the electrodes that occur during cell abuse. Characterization of cells after overcharging would be very useful from the safety view point. The information gained may help mitigate the consequences of overcharge by telling us the nature of the SEI, how it changes during overcharge, and, possibly, how to increase its robustness. Two sets of 1.5-Ah pouch cells, which contained NMC532/graphite chemistry, were fabricated at ORNL. PVDF (NMP-processed) was the binder in one set of cells; and CMC (aqueous processed), in the other. After formation, the cells were sent to SNL for overcharging. The cells were charged to 100, 120, 140, 160, 180 and failure (250 and 270% SOC). Argonne then characterized the abused cells after they were discharged to 3.0 V.

Figure II-440 shows images of the two sets of cells upon disassembly in an argon-atmosphere glove box.

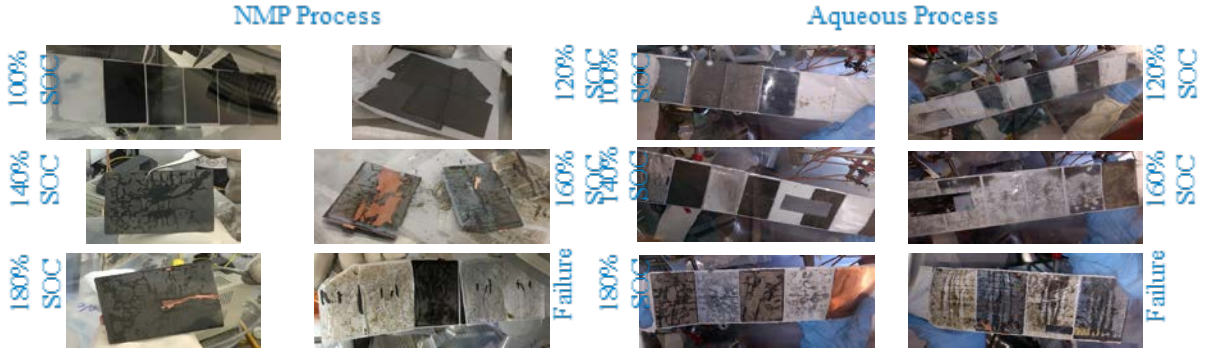


Figure II-440. Images of the anodes from the overcharged cells. The rectangular-shaped voids in some of the images are from sampling for microscopy.

In the SOC range of 140 to 180%, there was more damage to the anode laminate in the NMP-processed cells than in the aqueous-process ones. There was clearly a loss of adhesion of the active material to the copper foil.

Elemental analyses, given in Figure II-441 and Figure II-442 for NMP- and aqueous-processed electrodes, respectively, show the trends in transition metals and phosphorus from anode materials. The concentration of the transition metals increase with increasing %SOC, but stay in the original stoichiometric ratio, 5:3:2. Comparing the values given in Figure II-441 to those in Figure II-442 shows that the concentrations of the elements depends on the binder and processing conditions. At SOCs greater than 160%, the concentrations are greater in the electrodes processed using NMP than those processed using aqueous binders.

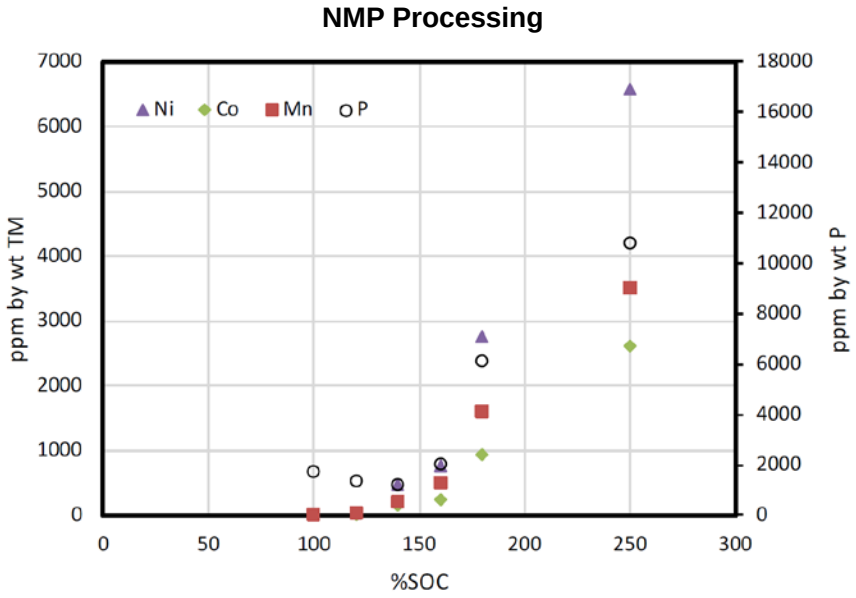


Figure II-441. Concentration of metals and phosphorus vs. %SOC for NMP-processed electrodes.

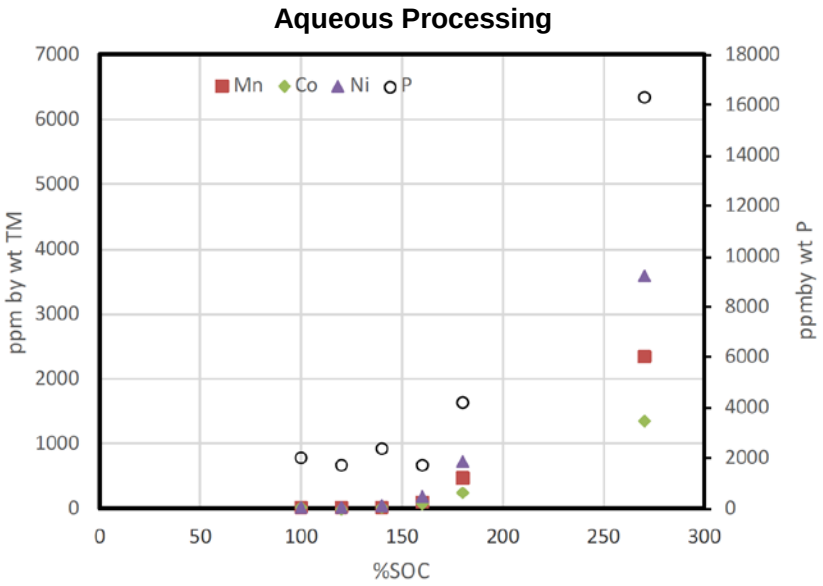


Figure II-442. Concentration of metals and phosphorus vs. %SOC for aqueous-processed electrodes.

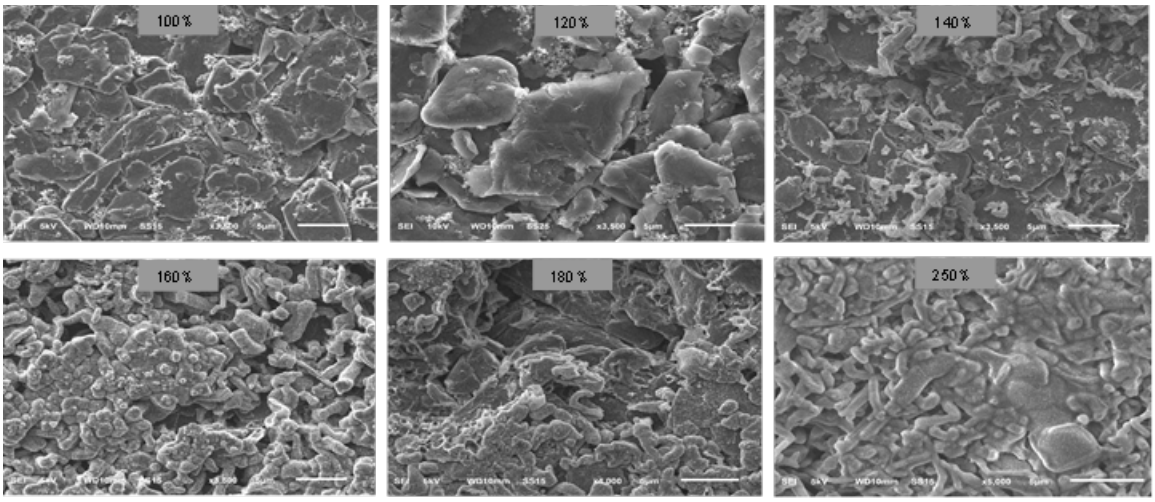


Figure II-443. SEM images of the surface of anodes from overcharged cells, NMP processing. The numbers shown in the grey boxes indicate the %SOC that the cell experienced during the overcharge experiment.

Other trends are seen on the surface, for example, of overcharged anodes. Figure II-443 and Figure II-444 show images of the surfaces of overcharged anodes from NMP and aqueous process, respectively. As seen from the figures, the surfaces of the electrodes changes in %SOC and with the binder/processing used. Examining the surfaces shows, for example, that the concentration of dendrite-like structures tends to increase with SOC. Additionally, the formation of dendrite-like structures is more severe and occurs at lower SOC in the NMP processed anodes than those from aqueous processing.

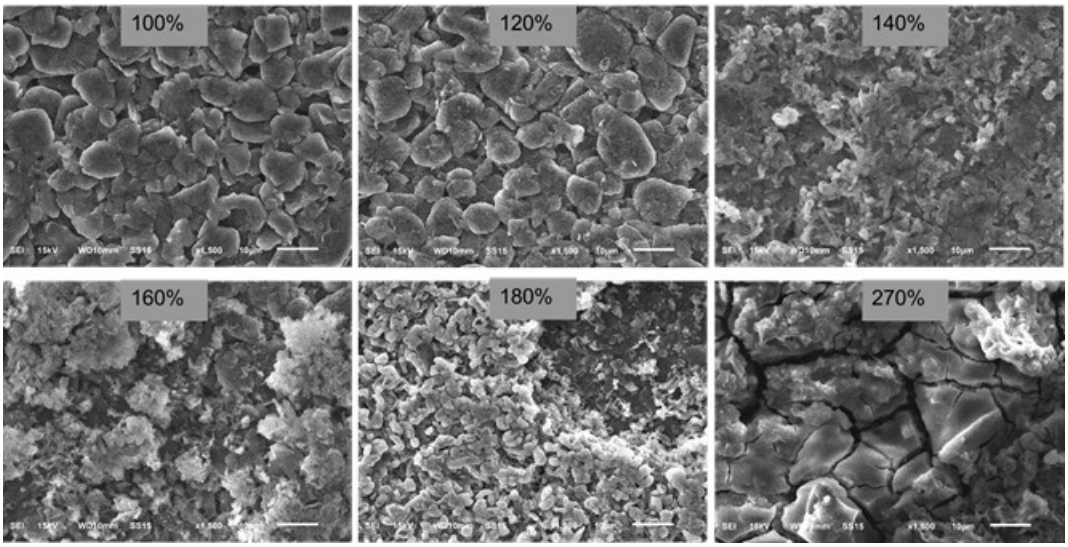


Figure II-444. SEM images of the surface of anodes from overcharged cells, aqueous processing. The numbers shown in the grey boxes indicate the %SOC that the cell experienced during the overcharge experiment.

In the XPS results from the anode, many SOC- and processing-dependent trends were seen. For example, Figure II-445 shows the Li1s region of two overcharged anodes. In the SOC range of 100 to 180%, the quantity of $Li_2O$-like material tends to increase with SOC. There was more $Li_2O$-like material on the anode surface in the NMP-processed example than on that in the aqueous-processed one. It is possible that this material influenced the morphology of the dendrite-like materials seen in Figure II-443 and Figure II-444. Similar trends were seen in the 3d binding-energy regions for the respective transition metals.

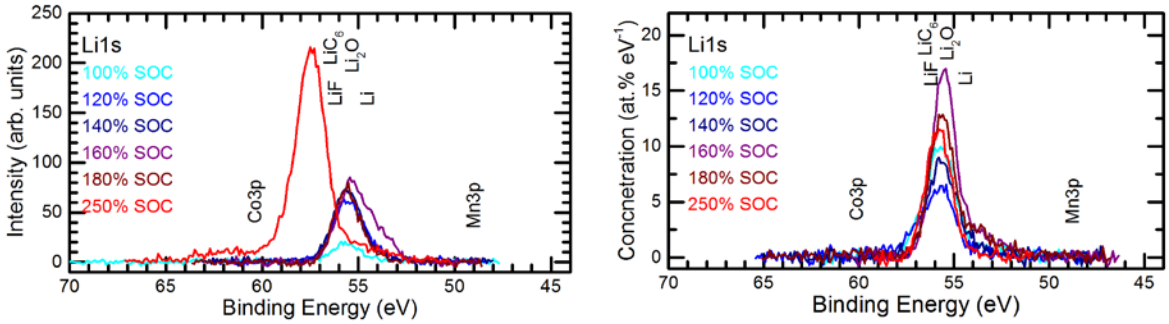


Figure II-445. XPS results from two anode materials (right) image from the NMP-processed material (left) image from the aqueous processed material.

On the cathode side of the cell, significant differences in the XPS spectra were seen. For example, in the O1s binding energy region, as shown in Figure II-446 a and 7b, the strength of the signal in the metal oxide ($MO_x$) region decreases markedly when the binder was changed from PVDF to CMC. This indicates that the film on the cathode surface is thinner on the latter than on the former.

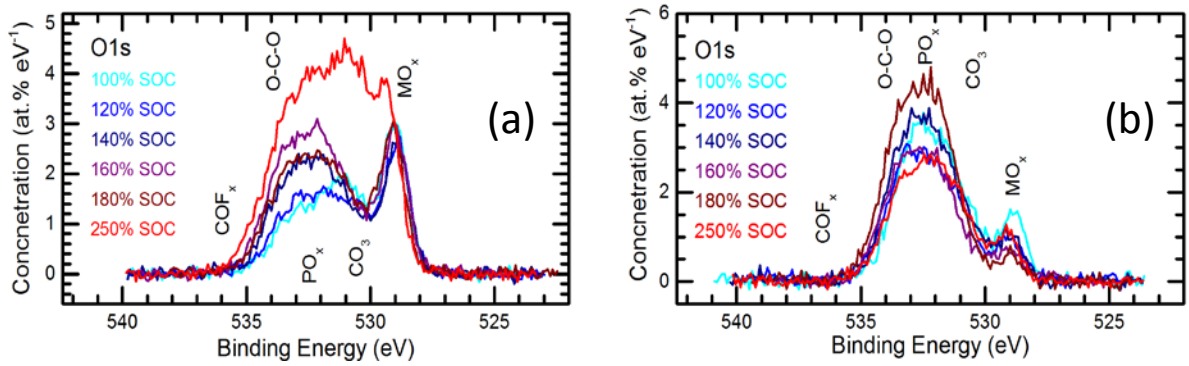


Figure II-446. (a) Concentration vs. binding energy in the O1s energy region from the NMP-processed cathodes. (b) Concentration vs. binding energy in the O1s energy region from the aqueous-processed cathodes.

In the F1s binding energy region of the spectrum, other changes were seen which correlated with the binder. From Figure II-447a and Figure II-447b, NMP- and aqueous-processed, respectively, there is a shift to higher binding energy when the binder was changed from PVDF to CMC. Here, the fluorine changed from being bound to a molecule similar to $Li_xPF_y$ to being in a compound analogous to $LiPF_6$. No other significant changes were seen in the XPS data from the cathode.

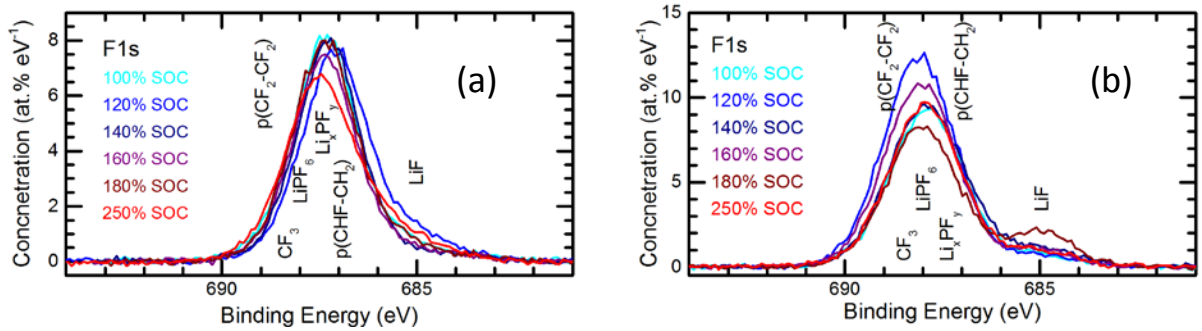


Figure II-447. (a) Concentration vs. binding energy in the F1s energy region from the NMP-processed cathodes. (b) Concentration vs. binding energy in the F1s energy region from the aqueous-processed cathodes.

## Conclusions

The binder/processing conditions play an important role in the abuse response of the NMC532/graphite cells. The binder alters the rate of, presumably, transition metal dissolution and transport to the anode. The concentrations of transition metals and phosphorus depend not only on SOC but also on the binder. The morphology and, perhaps, concentration of species on the surface of the electrodes also depend on it.

## Key Publications

1. XPS Characterization of Overcharged NMC and LFP Lithium Ion Cells. J. Bareño, N. Dietz Rago, Z. Du, Y. Sheng, J. Li, L.A. Steele, J. Lamb, S. Spangler, C. Grosso, D.L. Wood III, K. Fenton, and I. Bloom, Poster presented at the 10th International Conference on Advanced Lithium Batteries for Automobile Applications, Oakbrook, IL USA, October 22 - 25, 2017.

2. Effect of overcharge on lithium-ion cells containing $Li(Ni_{0.5}Mn_{0.3}Co_{0.2})O_2$ cathodes: NMP-soluble binder. I. Microstructural changes in the anode. N. Dietz-Rago, J. Bareño, J. Li, Z. Du, D. Wood, L. A. Steele, J. Lamb, et al., Journal of Power Sources (forthcoming).

3. Effect of overcharge on lithium-ion cells containing $Li(Ni_{0.5}Mn_{0.3}Co_{0.2})O_2$ cathodes: NMP-soluble binder. II — Chemical changes in the anode. I. Bloom, J. Bareño, N. Dietz-Rago, F. Dogan, D. Graczyk, Y. Tsai, S. Naik, et al., Journal of Power Sources (forthcoming).

4. Effect of overcharge on NMP-processed $Li(Ni_{0.5}Mn_{0.3}Co_{0.2})O_2$ / Graphite lithium ion cells with PVDF binder. II — Chemical changes in the cathode. J. Bareño, Nancy Dietz-Rago, F. Dogan-Key, D. Graczyk, Y. Tsai, S.Naik, S.-D. Han, et al., Journal of Power Sources (forthcoming).